



HAL
open science

Modeling gas-driven microstructural evolution in ODS-EUROFER steel by high dose helium and hydrogen ion implantation

Olga Emelianova

► **To cite this version:**

Olga Emelianova. Modeling gas-driven microstructural evolution in ODS-EUROFER steel by high dose helium and hydrogen ion implantation. Condensed Matter [cond-mat]. Université Paris-Saclay; National Research Nuclear University MEPhI (Moscou), 2020. English. NNT : 2020UPASP056 . tel-03510386

HAL Id: tel-03510386

<https://theses.hal.science/tel-03510386v1>

Submitted on 4 Jan 2022

HAL is a multi-disciplinary open access archive for the deposit and dissemination of scientific research documents, whether they are published or not. The documents may come from teaching and research institutions in France or abroad, or from public or private research centers.

L'archive ouverte pluridisciplinaire **HAL**, est destinée au dépôt et à la diffusion de documents scientifiques de niveau recherche, publiés ou non, émanant des établissements d'enseignement et de recherche français ou étrangers, des laboratoires publics ou privés.

Modeling gas-driven microstructural evolution in ODS-EUROFER steel by high dose helium and hydrogen ion implantation

**Thèse de doctorat de l'université Paris-Saclay
et National Research Nuclear University MEPhI**

École doctorale n° 576, Particules, Hadrons, Énergie, Noyau
Instrumentation, Imagerie, Cosmos et Simulation (PHENIICS)

Spécialité de doctorat : Énergie nucléaire

Unité de recherche : Université Paris-Saclay, CNRS, IJCLab, 91405, Orsay, France

Référent : Faculté des sciences d'Orsay

**Thèse présentée et soutenue en visioconférence totale, le
27/11/2020, par**

Olga EMELIANOVA

Composition du Jury

Frederico GARRIDO

Professeur, Université Paris-Saclay

Président

Marie-Laure DAVID

MdC HDR, Université de Poitiers

Rapporteur & Examinatrice

Robin SCHAEUBLIN

Professeur, ETH Zurich, Suisse

Rapporteur & Examineur

Michael P. SHORT

Professeur associé, MIT, États-Unis

Examineur

Pavel VLADIMIROV

Chercheur, KIT, Allemagne

Examineur

Aurélien GENTILS

CR CNRS, IJCLab

Directrice de thèse

Maria GANCHENKOVA

Professeur associé, NRNU MEPhI, Russie

Co-directrice de thèse

Vladimir BORODIN

Professeur, NRNU MEPhI, NRC KI, Russie

Co-directeur de thèse

Joël RIBIS

Chercheur, CEA Saclay

Invité

“I am among those who think that science has great beauty”

Marie Curie

ACKNOWLEDGEMENTS

First and foremost, I would like to thank my supervisors (thesis directors) Dr. Aurélie Gentils, Dr. Maria Ganchenkova and Dr. Vladimir Borodin for giving me the opportunity to fulfill this thesis project. Their guidance, overall support, constructive criticism, and patience have helped me to pass through the challenges of my research and, I believe, have made me a better scientist. I am grateful that I had supervisors who truly cared about my development, professional and personal growth.

I also want to extend my gratitude to SEMIRAMIS team at the JANNuS-Orsay/SCALP facility (IJCLab, Orsay, France). My thanks go to Dr. Cédric Baumier (IJCLab, Orsay, France), my colleague and friend, for my *in situ* ion beam implantation experience, his help during thousands of my transmission electron microscopy (TEM) sessions, unique tips on TEM operation and personal support; to Cyril Bachelet, Stéphane Renouf, Jérôme Bourçois and Sandrine Picard for the plenty of ion implantations in this project performed even under extreme *ex situ/in situ* ion beam and time-restricted conditions.

Appreciation also goes to David Troadec (IEMN, Lille, France) for the FIB sample preparation via the Renatech network. FIB samples prepared by David Troadec were the best I had ever seen.

Significant contributions to this project and to my overall experience were made by many other researchers and research groups. My special thanks go to Dr. Katia March (UPMC, Paris, France&ASU, Tempe, USA) and Dr. Yuriy Yagodzinsky (Aalto University, Espoo, Finland) for the fruitful collaboration on hydrogen task. Outstanding EELS and TDS results by Dr. March and Dr. Yagodzinsky, respectively, make the project results self-consistent. I deeply appreciate their help with advanced data analysis. I also would like to thank colleagues from IAM-AWP (KIT, Karlsruhe, Germany), Prof. Anton Möslang, Dr. Pavel Vladimirov and Rainer Lindau for the provided industrial materials and for many fruitful discussions prior to implementation of this project. The part of this project devoted to the model bi-layer system would not have been possible without collaborative efforts of our colleagues from NUST MISIS&MIPT (Moscow, Russia) and KFU (Kazan, Russia). My thanks go to Dr. Igor Golovchanskiy (NUST MISIS&MIPT), Dr. Igor Shchetinin (NUST MISIS), Dr. Vasilii Stolyarov (MIPT) and members of laboratory “The physics of magnetic nanostructures and spintronics” of KFU (Kazan, Russia) Amir Gumarov, Igor Yanilkin, Iskander Vakhitov and Prof. Lenar Tagirov for their help with fabrication and initial characterization of model thin film samples. I thank my colleague and friend from NRNU MEPHI Dr. Pavel Dzhumayev for the plenty of SEM investigation included and not included in this thesis, overall support and useful tips on TEM investigations and general material science.

I am confident that our collaborative efforts to understand the light gas effects in ODS alloys for applications in nuclear fusion and accelerator-driven particle sources will make a significant contribution to this research field.

I also acknowledge the defense committee members Prof. Frédérico Garrido (Université Paris-Saclay, France), Dr. Marie-Laure David (Université de Poitiers, France), Prof. Robin Schäublin (ETH Zurich, Switzerland), Dr. Michael P. Short (MIT, USA), Dr. Pavel Vladimirov (KIT, Germany) and Dr. Joël Ribis (CEA Saclay, France).

Thanks also go to Dr. Kirill Prikhodko (NRC KI, Moscow, Russia) and Dr. Michael Klimenkov (KIT, Karlsruhe, Germany) for igniting my passion for electron microscopy.

I would like to extend my gratitude to vice head of Material Science Department Prof. Boris Kalin and to head of Institute of Nuclear Physics and Engineering Dr. Natalya Barbashina of NRNU MEPHI for the personal and organizational support during thesis implementation.

I am also grateful to my teammates and colleagues from IJCLab Dr. Stephanie Jublot-Leclerc, Dr. Martin Owusu-Mensah, Marie-Jose Saleh-Afif, Maximilian Thees and from NRNU MEPHI Dr. Olga Krymskaya, Dr. Alexey Suchkov, Dr. Alexander Ivannikov and Dr. Ivan Fedotov besides offering support they were responsible for creating a good working atmosphere.

Thanks also go to the administrative staff of IJClab including Rejane Bodson, Sonia Martineau and Patricia Duarte for all the help and assistance relating to the administrative issues in the period of study.

I would like to thank the Vernadskiy scholarship program of French Embassy (Université Paris-Sud/Université Paris-Saclay), National Research Nuclear University MEPHI and Université Paris-Sud for the Ph.D. funding received for the duration of the thesis. The work has been carried out within the framework of the French Research Federation for Fusion Studies and EUROfusion consortium, and has received funding from the Euratom research and training program 2014-2018 and 2019-2020 under agreement No. 633053. The views and opinions expressed herein do not necessarily reflect those of the European Commission.

Finally, thanks to my mother, father, grandmother and to my partner Igor Golovchanskiy for their encouragement, patience, and love throughout the years.

Table of contents

TABLE OF CONTENTS	1
INTRODUCTION	5
CHAPTER 1 MATERIALS CHALLENGES OF GENERATION IV FISSION AND FUSION REACTORS AND ACCELERATOR DRIVEN SYSTEMS.....	11
1.1 Introduction	11
1.2 Materials challenges of fission and fusion systems	12
1.3 ODS steels.....	18
1.4 Radiation induced swelling	25
1.4.1 Effects of temperature, dose, and transmutant gases on void swelling	25
1.4.2 Helium effects on swelling.....	28
1.4.2.1 Helium bubble nucleation and growth	28
1.4.2.2 Heterogeneous nucleation of helium cavities and helium management in ODS-steels	34
1.4.2.3. Helium bubble coarsening	38
1.4.3 Hydrogen effects on swelling.....	40
1.4.4 Synergistic influence of helium and hydrogen on swelling.....	44
1.5 Conclusions	49
1.6 References	51
CHAPTER 2 EXPERIMENTAL TECHNIQUES	63
2.1 Materials and Sample Preparation	63
2.1.1 Characterization of industrial materials ODS-EUROFER and EUROFER 97.....	63
2.1.1.1 ODS-EUROFER and EUROFER 97 microstructure and elemental content	63
2.1.1.2 Sample preparation prior to implantation/irradiation.....	67
2.1.1.3 Sample preparation after ion implantation/irradiation	69
2.1.2 Fabrication and microstructural characterization of bi-layer Y ₂ O ₃ /FeCr system	70
2.1.2.1 Fabrication of bi-layer metal/oxide system.....	70
2.1.2.1.1 Substrate preparation	71
2.1.2.1.2 Deposition of the yttrium oxide (Y ₂ O ₃) thin film	72
2.1.2.1.3 Deposition of Fe-10%Cr thin film.....	72
2.1.2.2 Microstructure and elemental content of bi-layer Y ₂ O ₃ /FeCr system.....	73
2.1.2.3 Sample preparation prior to and after implantation/irradiation.....	78
2.2 Ion Implantation/Irradiation.....	79
2.2.1 Experimental setup	79
2.2.1.1 IRMA ion implanter.....	80
2.2.1.2 ARAMIS: a Tandem/Van de Graaff accelerator.....	80
2.2.1.3 Assembling the irradiation stage for <i>ex situ</i> ion implantations	81
2.2.2 Coupling IRMA or/and ARAMIS with TEM	82
2.2.3 Implantation/irradiation conditions	82
2.2.3.1 Dose calculation.....	83
2.2.3.2 Parameters of single-beam He ⁺ ion implantation into ODS-EUROFER and EUROFER 97	84
2.2.3.3 Parameters of <i>in situ</i> heavy ion Au ²⁺ and dual-beam He ⁺ +Au ²⁺ irradiation of ODS-EUROFER	87
2.2.3.4 Parameters of sequential dual-beam He ⁺ +H ⁺ ion implantation of ODS-EUROFER and EUROFER 9788	87

2.2.3.5 Parameters of ion implantation/irradiation of FeCr/Y ₂ O ₃ bi-layer system.....	91
2.3 Characterization techniques	94
2.3.1 X-ray Diffraction (XRD).....	94
2.3.2 Electron microscopy.....	95
2.3.2.1 Electron – matter interactions	96
2.3.2.2 Scanning electron microscopy (SEM)	98
2.3.2.3 Transmission electron microscopy (TEM).....	101
2.3.2.3.1 TEM/STEM operation modes	102
2.3.2.3.2 Bright field, high-angle annular dark field and HRTEM imaging.....	103
2.3.2.3.2.1 Diffraction contrast	103
2.3.2.3.2.2 Mass-thickness contrast	105
2.3.2.3.2.3 Phase contrast.....	105
2.3.2.3.2.4 Bright field imaging	106
2.3.2.3.2.5 Crystallographic structure imaging by HRTEM	106
2.3.2.3.2.6 HAADF imaging.....	109
2.3.2.3.3. Energy Dispersive X-ray spectroscopy (EDX).....	109
2.3.2.3.4 Electron Energy Loss Spectroscopy (EELS).....	111
2.3.2.3.4.1 Principles.....	111
2.3.2.3.4.2 The structure of EEL spectrum	112
2.3.2.3.4.3 EELS acquisition modes	113
2.3.2.3.4.4 Dual EELS	114
2.3.2.3.4.5 Sample thickness measurement by EELS	115
2.3.2.3.4.6 Hydrogen association with cavities by EELS	116
2.3.2.3.5 Void/bubble imaging	116
2.3.3 Thermal desorption spectroscopy.....	122
2.4 References	126

CHAPTER 3 HELIUM EFFECTS ON THE MICROSTRUCTURE EVOLUTION OF ODS-EUROFER STEEL134

3.1 Microstructure development in ODS-EUROFER steel during single-beam He⁺ ion implantation	135
3.1.1 General description of microstructural evolution.....	135
3.1.1.1 Distribution of bubbles vs. implantation depth.....	136
3.1.1.2 Distribution of bubbles over defect types	139
3.1.2 The relative importance of different defect microstructure components for helium accumulation depending on ion implantation conditions (temperature, ion flux, fluence)	141
3.1.2.1 Methodology of statistical analysis of bubble populations visible in TEM micrographs	142
3.1.2.2 Variation of helium bubble parameters as a function of He ⁺ ion implantation fluence	144
3.1.2.3 Variation of helium bubble parameters with He ⁺ ion implantation flux	149
3.1.2.4 Variation of helium bubble parameters with ion implantation temperature.....	153
3.1.2.5 Contributions of bubbles on different microstructural components to the total swelling and helium inventory.....	158
3.1.2.5.1 Methodology of swelling estimation	158
3.1.2.5.2 Fluence dependent variation of contributions from different bubble families to swelling and helium inventory.....	161
3.1.2.5.3 Flux dependence of contributions from different bubble families to swelling and helium inventory	165
3.1.2.5.4 Temperature dependence of contributions from different bubble families to swelling and helium inventory.....	169
3.1.2.5.5 General trends of swelling and helium inventory variations in reply to implantation condition variations	173
3.1.2.6 Swelling and helium inventory in ODS-EUROFER steel after post-implantation annealing.....	175
3.1.2.7 Sensitivity of the obtained data to the uncertainties in input parameters.....	179

3.1.3 The analysis of helium partitioning between bubbles at different microstructural defects and the estimation of cumulative swelling in EUROFER 97 in comparison to ODS-EUROFER	181
3.2 Microstructural evolution of ODS-EUROFER steel during dual-beam He⁺+Au²⁺ irradiation.....	186
3.2.1 Microstructural evolution of helium pre-implanted ODS-EUROFER steel during 4 MeV Au ²⁺ irradiation	186
3.2.2 Microstructural evolution of ODS-EUROFER steel during simultaneous dual-beam He ⁺ +Au ²⁺ irradiation	191
3.2.3 The mechanism of bubble-to-void transition acceleration by oxide nanoparticles	200
3.2.3.1 The basics of bubble-to-void transition theory	200
3.2.3.2 Gas bubble growth on second-phase particles	203
3.2.3.3 Discussion.....	211
3.3 Summary and Discussion.....	214
3.4 References	222
CHAPTER 4 SYNERGETIC EFFECTS OF HELIUM AND HYDROGEN ACCUMULATION ON THE MICROSTRUCTURAL EVOLUTION OF ODS-EUROFER STEEL	225
4.1 Microstructural response of ODS-EUROFER steel to sequential dual-beam He⁺+H⁺ ion implantation ..	227
4.1.1 Microstructural evolution of ODS-EUROFER steel pre-implanted with He ⁺ ions after H ⁺ ion implantation at elevated temperature	227
4.1.2 Microstructural evolution of ODS-EUROFER steel pre-implanted with He ⁺ ions after H ⁺ ion implantation at room temperature	233
4.1.2.1 Combination of room temperature implantation regimes	233
4.1.2.2 Combination of different temperature regimes	239
4.1.3 Conclusions	241
4.2. Uptake and trapping of hydrogen in ODS-EUROFER steel	242
4.2.1 Hydrogen trapping in helium-free ODS-EUROFER and EUROFER 97 steels	242
4.2.2 Hydrogen trapping in helium pre-implanted ODS-EUROFER and EUROFER 97 steels	244
4.2.2.1 Hydrogen trapping in ODS-EUROFER and EUROFER 97 steels pre-implanted with He ⁺ ions at room temperature	244
4.2.2.2 Hydrogen trapping in ODS-EUROFER steel pre-implanted with He ⁺ ions at 823 K.....	246
4.2.2.3 Activation analysis.....	248
4.2.2.4 Tentative identification of hydrogen traps	251
4.2.2.4.1 Hydrogen trapping mechanisms associated with peaks 1.1-1.3 at ~435-535 K (reversible traps)	252
4.2.2.4.2 Hydrogen trapping mechanisms associated with peaks 2 and 3 at ~610-800 K (irreversible traps)	253
4.2.2.4.3 Hydrogen trapping mechanisms associated with peak 4 at ~1000 K (irreversible traps)	254
4.2.3 Conclusions	255
4.3 Electron energy loss spectroscopy investigation of hydrogen association with helium bubbles in ODS-EUROFER steel.....	256
4.3.1 Analysis of raw EELS-SI data.....	256
4.3.2 Data processing using spectral difference method	262
4.3.3 Discussion and conclusions.....	273
4.4 Summary and discussion.....	276
4.4.1 The effects of helium and hydrogen interplay observed in the sequential dual-beam He ⁺ +H ⁺ ion implantations	276
4.4.2 The impact of results on the interpretation of triple-beam experiments used for modelling fusion and spallation environment	278
4.5 References	283

CHAPTER 5 ACCUMULATION OF HELIUM AND HYDROGEN IN A MODEL BI-LAYER $Y_2O_3/FeCr$ SYSTEM	289
5.1 Microstructural development in bi-layer $Y_2O_3/FeCr$ system after single-beam He^+ ion implantation at room and elevated temperature	291
5.1.1 He^+ ion implantation at room temperature	291
5.1.2 He^+ ion implantation at 823 K.....	293
5.2 Microstructural development in bi-layer $Y_2O_3/FeCr$ system after single-beam H^+ ion implantation at room temperature.....	295
5.3 Microstructural development in bi-layer $Y_2O_3/FeCr$ system after sequential dual-beam implantation with He^+ and H^+ ions at room temperature.....	297
5.4 Microstructural development in bi-layer $Y_2O_3/FeCr$ system after Kr^+ irradiation at room temperature	301
5.5 Discussion	302
5.5.1 Irradiation with heavy (Kr^+) ions	303
5.5.2 The effects of light gases on the microstructural development in the implanted bi-layer systems	304
5.5.2.1 Helium partitioning between oxide, matrix and interface.....	304
5.5.2.2 Hydrogen partitioning between oxide, matrix and interface.....	309
5.5.2.3 Possible synergism of helium and hydrogen influence on the implantation-induced damage in the oxide, metal matrix and at the interface.....	310
5.6 Summary	310
5.7 References	312
CONCLUSIONS AND FUTURE WORK.....	315
ANNEX I. LIST OF FIGURES	318
ANNEX II. LIST OF TABLES	330
ANNEX III. LIST OF ABBREVIATIONS	333
ANNEX IV. RÉSUMÉ DÉTAILLÉ EN FRANÇAIS	335
ANNEX V. DETAILED SUMMARY IN ENGLISH.....	351
ANNEX VI. SCIENTIFIC COMMUNICATIONS	366

Introduction

The challenges of meeting rapidly growing demand for energy have renewed a worldwide interest in advanced power energy plants, while the need for new clean sources of energy provides strong support to the quest for next generation energy devices. Given the advantages of high efficiency and fewer limitations from environmental impact, advanced Generation IV fission, fusion and accelerator driven systems (ADS) have a great potential to become an important part of current and future non-carbon energy sources with continuous mode of energy generation [1–4]. Advanced fission and fusion facilities service conditions are characterized by high temperatures ~550-1000°C, intense neutron radiation fields ~5-30 dpa/fpy (displacement damage per atom per full power year) and utilization of chemically aggressive coolants. The existing experience with structural materials in current light water reactors (LWRs) that operate at temperatures ~300 °C and displacement damage levels for core internal structures of 7-70 dpa for forty-years operating time [5,6] is insufficient to recommend similar materials for the above-mentioned heavy-duty operation conditions. The safety, reliability, and efficiency of new facilities will ultimately depend on developing new high-performance structural materials that can provide extended service under extremely hostile operation conditions.

The primary candidate structural materials for the forthcoming fission and fusion facilities are ferritic-martensitic steels [7–11]. However, some designs are expected to operate at temperatures well above the limit (~550°C) of reliable performance of these steels. According to modern views, one of the keys to improve properties of multifunctional steels is strengthening by very high density of ultrafine oxide nanoparticles [12–17]. Oxide strengthening eliminates the most serious drawback of otherwise very good ferritic-martensitic steel grades (such as EUROFER) – the insufficient creep ductility resistance at high temperatures. This makes oxide dispersion strengthened (ODS) steels especially attractive for forthcoming advanced energy facilities. The high density of nano-oxide particles dispersed in the steel matrix not only improves its mechanical properties for high-temperature applications, but also adds to its radiation stability [12–17]. In spite of intensive international research on ODS steels in the last decade, many fundamental questions concerning the nano-oxides usage for the improvement of steel properties remain under debate. An important issue is the relative role in material microstructure development played by nano-oxides in complex irradiation environments where intensive displacement damage is accompanied with the accumulation of extremely high levels of light gases - helium and hydrogen.

Two major risks of helium accumulation in ferritic and ferritic-martensitic steels are (i) the decrease of swelling incubation dose and (ii) high temperature irradiation embrittlement (HTIE). It is currently expected that nanosized oxide particles in ODS steel should be beneficial for mitigation of both swelling and high temperature embrittlement, providing additional recombination sites for point defects at the oxide particle/matrix interfaces and He trapping sites [15, 18–23]. However, ODS steels have very complicated microstructure with multiple sinks (grain boundaries, dislocations, second phase precipitates) competing for point defects and helium atoms, and the relative role of additional components such as oxide nanoparticles is far from obvious, especially having in mind a broad variety of nano-oxides (Y_2O_3 , $Y_2Ti_2O_7$, $Y_3Al_5O_{12}$, $YAlO_3$, etc.) employed in different steel grades. Depending on particular steel and testing conditions the fraction of helium bubbles affiliated with nano-oxides varies from 30-100% [17-19,23–26]. Taking into account that the nucleation and growth kinetics of helium bubbles is sensitive to multiple parameters of irradiation (dose, temperature and helium injection/generation rate) as well, the available literature knowledge remains unsystematic and often badly reproducible due to the lack of basic understanding of the involved microstructural mechanisms. Neither is it clear whether strong helium accumulation on nano-oxides bears no risks of undesirable consequences in terms of ODS-steel radiation tolerance [27,28].

The effects of hydrogen on the microstructural modification of ODS steels have been less extensively investigated than those of helium. It is commonly expected that in conventional steels

hydrogen would not be retained at high concentrations but recent investigations have shown that ODS steels are able to accumulate more hydrogen than in conventional materials [29,30]. The proposed explanation of this effect is hydrogen trapping by oxide-nanoparticles is plausible, but has no firm proofs. An open question remains also a synergy in the action of hydrogen and helium on the properties of ODS steels. Multi-ion beam irradiation experiments evidence that helium and hydrogen are able to act in a synergistic manner on the development of irradiation-induced defect microstructure [31–38] and promote notable extra swelling under intense displacement damage, but only in certain temperature range [32–34,38]. The mechanisms of such hydrogen effects remain unclear.

Mostly unsystematic experimental research of complex materials under complex radiations environment is not in a position to guide materials design because in order to recommend ODS steels for particular heavy-duty application, a designer must not only know its response to the effect of operation conditions (operation temperature history, damage and helium, hydrogen accumulation rates, etc.), but also have a possibility to make the reliable long-term predictions and extrapolations of the existing experimental data beyond the parameter range, where these data were obtained. To reach this goal it is necessary to perform systematic studies of the sensitivity of gas-driven microstructure to the variation of key parameters, which include the nano-oxide sizes and densities, gas content and processing temperatures.

In order to achieve this task, it is highly desirable to perform investigations using as much control over the experimental parameters as possible. From this point of view, the use of ion implantation technique for the imitation of microstructural changes in well-controlled conditions with a wide range of variable parameters combined with careful post-implantation characterization looks highly promising. One should keep in mind, however, that ion implantation experiments are affected by geometry limitations (such as the relatively low ion implantation depth). In order to allow extrapolation of the results to more general and relevant cases, the experimental research must be supplemented with relevant modeling in order to extract the general trends of gas-driven microstructure development from the environment-sensitive data and suggest the ways of applying the obtained knowledge in a broader context. Such a combination of experimental and modeling approaches is the guideline of the current PhD project.

The major objective of this PhD study is to systematically investigate fundamental trends in gas-driven microstructure development in ferritic-martensitic ODS steels in separate ion implantation experiments examining single parameter dependencies of accumulated gas content, gas accumulation and damage rates, and temperature, with particular attention to the role of oxide particles. The proposed experimental approach involves saturation of ODS-EUROFER steel samples with various amounts of helium and hydrogen atoms using ion implantation at the JANNuS-Orsay facility in well-controlled conditions. The characterization methods include various transmission electron microscopy (TEM) based techniques, as well as appropriate supplementary techniques. For better understanding of the basic mechanisms of helium interaction with oxides, the experiments on the industrial material are supplemented with those on model $Y_2O_3/FeCr$ bilayer systems and with relevant modeling.

Within the scope of this objective, this PhD study has the following aims:

1. Systematic investigation of the effects of helium and hydrogen accumulation on microstructural development and swelling of commercial ODS-EUROFER steel, including

- (i) the investigation of the efficiency of Y_2O_3 nanoparticles as helium trapping sites under irradiation with either single He ion beam or simultaneously with He and heavy ions (with strongly different He/dpa ratios);
- (ii) the estimation of potential risks associated with using oxide nanoparticles in a high He/dpa ratio environment.
- (iii) the investigation of the role of hydrogen in the evolution of different cavity populations in ODS steel in a high H/dpa ratio environment and the resulting hydrogen effects on swelling;

(iv) the study of hydrogen retention under single-beam H and sequential dual-beam $\text{He}^+ + \text{H}^+$ ion implantations at both low and high temperatures with particular attention on the role of Y_2O_3 nanoparticles in hydrogen trapping.

2. *Investigation of the effects of helium and hydrogen implantation into a model $\text{Y}_2\text{O}_3/\text{FeCr}$ bi-layer system*

(v) the elucidation of contributions from radiation defect production and helium/hydrogen accumulation on secondary microstructure development near metal/oxide interfaces;

(vi) the investigation of the temperature effects on helium partitioning between metal, interface and oxide layers;

(vii) the investigation of possible hydrogen partitioning between metal, interface and oxide;

(viii) the search for synergetic effects of He and H on microstructural development in systems with the metal/oxide interfaces.

The manuscript consists of five Chapters.

Chapter 1 summarizes materials challenges for Generation IV fission, fusion reactors and accelerator driven systems, covers relevant experimental and simulation results on cavity swelling in ferritic-martensitic and ODS alloys, and discusses possible mechanisms of helium and hydrogen influence on swelling.

Chapter 2 specifies experimental techniques used in the study and is mostly focused on ion implantation method and the various TEM-related techniques, which are the main characterization methods used in this study. The results on initial microstructural characterization of ODS-EUROFER steel and model $\text{Y}_2\text{O}_3/\text{FeCr}$ bilayer system are also provided in this chapter.

Chapter 3 presents the detailed analysis of He effects on the microstructure evolution in ODS-EUROFER steel during single-beam helium implantation and dual-beam irradiation with helium and gold ions in different regimes. The role of oxide nanoparticles in helium inventory and bubble-to-void transition is discussed.

Chapter 4 covers synergetic effects of helium and hydrogen accumulation on the microstructural evolution in ODS-EUROFER steel by means of a combination of TEM, TDS and electron energy loss spectroscopy investigations.

Chapter 5 covers gas-driven microstructure development in a model bi-layer $\text{Y}_2\text{O}_3/\text{FeCr}$ system. Helium and hydrogen accumulation pattern observed in industrial material are re-aligned in the frame of the results obtained for the model bi-layer $\text{Y}_2\text{O}_3/\text{FeCr}$ system.

All chapters include appropriate discussions and conclusions. General conclusions and perspectives of the work are presented in the final section of the manuscript.

The manuscript is a detailed work of the PhD thesis of Olga V. Emelianova in partial fulfilment of the doctoral thesis study performed under joint supervision of Université Paris-Saclay (Irène-Joliot Curie Physics of Two Infinities Laboratory (IJCLab - Université Paris-Saclay, CNRS); doctoral school Particules, Hadrons, Énergie, Noyau, Instrumentation, Imagerie, Cosmos and Simulation (PHENIICS, № 576) and National Research Nuclear University MEPhI (Institute of Nuclear Physics and Engineering, NRNU MEPhI doctoral school, specialty physics of Condensed Matter 01.04.07).

References

- [1] *Climate Change and Nuclear Power 2018*. Vienna: International Atomic Energy Agency, 2018.
- [2] P. Yvon, Ed., *Structural Materials for Generation IV Nuclear Reactors*. Woodhead Publishing, 2017.
- [3] G. R. Odette and S. Zinkle, Eds., *Structural Alloys for Nuclear Energy Applications*. Elsevier, 2019.

- [4] I. L. Pioro, Ed., *Handbook of Generation IV Nuclear Reactors*. Woodhead Publishing, 2016.
- [5] S. J. Zinkle and J. T. Busby, “Structural materials for fission & fusion energy,” *Mater. Today*, vol. 12, no. 11, pp. 12–19, 2009.
- [6] J. T. Busby, “Chapter 1 - Overview of structural materials in water-cooled fission reactors,” in *Structural Alloys for Nuclear Energy Applications*, G. R. Odette and S. Zinkle, Eds. Boston: Elsevier, 2019, pp. 1–22.
- [7] R. L. Klueh, “Analysis of swelling behaviour of ferritic/martensitic steels,” *Philos. Mag.*, vol. 98, no. 28, pp. 2618–2636, Oct. 2018.
- [8] S. J. Zinkle and G. S. Was, “Materials challenges in nuclear energy,” *Acta Mater.*, vol. 61, no. 3, pp. 735–758, 2013.
- [9] A. Bhattacharya and S. J. Zinkle, “1.12 - Cavity swelling in irradiated materials,” in *Comprehensive Nuclear Materials (Second Edition)*, R. J. M. Konings and R. Stoller, Eds. Oxford: Elsevier, 2020, pp. 406–455.
- [10] *Structural Materials for Liquid Metal Cooled Fast Reactor Fuel Assemblies-Operational Behaviour*, no. NF-T-4.3. Vienna: International Atomic Energy Agency, 2012.
- [11] F. A. Garner, M. B. Toloczko, and B. H. Sencer, “Comparison of swelling and irradiation creep behavior of fcc-austenitic and bcc-ferritic/martensitic alloys at high neutron exposure,” *J. Nucl. Mater.*, vol. 276, no. 1, pp. 123–142, 2000.
- [12] R. Lindau, A. Moeslang, M. Rieth, M. Klimiankou, E. Materna-Morris, A. Alamo, A.-A. F. Tavassoli, C. Cayron, A.-M. Lancha, P. Fernandez, N. Baluc, R. Schaubelin, E. Diegele, G. Filacchioni, J.W. Rensman, B.v.d. Schaaf, E. Lucon, W. Dietz, “Present development status of EUROFER and ODS-EUROFER for application in blanket concepts,” *Fusion Eng. Des.*, vol. 75–79, pp. 989–996, 2005.
- [13] S. Ukai, S. Ohtsuka, T. Kaito, Y. de Carlan, J. Ribis, and J. Malaplate, “10 - Oxide dispersion-strengthened/ferrite-martensite steels as core materials for Generation IV nuclear reactors,” in *Structural Materials for Generation IV Nuclear Reactors*, P. Yvon, Ed. Woodhead Publishing, 2017, pp. 357–414.
- [14] S. J. Zinkle, J. L. Boutard, D. T. Hoelzer, A. Kimura, R. Lindau, G. R. Odette, M. Rieth, L. Tan and H. Tanigawa, “Development of next generation tempered and ODS reduced activation ferritic/martensitic steels for fusion energy applications,” *Nucl. Fusion*, vol. 57, no. 9, p. 92005, 2017.
- [15] G. R. Odette and D. T. Hoelzer, “Irradiation-tolerant nanostructured ferritic alloys: Transforming helium from a liability to an asset,” *JOM*, vol. 62, no. 9, pp. 84–92, Sep. 2010.
- [16] G. R. Odette, M. J. Alinger, and B. D. Wirth, “Recent developments in irradiation-resistant Steels,” *Annu. Rev. Mater. Res.*, vol. 38, no. 1, pp. 471–503, Jul. 2008.
- [17] G. R. Odette, N. J. Cunningham, T. Stan, M. E. Alam, and Y. De Carlan, “Chapter 12 - Nano-oxide dispersion-strengthened steels,” in *Structural Alloys for Nuclear Energy Applications*, G. R. Odette and S. Zinkle, Eds. Boston: Elsevier, 2019, pp. 529–583.
- [18] P. D. Edmondson, C. M. Parish, Y. Zhang, A. Hallén, and M. K. Miller, “Helium bubble distributions in a nanostructured ferritic alloy,” *J. Nucl. Mater.*, vol. 434, no. 1, pp. 210–216, 2013.
- [19] A. I. Ryazanov, O. K. Chugunov, S. M. Ivanov, S. T. Latushkin, R. Lindau, A. Möslang, A. A. Nikitina, K. E. Prikhodko, E. V. Semenov, V. N. Unezhev, P. V. Vladimirov, “Tensile properties and microstructure of helium implanted EUROFER ODS,” *J. Nucl. Mater.*, vol. 442, no. 1, Supplement 1, pp. S153–S157, 2013.

- [20] T. Chen, H. Kim, J. G. Gigax, D. Chen, C.-C. Wei, F. A. Garner, L. Shao, “Radiation response of oxide-dispersion-strengthened alloy MA956 after self-ion irradiation,” *Nucl. Instruments Methods Phys. Res. Sect. B Beam Interact. with Mater. Atoms*, vol. 409, pp. 259–263, 2017.
- [21] Q. Li, C. M. Parish, K. A. Powers, and M. K. Miller, “Helium solubility and bubble formation in a nanostructured ferritic alloy,” *J. Nucl. Mater.*, vol. 445, no. 1, pp. 165–174, 2014.
- [22] C. M. Parish and M. K. Miller, “Aberration-corrected X-ray spectrum imaging and fresnel contrast to differentiate nanoclusters and cavities in helium-irradiated alloy 14YWT,” *Microsc. Microanal.*, vol. 20, no. 2, pp. 613–626, 2014.
- [23] C. M. Parish, K. A. Unocic, L. Tan, S. J. Zinkle, S. Kondo, L. L. Snead, D. T. Hoelzer, Y. Katoh, “Helium sequestration at nanoparticle-matrix interfaces in helium + heavy ion irradiated nanostructured ferritic alloys,” *J. Nucl. Mater.*, vol. 483, pp. 21–34, 2017.
- [24] T. Yamamoto, G. R. Odette, P. Miao, D. J. Edwards, and R. J. Kurtz, “Helium effects on microstructural evolution in tempered martensitic steels: In situ helium implanter studies in HFIR,” *J. Nucl. Mater.*, vol. 386–388, pp. 338–341, 2009.
- [25] G. R. Odette, P. Miao, D. J. Edwards, T. Yamamoto, R. J. Kurtz, and H. Tanigawa, “Helium transport, fate and management in nanostructured ferritic alloys: In situ helium implanter studies,” *J. Nucl. Mater.*, vol. 417, no. 1, pp. 1001–1004, 2011.
- [26] T. Yamamoto, Y. Wu, G. Robert Odette, K. Yabuuchi, S. Kondo, and A. Kimura, “A dual ion irradiation study of helium-dpa interactions on cavity evolution in tempered martensitic steels and nanostructured ferritic alloys,” *J. Nucl. Mater.*, vol. 449, no. 1–3, pp. 190–199, 2014.
- [27] B. Yao, D. J. Edwards, R. J. Kurtz, G. R. Odette, and T. Yamamoto, “Microstructure Characterization of Neutron Irradiated and Helium Injected PM2000, 14YW, and Modified F82H Alloys,” *Fusion Mater. Semiannul Prog. Rep. June 2012*, vol. DOE-ER-031, p. 26, 2012.
- [28] H. J. Jung, D. J. Edwards, R. J. Kurtz, T. Yamamoto, Y. Wu, and G. R. Odette, “Structural and chemical evolution in neutron irradiated and helium-injected ferritic ODS PM2000 alloy,” *J. Nucl. Mater.*, vol. 484, pp. 68–80, 2017.
- [29] E. Malitckii, Y. Yagodzinskyy, M. Ganchenkova, S. Binyukova, H. Hänninen, R. Lindau, P. Vladimirov, A. Moeslang, “Comparative study of hydrogen uptake and diffusion in ODS steels,” *Fusion Eng. Des.*, vol. 88, no. 9, pp. 2607–2610, 2013.
- [30] Y. Yagodzinskyy, E. Malitckii, M. Ganchenkova, S. Binyukova, O. Emelyanova, T. Saukkonen, H. Hänninen, R. Lindau, P. Vladimirov, A. Moeslang, “Hydrogen effects on tensile properties of EUROFER 97 and ODS-EUROFER steels,” *J. Nucl. Mater.*, vol. 444, no. 1, pp. 435–440, 2014.
- [31] K. Farrell and E. H. Lee, “Ion Damage in a Fe-10Cr-6Mo-0.5Nb Ferritic Steel,” *Radiation-Induced Changes in Microstructure: 13th International Symposium (Part I)*, vol. STP 955, pp. 498–507, Jan. 1987.
- [32] E. Wakai, T. Sawai, K. Furuya, A. Naito, T. Aruga, K. Kikuchi, S. Yamashita, S. Ohnuki, S. Yamamoto, H. Naramoto, S. Jistukawa, “Effect of triple ion beams in ferritic/martensitic steel on swelling behavior,” *J. Nucl. Mater.*, vol. 307–311, pp. 278–282, 2002.
- [33] E. Wakai, K. Kikuchi, S. Yamamoto, T. Aruga, M. Ando, H. Tanigawa, T. Taguchi, T. Sawai, K. Oka, S. Ohnuki, “Swelling behavior of F82H steel irradiated by triple/dual ion beams,” *J. Nucl. Mater.*, vol. 318, pp. 267–273, 2003.
- [34] T. Tanaka, K. Oka, S. Ohnuki, S. Yamashita, T. Suda, S. Watanabe, E. Wakai, “Synergistic effect of helium and hydrogen for defect evolution under multi-ion irradiation of Fe–Cr ferritic alloys,” *J. Nucl. Mater.*, vol. 329–333, pp. 294–298, 2004.

- [35] J. Marian, T. Hoang, M. Fluss, and L. L. Hsiung, “A review of helium–hydrogen synergistic effects in radiation damage observed in fusion energy steels and an interaction model to guide future understanding,” *J. Nucl. Mater.*, vol. 462, pp. 409–421, 2015.
- [36] Y. E. Kupriyanova, V. V. Bryk, O. V. Borodin, A. S. Kalchenko, V. N. Voyevodin, G. D. Tolstolutsкая, F.A. Garner, “Use of double and triple-ion irradiation to study the influence of high levels of helium and hydrogen on void swelling of 8–12% Cr ferritic-martensitic steels,” *J. Nucl. Mater.*, vol. 468, pp. 264–273, 2016.
- [37] D. Brimbal, L. Beck, M. Payet, and F. Jomard, “The synergistic effect of hydrogen and helium implantations in forming H₂ molecules in a Fe-12 wt.%Cr-ODS steel characterized by Raman spectroscopy and SIMS,” *Nucl. Instruments Methods Phys. Res. Sect. B Beam Interact. with Mater. Atoms*, vol. 461, pp. 191–196, 2019.
- [38] N. Zimmer, P. Vladimirov, M. Klimenkov, U. Jaentsch, R. Vila, V. Chakin, F. Mota, “Microstructural evolution of three potential fusion candidate steels under ion-irradiation,” *J. Nucl. Mater.*, vol. 535, p. 152160, 2020.

Chapter 1 Materials challenges of Generation IV fission and fusion reactors and accelerator driven systems

1.1 Introduction

Development of technologies and a sharp increase in world population require permanently increasing energy supply that is currently heavily based on fossil fuels. However, fossil fuel resources are limited, while their burning in the energy sector and in industrial activities produces a large amount of greenhouse gases, the most important contribution of ~60 % being that of carbon dioxide (CO₂), that are currently believed to be responsible for climate change [1]. According to Current Policies Scenario of International Energy Agency (IEA) from 2018 to 2040, the world's energy demand is expected to increase by ~2.3 % per year [2,3]. Following the current trend, CO₂ emission in 2030 will be ~15 GtCO₂e (GtCO₂e -gigatonne carbon dioxide equivalent per year) and ~32 GtCO₂e higher than can be allowed to keep the global warming below 2°C and 1.5°C (Paris Agreement limit), respectively. Although the energy consumption increase in 2019 was only ~1.3 % [2,3], it still leads in an upward march of CO₂ emission. The challenges of meeting rapidly growing demand for energy have renewed worldwide interest in advanced power energy plants, while the need for new clean sources of energy provides strong support to the quest for next generation energy devices. Renewable energy sources using solar, wind and water energy are promising candidates for future energy power plants in terms of mitigating CO₂ emission. The past decade was characterized by strong growth in the deployment of renewable energy technologies, especially solar photovoltaics and wind generation [3]. However, their application as major large-scale energy production technologies remains strongly restricted by relatively low efficiency of renewable energy sources and the non-continuous mode of energy generation.

In fact, nuclear power, as an essential low-carbon technology can largely contribute to the global objective of developing clean energy technologies for current and future generations [4]. It is especially suitable for large-scale, continuous electricity demands that require reliability. Currently, nuclear plants provide a significant fraction of non-carbon power generation around the world. Cumulatively, in 2019 they represented 11% of the world's electricity generation and consumption was provided by 443 operating power units (and even more in some countries, e.g. ~70% in France, ~50 % in Belgium, ~20 % in the US, Russian Federation and South Korea) [5]. Given the advantages of low cost, high efficiency and fewer limitations from environmental impact, nuclear power constitutes an important part of current and future energy sources. Although nuclear power plants have significant potential to contribute to further mitigation of CO₂ emission, these facilities also face a number of challenges, in particular the concerns around radiation exposure, radioactive waste, off-site effects of nuclear accidents and high capital costs [4]. These issues can be successfully solved by integrating in power industry advanced nuclear fuel cycle options based on combined use of light water reactors (LWRs) and such innovative systems as Generation IV (Gen IV) reactors [6,7] and Accelerator Driven Systems (ADS) with spallation neutron targets [8,9]. The advanced nuclear fuel cycle option offers significant advantages over commercially used LWRs combining breeding and waste management capacity with increased power conversion efficiency and passive safety. Radioactive waste mitigation in advanced nuclear fuel cycle is based on the partitioning and transmutation strategy which includes multi recycling of transuranic elements unloaded from LWRs in fast breeder reactors with further transmutation of selected isotopes from radioactive waste in ADS systems. While some of Gen IV concepts are already implemented in research reactors (sodium fast reactor), ADS systems are planned for longer term perspective due to complexity of final installations (ex. transmutation demonstration facility MYRRHA [9]). The current Gen IV designs include three fast reactor concepts (namely, sodium fast reactor (SFR), lead fast reactor (LFR), and gas-cooled fast reactor (GFR)), one thermal reactor concept (e.g. very high-temperature reactor (VHTR)) and two fast or thermal reactors, i.e. supercritical water reactor (SCWR) and molten salt reactor (MSR) [10,11].

Besides new design ideas based on advanced fission technology, nuclear fusion facilities are being developed as a next-generation technique for clean energy production [7,12]. Fusion technology has several advantages in comparison with fission, e.g.

- Abundant fuel. Deuterium is extracted from seawater, and tritium can be produced from transmutation of lithium using neutrons produced in the D-T fusion reaction;
- Energy efficiency. One kilogram of fusion fuel produces the same amount of energy as 10 million kilograms of fossil fuel;
- Safety. The amounts of fuel used in fusion devices are small, excluding massive uncontrolled nuclear accidents. Also, fusion reaction does not result in the production of transuranic elements, which is beneficial for both safety and ecology.

Several research fusion facilities, such as JET (UK), ASDEX and Wendelstein 7-X (Germany), West (France), and T-15 (Russia) are currently active [12]. A large-scale fusion facility, ITER, is under construction by joint efforts of EU, US and Japan. The construction of the demonstration fusion power facility DEMO is planned to start already in early 2040s.

Gen IV, ADS and fusion systems are expected to supply carbon-free electrical power in a sustainable amount to modern economies. However, in order to reach desired advantages in performance over the current nuclear fleet advanced fission and fusion systems have to be operated in much more severe regimes and environments than the modern LWRs and fast-breeder fission facilities. The safety, reliability, and efficiency of new facilities ultimately depend on high-performance structural materials that can provide extended service in severe operation conditions.

1.2 Materials challenges of fission and fusion systems

Compared to existing experience with structural materials in LWRs operated at temperature ~300°C and displacement damage levels for core internal structures of 7-70 displacements per atom (dpa) for forty-year operating time [5,13], the advanced fission and fusion designs call for higher temperatures and radiation doses [14-16]. To allow operation at such high temperatures, chemically aggressive coolants have to be utilized. In addition, changes of neutron spectra, the increased neutron fluxes, and high levels of transmutation products will lead to non-negligible accumulation of light gases (H, He) in the reactor core structural and functional materials. Even without irradiation effects, the thermo-mechanical challenges to complex multifunctional structures are daunting. The addition of irradiation triggers microstructural-microchemical evolution that tends to degrade performance-sustaining material properties, i.e. mechanical/thermo-physical properties and dimensional stability.

Typical operation conditions for nuclear fission, fusion and spallation designs are given in Fig. 1.1 and Table 1.1.

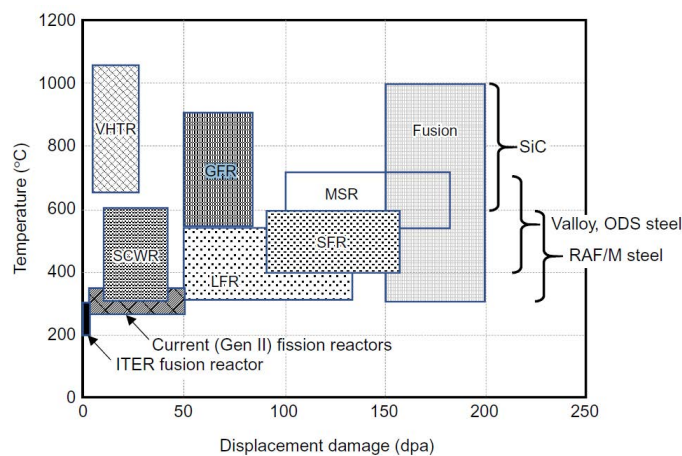


Fig. 1.1. Overview of operating temperatures and displacement damage regimes for structural materials in the current (generation II) and future Gen IV (VHTR, SCWR, LFR, GFR, SFR and MSR) and fusion energy systems [16].

Table 1.1. Comparison of neutron fluxes, displacement rates, He and H production (in Fe-based alloys) for fusion (DEMO FW), spallation (SINQ, European spallation source (ESS), Experimental Accelerator Driven System (XADS)), fission materials testing reactors (high flux reactor (HFR) and Jules Horowitz reactor (JHR)), and the fast neutron BOR60 reactor. Abbreviation fpy stands for ‘full power year’ [17,18].

Parameter	Technology							
	Fusion		Spallation			Fission		
	Demo FW*	SINQ	ESS, irr. riggs reflector	XADS* 1 MW Window	HFR position F8	BOR 60 Position D23	JTR*	
Energy	<14.1 MeV		≤ 1 GeV (p) and >100 MeV(n)			<1-2 MeV (most n’s)		
Total flux (cm⁻² s⁻¹)	n	1.3×10^{15}	2.7×10^{14}	6.5×10^{14}	1.2×10^{15}	3.8×10^{14}	2.3×10^{15}	2.5×10^{15}
	p	0	2.6×10^{14}	2.5×10^{12}	2.7×10^{14}	0	0	0
Damage (dpa/ fpy)	30	30	5-10	38	2.5	20	16	
He (appm/fpy)	320	2600	25-60	1320	0.8	5.8	4.4	
H (appm/fpy)	1240	11000	160-360	16260	1.9	14	10.6	
He/dpa	11	85	5-6	35	0.3	0.29	0.3	
H/dpa	41	35	33-36	430	0.8	0.7	0.7	

* - facilities under preparation or at the construction stage [17,18]

Basically, the behavior of structural materials in different irradiation environments is determined by the same underlying physics of radiation effects in solids [19-21], which involves:

- (1) point defect (vacancies and self-interstitial atoms (SIA)) generation as a result of fast neutron collisions with target atoms;
- (2) production of solid and gaseous impurity atoms in (n,γ) , (n,α) , and (n,p) transmutation reactions;
- (3) migration and interaction of self-point defects and impurity atoms with each other and with material microstructural features, resulting in the formation and evolution of secondary radiation damage (dislocation loops, gas bubbles and voids, sometimes stacking fault tetrahedra (SFT), etc.).

However, strong differences in material operation parameters, such as primary knock-on atom (PKA) energy spectra, damage rates, accumulated displacement doses, temperatures and initial material structures, can result in a broad spectrum of final material microstructures formed via defect production and evolution under neutron irradiation. Examples of typical microstructures developed in irradiated materials are given in Fig. 1.2, being listed in the order of increasing temperature where that or other effect is typically dominant [20,21].

Regardless of differences in irradiation regimes, there exist a number of principal performance-limiting phenomena arising from radiation effects on materials that can be summarized as follows: amorphization, hardening, decrease in thermal and electrical conductivity, mechanical property or corrosion degradation as a result of radiation-induced segregation and precipitation, dimensional instabilities (e.g. irradiation growth, irradiation creep and swelling), and high temperature embrittlement resulting from impurity (first of all, helium) accumulation at grain boundaries [14,20].

At very low homologous temperatures ($\sim 0.02-0.05 T/T_M$), when vacancies are immobile and SIA mobility is strongly suppressed, neutron irradiation can lead to radiation-induced amorphization. In practical terms, the effect is typically important for intermetallic and ceramic materials. Already at relatively low doses ($\sim 0.1-1$ dpa) amorphization is accompanied with notable (up to 5-30 %) swelling of such materials [20-22].

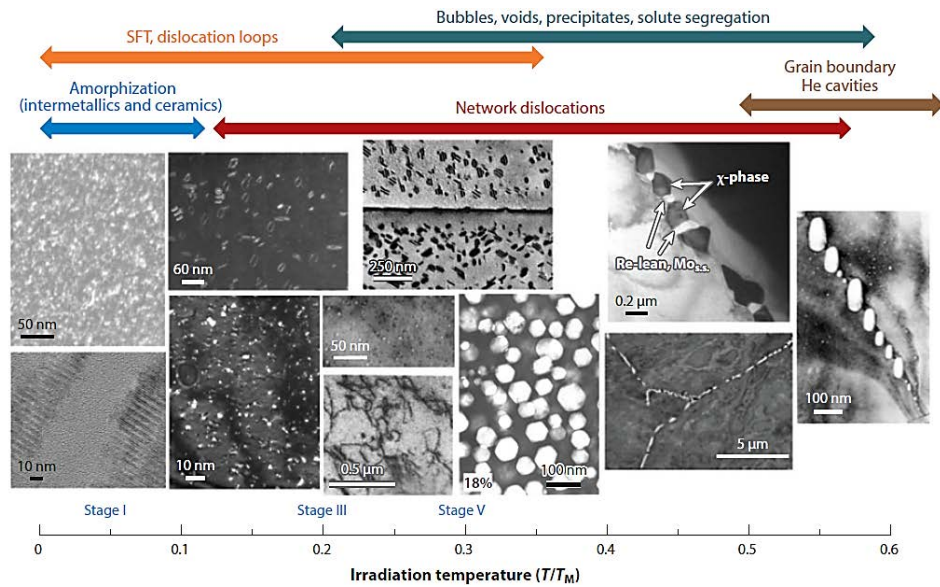


Fig. 1.2. Examples of representative microstructures in irradiated materials as a function of irradiation temperature. The approximate onset temperatures for Stages I, III, and V of defect recovery are listed above the temperature scale, corresponding to initiation of long-range self-interstitial-atom migration, vacancy migration, and thermal dissolution of small vacancy clusters, respectively. T_M is the melting temperature [21].

In metallic structural materials, lifetime-limiting radiation-induced phenomena are sensitive to the irradiation temperature [15,20,21]. At low temperatures ($<0.3-0.4 T/T_M$), where SIAs are already mobile while vacancies are relatively immobile, accumulation of defect clusters, in particular dislocation loops, takes place, promoting hardening at the damage dose range of 0.01–1 dpa [20]. Hardening reduces fracture toughness and sometimes shifts ductile-to-brittle transition to higher temperatures. In the intermediate temperature range ($\sim 0.2-0.5 T/T_M$), where both SIAs and vacancies are mobile, the complex evolution of wide range of defect cluster geometries results in dimensional instabilities due to swelling accompanied with vacancy clustering in cavities, phase instabilities driven by radiation-induced segregation and radiation-enhanced diffusion, irradiation creep and (in anisotropic metals) growth [20,21]. Defect cluster accumulation and evolution in this temperature range is dose, temperature and material type dependent. In fact, in the intermediate temperature range these degradation phenomena limit the maximum allowable damage dose. In the high temperature range ($>0.5 T/T_M$), thermodynamic equilibrium processes dominate and only minor microstructural changes occur [20]. However if significant amounts of badly soluble impurity atoms such as helium are introduced into the metal (typically for dose >10 dpa and $>100-1000$ He appm), cavities are nucleated in the grain interior and along grain boundaries. The accumulation of helium at grain boundaries and the formation of large grain boundary cavities weaken the boundaries and bear potential risk of promoting intergranular fracture of material under the action of sufficiently high external loads; the effect is referred to as high temperature irradiation embrittlement (HTIE). The low-temperature radiation-hardening and HTIE phenomena typically define the allowable range of operating temperatures for metallic structural materials in advanced nuclear concepts [21]. Within this temperature range, the major degradation phenomena for structural materials operating at the expected high damage levels are void swelling and phase instability [15].

Although, owing to high operating temperatures and neutron doses, the structural material response to radiation exposure in Gen IV fission, fusion and spallation concepts demonstrates certain similarities, the differences in neutron spectra can notably affect microstructural development [18,23]. The harder spectrum in fusion and spallation devices as compared to fission facilities (where the top neutron energies are on the average <2 MeV) is potentially able to modify both the primary damage production characteristics and the levels of transmutant elements with considerable impact on subsequent evolution of the secondary defect microstructure [14,18,23,24].

However, in terms of damage production no big differences were found for all three irradiation sources [14,18,23,24]:

- in all cases the point defect recombination within energetic displacement cascades results in surviving defect fraction of ~30% of the NRT dpa in spite of the large differences in the average PKA energy for fission (~10 keV), fusion (~50–100 keV) and spallation (~50–200 keV) neutron irradiation conditions;
- defect cluster geometry and the fractions of clustered vacancies and interstitials are also comparable for fission, fusion and spallation neutron irradiation conditions.

But in terms of transmutant production levels, fission, fusion and spallation environments are critically different. The high energy neutrons in fusion and spallation devices provoke much higher levels of secondary elements produced by neutron-induced transmutations or spallation reactions that can alter the microstructure and properties of irradiated materials [14,18,23,25,26]. For such practically important structural materials as steels, $^{54}\text{Fe}(n,\alpha)^{51}\text{Cr}$ (threshold at 2.9 MeV) and $^{54}\text{Fe}(n,p)^{54}\text{Mn}$ (0.9 MeV) reactions in spallation and fusion systems produce ~3 and ~1-2 orders of magnitude higher levels of He and H as compared to any fission reactor. High He and H generation rates invoke potential issues for material radiation stability, including He-enhanced radiation hardening and embrittlement ($<0.4 T_M$), He/H effects on void swelling and modified phase stability ($\sim 0.3\text{--}0.6 T_M$), and high probability of HTIE ($>0.5 T_M$) [15,23,25,27–29]. In addition, because the irradiated structural materials in fusion and spallation devices are the major source of long-term radioactivity, such elements as Mo, Nb, Ni, Co, Cu should be eliminated in the advanced structural materials and various impurity elements with high long-term radioactivity must be avoided or their concentration should be reduced in order to satisfy “clean” energy source condition [29–32].

Austenitic Fe-Cr-Ni steels with face-centered-cubic (*fcc*) structure are successfully used as basic structural materials of LWR core internals ($T < 350^\circ\text{C}$, doses up to ~80 dpa achieved during ≈ 40 years) [33,34], but their operating experience as fuel cladding under high damage rate or/and temperature in SFR/MTR has revealed that after a certain, relatively short incubation dose these steels are prone to insaturable swelling with the rate of ~1%/dpa [35]. As soon as void swelling reaches ~3-5%, swelling becomes the dominant factor that controls the physical and mechanical properties (e.g. irradiation creep) [28]. Typically, already >5% swelling is unacceptable based on engineering design considerations [15]. When void swelling of austenitic steels irradiated at $\leq 400^\circ\text{C}$ exceeds 10% (at ~80 dpa), the steels suffer from severe embrittlement due to the action of a complex mechanism involving stress concentration between voids, nickel segregation to void surfaces, and alteration of the martensite start temperature [28,33,35]. In addition, due to notable Ni content in austenitic steels, even under LWR neutron spectra the intense accumulation of transmutation He and H leads to He cavity growth at grain boundaries and promotes intergranular embrittlement [35]. At the typical fission reactor temperature of $\sim 300^\circ\text{C}$ He and H are assumed to be trapped by high density of nano-cavities especially at grain boundaries, but this additional hydrogen storage is believed to play a role in increased susceptibility of austenitic steels to intergranular failure (stress corrosion cracking (IGSCC)), as detected during post-irradiation slow strain rate testing [35]. When swelling exceeds 15–20%, a steel detail can even break due to deformations induced by swelling and irradiation creep, especially during fuel rod maintenance [28]. Summing up, swelling driven phenomena prompted by enhanced point defect production and He/H accumulation limit acceptable damage doses and prohibit conventional austenitic steel usage in severe radiation environments, especially those expected in fusion and spallation facilities.

Since it is virtually impossible to reduce the primary defect generation rates with a given material, the eventual fate of defects can be tailored by microstructure engineering during defect migration and interaction. According to Ref. [21] and references therein, three general strategies can be adopted to increase radiation tolerance of structural materials, namely, engineered high-sink-strength microstructures (introduction of a high density of point defect recombination centers), radiation-resistant matrix phases and point defect immobilization. Optimization of austenitic steels in terms of high-sink-strength tailoring

(increase of dislocation density by 15-30% cold-work and solute-cluster/precipitate number densities by Ti, P, Nb, V alloying) results in better recombination and annihilation of point-defects which mitigate cavity nucleation. Optimized austenitic steels demonstrate efficient delay of the steady-state swelling regime up to 50-100 dpa, but after incubation dose the swelling rate is the same as for basic steel variants (see Fig. 1.3). It is obvious that swelling resistance of even optimized austenitic steels is not sufficient to withstand the damage levels of 100-350 dpa expected in the advanced Gen IV, fusion and spallation facilities. Moreover, low-activation and HTIE phenomena remain a concern for optimized austenitic steels.

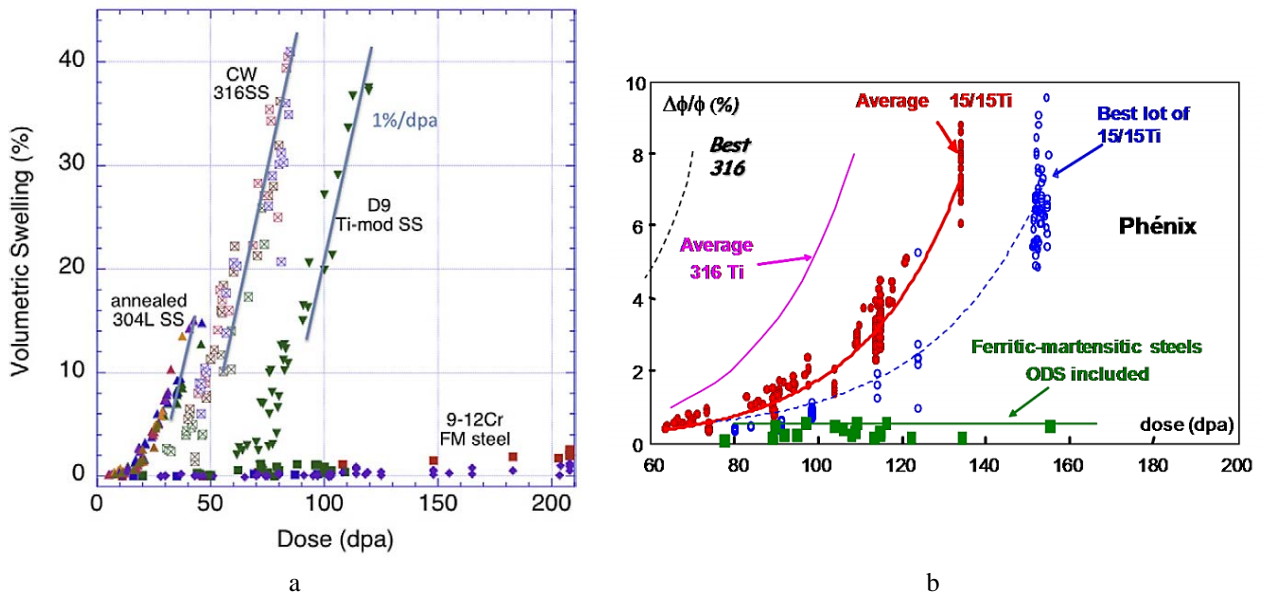


Fig. 1.3. Comparison of swelling and maximal deformation of austenitic and ferritic-martensitic steels irradiated at 400–550°C to high doses in fast fission reactor spectrum: (a) volumetric void swelling in 304L, 316 and Ti-modified (D9) austenitic stainless steels and in tempered ferritic-martensitic steels with 9–12% Cr [15]; (b) maximum deformation (in term of swelling) of irradiated fuel pin claddings from base type 316 and type 316 Ti-modified steel, austenitic alloy alloyed with Ti, P, V, Nb, and ferritic-martensitic steels [28].

A further improvement is to combine benefits of high-sink-strength microstructures with radiation-resistant matrix strategy. This approach is essentially implemented in ferritic and ferritic/martensitic (F/M) steels with body-centered-cubic (*bcc*) structure. Body-centered-cubic matrix exhibits generally superior radiation resistance in itself. Several factors have been suggested to contribute to low swelling levels of *bcc* alloys under both ion and neutron irradiation, including reduced in-cascade production of point defect clusters, lower dislocation bias and higher self-diffusion coefficients of point defects. F/M steels after normalization and tempering treatment typically demonstrate hierarchical tempered martensite structure (see Fig. 1.4). In such structure, prior-austenitic grains (PAGs) are subdivided into sub-grains and packets of lath martensite blocks with high dislocation density. Grain boundaries are preferentially decorated with relatively coarse $M_{23}C_6$ carbides ($M = Cr$ -rich), while fine MX-type carbonitrides ($M=Nb/Mo/W/Ta/V$, $X= C/N$) are located both in inter- and intragranular regions. It is apparent that, in contrast to austenitic steels, F/M steels exhibit a high number density of point defect trapping/recombination sites (see Fig. 1.4). At intermediate temperatures and doses (steady-state swelling regime), high sink strength of F/M steels efficiently suppresses cavity growth. High swelling incubation dose of ~150-200 dpa along with relatively low swelling rate of ~0.2 %/dpa of F/M steels in steady-state regime (see. Fig. 1.3) make them attractive for utilization in advanced future power generation facilities [15,22,28,36,37].

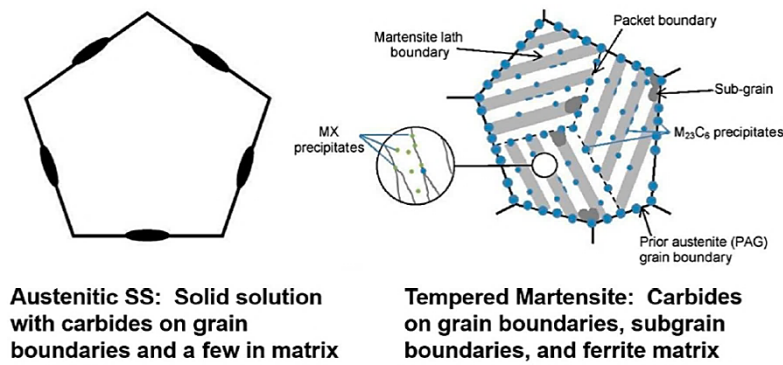


Fig. 1.4. Schematic diagram illustrating the difference in the microstructure of austenitic stainless steel and ferritic/martensitic steel [36].

However, excellent void swelling resistance demonstrated by F/M steels can be affected in fusion and spallation devices by the expected high levels of transmutant He and H that promote cavity nucleation and growth. Examples of He and H+He influence on swelling of F/M steels for fusion relevant environment simulated with ion implantation and fission neutron irradiation are shown in Fig. 1.5. The data for “pure” void swelling as a result of fission neutron and single-beam ion irradiations are provided for comparison. As can be seen in Fig. 1.5, the level of void swelling is notably higher for conditions where He and He+H are introduced at gas/dpa ratios relevant for fusion facilities [29]. Without He and/or He+H co-injection/transmutation, all F/M alloys demonstrate moderate or no swelling in fission reactor relevant conditions (fission neutrons or single-beam ion irradiation) up to incubation doses of ~200 dpa [29,37–39]. The introduction of either He or He+H reduces the swelling incubation dose down to 16.6-50 dpa for F/M steels depending on damage rate, He/dpa ratio, temperature and microstructure of a particular material [29,40–47]. At the first glance, the simultaneous He+H co-implantation leads to more efficient swelling acceleration; the reported swelling levels at the dose of 50 dpa reached 3.2% for F82H commercial steel [43] and 4-5% for Fe–9-12%Cr model alloys [45]. The incubation dose is typically smaller [25,29] for low-dose rate in-service radiation environments than for high-dose rate ion irradiations experiments. Thus, the lifetime limiting swelling level of >5% for F/M steels might be achieved in in-service conditions at doses even lower than ~50 dpa expected from ion-irradiation experiments [29].

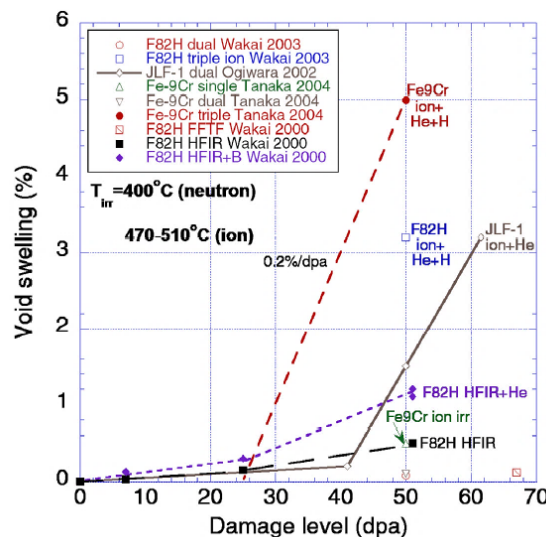


Fig. 1.5. Summary of the effects of simultaneous DT fusion relevant He and H production on volumetric void swelling in ion and fission neutron irradiated F/M steels. The experimental studies include simultaneous heavy ion and He or He + H implantation at 470–510°C and fission reactor (HFIR or FFTF) irradiation at 400 °C of standard or boron-doped (to generate He) samples. The multi-ion beam irradiations used implantation rates of 10-18 appm He/dpa and 40–70 appm H/dpa. The boron doped HFIR neutron irradiated F82H samples generated ~60 or ~300 appm He, mainly created at doses <1 dpa [29].

Hard neutron spectra and high radiation doses expected in advanced nuclear facilities impose additional demands on elemental content of F/M steels. With respect to swelling, chromium content in F/M steels should be limited to 9% in order to prevent the formation of δ -ferrite that is prone to notable void swelling [31]. Moreover, δ -ferrite together with radiation-induced α' phase formation is partially responsible for the reduction of fracture toughness at temperatures 50-400 °C [31].

In addition to superior swelling resistance, F/M steels have higher thermal conductivity and lower thermal expansion than austenitic steels, but the loss of creep strength above 550°C generally deteriorates their high temperature performance [28,31]. The loss of creep-rupture strength at high temperatures occurs due to the sub-grain structure destabilization and the reduction of the primary precipitate-strengthening as a result of coarsening of $M_{23}C_6$ and MX precipitates, respectively [48]. In order to comply with the low activation requirements, such important alloying elements in conventional F/M steels as Nb and Mo with long post-irradiation decay times are replaced with metallurgically equivalent Ta and W elements, giving rise to a new generation of F/M steels, so called reduced activation ferritic-martensitic (RAFM) steels [31,32,49–51]. But even the most advanced RAFM steels, in particular, F82H and EUROFER97 that are based on 9Cr2WVTa composition, have creep-rupture strength lower than the second generation of T91F/M steel (by 18% at 550 °C and 30% at 600 °C) [29,52,53]. Optimization of RAFM steels by means of thermo-mechanical treatments (TMT) and chemical composition tailoring eventually allow the operation limit to slightly exceed 550°C as a compromise between the high temperature creep properties and DBTT reduction [31,48,54,55].

For the higher temperature applications of RAFM steels, further improvement of their high temperature creep performance is required. Optimal creep strength can be obtained combining high density of fine and thermally/radiation stable precipitates and solid solution strengthening. A promising approach is steel strengthening with metal/oxide particles. Such oxide dispersion-strengthened (ODS) steels contain high-density distributions of small particles typically based on yttrium oxide (Y-O, Y-Ti-O, Y-Al-O). The basic idea behind the concept is that nano-oxides will act as barriers for dislocation motion and grain boundary migration even at those temperatures where carbides lose their efficiency as dislocation and grain boundary pinning centers and will control the high-temperature tensile properties and creep resistance. ODS steels have a potential to overcome the drawbacks of conventional F/M and RAFM steels in mechanical strength and, as commonly expected, to demonstrate improved radiation resistance as well [29,49,56–59].

1.3 ODS steels

The history of ODS alloys in nuclear power industry started in the mid-nineties of the last century (see e.g. [60]), mostly in relation to liquid metal fast breeder reactor cladding applications. First ferritic ODS alloys commercialized by Fischer and marketed by International Nickel Corporation were MA956 and MA957 [59]. Later large efforts in the development of ODS steel were made in Japan, U.S and Europe. However, due to currently restricted practical use, ODS steels are manufactured on a laboratory scale (~10 kg batch) or pilot plant scale (~few tons) in Germany, France, Japan and the Russian Federation. The mainstream of the research was for a long time concentrated on technological aspects of steel production and technology-oriented mechanical property testing. However, some early data on ODS steel behavior under irradiation can be found in literature [61]. A serious interest in these steels arose after it had been demonstrated that material alloying with high number densities of nanometer size oxide particles not only improved the steel mechanical properties for high-temperature applications, but also resulted in outstanding radiation stability [59].

Among different oxides, yttria is the most widely used for the production of ODS steel. The primary reason for choosing yttrium as dispersion oxide is the high thermal stability and low diffusion in Fe-Cr matrix [59]. However, one meets in the literature permanent attempts to further improve ODS steel performance playing with mixed Y-based (e.g. Y-Ti) oxides or choosing alternative oxide compositions.

Recent comparison of microstructure and mechanical properties [62] of Fe-13%Cr steels manufactured using hot isostatic pressing (HIP) and strengthened with MgO, La₂O₃, Ce₂O₃ and ZrO₂ with the common Y₂O₃ strengthened analog has revealed improved steel mechanical properties in terms of Charpy impact tests for steels strengthened with MgO and Ce₂O₃, but the best performance in terms of tensile behavior was still shown by Y₂O₃-alloyed steel.

As a result of poor solubility and wettability of rare earth oxides such as yttria in molten Fe [63], manufacturing of ODS-steels by classical casting methods fails due to coarsening and agglomeration of oxide particles during melting/solidification [64,65] and accumulation of oxides particles at the surface of ingots [66]. So at present ODS steels are mainly produced via mechanical alloying (MA), followed by powder metallurgy processing (PM). A common PM/MA route for the fabrication of ODS steels includes the following major steps [56,67,68] (see Fig. 1.6):

- selection of the steel composition,
- gas atomization of the steel to be dispersion hardened (master alloy),
- blending of the steel powder and suitable oxide powders, e.g. commercial 20-200 nm Y₂O₃,
- mechanical alloying of the blended mixture using e.g. planetary ball mills or attritor mills,
- canning and degassing,
- consolidation, e.g. by means of HIP or hot extrusion (HE),
- post-processing based on thermal, mechanical or thermo-mechanical treatment (TMT).

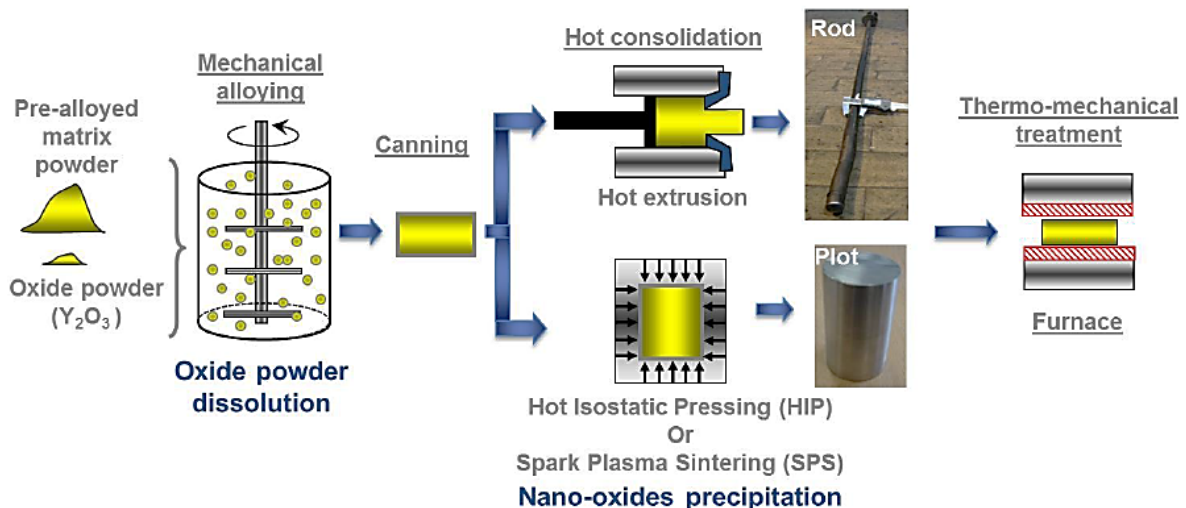


Fig. 1.6. A schematic illustration of PM/MA fabrication route of ODS steels [69].

There exist three major processes of ODS steel fabrication, namely premixed, partially pre-alloyed, and fully pre-alloyed process, that differ in the way of preparation of the raw material powder [56,68]. In the premixed process, Y₂O₃ powder is mixed with elemental powders (Fe, Cr, C, W, Ti, etc.), in the partially pre-alloyed one - with the major raw material powder, and in the fully pre-alloyed process -with the master alloy, respectively. The premixed process is the cheapest one, but it does not exclude metallic inclusion formation. For this reason, the pre-alloyed powder process (with master alloy) is utilized most widely. The pre-alloyed powder used is produced by vacuum melting followed by gas atomization. Atomization is usually carried out in Ar atmosphere. After atomization, the metallic powder and Y₂O₃ powder are mechanically alloyed under Ar or H atmosphere in a high-energy attritors, planetary ball mills or/and shaker mills, where Y₂O₃ is forced to decompose or nearly decompose in the metal matrix [67]. Milling stage is critical because Y₂O₃ oxide dispersion partially determines the refinement of nano-oxide clusters in produced steel. Multiple milling parameters responsible for powders refinement are cross-correlated with each other and with steel composition and initial powder quality. These parameters include milling energy and mill type, ball sizes and the ball to powder mass ratio, milling atmosphere, milling temperature and time, oxide and metal powder sizes and etc. The interaction

of decomposed Y and O atoms and/or yttria particle remnants with alloy powders during milling is critical for the subsequent formation of refined nano-oxide clusters, though it is still unclear which particular mechanisms dominate in any particular set of milling conditions [67]. After MA, the milled powder is sealed in steel cans and degassed at elevated temperatures to prevent its oxidation. At the next step, a well-established and effective consolidation process (HIP or HE) is applied to vacuum sealed cans [56,67,68]. As an alternative, other field-assisted techniques of MA powder consolidation, such as pulsed-current-assisted sintering (SPS), are currently under development. At milling stage, considerable energy is stored in the powder in the form of powder particle surface energy, while the sintering step reduces the total energy of the system allowing grains to remain small [59]. Both the milling time during MA step and the processing temperature at the consolidation step influence the grain and nano-oxide size in the final material. Extrusion and HIP at lower temperatures sometimes result in finer and more uniform grain sizes [59]. Consolidation temperatures typically range from 850°C to 1150°C. Extruded ODS steels display anisotropic grain morphology and crystallographic texture [59,67]; whereas HIPped ODS steels typically exhibit more random initial texture and equiaxed grain morphology. The structure anisotropy of the as-extruded steels have a direct effect on the mechanical properties; in particular, in ferritic ODS steels the transverse direction is less ductile than the extruded one [59]. Different post-consolidation thermo-mechanical treatments (TMTs) such as annealing, hot and/or cold rolling and etc, have been developed to avoid anisotropic grain structures and texture in order to improve ductility and fracture toughness, while retaining high strength and thermal stability [56,59,60,67,68]. Particular regimes of TMT depend on steel composition.

While well-controlled PM/MA routes are widely used in laboratory scale production of ODS-steels, their implementation at the industrial scale is limited by high costs and time expenses. Complementary and alternative fabrication routes of ODS steels are reviewed in Ref. [67].

Elemental compositions of ODS steels are designed to combine high temperature mechanical properties with corrosion resistance and radiation tolerance. Typical ODS steels alloying elements are C, Cr, W, Ti, Y, O, Mn, while Si, P, S and Ar are often traced as impurity elements [70]. Typical alloy compositions are collected in Table 1.2. The matrix phase composition of ODS depends strongly on the elemental content of the material, e.g. the amounts of ferrite and austenite stabilizing elements, first of all, C (austenite stabilizer) and Cr (ferrite stabilizer) [56,59,68] (see Fig. 1.7). Carbon is a key element for the formation of martensite and the main component of the most common carbides that contribute to precipitation strengthening. Chromium content exceeding 10 wt.% improves steel corrosion resistance, but in steels with 12 wt.% of Cr the formation of δ -ferrite phase occurs, which lowers fracture toughness. Suppression of δ -ferrite formation by adding C or/and Mn leads to extensive formation of $M_{23}C_6$ carbides or χ -phase under irradiation, implying potential risks of fracture toughness and embrittlement, respectively. Two major versions of *bcc* Fe-based ODS steels are (i) low-carbon ferritic ODS steels with 12-20%Cr and (ii) ferritic-martensitic ODS steels (F/M ODS) containing 9-11 wt.% Cr and ~0.1 wt.% C.

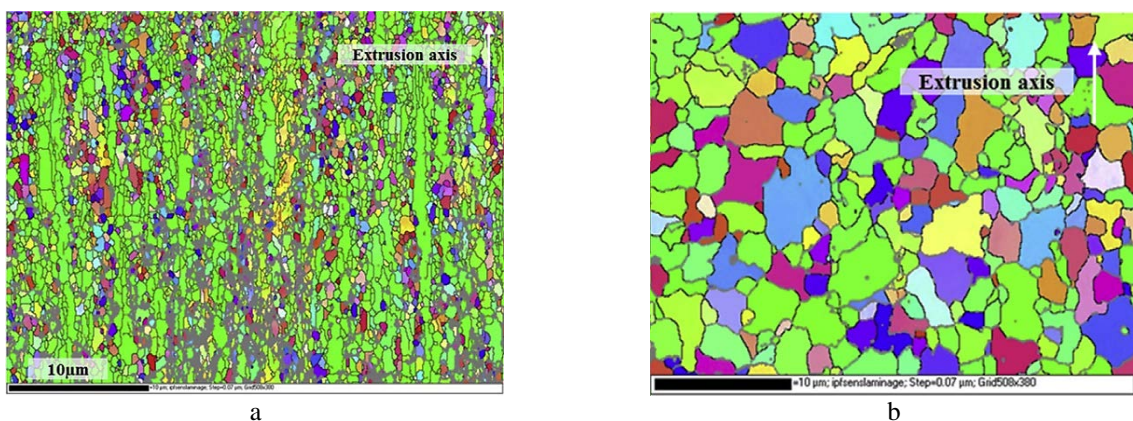


Fig. 1.7. Electron backscatter diffraction (EBSD) maps of a ferritic Fe-14Cr ODS alloy (a) and F/M Fe-9Cr ODS alloy (b) after hot extrusion [56].

Table 1.2. Examples of nominal key element contents (in wt.%) for ferritic (F) and F/M ODS steels (balance Fe with other elements at < 0.5 wt%) [59].

Alloy	Cr	W/Mo	Ti/Al	Y ₂ O ₃ /Y/O	C
MA957 (F)	14	-/0.3	1/-	0.25/-/-	0.01
12YWT (F)	12	2/-	0.3/-	0.24/-/0.09	0.06
15YWT (F)	15	2/-	0.2/4	0.35/-/-	0.03
14YWT (F)	14	1/-	0.4/-	0.3-0.6/-/-	0.02
NFA-1 (F)	14	3/-	0.3/-	-/0.2/0.125	0.03
ODS-EUROFER (F/M)	9	1.1/-	-/-	0.3-0.5/-/-	0.11
9Cr ODS (Japan) (F/M)	9	2/-	0.2/-	0.35/-/-	0.13
9Cr -ODS (France) (F/M)	9	1/-	0.2/-	0.3/-/-	0.1

Ferritic ODS steels have a single *bcc* phase up to their solidus temperature, staying outside the Fe-Cr γ -loop; in F/M ODS steels with 9-11% Cr there is reversible $\alpha \leftrightarrow \gamma$ transformation above 800-850°C. A typical F/M ODS steels heat treatment is similar to conventional F/M steels and includes austenitization at ~1050°C (in the γ -phase region), followed by cooling at slow or fast rates to produce different final microstructures, *bcc* α -ferrite or *bct* martensite, respectively and tempering at ~750-800 °C. In contrast to conventional steels, the grain size in ferritic-martensitic ODS steels remains nearly unchanged during austenitization even if the austenitization temperature increases up to 1300°C [56,68,71]. The major reason for the stable grain size is strong pinning (blocking) of austenite grain boundaries by nano-oxides. Slowly cooled ferritic steels are weak and hence the heat treatment of F/M ODS steels are selected so as to produce alloys with tempered martensite structure, which exhibits high strength and radiation resistance. In F/M ODS steel, the formed martensite morphology can be free of laths because martensite laths have not enough space to form within small grains of prior austenite [56,68,72]. Tempering of austenitized and quenched F/M steels results in additional formation of Cr-based carbides, hardness reduction and toughness improvement. Although microstructure of F/M ODS steel is basically tempered martensite, it has been shown [56,68] that heat-treated F/M ODS steel often exhibit a dual-phase structure consist of tempered martensite and residual ferrite. The main reason of residual ferrite formation is the incomplete reverse $\alpha \rightarrow \gamma$ transformation during the austenitization as a result of blocking of ferrite/austenite interfaces by nano-oxides. According to Refs.[56,68], the formation of residual ferrite phase occurs when the pinning force of nano-oxides against the motion of the $\alpha \rightarrow \gamma$ interface (ΔG) is higher than the chemical driving force of the reverse $\alpha \rightarrow \gamma$ transformation (F). F and ΔG are determined by the interfacial energy between α - and γ -phases, the size of nano-oxides, their volume fraction and the amount of austenite stabilizers [56,68]. For a particular case of 9Cr-ODS steel, the condition $F > \Delta G$ is satisfied, when Y₂O₃ content exceeds 0.35 wt.% [56,68,73]. Investigation performed on EU batch ODS-EUROFER with slightly lower Y₂O₃ content (0.3 wt.%) [74] has revealed that even though coarse regions morphologically similar to residual ferrite had appeared in the steel microstructure, they underwent martensitic transformation and corresponded to zones not mechanically alloyed with Y₂O₃, rather than to residual ferrite. The absence of residual ferrite was also reported in 9Cr-ODS with C content lowered to 0.012 % and Mn content increased to 1.0 % [75]. TMT of ferritic ODS steel aims to produce fully recrystallized single phase ferritic microstructure in order to reduce microstructure/property anisotropy and includes a set of annealing and cold- and/or hot-rolling processing [59]. Annealing temperature is chosen to be high enough to initiate recrystallization, but not too high to prevent nano-oxides coarsening and keep grain size small.

Similar to conventional RAFM steels, Ta and W are used as a replacement for Nb and Mo, to form relatively stable carbonitrides and provide solid solution strengthening, respectively, in both ferritic and F/M ODS steels. For the applications in aggressive corrosion environments (SCWR and LFR reactor concepts in Gen IV) ~4% of Al might be also added in ODS steels with high (>13 wt.%) Cr content to improve corrosion resistance [56,59]. As mentioned earlier, yttrium oxide particles are commonly used for dispersion strengthening. The low size and high number density of Y₂O₃ particles required to improve high temperature strength (and possibly to increase sink strength) of ODS steels are achieved by forced

decomposition of yttria powder at MA processing stage with subsequent re-precipitation of fine oxide particles during consolidation and annealing steps at high temperature $> 1000\text{ }^{\circ}\text{C}$. The co-addition of such elements as Ti, Al, Zr, Hf during MA processing stage can affect both nano-oxide size and number density via the influence on oxide decomposition and re-precipitation processes. The co-addition of Ti promotes the decomposition of Y_2O_3 at the MA stage and then precipitation of extremely fine and stable Y-Ti-O (typically $\text{Y}_2\text{Ti}_2\text{O}_7$, fewer $\text{Y}_2\text{Ti}_2\text{O}_5$) oxides with high density, hence significantly improving the creep strength [56,59,68]. Addition of Al results in several chemical forms of nano-oxides ($\text{Y}_3\text{Al}_5\text{O}_{12}$, YAlO_3 , and Al_2O_3) with no size and density improvement as compared to Al-free ODS steels. Moreover, aluminum addition results in an inhomogeneous dispersion of oxide particles and the reported mixed oxides have tendency for coarsening upon heating, causing degradation of high temperature mechanical strength [59,68]. Addition of Zr instead of Ti was also considered but the particles were found to be not as stable as (Y,Ti) nano-oxides [56]. However, additions of Hf or Zr help to refine the oxides in Al-containing steels [59,68]. Not only nano-oxide size and density are responsible for the ODS steel properties but also their compositions and structures.

Often nano-oxides maintain crystalline coherency or partial-coherency with ferritic matrix and a number of orientation relationships (OR), typically cube-on-cube and cube-on-edge, have already been described in the literature for Y_2O_3 and $\text{Y}_2\text{Ti}_2\text{O}_7$ [56,59,68]. The nano-oxide ORs are of interest because they affect interface energies, misfit strains, defect structures and consequently nano-oxides interaction with point defects, secondary gas impurities and dislocations. Atom probe tomography investigations reveal that along with well-formed near stoichiometric nano-oxides, a large number of coherent solute clusters or transition phases with Y, Ti, O, Cr and Fe is typically present in ODS steels [59,76].

Since nano-oxide coarsening or dissolution would reduce their beneficial contribution to alloy performance, the thermal stability of nano-oxides is a critical issue for ODS steel application in the in-service environment. A number of thermal stability studies on various ODS steels have been performed over a wide range of temperatures and times. The results for high Cr ferritic steels are summarized in Ref. [59]. In NFA steel, nano-oxides were found to be stable below $\sim 950\text{ }^{\circ}\text{C}$, while above $1200\text{ }^{\circ}\text{C}$ coarsening occurs rapidly within few to hundreds hours. However, nano-oxide stability in NFA steels depends on consolidation temperature during production: the lower is the consolidation temperature, the higher coarsening probability. Thermal stability study of ferritic steel MA 957 reveal that nano-oxides are resistant to coarsening up to temperatures in excess of $900\text{ }^{\circ}\text{C}$ for annealing times up to 32 000 h and up to $1300\text{ }^{\circ}\text{C}$ for 24 h thermal exposures [29,59]. Data on thermal stability of nano-oxides in ferritic-martensitic ODS steels (NMS) are relatively limited. Thermal stability of Y_2O_3 and Y-Ti-O oxides was confirmed up to $800\text{ }^{\circ}\text{C}$ during 4000 h and to $700\text{ }^{\circ}\text{C}$ during 10000 h in ODS-EUROFER [77] and 9Cr ODS [78], respectively. At the same time, notable coarsening of Y_2O_3 particles occurs in ODS-EUROFER after 8 h at $1350\text{ }^{\circ}\text{C}$ [79]. In fact, most of the thermal stability studies reach similar conclusions: thermal coarsening of nano-oxides will be negligible in both ferritic and ferritic-martensitic steels under the proposed in-service temperature range $\sim 600\text{--}900\text{ }^{\circ}\text{C}$, though some minor changes, e.g. in Ti/Y ratio and coherency state of the oxide-nanoparticle matrix interfaces, possibly occur for some steels [59].

As far as mechanical properties of ODS steels are concerned, the optimization of elemental composition and TMT make it possible to attain high tensile and thermal creep strengths with suitable ductility and fracture toughness [29,49,56,59,68]. Fig. 1.8 provides data on thermal creep strength of ODS steels, as well as conventional F/M and RAFM steels at $650\text{ }^{\circ}\text{C}$. It is obvious that both ferritic ODS and F/M ODS steels have superior high-temperature thermal creep strength compared to conventional F/M and RAFM steels.

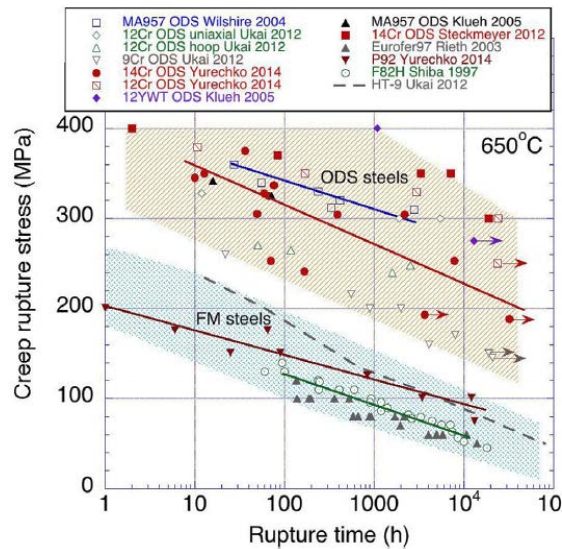


Fig. 1.8. Comparison of the thermal creep behavior at 650 °C for ODS steels versus conventional F/M and RAFM steels [29].

Some quantitative difference in creep strength values of ferritic ODS and F/M ODS steels is related to their microstructure. Due to their isotropic structure, F/M ODS steels have approximately isotropic creep properties; while in ferritic ODS steels the strength is higher in the extrusion direction. The best versions of F/M ODS steels have comparable, or slightly better, creep strengths than ferritic ODS in transverse orientations, while for the most favorable orientations of ferritic ODS steels the creep strengths are much higher than for F/M ODS [56,59,68]. The highest achieved creep strength and corresponding creep rupture lifetime at a given stress are nearly 3 and 1000 times higher for ferritic ODS steels than for conventional steels [29].

The choice of ferritic or F/M ODS steel version depends on a particular application, i.e. temperature, stress, neutron spectrum and dose, as well as the presence of corrosion environment. F/M ODS steels are well suited for application below 700 °C in order to maintain the tempered martensitic structure, while ferritic ODS steels can be used up to temperature exceeding 800 °C and their high Cr content is potentially more favorable for applications in corrosive environment. But although ferritic ODS steels allow higher application temperatures and high-temperature creep strength, F/M ODS steels also have important advantages, in particular:

(i) the microstructure of F/M ODS steels can be easier controlled by reversible α - γ transformation as compared to irreversible recrystallization of ferritic ODS steels. This allows, in particular, much easier fabrication and relatively isotropic mechanical properties;

(ii) F/M ODS steels generally demonstrate more favorable fracture toughness properties, e.g. lower DBTT and higher upper shelf fracture energy;

(iii) with respect to irradiation resistance, very high point defect sink strength in F/M ODS steels is associated not only with nano-oxides presence, but also with essential fine-scale hierarchical features (high-angle and low-angle grain boundaries, etc.) tolerating less strict control of nano-oxide size and number density. In addition, low Cr content (8-10 wt.%) prevents α' phase formation and the accompanying reduction of fracture toughness at high neutron doses.

Generally, small grain size, high dislocation and nano-oxides densities in ODS steels should reduce excess point defect levels and thus the related displacement damage effects in comparison with conventional F/M steels. However, to ensure the stability of microstructure parameters, nano-oxides should be not only thermal, but also radiation resistant. There is a large scatter in literature data concerning irradiation stability of nanoparticles in ODS-steels, as summarized in a recent review [80]. Both size and number density were observed to increase, decrease, or remain stable during irradiation. With respect to the crystal structure, irradiation results in the oxide/matrix interfaces to become more diffuse, faceted structures become smoother and in some cases full nano-oxide amorphization was

reported. It is also suggested that nano-oxides amorphization depends on three major parameters: the nature and size of the oxide particle, the irradiation dose, and the irradiation temperature. Typically, the probability of amorphization increases with the dose increase and the temperature decrease. Four fundamental mechanisms for nano-oxide evolution in ODS steels under irradiation were proposed: ballistic dissolution, Ostwald ripening, irradiation-enhanced diffusion, and homogeneous nucleation. The authors of Ref. [80] based on their analysis of experimental data suggest that multiple mechanisms are active in controlling irradiation-induced evolution of nano-oxides. However, the majority of studies agrees that nano-oxides are either relatively stable under both neutron and ion irradiations at elevated temperatures, or demonstrate a moderate trend to inverse coarsening [59].

Radiation resistance of ODS steels was recently investigated under single-, dual-, and triple-ion beam implantation/irradiation and fission neutron irradiation [41,42,45,81–83,85-89]. Based on preliminary irradiation studies, ODS steels manifest superior radiation resistance as compared to conventional and RAFM steels. In particular, void swelling after single-ion irradiation of ODS steels is low (<5%) up to doses of 500 dpa, while conventional FM steels exhibit good void swelling resistance up to 200–400 dpa (see Fig. 1.9).

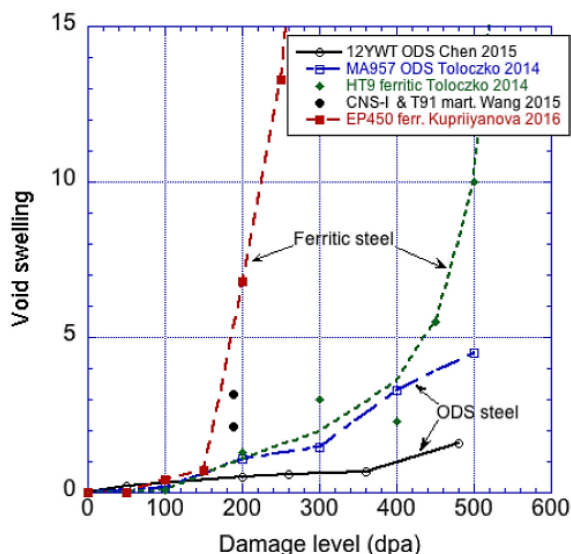


Fig. 1.9. Comparison of void swelling under single ion irradiation at 450–480°C in conventional F/M steels and ODS steels [29].

In the absence of light gases in the steel matrix, superior radiation resistance of ODS-steels is often ascribed to efficient recombination of vacancies and self-interstitials at the nano-oxide/matrix interfaces, which should reduce excess point defect super saturations and mitigate radiation damage effects [19,21]. The efficiency of nano-oxides as recombination centers depends on the efficiency of mobile defect trapping by the particles [59], which is, in turn, determined by particular interface properties and can vary for different ODS steels. Since nano-oxide number density in ODS steels is typically two orders of magnitude higher than typical void nuclei number densities at irradiation temperatures of 400–500 °C, the probability of point defect recombination at nano-oxides/matrix interfaces might also be high [29]. However, the displacement damage mitigating effect of nano-oxides via recombination has not been fully confirmed and, moreover, cavities at the oxide/matrix interfaces were observed after heavy ion irradiation without He and H [81].

As mentioned earlier, He implantation, as well as He and H co-implantation, tends to lower the incubation swelling dose. Relatively low or no swelling was also reported under synergetic influence of damage, He or He+H in ODS steels [41,42,45,59,86,87]. It is suggested that the large number of fine nano-oxides in ODS steels serves as gas impurity trapping centers and consequently prevents both void nucleation and HTIE. Significant efforts of many research groups (partially summarized in Ref. [59]) confirm the efficiency of nano-oxides in He trapping and lowering the void swelling, while information

about H interaction with nano-oxides and its influence on swelling even in conventional F/M and RAFM steels is quite limited. In addition, little is known about the resistance of ODS steels to HTIE. It should be also noted that in the available experimental datasets the achieved damage doses typically do not exceed ~50 dpa, and some indications of transition to steady-state swelling regime in the presence of He and He+H in ODS steels have already been reported [86,89]. Furthermore, introduction of fine scaled nano-oxides in ODS steels is unable to completely suppress He cavity nucleation at grain boundaries even at temperatures $< 0.5 T_M$.

ODS steel testing using ion and fission neutron irradiations cannot fully reproduce dose rates and He/H dpa ratios expected for Gen IV, spallation and especially fusion facilities, so that the microstructural evolution in simulated and in-service environments can vary significantly. Relatively different base microstructure as compared to conventional F/M and RAFM steels, as well as principally new structural components - ceramic nano-oxides embedded in the metal matrix with not well-known performance under irradiation - make direct extrapolation of swelling trends from conventional to ODS steels quite uncertain.

Summing up, the available data are insufficient to guarantee ODS steel swelling resistance for novel energy applications, especially when high levels of light gases are expected to accumulate in the steel matrix. In the absence of relevant testing devices, the best strategy for prediction of ODS steel behavior in expected radiation conditions is the investigation of physical mechanisms that govern microstructural evolution. The available literature data on He and H effects on microstructure development in F/M and ODS steels and the underlying mechanisms are discussed in more detail in the next sections.

1.4 Radiation induced swelling

1.4.1 Effects of temperature, dose, and transmutant gases on void swelling

Neutron and ion irradiations induce radiation damage in solids displacing a large number of atoms and creating both isolated Frenkel pairs and displacement collision cascades, where atoms are collectively displaced in localized regions at picosecond time scale. Once a cascade cools down, only a fraction of created displacements survives in the form of point defects. Radiation induced changes in the microstructure result from migration, interaction and agglomeration of surviving point defects, and are thus sensitive to point defect characteristics, such as formation energies and volumes, migration barriers and binding energies with other defects. In metallic alloys, including steels, vacancy formation energies are typically noticeably lower than those of self-interstitial atoms (SIAs), while their migration energies are, on the contrary, noticeably higher. As a result, measurable vacancy migration starts at much higher temperatures than that of SIAs, which are typically mobile even at cryogenic temperatures. The binding between vacancies is also generally noticeably weaker than for SIAs. If irradiation temperature is sufficiently high to promote vacancy migration, vacancies can cluster and vacancy cluster growth can lead to formation of 3-D open-volume defects that are usually referred to as cavities or voids [22]. Since vacancies and interstitials are produced by irradiation in pairs, the missing matter inside the cavities is compensated by volume expansion of irradiated material, which is called cavity swelling. Although cavity formation is only one of several phenomena leading to material volume increase under ion or neutron irradiation, the others being e.g. lattice parameter expansion and amorphization, in practical applications the term ‘swelling’ is synonymous of cavity swelling [22].

Swelling is sensitive to various parameters of irradiation, the most important being irradiation temperature, dose, dose rate and the presence of secondary gas impurities. Swelling temperature dependence is controlled by relative mobility of point defects and can be described referring to point defect recovery stages (see Fig. 1.10) as described in Ref. [22]. Below recovery stage I ($< 0.01-0.05 T_M$) all point defects are immobile and ballistic damage might induce amorphization and notable swelling, but

the effect is mostly relevant to ceramics. Starting from recovery stage I (at $\sim 0.01-0.05 T_M$), SIAs become mobile and defect-cluster swelling regime occurs at temperatures between recovery stages I and III, where vacancies are relatively immobile and only mobile SIA anneal on preexisting structural defects (such as dislocations) or precipitate in clusters, typically in the form of interstitial dislocation loops. In this temperature range swelling results mostly from point defect accumulation and clustering, but in some materials it is still accompanied with disordering. Defect-cluster swelling is mostly a problem of ceramics, where it can reach $\sim 1-5\%$, but for metals it is relatively low, $\sim 0.1\%$. At temperatures of $\sim 0.2-0.3 T_M$ (above recovery stage III) vacancies became mobile. As a result of sufficient mobility and positive vacancy-to-vacancy binding energy vacancy clustering becomes possible, enabling the development of cavity swelling, but only provided irradiation conditions are favorable for cavity growth by further vacancy absorption.

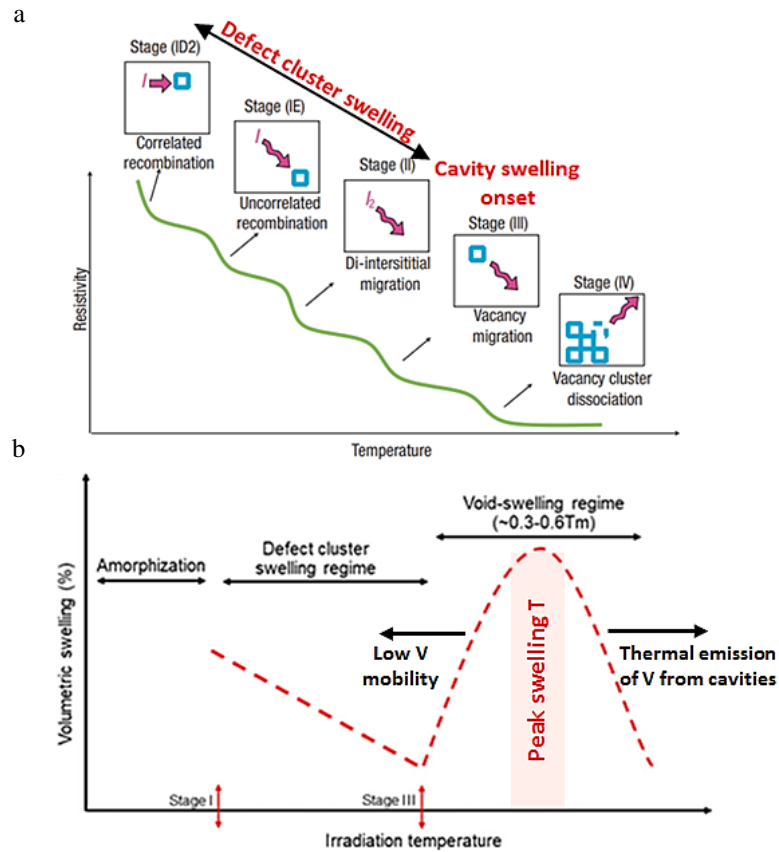


Fig. 1.10. Correlation of different swelling regimes with the point defect mobility onset temperatures. (a) Schematic representation of different recovery stages as a function of temperature and associated mechanisms proposed for electron-irradiated Fe. Labels I, I2 and squares refer to mono- and di-interstitials and vacancies. (b) A simplified representation of three main volumetric swelling regimes that most materials follow under irradiation [22].

Commonly, the cavity growth is macroscopically described in terms of kinetic rate theory approach [90–96]. According to it, cavity growth can only happen when cavity size exceeds some critical value r^* . The growth or shrinkage of an individual cavity is determined by the relation between point defect absorption and emission rates. The absorption rate of vacancies and, consequently, cavity growth are fundamentally linked to the concept of ‘bias’ [91]. Long-range elastic interaction between dislocations and point defects, being stronger for SIAs than for vacancies, makes dislocations more preferable sinks for SIAs as compared to other sink types, enabling excess flow of vacancies to other sinks with weaker preference for interstitial absorption, such as cavities and unbiased sinks. The misbalance in vacancy and SIA currents to different sinks can be conveniently calibrated in terms of effective vacancy supersaturation, which is the share of all vacancies available to unbiased sinks due to preferential interstitial absorption of SIAs at dislocations. As a result, the efficient vacancy supersaturation depends

not only on the absolute values of Frenkel pair generation rates by irradiation and the total point defect sink strength, but also on the balance of point defect sources and sinks (neutral and biased) [90–96].

For a simplistic model, where only cavities and dislocations dominate in the sink ensemble, the partitioning of vacancies and SIAs between dislocations and cavities is sensitive to the ratio of their point defect sink strengths,

$$Q = \frac{Z_{i,v}^d \rho_d}{Z_{i,v}^c 4\pi r \bar{N}_c}, \quad (1.1)$$

Where $Z_{i,v}^d$ and $Z_{i,v}^c$ are the so-called bias factors of dislocations and cavities, respectively (subscripts i and v stand for interstitials and vacancies), ρ_d is the total dislocation density, \bar{r} and \bar{N}_c are the average cavity size and cavity number density. For unbiased sinks, such as voids, $Z_{i,v}^c$ is unity, while the difference between dislocation bias factors between vacancies and interstitials can be disregarded in parameter Q . As can be easily shown, the critical radius r^* for void growth is very sensitive to the value of Q . At both high and low dislocation densities r^* is relatively large and all cavities in the subcritical size range are unable to grow. At low dislocation densities the bias for vacancies is low, whereas too high dislocation densities suppress point defect concentrations in the matrix [95]. The smallest r^* is achieved when the dislocation sink strength balances the cavity sink strength ($Q=1$).

Returning to the swelling dependence on temperature, cavity swelling in the 0.3-0.6 T_M temperature range occurs due to vacancy clustering and cavity growth. Cavity number density decreases approximately logarithmically and average cavity size increases monotonically with the increase of irradiation temperature so that cavity swelling variation with temperature follows a bell-shaped curve. At low temperatures, the low vacancy mobility, accompanied with high sink strength (due to large number of vacancy clusters and high density of radiation induced dislocation loops) suppresses vacancy supersaturation and limits the cavity nucleation and growth via a combination of sink- and recombination-dominant vacancy annihilation mechanisms [22,95]. At higher temperatures, easy vacancy emission from cavities controls vacancy currents in the cavity vicinity and limits their growth. At sufficiently high temperatures the vacancy thermal emission from cavities exceeds the inflow of radiation-produced vacancies from the bulk, so that even preexisting cavities dissolve. The maximum cavity swelling is reached at an intermediate temperature, which is typically referred to as the peak swelling temperature. For all F/M and ODS steels the peak swelling temperature falls within the operation temperature range of Gen IV, fusion and spallation facilities, so that swelling of steels can be a serious hazard for reactor operation safety.

The damage dose dependence of cavity swelling can be divided into low-swelling incubation or transient stage followed by the steady-state swelling stage (see Fig. 1.11). In some cases, swelling saturation can be expected at very high doses, e.g. for electron irradiation with surface sink, ion irradiation with injected ion effects or when void lattice formation in refractory alloys appears [22].

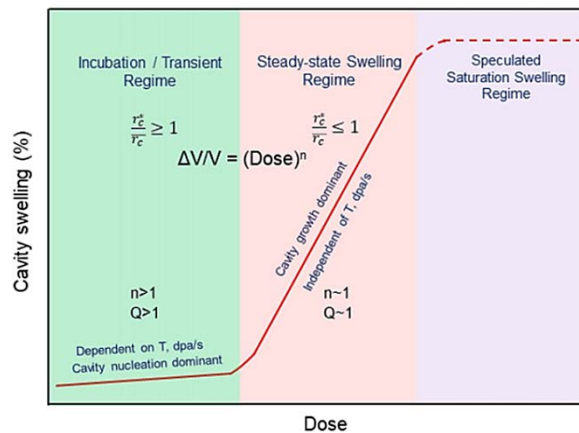


Fig. 1.11. A scheme of the cavity swelling evolution as a function of irradiation dose [22].

At each stage the dose dependence of cavity swelling can be roughly described as $\Delta V/V \propto (dose)^n$ [96]. At the incubation stage, cavity number density increases without notable increase of cavity sizes up to a threshold dose and evolution of dislocation structure takes place at the same time; the balance of sink strengths is such that $Q > 1$ and $n > 1$. The swelling rate is low and is controlled by cavity nucleation. Any factor that changes the sink strength balance and affects cavity nucleation can strongly influence the incubation stage duration. Thus, the duration of incubation period is determined by the initial and irradiation-induced microstructure kinetics, which, in turn, depends on irradiation conditions, i.e. irradiation temperature and dose rate [22,90–96]. Low temperatures and high dose rates typically prolong incubation period. The extended swelling incubation dose in F/M steels in comparison with austenitic steels is due, in particular, to higher density of point defect sinks. At a certain dose, when the cavity number density already saturates and the average cavity size becomes sufficiently large so that the cavity sink strength becomes comparable to that of the evolved dislocation structure and Q approaches unity, an accelerated bias-driven cavity growth occurs thanks to increased vacancy currents towards the cavities. As a result, cavity swelling reaches the second, steady-state stage characterized by practically linear swelling increase with irradiation dose ($n \sim 1$). Once the steady-state regime starts, high swelling values can be achieved at a relatively short time/dose scale. The steady-state swelling rate is weakly dependent on dose rate and temperature [22], but demonstrates sensitivity to material crystal structure. In particular, for ferritic or F/M steels with *bcc* crystal structure it is typically lower (~ 0.2 %/dpa) than for *fcc* austenitic steels (~ 1 %/dpa).

Dose rate effects on swelling are investigated worse than temperature and dose influence. However, it is generally accepted that the increase in dose rate shifts the peak swelling temperature to higher values and prolongs the incubation stage.

Irradiation resistance of materials is characterized by the duration of the incubation stage and, to a less extent, by swelling rate in the steady-state regime.

1.4.2 Helium effects on swelling

1.4.2.1 Helium bubble nucleation and growth

Helium is badly soluble in metals, including iron-based alloys. Due to low migration energy of ~ 0.02 eV [97], interstitial He diffuses easily in *bcc* iron. The accumulation of He in steels in reactor environment is always accompanied with displacement damage. Helium-to-vacancy binding energy largely exceeds vacancy-to-vacancy binding energy in *bcc* iron. In particular, for He atom trapped in a single vacancy the binding energy is estimated to vary within 2.3–3.7 eV [97–100], while binding energy between vacancies in *bcc* Fe does not exceed 0.3 eV [97]. Interstitial He atoms are easily trapped by vacancies and form He_nV_m clusters with relatively low mobility, with rare exceptions (in particular HeV_3 clusters are expected to be highly mobile [101]). Therefore, introduction of He into *bcc* Fe-based alloys promotes vacancy cluster stabilization. For small He_nV_m clusters, the He binding energy depends on helium-to-vacancy ratio and decreases from ~ 3.7 eV as n/m increases, but does not fall below ~ 1.8 eV even for unrealistically high ratio of $n/m = 4$ [97]. In that way He_nV_m with high binding energy might act as traps for interstitial He and small He_nV_m clusters and gradually grow as bubbles, i.e. helium-filled cavities whose tendency to shrink via vacancy emission is counterbalanced by the internal pressure of captured He atoms.

Similar to voids, helium bubble growth can be described in the framework of kinetic rate theory. The model describing the kinetics of bubble growth and eventual transformation into voids was originally suggested in Ref. [91] and is sometimes referred to as the critical bubble model (CBM) [19,58,94,102]. According to it, the rate of defect annihilation or accumulation at sinks is given by

$$R_{i,v} = D_{i,v} X_{i,v} Z_{i/i,v}, \quad (1.2)$$

where i and v denote vacancies and SIAs, D is the defect diffusion coefficient, X - the atomic defect fraction (concentration), and Z_i - the total defect sink strength (in m^{-2}). The total defect sink strength is a sum of individual sink strengths, $Z_i = \sum_j Z_j$, where $j=d, i, c$ for dislocations, incoherent precipitate/grain boundary interfaces, and cavities, respectively. The strengths of spherical sinks (cavities and incoherent precipitates) for both vacancies and SIAs are approximated as $Z_s \approx 4\pi r_s N_s$, where r_s and N_s are the average sink radius and number density, respectively. Dislocations are described as interstitially biased sinks with the strength $Z_d \approx \rho_d$ for vacancies and $Z_d \approx (1+B)\rho_d$ for SIAs, where ρ_d and B are dislocation density and bias factor, respectively. At a quasi-steady-state, the primary defect generation rate G is exactly balanced by the rate of point defect loss through different channels, including recombination, annihilation and accumulation at sinks. Ignoring recombination, which is always a good approximation close to the peak swelling temperatures, one gets $D_j X_j = G / Z_{ij}$. Assuming that the defect sinks are limited to cavities and dislocations, the excess flow of vacancies to neutral sinks (cavities) is [58,102]

$$D_v X_v - D_i X_i = (\eta B G Z_d) / \left((Z_c + Z_b) (Z_c + Z_d (1+B)) \right) + D_v X_{ve}, \quad (1.3)$$

where X_{ve} is the thermal vacancy concentration that exists in the absence of irradiation and η ($\approx 1/3$ when the primary damage is produced predominantly in cascade regime) - the ratio of net vacancy to dpa production.

In the classical CBM, the main effect of He captured in the bubble on the bubble growth is the modification of the rate of thermal vacancy emission from the bubble by helium gas pressure p , which counteracts the surface tension [19,93]. The change rate of bubble radius r is described in CBM as

$$\frac{dr}{dt} = \frac{1}{r} \left(D_v X_v - D_i X_i - D_v X_{ve} \exp \left(\left(\frac{2\gamma}{r} - p \right) \frac{\Omega}{kT} \right) \right), \quad (1.4)$$

where the term $X_{ve} \exp \left(\left(\frac{2\gamma}{r} - p \right) \frac{\Omega}{kT} \right)$ is the concentration of vacancies in local equilibrium at the cavity surface, γ - the surface tension, and Ω - the atomic volume. Equilibrium cavity radii, separating the regions of stable or unstable bubble growth, are defined by the condition $dr / dt = 0$, which is equivalent to

$$\left(D_v X_v - D_i X_i - D_v X_{ve} \exp \left(\left(\frac{2\gamma}{r} - p \right) \frac{\Omega}{kT} \right) \right) = 0, \quad (1.5)$$

where $D_v X_{ve}$ is approximately the self-diffusion coefficient, D_{sd} . The helium pressure can be expressed in terms of the cavity size as

$$p = \frac{3Kn_g kT}{4\pi r^3}, \quad (1.6)$$

where n_g is the number of He atoms in the cavity and K - the gas compressibility factor. In an alternative form, equation (1.5) can be written down as

$$\left(\frac{2\gamma}{r} - \frac{3Kn_g kT}{4\pi r^3} \right) \frac{\Omega}{kT} = \ln S, \quad (1.7)$$

where $S = (D_v X_v - D_i X_i) / D_{sd}$ is the effective vacancy supersaturation. For a given He content, this third order equation has two real roots (see blue curve in Fig. 1.12): the smaller root is the stable bubble radius r_b and the larger root is the unstable void radius r_v^* .

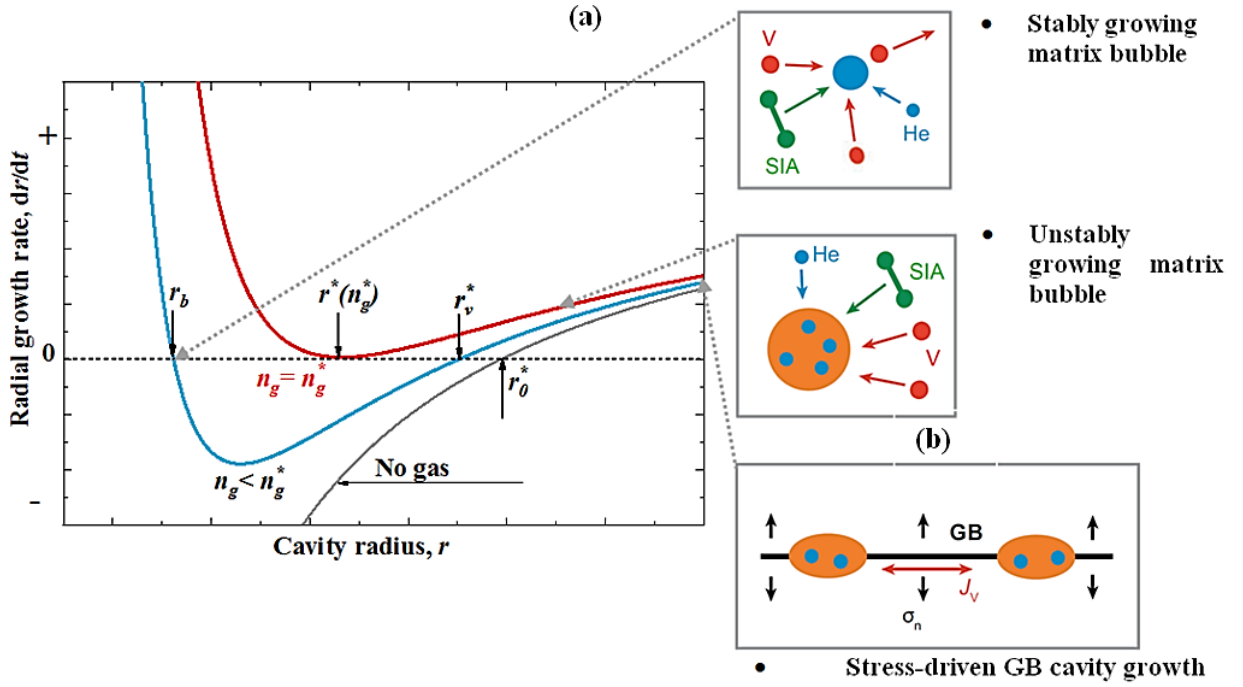


Fig. 1.12. (a) The dependence of the cavity radius growth rate on cavity radius showing stable bubble (r_b) and metastable void (r_v^*) radii for $n_g < n_g^*$, as well as $r^* = r_v^* = r_b$ condition at n_g^* . Here n_g is He content in a bubble and n_g^* is the critical number of gas atoms at which the bubble transforms to a growing void at the critical radius r^* . (b) Stress-driven growth of creep cavities formed on grain boundary (GB) bubbles. Based on [58].

With $r < r_b$, the growth rate is positive and such bubbles grow stably (r_b increases) until $r = r_b$ is reached. With the radius $r_b < r_c < r_v^*$, the bubble is unable to sustain a net vacancy absorption, the growth rate is negative and the cavity shrinks down to $r = r_b$. When He bubble size achieves $r \geq r_v^*$, the bubble does not need internal helium support any more and grows continuously in the same mode as gas-free voids or creep cavities (under grain boundary stress) by preferential absorption of radiation-generated vacancies. This scenario leads to void swelling via so-called bias-driven void growth. For comparison, the growth rate for a cavity containing no gas is shown with the grey curve in Fig. 1.12, where r_0^* denotes the critical radius. The reduction of thermal vacancy emission from cavity surfaces due to He pressure results in $r_b < r_0^*$; hence He facilitates cavity nucleation. Moreover, as shown in Ref. [90], r_0^* is about 1.5 times larger than the critical radius r^* of a cavity containing He gas and thus He makes achieving the critical radius easier.

During irradiation, mobile He atoms are captured by bubbles, so that He content (n_g) in the bubbles increases, causing the decrease of r_v^* and increasing the actual bubble size r_b . When a critical He content (n_g^*) is reached, equation (1.7) has a single root $r^* = r_v^* = r_b$, usually referred to as the critical radius for bubble-to-void transition (see Fig. 1.12, red curve). The accumulation of He beyond n_g^* leads to the situation when critical radii do not exist anymore, the bubble grows rate is always positive and the bias-driven cavity growth is unavoidable.

The ideas of the critical bubble model remain applicable not only to bubbles in the matrix, but to bubbles formed heterogeneously at interfaces as well. Quite generally, n_g^* and r^* can be written down as [102]

$$n_g^* = \frac{32F_v \theta_1 \gamma^3 \Omega^2}{27(kT)^3 (\ln(S))^2}, \quad (1.8)$$

$$r^* = \frac{4\theta_2 \gamma \Omega}{3kT \ln(S)}, \quad (1.9)$$

where θ_1 and θ_2 are corrections for non-ideal gas behavior and F_V -the shape factor that equals $4\pi/3$ for a spherical bubble/void in the matrix or less for heterogeneous nucleation at interfaces. Both n_g^* and r^* are affected by the matrix-cavity interface energy, stress fields at the bubble site and the vacancy supersaturation (S). Tuning these parameters by microstructure tailoring provides opportunities to keep $r < r^*$ in order to control bubble development and the vacancy flux required for continuous growth of voids. S can be related to D_{sb} , Z , G , B , and various sink strengths during the incubation period

$$S = \left((\eta GBZ_d) / \left((Z_b + Z_d)(Z_d(1+B) + Z_b) \right) / D_{sd} + 1 \right). \quad (1.10)$$

In simple terms, the incubation dose ϕ^* (in dpa) needed to form a large population of growing voids is [58,102]

$$\phi^* \approx \frac{10^6 \Omega n_g^* N_b}{He / dpa}, \quad (1.11)$$

where N_b is the number density of bubbles. High N_b increases ϕ^* via increasing the neutral sink strength, thus decreasing S , and partitioning of He to more numerous bubble sites.

Mobile He can be trapped not only by vacancies in the matrix but also on dislocations, at precipitate interfaces, and in grain boundaries (GBs), so that He bubbles can nucleate and grow in association with these microstructural features. Generally CBM treatment for He bubble evolution can be applied for all mentioned bubble populations. In particular, for the He-filled cavities at grain boundaries the stress-induced cavity growth rate which can promotes HTIE is [102]

$$\frac{dr}{dt} = \frac{D_{gb}\delta}{4\pi r^2} \left(1 - \exp \left(\left(\frac{2\gamma}{r} - p - \sigma \right) \frac{\Omega}{kT} \right) \right), \quad (1.12)$$

where D_{gb} , δ and σ are the GB diffusion coefficient, GB thickness and the tensile stress normal to the grain boundary, which generates a flux of vacancies to boundary cavities, respectively. Similar to He bubbles in matrix, bubble-to-void conversion may take place in case if the vacancy absorption at the grain boundary is suppressed; critical cavity radius and He content for He-filled cavity at GBs are

$$n_g^* = \frac{32F_V\pi\gamma^3}{27kT\sigma^2}, \quad (1.13)$$

$$r^* = \frac{0.75\gamma}{\sigma}, \quad (1.14)$$

This treatment can also be modified to account for a real gas equation of state.

In order to correctly predict swelling behavior of steels via multi-scale models of He transport and redistribution taking into account steel structure and chemical content, temperature, dose, dose rate, and the He/dpa, the model variables should adequately parameterized, calibrated and validated through the comparison of estimated and experimental results.

One of the conclusions of CBM is the prediction that only a part of bubbles in the material convert into voids, namely those that reach the critical radius first. When the number density of voids grows, the effective vacancy supersaturation falls down and the critical radius increases, precluding the bubble-to void transformation for remaining bubbles. As a result, a characteristic feature of helium driven void nucleation is the formation of bi-modal cavity size distribution, where relatively large void-like cavities coexist with the high density of comparatively small gas bubbles. Experimental observations of bi-modal cavity size distributions composed by growing voids and stable bubbles are quite common for austenitic steels in situations, where He is introduced together with ballistic damage; see Ref. [102] and references therein. In contrast, the microstructure of F/M and especially ODS-steels is favorable for nucleation of very high number density of stable He bubbles due to He trapping at multiple pre-existing microstructural features, so that the bubble-to-void conversion and bi-modal cavity distribution formation in these steels is expected to be much less common. Nonetheless, bi-modal cavity distributions, indicating the onset of uncontrolled steady-state swelling, were reported for ion and neutron irradiated F/M steels HT9 [38,47,103], Fe-9Cr-6Mo steel [40], Fe-14Cr [41], 9Cr-2WVTa [89], EUROFER97 [104,105],

F82H [106,107] and some ODS steels [89,108–110]. Examples of such bimodal cavity structures are shown in Fig. 1.13(a,b).

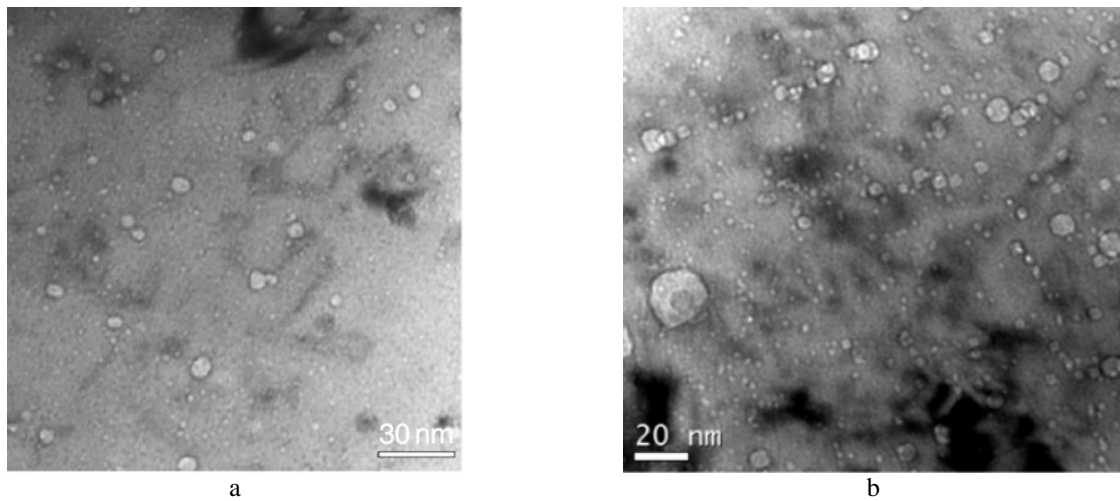


Fig. 1.13. Bimodal cavity distributions in: (a) F/M steel F82H spallation proton-neutron irradiated to 20.3dpa/1800 appm He at $\sim 400^{\circ}\text{C}$ [102] and (b) ODS steel 14YW neutron irradiated to 21.2 dpa/1230 appm He at 500°C [108].

In some cases [102,107,108,110], larger cavities were associated with precipitate/matrix interfaces (see Fig. 1.14), rather than located in the bulk.

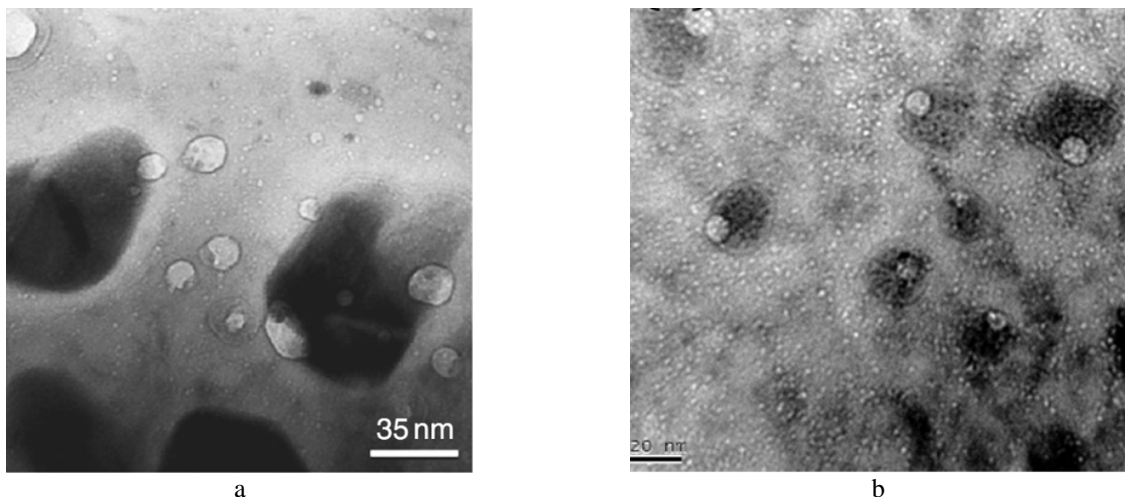


Fig. 1.14. Large cavity distribution in: (a) F/M steel F82H spallation proton-neutron irradiated to 20.3 dpa/1800 appm He at $\sim 400^{\circ}\text{C}$ [102] and (b) PM 2000 ODS steel neutron irradiated to 21.2 dpa/ 1230 appm at 500°C [108].

Multi-beam ion and neutron/He irradiation experiments indicate that void swelling in F/M steels has its maximum near $450\text{--}500^{\circ}\text{C}$ [111] and steady-state swelling onset typically requires He/dpa ratio $\sim 10\text{--}40$ appm/dpa [22]. However, the range of doses and He/dpa ratios at which bi-modal size distribution occurs in different F/M and ODS steels scatters in neutron and different multi-beam experiments, so that even at relatively close temperatures, He/dpa and doses both bimodal and unimodal cavity distributions were reported. Therefore, more systematic studies of swelling development are required for both F/M and ODS steels. In reactor studies, the flux of neutrons controls radiation damage rate, temperature, and helium generation rate interdependently, which reduces the range of possible parameters variation. In contrast, ion-beam simulation experiments present more freedom for independent parameter variation and studying the parametric dependencies of swelling. Recently, systematic investigation was performed on T91 F/M steel under dual ion irradiation over a range of temperature, helium injection rates, and damage rates [46]. It was found that the experimentally observed cavity nucleation kinetics nicely follows the

predictions of CBM except for the case of high damage rates. For the best of our knowledge, no such systematic experimental investigations have been yet published for ODS steels that have more complex microstructure. Although some advanced experimental efforts were made for 14YWT, 12YWT, MA957 and PM 2000 ODS steels in neutron *in situ* helium injection (ISHI) experiments [102], the range of variables such as He/dpa, dose rate and temperature was still quite narrow.

Although helium stipulates bubble nucleation and generally promotes void formation, very high concentrations of bubbles associated with high He generation rates can suppress swelling due to prolongation of swelling incubation time. Such behavior was reported e.g. for *bcc* Fe irradiated using self-ions to 157 dpa and simultaneously implanted with helium with either 0 or 17 appm He/dpa injection rates [112]. Notable swelling reduction from 12% to 1% was measured in the He co-injection regime. The swelling suppression occurred as a result of cavity size decrease from 60–80 nm without He to less than 10 nm for the case with He, accompanied with roughly an order of magnitude increase of cavity number density with He.

The non-monotonic dependence of cavity swelling on He/dpa ratio was discussed in Refs. [22,25,95] in terms of the sink strength ratio Q (see Fig. 1.15). As far as He/dpa ratio is small and the gas-filled cavities consume relatively small share of radiation-generated point defects, transformation of cavities to voids is suppressed by low efficient vacancy supersaturation due to high dislocation density, $Q \gg 1$. The same problem is met in the opposite case of excessively high He/dpa ratio, where large numbers of small cavities form and the sink strength becomes dominated by cavities $Q \ll 1$. Only at intermediate He/dpa ratios, where the point defect loss on evolving cavities becomes comparable to that on dislocations, there appears a chance for eventual bubble-to-void conversion and the onset of insaturable swelling.

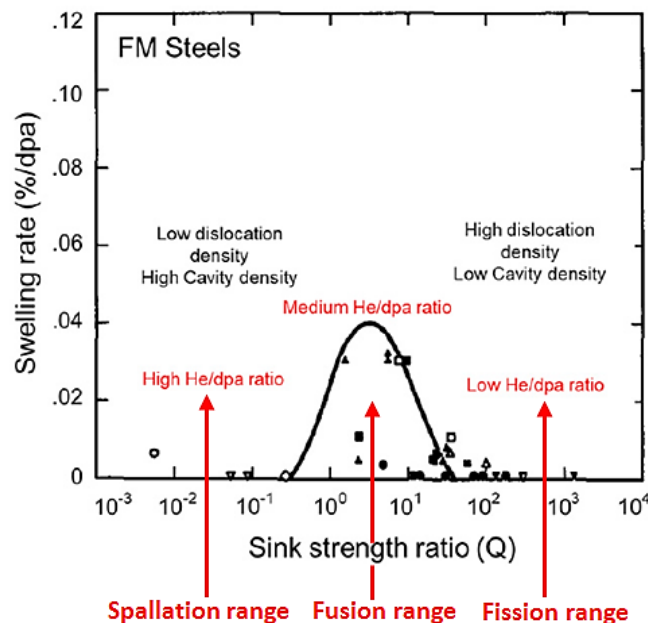


Fig. 1.15. Variation of cavity swelling rate in F/M steels as a function of sink strength ratio (Q). The areas where swelling can be suppressed by excess cavity nucleation (high He/dpa ratio) and by high dislocation density (low He/dpa ratio) are highlighted [22].

From application point of view, the most critical He/dpa ratios in terms of void swelling are expected for fusion irradiation environment, whereas in fission and spallation facilities high and low He/dpa ratios will possibly be favorable for suppression of void swelling in dislocation and cavity sink dominated regimes, respectively.

1.4.2.2 Heterogeneous nucleation of helium cavities and helium management in ODS-steels

It is obvious that at least for fusion environment with high damage rates, high temperatures and intermediate He/dpa ratio successful suppression of bubble-to-void conversion and mitigation of HTIE is the key requirement for radiation-resistant materials. Suppression of bubble-to-void conversion can be achieved in different ways, either by decreasing the sizes of He bubbles themselves or by increasing the critical size r^* that bubbles should reach for such a transition. Therefore two major pathways for suppression of bubble-to-void conversion and protection of grain boundaries from HTIE are

(i) partitioning of He between large numbers of fine-scale He bubbles via heterogeneous bubble nucleation;

(ii) misbalancing the cavity versus dislocation sink strengths ($Q \ll 1$ or $Q \gg 1$) via increasing either dislocation density or the concentration of neutral sinks. In practice, it is difficult to keep sink density low in the void swelling regime; therefore the main strategy is tailoring of radiation-stable high sinks strength microstructure.

Currently, both pathways are practically implemented in ferritic or F/M ODS steels that combine inherently swelling resistant *bcc* matrix with high number density of stable nano-oxides. Key elements of swelling resistance in a particular class of ODS steels, i.e. nanostructured ferritic alloys (NFA), in comparison with conventional F/M steels are illustrated in Fig. 1.16. The characteristics of F/M ODS alloys with martensitic or dual-phase microstructure are generally similar.

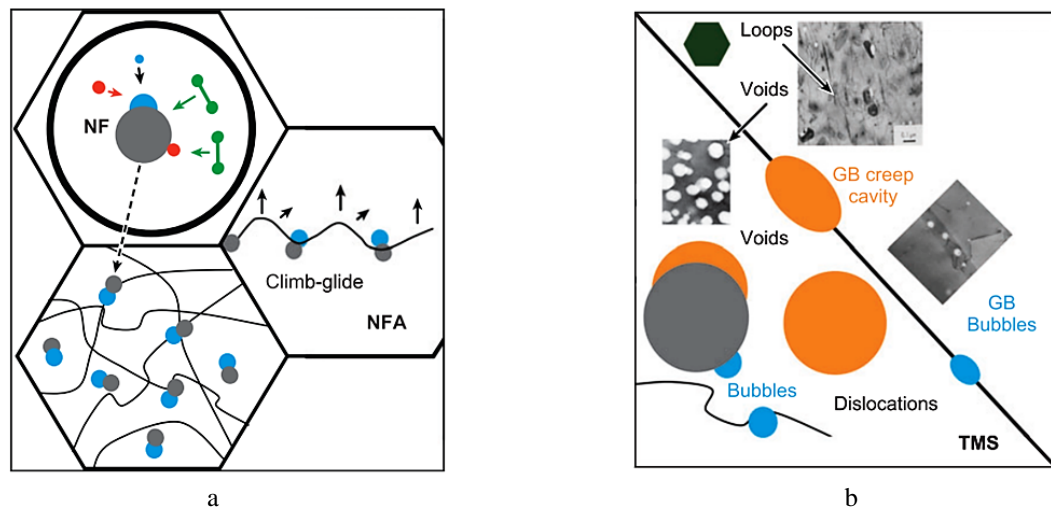


Fig. 1.16. Key elements of swelling resistance of ODS NFA steels (a) versus conventional F/M steels (b) [58].

On the one hand, additional population of bubbles on oxide particles increases the total sink strength for point defects and thus contributes to the increase of the critical transition size. However, the relative importance of this increase is not evident because ODS steels are very complex materials with high densities of other possible point defect sinks. On the other hand, the beneficial role of oxide nanoparticles is mostly attributed to their ability to act as nucleation centers for small He bubbles [41,57–59,83,85,113–116]. With a fixed He content an artificial increase of the bubble number density efficiently decreases the average bubble size and thus prevents or strongly postpones the conversion of bubbles to voids. Bubble nucleation at α -Fe/nano-oxide interfaces requires He trapping and migration, which depends on He and vacancy trapping and migration energies. These parameters depend on particular metal/oxide interface structure and chemistry. Up to now there is no well-established database on these parameters for all existing ODS related metal/oxide system. At the moment, the most fully studied are *bcc* Fe/ $Y_2Ti_2O_7$ interfaces [114,117]. The available first-principles literature data [114,117,118] suggest that solution energies of He atoms in $Y_2Ti_2O_7$ and Y_2O_3 oxides and at their interfaces with *bcc* Fe are similar

(<1 eV) and noticeably lower than inside *bcc* Fe, both in vacancy positions inside the matrix and at grain boundaries (~2 eV). In other words, He is trapped in $Y_2Ti_2O_7$ and Y_2O_3 nanoparticles and at their interfaces easier than in the steel matrix. Similarly, vacancy formation energies at Fe/ $Y_2Ti_2O_7$ interfaces are claimed to be lower than inside iron matrix or at grain boundaries. Based on these calculations, the following mechanism of He bubble nucleation was suggested for *bcc*-Fe/ $Y_2Ti_2O_7$ system (see Fig. 1.17) [114,116,117]:

(i) Helium atoms insoluble in *bcc* Fe migrate towards nano-oxides and are trapped inside nanoparticles until all the available trapping positions are saturated.

(ii) He solution energy is slightly higher at the interface than in the oxides and the trapped helium does not promote cavity nucleation. But if a bubble at the interface is nucleated e.g. via stochastic nucleation mechanism and reaches a certain size <1 nm, the He energy in the empty cavity would be lower than in the oxide, resulting in He outflow from the particle into the interfacial bubble, forcing it to grow.

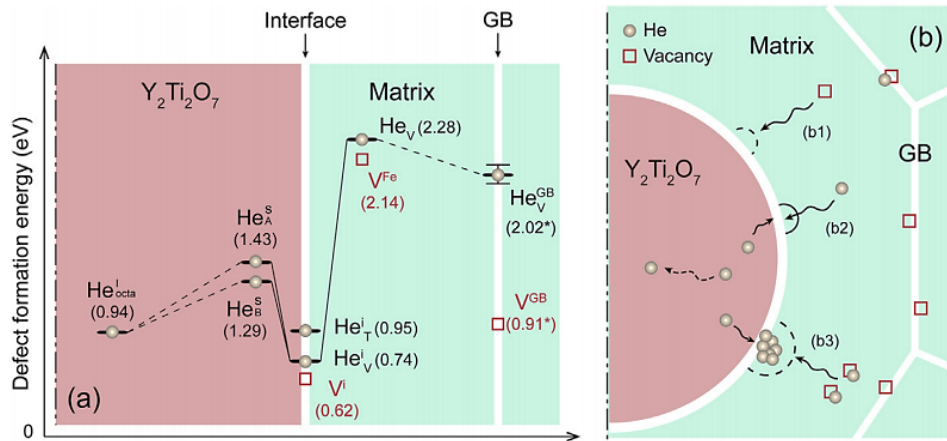


Fig. 1.17. (a) Energies of forming vacancies and trapping He at different locations in NFAs. Locations include the ferrite matrix, the bulk oxides, the oxide interfaces, and the iron grain boundaries. (b) The schematic formation of interfacial He bubbles in NFAs (ODS steel) [117].

According to this mechanism, nano-oxides with large numbers of structural vacancies that might accommodate He atoms can serve as efficient He storage places for filling interfacial He bubbles, so that quite large He concentrations can be managed in ODS steels with high oxide number density. He storage inside $Y_2Ti_2O_7$ particles is consistent with experimental observations that larger bubbles are associated with larger oxides [116]. For *bcc* Fe/ $Y_2Ti_2O_7$ system, bubbles were found to preferentially form at corner {111} facets of $Y_2Ti_2O_7$ with higher interface energy; sometimes multiple bubble formation was reported and bubble growth was observed up to ~75% of the oxide size (typically not exceeding 6 nm in the investigated 14YWT alloy) [116].

However, the proposed mechanism of He bubble nucleation at oxide/matrix interfaces is hardly universal because He and vacancy energies are very sensitive to the availability of potential residence sites at the interfaces. Such residence sites for He and vacancies can vary significantly depending on interface configuration, particle chemistry, size and structure. The chemistry of nano-oxide/matrix interfaces in commercial ODS steels is complicated and can involve segregation of Cr, V, etc. [119]. In contrast to $Y_2Ti_2O_7$ and Y_2O_3 , He solution energies in $YAlO_3$, $Y_3Al_5O_{12}$, Al_2O_3 and TiO_2 are similar to or just slightly lower than for substitutional He in *bcc* Fe matrix and grain boundaries [120], so that the efficiency of He storage inside these oxides remains an open question. In addition, bubble nucleation requires not only He trapping, but also diffusion of He atoms, vacancies and/or He_nV_m clusters. While some data is available for He diffusion in oxides [121], the knowledge of interfacial diffusion parameters is lacking. But in spite of the fact that exact mechanisms of He trapping and bubble growth at nano-oxides

remain unknown, most of the studies agree in that typically He bubble formation associated with nano-oxides is quite efficient [41,83,85,104,108,109,113,115,116,122–125].

ODS steels have, in addition to oxide particles, a variety of microstructural features. Experimental and theoretical studies suggest He affinity to grain boundaries, dislocations, prismatic dislocation loops and carbide precipitates [22,42,102,126,127]. Since all of these are also sinks for vacancies, He bubble populations generally form on all these microstructural features (see Fig. 1.18). In such conditions, relative importance of nano-oxides in development of high densities of tiny bubbles and, consequently, in suppression of bubble-to-void conversion is not obvious and depends on the overall He behavior in response to complex microstructure. The abundances of He bubble nucleation sites leads to the situation where, according to the majority of experimental studies, the effective He bubble nucleation on nano-oxides looks quantitatively different to nucleation on the other microstructural features. If bubble-to-void conversion has not yet occurred and the sizes of bubbles on different microstructural features are similar, bubble number density or fraction reflects the amount of He trapped by a particular bubble population.

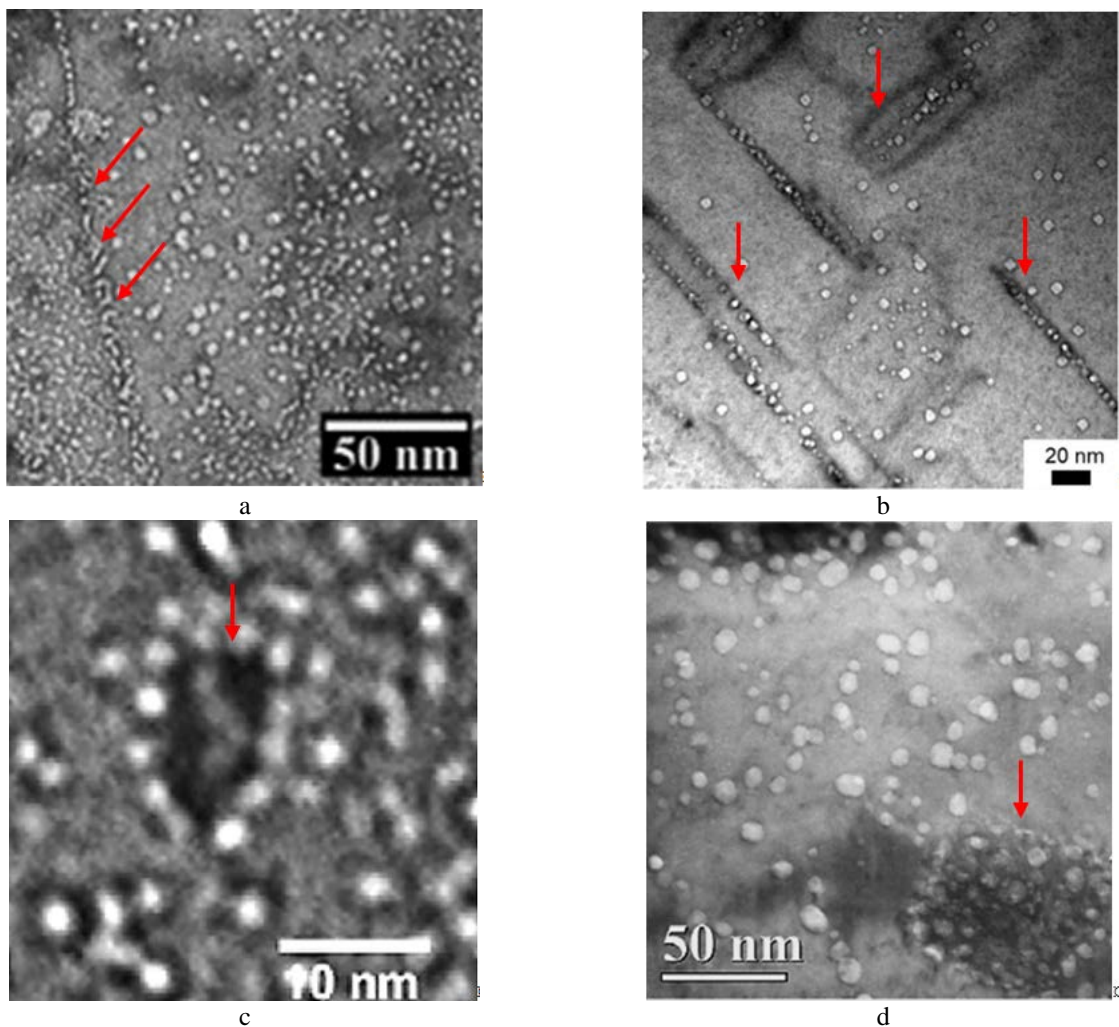


Fig. 1.18. He induced cavity nucleation :(a) at grain boundaries in 14YWT [115]; (b) on prismatic dislocation loops in ultra-high purity Fe14%Cr alloy [22]; (c) Ti(C,N) precipitate [124] and (d) $M_{23}C_6$ carbide in F82H [126].

In MA957 steel neutron irradiated to 9-25 dpa at 500 °C with ~1500 He appm (ISHI experiment) the formed nanometer-scale bubbles were found to be preferentially associated with dislocations and oxide precipitate interfaces, while grain boundaries appeared to be relatively bubble free [59,123,128]. Nearly all oxide precipitates were decorated with small bubbles. Quantitatively similar trends were observed for MA 957 and PM2000 steels dual-beam ion irradiated to higher doses of ~10-80 dpa with higher He contents of ~400-3900 appm in the temperature range 500-650 °C [85]. All oxide precipitates were decorated with small He bubbles and the density of bubbles was just slightly higher than the nano-

oxide number density. However, some grain boundary He bubbles were larger than in the matrix in MA 957 steel in ~80 dpa–3800 appm He irradiation condition. The authors of Ref. [85] tend to associate these larger grain boundary bubbles with larger nano-oxides located at grain boundaries. Some studies [41] reveal that bubble number density in K3 ODS steel after dual-beam ion irradiation at 425 °C to the dose of 10-40 dpa with 1000 appm He can exceed the number density of nano-oxides by more than an order of magnitude, still keeping bubble/oxide association level close to 100%. The major reason for such intense He bubbles nucleation is ascribed to the presences of amorphous nanoclusters (<2 nm in diameter) along with crystalline nano-oxides. In contrast, unexpectedly low fraction ~30-40% of bubbles affiliated with nano-oxides along with efficient bubble nucleation in both grain interior and at grain boundaries was detected in 9Cr and Fe-12Cr-5Al ferritic ODS steels after dual-beam ion irradiation at 650 °C to 50 dpa and ~750 appm He [125].

Bubble partitioning between microstructural components after irradiation with lower dose and higher He content differs from the results of Refs. [59,85,123,128]. The fraction of nano-oxides hosting He bubbles was found to be ~70% in ODS-EUROFER steel ion irradiated to the dose of 0.23 dpa with ~1000 appm of He [113]. In 14YWT steel after single He⁺ beam irradiation at 400 °C with ~10 dpa and ~12 at.% He, only ~49% of bubbles were associated with nano-oxides and bubbles efficiently nucleated also in the grain interior, on grain boundaries (see Fig. 1.18 (a)) and on dislocations with corresponding fractions of 20, 14 and 12 % [115]. Relatively low bubble fraction of ~4% was found on coarse carbides. Note that bubbles on grain boundaries, dislocations and precipitates had slightly different average sizes. The authors of Ref. [115] associate the formation of a notable fraction of grain boundary bubbles in particular with the presence of nano-oxides on grain boundaries. Low temperature and extremely high He generation rates can eventually inhibit any preferences for He bubble nucleation in ODS steels. In particular, RT single-beam He⁺ irradiations of F82H-ODS [129], EU-ODS EUROFER [130] and 14YWT [131] at high He fluxes suggest that microstructural features like grain boundaries, oxides or dislocations have no effect on He bubbles formation. Long-term post-implantation annealing of 14YWT at 750 °C did not change the He bubble partitioning between microstructural features, i.e. 91 %, 5%, 4% and 0.3% of visible bubbles corresponded to grain matrix, nano-oxides, grain boundaries and Ti(N,O,C) precipitates, respectively. However, the bubble growth rate varied in different bubble population during annealing; bubbles in grain boundary and nano-oxide bubble populations grew 1.5-2 times more intense. Although in all above mentioned studies He bubbles in ODS steels remained small even at quite high levels of accumulated He and the bubble size distributions were relatively unimodal without any signs of bubble-to-void conversion, the typical sizes of bubbles on different microstructural defects were different [85,115,131]. Evidently, the bubble population with the largest typical size has the largest chances to reach the critical size first. From this point of view, bubbles on oxides and grain boundaries are potentially in the group of risk.

Judging from quite limited literature data, ODS ferritic/martensitic steels have good resistance to HTIE [29]. However, relatively intense He bubble formation at grain/lath boundaries in some ODS steels saturated with high He content along with the observed reduction in creep rupture lifetime in short-term high-stress tests on Fe–14CrWTi ODS steel ion implanted with ~1000 appm He at 650 °C [132] leave HTIE probability under in-service environment an open question.

In the current literature one can find only a few reports mentioning bimodal size distribution of cavities and consequently bubble-to-void transition in ODS alloys 17Y3, 12Y1, PM2000 and 14YW [89,108–110]. Importantly, large cavities formed in PM2000 and 14YW steels neutron irradiated at 500°C to ~21 dpa with ~1200 appm He (ISHI experiment) and interpreted by the authors as voids were always associated with nano-oxides (see Fig. 1.19). It is noteworthy that cavities formed on small crystalline Y₂O₃ particles were located at the oxide/matrix interfaces, whereas internal void growth occurred in large YAlO₃ particles amorphized during irradiation. The reason for such differences remains unclear.

Generally, bimodal size distribution in swelling-favorable irradiation conditions (high T and moderate He/dpa ratio) were observed in irradiated ODS steels containing low number densities of oxide particles ($<1 \times 10^{21} \text{ m}^{-3}$). In contrast, unimodal size distributions were observed in ODS steels containing high ($\geq 1 \times 10^{23} \text{ m}^{-3}$) number densities of oxide particles. In fact, both oxide number density and size can be used for designing swelling-resistant ODS steels. As reported in Ref. [133] for ZrO_2 and HfO_2 alloyed ODS steels, He cavity sizes and swelling percentage are sensitive to variations of oxide particle size below an effective size $\sim 3.5\text{--}4 \text{ nm}$. The grain size was also suggested to be a key parameter controlling swelling behavior of ODS steels at high temperatures and He generation rates [134].

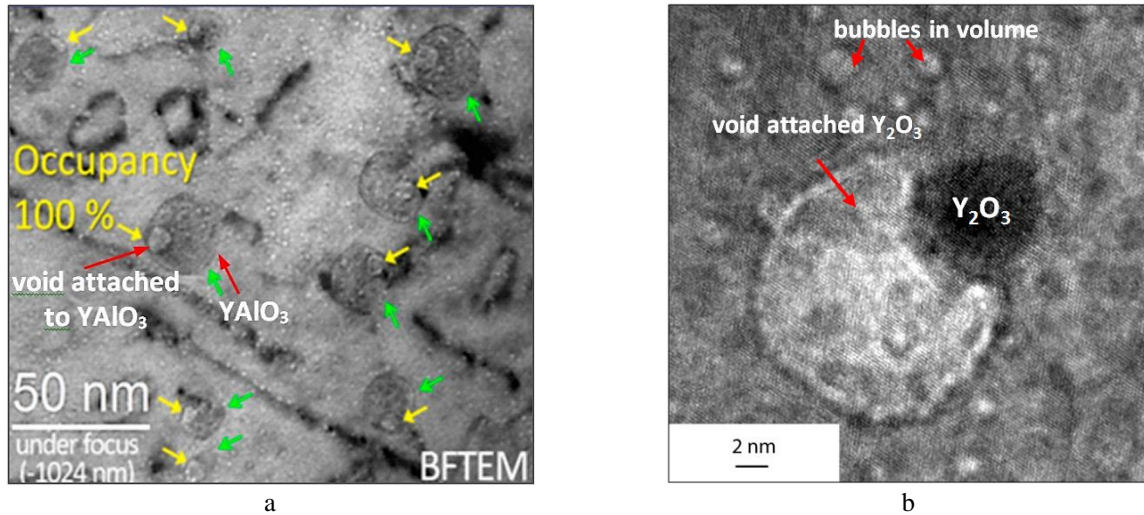


Fig. 1.19. Cavities associated with different nano-oxides in ODS steels neutron irradiated at 500 °C to 21 dpa with $\sim 1200 \text{ appm He}$: (a) amorphous YAlO_3 in PM 2000 [110]; (b) crystalline Y_2O_3 in 14YW [108].

Summing up, helium influence on swelling behavior of ODS materials is highly sensitive to both irradiation conditions and alloy design. Efficient He trapping at nano-oxide/matrix interfaces or inside nano-oxides does not guarantee efficient swelling suppression. In fact, the efficiency of this swelling mitigation strategy depends on the mechanisms of He bubble nucleation/growth at such interfaces and on overall He partitioning between all microstructural components of a particular alloy. In the case of multiple bubble formation in a manner reported for carbide- and $\text{Y}_2\text{Ti}_2\text{O}_7$ /matrix interfaces and in the absence of bubble coalescence, the concept of He trapping on nano-particles should work. However, when He atoms or/and He_nV_m clusters at oxide/matrix interfaces are sufficiently mobile and only one relatively large bubble per particle evolves, the probability of bubble-to-void conversion increases. Moreover, as noticed earlier, non-spherical bubbles on precipitates require less helium in order to reach critical parameters for bubble-to-void transition.

1.4.2.3. Helium bubble coarsening

Helium bubble coarsening typically occurs when metals are annealed at high temperatures (higher than the temperature of bubble nucleation and growth) [135–137]. At a constant He content in the material, bubble coarsening leads to increased average bubble size and reduced bubble number density. Two qualitatively different mechanisms of bubble coarsening upon annealing have been suggested in the literature:

(a) bubble migration and coalescence (MC). In the framework of this mechanism, bubble coarsening is governed by migrating bubbles. Bubble migration occurs as a result of random rearrangements of the bubble surface by diffusion of matrix atoms, preferably by surface diffusion [136–138].

(b) Ostwald ripening (OR). OR is driven by different equilibrium pressures in bubbles of different sizes. As a result of thermal activation, He atoms and/or vacancies de-trap from small bubbles and

become re-absorbed by the larger bubbles. Small bubbles shrink and even vanish to feed the larger ones [136,137].

Generally, MC and OR are expected to dominate at relatively low and high temperatures (and/or high and low helium concentrations), respectively [136]. However, the activation energy for OR mechanism is determined by the energy of He de-trapping from bubbles, which in F/M steels is much higher than that for MC mechanism, so that in these steels Ostwald ripening of He bubbles looks highly improbable. In practice, only MC mechanism was confirmed experimentally.

He bubble coarsening upon post-irradiation annealing was reported in *bcc* Fe-based alloys with and without oxide strengthening [129,139–141]. Direct evidence of bubble coarsening via MC mechanism was given in Ref. [139] under *in situ* annealing of *bcc* Fe and Fe–9Cr alloy in the temperature range of 650-1000°C. In *bcc* Fe-based alloys, small He bubbles were shown to perform Brownian (random) migration both in the interior of grains [139] and along grain boundaries [140]. The coarsening of helium bubbles inside a grain is dominated by simple bubble coalescence; while that at grain boundaries might be mediated by the coupling of the metal matrix interface diffusion and non-zero grain boundary fluxes [138,142]. He bubble mobility is sensitive to material microstructure, bubble size, bubble shape, annealing temperature and the presence of stress fields and pressure gradients [138,142]. In industrial Fe-based alloys with complex microstructure bubbles cannot easily move in the matrix, since there are many obstacles that prevent the movement. As a result, the mobility of bubbles in Fe–9Cr was shown to be much lower than that in pure Fe [139]. The authors of Ref. [139,140] suggest that retarded bubble motion is a consequence of Cr segregation on the bubble surface which decreases of the bubble surface diffusion. Comparison of bubble coarsening behavior between pure Fe and commercial ferritic F82H-IEA steel [129] shows the same effect as in Refs. [139,140], i.e. bubble mobility is reduced in a more complex alloy with Cr addition.

Unexpectedly, bubbles after annealing were found to be larger in ODS steel than in its non-ODS counterpart with less complex microstructure [129,141]. The authors of Ref. [129] suggest that bubble coarsening in F82H-ODS after annealing may be due to higher sink strength in comparison with the base F82H, suggesting that during the post-irradiation annealing at 650 °C relatively weakly trapped He atoms or He clusters diffuse into cavities after de-trapping from grain boundaries, dislocations and oxide/matrix interfaces. In EU-ODS EUROFER [141] the authors tend to associate higher bubble size with effect of vacancies remaining after special manufacturing, suggesting that the annealing temperature of 450 °C favors vacancy mobility and promotes creation and growth of He bubbles. However, both assumptions cannot explain the observed bubble density decrease. Summing up, neither MC, nor OR match well the results of Refs. [129,141]; thus the mechanisms of relatively intense bubble coarsening in ODS-steels under annealing treatment are not fully understood.

To the best of our knowledge, direct experimental evidence of coarsening via MC mechanism was not reported so far for *bcc* Fe-based alloys under the influence of damage/accumulation and high temperature. However He bubbles migration, coalescence, coarsening, and shrinkage were found under *in situ* irradiation of Al, Cu, Au and austenitic alloy Fe-16Cr-1 Ni [142]. The underlying mechanisms of bubble coalescence under irradiation can differ from those acting during high-temperature annealing. Two additional mechanism of bubble coalescence under high-energy ion irradiation have been suggested: displacement of matrix atoms out of the volume between two bubbles or cascade-induced migration of the bubbles [142]. Although He bubbles show random motion under high-energy ion beam irradiation, both mobility increase and decrease were reported. It is suggested that bubble motion at higher-temperature irradiation is driven by thermal motion, which is more efficient than the thermal spike effects caused by cascades.

Migration of helium bubbles along grain boundaries and interfaces can be accelerated as compared to the grain interior [138,140,142]. Thus, taking onto account relatively intense bubble coarsening in ODS-steels, in practice the phenomenon can be of concern for HTIE.

1.4.3 Hydrogen effects on swelling

Potential influence of hydrogen on swelling is far from being fully understood, but, in general terms, hydrogen can be involved in cavity nucleation, or cavity growth, or both. Hydrogen solubility in *bcc* Fe-based alloys is generally higher than that of He (~ 0.1 -1 appm between 400-600 °C) [143], but still notably below concentrations that will be accumulated in reactor in-service environment. Therefore, the absolute majority of accumulated H should be accommodated somewhere. Since H is a fast diffuser in *bcc* Fe-based alloys [144,145], in the absence of irradiation it is commonly not expected to be retained at high concentrations, especially at high temperatures typical for reactor operation conditions. However, irradiation produces in the structural steels multiple defects that are able to trap hydrogen, decrease its apparent diffusivity and results in notable hydrogen accumulation [146–148]. Potential hydrogen trapping sites in steels include e.g. solute impurities, dislocations (strain fields and core), grain boundaries, vacancies, different precipitates and their interfaces with the matrix, etc. [143,149–151]. The efficiency of hydrogen trapping depends on hydrogen binding energies to traps and the volumetric number density of trapping sites. Permeation, diffusivity and thermal desorption measurements suggest that H binding energy to the solute atoms, grain boundaries and dislocations is relatively low in the range of ~ 0.03 -0.38 eV, whereas vacancies, carbide and oxide precipitates have much higher affinity to H and their binding energy with H fall in the range of 0.35-0.81 eV.

Similar to helium, hydrogen-to-vacancy binding energy exceeds vacancy-to-vacancy binding energy in *bcc* Fe. In particular, for single H atom trapped in a single vacancy the semi-empirical molecular statics and first principal simulations suggest the binding energy of ~ 0.53 -0.56 eV, while experimental measurements show slightly wider range of 0.5-0.81 eV [151–157]. That is, though hydrogen can potentially be trapped in vacancies, its binding energy is significantly lower than that of He. Interaction of He with *bcc* Fe matrices is of a purely elastic origin, while for H atoms both elastic and chemical aspects contribute. As a result, while He prefers the central region of a vacant site, H is trapped at the periphery of a vacancy [153,158]. Up to 5-6 hydrogen (see Fig. 1.20) can be trapped at tetrahedral positions at the periphery of a single vacancy in *bcc* Fe [152–156], reducing the efficient vacancy formation energy [153,154]. As the H/V ratio increases up to 5, the binding energy of H atom to a vacancy decreases down to 0.29-0.34 eV [154,155]. Alloying elements typically present in commercial steels, such as C, Cr, Al, Ti, V, Mn, Si and etc, play a minor role when H is in the presence of a vacancy in bulk *bcc* Fe [157].

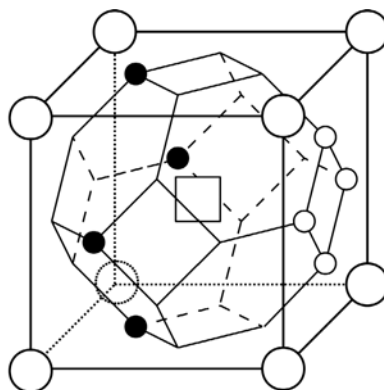


Fig. 1.20. Typical configuration of a VH_5 cluster. When 4 tetrahedral sites are occupied by H atoms (black small circles), only one of the tetrahedral sites marked with white small circles can be occupied to form VH_5 [153].

According to the literature, hydrogen can influence cavity growth via various mechanisms, e.g. plastic deformation near free surfaces (“blistering”), plastic deformation by loop punching, and H trapping in H_nV_m clusters which promotes cavity growth or coalescence [159]. As far as radiation-induced cavity swelling is concerned, the latter is the most likely scenario for hydrogen influence on bubble growth.

Molecular dynamics studies of H_nV_m cluster migration indicate that their mobility is low, except for H_mV_3 [155]. More typical is cluster dissociation that permits vacancies and H atoms to migrate separately. Hydrogen effect on the cavity growth is expected to be a consequence of H atom trapping in small H-vacancy complexes and stabilizing them against vacancy desorption so that they could grow via attraction of additional vacancies produced in the bulk by irradiation [153–155].

While both helium and hydrogen stabilize small vacancy clusters, the mechanisms of their action are different. Helium atoms are accumulated in the central part of a cluster in the form of dense gas and prevent vacancy emission from cluster exerting internal pressure on bubble walls. In contrast, hydrogen atoms preferably decorate cavity walls, while hydrogen contribution to internal pressure is relatively insignificant, if any. Hydrogen molecule does not survive in a single vacancy and, even if artificially placed in the center of vacancy in a computer experiment, dissociates to separate hydrogen atoms decorating vacancy periphery [154,155]. The same is true for small cavities, where H covers cavity facets. According to Ref. [156] H_2 molecule is unstable in vacancy clusters with the sizes lower than 5-6 vacancies. Only after a cavity is large enough and only when the cavity surface is fully saturated with hydrogen atoms, hydrogen molecules placed inside the cavity are able to survive (see Fig. 1.21). However, as shown in Ref. [160], in even in a nine-vacancy cavity decorated with 24 H atoms bond length between two H atoms remains higher than in H_2 molecule in vacuum, so that H pairs are rather weakly bound dimers than molecules. According to Ref. [160], at low temperatures the smallest H bubble in *bcc* Fe able to accommodate hydrogen molecules is a 27-vacancy cavity decorated with 54 H atoms (with the radius 0.418 nm). Similar location H in bubbles and conditions for H_2 formation were proposed in tungsten [161].

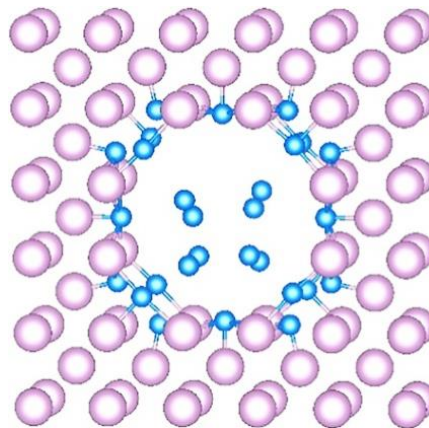


Fig. 1.21. Atomic structure of the fully H-decorated cavity in *bcc* Fe. Iron atoms are in violet, adsorbed atomic H and H_2 complexes (H dimers) - in blue [160].

At elevated temperatures and moderate H concentrations vacancy traps in *bcc* Fe can hardly be fully covered with hydrogen atoms due to relatively low binding energy of H to H_nV_m [162], so that the nucleation of H_nV_m clusters with critical size and a notable H bubble growth via direct H and vacancies collection are unlikely.

Hydrogen-promoted bubble development accompanying H^+ implantation to high doses is theoretically not forbidden and e.g. for tungsten was reported at low [163] and even elevated temperatures [164]. However, the binding energy of H to a single vacancy in tungsten is quite high (~ 1.18 - 1.41 eV [165]), so that the presence of H bubbles in tungsten even at elevated temperature is not surprising. However, the H-vacancy binding in Fe-based alloys is noticeably lower (~ 0.5 - 0.6 eV), so the formation of hydrogen bubbles should be restricted to relatively low temperatures that are not often studied experimentally. In fact, we found only a single, very recent experimental demonstration of H induced cavity nucleation in F/M Fe-10Cr steel after room temperature H^+ implantation (see Fig. 1.22) [166].

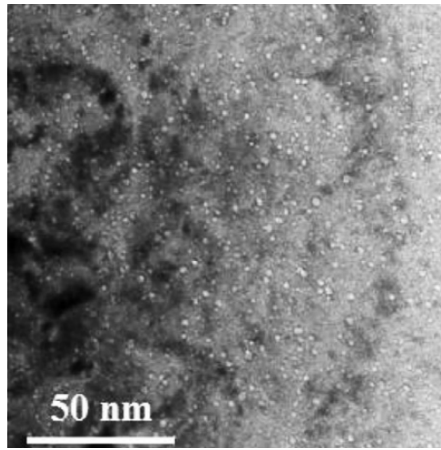


Fig. 1.22. Hydrogen induced cavities in Fe-10Cr steel after implantation with 260 keV H^+ to the fluence of 1×10^{18} ions/cm² (2.5 dpa at peak position) [166].

However, the effects of hydrogen can be more complicated than discussed above, having in mind an unusually strong effect of hydrogen introduction on swelling reported for the ferrite phase in EP 450 (12 Cr F/M) steel under simultaneous influence of damage production by dual-beam heavy ion (Cr^{3+}) and H^+ irradiation to dose 50 dpa at 480°C [84]. Fig. 1.23 shows the evolution of microstructure in EP 450 steel irradiated without hydrogen co-implantation (Fig. 1.23(a)) and with H co-injection at rates 20-200 appm/dpa (Fig. 1.23(c-d)). Cavity parameter variation depending on H/dpa ratio is shown in Fig. 1.24.

H co-injection has led to pronounced increase of cavity number density and reduction of cavity size, as compared to heavy ion irradiation only. The increase of co-injected H concentration from 0 to 1000 H appm (at 20 appm H/dpa) reduced cavity size from 17 to 8 nm, while cavity number density sharply increased from 2×10^{14} cm⁻³ to 2×10^{16} cm⁻³. With further increase of H/dpa ratio cavity parameters changed only weakly, the number density practically saturated, while cavity size slightly decreased. As a result, swelling dependence on H/dpa ratio was non-monotonic with the maximum at 100 appm H/dpa (5000 appm). Qualitatively similar results were reported in Ref. [84] for the case of He co-injection with the same damage dose and in the range of He concentrations 100-8000 appm, H tends to produce lower densities of larger cavities as compared to He. The authors explain such difference in terms of higher H mobility as compared to slower diffusing He [84]. If these experimental data are correct, they suggest a possibility of vacancy cluster stabilization by hydrogen and a notable H effect on cavity nucleation even at elevated temperature. However, in contrast to Ref. [84], in the Fe-9Cr and Fe-12Cr alloys dual-beam (Fe^{3+} (10.5 MeV)+ H^+ (380 keV)) irradiated to the same dose with H co-injection at comparable rate of 40 appm/dpa no cavities were found [45], which suggests that H has little or no effect on cavity nucleation.

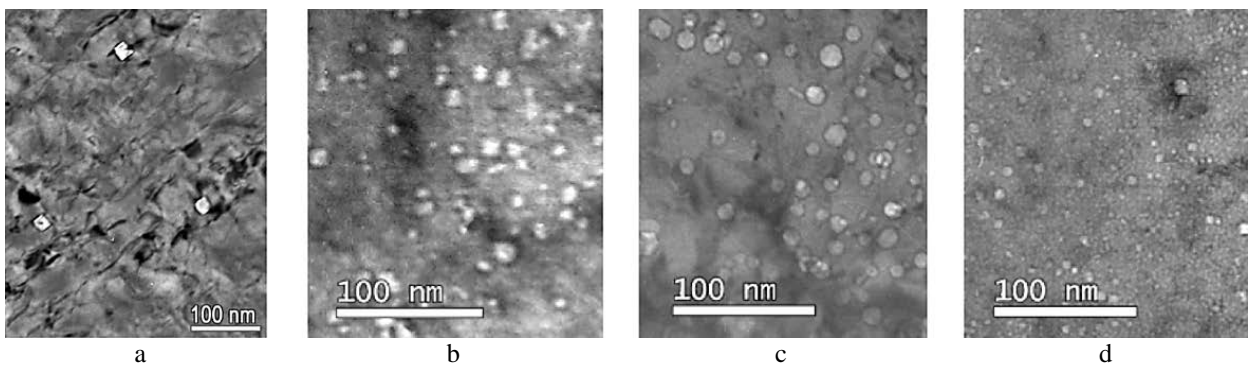


Fig. 1.23. Cavity development in ferrite phase of EP-450 steel after simultaneous irradiation at 480 °C with 1.8 MeV Cr^{3+} ions to 50 dpa and 20 keV H^+ ions at different H injection rates: (a) 0 appm H; (b) 1000 appm H; (c) 5000 appm H; (d) 10000 appm H [84].

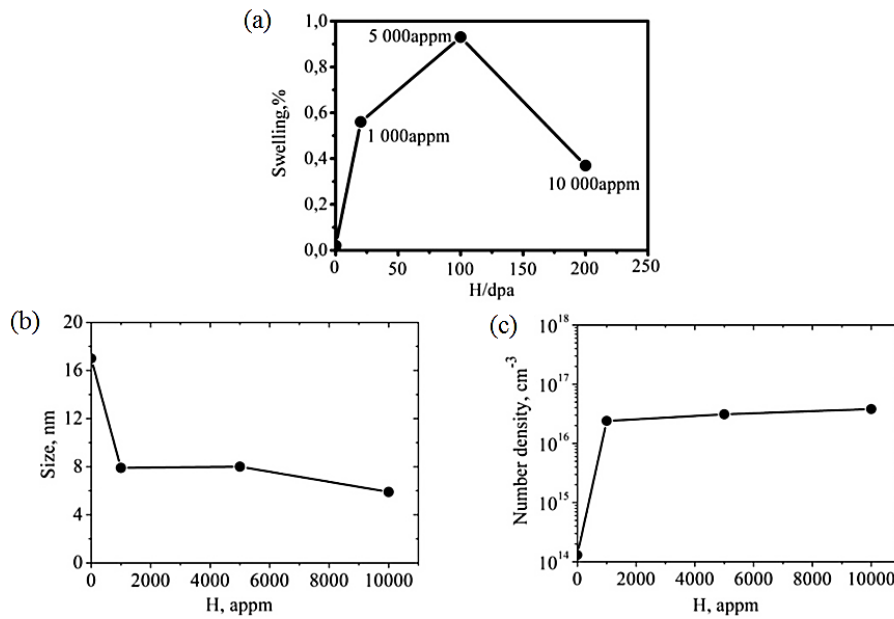


Fig. 1.24. Swelling (a) cavity size (b) and cavity number density (c) of EP-450 steel after simultaneous irradiation at 480 °C with 1.8 MeV Cr³⁺ ions and 20 keV H⁺ ions to 50 dpa as a function of H/dpa ratio [84].

In addition to homogeneous bubble formation, the possibility of heterogeneous H bubble nucleation can't be generally excluded for F/M and ODS steels, particularly because the estimated binding energies of H to precipitates such as NbC (~0.7 eV) [167], TiC (~0.48-1.12 eV) [151], Cr-based carbides (~0.69 eV) [149] and Y₂O₃ particles (~0.35-0.73 eV) [149,168] are relatively high and some H amount can be stored at their interfaces or inside precipitates themselves. Although, to the best of our knowledge, heterogeneously nucleated H bubbles have not been experimentally observed in *bcc* Fe-based or any other *bcc* alloys, the possibility of H bubbles nucleation and growth at metal/oxide interfaces was recently demonstrated for *fcc* Al [169–171]. In Al/Al₂O₃ system, H induced cavities were nucleated at the interface after hydrogen saturation at 20 °C (see Fig. 1.25 (a)). During annealing up to 200 °C cavities grew by a mechanism similar to Ostwald ripening and finally, a giant cavity appears at the metal/oxide interface (see Fig. 1.25 (b-d)).

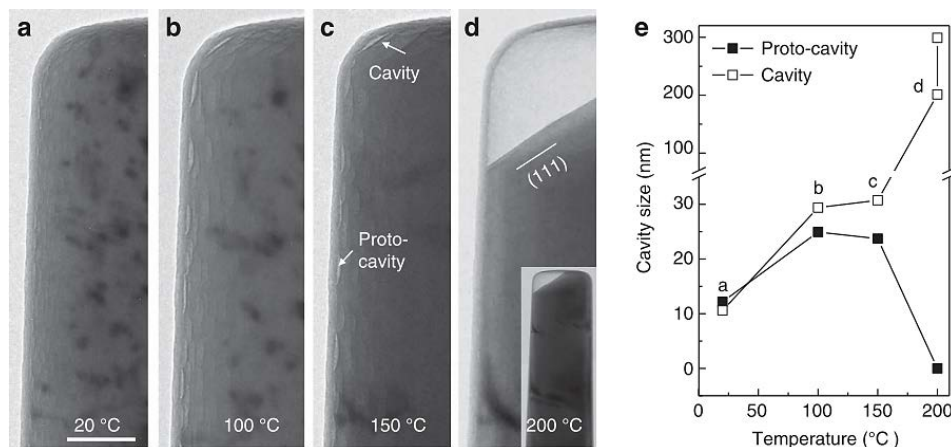


Fig. 1.25. H saturated Al/Al₂O₃ pillar at (a) 20°C; (b) 100°C; (c) 150°C; and (d) 200°C, respectively; (e) size evolution of proto-cavities and the cavity with temperature. From 20 to 10 °C, proto-cavities grow, but as the cavity on the corner begins to grow, the proto-cavities shrink. Scale bar corresponds to 100 nm [170].

Hydrogen thermal desorption and permeation investigations [168,172,173] have shown that ODS steels can accumulate more H in comparison with its non-ODS counterparts. The authors of

Refs. [168,172,173] suggest that H trapping by the Y_2O_3 nano-oxides is the main reason for such phenomena. If large enough amounts of H would be trapped by nano-oxides, similar to He case, H bubbles can be nucleated at oxide/matrix interfaces. However, according to recent first-principles calculations, the ratio between solution energies of H in oxide and Fe is opposite to that for He, that is H atom solution energies at different positions inside crystalline Y_2O_3 fall in the range of 2.4- 2.7 eV [174], while H solution energy in α -Fe is only 0.21 eV [157]. The same trend was also found for $Y_2Ti_2O_7$, Y_2TiO_5 , $Y_3Al_5O_{12}$ and $YAlO_3$ oxides [174]. Based on the reported energies, one can conclude that the majority of ODS-related oxides cannot accumulate H inside them. In that way, particle-related potential of H storage is restricted only to oxide/matrix interfaces and hence only relatively low amount of trapped hydrogen can support interfacial bubble nucleation. Although solution energies of H for the ODS-related oxide/*bcc*-Fe interfaces have not been reported in literature so far, estimated H binding energy to vacancies implies that H_nV_m may become nuclei for H bubbles formation not only in *bcc* Fe matrix, but also at the nano-oxides matrix interface.

1.4.4 Synergistic influence of helium and hydrogen on swelling

As mentioned in section 1.2, significant amounts of He and H will be generated simultaneously under fusion and spallation environment. Both gases can stabilize vacancy clusters and therefore their potential synergetic effect on swelling is of great interest.

It is hard to distinguish He and He+H effects in neutron irradiation experiments (*e.g.* on spallation facilities). For this reason, the majority of results in the literature are obtained by means of numerical simulations and imitation experiments that use sequential and simultaneous multi-beam ion implantation/irradiation.

Both first principles [175] and classical molecular dynamic (MD) [176] simulations reveal that direct interaction between He and H is negligible. Therefore, the most evident idea that a synergy of He and H influence on cavity development arises from their direct interaction can be abandoned. More reasonable seems an assumption that synergetic action of He and H is related to the fact that both gases are able to stabilize small vacancy complexes. When He and H are simultaneously introduced into iron or *bcc* steels, mixed $He_nH_mV_k$ clusters may form along with He_nV_m and H_nV_m clusters [175,176]. The binding of gas atoms in mixed clusters follows the same trends as in binary gas-vacancy clusters (see Fig. 1.26):

(i) H atoms are less strongly bound to vacancies than He atoms and the binding of both gases reduces with the increase of gas atom number in a cluster.

(ii) Helium fills the interior of clusters, while hydrogen prefers to decorate cluster periphery, whatever the cluster size.

Generally, H binding is more sensitive to He presence than *vice versa*. The strongest synergy in the He and H interaction with vacancies can be expected at relatively high n/k and/or m/k ratios. For example, when a He atom is placed into a single-vacancy based cluster He_nH_mV ($n=1-2$, $m=1-3$) in *bcc* iron, the hydrogen binding energy decreases by ~ 0.1 eV [175]. In $H_mHe_nV_6$ clusters, hydrogen has larger binding energy when He is present than in the absence of it [176].

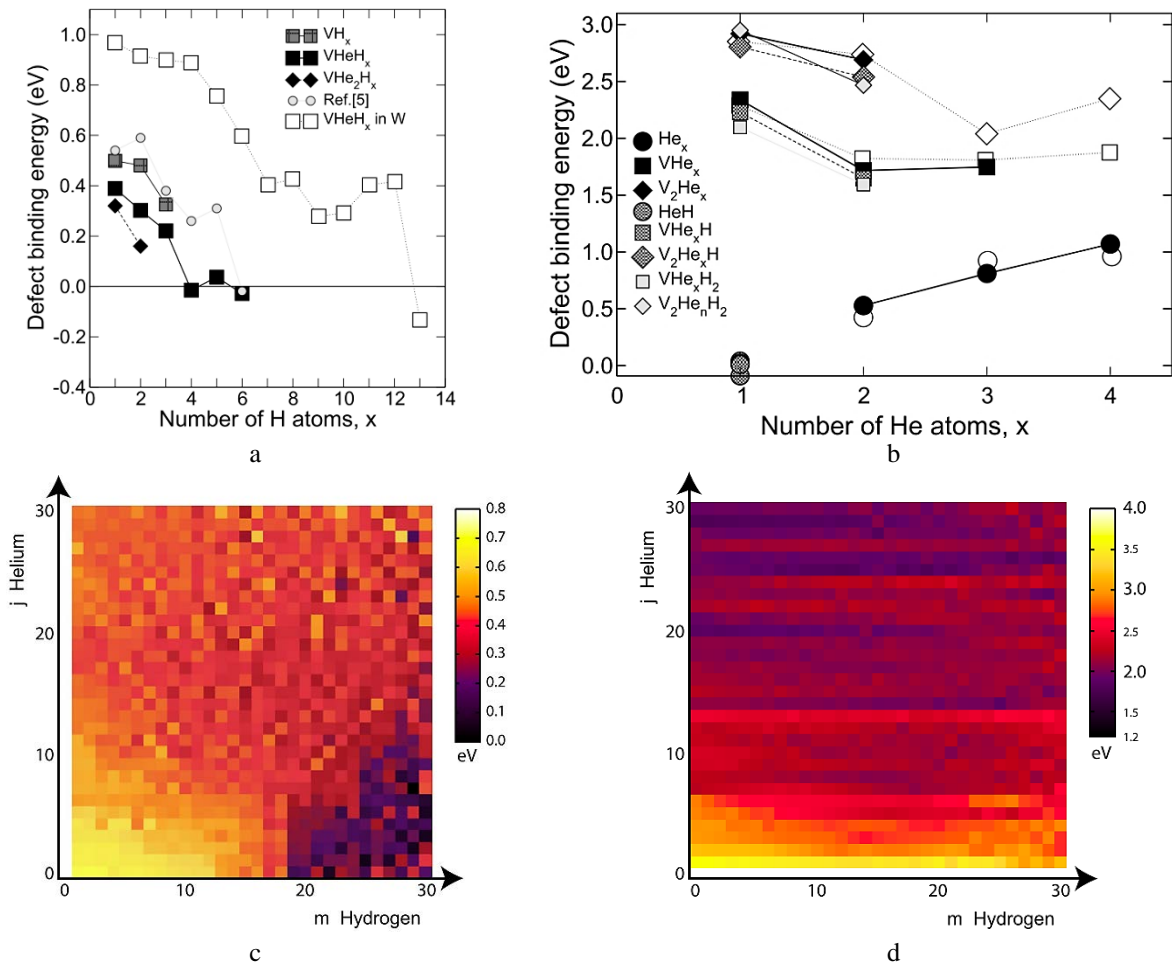


Fig. 1.26. Calculated binding energies of H and He in *bcc* Fe. (a) H to H_x and $VHeH_x$ clusters [175]; (b) He to $V_nHe_mH_p$ clusters [175], (c) H to $H_mHe_jV_6$ clusters [176], (d) He to $H_mHe_jV_6$ [176].

The authors of Ref. [176] suggest a mechanism of possible synergetic He and H action on bubble growth via forced interstitial or dislocation loop emission. It is assumed that strongly overpressurized He bubbles can eject surface atoms into interstitial positions and these interstitials might diffuse away into the matrix, while the associated increase of the cavity volume is accompanied with the increase of bubble surface that can trap more H atoms. In turn, the accumulation of H atoms at the surface reduces the energy and the He/V ratio required for interstitial emission. It is clear, however, that such a mechanism, even though not impossible, in practice it can be realized only under conditions where high He concentrations in the matrix are accompanied with very strong deficiency of vacancies that might be captured in the bubbles and relax their internal pressure in much less energetically demanding way. When bubble growth in *bcc* Fe-based alloys occurs at close to reactor in-service (i.e. elevated) temperature, continuous supply of radiation-produced vacancies and relatively moderate He generation rates of 0.3-85 appm/dpa guarantee that bubbles remain nearly under equilibrium and He/V ratio typically doesn't exceed 0.5-1 [177,178]. The internal gas pressure of equilibrium bubbles is insufficient to force SIA emission, so that the suggested mechanism is hardly of any importance in relevant situations.

In addition to theoretical considerations, H trapping at the periphery of mixed clusters or at the inner surface of He bubbles nicely agrees with experimental observations of increased H/D retention or/and the development of efficient H/D traps in *bcc* Fe [146,179] and ferritic-martensitic steels [180–183] after low (RT-350°C) temperature H injection into He pre-implanted samples. The H binding energy to He bubbles is expected to be at the level of ~0.78-0.8 eV [146,183].

The effect of additional presence of mixed $He_nH_mV_k$ clusters on the mean cavity/cluster size in *bcc* Fe-based alloys was investigated by rate theory simulations in Refs. [86,175]. Calculations up to doses ≤ 1 dpa with fusion relevant He/H/dpa ratio (~10 He appm/dpa and ~40 H appm/dpa) predict that at

450-470 °C the mean bubble/cluster diameter would be ~15-50% larger when H and He are present simultaneously, in comparison to the presence of He alone (see Fig. 1.27 (a)). The study of the effect of He/H insertion ratio on mean bubble size has demonstrated [86] that the higher is the content of He relative to H, the lower the bubble diameter. When He/H ratio exceeds 80/40, the mean bubble diameter saturates at about 1.2 nm, i.e. smaller than 1.8 nm predicted for fusion-relevant ratio of 10/40 (see Fig. 1.27 (b)).

For not too small bubbles, H might increase He bubble growth rate in two ways:

(i) H trapped at the bubble surface might change cavity surface energy and thus the efficiency of thermal vacancy emission, or

(ii) if the size of a bubble exceeds certain size, e.g. ~27 vacancies as suggested in Ref. [160], and sufficient number of H atoms is accumulated to saturate bubble surface, H might form molecules inside bubble. Molecular H would increase the internal gas pressure.

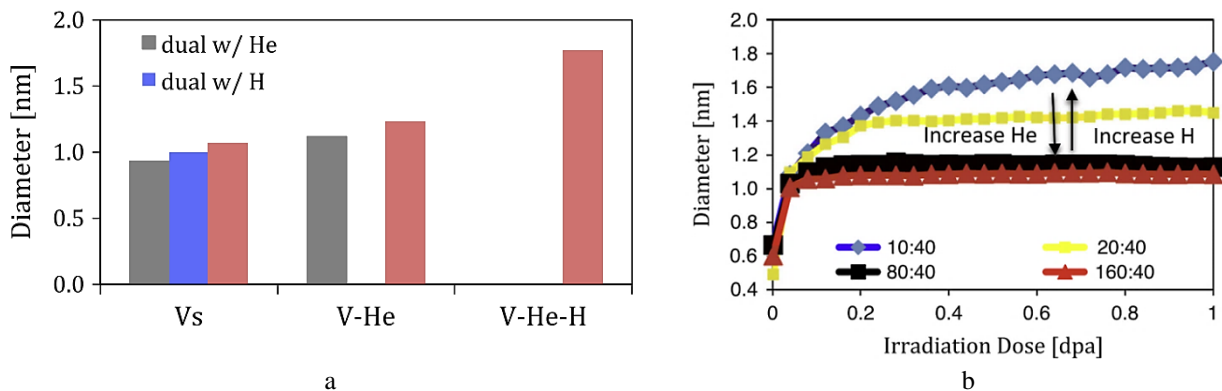


Fig. 1.27. (a) The mean bubble diameter after irradiation to 1 dpa with 10 appm He/dpa and 40 appm H/dpa at 743 K in dual and triple ion-beam irradiation conditions calculated using rate theory approach. (b) Evolution of the mean bubble diameter with dose at 743 K as a function of the He/H ratio [86].

The relative importance of these two modes of hydrogen influence on cavity growth is very different. Hydrogen binding to bubble/void surface was widely discussed in the literature on thermal-desorption and nuclear reaction analysis measurements in *bcc* Fe-based alloys (e.g. Refs. [146,183]), while there exists the only experimental investigation of H₂ molecule formation in Fe-12wt. %Cr-ODS steel irradiated at room temperature in a variety of regimes, including single-beam H⁺, dual-beam He⁺/H⁺ and Fe⁺/H⁺, and triple-beam Fe⁺/He⁺/H⁺ [184]. While atomic hydrogen was found after implantation in all samples, the presence of molecular hydrogen was demonstrated using Raman spectroscopy only in those irradiation regimes that included He implantation. For this reason, the authors of Ref. [184] associate the presence of molecular hydrogen with the cavities promoted by He atoms.

Considerable efforts were made by several research groups to experimentally simulate swelling kinetics under synergetic action of damage production and He⁺/H⁺ generation in triple ion beam (heavy ion+He⁺+H⁺) irradiation experiments [42–45,84,86,87,185,186]. As already mentioned earlier, the most critical He/dpa ratios in terms of transition to steady-state void swelling regime are expected for fusion irradiation environment. Therefore, most of the studies were performed using fusion relevant He/H/dpa ratio. Comparison of swelling of model ferritic and F/M steels after triple ion beam (self ion+He⁺+H⁺) and dual (self ion+He⁺) irradiation experiments reveals that additional H⁺ beam leads to pronounced swelling increase (see e.g. Fig. 1.28) [42–45].

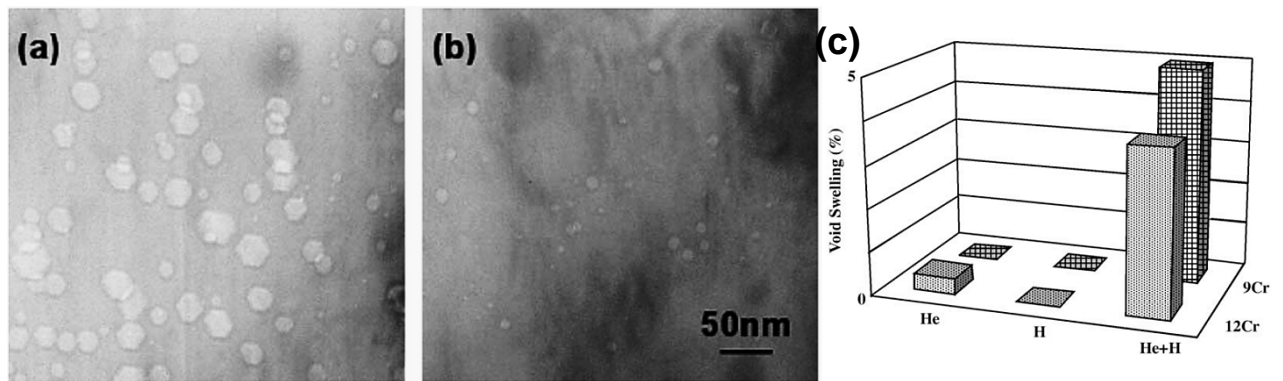


Fig. 1.28. Cavities developed in F82H steel irradiated at 470°C to 50 dpa in (a) triple ion beam regime Fe+He+H with 18 appm He/dpa and 70 appm H/dpa and (b) in dual ion beam regime Fe+He with 18 appm He /dpa, respectively [44]. (c) Swelling in 9Cr and 12Cr alloys irradiated at 510 °C to 50 dpa in triple ion beam regime Fe+He+H and in dual ion beam regimes with 10 appm He /dpa and 40 appm H/dpa [45].

The exact mechanisms of synergetic influence of He and H on swelling promotion remain unclear, but, in general terms, synergy between two gases and radiation defects (vacancies) might take place either at cavity nucleation stage, or during cavity growth, or both. The data on cavity size reported for ferritic and F/M steels after dual and triple-beam experiments at peak swelling temperature are summarized in Table 1.3.

As can be noticed in Table 1.3, at the peak swelling temperature cavity number density mostly tends to be lower after triple-beam irradiation, while cavity sizes are notably larger as compared to dual-beam regime. Such behavior implies that at the peak swelling temperature synergetic influence of radiation defects, He and H affects cavity growth rather than cavity nucleation. The notable increase of swelling and cavity size in triple-beam experiments at peak swelling temperature [42–45] was always accompanied with the development of bi-modal cavity distribution, whereas only unimodal cavity distribution was found in dual-beam irradiated samples at the same temperatures and He concentrations. The bimodal size distribution typically indicates the transition to bias-driven cavity growth and strongly suggests that additional H⁺ beam in triple-beam experiments facilitates bubble-to-void conversion.

Table 1.3. Comparison of average cavity sizes $\langle d \rangle$, average cavity number density $\langle N \rangle$ and swelling detected in commercial ferritic and ferritic-martensitic steels after dual and triple-beam irradiations simulating fusion conditions

Ref.	[43,44]	[45]	[42]
Material	F82H steel	12 Cr	EUROFER 97
Irradiation conditions	50 dpa, 900 appm He 3500 appm H	50 dpa, 500 appm He, 2000 appm H	40 dpa, 500 appm He, 2000 appm H
Temperature, °C	470	510	673/723
$\langle N \rangle 10^{21} \text{ m}^{-3}$, Fe+He/ Fe+He+H	5.1/4.6	6.4/0.03	94/15
$\langle d \rangle$ nm, Fe+He/ Fe+He+H	6.7/11.2	15/50	1.2/4.8
Swelling, Fe+He/ Fe+He+H %	0.08/3.2	~0.5 /4	>0.02/0.5

As already discussed, the effect of He on cavity evolution can be due to the trapping of H on cavity walls, which might change the surface energy and thus the efficiency of thermal vacancy emission, and the accumulation of molecular hydrogen inside cavities that would increase the internal gas pressure. None of these mechanisms have been confirmed so far. In addition, H concentration remaining in F82H steel sample one week after triple-beam irradiation simulating spallation environment was below the detection limit (of 0.13 at. %) [43]. Therefore, verification of H role in swelling development requires an unequivocal confirmation of its presence in radiation induced cavities, which is always challenging.

Straightforward hydrogen detection is hindered by low hydrogen mass and typically small cavity size in irradiated steels. H association with cavities was proven only in several rare cases by electron energy loss spectroscopy (EELS) investigations [42,187–190]. Due to spatial and concentration limitations for H detection by EELS, its association with cavities can be confirmed only when cavities have sufficient size and trapped H amount. Despite the available investigations, H state in He bubbles or cavities remains still uncertain.

Though swelling was always found to be higher when both H and He were involved in cavity development, whatever temperature and He/H/dpa ratio, cavity parameters and the level of swelling increase were found to be also sensitive to temperature [42–45] and He/H injection ratio [43,44] (see Fig. 1.29). Strictly speaking, bimodal cavity size distribution and sharp swelling increase in ferritic and F/M steels after irradiation in triple-beam conditions were observed and directly associated with synergistic influence of displacement damage, He and H only in a rather narrow temperature window of 450 – 550 °C (e.g. area A in Fig. 1.29). The enhancement of swelling for high He/H to dpa ratio at 600 °C is associated by the authors of Ref. [43] with synergistic effect of displacement damage and high He concentration. At temperatures higher or lower than the mentioned temperature window only moderate increase of cavity size as a result of displacement damage and He and H introduction occurred, which is consistent with rate theory simulations that predict ~15-50 % increase of cavity/cluster size due to the presence of mixed $H_nH_mV_k$ clusters [86,175]. The authors of Refs. [86,186] suggest also that the enhanced swelling under triple-beam in the mentioned temperature window, as well as the peak swelling temperature might vary depending on material microstructure and elemental content.

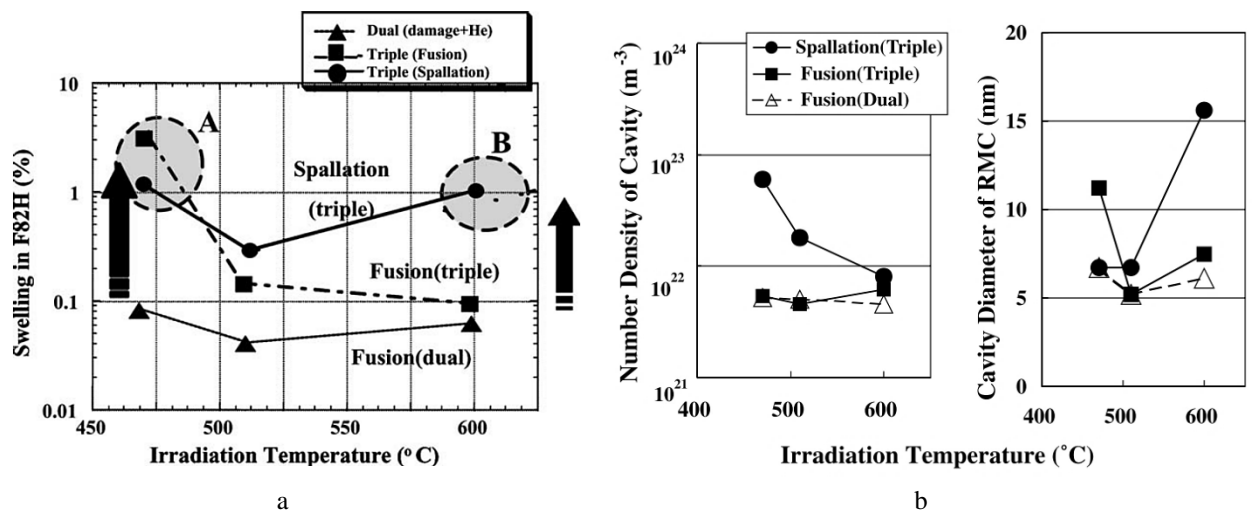


Fig. 1.29. (a) Swelling and (b) number density and mean cube root diameter of cavities formed in F82H steel after self ion irradiated to 50 dpa in fusion-relevant dual-beam experiment with 18 appm He/dpa, fission-relevant triple-beam experiment with 18 appm He/dpa and 70 appm H/dpa, and spallation-relevant triple -beam experiment with 180 appm He/dpa and 1700 appm H/dpa [43].

According to the majority of reported triple-beam data, swelling detected in commercial ODS-steels even under triple-beam ion irradiation conditions was quite limited [42,45,87]. Notable swelling under triple-beam conditions was reported only in Refs. [86,186] and [42] for K3-ODS and HIP-13Cr-ODS (material after hipping without heat treatment), respectively. In both ODS materials, the large cavities that had undergone bubble-to-void conversion were observed outside of the expected temperature window, i.e. at 350° C in HIP-13Cr-ODS and at 600/625°C in K3-ODS, when the irradiation conditions were not so far from those shown in Table 1.3 for conventional ferritic and F/M steels. More importantly, cavities in ODS steels were situated in local areas of the samples. In HIP-13Cr-ODS irradiated to 40 dpa with co-injection of 13 appm He/dpa and 50 appm H/dpa, cavities were attached to Y₂O₃ nanoparticles. Diffraction and chemical studies in Refs. [86,186] have revealed that in the case of K3-ODS steel irradiated to 30-40 dpa with co-injection of 15 appm He/dpa and 40 appm H/dpa a nanoscale

H(Fe,Cr,Al)₅O₈ compounds were co-located with trace amounts (~0.17 at.%) of yttrium at the large cavity sites. It was suggested that yttrium presence within hydroxide indicated decomposition and dissolution of oxide nanoparticles/clusters previously located in the region, while the formation of hydroxide compound resulted from synergistic action of displacement damage (ballistic effect) and the availability of a steady-state concentration of hydrogen introduced via implantation.

1.5 Conclusions

ODS steels manifest high radiation stability, in particular - low void swelling, under fission neutron spectra and are considered as candidate materials for advanced fission and fusion facilities with much more severe radiation environment than in modern nuclear reactors owing to higher operation temperatures (>650 °C), higher damage levels, and high rates of helium and hydrogen accumulation. Large concentrations of helium/hydrogen can negatively affect radiation tolerance of ODS steels, particularly via reduction of the void swelling incubation dose. The most critical He/dpa ratios in terms of void swelling are expected for fusion irradiation environment. There are still no research facilities with relevant neutron spectra to correctly reproduce fusion radiation environment. In addition to swelling issue, severe radiation environment and high temperatures involve potential risk of high temperature irradiation embrittlement (HTIE) caused by helium accumulation at grain boundaries. It is generally believed that stable nano-oxide particles in ODS steels should be beneficial for decreasing both swelling and HTIE, providing additional trapping sites for point defects and He.

However, it is not *a priori* obvious how efficient in quantities terms are nano-oxides as point defect sinks and gas trapping centers in comparison to the other structural features, especially in complex F/M ODS steels. It is not even proven that all ODS-related oxide/matrix interfaces or oxides themselves serve as He trapping sites. Moreover, there is no guarantee that under high He concentration nano-oxides of all types are able to strongly suppress heterogeneous bubble nucleation, in particular at grain boundaries. Heterogeneous bubble nucleation on various microstructural features remains highly probable in relevant conditions and different bubble populations can have different characteristic sizes. The bubble population with the largest typical size has the largest chances to reach the critical size first and to give rise to steady-state void swelling. Bubbles on second phase precipitates are in the group of largest risk because such bubbles require less gas atoms to reach any predefined diameter than bubbles in the bulk. In that way, there is no guarantee that strong helium accumulation on nano-oxides would not lead to undesirable effects in terms of ODS-steel radiation tolerance. For the best of our knowledge, no systematic experimental investigations have been performed so far on ODS steel microstructural development under synergetic helium and displacement damage action over a range of temperatures, helium injection rates, and damage rates.

Published data on hydrogen effects on swelling are far less extensive than in the case of He effects even in *bcc* iron, which is the basic constituent of ODS steels. Owing to high hydrogen diffusion rate in iron, it remains unclear whether and how hydrogen influences bubble nucleation and growth, and what are the restrictive parameters. Taking into account general complexity on detection of hydrogen distribution in metals, one has to hardly rely on modeling and simulation efforts. Only relatively limited data on hydrogen interaction with vacancies, dislocations and grain boundaries in *bcc* iron have been reported in the literature. Few papers are discussing hydrogen bubble nucleation and growth under the ultra-high hydrogen concentration conditions. Nothing is known about hydrogen interaction with ODS-related interfaces. From the limited simulation data, hydrogen trapping inside ODS-related oxides is unfavorable, in contrast to helium. Direct hydrogen bubbles nucleation and growth at least in ODS steel matrix under in-service conditions is unlikely. Therefore, hydrogen effects on swelling are regularly discussed in terms of synergetic influence with displacement damage and helium.

Up to now, the most advanced way of experimental evaluation of synergy between displacement damage, helium and hydrogen in ODS steel microstructural development is the use of triple-beam ion

irradiation experiments. Such experiments have revealed potentially strong swelling increase in ferritic and ferritic-martensitic steels when hydrogen intervenes into already fragile balance between helium and displacement damage. Although ODS steels seem to be more resistant in such severe radiation condition, some indications of undesirable nano-oxide performance as nuclei for large bubbles require deeper attention. Unfortunately, the simultaneous action of multiple effects in such complex experiments as triple-beam irradiations makes it hard to clarify the contributions of individual microstructural components (oxide particles, dislocations, grain boundaries, etc.) and processing parameters (type and amount of gas impurities, temperature, etc.) to the microstructure evolution.

In fact, saturation of ferritic and ferritic-martensitic steels with oxide particles introduces a principally new variable, oxide/metal interfaces, with rather poorly known properties. Small size of nano-oxides, their complex chemistry and non-obvious interfacial structure, all related to production route, make the irradiation stability studies at these interfaces very challenging. Therefore, simplified planar systems, such as deposited bi-layered thin films with well-controlled chemistry and interfacial structure, attract considerable interest as templates for studying nano-oxide interaction with secondary gas impurities and displacement damage. Success of this approach was recently demonstrated on ODS related systems [191–195].

Despite of all experimental and modeling efforts, the overall picture of helium and especially hydrogen promoted microstructure development in ODS steels remains incomplete and not self-consistent. In the absence of relevant irradiation testing facilities, the most successful strategy is to combine target experiments in well-controlled conditions with theory and simulations to develop fundamental basis of predictive models of radiation-induced material degradation and to provide more reliable guidelines for radiation-resistant materials engineering.

1.6 References

- [1] “Paris Agreement, United Nations Framework Convention on Climate Change, Bonn (2015).”
- [2] “United Nations Environment Programme (2019). Emissions Gap Report 2019. UNEP, Nairobi”
- [3] “IEA (2019), World Energy Outlook 2019, IEA, Paris” <https://www.iea.org/reports/world-energy-outlook-2019>.
- [4] *Climate Change and Nuclear Power 2018*. Vienna: International Atomic Energy Agency, 2018.
- [5] J. T. Busby, “Chapter 1 - Overview of structural materials in water-cooled fission reactors,” in *Structural Alloys for Nuclear Energy Applications*, G. R. Odette and S. Zinkle, Eds. Boston: Elsevier, 2019, pp. 1–22.
- [6] P. Yvon, Ed., *Structural Materials for Generation IV Nuclear Reactors*. Woodhead Publishing, 2017.
- [7] G. R. Odette and S. Zinkle, Eds., *Structural Alloys for Nuclear Energy Applications*. Elsevier, 2019.
- [8] “Status of accelerator driven systems research and technology development,” International Atomic Energy Agency, Vienna, 2015.
- [9] “MYRRHA project”. <https://myrrha.be/myrrha-project/myrrha-phased-implementation/>
- [10] D. Buckthorpe, “1 - Introduction to Generation IV nuclear reactors,” in *Structural Materials for Generation IV Nuclear Reactors*, P. Yvon, Ed. Woodhead Publishing, 2017, pp. 1–22.
- [11] I. L. Pioro, Ed., *Handbook of Generation IV Nuclear Reactors*. Woodhead Publishing, 2016.
- [12] “Eight European fusion devices, one common goal”. <https://www.euro-fusion.org/devices/>
- [13] S. J. Zinkle and J. T. Busby, “Structural materials for fission & fusion energy,” *Mater. Today*, vol. 12, no. 11, pp. 12–19, 2009.
- [14] L. K. Mansur, A. F. Rowcliffe, R. K. Nanstad, S. J. Zinkle, W. R. Corwin, and R. E. Stoller, “Materials needs for fusion, Generation IV fission reactors and spallation neutron sources – similarities and differences,” *J. Nucl. Mater.*, vol. 329–333, pp. 166–172, 2004.
- [15] S. J. Zinkle and G. S. Was, “Materials challenges in nuclear energy,” *Acta Mater.*, vol. 61, no. 3, pp. 735–758, 2013.
- [16] R. J. Kurtz and G. R. Odette, “Chapter 3 - Overview of reactor systems and operational environments for structural materials in fusion reactors,” in *Structural Alloys for Nuclear Energy Applications*, G. R. Odette and S. Zinkle, Eds. Boston: Elsevier, 2019, pp. 51–102.
- [17] S. M. González de Vicente, J.-L. Boutard, S. J. Zinkle, and H. Tanigawa, “Materials testing facilities and programmes for fission and ion implantation damage,” *Nucl. Fusion*, vol. 57, no. 9, p. 92011, 2017.
- [18] P. Vladimirov and A. Möslang, “Comparison of material irradiation conditions for fusion, spallation, stripping and fission neutron sources,” *J. Nucl. Mater.*, vol. 329–333, no. Part A, pp. 233–237, 2004.
- [19] G. S. Was, *Fundamentals of Radiation Materials Science*. New York, NY: Springer New York, 2017.
- [20] S. J. Zinkle, “1.04 - Radiation-induced effects on microstructure,” in *Comprehensive Nuclear Materials (Second Edition)*, R. J. M. Konings and R. Stoller, Eds. Oxford: Elsevier, 2020, pp. 91–129.

- [21] S. J. Zinkle and L. L. Snead, “Designing radiation resistance in materials for fusion energy,” *Annu. Rev. Mater. Res.*, vol. 44, no. 1, pp. 241–267, Jul. 2014.
- [22] A. Bhattacharya and S. J. Zinkle, “1.12 - Cavity swelling in irradiated materials,” in *Comprehensive Nuclear Materials (Second Edition)*, R. J. M. Konings and R. Stoller, Eds. Oxford: Elsevier, 2020, pp. 406–455.
- [23] S. J. Zinkle and A. Möslang, “Evaluation of irradiation facility options for fusion materials research and development,” *Fusion Eng. Des.*, vol. 88, no. 6, pp. 472–482, 2013.
- [24] R. E. Stoller, “1.11 - Primary radiation damage formation,” in *Comprehensive Nuclear Materials*, R. J. M. Konings, Ed. Oxford: Elsevier, 2012, pp. 293–332.
- [25] R. E. Stoller, “The influence of helium on microstructural evolution: Implications for DT fusion reactors,” *J. Nucl. Mater.*, vol. 174, no. 2, pp. 289–310, 1990.
- [26] F. A. Garner and L. R. Greenwood, “Neutron irradiation effects in fusion or spallation structural materials: Some recent insights related to neutron spectra,” *Radiat. Eff. Defects Solids*, vol. 144, no. 1–4, pp. 251–286, Jun. 1998.
- [27] M. R. Gilbert, S. L. Dudarev, D. Nguyen-Manh, S. Zheng, L. W. Packer, and J.-C. Sublet, “Neutron-induced dpa, transmutations, gas production, and helium embrittlement of fusion materials,” *J. Nucl. Mater.*, vol. 442, no. 1, Supplement 1, pp. S755–S760, 2013.
- [28] *Structural Materials for Liquid Metal Cooled Fast Reactor Fuel Assemblies-Operational Behaviour*, no. NF-T-4.3. Vienna: International Atomic Energy Agency, 2012.
- [29] S. J. Zinkle, J. L. Boutard, D. T. Hoelzer, A. Kimura, R. Lindau, G. R. Odette, M. Rieth, L. , and H. Tanigawa, “Development of next generation tempered and ODS reduced activation ferritic/martensitic steels for fusion energy applications,” *Nucl. Fusion*, vol. 57, no. 9, p. 92005, 2017.
- [30] L. Petrizzi, P. Batistoni, and M. Pillon, “Comprehensive activation calculations of reference materials for long term reactor concepts,” *Fusion Eng. Des.*, vol. 69, no. 1, pp. 593–599, 2003.
- [31] N. Hashimoto, R. Kasada, B. Raj, and M. Vijayalakshmi, “3.05 - Radiation effects in ferritic steels and advanced ferritic-martensitic steels,” in *Comprehensive Nuclear Materials (Second Edition)*, R. J. M. Konings and R. Stoller, Eds. Oxford: Elsevier, 2020, pp. 226–254.
- [32] C. Cabet, F. Dalle, E. Gaganidze, J. Henry, and H. Tanigawa, “Ferritic-martensitic steels for fission and fusion applications,” *J. Nucl. Mater.*, vol. 523, pp. 510–537, 2019.
- [33] O. K. Chopra, *Degradation of LWR core internal materials due to neutron irradiation*. US Nuclear Regulatory Commission, Office of Nuclear Regulatory Research, 2010.
- [34] O. K. Chopra and A. S. Rao, “A review of irradiation effects on LWR core internal materials – Neutron embrittlement,” *J. Nucl. Mater.*, vol. 412, no. 1, pp. 195–208, 2011.
- [35] F. A. Garner, “4.02 - Radiation damage in austenitic steels,” in *Comprehensive Nuclear Materials*, R. J. M. Konings, Ed. Oxford: Elsevier, 2012, pp. 33–95.
- [36] R. L. Klueh, “Analysis of swelling behaviour of ferritic/martensitic steels,” *Philos. Mag.*, vol. 98, no. 28, pp. 2618–2636, Oct. 2018.
- [37] F. A. Garner, M. B. Toloczko, and B. H. Sencer, “Comparison of swelling and irradiation creep behavior of fcc-austenitic and bcc-ferritic/martensitic alloys at high neutron exposure,” *J. Nucl. Mater.*, vol. 276, no. 1, pp. 123–142, 2000.
- [38] K. Asano, Y. Kohno, A. Kohyama, and G. Ayrault, “Microstructural evolution of HT9 under dual-beam charged particle irradiation,” *J. Nucl. Mater.*, vol. 155–157, pp. 912–915, 1988.

- [39] J. Van den Bosch, O. Anderoglu, R. Dickerson, M. Hartl, P. Dickerson, J.A. Aguiar, P. Hosemann, M.B. Toloczko, S.A. Maloy, "SANS and TEM of ferritic–martensitic steel T91 irradiated in FFTF up to 184 dpa at 413°C," *J. Nucl. Mater.*, vol. 440, no. 1, pp. 91–97, 2013.
- [40] K. Farrell and E. H. Lee, "Ion damage in a Fe-10Cr-6Mo-0.5Nb ferritic Steel," *Radiation-Induced Changes in Microstructure: 13th International Symposium (Part I)*, vol. STP 955, pp. 498–507, Jan. 1987.
- [41] L. L. Hsiung, M. J. Fluss, S. J. Tumey, B. W. Choi, Y. Serruys, and F. Willaime, "Formation mechanism and the role of nanoparticles in Fe-Cr ODS steels developed for radiation tolerance," *Phys. Rev. B*, vol. 82, p. 184103, 2010.
- [42] N. Zimmer, P. Vladimirov, M. Klimenkov, U. Jaentsch, R. Vila, V. Chakin, F. Mota, "Microstructural evolution of three potential fusion candidate steels under ion-irradiation," *J. Nucl. Mater.*, vol. 535, p. 152160, 2020.
- [43] E. Wakai, K. Kikuchi, S. Yamamoto, T. Aruga, M. Ando, H. Tanigawa, T. Taguchi, T. Sawai, K. Oka, S. Ohnuki, "Swelling behavior of F82H steel irradiated by triple/dual ion beams," *J. Nucl. Mater.*, vol. 318, pp. 267–273, 2003.
- [44] E. Wakai, T. Sawai, K. Furuya, A. Naito, T. Aruga, K. Kikuchi, S. Yamashita, S. Ohnuki, S. Yamamoto, H. Naramoto, S. Jistukawa, "Effect of triple ion beams in ferritic/martensitic steel on swelling behavior," *J. Nucl. Mater.*, vol. 307–311, pp. 278–282, 2002.
- [45] T. Tanaka, K. Oka, S. Ohnuki, S. Yamashita, T. Suda, S. Watanabe, E. Wakai, "Synergistic effect of helium and hydrogen for defect evolution under multi-ion irradiation of Fe–Cr ferritic alloys," *J. Nucl. Mater.*, vol. 329–333, pp. 294–298, 2004.
- [46] S. Taller and G. S. Was, "Understanding bubble and void nucleation in dual ion irradiated T91 steel using single parameter experiments," *Acta Mater.*, vol. 198, pp. 47–60, 2020.
- [47] S. Taller, Z. Jiao, K. Field, and G. S. Was, "Emulation of fast reactor irradiated T91 using dual ion beam," *J. Nucl. Mater.*, vol. 527, p. 151831, 2019.
- [48] R. L. Klueh, "Reduced-activation steels: Future development for improved creep strength," *J. Nucl. Mater.*, vol. 378, no. 2, pp. 159–166, 2008.
- [49] R. Lindau, A. Moeslang, M. Rieth, M. Klimiankou, E. Materna-Morris, A. Alamo, A.-A. F. Tavassoli, C. Cayron, A.-M. Lancha, P. Fernandez, N. Baluc, R. Schaubelin, E. Diegele, G. Filacchioni, J.W. Rensman, B.v.d. Schaaf, E. Lucon, W. Dietz, "Present development status of EUROFER and ODS-EUROFER for application in blanket concepts," *Fusion Eng. Des.*, vol. 75–79, pp. 989–996, 2005.
- [50] H. Tanigawa, Y. Someya, H. Sakasegawa, T. Hirose, and K. Ochiai, "Radiological assessment of the limits and potential of reduced activation ferritic/martensitic steels," *Fusion Eng. Des.*, vol. 89, no. 7, pp. 1573–1578, 2014.
- [51] A. Kohyama, A. Hishinuma, D. S. Gelles, R. L. Klueh, W. Dietz, and K. Ehrlich, "Low-activation ferritic and martensitic steels for fusion application," *J. Nucl. Mater.*, vol. 233–237, pp. 138–147, 1996.
- [52] T. Muroga, M. Gasparotto, and S. J. Zinkle, "Overview of materials research for fusion reactors," *Fusion Eng. Des.*, vol. 61–62, pp. 13–25, 2002.
- [53] P. Fernández, A. M. Lancha, J. Lapeña, R. Lindau, M. Rieth, and M. Schirra, "Creep strength of reduced activation ferritic/martensitic steel Eurofer 97," *Fusion Eng. Des.*, vol. 75–79, pp. 1003–1008, 2005.
- [54] J. Hoffmann, M. Rieth, L. Commin, P. Fernández, and M. Roldán, "Improvement of reduced activation 9%Cr steels by ausforming," *Nucl. Mater. Energy*, vol. 6, pp. 12–17, 2016.

- [55] B. Raj and M. Vijayalakshmi, “4.03 - Ferritic steels and advanced ferritic–martensitic steels,” in *Comprehensive Nuclear Materials*, R. Konings, Ed. Oxford: Elsevier, 2012, pp. 97–121.
- [56] S. Ukai, S. Ohtsuka, T. Kaito, Y. de Carlan, J. Ribis, and J. Malaplate, “10 - Oxide dispersion-strengthened/ferrite-martensite steels as core materials for Generation IV nuclear reactors,” in *Structural Materials for Generation IV Nuclear Reactors*, P. Yvon, Ed. Woodhead Publishing, 2017, pp. 357–414.
- [57] G. R. Odette and D. T. Hoelzer, “Irradiation-tolerant nanostructured ferritic alloys: Transforming helium from a liability to an asset,” *JOM*, vol. 62, no. 9, pp. 84–92, Sep. 2010.
- [58] G. R. Odette, M. J. Alinger, and B. D. Wirth, “Recent developments in irradiation-resistant steels,” *Annu. Rev. Mater. Res.*, vol. 38, no. 1, pp. 471–503, Jul. 2008.
- [59] G. R. Odette, N. J. Cunningham, T. Stan, M. E. Alam, and Y. De Carlan, “Chapter 12 - Nano-oxide dispersion-strengthened steels,” in *Structural Alloys for Nuclear Energy Applications*, G. R. Odette and S. Zinkle, Eds. Boston: Elsevier, 2019, pp. 529–583.
- [60] J.-J. Huet, “Possible fast-reactor canning material strengthened and stabilized by dispersion,” *Powder Metall.*, vol. 10, no. 20, pp. 208–215, Sep. 1967.
- [61] M. L. Hamilton, D. S. Gelles, R. J. Lobsinger, G. D. Johnson, W. F. Brown, M. M. Paxton, R. J. Puigh, C. R. Eiholzer, C. Martinez, M. A. Blotter, “Fabrication technological development of the oxide dispersion strengthened alloy MA957 for fast reactor applications,” Mar 2000, (PNNL-13168), United States.
- [62] J. Hoffmann, M. Rieth, R. Lindau, M. Klimenkov, A. Möslang, and H. R. Z. Sandim, “Investigation on different oxides as candidates for nano-sized ODS particles in reduced-activation ferritic (RAF) steels,” *J. Nucl. Mater.*, vol. 442, no. 1, pp. 444–448, 2013.
- [63] K. Verhiest, S. Mullens, J. Paul, I. De Graeve, N. De Wispelaere, S. Claessens, A. DeBremaecker, K. Verbeken, “Experimental study on the contact angle formation of solidified iron–chromium droplets onto yttria ceramic substrates for the yttria/ferrous alloy system with variable chromium content,” *Ceram. Int.*, vol. 40, no. 1, Part B, pp. 2187–2200, 2014.
- [64] Z. Shi and F. Han, “The microstructure and mechanical properties of micro-scale Y_2O_3 strengthened 9Cr steel fabricated by vacuum casting,” *Mater. Des.*, vol. 66, pp. 304–308, 2015.
- [65] Z. Shi and F. Han, “Microstructures and properties of cast T91-ODS alloys,” *Mater. Res. Innov.*, vol. 19, no. sup5, pp. S5-832-S5-835, May 2015.
- [66] V. K. Sikka, D. Wilkening, J. Liebetrau, and B. Mackey, “Melting and casting of FeAl-based cast alloy,” *Mater. Sci. Eng. A*, vol. 258, no. 1, pp. 229–235, 1998.
- [67] F. Bergner, I. Hilger, J. Virta, J. Lagerbom, G. Gerbeth, S. Connolly, Z. Hong, P. S. Grant and T. Weissgärber, “Alternative fabrication routes toward oxide-dispersion-strengthened steels and model alloys,” *Metall. Mater. Trans. A*, vol. 47, no. 11, pp. 5313–5324, 2016.
- [68] S. Ukai, “4.08 - Oxide dispersion strengthened steels,” in *Comprehensive Nuclear Materials*, R. Konings, Ed. Oxford: Elsevier, 2012, pp. 241–271.
- [69] A. Chauhan, “Deformation and damage mechanisms of ODS steels under high-temperature cyclic loading,” Karlsruhe Institut für Technologie (KIT), 2018.
- [70] M. Inoue, T. Kaito, and S. Ohtsuka, “Research and development of oxide dispersion strengthened ferritic steels for sodium cooled fast breeder reactor fuels,” 2008, pp. 311–325.
- [71] K. D. Zilnyk, V. B. Oliveira, H. R. Z. Sandim, A. Möslang, and D. Raabe, “Martensitic transformation in Eurofer-97 and ODS-Eurofer steels: A comparative study,” *J. Nucl. Mater.*, vol. 462, pp. 360–367, 2015.

- [72] V. S. M. Pereira, H. Schut, and J. Sietsma, "A study of the microstructural stability and defect evolution in an ODS Eurofer steel by means of electron microscopy and positron annihilation spectroscopy," *J. Nucl. Mater.*, vol. 540, p. 152398, 2020.
- [73] M. Yamamoto, S. Ukai, S. Hayashi, T. Kaito, and S. Ohtsuka, "Formation of residual ferrite in 9Cr-ODS ferritic steels," *Mater. Sci. Eng. A*, vol. 527, no. 16, pp. 4418–4423, 2010.
- [74] A. Das, P. Chekhonin, E. Altstadt, F. Bergner, C. Heintze, and R. Lindau, "Microstructural characterization of inhomogeneity in 9Cr ODS EUROFER steel," *J. Nucl. Mater.*, vol. 533, p. 152083, 2020.
- [75] G. Wang, Y. Li, J. Zhang, F. Bao, Y. Wei, Q. Shi, X. Shi, Y. Shan, K. Yang, "Design and preliminary characterization of a novel carbide-free 9Cr-ODS martensitic steel," *Fusion Eng. Des.*, vol. 160, p. 111824, 2020.
- [76] S. Rogozhkin, A. Bogachev, O. Korchuganova, A. Nikitin, N. Orlov, A. Aleev, A. Zaluzhnyi, M. Kozodaev, T. Kulevoy, B. Chalykh, R. Lindau, J. Hoffmann, A. Moeslang, P. Vladimirov, M. Klimenkov, M. Heilmaier, J. Wagner, S. Seils, "Nanostructure evolution in ODS steels under ion irradiation," *Nucl. Mater. Energy*, vol. 9, pp. 66–74, 2016.
- [77] K. D. Zilnyk, K. G. Pradeep, P. Choi, H. R. Z. Sandim, and D. Raabe, "Long-term thermal stability of nanoclusters in ODS-Eurofer steel: An atom probe tomography study," *J. Nucl. Mater.*, vol. 492, pp. 142–147, 2017.
- [78] P. Zheng, Y. Li, J. Zhang, J. Shen, T. Nagasaka, T. Muroga, H. Abe, "On the thermal stability of a 9Cr-ODS steel aged at 700 °C up to 10000 h - Mechanical properties and microstructure," *Mater. Sci. Eng. A*, vol. 783, p. 139292, 2020.
- [79] M. J. R. Sandim, I. R. Souza Filho, E. H. Bredda, A. Kostka, D. Raabe, and H. R. Z. Sandim, "Short Communication on 'Coarsening of Y-rich oxide particles in 9%Cr-ODS Eurofer steel annealed at 1350 °C,'" *J. Nucl. Mater.*, vol. 484, pp. 283–287, 2017.
- [80] J. P. Wharry, M. J. Swenson, and K. H. Yano, "A review of the irradiation evolution of dispersed oxide nanoparticles in the b.c.c. Fe-Cr system: Current understanding and future directions," *J. Nucl. Mater.*, vol. 486, pp. 11–20, 2017.
- [81] T. Chen, H. Kim, J. G. Gigax, D. Chen, C.-C. Wei, F.A. Garner, L. Shao, "Radiation response of oxide-dispersion-strengthened alloy MA956 after self-ion irradiation," *Nucl. Instruments Methods Phys. Res. Sect. B Beam Interact. with Mater. Atoms*, vol. 409, pp. 259–263, 2017.
- [82] Z. Zhang, T. A. Saleh, S. A. Maloy, and O. Anderoglu, "Microstructure evolution in MA956 neutron irradiated in ATR at 328 °C to 4.36 dpa," *J. Nucl. Mater.*, vol. 533, p. 152094, 2020.
- [83] P. Song, D. Morrall, Z. Zhang, K. Yabuuchi, and A. Kimura, "Radiation response of ODS ferritic steels with different oxide particles under ion-irradiation at 550 °C," *J. Nucl. Mater.*, vol. 502, pp. 76–85, 2018.
- [84] Y. E. Kupriyanova, V. V. Bryk, O. V. Borodin, A. S. Kalchenko, V. N. Voyevodin, G. D. Tolstolutskaia, F. A. Garner, "Use of double and triple-ion irradiation to study the influence of high levels of helium and hydrogen on void swelling of 8–12% Cr ferritic-martensitic steels," *J. Nucl. Mater.*, vol. 468, pp. 264–273, 2016.
- [85] T. Yamamoto, Y. Wu, G. Robert Odette, K. Yabuuchi, S. Kondo, and A. Kimura, "A dual ion irradiation study of helium-dpa interactions on cavity evolution in tempered martensitic steels and nanostructured ferritic alloys," *J. Nucl. Mater.*, vol. 449, no. 1–3, pp. 190–199, 2014.

- [86] J. Marian, T. Hoang, M. Fluss, and L. L. Hsiung, “A review of helium–hydrogen synergistic effects in radiation damage observed in fusion energy steels and an interaction model to guide future understanding,” *J. Nucl. Mater.*, vol. 462, pp. 409–421, 2015.
- [87] D. Brimbal, L. Beck, O. Troeber, E. Gaganidze, P. Trocellier, J. Aktaa, R. Lindau, “Microstructural characterization of Eurofer-97 and Eurofer-ODS steels before and after multi-beam ion irradiations at JANNUS Saclay facility,” *J. Nucl. Mater.*, vol. 465, pp. 236–244, 2015.
- [88] E. Aydogan, S.A. Maloy, O. Anderoglu, C. Sun, J.G. Gigax, L. Shao, F.A. Garner, I.E. Anderson, J.J. Lewandowski, “Effect of tube processing methods on microstructure, mechanical properties and irradiation response of 14YWT nanostructured ferritic alloys,” *Acta Mater.*, vol. 134, pp. 116–127, 2017.
- [89] I.-S Kim, J. D Hunn, N. Hashimoto, D. L Larson, P. J Maziasz, K Miyahara, E. H Lee, “Defect and void evolution in oxide dispersion strengthened ferritic steels under 3.2 MeV Fe⁺ ion irradiation with simultaneous helium injection,” *J. Nucl. Mater.*, vol. 280, no. 3, pp. 264–274, 2000.
- [90] L. K. Mansur and W. A. Coghlan, “Mechanisms of helium interaction with radiation effects in metals and alloys: a review,” *J. Nucl. Mater.* 119, vol. 119, pp. 1–25, 1983.
- [91] A. D. Brailsford and R. Bullough, “The theory of sink strength,” *Philos. Trans. R. Soc. London. Ser. A, Math. Phys. Sci.*, vol. 302, pp. 88–136, 1981.
- [92] A. D. Brailsford and R. Bullough, “The rate theory of swelling due to void growth in irradiated metals,” *J. Nucl. Mater.*, vol. 44, no. 2, pp. 121–135, 1972.
- [93] V. A. Borodin, “Radiation induced swelling,” *State-of-the-art Report on Structural Materials Modelling, Report NEA/NSC/R(2016)5, OECD*, pp. 165–225, 2016.
- [94] V. A. Borodin, “Generalized rate theory for spatially inhomogeneous systems of point defect sinks,” *Physica A: Statistical Mechanics and its Applications*, vol. 211, no. 2–3, pp. 279–316, Nov. 1994.
- [95] E. H. Lee and L. K. Mansur, “Unified theoretical analysis of experimental swelling data for irradiated austenitic and ferritic/martensitic alloys,” *Metall. Trans. A*, vol. 21, no. 4, pp. 1021–1035, 1990.
- [96] L. K. Mansur, “Theory of transitions in dose dependence of radiation effects in structural alloys,” *J. Nucl. Mater.*, vol. 206, no. 2, pp. 306–323, 1993.
- [97] C.-C. Fu and F. Willaime, “Ab initio study of helium in alpha-Fe: Dissolution, migration, and clustering with vacancies,” *Phys. Rev. B*, vol. 72, no. 6, p. 64117, Aug. 2005.
- [98] K. Morishita, R. Sugano, and B. D. Wirth, “MD and KMC modeling of the growth and shrinkage mechanisms of helium–vacancy clusters in Fe,” *J. Nucl. Mater.*, vol. 323, no. 2, pp. 243–250, 2003.
- [99] K. Morishita, R. Sugano, B. D. Wirth, and T. Diaz de la Rubia, “Thermal stability of helium–vacancy clusters in iron,” *Nucl. Instruments Methods Phys. Res. Sect. B Beam Interact. with Mater. Atoms*, vol. 202, pp. 76–81, 2003.
- [100] G. Lucas and R. Schäublin, “Stability of helium bubbles in alpha-iron: A molecular dynamics study,” *J. Nucl. Mater.*, vol. 386–388, pp. 360–362, 2009.
- [101] V. A. Borodin and P. V Vladimirov, “Diffusion coefficients and thermal stability of small helium–vacancy clusters in iron,” *J. Nucl. Mater.*, vol. 362, no. 2, pp. 161–166, 2007.
- [102] Y. Dai, G. R. Odette, and T. Yamamoto, “The effects of helium in irradiated structural alloys,” in *Comprehensive Nuclear Materials*, vol. 1, Elsevier Inc., 2012, pp. 141–193.
- [103] C. Zheng, E. R. Reese, K. G. Field, T. Liu, E. A. Marquis, S. A. Maloy, D. Kaoumi, “Microstructure response of ferritic / martensitic steel HT9 after neutron irradiation: Effect of temperature,” *J. Nucl. Mater.*, vol. 528, p. 151845, 2020.

- [104] T. Yamamoto, G.R. Odette, P. Miao, D.T. Hoelzer, J. Bentley, N. Hashimoto, H. Tanigawa, R.J. Kurtz, “The transport and fate of helium in nanostructured ferritic alloys at fusion relevant He/dpa ratios and dpa rates,” *J. Nucl. Mater.*, vol. 367–370, pp. 399–410, 2007.
- [105] V. Krsjak, J. Degmova, J. S. Veternikova, C. F. Yao, and Y. Dai, “Experimental comparison of the (ODS)EUROFER steels implanted by helium ions and irradiated in spallation neutron target,” *J. Nucl. Mater.*, vol. 523, pp. 51–55, 2019.
- [106] E. Wakai, M. Ando, T. Sawai, K. Kikuchi, K. Furuya, M. Sato, K. Oka, S. Ohnuki, H. Tomita, T. Tomita, Y. Kato, F. Takada, “Effect of gas atoms and displacement damage on mechanical properties and microstructures of F82H,” *J. Nucl. Mater.*, vol. 356, no. 1, pp. 95–104, 2006.
- [107] X. Jia and Y. Dai, “Microstructure of the F82H martensitic steel irradiated in STIP-II up to 20 dpa,” *J. Nucl. Mater.*, vol. 356, no. 1, pp. 105–111, 2006.
- [108] B. Yao, D. J. Edwards, R. J. Kurtz, G. R. Odette, and T. Yamamoto, “Microstructure characterization of neutron irradiated and helium injected PM2000, 14YW, and modified F82H alloys,” *Fusion Mater. Semiannul Prog. Rep. June 2012*, vol. DOE-ER-031, p. 26, 2012.
- [109] H. J. Jung, D. J. Edwards, R. J. Kurtz, G. R. Odette, Y. Wu, and T. Yamamoto, “Microstructural summary of ODS ferritic alloys (14YW, 14YWT, 12YWT, MA957FR, PM2000) and RAFM steels (F82H Mod.3-CW, Eurofer97) from JP27 in-situ He injection (ISHI) Experiment at 500°C,” *Fusion Mater. Semiannul Prog. Rep. June 2015*, vol. DOE-ER-031, p. 55, 2015.
- [110] H. J. Jung, D. J. Edwards, R. J. Kurtz, T. Yamamoto, Y. Wu, and G. R. Odette, “Structural and chemical evolution in neutron irradiated and helium-injected ferritic ODS PM2000 alloy,” *J. Nucl. Mater.*, vol. 484, pp. 68–80, 2017.
- [111] H. Tanigawa, K. Shiba, A. Moeslang, R. E. Stoller, R. Lindau, M. A. Sokolov, G. R. Odette, R. J. Kurtz, S. Jitsukawa, “Status and key issues of reduced activation ferritic/martensitic steels as the structural material for a DEMO blanket,” *J. Nucl. Mater.*, vol. 417, no. 1, pp. 9–15, 2011.
- [112] A. Bhattacharya, E. Meslin, J. Henry, B. Décamps, and A. Barbu, “Dramatic reduction of void swelling by helium in ion-irradiated high purity α -iron,” *Mater. Res. Lett.*, vol. 6, no. 7, pp. 372–377, Jul. 2018.
- [113] A. I. Ryazanov, O. K. Chugunov, S. M. Ivanov, S. T. Latushkin, R. Lindau, A. Möslang, A. A. Nikitina, K. E. Prikhodko, E. V. Semenov, V. N. Unezhev, P. V. Vladimirov, “Tensile properties and microstructure of helium implanted EUROFER ODS,” *J. Nucl. Mater.*, vol. 442, no. 1, Supplement 1, pp. S153–S157, 2013.
- [114] L. Yang, Y. Jiang, G. R. Odette, T. Yamamoto, Z. Liu, and Y. Liu, “Trapping helium in $Y_2Ti_2O_7$ compared to in matrix iron: A first principles study,” *J. Appl. Phys.*, vol. 115, no. 14, p. 143508, Apr. 2014.
- [115] P. D. Edmondson, C. M. Parish, Y. Zhang, A. Hallén, and M. K. Miller, “Helium bubble distributions in a nanostructured ferritic alloy,” *J. Nucl. Mater.*, vol. 434, no. 1–3, pp. 210–216, 2013.
- [116] T. Stan, Y. Wu, J. Ciston, T. Yamamoto, and G. R. Odette, “Characterization of polyhedral nano-oxides and helium bubbles in an annealed nanostructured ferritic alloy,” *Acta Mater.*, vol. 183, pp. 484–492, 2020.
- [117] L. Yang, Y. Jiang, Y. Wu, G. R. Odette, Z. Zhou, and Z. Lu, “The ferrite/oxide interface and helium management in nano-structured ferritic alloys from the first principles,” *Acta Mater.*, vol. 103, pp. 474–482, 2016.
- [118] D. Sun, R. Li, J. Ding, S. Huang, P. Zhang, Z. Lu, J. Zhao, “Helium behavior in oxide dispersion strengthened (ODS) steel: Insights from ab initio modeling,” *J. Nucl. Mater.*, vol. 499, pp. 71–78, 2018.

- [119] M. Klimenkov, R. Lindau, and A. Möslang, “New insights into the structure of ODS particles in the ODS-Eurofer alloy,” *J. Nucl. Mater.*, vol. 386–388, pp. 553–556, 2009.
- [120] P. Erhart, “A first-principles study of helium storage in oxides and at oxide-iron interfaces,” *J. Appl. Phys.*, vol. 111, no. 11, 2012.
- [121] D. Sun, P. Zhang, J. Ding, and J. Zhao, “Helium behavior in different oxides inside ODS steels : A comparative ab initio study,” *J. Nucl. Mater.*, vol. 507, pp. 101–111, 2018.
- [122] C. Lu, Z. Lu, X. Wang, R. Xie, Z. Li, M. Higgins, C. Liu, F. Gao and L. Wang, “Enhanced radiation-tolerant oxide dispersion strengthened steel and its microstructure evolution under helium-implantation and heavy-ion irradiation,” *Scientific Reports*, vol. 7, no. 1, p. 40343, 2017.
- [123] G. R. Odette, P. Miao, D. J. Edwards, T. Yamamoto, R. J. Kurtz, and H. Tanigawa, “Helium transport, fate and management in nanostructured ferritic alloys: In situ helium implanter studies,” *J. Nucl. Mater.*, vol. 417, no. 1, pp. 1001–1004, 2011.
- [124] P. D. Edmondson, C. M. Parish, Y. Zhang, A. Hallén, and M. K. Miller, “Helium entrapment in a nanostructured ferritic alloy,” *Scripta Materialia*, vol. 65, no. 8, pp. 731–734, 2011.
- [125] C. M. Parish, K. A. Unocic, L. Tan, S. J. Zinkle, S. Kondo, L. L. Snead, D.T. Hoelzer, Y. Katoh, “Helium sequestration at nanoparticle-matrix interfaces in helium + heavy ion irradiated nanostructured ferritic alloys,” *J. Nucl. Mater.*, vol. 483, pp. 21–34, 2017.
- [126] B. Mazumder, M. E. Bannister, F. W. Meyer, M. K. Miller, C. M. Parish, and P. D. Edmondson, “Helium trapping in carbide precipitates in a tempered F82H ferritic–martensitic steel,” *Nucl. Mater. Energy*, vol. 1, pp. 8–12, 2015.
- [127] J.-L. Cao, W. Xiao, Q. Cao, and B.-L. He, “First-principles study of helium trapping in carbide precipitates (Cr_{23}C_6) in ferritic-martensitic steels,” *Fusion Sci. Technol.*, vol. 74, no. 3, pp. 177–185, Oct. 2018.
- [128] T. Yamamoto, G. R. Odette, P. Miao, D. J. Edwards, and R. J. Kurtz, “Helium effects on microstructural evolution in tempered martensitic steels: In situ helium implanter studies in HFIR,” *J. Nucl. Mater.*, vol. 386–388, pp. 338–341, 2009.
- [129] S. Chen, Y. Wang, N. Hashimoto, and S. Ohnuki, “Post-irradiation annealing behavior of helium in irradiated Fe and ferritic-martensitic steels,” *Nucl. Mater. Energy*, vol. 15, pp. 203–207, 2018.
- [130] M. Roldán, P. Fernández, J. Rams, D. Jiménez-Rey, E. Materna-Morris, and M. Klimenkov, “Comparative study of helium effects on EU-ODS EUROFER and EUROFER97 by nanoindentation and TEM,” *J. Nucl. Mater.*, vol. 460, pp. 226–234, 2015.
- [131] Q. Li, C. M. Parish, K. A. Powers, and M. K. Miller, “Helium solubility and bubble formation in a nanostructured ferritic alloy,” *J. Nucl. Mater.*, vol. 445, no. 1–3, pp. 165–174, 2014.
- [132] J. Chen, P. Jung, T. Rebac, F. Duval, T. Sauvage, Y. de Carlan, M. F. Barthe, “Helium effects on creep properties of Fe–14CrWTi ODS steel at 650°C,” *J. Nucl. Mater.*, vol. 453, no. 1, pp. 253–258, 2014.
- [133] W. Xu, L. Li, J. A. Valdez, M. Saber, Y. Zhu, C. C. Koch, R. O. Scattergood, “Effect of nano-oxide particle size on radiation resistance of iron-chromium alloys,” *J. Nucl. Mater.*, vol. 469, pp. 72–81, 2016.
- [134] L. Fave, M. A. Pouchon, M. Döbeli, M. Schulte-Borchers, and A. Kimura, “Helium ion irradiation induced swelling and hardening in commercial and experimental ODS steels,” *J. Nucl. Mater.*, vol. 445, no. 1, pp. 235–240, 2014.

- [135] B. N. Singh and H. Trinkaus, “An analysis of the bubble formation behaviour under different experimental conditions,” *J. Nucl. Mater.*, vol. 186, no. 2, pp. 153–165, 1992.
- [136] H. Trinkaus and B. N. Singh, “Helium accumulation in metals during irradiation – where do we stand?,” *J. Nucl. Mater.*, vol. 323, no. 2, pp. 229–242, 2003.
- [137] S.-H. Li, J.-T. Li, and W.-Z. Han, “Radiation-induced helium bubbles in metals,” *Materials (Basel)*, vol. 12, no. 7, p. 1036, Mar. 2019.
- [138] J. Gao, H. Huang, X. Liu, C. Wang, J. F. Stubbins, and Y. Li, “A special coarsening mechanism for intergranular helium bubbles upon heating: A combined experimental and numerical study,” *Scripta Materialia*, vol. 147, pp. 93–97, 2018.
- [139] K. Ono, K. Arakawa, and K. Hojou, “Formation and migration of helium bubbles in Fe and Fe–9Cr ferritic alloy,” *J. Nucl. Mater.*, vol. 307–311, pp. 1507–1512, 2002.
- [140] K. Ono, M. Miyamoto, and K. Arakawa, “Dynamical interaction of helium bubbles with grain boundaries in Fe and Fe–9Cr ferritic alloy,” *J. Nucl. Mater.*, vol. 367–370, pp. 522–526, 2007.
- [141] M. Roldán, P. Fernández, J. Rams, F. J. Sánchez, and A. Gómez-Herrero, “Nanoindentation and tem to study the cavity fate after post-irradiation annealing of He implanted EUROFER97 and EU-ODS EUROFER,” *Micromachines*, vol. 9, no. 12, p. 633, Nov. 2018.
- [142] S.-M. Liu, S.-H. Li, and W.-Z. Han, “Revealing the dynamics of helium bubbles using in situ techniques,” *JOM*, vol. 72, no. 6, pp. 2352–2362, 2020.
- [143] F. G. Wei and K. Tsuzaki, “13 - Hydrogen trapping phenomena in martensitic steels,” in *Woodhead Publishing Series in Metals and Surface Engineering, Gaseous Hydrogen Embrittlement of Materials in Energy Technologies*, vol. 2, R. P. Gangloff and B. P. Somerday, Eds. Woodhead Publishing, 2012, pp. 493–525.
- [144] J. Vökl and G. Alefeld, “Diffusion of hydrogen in metals,” In: *Alefeld G., Vökl J. (eds) Hydrogen in Metals I. Topics in Applied Physics*, vol 28, Springer, Berlin, Heidelberg, 1978, pp. 321–348.
- [145] D. Di Stefano, M. Mrovec, and C. Elsässer, “First-principles investigation of quantum mechanical effects on the diffusion of hydrogen in iron and nickel,” *Phys. Rev. B*, vol. 92, no. 22, p. 224301, Dec. 2015.
- [146] S. M. Myers, D. M. Follstaedt, F. Besenbacher, and J. Boettiger, “Trapping and surface permeation of deuterium in He-implanted Fe,” *J. Appl. Phys.*, vol. 53, no. 12, pp. 8734–8744, Dec. 1982.
- [147] O. V. Ogorodnikova, Z. Zhou, K. Sugiyama, M. Balden, Y. Gasparyan, and V. Efimov, “Surface modification and deuterium retention in reduced-activation steels under low-energy deuterium plasma exposure. Part I: undamaged steels,” *Nucl. Fusion*, vol. 57, no. 3, p. 36010, 2016.
- [148] V. N. Voyevodin, S. A. Karpov, I. E. Kopanets, V. V Ruzhytskyi, G. D. Tolstolutsкая, and F. A. Garner, “Influence of displacement damage on deuterium and helium retention in austenitic and ferritic-martensitic alloys considered for ADS service,” *J. Nucl. Mater.*, vol. 468, pp. 274–280, 2016.
- [149] S. K. Dwivedi and M. Vishwakarma, “Effect of hydrogen in advanced high strength steel materials,” *Int. J. Hydrogen Energy*, vol. 44, no. 51, pp. 28007–28030, 2019.
- [150] S. Frappart, A. Oudriss, X. Feaugas, J. Creus, J. Bouhattate, F. Thébault, L. Delattre, H. Marchebois, “Hydrogen trapping in martensitic steel investigated using electrochemical permeation and thermal desorption spectroscopy,” *Scripta Materialia*, vol. 65, no. 10, pp. 859–862, 2011.
- [151] H. K. D. H. Bhadeshia, “Prevention of Hydrogen Embrittlement in Steels,” *ISIJ Int.*, vol. 56, no. 1, pp. 24–36, 2016.

- [152] K. Ohsawa, K. Eguchi, H. Watanabe, M. Yamaguchi, and M. Yagi, “Configuration and binding energy of multiple hydrogen atoms trapped in monovacancy in bcc transition metals,” *Phys. Rev. B*, vol. 85, no. 9, p. 94102, Mar. 2012.
- [153] H. Sugimoto and Y. Fukai, “Hydrogen-induced superabundant vacancy formation in bcc Fe: Monte Carlo simulation,” *Acta Mater.*, vol. 67, pp. 418–429, 2014.
- [154] Y. Tateyama and T. Ohno, “Stability and clusterization of hydrogen-vacancy complexes in α -Fe: An ab initio study,” *Phys. Rev. B*, vol. 67, no. 17, p. 174105, May 2003.
- [155] E. Hayward and C.-C. Fu, “Interplay between hydrogen and vacancies in α -Fe,” *Phys. Rev. B*, vol. 87, no. 17, p. 174103, May 2013.
- [156] E. Hayward, R. Hayward, and C.-C. Fu, “Predicting distinct regimes of hydrogen behavior at nano-cavities in metals,” *J. Nucl. Mater.*, vol. 476, pp. 36–44, 2016.
- [157] W. A. Counts, C. Wolverton, and R. Gibala, “First-principles energetics of hydrogen traps in α -Fe: Point defects,” *Acta Mater.*, vol. 58, no. 14, pp. 4730–4741, 2010.
- [158] B. Irigoyen, R. Ferullo, N. Castellani, and A. Juan, “The interaction of hydrogen with an Fe vacancy: a molecular orbital simulation,” *J. Phys. D. Appl. Phys.*, vol. 29, no. 5, pp. 1306–1309, 1996.
- [159] J. B. Condon and T. Schober, “Hydrogen bubbles in metals,” *J. Nucl. Mater.*, vol. 207, pp. 1–24, 1993.
- [160] W.T. Geng, L. Wan, J.-P. Du, A. Ishii, N. Ishikawa, H. Kimizuka, S. Ogata, “Hydrogen bubble nucleation in α -iron,” *Scripta Materialia*, vol. 134, pp. 105–109, 2017.
- [161] J. Hou, X.-S. Kong, X. Wu, J. Song, and C. S. Liu, “Predictive model of hydrogen trapping and bubbling in nanovoids in bcc metals,” *Nat. Mater.*, vol. 18, no. 8, pp. 833–839, 2019.
- [162] E. R. M. Davidson, T. Daff, G. Csanyi, and M. W. Finnis, “Grand canonical approach to modeling hydrogen trapping at vacancies in α -Fe,” *Phys. Rev. Mater.*, vol. 4, no. 6, p. 63804, Jun. 2020.
- [163] J. Zhang, J. Zhao, W. Jiang, X. Guan, H. Peng, Z. Zhu and T. Wang, “Formation of bubbles and blisters in hydrogen ion implanted polycrystalline tungsten,” *Radiat. Eff. Defects Solids*, vol. 173, no. 11–12, pp. 1027–1036, Dec. 2018.
- [164] W. Hu, F. Luo, Z. Shen, L. Guo, Z. Zheng, Y. Wen, Y. Ren, “Hydrogen bubble formation and evolution in tungsten under different hydrogen irradiation conditions,” *Fusion Eng. Des.*, vol. 90, pp. 23–28, 2015.
- [165] G.-H. Lu, H.-B. Zhou, and C. S. Becquart, “A review of modelling and simulation of hydrogen behaviour in tungsten at different scales,” *Nucl. Fusion*, vol. 54, no. 8, p. 86001, 2014.
- [166] P. Jin, T. Shen, M. Cui, Y. Zhu, B. Li, T. Zhang, J. Li, S. Jin, E. Lu, X. Cao, Z. Wang, “Study on vacancy-type defects in SIMP steel induced by separate and sequential H and He ion implantation,” *J. Nucl. Mater.*, vol. 520, pp. 131–139, 2019.
- [167] E. Wallaert, T. Depover, M. Arafin, and K. Verbeken, “Thermal desorption spectroscopy evaluation of the hydrogen-trapping capacity of NbC and NbN Precipitates,” *Metall. Mater. Trans. A*, vol. 45, no. 5, pp. 2412–2420, 2014.
- [168] E. Malitckii, Y. Yagodzinskyy, M. Ganchenkova, S. Binyukova, H. Hänninen, R. Lindau, P. Vladimirov, A. Moeslang, “Comparative study of hydrogen uptake and diffusion in ODS steels,” *Fusion Eng. Des.*, vol. 88, no. 9, pp. 2607–2610, 2013.

- [169] D.-G. Xie, Z.-J. Wang, J. Sun, J. Li, E. Ma, and Z.-W. Shan, “In situ study of the initiation of hydrogen bubbles at the aluminium metal/oxide interface,” *Nat. Mater.*, vol. 14, no. 9, pp. 899–903, 2015.
- [170] M. Li, D.-G. Xie, E. Ma, J. Li, X.-X. Zhang, and Z.-W. Shan, “Effect of hydrogen on the integrity of aluminium–oxide interface at elevated temperatures,” *Nat. Commun.*, vol. 8, no. 1, p. 14564, 2017.
- [171] M. Li, D. Xie, and Z. Shan, “In situ TEM study of the hydrogen effect on the interface between al and its oxide at room and elevated temperature,” *Microsc. Microanal.*, vol. 23, no. S1, pp. 1990–1991, 2017.
- [172] Y. Yagodzinskyy, E. Malitckii, M. Ganchenkova, S. Binyukova, O. Emelyanova, T. Saukkonen, H. Hänninen, R. Lindau, P. Vladimirov, A. Moeslang, “Hydrogen effects on tensile properties of EUROFER 97 and ODS-EUROFER steels,” *J. Nucl. Mater.*, vol. 444, no. 1, pp. 435–440, 2014.
- [173] G. A. Esteban, A. Peña, F. Legarda, and R. Lindau, “Hydrogen transport and trapping in ODS-EUROFER,” *Fusion Eng. Des.*, vol. 82, no. 15, pp. 2634–2640, 2007.
- [174] D. Sun, J. Ding, Y. Yang, P. Zhang, and J. Zhao, “First-principles investigation of hydrogen behavior in different oxides in ODS steels,” *Int. J. Hydrogen Energy*, vol. 44, no. 31, pp. 17105–17113, 2019.
- [175] C. J. Ortiz, R. Vila, and J. M. Pruneda, “Ab initio study of helium and hydrogen interactions in alpha-Fe,” *arXiv:1205.6374v2 [cond-mat.mtrl-sci.]*, 2012.
- [176] E. Hayward and C. Deo, “Synergistic effects in hydrogen–helium bubbles,” *J. Phys. Condens. Matter*, vol. 24, no. 26, p. 265402, 2012.
- [177] A. Caro, J. Hetherly, A. Stukowski, M. Caro, E. Martinez, S. Srivilliputhur, L. Zepeda-Ruiz, M. Nastasi, “Properties of helium bubbles in Fe and FeCr alloys,” *J. Nucl. Mater.*, vol. 418, no. 1, pp. 261–268, 2011.
- [178] R. E. Stoller and Y. N. Osetsky, “An atomistic assessment of helium behavior in iron,” *J. Nucl. Mater.*, vol. 455, no. 1, pp. 258–262, 2014.
- [179] Q. Xu and J. Zhang, “Effects of He, D interaction on thermal desorption of He and D₂ and microstructural evolution in pure Fe,” *J. Nucl. Mater.*, vol. 479, pp. 255–259, 2016.
- [180] Y. Yamauchi, K. Gotoh, Y. Nobuta, T. Hino, S. Suzuki, and M. Akiba, “Deuterium retention and desorption behavior of reduced activated ferritic steel with surface damage due to high energy helium ion irradiation,” *Fusion Eng. Des.*, vol. 85, no. 10, pp. 1838–1840, 2010.
- [181] Y.-P. Xu, T. Lu, X.-C. Li, F. Liu, H.-D. Liu, J. Wang, Z.-Q. An, F. Ding, S.-H. Hong, H.-S. Zhou, G.-N. Luo, “Influence of He ions irradiation on the deuterium permeation and retention behavior in the CLF-1 steel,” *Nucl. Instruments Methods Phys. Res. Sect. B Beam Interact. with Mater. Atoms*, vol. 388, pp. 5–8, 2016.
- [182] D. Hamaguchi, H. Iwakiri, T. Kawamura, H. Abe, T. Iwai, K. Kikuchi, N. Yoshida, “The trapping behavior of deuterium in F82H ferritic/martensitic steel,” *J. Nucl. Mater.*, vol. 386–388, pp. 375–378, 2009.
- [183] G. D. Tolstolutskaia, V. V Ruzhyskiy, V. N. Voyevodin, I. E. Kopanets, S. A. Karpov, and A. V Nikitin, “The role of radiation damage on retention and temperature intervals of helium and hydrogen detrapping in structural materials,” *J. Nucl. Mater.*, vol. 442, no. 1, Supplement 1, pp. S710–S714, 2013.
- [184] D. Brimbal, L. Beck, M. Payet, and F. Jomard, “The synergistic effect of hydrogen and helium implantations in forming H₂ molecules in a Fe-12 wt.%Cr-ODS steel characterized by Raman spectroscopy and SIMS,” *Nucl. Instruments Methods Phys. Res. Sect. B Beam Interact. with Mater. Atoms*, vol. 461, no. June, pp. 191–196, 2019.

- [185] M. Roldán, P. Fernández, R. Vila, A. Gómez-Herrero, and F. J. Sánchez, “The effect of triple ion beam irradiation on cavity formation on pure EFDA iron,” *J. Nucl. Mater.*, vol. 479, pp. 100–111, 2016.
- [186] M. J. Fluss, L. L. Hsiung, and J. Marian, “Dual and triple ion-beam irradiations of Fe, Fe(Cr) and Fe(Cr)-ODS. Final Report: IAEA SMORE CRP,” United States, 2011.
- [187] K. Hojou, S. Furuno, K. N. Kushita, N. Sasajima, and K. Izui, “EELS analysis of SiC crystals under hydrogen and helium dual-ion beam irradiation,” *Nucl. Instruments Methods Phys. Res. Sect. B Beam Interact. with Mater. Atoms*, vol. 141, no. 1, pp. 148–153, 1998.
- [188] W. R. McKenzie, M. Z. Quadir, M. H. Gass, and P. R. Munroe, “Focused Ion beam implantation of diamond,” *Diam. Relat. Mater.*, vol. 20, no. 8, pp. 1125–1128, 2011.
- [189] M. S. Blackmur, S. Dumbill, I. MacLaren, D. Hernandez-Maldonado, P. D. Styman, M. Gass, R. J. Nicholls, J. M. Hyde, Q. M. Ramasse, K. J. Annand, J. S. Smith, N. Gotham, “The association of hydrogen with nanometre bubbles of helium implanted into zirconium,” *Scripta Materialia*, vol. 152, pp. 102–106, 2018.
- [190] M. Klimenkov, P. Vladimirov, J. Hoffmann, N. Zimmer, A. Möslang, and V. Kuksenko, “First simultaneous detection of helium and tritium inside bubbles in beryllium,” *Micron*, vol. 127, p. 102754, 2019.
- [191] N. Li, S. K. Yadav, Y. Xu, J. A. Aguiar, J. K. Baldwin, Y. Q. Wang, H. M. Luo, A. Misra and B. P. Uberuaga, “Cr incorporated phase transformation in Y_2O_3 under ion irradiation,” *Scientific Reports*, vol. 7, no. 1, p. 40148, 2017.
- [192] A. Mairov, D. Frazer, P. Hosemann, and K. Sridharan, “Helium irradiation of Y_2O_3 -Fe bilayer system,” *Scripta Materialia*, vol. 162, pp. 156–160, 2019.
- [193] T. C. Kaspar, M. E. Bowden, C. M. Wang, V. Shutthanandan, N. R. Overman, R. M. van Ginhoven, B. D. Wirth, R. J. Kurtz, “Epitaxial Fe/ Y_2O_3 interfaces as a model system for oxide-dispersion-strengthened ferritic alloys,” *J. Nucl. Mater.*, vol. 457, pp. 352–361, 2015.
- [194] T. Stan, Y. Wu, P. B. Wells, H. D. Zhou, and G. R. Odette, “Epitaxial Fe thin films on $\{100\}$ $Y_2Ti_2O_7$: Model interfaces for nano-oxide dispersion strengthened steels,” *Metall. Mater. Trans. A*, vol. 48, no. 11, pp. 5658–5666, 2017.
- [195] T. Stan, “The role of oxides in nanostructured ferritic alloys and bilayers: Interfaces, helium partitioning and bubble formation,” 2017.

Chapter 2 Experimental techniques

2.1 Materials and Sample Preparation

In this section the procedures of material fabrication for industrial materials ODS-EUROFER and EUROFER 97 and for fabricated Y_2O_3 -FeCr bi-layer system are described and sample preparation routine prior to the ion implantation/irradiation is specified. Microstructures of as-supplied industrial materials ODS-EUROFER and EUROFER 97, as well as-fabricated model bi-layer are described. The techniques used for collecting the data will be explained when required.

2.1.1 Characterization of industrial materials ODS-EUROFER and EUROFER 97

2.1.1.1 ODS-EUROFER and EUROFER 97 microstructure and elemental content

This section is focused on reduced activation ferritic-martensitic (RAFM) oxide dispersion strengthened (ODS) steel ODS-EUROFER as the main industrial material investigated in this thesis. Data for its non-ODS counterpart EUROFER 97 steel are provided for relevant comparison.

Both industrial materials ODS-EUROFER and EUROFER 97 were supplied by Karlsruhe Institute of Technology (KIT). The chemical composition of these steels is summarized in Table 2.1.

Table 2.1. Chemical composition of ODS- EUROFER and EUROFER-97 steels (in wt.%) [1–3].

Element	C	Cr	Si	Mn	V	W	Ta	Y	O	Fe
ODS-EUROFER	0.07	8.92	0.11	0.41	0.19	1.11	0.08	0.19	0.14	Balance
EUROFER 97	0.12	8.91	0.04	0.48	0.20	1.08	0.14	–	–	Balance

The EUROFER97 samples originate from batch E83697 and were manufactured by Boehler Austria GmbH. The processing route of EUROFER 97 steel includes conventional ladle metallurgy, refining via vacuum arc re-melting, and hot rolling in the austenitic field. ODS-EUROFER was produced using powder metallurgy technique that included mechanical alloying of EUROFER 97 powder with 0.3% yttrium at Plansee GmbH, followed by hot isostatic pressing (HIP) and hot cross-rolling in the austenitic temperature range (1150°C). For details, see Ref. [1].

Both steels were supplied in heat treated condition which is referred to below as ‘as-supplied’ state. The samples of EUROFER 97 were austenitized for 30 min at 980°C, quenched in air and then tempered for 2 h at 760°C. ODS-EUROFER samples were austenitized at 1100°C for 30 min, quenched and then tempered at 750°C for 2 h.

Detailed microstructural studies of non-irradiated ODS-EUROFER [4–21] and EUROFER 97 [6,7,9,11,22–24] are already available in literature; some additional details are given in this section for clarity. The scanning (SEM) and transmission (TEM) electron microscopy investigations of ODS-EUROFER and EUROFER 97 steels in as-supplied state were carried out using SEM Zeiss Evo 50 XVP (NRNU MEPhI, Russian Federation) and TEM FEI TECNAI G² 20 Twin (JANNuS-Orsay, at CSNSM, Univ. Paris-Sud and CNRS (now IJCLab, CNRS/IN2P3 and University Paris-Saclay), France), respectively. The basic principles of these techniques are illustrated in section 2.3.2 below. Sample preparation of as-supplied samples for SEM and TEM investigations is described in section 2.1.1.2.

Figs. 2.1(a,c) and 2.1(b,d) show typical SEM/TEM images of ODS-EUROFER and EUROFER 97 steels in as-supplied state, respectively. Microstructure of both steels is characterized by elongated grains with some carbide precipitation preferentially along grain boundaries. ODS-EUROFER contains also Y_2O_3 nanoparticles visibly homogeneously distributed inside the grains (see inset in Fig. 2.1(c)). As can be seen in Fig. 2.1(a,b), ODS-EUROFER steel has noticeably finer grain structure than EUROFER

97. Smaller grains in ODS-EUROFER steel are a consequence of finely-dispersed Y_2O_3 nanoparticles that provide strong pinning effects on austenite grain growth during steel austenitization [7,11]. No retained austenite was present in both steels in as-supplied state [7,10].

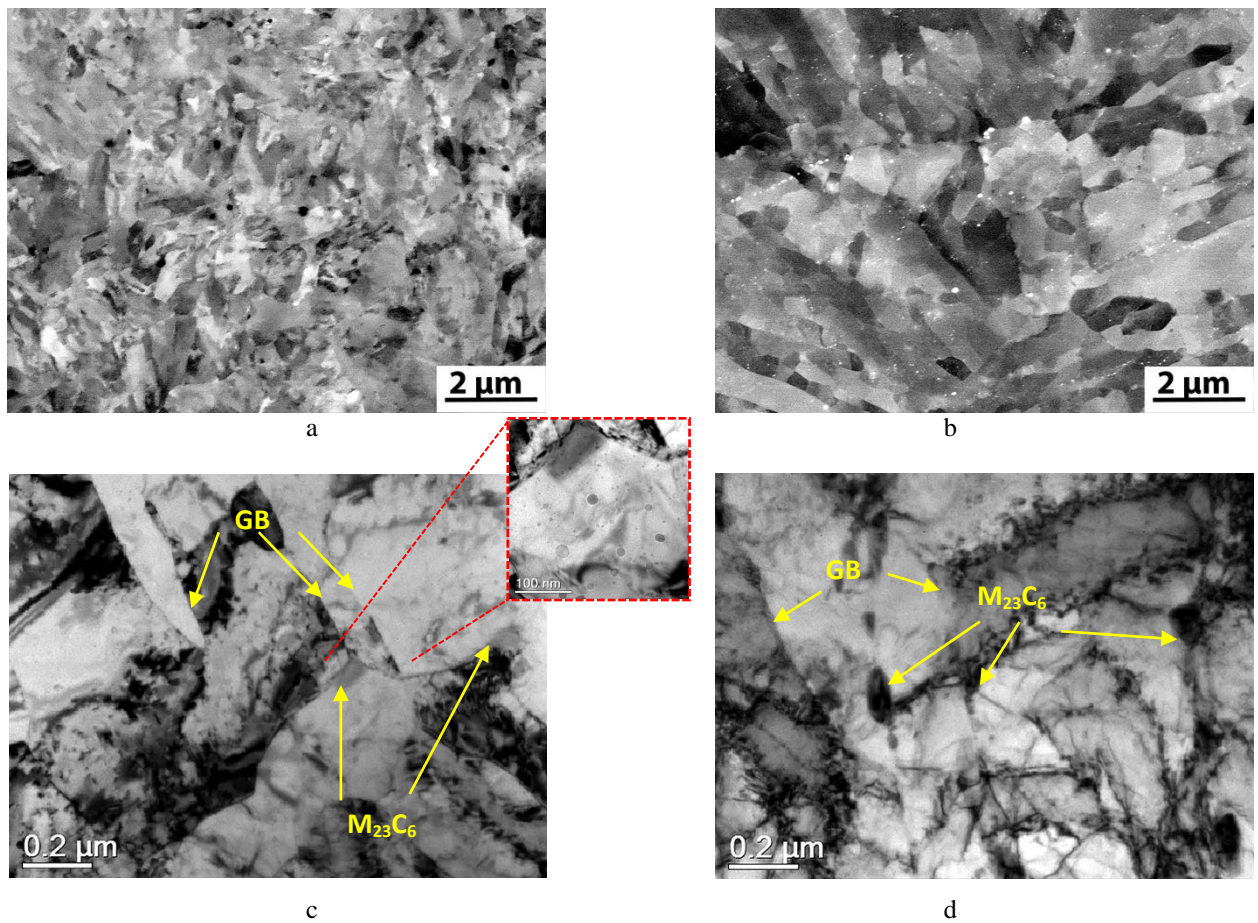


Fig. 2.1. Typical microstructure of ODS-EUROFER (a,c) and EUROFER 97 steel in as-supplied state (b,d). (a,b) BSE SEM image; (c,d) BF TEM (imaging conditions $\sim 0.5 \mu\text{m}$ underfocus). The inset shows an array of Y_2O_3 nanoparticles in ODS-EUROFER steel at a higher magnification.

As-supplied EUROFER 97 steel has a fully martensitic structure with martensite laths, blocks and packets [6,7,22,23]. A typical size of martensite grains in EUROFER 97 is $\sim 6.7\text{-}2 \times 0.5 \mu\text{m}$ [22,23]. For ODS-EUROFER with 0.5 wt.% of Y_2O_3 , duplex microstructure with residual ferrite and martensite grains was reported after heat treatment similar to that used in this thesis [6]. However, although the presence of residual ferrite was observed in many 9Cr ODS steels, see e.g. [25–28], its formation in ODS-EUROFER is unusual because a fully martensitic microstructure is expected to form after austenitization, similar to those in the base material EUROFER 97 which contains low content of ferrite stabilizers such as Ti, Cr and W. It is believed [25–28] that the main reason of residual ferrite phase formation in 9Cr ODS steels is the incomplete reverse transformation of ferrite to austenite during the austenitization at 1100°C due to the blocking of ferrite/austenite interfaces by oxide nanoparticles in the matrix. Thus, the possibility of residual ferrite formation depends not only on the concentration of ferrite stabilizers but also on the concentration of Y_2O_3 or/and Ti/O. Residual ferrite grains are frequently identified as regions with relatively coarse and sometimes elongated grains. Recently, coarse-grain regions were found in spark plasma sintered ODS-EUROFER with 0.3 wt.% of Y_2O_3 and reported as residual ferrite [13]. However, detailed investigation performed on EU batch ODS-EUROFER with 0.3 wt.% of Y_2O_3 (the same material as used in this thesis) [10,12] has revealed that, in contrast to Ref. [13], coarse regions underwent martensitic transformation and corresponded to zones not mechanically alloyed with Y_2O_3 rather than to residual ferrite grains. The volume fraction of regions with coarse grains was estimated to be $\sim 4\%$ [10]. The absence of residual ferrite in ODS-EUROFER steel with 0.3 wt.% of Y_2O_3 is in agreement with the

results of Ref. [25] that show fully martensitic structure in 9Cr ODS steels with the weight content of Y_2O_3 below certain limit. Though we did not pursue a detailed search for the presence of residual ferrite, the results of Ref. [10] obtained on the same material assure us that ODS-EUROFER used in this thesis has essentially tempered martensitic microstructure.

Small grain size of ODS-EUROFER steel together with limited TEM investigation area and strong diffraction contrast makes the combination of conventional SEM and TEM microscopy insufficient to identify exact grain size in this material. Since the density of grain boundaries is one of the critical input parameters required for swelling estimation, the electron backscatter diffraction (EBSD) technique [29] was used in this study to image the microstructure of ODS-EUROFER at the grain and sub-grain scales. The EBSD measurements were carried out in Zeiss Evo 50 XVP scanning electron microscope (SEM) equipped with a LaB_6 electron filament and a Nordlys S EBSD detector. The microscope operated at accelerating voltage of 20 kV. The step size used was $0.40\ \mu m$ and the mapped area was $8 \times 8\ \mu m$. The EBSD data analysis was done using HKL Channel 5 software. Fig. 2.2(a-c) provides the results of EBSD mapping.

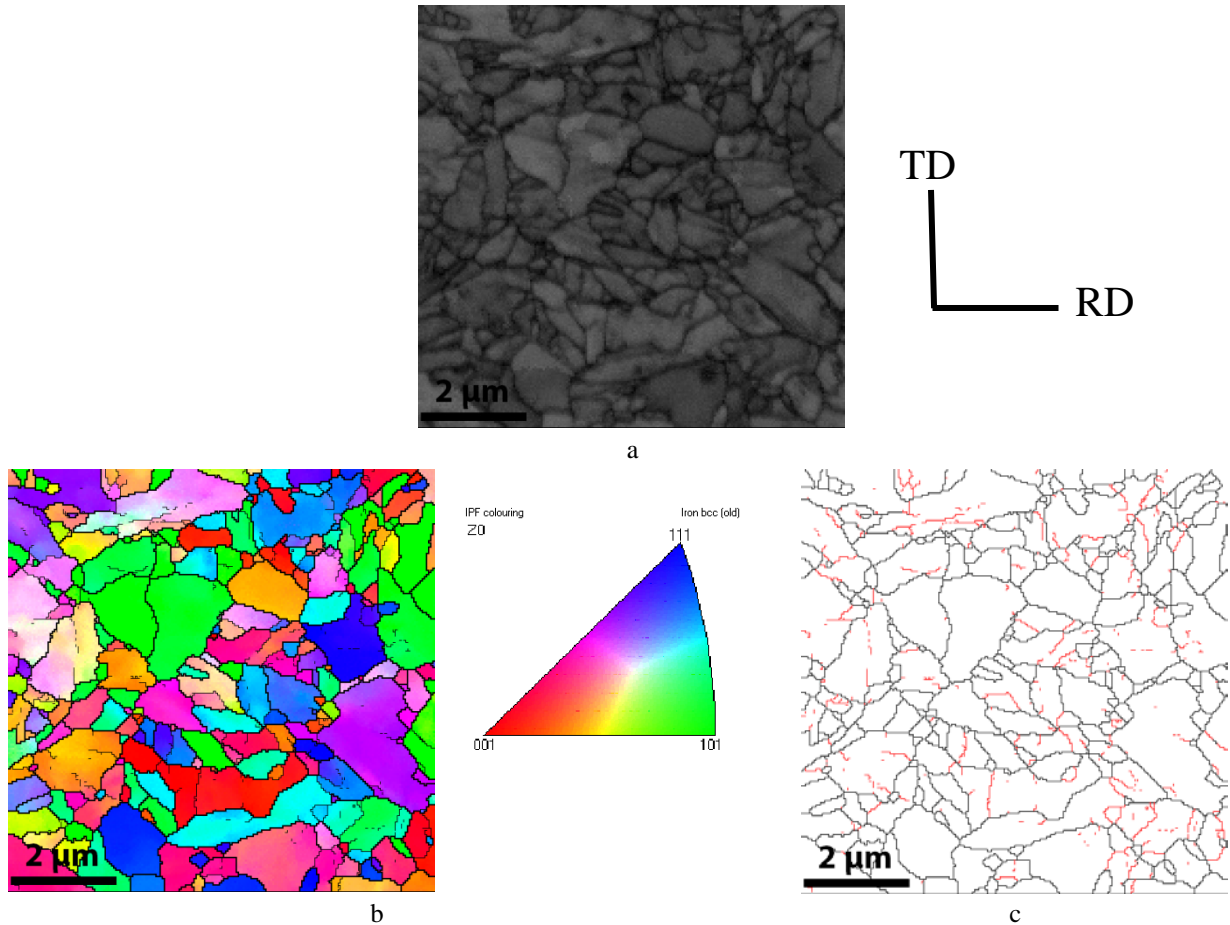


Fig. 2.2. EBSD mapping of ODS-EUROFER in as-supplied state: (a) EBSD pattern quality map; (b) orientation image maps from EBSD data; high angle grain boundaries with misorientation angle $\geq 15^\circ$ (HAGBs) are shown as bold black lines and low angle grain boundaries (LAGBs) with misorientation between 2° and 15° are thin black lines; (c) grain boundary map showing HAGBs as black lines and LAGBs as red lines. Rolling (RD) and transverse (TD) directions marked in panel (a) are valid for all panels.

Fig. 2.2(b) shows the inverse pole figure map of ODS-EUROFER, giving crystalline orientations on the scanned area. Fig. 2.2(c) shows the results of mesotexture determined in as-supplied ODS-EUROFER. Grain colors related to grain orientation are expressed in the standard triangle. ODS-EUROFER steel has weak crystallographic texture, as expected for hot-rolled steels following martensitic transformation [30]. The black lines shown in Fig. 2.2(c) correspond to high-angle grain boundaries (HAGBs) with misorientation angles $\geq 15^\circ$, while red lines correspond to low-angle grain boundaries

misorientation angles $\sim 2\text{-}15^\circ$. Grains with irregular morphology were sometimes found. HAGBs dominate in ODS-EUROFER steel (see Fig. 2.2(c)). LAGBs are also present in a lower fraction $\sim 24\%$. It should be mentioned that a significant amount of dislocation boundaries with low misorientations might be present in the investigated material but their quantification by SEM EBSD technique is challenging. Only misorientations above 2° should be taken into account since grain boundaries with misorientations below this limit cannot be properly indexed by SEM EBSD. Two peaks at $\sim 2^\circ$ and 59° can be seen in the grain misorientation distribution histogram obtained from mesotexture EBSD data and displayed in Fig. 2.3. A similar distribution was reported for quenched [7] and quenched/tempered [11,20] ODS-EUROFER steel. According to Ref. [7], the maximum at $\sim 2^\circ$ is presumably related to lath boundaries or dislocation substructures, while the maximum at $\sim 60^\circ$ is related to the crystallographic nature of the martensitic transformation itself (selection variants) and corresponds to packet or/and block boundaries. The average grain size in as-supplied ODS-EUROFER measured over 500 grains is found to be $\sim 0.7 \times 0.32 \mu\text{m}$. Although rare coarse grain regions (not shown) similar to those reported in Ref. [10] were detected on SEM EBSD maps, these regions were not met on TEM images in zones where He bubbles parameters were investigated (see sections 3.1.2.2-3.1.2.4, 3.1.2.6, 3.2.1, 3.2.2, 4.1.1, 4.1.2 and 4.3 below).

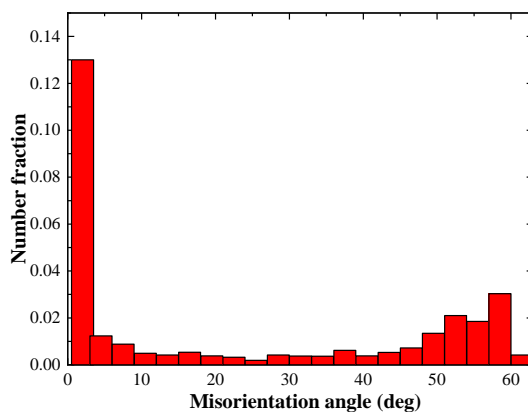


Fig. 2.3. Grain misorientation distribution in ODS-EUROFER steel in as-supplied state.

According to the literature data, dislocation density in ODS-EUROFER is by up to a factor of two higher than in EUROFER 97, but is still quite moderate due to static recovery during the tempering treatment [6,8,13].

The grain boundary inclusions with globular shape and average size of ~ 100 nm detected in both ODS-EUROFER and EUROFER 97 are $M_{23}C_6$ type precipitates rich in Cr, Fe and W [10,18,22,23]. The volume density of $M_{23}C_6$ carbides in ODS-EUROFER steels is only half of that in its non-ODS counterpart, possibly due to the lower carbon content. MX (TaC and VN) carbonitride particles with the average size of ~ 20 nm are found inside grains of EUROFER 97, while for ODS-EUROFER the presence of such particles has not been reported [7,11,13]. The common explanation [7] for this difference is the enrichment of Y_2O_3 particles in Ta and V during the high-energy milling [11,17,31], which results in depletion of steel matrix in these elements and suppression of MX particle formation.

Numerous dispersed Y_2O_3 particles with typical diameters ranging from 3 to 40 nm were located mostly inside ODS-EUROFER grains. As demonstrated in the inset in Fig. 2.1(c), the spatial particle distribution is relatively uniform inside particular grain. However, variations of particle number density from grain to grain and from one TEM sample to another were noticed. Low contrast of oxide particles on TEM images makes particle identification quite challenging. The average particle diameter of ~ 12 nm determined in this study through statistical analysis of ~ 1000 particles on different TEM samples agrees well with the literature data [4,8,16,18].

Literature sources (e.g. [8,9,14,19,21]) report quite different number densities of Y_2O_3 nanoparticles varying from $5 \times 10^{21} \text{ m}^{-3}$ [8] to $\sim 1 \times 10^{23} \text{ m}^{-3}$ [9,19] even for the same batch of ODS-

EUROFER. As a reasonable estimated number density of oxide particle for the evaluation of bubble number density, swelling and He fraction, the value of $1 \times 10^{22} \text{ m}^{-3}$ was used in sections 3.1.2.2-3.1.2.6, 3.1.3, 3.2.1-3.2.2, 4.1.1 and 4.1.2 below. Possible consequences of the uncertainty in Y_2O_3 nanoparticle number density evaluation on the swelling and accumulated He fraction estimation are discussed in section 3.1.2.7.

Typical microstructural parameters of ODS-EUROFER and EUROFER steel in as-supplied condition are summarized in Table 2.2. Densities of grain and carbide boundaries per unit ODS-EUROFER volume were calculated as a ratio between their surface to volume using the parameters obtained by SEM EBSD and TEM investigations and assuming that both microstructural features have ellipsoidal shape.

Table 2.2. Typical microstructural parameters of ODS-EUROFER and EUROFER steel in as-supplied state.

Microstructural component		ODS-EUROFER	Ref.	EUROFER 97	Ref.
Grain boundaries	Mean grain length (10^{-6} m)	0.70	This study	6.70	[22,23]
	Mean grain width (10^{-6} m)	0.32	This study	0.50	[22,23]
	Volume density (10^6 m^{-1})	7.7	This study	not calculated	-
Dislocations	Density (10^{14} m^{-2})	1.3-1.80	[6,8]	0.90	[6]
Carbides M_{23}C_6	Mean diameter (10^{-6} m)	1.10	This study	1.00	[22,23]
	Number density (10^{19} m^{-3})	0.8-2.70	[10,18]	4.18	[22]
	Volume density (10^5 m^{-1})	9.2	This study	not calculated	-
Y_2O_3 nano-oxides	Mean diameter (10^{-9} m)	12.00	[16]	-	-
	Number Density (10^{21} m^{-3})	10.00	[18]	-	-
MX precipitates	Mean Diameter (10^{-9} m)	-	-	20.00	[22,23]
	Number Density (10^{21} m^{-3})	-	-	1.00	[22-24]

2.1.1.2 Sample preparation prior to implantation/irradiation

Principal steps of the procedure of sample preparation from ODS-EUROFER and EUROFER 97 steels are shown in Fig. 2.4. As-supplied ODS-EUROFER and EUROFER 97 slabs were cut into $30 \times 4.5 \times 0.5 \text{ mm}$ bars parallel to the rolling plane by spark erosion cutting (SEC). During SEC, high frequency sparks are applied across a $10\text{-}50 \text{ }\mu\text{m}$ gap between a metal wire and the cut area on the material. The sparks result in material removal without cold working, which is a concern in conventional mechanical cutting [32]. Specimens are prepared for mechanical grinding/polishing by mounting them on a metal block to ensure that TEM discs used for ion implantation/irradiation have a flat planar surface. The metal block was heated on a hot plate up to 100°C to melt Crystal glue, which bonded the samples to the block. During the second preparation step, specimens were mechanically wet-grinded from both sides using SiC paper starting with grit 320, and working the grits up to 1200. After that specimens were ultrasonically cleaned successively in acetone and ethanol for 5 minutes. Samples of three different geometries were prepared for further implantations and investigations with TEM and TDS techniques. These sample types are referred to below as:

- *TEM bulk discs* - 3 mm discs with main thickness $100 \text{ }\mu\text{m}$, electropolished from one side. TEM results obtained on these specimens after ion implantation are reported in sections 3.1.1.-3.1.3, 4.1 and 4.3;
- *TEM thin foils* - 3 mm discs with main thickness $100 \text{ }\mu\text{m}$, electropolished from backside or from both sides to electron transparency. TEM results obtained on these samples are reported in sections 3.2.1 and 3.2.2.
- *TDS samples* - $15 \times 4.5 \times 0.1 \text{ mm}$ bars prepared by mechanical polishing. TDS results obtained on these samples are reported in section 4.2.

The required 3mm disks for *TEM bulk discs* and *TEM thin foils* were punched out from the steel bars using a puncher [32]. Steel samples for the TDS measurements were used directly in the shape of

bars with the sizes 15×4.5×0.1 mm. At the next preparation step samples of all types (TEM bulk discs, TEM thin foils, and TDS samples) were wet-polished from both sides using diamond suspension beginning with grain size 9 μm, and working up grain size to 1 μm. Mechanical polishing always introduces a thin layer of plastic deformation on the sample surface, even if fine grained suspension with the grain size as low as 1 μm is applied. Considering that in all implantation/irradiation regimes used quite thin subsurface region of investigated materials is affected during ion bombardment and further investigations, additional processing was necessary to eliminate the mechanically damaged surface layer.

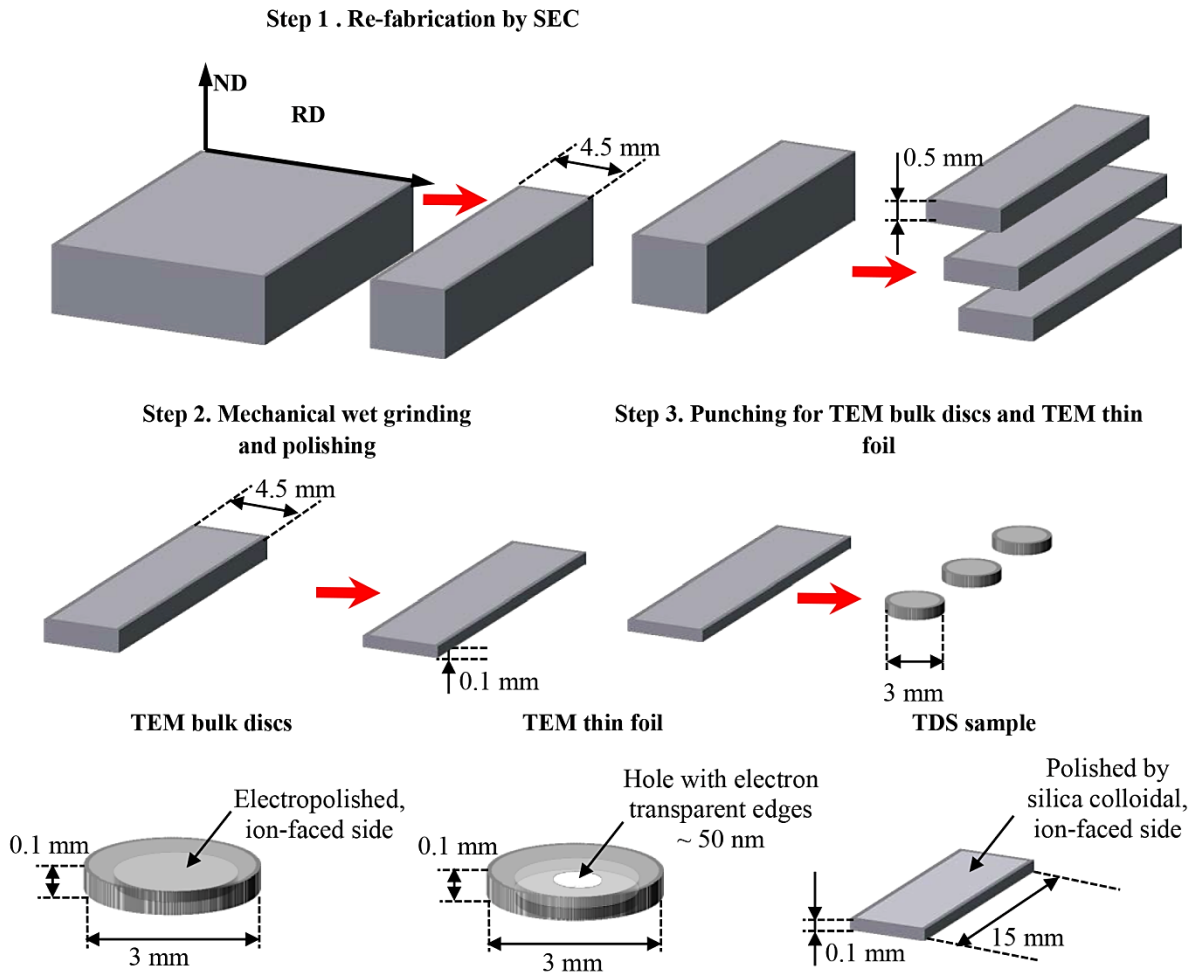


Fig. 2.4. A scheme of ODS-EUROFER and EUROFER97 sample preparation procedure used prior to ion implantation or irradiation.

In the case of *TEM bulk discs*, mechanically polished samples with diameters of 3 mm were further electropolished from one side using a twin-jet Struers Tenupol-5 unit with a 10% perchloric acid and 90% ethanol solution at the temperature of -20°C for 40 seconds, followed by cleaning successively in ethanol and methanol. Electropolishing in this regime removed ~10 μm thick layer from the sample surface, which exceeds the estimated thickness of damaged layer of ~3 μm.

TEM thin foils were prepared in a similar way, but electropolishing was conducted on both sides of specimens until a hole was created at the center. The region closest to the hole was very thin (ideally <50 nm) and thus ready for direct TEM observation.

At the next preparation step, *TEM bulk discs* and *TEM thin foils* were cleaned from both sides by ion milling system PIPS 693 using the ion beam of 3 eV voltage and 5–6° etching angle for 2 minutes in order to remove thin oxide layer formed on the steel surface after electropolishing. *TEM thin foils* were

checked by TEM just after electropolishing and after ion milling in order to assure that no visible defects formed after ion cleaning in the applied regime.

Considering that TDS technique is a very sensitive method for the hydrogen detection, a special finishing preparation recipe was used for this sample type in order to exclude additional hydrogen introduction during electropolishing. *TDS samples* were wet mechanical polished for 20 minutes using fine grained silica colloidal suspension (40 nm particle size). This suspension is designed to minimize the layer of surface deformation by means of both dispersing action of fine grained silica as well as chemical mechanical polishing (CMP) action (suspension pH > 9.5).

At the final preparation step, samples of all types were plasma cleaned for 7 minutes by pure Ar using Gatan Solarus 950 plasma unit in order to remove the rest of carbon and oxygen contamination. After preparation procedure and up to the implantation/irradiation, samples were stored under vacuum.

Samples used for initial microstructure characterization by SEM and TEM techniques (see section 2.1.1.1) were prepared following the same route as *TDS samples* and *TEM thin foils*, respectively.

2.1.1.3 Sample preparation after ion implantation/irradiation

Two different types of samples for TEM investigations were obtained from implanted *TEM bulk discs* (sections 3.1.1-3.1.3, 3.2.1, 4.1 and 4.3), namely planar-view and cross-sectional samples.

Planar-view sample preparation was conducted by backside twin-jet electropolishing [32] using the same recipe as for samples prior to implantation, but electropolishing was performed up to electron transparency. During electropolishing the ion-facing side of the sample was protected by light transparent plastic film. A typical BF TEM overview image of electron transparent areas in plain-view sample prepared by backside electropolishing is given in Fig. 2.5.

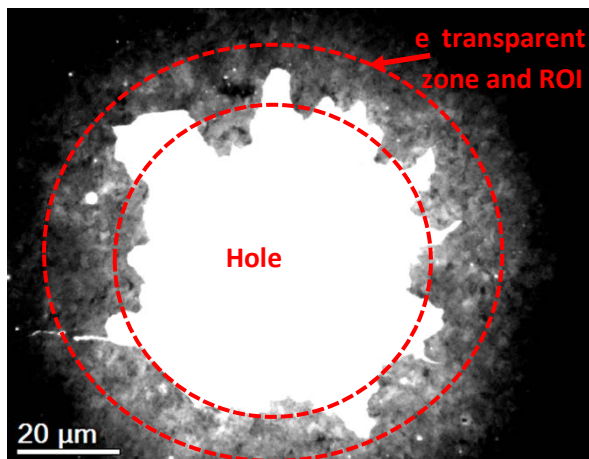


Fig. 2.5. Typical BF TEM overview image of plane-view sample displaying a hole at the center surrounded by electron transparent areas (TEM ROI).

After electropolishing, samples were cleaned from both sides by ion milling (PIPS 693) with 1 keV ion beam and 4–5° etching angle for 2 minutes. The cross-sectional TEM samples were prepared by focus ion beam (FIB) lift-out technique [33]. The major part of TEM investigations in this thesis focused on the gas/radiation induced cavities evolution. As will be shown later, the low energy ion implantation used in this thesis resulted in quite narrow implanted zone ~100 nm thick. Thus, the region of interest (ROI) for TEM investigations is quite narrow on cross-sectional FIB samples, in contrast to planar view samples (see section 3.1.1.1), where ROI is limited only by the area of thin enough electron transparent zones (electron mean free path (MFP) of 200 keV electrons in Fe is ~70-100 nm). Also, according to Ref. [34], the best samples for TEM cavity investigation in metals (conductive materials) are samples produced by electro-polishing. Such samples are free from ion induced artifacts that are typical for any ion based preparation. Taking into account both limitations, backside electropolishing technique

was used for the preparation of the major part of TEM probes from implanted *TEM bulk discs* of ODS-EUROFER and EUROFER 97 steels.

Cross-sectional TEM FIB samples of ODS-EUROFER were utilized only in sections 3.1.1.1 and 4.3 for the investigation of bubble size distribution relative to ion concentration profile and for electron energy loss spectroscopy (EELS) investigation of hydrogen trapped in He bubbles. The technique of cross-sectional FIB samples preparation is the same as that used for bi-layer metal/oxide system (see section 2.1.2.3 below for detailed description).

TEM thin foils used in sections 3.2.1 and 3.2.2 were not subjected to any special treatment after ion irradiation. After preliminary TEM examination these samples were cleaned from both sides by ion milling (PIPS 693) with a 1 keV ion beam and 4–5° etching angle for 2 minutes.

After implantation all samples were stored under vacuum. Prior to TEM investigations all samples were subjected to pure Ar plasma cleaning for 3 minute (Gatan Solarus 950 plasma unit) to remove the remaining carbon and oxygen contaminations.

TDS samples were not subjected to any special sample preparation treatment after implantation; they were transferred and stored under vacuum conditions until TDS measurements.

2.1.2 Fabrication and microstructural characterization of bi-layer $Y_2O_3/FeCr$ system

2.1.2.1 Fabrication of bi-layer metal/oxide system

Model thin film samples studied in this thesis were fabricated at the laboratory of Physics of magnetic nanostructures and spintronics of the Institute of Physics, Kazan Federal University (Russian Federation) employing an ultra-high vacuum (UHV) setup for deposition and analysis of thin film structures.

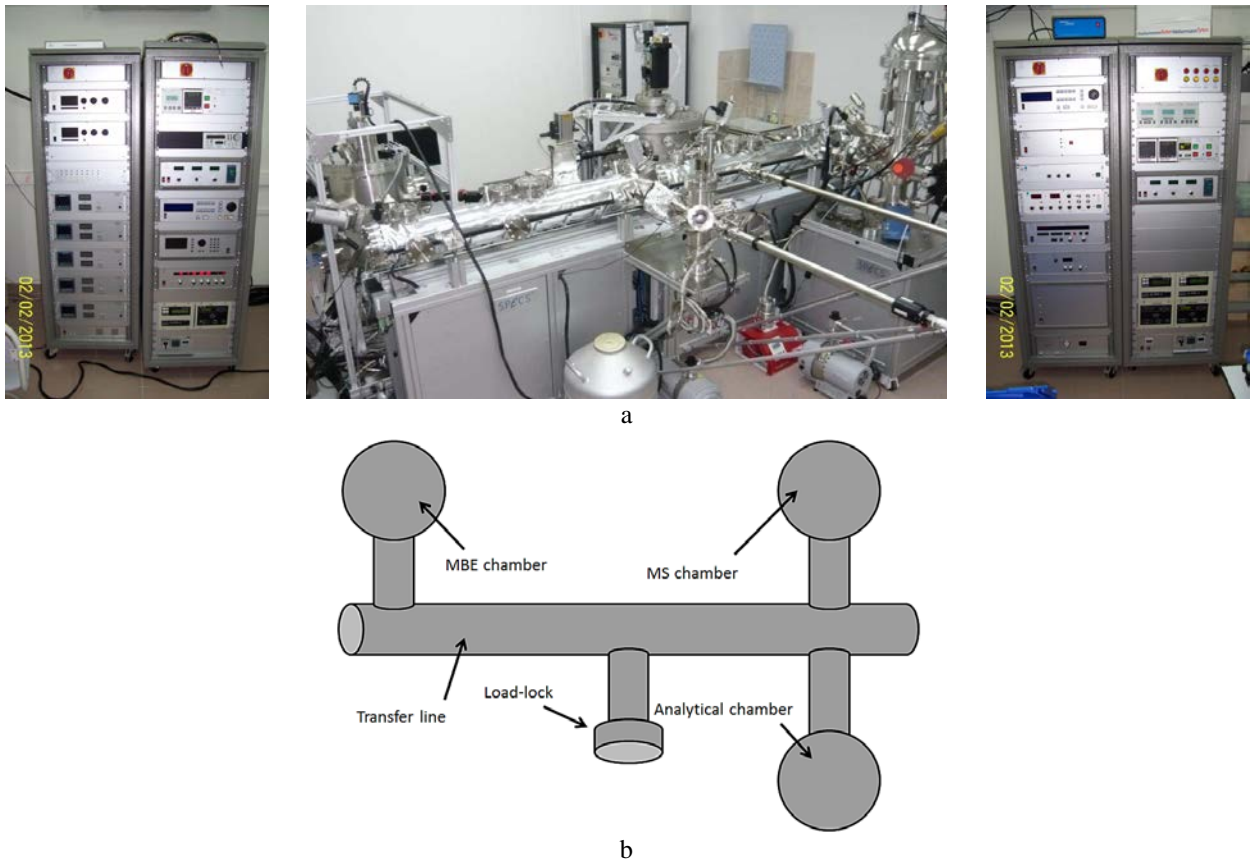


Fig. 2.6. (a) Overview and (b) schematic illustration of the UHV setup used for deposition and analysis of thin film structures.

The setup consists of three main operation chambers (see Fig. 2.6), namely, the magnetron sputtering (MS) chamber, the molecular beam epitaxy (MBE) chamber and the analytical chamber. The MS chamber supports base vacuum better than 5×10^{-7} Pa; it is equipped with the heating rotating substrate table and with six deposition positions that are powered by DC, AC or pulsed DC power sources. The target positions are equipped with additional gas supply that allows performing reactive MS deposition of oxide or nitride thin films. The control over the deposition kinetics is carried out via a quartz-crystal monitor (QCM).

The basics of the magnetron sputtering can be described as follows. A sputtered target is fixed next to magnets in the magnetron. These magnets form a specific distribution of magnetic field in the vicinity to the target. Sputtering process occurs when plasma of inert gas with high molecular weight (typically, Ar) is ignited and maintained next to the target and a high voltage is applied to the target-cathode. Electrons which are present in the plasma are accelerated away from the cathode causing a steady-state ionization of Ar atoms. The positive gas ions are accelerated towards the negatively charged target, leading to high energy collisions with the surface of the target and the sputtering of target atoms, which are transferred to the substrate. Strong magnets of the magnetron confine the electrons in the plasma near the surface of the target that increases the density of the plasma and the sputtering rate. In the case of reactive MS, a reactive gas (O_2 for instance) is supplied additionally to the chamber, which causes oxidization of the sputtered material at the substrate, at the target surface, or during the transfer from the target to the substrate. A detailed overview of the reactive MS technique can be found in Ref. [35].

The MBE chamber supports the base vacuum better than 3×10^{-8} Pa. The chamber is equipped with a heating substrate table, with an Ar ion gun for cleaning and etching of sample surface, and with up to nine target positions that are the effusion cells with thermal and the e-beam evaporation positions. The MBE chamber is additionally equipped with reflection high-energy electron diffraction (RHEED) and low energy electron diffraction (LEED) units for precise *in situ* monitoring of the crystal structure of substrates and deposited films.

The basics of the MBE can be described as follows. The target material is loaded into a crucible. The crucible is heated in UHV conditions above the melting point of the target material using either the ohmic heating or e-beam heating. Thermally desorbed atoms of the target material are transferred to the substrate. Importantly, the desorption process in UHV conditions ensures a unidirectional kinematic flow of atoms or molecules with no or a small number of collisions among them. A precise control of the beam fluxes and growth conditions of MBE technique enables a layer-by-layer growth of various thin films. A detailed overview of modern MBE techniques can be found in Ref. [36].

A layer-by-layer composition of fabricated samples can be studied in the analytical chamber that is equipped with a set of spectroscopy techniques, including X-ray photoemission spectroscopy (XPS), Auger spectroscopy, and the mass spectrometry of secondary ions (SIMS). Additionally the chamber is equipped with an Ar ion gun and a heater for cleaning, etching or annealing of studied samples.

All three operation chambers are connected to each other and with the load-lock via the UHV transfer line with the base vacuum better than 3×10^{-8} Pa. This allows transfer of a sample between the operation chambers in UHV conditions with no exposure to the air, which provides an opportunity for alternation of deposition methods, materials, as well as for *in situ* analysis of fabricated samples at different technological stages.

In this study, bi-layer FeCr/Y₂O₃ metal/oxide films were deposited on single crystal ceramic substrates in 2 stages combining the reactive MS deposition of Y elemental target in oxygen atmosphere and MBE deposition of elemental Fe and Cr metals using thermal effusion.

2.1.2.1.1 Substrate preparation

Three different epi-polished single-crystal substrates were used: (001)-oriented MgO, (100) SrTiO₃, and (110) YSZ. All substrates were $5 \times 5 \times 0.5$ mm³ in size and were supplied by *Crystal*

GmbH (Germany). A molybdenum substrate holder was used for deposition with 6 substrate positions (see Fig. 2.7). Prior to deposition of thin films, the substrates were annealed in ultra-high vacuum (better than 3×10^{-8} Pa) at 600 °C for 20 min. These means improve epitaxial quality of substrate surface. Single-crystalline low-energy electron diffraction (LEED) patterns were obtained after vacuum annealing procedure for all substrates. An example of LEED pattern for (001) SrTiO₃ substrate is shown in Fig. 2.8.

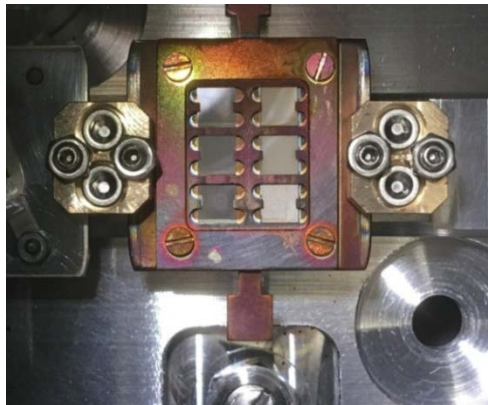


Fig. 2.7. Samples fixed on the deposition holder.

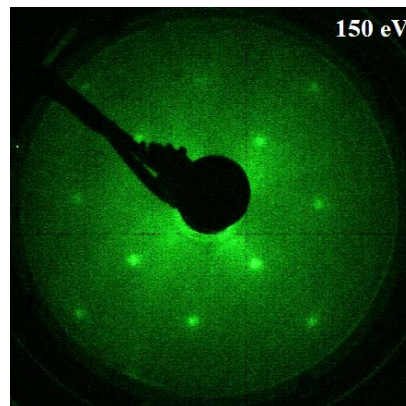


Fig. 2.8. LEED pattern of a pure SrTiO₃ (001) surface.

2.1.2.1.2 Deposition of the yttrium oxide (Y₂O₃) thin film

Deposition of Y₂O₃ thin films was performed by DC reactive magnetron sputtering of 99.99% purity elemental Y target in argon-oxygen environment at Ar flow rate 50 sccm and O₂ flow rate 1 sccm. The purity of working (Ar) and reactive (O₂) gases was 99.9999%. The residual and working pressure of gas mixture were 6.5×10^{-7} Pa and 0.6 Pa, respectively. The substrates were kept at 600 °C during the deposition process. The heating was accomplished through radiative heat transfer from a tungsten filament. Depositions were performed within ultrahigh vacuum chamber (BESTEC, Germany). The power of the DC generator was fixed at 43 W. Film growth was controlled by a calibrated quartz-crystal monitor (by INFICON, Switzerland). The resulting growth rate was ~20 nm/h. In order to obtain relatively uniform thickness of films, substrate table was rotated during the deposition with the rate of 5 rpm. The angle of magnetron target to the surface of the substrate table was set at 45°. Despite rotation of substrates during the deposition process, the design of the substrate holder does not allow to obtain uniform film thickness. Thus, only central area of samples with the size of 2×2 mm² was used for further analysis by means of transmission electron microscopy (TEM).

2.1.2.1.3 Deposition of Fe-10%Cr thin film

The top layer of metal/oxide bi-layer system consisting of Fe-10%Cr alloy was deposited by co-deposition of elemental Fe and Cr molecular beam sources using ultra-high vacuum (UHV) molecular beam epitaxy system (MBE, by SPECS GmbH, Germany). Concentration of Cr in the alloy was monitored by variation of the temperature coefficient by means of calibration sensor. The base vacuum in the MBE chamber was better than 3×10^{-8} Pa. During the deposition of Fe-Cr film the temperature of substrates was 400 °C. The growth rate was controlled by a calibrated QCM (by INFICON, Switzerland). The resulting deposition rates were ~23 nm/h for Fe and 0.26 nm/h for Cr. At the final stage samples were annealed in UHV conditions ($< 5 \times 10^{-7}$ Pa) at 600 °C for 20 minutes.

2.1.2.2 Microstructure and elemental content of bi-layer $Y_2O_3/FeCr$ system

This section presents the results on microstructural characterization of as-fabricated samples of model bi-layer $Y_2O_3/FeCr$ system by means of X-ray diffraction (XRD) and transmission electron microscopy (TEM). The basic principles of applied techniques are described in section 2.3.1 below.

XRD studies were carried out in the Center for X-ray Research and Diagnostics of Materials of the National University of Science and Technology (Russian Federation) using a Rigaku SmartLab diffractometer with monochromatic CuK_{α} radiation. The out-of-plane symmetrical-reflection XRD measurements were conducted using parallel beam optics [37,38] in the angle interval of $20-120^\circ$ with a step of 0.05° and the dwell time of 1 s per point. Fig. 2.9(a-c) shows XRD pattern for $Y_2O_3/FeCr$ bi-layers deposited on (001)-oriented MgO, (110) YSZ, and (100) SrTiO₃, respectively. XRD data show that for all deposited films the Y_2O_3 layer matches the crystallography information for cubic yttrium oxide in the PDF database (PDF Card No. 03-065-3178), namely - space group Ia3 (206), $a = b = c = 1.060$ nm, and $\alpha = \beta = \gamma = 90^\circ$. Fe-Cr layer for all deposited films matches the crystallography information on cubic bcc FeCr alloy in the PDF database (PDF Card No.: 01-077-7598), namely - space group Im-3m (229), $a = b = c = 0.2878$ nm, and $\alpha = \beta = \gamma = 90^\circ$.

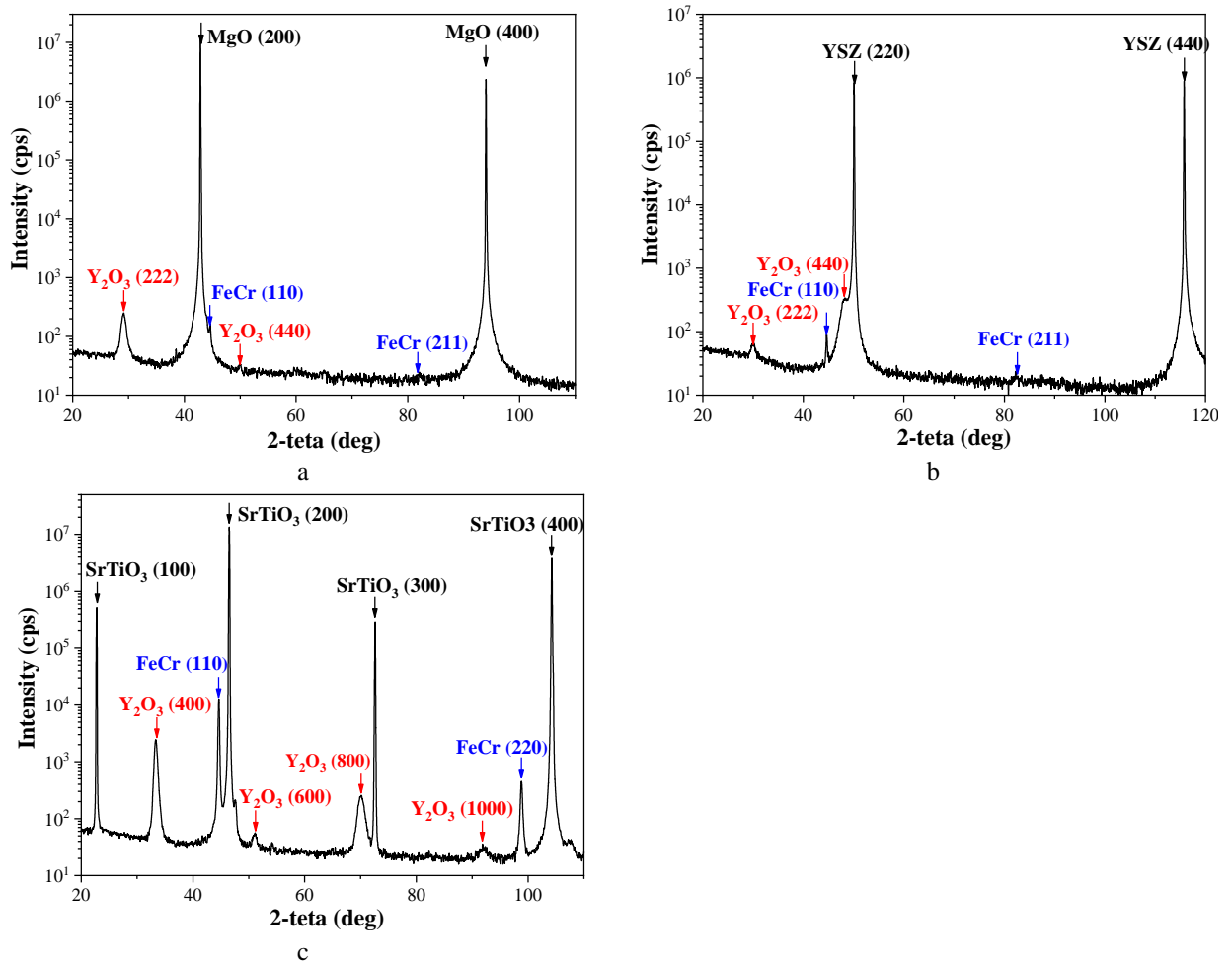


Fig. 2.9. XRD patterns for $Y_2O_3/FeCr$ thin films deposited on: (a) MgO(100); (b) YSZ(110) and (c) SrTiO₃(100) substrates.

The XRD pattern plotted in Fig. 2.9(a) shows that the Y_2O_3 layer deposited on (100) MgO substrate is predominantly oriented in the Y_2O_3 [222] direction, although a small contribution from Y_2O_3 [440] is also visible. For the FeCr layer deposited on top of (111)&(110) Y_2O_3 || (100)MgO, two peaks corresponding to orientations [110] and [211] are observed.

The Y_2O_3 layer deposited on (110) YSZ substrate (Fig. 2.9(b)) demonstrates two peaks that reflect to the Y_2O_3 [222] and [440] directions. The intensity of the peak corresponding to [440] is higher. The FeCr layer deposited on top of (111)&(110) Y_2O_3 || (110) YSZ shows two peaks with relatively weak intensities with the same orientations [110] and [211] as in the case of (111)&(110) Y_2O_3 || (100) MgO system.

The presence of more than one crystalline orientation (different from the substrate) for Y_2O_3 layers deposited on (100) MgO and (110) YSZ indicates that no single crystal epitaxy was achieved for Y_2O_3 layer. Consequently no epitaxial orientation of FeCr layers relative to $\text{Y}_2\text{O}_3/\text{MgO}(100)$ and $\text{Y}_2\text{O}_3/\text{YSZ}(110)$ are expected.

Fig. 2.9(c) shows XRD pattern for FeCr/ Y_2O_3 /SrTiO₃(100), where Y_2O_3 (400), (600), (800) and (1000) reflections are visible. Two peaks reflected to FeCr [110] and [220] directions are present. The absence of Y_2O_3 and FeCr peaks corresponding to other crystalline orientations implies the formation of single crystalline layers of Y_2O_3 and FeCr with possible epitaxial relationship between layers. The XRD patterns show that Y_2O_3 and FeCr are oriented out-of-plane with the (100) and (110) planes parallel to the film surface. However, for the FeCr film the (110) surface is the close-packed surface and is thus typically favored as a growth surface even if no in-plane orientation is present. Hence, the epitaxial matching to Y_2O_3 needed more detailed verification.

Therefore, detailed cross-sectional TEM and high resolution transmission electron microscopy (HRTEM) studies were carried out using TEM FEI TECNAI G² F20 S-Twin (Systems for microscopy and analysis (SMA), Russian Federation) to investigate the structure of FeCr- Y_2O_3 interface. A typical cross-sectional BF TEM micrograph of the model bi-layer Y_2O_3 /FeCr system is shown in Fig. 2.10. The individual layer thicknesses for the first FeCr and the second Y_2O_3 are ~80 nm.

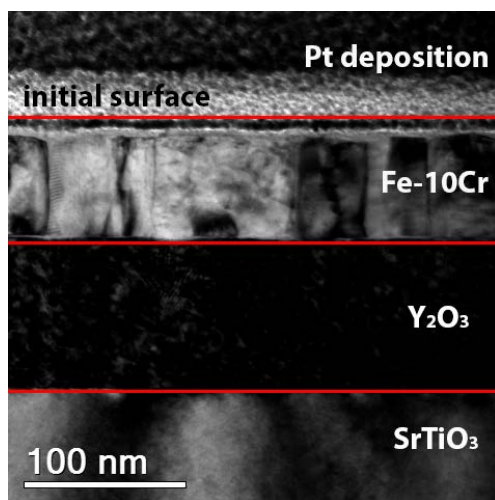


Fig. 2.10. BF TEM image of as-fabricated bi-layer Y_2O_3 /FeCr system deposited on SrTiO₃(100) substrate.

The Y_2O_3 layer appears in the BF image in dark contrast along the entire investigated sample. No visible grain structure indicates a well-ordered single crystalline Y_2O_3 layer deposited on SrTiO₃ substrate. In contrast, the FeCr layer exhibits columnar grain structure above Y_2O_3 (100) film. The transverse grain size in FeCr is small, about 40 nm on the average. Some of FeCr grains appear in dark and some in weak contrast in the BF image. Since the substrate and consequently the Y_2O_3 layer are oriented, the weak contrast of some grains in FeCr layer indicates that they are poorly oriented as compared to the dark FeCr grains.

HRTEM cross-sectional image taken close to [100] substrate zone axis and [110] zone axis of Y_2O_3 and corresponding Fast Fourier Transform (FFT) image of the middle part of model bi-layer Y_2O_3 /FeCr system are shown in Fig. 2.11(a,b). In both images, the single crystalline nature of Y_2O_3 (100) film is clearly visible. Several in-plane orientations for FeCr and Y_2O_3 are found among the samples analyzed. The most commonly observed in-plane orientation relationships (ORs) between Y_2O_3 and FeCr

layers, namely, $[\bar{1}10]_{\text{FeCr}} \parallel [001]_{\text{Y}_2\text{O}_3}$, $[110]_{\text{FeCr}} \parallel [1\bar{1}0]_{\text{Y}_2\text{O}_3}$ & $(001)_{\text{FeCr}} \parallel (110)_{\text{Y}_2\text{O}_3}$ and $[\bar{1}10]_{\text{FeCr}} \parallel [001]_{\text{Y}_2\text{O}_3}$, $[11\bar{2}]_{\text{FeCr}} \parallel [1\bar{1}0]_{\text{Y}_2\text{O}_3}$ & $(111)_{\text{FeCr}} \parallel (110)_{\text{Y}_2\text{O}_3}$ are shown in Figs. 2.11(a) and 2.11(b), respectively. According to the presented HRTEM data, these in-plane orientations correspond to the following out-of-plane relations $[001]_{\text{FeCr}} \parallel [110]_{\text{Y}_2\text{O}_3}$ & $(\bar{1}10)_{\text{FeCr}} \parallel (001)_{\text{Y}_2\text{O}_3}$ and $[111]_{\text{FeCr}} \parallel [110]_{\text{Y}_2\text{O}_3}$ & $(\bar{1}10)_{\text{FeCr}} \parallel (001)_{\text{Y}_2\text{O}_3}$, respectively. HRTEM and FFT patterns (Fig. 2.11(b)) are similar to those obtained in Ref. [4] for an Y_2O_3 particle oriented along $[110]$ zone axis and embedded in FeCr matrix oriented along $[111]$ zone axis in ODS-EUROFER steel.

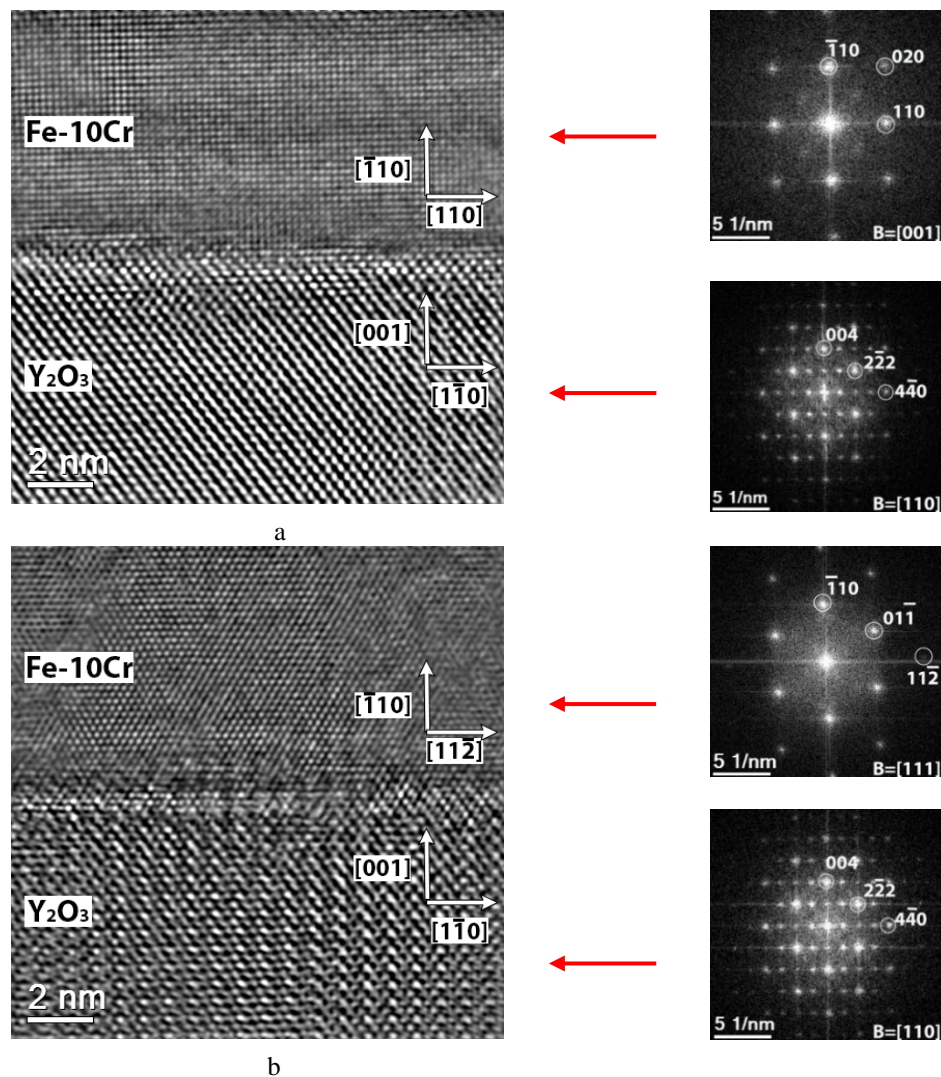


Fig. 2.11. HRTEM images and corresponding FFT images for two different as-fabricated bi-layer $\text{Y}_2\text{O}_3/\text{FeCr}$ systems deposited on SrTiO_3 (100) substrate. In-plane orientation relationships of films are: (a) $[110]_{\text{FeCr}} \parallel [1\bar{1}0]_{\text{Y}_2\text{O}_3}$ & $(001)_{\text{FeCr}} \parallel (110)_{\text{Y}_2\text{O}_3}$ and (b) $[11\bar{2}]_{\text{FeCr}} \parallel [1\bar{1}0]_{\text{Y}_2\text{O}_3}$ & $(111)_{\text{FeCr}} \parallel (110)_{\text{Y}_2\text{O}_3}$.

Elemental content of as-fabricated bi-layer $\text{Y}_2\text{O}_3/\text{FeCr}$ system was analyzed using energy dispersive X-ray spectroscopy in the scanning transmission electron microscopy (STEM) mode. Fig. 2.12(b-e) demonstrates qualitative elemental distributions in a typical region of as-fabricated system obtained by EDX together with a high angular annular dark field (HAADF) STEM image (Fig. 2.12(a)) of the area used for the elemental mapping. A uniform distribution of iron and yttrium within corresponding films can be noticed. Although chromium and oxygen are also distributed quite uniformly within the FeCr film, a pronounced chromium and possibly oxygen enrichment is visible in the interfacial

region. Some amount of oxygen is found in the FeCr film, which might be a result of film surface oxidation during sample preparation or/and TEM observations.

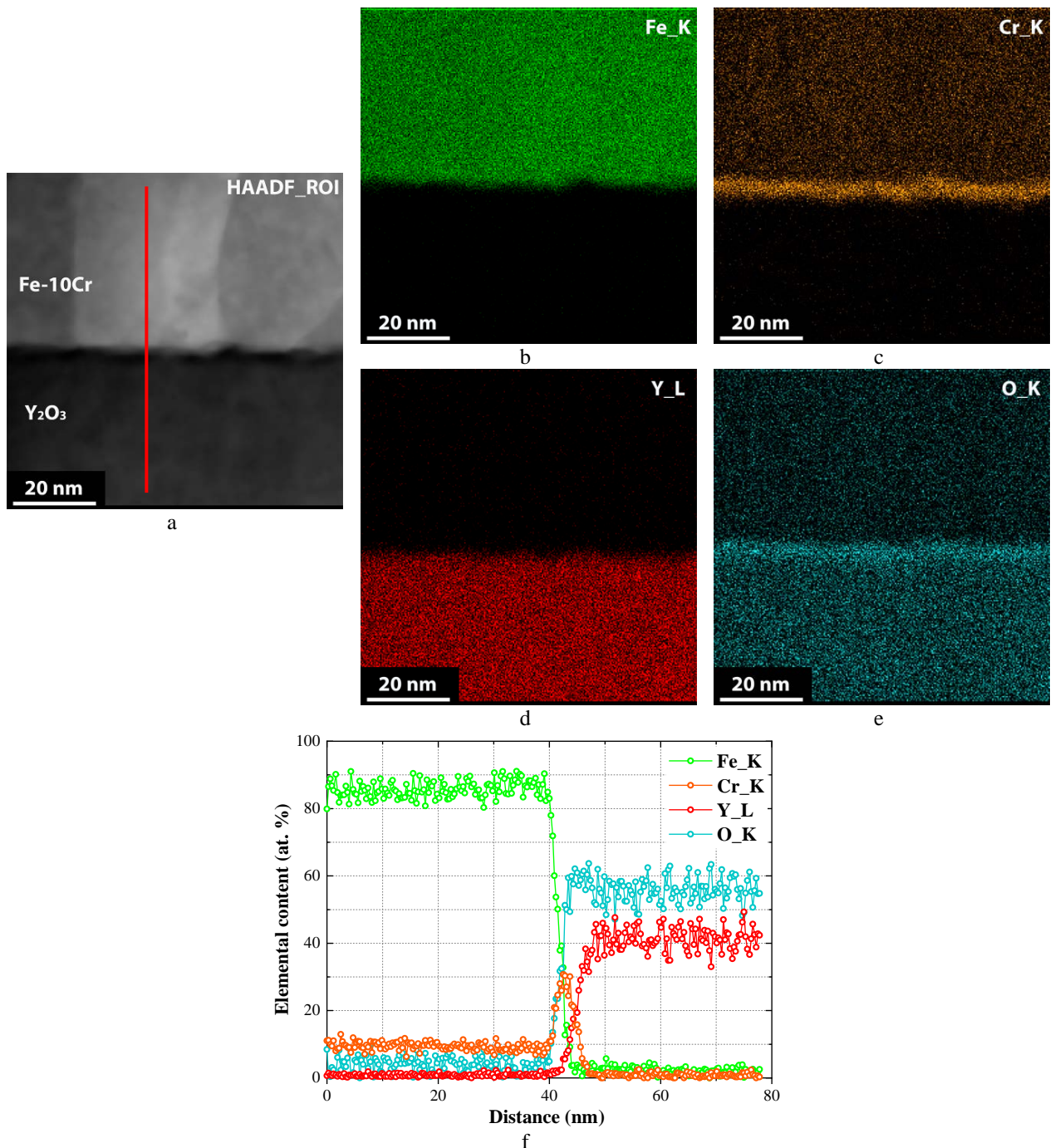


Fig. 2.12. (a) HAADF STEM image of the area used for the elemental mapping; (b-c) STEM EDX elemental maps of as-fabricated bi-layer Y₂O₃/FeCr system deposited on SrTiO₃ (100); (f) EDX line scan across the interface. Red line in panel (a) indicates the position of EDX line scan.

Fig. 2.12(f) shows the distribution profiles of chemical elements across interfaces (bottom-up direction) and clearly demonstrates chromium segregation up to 30 at.% at the interface. The thickness of chromium enriched layer doesn't exceed 5 nm. Similar chromium segregation around Y₂O₃ particles in ODS-EUROFER steel were reported in Refs. [17,31]. Also, minor oxygen enrichment can be noticed close to the interfacial area. The formation of Cr_xO_y or (Fe,Cr)_xO_y at the interface seems unlikely because chromium enrichment appears directly at the interface while the oxygen enrichment mostly corresponds to the top sub-layer of yttria film. It should be noted that O-K_α (525 eV) and Cr-L_α (572 eV) lines in EDX

spectra are overlapped. Therefore, the visible oxygen enrichment is most probably an artifact that appears due to Cr-L_α line presence. The ratio of Y and O signals within the yttria film corresponds to the stoichiometry of Y₂O₃ within the accuracy of performed measurements. In the FeCr film, the chemical concentration of iron is slightly lower than 90 at.%. Since the chromium concentration calculated from separate Cr-K_α line doesn't deviated from the nominal value 10%, the detected iron depletion seems also to be an artifact due to O-K_α and Cr-L_α lines overlapping. However, it cannot be firmly excluded that the minor incompatibility of iron and chromium chemical profiles is caused by the presence of 3-5 at.% of oxygen in this film due to surface oxidation of the sample.

2.1.2.3 Sample preparation prior to and after implantation/irradiation

In order to prevent contamination of samples with oxygen and carbon after preparation, the as-fabricated samples of metal/oxide bi-layer system were stored and transported under vacuum. No specific processing was applied to as-fabricated samples prior to ion implantation/irradiation. Before implantation, bi-layer samples were removed from the transportation boxes and mounted onto a sample holder and an irradiation stage for *ex situ* ion implantations (see section 2.2.1.3). The sample holder was specially designed for this sample type in order to fit implantation setup and sample geometry.

The same technique of samples preparation for TEM characterization was used for both as-fabricated samples and samples after implantation/irradiation.

The fabricated model system is a multiphase, highly heterogeneous material which consists of thin ceramic (insulator) and metal (conductive) layers. This kind of samples is difficult to handle by conventional TEM sample preparation techniques. Also, microstructural investigations of the bi-layer system were mostly conducted in HRTEM mode requiring a specific sample orientation. The preparation of TEM samples by FIB technique is obligatory in this case in spite of the risks of undesirable damage induced by ion bombardment, Ga ion implantation into the sample and re-deposition of sputtered matter.

The cross-sectional TEM samples were prepared by means of FIB lift-out technique at the Institut d'électronique, de Microélectronique et de Nanotechnologie (Lille, France) using Strata dual-beam 235 (FEI, USA) microscope composed of an electron column (SEM) and an ion column (FIB) and three internal micromanipulators Kleindiek. SEM allows to observe sample and to localize the area of interest. FIB allows depositing material or etching the sample.

The main steps involved in FIB lift-out preparation are [33]:

- Pt strip deposition over the sample to protect the outer surface of interest from Ga ion implantation and damage
- Trench milling on both sides of ROI at high voltage (30 kV)
- Ion-milling the release cuts to the sample (30 kV)
- Attachment of the Kleindiek manipulator to the sample
- Lifting-out the sample from the trench followed by mounting on TEM copper or molybdenum grid
- Final sample thinning from both sides (30 kV)
- Low voltage (5 kV) cleaning to remove amorphization on each side of the sample.

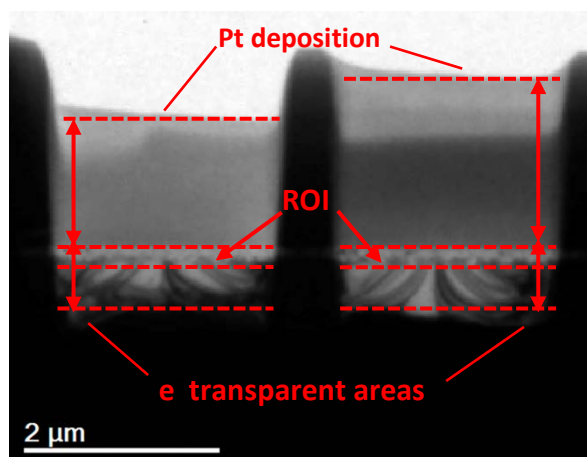


Fig. 2.13. Typical BF TEM overview image of investigated FIB probe showing the electron transparent areas, ROI for TEM investigations and Pt protection layer.

FIB samples were cut roughly parallel to the $\langle 100 \rangle$ direction of SrTiO_3 substrate. Final thinning was conducted to a depth of ~ 500 nm to ensure that the entire region of interest ~ 200 nm thick was captured. In order to improve measurement statistics, each prepared FIB sample contained 2-4 electron

transparent windows with the final thickness of < 40 nm and the length of ~ 2 μm . A typical BF TEM overview image of investigated FIB probe is given in Fig. 2.13.

2.2 Ion Implantation/Irradiation

In this study, ion implantation and ion irradiation techniques were used to achieve well controlled gas atom incorporation and damage simulation in investigated materials. This section covers the experimental setup and techniques used during ion beam implantation and irradiation. Samples of ODS-EUROFER and EUROFER 97 steels, as well as model bi-layer thin film ($\text{FeCr}/\text{Y}_2\text{O}_3$) samples have been implanted/irradiated with He^+ , H^+ , Au^{2+} and Kr^+ ions in different *ex situ* and *in situ* regimes at the Centre de Sciences Nucléaires et de Sciences de la Matière (CSNSM), Univ. Paris-Sud and CNRS (now IJCLab, CNRS/IN2P3 and University Paris-Saclay), using the JANNuS-Orsay/SCALP facility. Several factors contribute to a successful ion implantation/irradiation, including a specialized irradiation setup, stage and holder design, temperature control, estimation of implanted ion and displacement damage distributions. These aspects are described in the current section.

2.2.1 Experimental setup

The setup of JANNuS-Orsay/SCALP facility [39] (principal scheme is shown in Fig. 2.14), includes a 2 MV Tandem/Van de Graaff Accelerator (ARAMIS) and a 190 kV ion implanter (IRMA) that can be additionally coupled with a 200 kV Transmission Electron Microscope (TEM FEI TecnaiG² 20), allowing *in situ* observation of material microstructure evolution induced by single-beam or dual-beam ion implantation/irradiation.

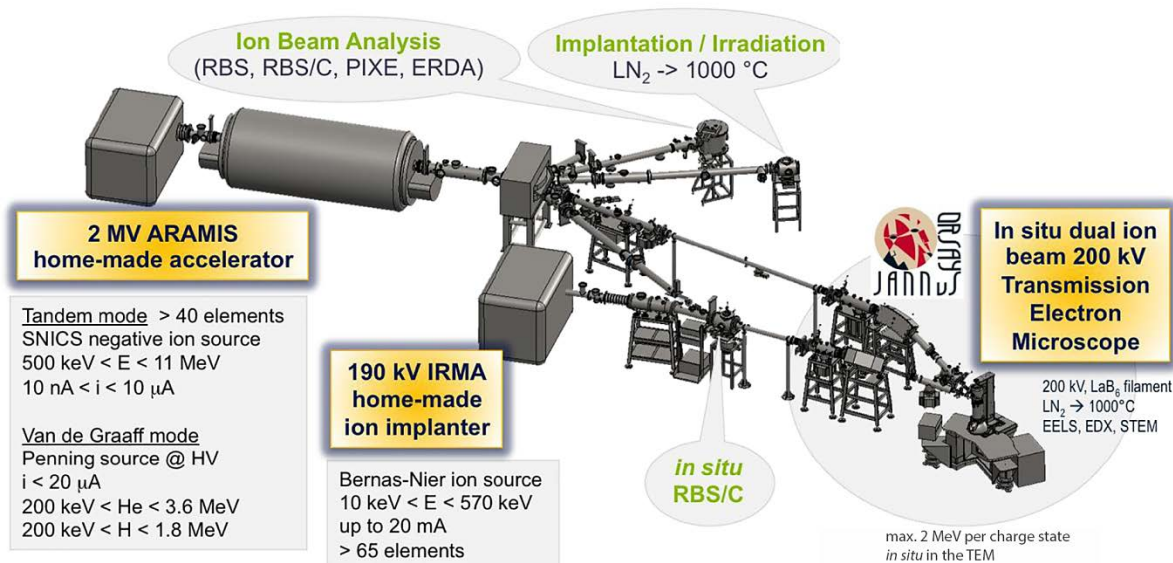


Fig. 2.14. An overview of the JANNuS-Orsay/SCALP facility [39].

Five beam lines are connected to IRMA and ARAMIS accelerators. Two beam lines are dedicated to ion implantation/irradiation and one is for ion beam analysis such as Rutherford Backscattering Spectrometry (RBS, RBS/C), Elastic Recoil Detection Analysis (ERDA), and Particle Induced X-ray Emission (PIXE). Other lines are used for coupling IRMA and ARAMIS accelerators with Transmission electron microscope Tecnai G² 20 Twin (FEI).

JANNuS-Orsay equipment can operate at a chosen temperature in the range of 77–1300 K according to different modes:

- *ex situ* ion implantation on IRMA ion implanter;
- *ex situ* ion implantation/irradiation or ion beam analysis on ARAMIS ion accelerator;

- *in situ* ion implantation by means of coupling TEM and IRMA ion implanter;
- *in situ* ion implantation/irradiation by means of coupling TEM and ARAMIS ion accelerator;
- *in situ* ion implantation/irradiation by means of coupling TEM, IRMA ion implanter and ARAMIS ion accelerator.

Below in this section ion implantation/irradiation details are discussed with regard to implantation regimes applied in this study.

2.2.1.1 IRMA ion implanter

IRMA is a homemade 190 kV ion implanter equipped with a reduced version of Bernas-Nier positive ion source [40] that can deliver large variety of ion beams. The basic structure of IRMA ion implanter is fairly standard:

- an isotope separator is isolated from the ground;
- the selected ion beam is post-accelerated, if needed, and then refocused by a lens;
- the beam enters an electrostatic XY scanner, and is then deflected by approximately 7° in order to eliminate neutrals;
- various configurations of the target chamber (and different target holders) are available [41].

The target chamber of implanter is evacuated with a turbomolecular pump and is equipped with independent liquid nitrogen trap providing a vacuum of $\sim 2 \times 10^{-5}$ Pa. The beam energy ranges from 5 keV to 570 keV, depending on the possibility of doubly or triply charged ion production. The ion flux provided by IRMA implanter can reach up to 1×10^{13} cm⁻²s⁻¹. The ion current measurements provide an absolute accuracy within <10 % by means of the direct target connection to a current integrator protected by an electron repeller. Beam-scanning system of IRMA implanter provides frequencies 400 and 80 Hz in horizontal and vertical directions, respectively, which ensures a full, uniform implantation dose at the surface area of up to 100×100 mm². The temperature control is achieved by thermocouple sensor measurements with several temperature probes. The accuracy of temperature measurements is found to be ± 10 K.

The detailed characteristics of IRMA ion implanter can be found in Ref. [40].

2.2.1.2 ARAMIS: a Tandem/Van de Graaff accelerator

ARAMIS is a homemade 2 MV tandem accelerator which can be used either as a tandem, by injecting negative ions from an external Cs sputtering source (SNICS), or as a single-ended Van de Graaff accelerator, using a positive Penning ion source located in the high voltage terminal. In tandem mode, more than 35 elements can be produced and accelerated to energies between 400 keV and 11 MeV. The single-ended operating mode is used to produce H, He or noble gas ion beams from 200 keV to 3 MeV. Various configurations of the target chamber (and different target holders) are available. The typical flux range provided by ARAMIS accelerator, depending on ions type and energies, is between 1×10^9 cm⁻²s⁻¹ and 5×10^{11} cm⁻²s⁻¹.

The target chamber of accelerator is evacuated with a turbomolecular pump and equipped with independent liquid nitrogen trap providing a vacuum of $\sim 2 \times 10^{-5}$ Pa. The ion current measurements provide an absolute accuracy of < 10 % by means of direct target connection to a current integrator protected by an electron repeller. The uniformity of dose at the surface area up to 100×100 mm² is achieved by means of 10 mm ion beam rastering with the frequencies of 400 and 80 Hz in horizontal and vertical directions, respectively. The temperature control is achieved by thermocouple sensor measurements with several temperature probes. The accuracy of temperature measurement is within ± 10 K.

The detailed characteristics of ARAMIS Tandem/Van de Graaff accelerator can be found in Refs. [42,43].

2.2.1.3 Assembling the irradiation stage for *ex situ* ion implantations

Assembling the irradiation stage consists of several steps. Samples prepared according to the procedure described in the section 2.1.1.2 are mounted onto molybdenum sample holders with different geometry and cleaned by Ar plasma for 5 minutes. Sample holders are specially designed for the particular sample type in order to fit implantation setup and sample geometry. All samples are mounted to the appropriate sized slots in the bottom or the top plate of the holders and mechanically fixed by another flat holder plate to ensure thermal contact between both parts of molybdenum holder and samples. Holders for implantation of samples for TDS measurements and for the implantation of thin films were designed and produced during implementation of this thesis.

Next, sample holders are mechanically fixed on the top of irradiation stage. One or two of K-type thermocouples are attached directly to the sample holder. The K-type thermocouples operate at temperatures up to ~1300 K, and are made of Chromel (90% Ni and 10%Cr) /Alumel (95% Ni, 2% Mn, 2% Al and 1% Si) wires. During *ex situ* implantation using either IRMA implanter or ARAMIS accelerator, the heating stage designed for implantations at temperatures up to 1273 K was used. The overview of the heating stage is given in Fig. 2.15.

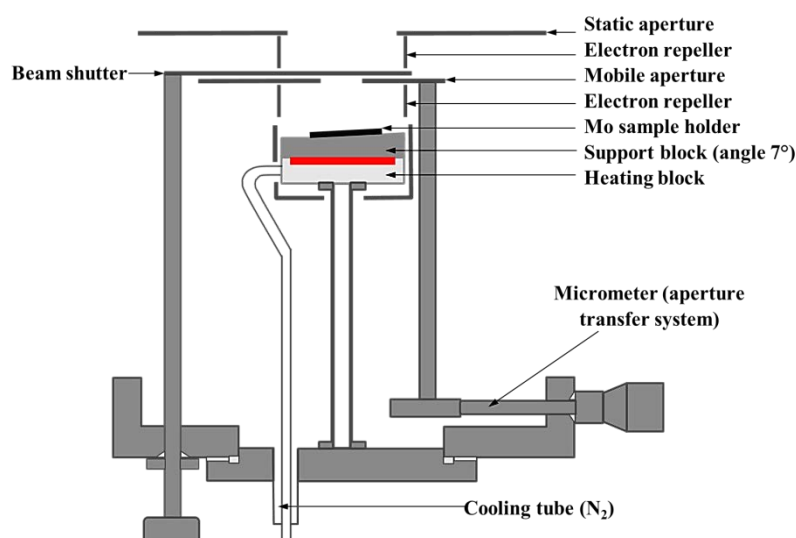


Fig. 2.15. A scheme of goniometric heating stage for *ex situ* implantation in IRMA and ARAMIS chambers.

Implantation heating stage setup is attached to, but electrically isolated from vacuum chamber. It consists of heating copper block, support stainless steel block, electron repellers and aperture assembly. The stainless steel part is produced with the inclination of 7° in order to prevent ion channeling and is mechanically fixed on the heating block. The heating block is equipped with a heater and a cooling loop. The heater is composed of a coaxial cable with tungsten filament core separated by dielectric insulator from a stainless steel shield. Thus, the heater is electrically isolated from the sample holder. Cooling is provided by means of compressed air. Prior to irradiation, the static and mobile apertures are aligned to the samples to prevent the aperture from shadowing a part of the samples. Both apertures are electrically isolated from the sample holder. Electrically isolated heater and apertures allow direct ion beam current measurements on the sample holder by connection with current integrator protected by an electron repeller.

2.2.2 Coupling IRMA or/and ARAMIS with TEM

As mentioned in the beginning of the section, the TEM setup can be coupled with accelerators in 3 different modes: (i) TEM+IRMA ion implanter, (ii) TEM+ARAMIS ion accelerator and (iii) TEM in dual ion beam mode TEM+IRMA+ARAMIS [39,44]. The ion beams are injected in the TEM with the angle of 22° in the vertical plane and with the angle of 45° between them in the horizontal plane (see Fig. 2.16). At the entrance of the TEM, the transverse dimensions of the two beams have to be around 3 mm diameter.

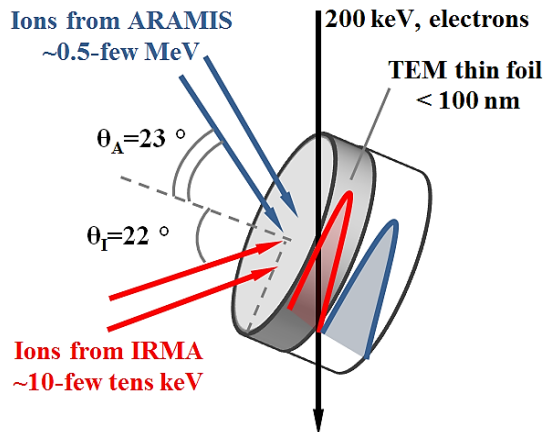


Fig. 2.16. Scheme of ion beam injection under the IRMA+ ARAMIS +TEM mode.

Inside the TEM, the typical range of ion beam energies is within 10–500 keV for IRMA 190 kV ion implanter and 0.5–6 MeV for 2 MV ARAMIS ion accelerator. Maximum energy of ion beams coming from ARAMIS is limited to be 2 MeV per charge state due to the deflection of the ion beam going to the TEM. Dynamical TEM observation is possible using one or two ion beam lines, depending on the tilt angle values, the shape of TEM thin foil, the location of TEM transparent area, the mass and energy of incident ion beams, etc. The magnetic field of the TEM objective lens deflects light and low energy element (below 100 keV N^+) ions coming from IRMA beam line. In order to prevent it, the objective lens must be switched

off during *in situ* ion implantation of such elements. Therefore only sequential observation is possible for such implantation conditions. The typical flux range used in the microscope, depending on elements and energies, is between approximately $1 \times 10^9 \text{ cm}^{-2} \text{ s}^{-1}$ and $5 \times 10^{11} \text{ cm}^{-2} \text{ s}^{-1}$.

The Transmission Electron Microscope (TEM) is a 200 kV FEI Tecnai G² 20 Twin equipped with a LaB₆ filament, with a spatial resolution of 0.27 nm (TEM mode). Images and videos are recorded by means of 2k×2k CCD high-resolution camera, with 30 frames per second recording, or a high speed and wide area-imaging camera. Several analytical techniques are also coupled to the microscope, e.g. Electron Energy Loss Spectroscopy (EELS) and Energy-Dispersive X-ray Spectroscopy (EDXS).

Specialized ultrathin TEM samples holder with α tilt angle up to 70° and β tilt angle up to 30° are used for room temperature irradiation and irradiations up to 1000°C (up to 1300°C without β tilt) in order to prevent ion beam shadowing effects. During the coupling of IRMA/ARAMIS setup with the microscope, the vacuum control in the sample chamber is provided by the TEM vacuum system using ion getter, turbo-molecular pump and liquid nitrogen trap which allows achieving vacuum of $\sim 10^{-5}$ Pa.

2.2.3 Implantation/irradiation conditions

This section covers ion implantation details with respect to particular implantation regimes applied in this study. The approach and parameters utilized for the dose calculation are provided. Methodology, sample geometry, the mode of experiment (*ex situ* or *in situ*), implantation parameters including fluence, flux, temperature along with the dose and concentration profile estimates by SRIM code are specified for each implantation regime. Section 2.2.3.2 covers parameters used during single-beam He^+ ion implantation of ODS-EUROFER and EUROFER 97. Details of dual-beam He^+ + Au^{2+} irradiation and sequential dual-beam implantation of ODS-EUROFER steel with He^+ and H^+ ions are provided in sections 2.2.3.3 and 2.2.3.4, respectively. Section 2.2.3.5 summarizes implantation details used for the model bi-layer FeCr/Y₂O₃ system.

2.2.3.1 Dose calculation

The implantation dose is directly related to the current of the incident ion beam either on the implantation sample holder for the *ex situ* implantation regimes, or measured by open Faraday cup located 3 cm away of the sample for the *in situ* implantation regimes. Thus, the beam current on the area of interest is monitored throughout the ion implantation to provide an appropriate fluence delivered to the samples.

In case of *ex situ* ion implantation regime, the stage and the holder are electrically isolated from the rest of the beam line, the heating filament and the aperture (see Fig. 2.15). Therefore, the beam current is measured by collecting the total charge from the area limited by the chosen aperture on Mo sample holder (on top of the stage setup), using a cable directly connected from the exterior of the vacuum chamber to a monitoring PC. The monitoring PC records the μC of charge collected from area limited by chosen aperture per second. The number of counts recorded and integrated during the implantation time is then used to determine the implantation parameters in terms of flux (ions/cm²/s) and fluence (ions/cm²).

In case of *in situ* implantation regime via coupling IRMA implanter or/and ARAMIS accelerator with TEM, the dose measurements cannot be directly performed on the sample. Therefore, IRMA and ARAMIS ion beam ports are equipped with open Faraday cups located at around 3 cm away from the sample (thanks to the modified polar pieces), so that the current is also monitored continuously during the ion irradiation. The error of the measured fluence under irradiation is estimated to be less than 1%, giving the accuracy and reproducibility of the dose rate within 10% at the worst.

Using the fluence and flux values measured by the technique described above, the cumulative concentration of implanted ions, ion accumulation rate, damage rate and cumulative dose are estimated with the Stopping and Range of Ions in Matter (SRIM) 2013 program [45]. For this thesis, the SRIM calculations were detailed calculations with full damage cascades using a total of 350 000 incident ions. A large number of incident ions are chosen to improve counting statistics. The displacement energies of $E_d = 40$ eV for Fe atoms [46] and $E_d = 57$ eV for Y and O atoms [47] were used for calculations.

Damage dose, dose rate, concentration of implanted ions (He, H, Au, and Kr) and appropriate accumulation rates of implanted elements were estimated according to the following equations:

$$R_D = \frac{\varphi \times R_{DS} \times 10^8}{N}, \quad (2.1)$$

where R_D (dpa/s) is the dose rate, while φ (ion/cm²/s), N (at/cm³) and R_{DS} (displ./ion/Å) (displ./ion/Å) are the implantation flux, the atomic density and the damage rate calculated by SRIM for selected ion, respectively. The atomic density for ODS-EUROFER, EUROFER 97 and Fe-10Cr thin film is assumed to be the same and equal to $N = 8.48 \times 10^{22}$ atoms/cm³, while for the Y₂O₃ thin film $N = 6.68 \times 10^{22}$ atoms/cm³. The damage dose, D (dpa) is estimated as

$$D = R_D \times t, \quad (2.2)$$

where t (s) is the implantation time.

The accumulation rate of implanted element, R_C (appm/s), was estimated as

$$R_C = \frac{\varphi \times R_{CS} \times 10^6}{N}, \quad (2.3)$$

where R_{CS} (at×cm⁻³/at×cm⁻²) is the damage rate calculated by SRIM for selected ion. Correspondingly, the concentration of implanted element, C (appm), was calculated as

$$C = R_C \times t. \quad (2.4)$$

2.2.3.2 Parameters of single-beam He⁺ ion implantation into ODS-EUROFER and EUROFER 97

In order to systematically investigate the gas-driven evolution of ODS-EUROFER steel, different *ex situ* implantation options using single He⁺ beam were applied. A set of experiments with 10 keV He⁺ ion beam was performed on 3 mm in diameter disc samples with a thickness of 100 μm (*TEM bulk discs*) using IRMA ion implanter with the stage setup specified in section 2.2.1. Ion injection was performed in the direction normal to the sample surface.

The selection of the appropriate energy of He⁺ ions for the current experiments, namely 10 keV, was motivated by relatively low production of radiation-induced vacancies, suitable region for TEM analysis using standard sample geometry and homogenous bubble size distribution via helium implantation depth. The reasons for this particular energy choice are discussed in detail in section 3.1.1.1 below. Typical concentration profile of implanted ions and damage at this ion energy are shown in Fig. 2.17; the calculation is for the fluence of $5 \times 10^{15} \text{ cm}^{-2}$ in pure Fe.

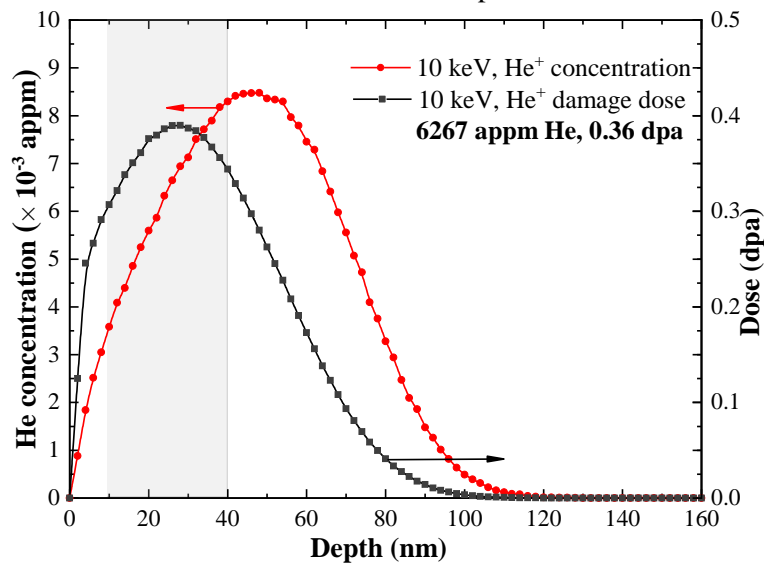


Fig. 2.17. SRIM-calculated depth profiles of implanted atoms (appm) and dose (dpa) in pure Fe implanted with 10 keV He⁺ ions to the fluence of $5 \times 10^{15} \text{ cm}^{-2}$.

SRIM calculations predict damage and He implanted profile in steel to fall between 0 nm and 140 nm from the sample surface, with the damage and implantation (R_p) peaks occurring at depths of 28 and 48 nm for 10 keV He⁺ ions arriving normally to the sample surface. Because the implantation and damage profile generated by He⁺ ions are not uniform, it is important to define a specific depth at which all concentration and dose calculations and TEM analysis will be performed. As described in section 3.1.1.1 below, this region is chosen to lie from 10 to 40 nm from the initial sample surface (as indicated by grey shaded area in Fig. 2.17) in order to obtain relatively ample statistics with the high accuracy of bubble size determination and to avoid the influence of surface effects.

During the experimental procedure of single-beam He⁺ implantation into ODS-EUROFER steel samples, the fluence, flux and temperature were varied in the ranges of 1×10^{15} - $1 \times 10^{16} \text{ cm}^{-2}$, 5×10^{11} - $5 \times 10^{12} \text{ cm}^{-2} \text{ s}^{-1}$, and 293-923 K, respectively. For implantations performed at elevated temperatures, the sample holder setup was heated up to required temperature prior to implantation under vacuum with heating rate $\sim 20 \text{ K/min}$. Samples of ODS-EUROFER implanted at 293 K were additionally subjected to post-implantation annealing during 90 minutes under vacuum. In order to compare the general trends of ODS-EUROFER steel microstructural evolution under helium implantation with the behavior of oxide-free material, EUROFER 97 steel was implanted with 10 keV He⁺ ions at 823 K with the flux of $5 \times 10^{11} \text{ cm}^{-2} \text{ s}^{-1}$ to the fluence of $1 \times 10^{16} \text{ cm}^{-2}$.

The experimental implantation parameters and those calculated by SRIM for various fluence, flux and temperature regimes are summarized in Table 2.3. The average values are calculated for the peak region and region of interest investigated by TEM (10-40 nm from surface, marked ROI in the Table). Results from these calculations indicate around 20% difference between 2 positions. Later on, all parameters regarding the implantation conditions are assumed to be given for the described region of interest. According to the data in Table 2.3, the fluence variation from 1×10^{15} to 1×10^{16} cm^{-2} results in the increase of He concentration from 1.25×10^3 to 1.25×10^4 appm, and damage dose from 0.07 to 0.73 dpa in the region of interest under the constant He accumulation rate 0.63 appm/s, dose rate 3.63×10^{-5} dpa/s and He/dpa ratio 1.7×10^4 appm/dpa. Flux change from 5×10^{11} to 5×10^{12} $\text{cm}^{-2}\text{s}^{-1}$ leads to the growth of He accumulation rate from 0.63 to 6.27 appm/s and dose rate from 3.6×10^{-5} to 3.6×10^{-4} dpa/s with the same final He concentration of 6.3×10^3 appm, damage dose 0.39 dpa and He/dpa ratio 1.7×10^4 appm/dpa. A set of implantations with variable temperature (excluding implantation at RT) was performed at the same fluence and flux, giving the final He concentration of 6.3×10^3 appm, damage dose 0.39 dpa, He accumulation rate of 0.6 appm/s, dose rate 3.6×10^{-5} dpa/s and He/dpa ratio 1.7×10^3 appm/dpa. Duration of post-implantation annealing for samples after RT implantation was chosen the same as the duration of implantation with the flux of 1×10^{12} $\text{cm}^{-2}\text{s}^{-1}$ to the fluence of 5×10^{15} cm^{-2} at $T=823$ K; corresponding calculated parameters are: He concentration of 6.3×10^3 appm, damage dose 0.39 dpa, He accumulation rate 1.3 appm/s, dose rate 7.3×10^{-5} dpa/s and He/dpa ratio 1.7×10^4 appm/dpa.

Table 2.3. Summary of implantation conditions with 10 keV He⁺ ions.

Parameters	Fluence variation			Flux variation		Temperature variation		
Flux, cm ⁻² s ⁻¹	5.00×10 ¹¹	5.00×10 ¹¹	5.00×10¹¹	1.00×10¹²	5.00×10¹²	1.00×10 ¹²	5.00×10 ¹¹	5.00×10 ¹¹
Fluence, cm ⁻²	1.00×10¹⁵	5.00×10¹⁵	1.00×10¹⁶	5.00×10 ¹⁵	5.00×10 ¹⁵	5.00×10 ¹⁵	5.00×10 ¹⁵	5.00×10 ¹⁵
T, K	823	823	823	823	823	293 and PIA at 823 K	723	923
Peak dose rate, dpa/s	3.90×10 ⁻⁵	3.90×10 ⁻⁵	3.90×10 ⁻⁵	7.80×10 ⁻⁵	3.90×10 ⁻⁴	7.80×10 ⁻⁵	3.90×10 ⁻⁵	3.90×10 ⁻⁵
ROI dose rate, dpa/s	3.63×10 ⁻⁵	3.63×10 ⁻⁵	3.63×10⁻⁵	7.27×10⁻⁵	3.63×10⁻⁴	7.27×10⁻⁵	3.63×10 ⁻⁵	3.63×10 ⁻⁵
Peak dose, dpa	0.08	0.39	0.78	0.39	0.39	0.39	0.39	0.39
ROI Dose, dpa	0.07	0.36	0.73	0.36	0.36	0.36	0.36	0.36
Peak He accumulation rate, appm/s	0.85	0.85	0.85	1.70	8.48	1.70	0.85	0.85
ROI He accumulation rate, appm/s	0.63	0.63	0.63	1.25	6.27	1.25	0.63	0.63
Peak He concentration, appm	1695	8477	16954	8477	8477	8477	8477	8477
ROI He concentration, appm	1253	6267	12533	6267	6267	6267	6267	6267
ROI appm/dpa ratio	1.72×10 ⁴	1.72×10 ⁴	1.72×10 ⁴					

2.2.3.3 Parameters of *in situ* heavy ion Au²⁺ and dual-beam He⁺+Au²⁺ irradiation of ODS-EUROFER

Investigation of helium accumulation and irradiation damage synergetic influence on gas-driven microstructure development in ODS-EUROFER steel was performed using two dual ion beam implantation regimes with He⁺ and Au²⁺ ions:

- Simultaneous *in situ* dual-beam irradiation (by means of coupling IRMA, ARAMIS and TEM) with 10 keV He⁺ ions at the flux of $5 \times 10^{11} \text{ cm}^{-2}\text{s}^{-1}$ to the fluence of $5 \times 10^{15} \text{ cm}^{-2}$ and 4 MeV Au²⁺ with the flux $4 \times 10^{11} \text{ cm}^{-2}\text{s}^{-1}$ to the fluence of $4.5 \times 10^{15} \text{ cm}^{-2}$ at 823 K;
- Sequential implantation: *ex situ* (IRMA implanter) with 10 keV He⁺ ions at the flux of $5 \times 10^{11} \text{ cm}^{-2}\text{s}^{-1}$ to the fluence of $5 \times 10^{15} \text{ cm}^{-2}$ at RT followed by *in situ* irradiation (by coupling ARAMIS and TEM) with 4 MeV Au²⁺ with the flux of $4 \times 10^{11} \text{ cm}^{-2}\text{s}^{-1}$ to the fluence of $4.5 \times 10^{15} \text{ cm}^{-2}$ at 823 K.

Under simultaneous *in situ* dual-beam regime, TEM thin foils of ODS-EUROFER steel prepared by two-side electro-polishing technique were irradiated with 4 MeV Au²⁺ ions and simultaneously implanted with 10 keV He⁺ ions. The energy of He⁺ ions was the same as during the single helium beam implantation experiments. Energy of Au²⁺ ions was selected in order to minimize sputtering and the influence of injected interstitials on bubble nucleation in the region of interest [48,49]. Due to the geometry of the facility, the thin foils were tilted off of the optical axis so that both the Au²⁺ and He⁺ ion beams made an angle of 23° with the sample surface normal direction. In order to prevent deflection of light and low energy He⁺ ions coming from IRMA beam line, TEM objective lens was switched off during *in situ* experiment. Therefore only sequential observation was possible for this implantation regime. The damage and He concentration profiles for simultaneous *in situ* dual-beam irradiation resulting from SRIM calculations are displayed in Fig. 2.18(a) and in Table 2.4. The flux and fluence of Au²⁺ ion beam was chosen so that the Au²⁺ ion irradiation had the same duration as He⁺ implantation in dual-beam experiments. The Au²⁺ ion flux was kept close to $4 \times 10^{11} \text{ cm}^{-2}\text{s}^{-1}$, which, together with He⁺ ions, provides damage generation rate of $2.2 \times 10^{-3} \text{ dpa/s}$ in the region of interest (10-60 nm from the sample surface), while the total number of displacements induced by both Au²⁺ and He⁺ ion beams during irradiation is 24.6 dpa. The region of interest for simultaneous dual-beam regime was slightly thicker than the one used for the TEM analysis for the single-beam implantation experiments due to significant surface damage and oxidation that occurred on TEM sample. The He⁺ ion flux was $5 \times 10^{11} \text{ cm}^{-2}\text{s}^{-1}$, corresponding to He accumulation rate of about 0.7 appm/s, so that He concentration by the end of irradiation reached $7.1 \times 10^3 \text{ appm}$. For similar fluences of He⁺ and Au²⁺ ions, the averaged ratio of He concentration to dpa over the region of interest is about 323 appm/dpa.

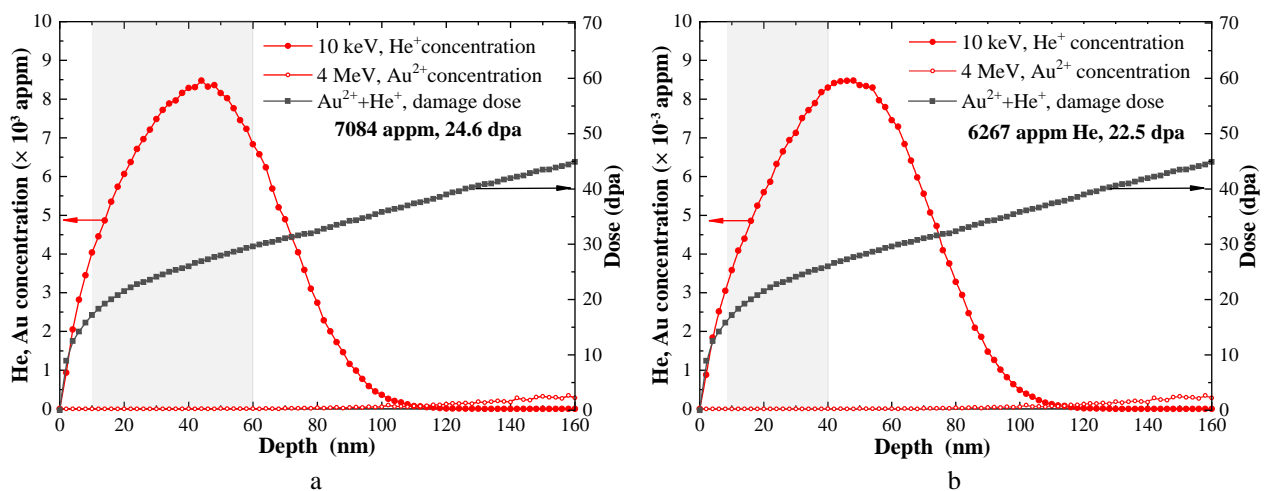


Fig. 2.18. SRIM-calculated depth profiles of implanted atoms (appm) and dose (dpa) in pure Fe implanted with 10 keV He⁺ ions to the fluence of $5 \times 10^{15} \text{ cm}^{-2}$ and irradiated with 4 MeV Au²⁺ to the fluence of $4.5 \times 10^{15} \text{ cm}^{-2}$ under: (a) simultaneous *in situ* dual ion beam regime and (b) sequential regimes with *ex situ* He⁺ pre-injection.

During sequential implantation conditions, a 3 mm in diameter ODS-EUROFER steel discs with the thickness of 100 μm (*TEM bulk discs*) were subjected to 10 keV He^+ pre-injection normal to the sample surface inside the IRMA chamber. Flux and fluence of He^+ ions were chosen to be the same as under simultaneous *in situ* dual-beam regime. After He^+ pre-implantation, *TEM thin foils* were prepared using one-side electropolishing technique, cleaned by Ar^+ ion beam with the energy of 1.5 keV for 3 minutes in PIPS GATAN ion polishing system. Then *in situ* 4 MeV Au^{2+} irradiation was performed inside the TEM column. Due to the geometry of the facility, the He^+ pre-implanted thin foils were tilted off of the optical axis so that the Au^{2+} beam made an angle of 23° with the sample surface normal direction. Flux and fluence of Au^{2+} ions was chosen to be the same as under simultaneous *in situ* dual-beam regime. The damage and He concentration profiles for sequential implantation resulting from SRIM calculations are displayed in Fig. 2.18(b) and in Table 2.4. Applied Au^{2+} ion flux produces 1.96×10^{-3} dpa/s in the region of interest 10-40 nm. The number of displacements induced by Au^{2+} and He^+ implantation is 22.5 dpa. The He^+ ion flux used corresponds to He production rate of about 0.6 appm/s, so that the final He concentration after implantation reaches 6.3×10^3 appm. For similar fluences of He^+ and Au^{2+} ions the averaged ratio of He concentration to dpa over the region of interest is about 279 appm/dpa. From the data presented, it is clear that irradiation under simultaneous *in situ* dual-beam and sequential regime result in similar He accumulation rate, dose rate, He concentration and desired dose. Thus, results of TEM microstructural investigations between two regimes are directly comparable.

Table 2.4. Summary of implantation/irradiation conditions with 10 keV He^+ ions and 4 MeV Au^{2+} ions.

Parameters	Sequential implantation/irradiation		Simultaneous irradiation	
	He^+	Au^{2+}	He^+	Au^{2+}
Flux, $\text{cm}^{-2}\text{s}^{-1}$	5.00×10^{11}	4.00×10^{11}	5.00×10^{11}	4.00×10^{11}
Fluence, cm^{-2}	5.00×10^{15}	4.50×10^{15}	5.00×10^{15}	4.50×10^{15}
T, K	293 K	823 K	823 K	823 K
ROI dose rate, dpa/s	3.63×10^{-5}	1.96×10^{-3}	2.19×10^{-3}	
ROI Dose, dpa	22.46		24.64	
ROI He accumulation rate, appm/s	0.63	-	0.71	-
ROI He concentration, appm	6267	-	7084	-
ROI appm/dpa ratio	1.72×10^4	2.79×10^2	3.23×10^2	

2.2.3.4 Parameters of sequential dual-beam $\text{He}^+ + \text{H}^+$ ion implantation of ODS-EUROFER and EUROFER 97

In order to investigate synergetic effect of helium and hydrogen accumulation on the evolution of bubble population in ODS-EUROFER steel, a set of experiments was carried out in sequential *ex situ* mode with the IRMA ion implanter in the following regimes:

- *High temperature regime* includes pre-implantation with 10 keV He^+ ions with the flux of $1 \times 10^{12} \text{ cm}^{-2}\text{s}^{-1}$ to fluence $5 \times 10^{15} \text{ cm}^{-2}$ at 823 K followed by 5 keV H^+ implantation with the flux of $7 \times 10^{12} \text{ cm}^{-2}\text{s}^{-1}$ to the fluence of $1 \times 10^{17} \text{ cm}^{-2}$ at 823 K.
- *Low temperature regime* includes pre-implantation with 10 keV He^+ ions with the flux of $5 \times 10^{11} \text{ cm}^{-2}\text{s}^{-1}$ to the fluences of $5 \times 10^{15} \text{ cm}^{-2}$ and $1 \times 10^{16} \text{ cm}^{-2}$ at RT followed by 5 keV H^+ implantation with the flux of $7 \times 10^{12} \text{ cm}^{-2}\text{s}^{-1}$ to the fluence of $1 \times 10^{17} \text{ cm}^{-2}$ at RT. A part of samples was subjected to post-implantation annealing during 90 minutes at 823 K under vacuum.

- *Combined temperature regime* includes pre-implantation with 10 keV He⁺ ions with the flux of $5 \times 10^{11} \text{ cm}^{-2}\text{s}^{-1}$ to the fluence of $1 \times 10^{16} \text{ cm}^{-2}$ at T=823 K followed by 5 keV H⁺ implantation with the flux of $7 \times 10^{12} \text{ cm}^{-2}\text{s}^{-1}$ to the fluence of $1 \times 10^{17} \text{ cm}^{-2}$ at RT.

Samples of two different geometries were studied for the purpose of TEM and TDS examinations. For the TEM analysis, 3mm discs with thickness 100 μm were implanted under high, low and combined temperature regimes (*TEM bulk discs*), while samples for TDS analysis were bars with sizes 10 mm \times 4 mm and thickness around 100 μm implanted under low temperature regime. In order to compare the hydrogen uptake and trapping in ODS-EUROFER steel after sequential implantation with He⁺ and H⁺ ion beams with the behavior of oxide-free material, EUROFER 97 steel was implanted sequentially at RT with the He⁺ ion flux of $5 \times 10^{11} \text{ cm}^{-2}\text{s}^{-1}$ to the fluence of $5 \times 10^{15} \text{ cm}^{-2}$ and with H⁺ flux $7 \times 10^{12} \text{ cm}^{-2}\text{s}^{-1}$ to the H⁺ fluence $1 \times 10^{17} \text{ cm}^{-2}$. In addition, implantations of ODS-EUROFER and EUROFER 97 samples by single H⁺ beam with the ion flux of $7 \times 10^{12} \text{ cm}^{-2}\text{s}^{-1}$ to the fluence of $1 \times 10^{17} \text{ cm}^{-2}$ were performed for the target comparison of TDS data.

The energy of 10 keV for He⁺ ions was used to be consistent with the other sets of experiments. The energy selected for H⁺ beam was 5 keV in order to get the peak concentrations of He and H at a similar depth from sample surface. Fig. 2.19 shows concentration profiles of implanted He⁺/H⁺ ions and cumulative damage profile predicted by SRIM for the He and fluencies of $5 \times 10^{15} \text{ cm}^{-2}$ and $1 \times 10^{17} \text{ cm}^{-2}$.

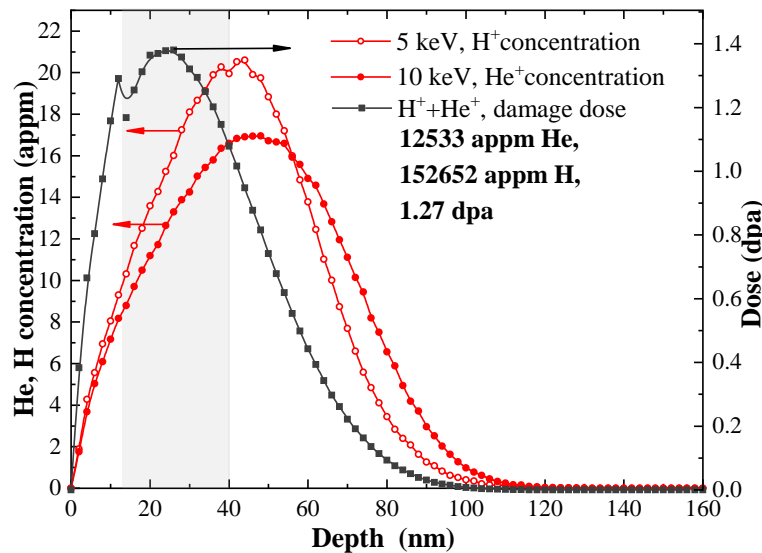


Fig. 2.19. SRIM-calculated depth profiles of implanted atoms (appm) and dose (dpa) in pure Fe implanted with 10 keV He⁺ ions to the fluence of $1 \times 10^{16} \text{ cm}^{-2}$ and with 5 keV H⁺ to the fluence of $1 \times 10^{17} \text{ cm}^{-2}$

Description of He damage and concentration distributions was provided in section 2.2.3.2. For 5 keV H⁺ ions perpendicularly incident on sample surface, SRIM predicts cumulative He+H damage and implanted H profiles located between 0 nm and 120 nm below the sample surface. The peaks of the damage and H implantation (R_p) occur at the depths of 28 and 50 nm. Like in the case of single He⁺ beam implantation regime, the region from 10 to 40 nm from the initial sample surface (indicated by grey bar in Fig. 2.19) was chosen for TEM analysis of planar view samples.

The experimental implantation parameters and parameters calculated by SRIM for all three used implantation regimes are summarized in Table 2.5. The applied H⁺ ion flux generates radiation damage at the rate of $3.8 \times 10^{-5} \text{ dpa/s}$ and corresponds to H accumulation rate of about 10.7 appm/s, so that the final hydrogen concentration reaches $1.5 \times 10^5 \text{ appm}$ for all regimes. The He⁺ ion flux was either $5 \times 10^{11} \text{ cm}^{-2}\text{s}^{-1}$ (high T regime) or $1 \times 10^{12} \text{ cm}^{-2}\text{s}^{-1}$ (low and combined T regime) corresponding to He accumulation rates of about 0.6 appm/s or 1.3 appm/s, and dose accumulation rates of $3.6 \times 10^{-5} \text{ dpa/s}$ or $7.3 \times 10^{-5} \text{ dpa/s}$, respectively. He concentration reaches $6.3 \times 10^3 \text{ appm}$ for high T and low T regimes and $1.25 \times 10^4 \text{ appm}$ for combined and low T regimes. The number of displacements induced by H⁺ and He⁺ implantations is found to be 0.9 dpa for high T and low T regimes and 1.3 dpa for combined and low T regimes. The averaged ratio of He/H concentration to dpa over the region of interest is about $2.8 \times 10^5 \text{ H appm/dpa}$ and $1.7 \times 10^4 \text{ He appm/dpa}$.

Table 2.5. Summary of implantation conditions with 10 keV He⁺ and 5 keV H⁺ ions.

Parameters	High T implantation with He and room T implantation with H						
	Room T implantation			High temperature implantation			
	Single-beam	Sequential		Sequential		Sequential	
	H ⁺	He ⁺	H ⁺	He ⁺	H ⁺	He ⁺	H ⁺
Flux, cm⁻²s⁻¹	7.00×10 ¹²	5.00×10 ¹¹	7.00×10 ¹²	5.00×10 ¹¹	7.00×10 ¹²	1.00×10 ¹²	7.00×10 ¹²
Fluence, cm⁻²	1.00×10 ¹⁷	5.00×10 ¹⁵ / 1.00×10 ¹⁶	1.00×10 ¹⁷	1.00×10 ¹⁶	1.00×10 ¹⁷	5.00×10 ¹⁵	1.00×10 ¹⁷
T, K	293	293 and PIA		823	293	823 K	
Peak dose rate, dpa/s	4.53×10 ⁻⁵	3.90×10 ⁻⁵	4.53×10 ⁻⁵	3.90×10 ⁻⁵	4.53×10 ⁻⁵	7.80×10 ⁻⁵	4.53×10 ⁻⁵
ROI dose rate, dpa/s	3.80×10 ⁻⁵	3.63×10 ⁻⁵	3.80×10 ⁻⁵	3.63×10 ⁻⁵	3.80×10 ⁻⁵	7.27×10 ⁻⁵	3.80×10 ⁻⁵
Peak dose, dpa	0.65	1.04 / 1.43			1.43	1.04	
ROI Dose, dpa	0.54	0.91 / 1.27			1.27	0.91	
Peak He/H accumulation rate, appm/s	14.42	0.85	14.42	0.85	14.42	1.70	14.42
ROI He/H accumulation rate, appm/s	10.69	0.63	10.69	0.63	10.69	1.25	10.69
Peak He/H concentration, appm	206050	8477 / 16954	206050	16954	206050	8477	206050
ROI He/H concentration, appm	152652	6267 / 12533	152652	12533	152652	6267	152652
ROI appm/dpa ratio	2.81×10 ⁵	1.72×10 ⁴	2.81×10 ⁵	1.72×10 ⁴	2.81×10 ⁵	1.72×10 ⁴	2.81×10 ⁵

2.2.3.5 Parameters of ion implantation/irradiation of FeCr/Y₂O₃ bi-layer system

In order to better understand the role of oxide/iron matrix interfaces in gas-driven evolution of ODS-EUROFER steel, samples of model FeCr-Y₂O₃ bi-layer system were subjected to *ex situ* ion implantation with single-beam He⁺ at RT/823 K and H⁺ beam at RT, as well as to sequential dual-beam implantation with He⁺+H⁺ ion beams at RT.

Ion implantation with 17 keV He⁺ and 10 keV H⁺ was performed normally to the sample surface on IRMA ion implanter using the He⁺ flux of $5 \times 10^{12} \text{ cm}^{-2} \text{ s}^{-1}$ to the fluence of $1 \times 10^{17} \text{ cm}^{-2}$ and the H⁺ flux of $1 \times 10^{13} \text{ cm}^{-2} \text{ s}^{-1}$ to the fluence of $2 \times 10^{17} \text{ cm}^{-2}$ (see Fig. 2.20). The energies for He⁺ and H⁺ ions were selected so as to obtain the peaks of implanted ion concentration close to the interface between Fe-10%Cr and Y₂O₃ thin films. Sequential implantation was performed at RT using the same parameters of He⁺ and H⁺ beams as during the single-beam implantation regime. The role of vacancies in bubble population development was verified by means of single-beam 2 MeV Kr⁺ irradiation (normally to the sample surface) with the flux of $2 \times 10^{11} \text{ cm}^{-2} \text{ s}^{-1}$ to the fluence of $3.6 \times 10^{15} \text{ cm}^{-2} \text{ s}^{-1}$ at RT using ARAMIS accelerator. The type (Kr⁺), energy, flux and fluence of irradiating ions were selected so as to obtain dose rate and accumulated dose similar to the single-beam He⁺ ion implantation and, at the same time, to minimize Kr concentration in the region of interest.

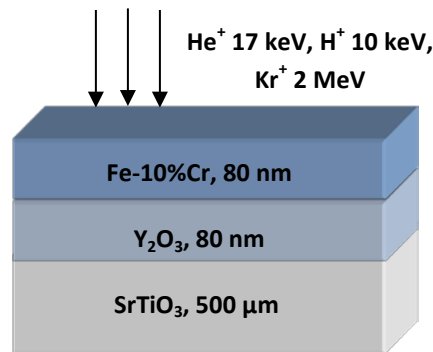


Fig. 2.20. Implantation scheme of FeCr/Y₂O₃ bi-layer system.

SRIM calculated concentration profile of He/H/Kr and corresponding damage profiles are shown in Fig. 2.21. The experimental and calculated by SRIM parameters for four implantation regimes are summarized in Table 2.6. The average values of damage rate, cumulative damage dose, ion accumulation rate and ion concentration presented in Table 2.6 are given for the interface position between FeCr and Y₂O₃ films (80 nm from the sample surface), the middle of the FeCr film (40 nm) and the middle of the Y₂O₃ film (120 nm).

During single-beam implantation, He⁺ ions generated damage at the rates of $2.8 \times 10^{-4} \text{ dpa/s}$ and $8.3 \times 10^{-5} \text{ dpa/s}$ at FeCr and Y₂O₃ sides of the interface between the films, respectively. The total accumulated numbers of displacements induced by He⁺ ions at the same interface positions are estimated to be 5.5 and 1.7 dpa. At the film middle positions the numbers of displacements are found to be 6.6 dpa for the FeCr film and 0.90 dpa for the Y₂O₃ film. The ion flux used provides He accumulation rates at the interface equal to 4.9 appm/s for FeCr side and 6.1 appm/s for the Y₂O₃ side, while the final He concentrations reach 99.2×10^3 and 121.9×10^3 appm. In comparison with the values calculated for the interface, slightly lower He accumulation rates of 4.0 appm/s and 3.9 appm/s are estimated for the middles of FeCr and Y₂O₃ films. With the high fluence used, these slightly lower He accumulation rates result in notably lower He concentration at the middles of both films, namely 80.8×10^3 and 79.6×10^3 appm for FeCr and Y₂O₃ films, respectively.

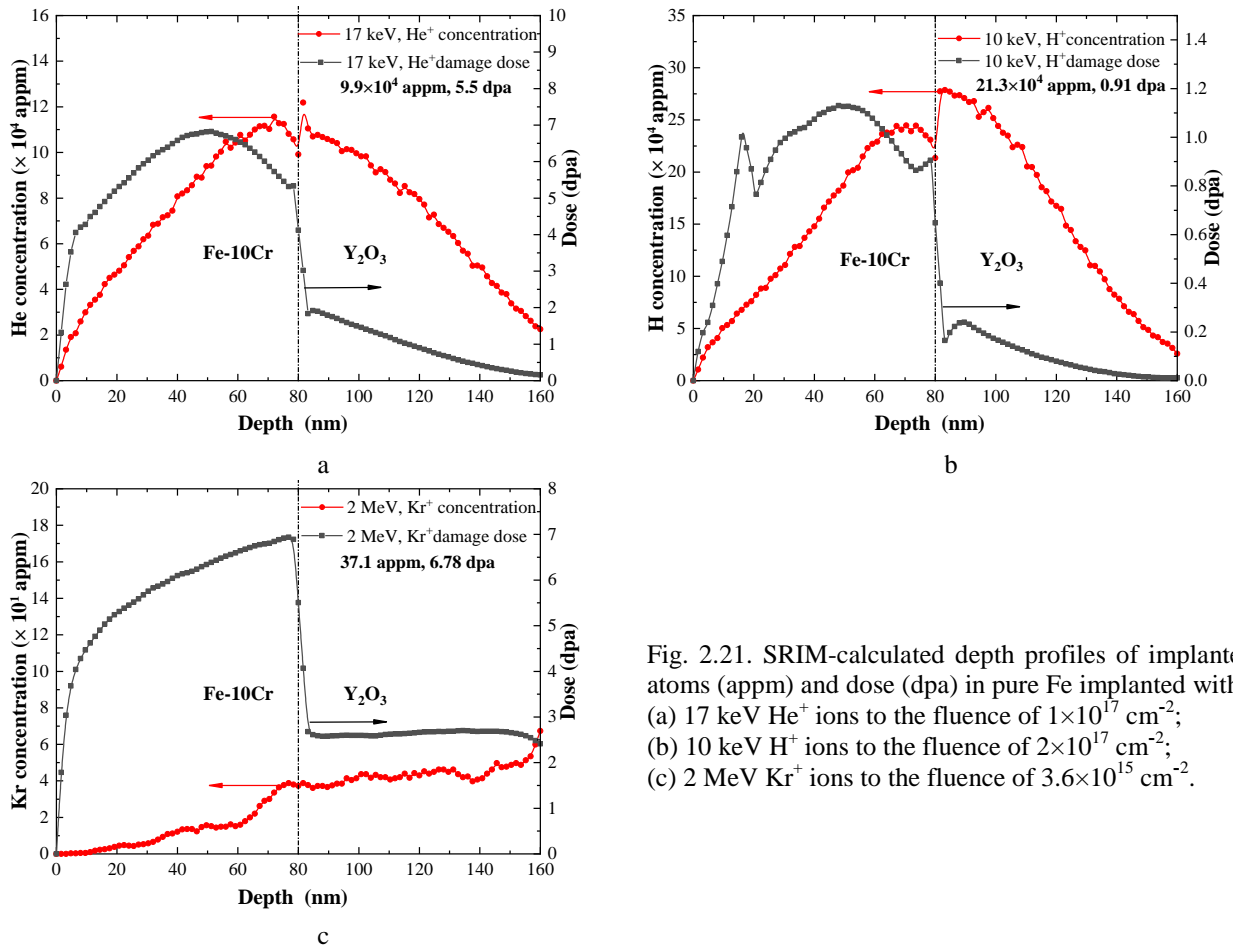


Fig. 2.21. SRIM-calculated depth profiles of implanted atoms (appm) and dose (dpa) in pure Fe implanted with: (a) 17 keV He⁺ ions to the fluence of 1×10^{17} cm⁻²; (b) 10 keV H⁺ ions to the fluence of 2×10^{17} cm⁻²; (c) 2 MeV Kr⁺ ions to the fluence of 3.6×10^{15} cm⁻².

Implantation with single H⁺ beam with the flux of 1.0×10^{13} cm⁻²s⁻¹ results in dose accumulation rate of 4.6×10^{-5} dpa/s at the interface on the FeCr side and 6.4×10^{-6} dpa/s on the Y₂O₃ side. The total number of displacements induced by H⁺ implantation is 0.9 dpa at the FeCr side and 0.1 dpa at the Y₂O₃ side of the interface. In the middles of thin films the numbers of displacements are 1.1 dpa for FeCr film and 0.08 dpa for Y₂O₃ film. The H accumulation rates are found to be 10.7 appm/s and 13.9 appm/s for the FeCr and Y₂O₃ sides of the interface, while the final H concentrations reach 21.3×10^4 and 27.7×10^4 appm. In the middle of FeCr and Y₂O₃ films, H accumulation rates are 7.4 appm/s and 8.4 appm/s, respectively. The applied H⁺ fluence results in the final hydrogen concentration of 14.8×10^4 appm in the middle of FeCr film and 16.8×10^4 appm in the middle of Y₂O₃ film.

As already mentioned at the beginning of this section, fluence, flux and temperature for both sequential He⁺+ H⁺ implantation regimes were kept the same as for the single-beam He⁺ and H⁺ regimes, so that the damage rates, ion accumulation rates and ion concentrations are the same as stated above. Sequential implantation results in damage dose at the interface of 6.4 dpa at the FeCr side and 1.8 dpa at the Y₂O₃ side. In this regime, the damage dose in the middle of FeCr film is 7.7 dpa, while in the middle of Y₂O₃ film it is 0.98 dpa. The final H concentration is twice as high as the final He concentration, which is very close to that expected in fusion blanket system.

Single-beam irradiation with Kr⁺ ions produces 3.8×10^{-4} dpa/s and 1.6×10^{-4} dpa/s at the interface between films on FeCr and Y₂O₃ sides, respectively. The number of displacements induced by Kr⁺ ions is calculated to be 6.8 dpa and 2.8 dpa in the same interface positions. In the layer middle positions, the numbers of displacements are found to be 6.10 dpa for the FeCr film and 2.7 dpa for the Y₂O₃ film. The accumulation rate and final concentration of implanted ions at the interface and in both films observed under Kr⁺ irradiation are roughly three orders of magnitude lower than those for He⁺ or H⁺ ions, and thus are negligible. The highest calculated Kr concentration observed at the middle of Y₂O₃ film doesn't exceed 45 appm. SRIM calculations demonstrate similar dose rates and doses at the interface under

single-beam He⁺ ion implantation and Kr⁺ irradiation. Therefore, appropriate selection of the Kr⁺ irradiation parameters allows direct comparison of possible bubble/void populations observed in these regimes along with the opportunity to clarify the relative importance of implanted He atoms and radiation-generated vacancies in bubble/void nucleation at FeCr/Y₂O₃ interfaces.

Table 2.6. Summary of implantation conditions for bi-layer Y₂O₃/FeCr system.

Parameters	Sequential				
	Single-beam	Single-beam	He ⁺ 17 keV+H ⁺ 10 keV		Single-beam
	He ⁺ 17 keV	H ⁺ 10 keV	He ⁺	H ⁺	Kr ⁺ 2MeV
Flux, cm⁻²s⁻¹	5.00×10 ¹²	1.00×10 ¹³	5.00×10 ¹²	1.00×10 ¹³	2.00×10 ¹¹
Fluence, cm⁻²	1.00×10 ¹⁷	2.00×10 ¹⁷	1.00×10 ¹⁷	2.00×10 ¹⁷	3.60×10 ¹⁵
T, K	293 and 823	293	293	293	293
Interface dose rate FeCr side/ Y₂O₃ side, dpa/s	2.75×10 ⁻⁴ /8.32×10 ⁻⁵	4.55×10 ⁻⁵ /6.37×10 ⁻⁶	2.75×10 ⁻⁴ /8.32×10 ⁻⁵	4.55×10 ⁻⁵ /6.37×10 ⁻⁶	3.77×10 ⁻⁴ /1.55×10 ⁻⁴
FeCr dose rate, dpa/s	3.30×10 ⁻⁴	5.41×10 ⁻⁵	3.30×10 ⁻⁴	5.41×10 ⁻⁵	3.39 ×10 ⁻⁴
Y₂O₃ dose rate, dpa/s	4.50×10 ⁻⁵	4.07×10 ⁻⁶	4.50×10 ⁻⁵	4.07×10 ⁻⁶	1.48 ×10 ⁻⁴
Interface dose FeCr side/ Y₂O₃ side, dpa	5.51/1.66	0.91/0.13	6.42/1.79		6.78/2.78
FeCr dose, dpa	6.59	1.08	7.67		6.10
Y₂O₃ dose, dpa	0.90	0.08	0.98		2.67
Interface ion accumulation rate FeCr side/ Y₂O₃ side, appm/s	4.96/6.09	10.67 / 13.87	4.96/6.09	10.67 / 13.87	2.06×10 ⁻³ / 2.12×10 ⁻³
FeCr ion accumulation rate, appm/s	4.04	7.39	4.04	7.39	0.79 ×10 ⁻³
Y₂O₃ ion accumulation rate, appm/s	3.98	8.38	3.98	8.38	2.50×10 ⁻³
Interface ion concentration FeCr side/ Y₂O₃ side, appm	99.15×10 ³ /121.87×10 ³	213.42×10 ³ /277.32×10 ³	99.15×10 ³ /121.87×10 ³	213.42×10 ³ /277.32×10 ³	37.14/38.17
FeCr concentration, appm	80.77×10 ³	147.81×10 ³	80.77×10 ³	147.81×10 ³	14.15
Y₂O₃ concentration, appm	79.56×10 ³	167.50×10 ³	79.56×10 ³	167.50×10 ³	44.91

2.3 Characterization techniques

The purpose of this section is to introduce the material characterization techniques and the analysis tools used in this thesis. Since the results presented in this thesis are mainly based on transmission electron microscopy (TEM) analysis, the main part of the section provides description of this technique. Basic principles of other techniques applied to the materials characterization, i.e. X-ray diffraction, scanning electron microscopy and thermal desorption spectroscopy are discussed briefly.

2.3.1 X-ray Diffraction (XRD)

X-ray Diffraction is a non-destructive and rapid method of the structural-sensitive material analysis [50]. It was used in this thesis for preliminary analysis of phases and preferred crystal orientations of as-fabricated thin film $Y_2O_3/FeCr$ system. XRD studies were carried out in the Center for X-ray Research and Diagnostics of Materials of the National University of Science and Technology (Russian Federation) using a Rigaku SmartLab diffractometer with CuK_α radiation. Out-of-plane XRD measurements were performed using parallel beam optics under symmetrical reflection mode. Additional experimental details and acquisition parameters are provided in section 2.1.2.2.

The basics of X-ray diffraction method can be described as follows. An X-ray beam is generated by a cathode ray tube, filtered (to produce monochromatic radiation), collimated and directed onto a sample. Since the wavelength of X-rays is comparable to the unit-cell spacing in crystals, X-rays are diffracted on regularly arrangements of atoms that constitute crystals. The interaction of the incident X-ray beam with the sample produces a diffracted beam that provides constructive interference when Bragg's law conditions are satisfied [38,50,51]

$$n\lambda = 2d_{hkl} \sin \theta \quad (2.5)$$

where n is an integer (the diffraction order), λ - the X-ray wavelength, d_{hkl} - the spacing between planes in the atomic lattice and θ - the scattering (or Bragg) angle between the incident beam and the scattering planes. Constructive interference of X-ray beams diffracted at Bragg angles from each set of lattice planes results in XRD intensity peaks. A XRD pattern is obtained by measuring the intensity of diffracted beams as a function of scattering angle. The positions and intensities of XRD peaks contain information about the ideal crystal structure. The shape of the peaks bears information about defects in the structure. A structure of investigated phase can usually be identified based on the obtained XRD pattern using standard XRD pattern databases.

For symmetrical-reflection XRD measurements (such as a conventional $2\theta/\theta$ method) the angles of incident and diffracted beams relative to the sample surface are the same (θ) [38]. These measurements are used to collect diffracted X-rays from lattice planes that are parallel to the sample surface. If a sample (e.g. a thin film) has strong preferred orientation, only beams diffracted from certain (hkl) set of reflections can be detected. In the symmetrical-reflection mode, X-rays have high penetration depth of ~several μm , strong substrate contribution to XRD pattern is hard to avoid, so that typically weak diffraction intensities from thin films can be even masked. Asymmetrical-reflection measurements stand for diffraction signal from planes that are inclined to sample surface [37,38]. The X-Ray penetration depth can be as low as 100 nm.

Typically, X-ray diffraction techniques can be divided into two groups with respect to thin film sample geometry: "out-of-plane" and "in-plane" [52]. For out-of-plane XRD, the beam scattering vector is directed out of the sample surface, which is possible for both symmetrical and asymmetrical-reflection measurements. In the in-plane XRD geometry, X-rays reflected from lattice planes that are perpendicular to sample surface (i.e. with plane normals parallel to the sample surface) are collected. Out-of plane and in-plane XRD measurements are complementary for epitaxial thin films. Geometries for out-of-plane and in-plane XRD measurements are shown in Fig. 2.22.

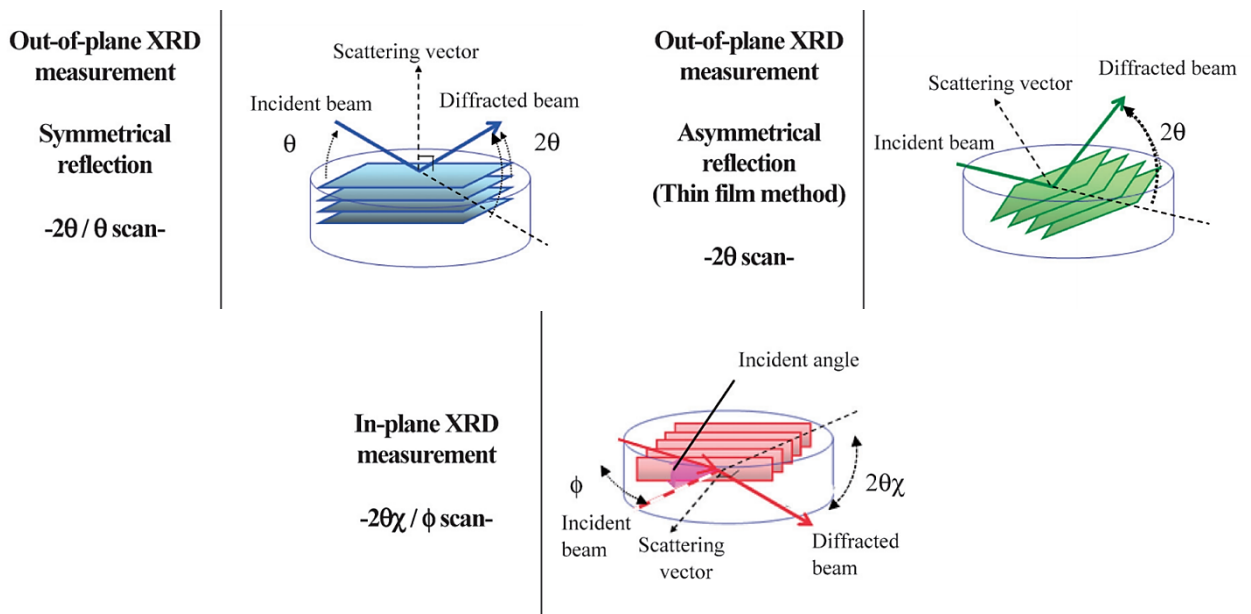


Fig. 2.22. Geometries for out-of-plane and in-plane XRD measurements [53].

Two types of X-ray optics are used for out-of-plane diffraction measurements: focusing (typically Bragg-Brentano) and parallel-beam. With parallel-beam optics it is possible to perform symmetrical-reflection and asymmetrical-reflection measurements. Parallel-beam acquisition also avoids aberrations which are typical for focusing optics. Focusing optics is suitable only for out-of-plane symmetrical-reflection measurements.

2.3.2 Electron microscopy

The electron microscopy uses a high-energy electron beam as a means to probe material's structure. Modern electron microscopy (EM) combines a set of different techniques that provide unique possibilities to gain insights into topology, morphology, structure and composition of materials [54,55]. Thanks to the short electron wavelength, electron microscopes can produce high-resolution images sampling length scales from the micro to the sub-angstrom, while strong interaction of electrons with matter generates a wide variety of useful signals. In practice, the resolution of electron microscopes is limited by spherical, chromatic aberrations and astigmatism rather than by electron wavelength.

Crudely described, electron microscopes combine an electron gun, electromagnetic/ electrostatic lenses to manipulate electron beam paths and detection systems. There exist two types of electron guns: thermionic (W filament, LaB₆), and field emission (Schottky, cold field emission gun (CFEG)) ones. Since, according to the de Broglie's equation, the wavelength of electrons is inversely proportional to their energy, electron microscopy techniques require high-energy electron beam. Because of the strong interaction of high-energy electrons with matter, high vacuum has to be maintained in the microscope column, in order to avoid undesirable electron scattering on gas atoms. Electron microscopy techniques include scanning electron microscopy (SEM), transmission electron microscopy (TEM), also called conventional transmission electron microscopy (CTEM), and scanning transmission electron microscopy (STEM).

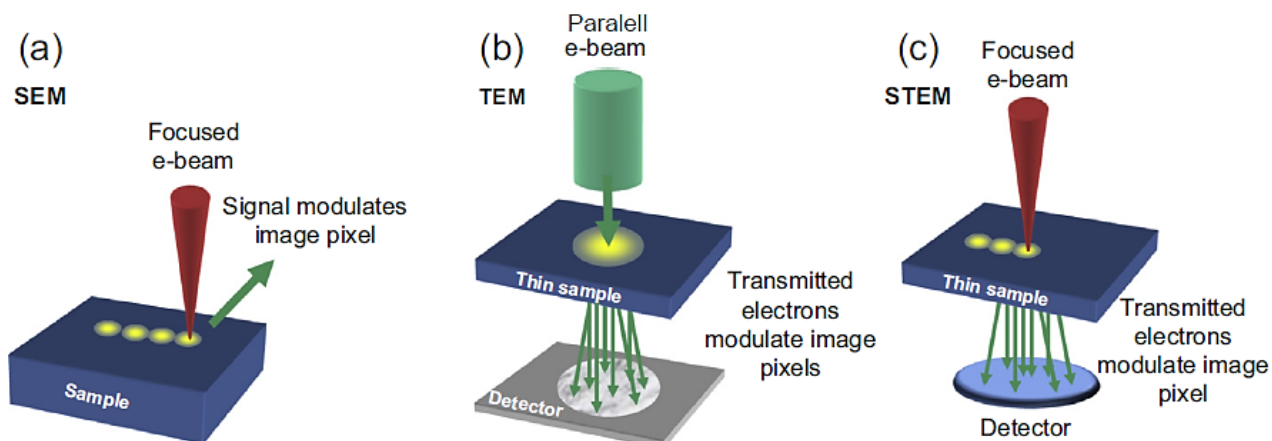


Fig. 2.23. Schematic of SEM, TEM, and STEM imaging principles. (a) Serial collection of data by SEM (b) Parallel image acquisition by TEM. (c) Serial collection of transmitted electrons in STEM [56].

In SEM (see Fig. 2.23(a)) the electron beam is focused to a spot and scans the sample surface of bulk sample pixel-by-pixel [54,56,57]. Electron beam energy in SEM ranges from 0.2 to 50 keV. 5-30 keV electrons are used for routine imaging, while <5 keV electrons are used to reduce electron penetration and achieve higher resolution secondary electron (SE) imaging. The signals emitted by sample and collected by detectors in series are combined to form an image whose dimensions/pixel distribution depends on the scan pattern. Analytical techniques, such as characteristic X-ray (EDX or/and WDX) analysis and electron backscatter diffraction (EBSD), require installation of additional detectors. Although the usual thickness of the sample for SEM analysis is several millimeters, and length up to several centimeters, the typical interaction volume is much thinner and depends on the electron scattering range. Typically, SEM signals are generated at depths ranging from ~100 nm for SE to ~5 μm for characteristic X-ray analysis.

In TEM, the electron beam is incident onto a defined area of a sample (Fig. 2.23(b)) [55,56,58]. Electron energy in TEM typically ranges from 80 to 300 keV. Electrons transmitted through the ultra-thin (typically, <100 nm sample) are focused by lenses and collected immediately by a parallel detector to form an image.

Modern TEMs are equipped with extra scan coils which scan a highly focused beam (with less than 0.1 nm diameter in advanced TEM), enabling detection of transmitted electron beam in pixel-by-pixel manner. This scanning mode with transmitted signal collection is called scanning transmission electron microscopy (STEM) [55,56,59]. Under both operation regimes TEM and STEM, installation of additional detection systems allows analysis of characteristic X-ray (EDX) and electron energy loss (EELS). In contrast to SEM, the generation depth of characteristic X-rays is limited by sample thickness. STEM mode is extremely useful for sequential chemical analysis by EDX or EELS across areas of the sample.

2.3.2.1 Electron – matter interactions

The variety of collected data in EM is based on the multitude of signals that are caused by various interactions of high energy electrons with solids. Interpretation of EM results requires understanding of the electron-matter interaction. When high energy incident electrons hit a solid, the key signals emitted from the solid [55,56,58] are scattered (backscattered or transmitted) electrons, secondary electrons (Auger and SEs), X-ray radiation, visible light emission, phonons and plasmons (see Fig. 2.24).

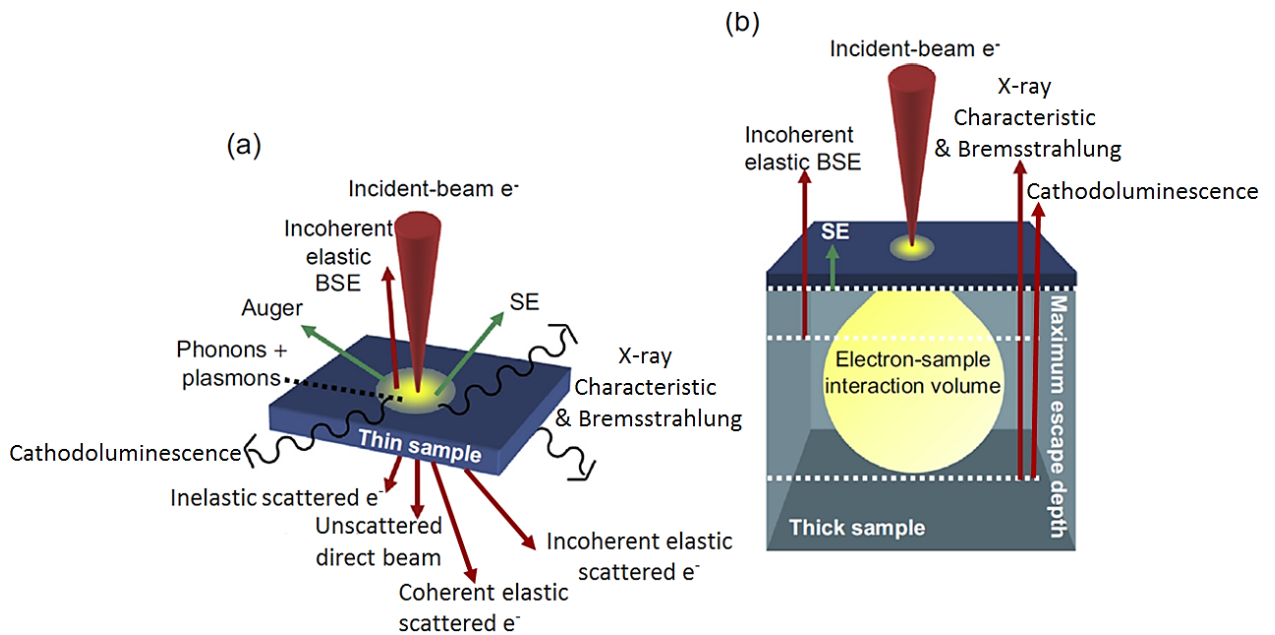


Fig. 2.24. The interaction of incident-beam electrons with solids. Useful signals generated by electron-matter interactions in a thin (TEM) (a) and a thick (b) sample. From Ref. [56].

High energy incident electrons are charged particles that might interact with the atoms (both nuclei and electrons) of an investigated sample. Basically when incident electron interacts with either nuclei or/and electron clouds of isolated atom it undergoes elastic (quasi-elastic) or inelastic scattering.

Elastic scattering

During an elastic electron-solid interaction, no energy transfer from the high energy incident electron to the solid occurs and electron still carries its original energy after transmission through the sample. Elastic scattering can occur in one of two ways, both of which involve Coulomb forces. When high-energy incident electron passes the outer, weakly bound electron shells, where the positive nucleus potential is screened, it interacts primarily with the electron cloud and scattering occurs at relatively low angles typically $< 8\text{-}10$ mrad. Such low-angle scattering is also called *coherent scattering*. The intensity of coherent scattering is strongly affected by the arrangement of atoms within the solid. If an incident electron interacts with tightly bound inner (or core) shell electrons of an atom it is attracted by the positive nucleus and can strongly deviate from its initial trajectory. Such high-angle (> 50 mrad) scattering is also called *incoherent scattering* [55,58,60]. Even complete electron backscattering can occur (backscattered electrons, BSE). Coulomb force depends on charge, and consequently increases with increasing atomic number Z . If incoherently scattered electrons are collected for image formation, the signal intensity directly relates to Z (Z contrast) giving rise to qualitative chemical information.

Elastically scattered electrons contribute to diffraction and image formation in both SEM and TEM. Thin sample in TEM permits electrons to be scattered in both forward and backward directions. However, only electrons scattered forward (both coherent and incoherent) are detected in TEM. A notable portion of electrons transmitted through the sample without any interaction contributes in TEM to the direct beam which propagates in the same direction as the incident beam. Bulk samples used in SEM allow only detection of incoherently elastically scattered BSEs.

Inelastic scattering

The interaction of high-energy incident electron with a nucleus or an electron cloud in a solid sometimes results in significant energy exchange (from parts of eV to thousands of eV). Inelastic scattering is almost always incoherent and typically occurs at low angles (< 20 mrad). The energy of the electron after the inelastic interaction is reduced by a certain amount ΔE . This energy loss can be directly measured by Electron Energy Loss Spectroscopy (EELS) and used for further analysis implemented in

TEM [61]. Moreover, the energy transferred to the sample generates different secondary signals (see Fig. 2.24). Some of these are used by various methods of analytical SEM and TEM microscopy. Inelastic electron scattering gives rise to the following effects [54–56, 58–60]:

Single-electron excitations:

(i) *Inner-shell excitation.* When an incident electron transfers a part of its energy to an inner-shell electron (K, L, M, . . .) with binding energies of the order of hundreds to thousands of eV, the inner-shell electron is excited through transitions from core levels to empty states above the Fermi level (in solid) or ejected into a vacuum (in isolated atom). If atom is excited, it then goes back to its ground state by emission of X-ray photon (characteristic X-rays) or Auger (outer-shell) electron. The wavelength of emitted X-ray photon is characteristic of each atomic species and can be utilized for chemical analysis in both SEM and (S)TEM.

(ii) *Emission of secondary electrons (SEs)* occurs when incident electron transfers a part of its energy to outer shell or valence electron. Outer shell electrons are weakly bound to ions and thus the transfer of only a small quantity of energy is sufficient to eject them into the vacuum. SEs have low energies (typically below 50 eV) and are used in SEM for the examination of surface topography.

(iii) *Cathodoluminescence (CL)* originates from the excitation of electron-hole pairs from the valence band into the conduction band by energy transfer from incoming high energy electron beam. Recombination of excited conduction band electrons with the holes results in the emission of a photon carrying the excess energy. CL spectroscopy has applications in the study of semiconductors and impurity effects therein by both SEM and TEM.

Collective electron excitations:

(i) *Phonons.* At finite temperatures, atoms in a crystal oscillate around their lattice sites. These collective oscillations are often interpreted in terms of phonons. Phonons might be initiated by the transfer of energy from an incoming high-energy electron. An incident electron can generate (and absorb) collective vibrations in any solid (even amorphous). Energy transmitted from the electron to collective atom oscillations is very low (a few tens of meV at best), but the electron-phonon interaction can result in electron scattering to quite large angles (5–15 mrad). Excitation of lattice vibrations contributes to heating of the sample (that can lead to beam damage) and to diffuse background intensity between the Bragg intensity maxima in diffraction patterns. Phonon-scattered electrons carry no useful chemical or contrast information in EM.

(ii) *Plasmons.* An incoming electron excites weakly bound outer-shell electron. The conduction band electrons compensate the unbalanced charge distribution resulting in the oscillations of the conduction electron density, or bulk (volume) plasmons. Bulk plasmon oscillations can be launched by energy loss of 5–30 eV and can occur in any material with weakly bound or quasi-free electrons, but predominantly in metals. Bulk plasmon peaks have notable intensity on EEL spectra (TEM). Metal-dielectric interfaces might also be polarized by an incident electron resulting in charge density oscillation, so-called surface (interface) plasmons. Surface plasmons occur at a lower energy loss than bulk plasmons, usually below 10 eV. Plasmons can be utilized for the indirect chemical analysis or analysis of electronic structure by means of EELS (TEM).

(iii) *Bremsstrahlung.* The slowing down of electrons by the Coulomb interaction with ions generates X-rays with the energies up to that incident electron beam. The bremsstrahlung has a continuous energy spectrum on which the characteristic X-rays are superimposed. Bremsstrahlung X-rays are relatively useless and obscure characteristic X-ray peaks.

2.3.2.2 Scanning electron microscopy (SEM)

Scanning electron microscopy (SEM) technique was utilized in this thesis for microstructural characterization of as-supplied industrial materials (ODS-EUROFER and EUROFER 97) at the grain and sub-grain scales. SEM investigations were carried out using SEM Zeiss Evo 50 XVP (NRNU MEPhI,

Russian Federation). The microscope has LaB₆ electron gun and is equipped with EDX detector INCA X-act, WDX detector Wave 500 and Nordlys S EBSD detector. The point resolution of Zeiss Evo 50 XVP is 3 nm. Additional experimental details and acquisition parameters are provided in section 2.1.1.1. The principal scheme of a SEM and overview of Zeiss Evo 50 XVP setup are shown in Fig. 2.25.

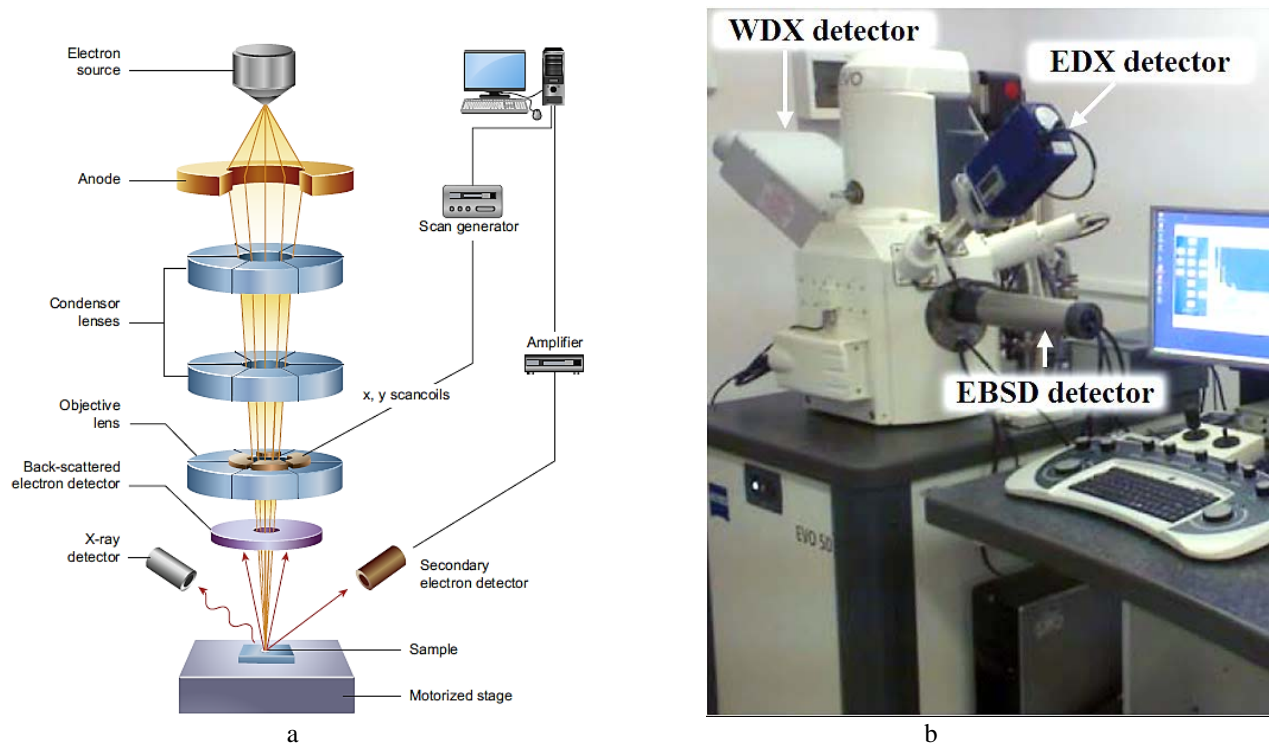


Fig. 2.25. (a) A scheme of the core components of SEM microscope [56]. (b) A picture of Zeiss Evo 50 XVP SEM microscope with analytical detectors.

Backscattered (BSEs) and secondary electrons (SEs) are primarily utilized for SEM image formation. BSE and SE signals carry different types of information. SEs leave the sample with the energy of typically 1–10 eV; the upper energy limit is specified as 50 eV. Since the energy of SE is very small, the electrons emitted at deep regions are quickly absorbed by the sample. Only SEs generated within ~10 nm of the surface are able to be emitted into the vacuum and be detected. Since SEs are emitted from the sample surface, their detection in SEM is useful for investigation of surface morphology. This mode also has the highest resolution in SEM up to ~1 nm. The most common SE detector is the Everhart-Thornley detector. In contrast to SEs, BSE are high-energy incident-beam electrons re-emitted from the sample due to elastic scattering mainly on atomic nuclei (Rutherford scattering events). Since BSEs have higher energy than SE, information from relatively deep regions up to ~300-500 nm is contained in BSE images. As mentioned previously, high-angle electron scattering strongly depends on the atomic charge number Z , therefore BSE are sensitive to the sample composition. The larger is Z of constituent atoms in the sample, the higher is BSE yield. Hence, areas that consist of heavy atoms appear bright in BSE images. BSEs are also used for electron backscatter diffraction (EBSD) methodology. The resolution for BSE images is ~10-50 nm because of the larger source size of these high-energy electrons. The most common BSE detectors are solid state detectors, which typically contain p-n junctions. In this thesis only BSE signal detection (including EBSD analysis) was used, hence composition and orientation based information required for the investigations is yielded BSE.

EBSD SEM technique detects and analyses BSEs that undergo coherent (Bragg) electron diffraction on atoms and are subsequently emitted with special angular distributions [29]. EBSD BSE detector comprises a phosphor screen to collect the diffracted BSEs over a large solid angle and special holder to tilt the sample at 70° to the incident electron beam. Under these conditions, the beam of electrons is directed at a point of interest on a tilted crystalline sample. A fraction of the electrons is

inelastically scattered on sample atoms (small energy loss) and forms a divergent source of electrons close to the surface of the sample. Electrons incident on atomic planes at angles which satisfy the Bragg condition are diffracted to form a set of paired large-angle cones that correspond to each diffracting plane [29,62]. The electron beam scattering pattern (EBSP or Kikuchi pattern) produced on the phosphor screen contains characteristic Kikuchi bands which are formed where the regions of enhanced electron intensity intersect the screen (see Fig. 2.26). The center lines of the Kikuchi bands correspond to where the diffracting planes intersect with the phosphor screen. Hence, each Kikuchi band might be indexed by the Miller indices of the diffracting crystal plane which formed it. The intersections of the Kikuchi bands correspond to zone axes in the crystal. The EBSP pattern seen is a gnomonic projection of the diffracted cone.

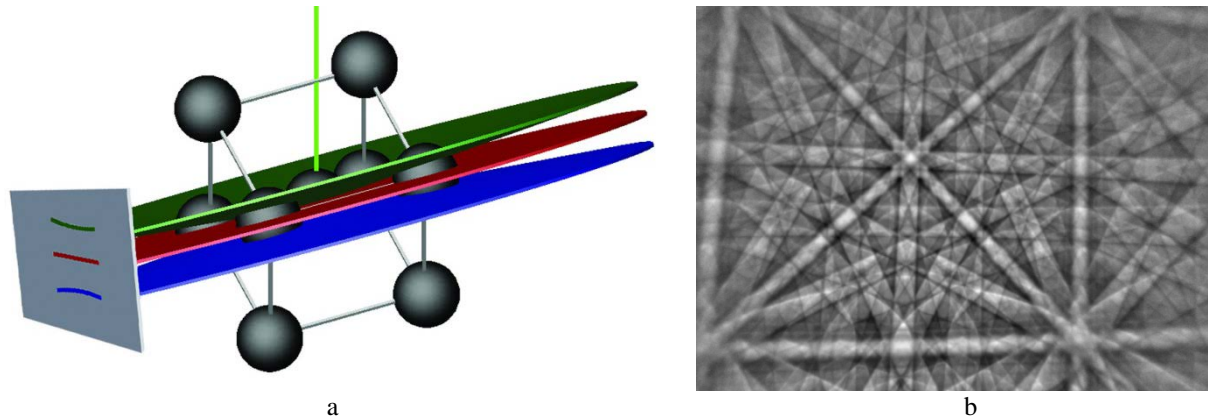


Fig. 2.26. (a) The cones (green and blue) generated by electrons from a divergent source which satisfy the Bragg conditions on a single lattice plane. These cones project onto the phosphor screen, and form the Kikuchi bands which are visible in the EBSP. (b) Generated EBSP pattern [62].

Electron beam scanning in SEM provides the opportunity to acquire EBSP patterns in pixel-to-pixel manner (EBSD mapping) with a defined pixel size [29]. A smaller step size is usually recommended for precision analysis. Each point on ROI of single- or polycrystalline sample can be then indexed with particular orientation and crystal phase. To relate Kikuchi bands in EBSP to crystal phase and its orientation available commercial software is used. Mathematical routine [62] includes modified Hough transform to identify the positions of the Kikuchi bands and compare the calculated angles between bands with a list of interplanar angles for the analyzed structure based on a selected number of reflecting planes in the reference crystal structure. In polycrystalline samples, grains are defined based on the difference in crystallographic orientation between two crystallites. The identification of grains with EBSD requires the definition of a critical misorientation angle, so that all boundary segments with an angle higher than the critical one are considered as grain boundaries [62]. Critical misorientation angle indicating the presence of a high-angle boundary between two crystallites is typically 10-15°. It is recommended to have at least 500 grains for the sampling the grain size information to be statistically meaningful [63]. Superposition of individual phase distributions and misorientation maps allow the determination of grain sizes within the investigated sample area. Post-processed EBSD data is useful for acquiring information about crystal phase and its orientation, grain size, local texture (preferred directional orientation), point-to-point orientation correlations and etc.

Energy or wavelength dispersive X-Ray (EDX or WDX) spectrometers might be coupled to SEM microscope to detect energy or wavelength of emitted characteristic X-rays (see section 2.3.2.1) [56,57,59]. Both techniques provide an opportunity of qualitative and quantitative chemical analysis with measurable elemental range varying from boron to uranium. Although both WDX and EDX spectrometers are constructed to measure characteristic X-ray radiation, spectral resolution of WDX (energy conversion ~20 eV) is relatively better than EDX (~140 eV). SEM based EDX or WDX techniques were used in this thesis for characterization of as-supplied/ as-fabricated materials.

2.3.2.3 Transmission electron microscopy (TEM)

The main part of results presented in this study was obtained by means of TEM analysis. The principle scheme of a TEM and overview of FEI Tecnai G2 20 twin setup are shown in Fig. 2.27.

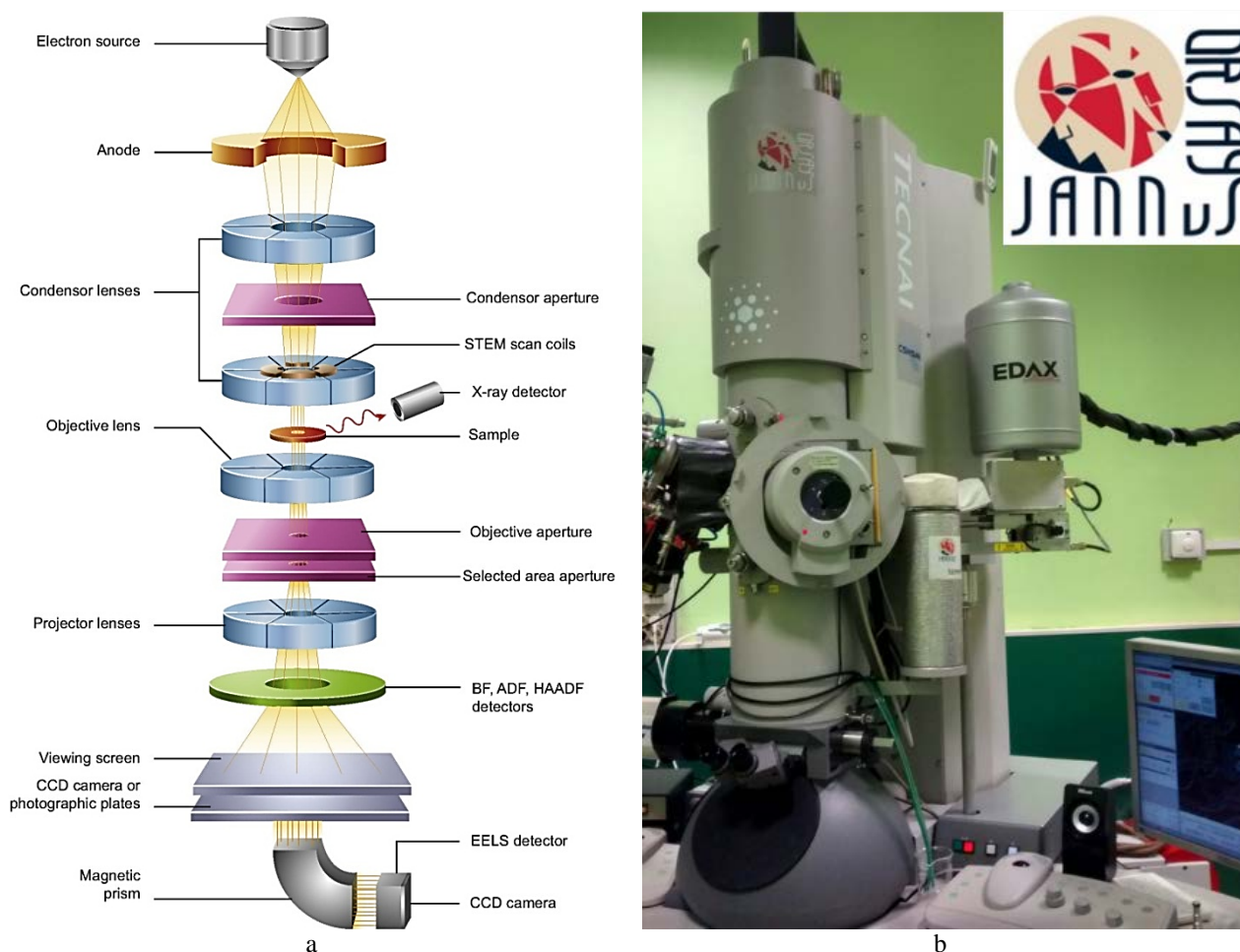


Fig. 2.27. (a) A scheme of the core components of an TEM microscope [56]. (b) A picture of FEI Tecnai G2 20 twin at JANNuS-Orsay facility.

Three different TEMs have been employed in this study, including:

(i) **FEI Tecnai G² 20 twin** (IJCLab (former CSNSM)/JANNuS-Orsay facility, Orsay, France [64,65]) with LaB₆ thermionic gun operating at 200 kV and spatial resolution 0.27 and 1 nm in TEM and STEM mode, respectively, equipped with EDX spectrometer and a Gatan Image Filter (GIF TRIDIEM). The microscope was used to perform TEM characterization in bright-field (BF) mode (size and density of cavities, carbides, Y₂O₃ nanoparticles in ODS-EUFOFER/EUROFER 97, as well as the thickness of layers, grain size, size and density of cavities in model bi-layer system). EELS technique was utilized for thickness measurements of TEM samples.

(ii) **FEI Tecnai G² F20 S-Twin** (Systems for microscopy and analysis (SMA), Moscow, Russian Federation): Schottky field emission gun operating at 200 k, spatial resolution 0.24 and 0.19 nm in TEM and STEM mode, respectively. TEM is equipped with an EDX spectrometer EDAX Apollo (AMETEK, USA) with energy resolution 125 eV and a Gatan Image Filter (GIF 2001). The microscope was used to perform high-resolution TEM (HRTEM) imaging of ODS-EUFOFER and model bi-layer system, EDX mapping with high-angle annular dark field (HAADF) imaging (model bi-layer system). EELS technique was utilized for thickness measurements of TEM samples.

(iii) **JEOL ARM-200F** (Eyring Materials Center of Arizona State University, Tempe, USA): Schottky field emission gun operating at 200 kV, spatial resolution 0.11 and 0.08 nm in TEM and STEM

mode, respectively. TEM is equipped with a Gatan Enfimum Dual Energy Electron Loss Spectrometer with base energy resolution 0.1 eV (0.56 eV with energy spread of Schottky FEG). The equipment operated at 200 kV and had a Zero-Loss Peak (ZLP). JEOL ARM-200F was used to perform EELS spectrum imaging (EELS-SI) with HAADF imaging to investigate possible hydrogen association with helium bubbles in ODS-EUROFER steel.

Basically TEM is constructed to display and analyze the non-uniform distribution of elastically scattered electrons transmitted through an ultra-thin sample in two different modes:

- the spatial distribution of scattering in real space contrast images of the sample (imaging mode)
- the angular distribution of scattering in reciprocal (k) space, such scattering patterns are called diffraction patterns (diffraction mode)

Imaging or/and diffraction are possible in both operational modes TEM and STEM.

Coupling TEM or STEM imaging with analytical electron microscopy techniques (AEM) such as EDX and EELS allows correlating spectroscopic information provided by inelastically scattered electrons and secondary signals with particular structural elements - multilayers, precipitates defects, etc.

2.3.2.3.1 TEM/STEM operation modes

In TEM, a stationary parallel incident electron beam passes through the sample. To translate the transmitted electron scatter into contrast, TEM uses objective aperture on either the direct beam (unscattered electrons) or diffracted beam (electrons scattered with low angles) or both and forms BF, DF or HRTEM images, respectively. In STEM, the sample is raster-scanned by a convergent electron beam (probe). STEM resolution is determined by the probe size. The direct or scattered beams are selected in an equivalent way, but use detectors rather than apertures.

The electron wave can change both its amplitude and its phase as it traverses the sample and both types of change can give rise to image contrast namely, amplitude (diffraction or/and mass thickness) and phase contrast. Although, all types of contrast actually contribute to an image in TEM or STEM, usually only one of them tends to dominate. Comparison of the main contrasts appearing in TEM and STEM modes is given in Fig. 2.28.

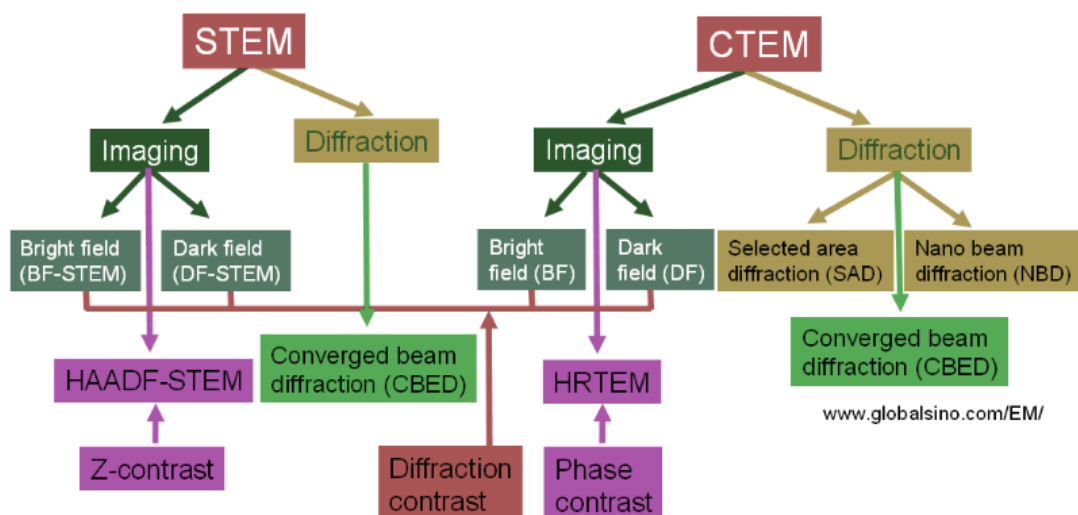


Fig. 2.28. Summary of the dominant contrast mechanisms in TEM and STEM operation modes [66].

The diffraction (or Bragg's) contrast dominates on BF/DF TEM images. HRTEM is phase contrast imaging technique based on the interference between unscattered and diffracted electron waves (small angle scattering).

Although STEM acquires images in BF, DF and HAADF modes, HAADF mode (scattering angles >50 mrad) is specific to STEM operation. Using the HAADF ensures that Bragg effects are avoided and mass-thickness contrast or its particular type Z-contrast dominates in the images. In terms of electron waves, the most obvious distinction between HAADF STEM and TEM is that TEM imaging involves coherent waves, therefore phase relationship and interferences can be achieved, while HAADF STEM involves incoherent waves.

The illumination geometry defines the coherence in TEM; whereas the geometry of the detector determines the degree of coherence of STEM image formation. TEM and STEM are related by the reciprocity theorem [67]. As a consequence, operating the STEM with a small or medium convergence angle simulates TEM with a small or medium objective aperture, hence BF TEM and BF STEM images are quite similar and diffraction contrast dominates on both images. STEM operating with a small collection angle (typically aberration-corrected STEM) places a very small slice of reciprocal space onto the BF detector; it is equivalent to TEM's nearly parallel illumination. As a result, under these conditions phase contrast might be observed in STEM BF images [68–70].

It should be noted that STEM mode is a quite universal operation mode. The versatility of STEM is based on opportunity of spot-wise detection of a variety of different secondary signals. Combination of STEM imaging with EELS or EDX spectroscopy provides a unique opportunity of local element analysis with high spatial resolution (up to atomic).

2.3.2.3.2 Bright field, high-angle annular dark field and HRTEM imaging

This section describes the basics of TEM/STEM-related contrast formation necessary for the interpretation of images in this thesis.

2.3.2.3.2.1 Diffraction contrast

Similar to X-rays, wavelength of high energy electrons is comparable to the unit-cell spacing in crystals. The interaction of the incident-beam electron wave with the regularly arranged atoms on a lattice results in constructive interference, when Bragg's law is satisfied:

$$n\lambda = 2d_{hkl} \sin \theta \quad (2.6)$$

where n is an integer, λ - the wavelength of the incident electron wave, d_{hkl} - the spacing between planes and θ - the scattering or Bragg angle between the incident electron wave and the scattering planes.

Description of diffraction can be conveniently done in reciprocal space using the Ewald sphere construction. A sphere with radius $1/\lambda$ includes the origin of the reciprocal lattice. For each reciprocal lattice point (relrod) located on the Ewald sphere of reflection, the Bragg condition is satisfied and a diffraction spot arises. In the resulting diffraction pattern the reciprocal lattice vector \vec{g}_{hkl} relating the transmitted and diffracted spots, is referred as the diffraction vector, its magnitude is $|\vec{g}_{hkl}| = d_{hkl}^{-1}$. The reciprocal lattice vector corresponds to the diffraction vector from (000) to (hkl) spot in the diffraction pattern. The radius of Ewald sphere k ($k=1/\lambda$) is much larger than \vec{g}_{hkl} . Hence, the surface of the Ewald sphere is almost planar in comparison with the array of relrods.

The relrods of thin TEM samples are elongated so that the Ewald sphere intersects several of them even if the Bragg condition is not exactly fulfilled (excitation error $S = |\vec{g}_{hkl}| \Delta\theta$) and, as the result, many reflections appear simultaneously. Excitation error is the measure of deviation from the exact Bragg condition, the intensity of the diffracted beam is strongly depends on S (see Fig. 2.29).

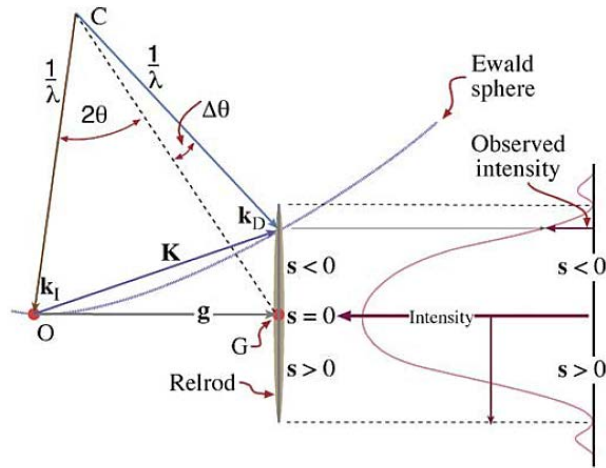


Fig. 2.29. The relrod at \bar{g}_{hkl} when the beam is $\Delta\theta$ away from the exact Bragg condition. The Ewald sphere intercepts the relrod at a negative value of S. The intensity of the diffracted beam as a function of where the Ewald sphere cuts the relrod is shown on the right of the diagram. In this case the intensity has fallen to almost zero [55].

Diffraction can be used to create contrast in TEM images. In TEM, as shown in Fig. 2.30, the objective aperture inserted into the back focal plane of the objective lens allows forming an image by selecting only the direct beam (bright field (BF-TEM) mode) or one of the diffracted beams (dark field (DF-TEM) mode). The resulting contrast on image is named diffraction or Bragg contrast.

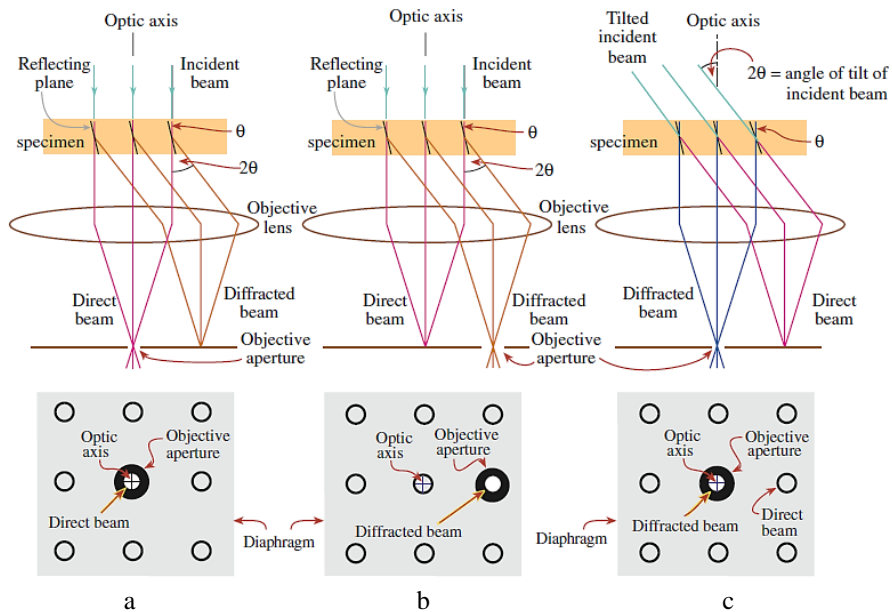


Fig. 2.30. Ray propagation diagrams showing how the objective lens and objective aperture are used in combination to produce: (a) a BF image by direct electron beam; (b) a displaced-aperture DF image with a specific off-axis scattered beam and (c) a DF image where the incident beam is tilted so that the scattered beam emerges on the optic axis [55].

When a crystal is oriented close to a zone axis, many electrons are strongly scattered to contribute to the intensities in the diffracted beams. Regions of the sample with high scattering appear dark in the BF TEM image. On the other hand, such areas may appear bright in the DF TEM image if they diffract into the area of reciprocal space (particular atomic plane or planes) that is selected by the objective aperture.

2.3.2.3.2 Mass-thickness contrast

Mass-thickness contrast arises from incoherent elastic scattering (Rutherford scattering) of electrons. In TEM, electron scattering occurs most likely in the forward direction; hence, in contrast to SEM, the probability for backscattering is small. The statistical prediction of electron-matter interactions requires the probability laws as provided by quantum mechanics. The concept of the cross-section expresses the probability of scattering. If the sample has thickness t , then the probability of scattering from the sample is given by

$$\sigma_{total}t = \frac{N_A \sigma \rho}{A}, \quad (2.7)$$

where σ_{total} is the cross section for scattering from the sample, N_A is the Avogadro's number, σ is the cross section for a given atom (Rutherford or modified Rutherford cross-section), ρ - the density and A - the atomic weight of scattering atoms in the sample

When the incident-beam electron passes close to a nucleus, it interacts mostly with the nucleus and the scattering angle will be relatively large and Rutherford differential cross section for this high-angle scattering by the nucleus alone is

$$d\sigma = \frac{Z^2 e^4}{16(4\pi\epsilon_0 E_0)^2} \cdot \frac{d\Omega}{\sin^4\left(\frac{\theta}{2}\right)}, \quad (2.8)$$

where Z is the atomic number, E_0 - the energy of incident electron beam, and θ - the scattering angle.

If a beam electron passes far from the nucleus, only the screening of nucleus by electrons became important and the scattering angle is small (<50 mrad). Modified Rutherford differential cross section is then applicable

$$d\sigma = \frac{Z^2 \lambda_R^4}{64\pi^4 a_0^2 (4\epsilon_0 E_0)^2} \cdot \frac{d\Omega}{\left[\sin^2\left(\frac{\theta}{2}\right) + \frac{\theta_0^2}{4}\right]^2}, \quad (2.9)$$

where λ_R is the relativistically corrected electron wavelength, a_0 - the Bohr radius of the scattering atom and $\theta_0 = 0.117Z^{1/3} / E_0^{1/2}$ - the screening parameter.

Summing up, the probability of high-angle scattering from the TEM sample is proportional to $Z^2 t$, so that the intensity at high scattering angles grows with the increase of the atomic number and sample thickness. In the case of constant thickness, the contrast is determined solely by atomic number (Z-contrast).

2.3.2.3.3 Phase contrast

Phase contrast images result from the interference of diffracted beams with each other and with the direct beam. This contrast mechanism can be difficult to interpret due to its high sensitivity to many factors: the appearance of the image varies with small changes in the thickness, orientation, or scattering factor of the sample, and variations in the focus or astigmatism of the objective lens. When a TEM sample is very thin, it is usually assumed that the sample does not change the amplitude, but introduces local changes in the phase of the electron wave (weak-phase objects approximation). In order to convert a small phase shift into amplitude variations (change of contrast due to interference), an extra phase shift must be added so that the phase difference between the diffracted and transmitted wave is equal to π . In conventional TEMs this phase shift is introduced by slightly defocusing the objective lens (Scherzer defocus). Very often phase contrast is associated with HRTEM imaging of lattice fringes; but, in fact, phase contrast appears in most TEM images even at relatively low magnifications. Particular

examples of phase contrast at low magnification are imaging of microscopic strain in materials with Moiré fringes, cavities and end-on dislocations /edge-on grain boundaries with Fresnel contrast (fringes).

2.3.2.3.2.4 Bright field imaging

BF imaging conditions can be set in both TEM and STEM modes. Since the convergence angle of the TEM illumination corresponds to the acceptance angle of the BF STEM detector and the objective aperture in TEM to the probe-forming aperture in STEM, BF STEM and BF TEM images might be considered equivalent. Since BF TEM imaging was used in this thesis as more common for radiation-induced damage characterization, only BF TEM imaging is considered further in this section.

BF TEM mode displays a mixture of phase, mass-thickness and diffraction contrasts. In BF TEM imaging conditions, sample regions of high scattering appear dark indicating regions of high Z, thickness or strong diffraction effects. In BF images of amorphous samples mass-thickness contrast dominates. BF images of crystalline samples are mostly formed by diffraction contrast. Characteristics of images with dominating diffraction contrast (both BF and DF) are sensitive to the chosen diffraction conditions. As mentioned previously, even if the Bragg condition is not exactly satisfied, many reflections may appear simultaneously. To get strong diffraction contrast in both BF and DF images, the two-beam conditions are used [34,71]. Diffraction conditions are often characterized by the excitation error S or normalized excitation error $\omega = S\xi_g$ (where ξ_g is the extinction distance that depends on the material, reflection, and λ). When for a particular diffracted beam g_{hkl} parameter ω is close to zero (the TEM sample is tilted so that one set of diffracting planes (hkl) is at, or very close to, the Bragg condition), this beam will appear in the diffraction pattern with intensity similar to that of the forward-scattered (or ‘incident’) beam. In this case a strong dynamical interaction between the two beams takes place; this diffraction condition is referred to as *dynamical two-beams conditions* and BF images - as “dynamical images” [71]. In two-beam dynamical conditions, sometimes called strong two-beam conditions, the image contrast is sensitive to weak lattice strains, and they are well-suited to the investigation of the sign of the long-range elastic strain fields of small clusters and dislocation loops. Due to strong dynamical interaction between the two beams, the resulting BF dynamical image may look quite complicated.

When it is desirable to avoid the dynamical contrast, two-beam kinematical conditions are used. In that case a two-beam condition is set up with a typically positive ω (achieved by simply tilting the TEM sample away from the Bragg condition). When a specific excitation error $\omega \geq 1/\xi_g$ is used, the diffraction conditions are referred to as defined kinematical two-beam conditions (and BF images - as “defined kinematic”). Diffraction conditions without strong excitation of a low-order reflection are called undefined *kinematical condition* (BF images are “undefined kinematic”). The simplified contrast under kinematical conditions often offers notable advantages [71,72]; e.g. for imaging of voids and bubbles. Fresnel contrast appears more obvious in out-of-focus conditions and for imaging small dislocation loops or clusters the strain-field contrast is expected to be more confined to their physical size. For this reason, BF kinematical conditions have often been used to image voids/bubbles as well as small dislocation loops.

2.3.2.3.2.5 Crystallographic structure imaging by HRTEM

HRTEM is a technique to obtain phase contrast lattice image or a crystal structure image from a thin sample. HRTEM images are interference patterns formed from the phase relationships of diffracted and transmitted electron waves. HRTEM images are best understood in terms of Fourier transforms. The diffracted electron wavefunction, ψ , is the Fourier transform of the scattering factor distribution in the material. The scattering factor distribution follows the atom arrangement in the material [73].

The most obvious instrumental distinction between HRTEM and BF/DF imaging is the number of beams collected by the objective aperture or an electron detector. BF or DF TEM image requires that a single-beam is selected by means of the objective aperture. To resolve atomic periodicity in HRTEM, an aperture that incorporates a range, $\delta k = 2\pi/d_{hkl}$, where δk is in terms of “reciprocal-lattice vector” the spatial frequency for a particular direction. HRTEM imaging requires objective aperture large enough to include both the transmitted beam and at least one diffracted beam.

The formation of HRTEM images includes two principal steps:

1. interaction of incident parallel electron beam, considered as a plane wave, with the crystal;
2. transfer of wave output (resulting modulations of its phase and amplitude) to electron optics system of the microscope.

Basic principles of HRTEM imaging are present below as described in Ref. [55].

Electron optics system of the microscope suffers from aberrations, including astigmatism, chromatic (C_c) aberration and, most importantly, spherical aberration (C_s) of objective which forms an image. They reduce the image quality so that a point in the sample becomes an extended region (disk) in the image. Each point on the sample may be different, the sample might be described by sample transmission function $f(\vec{r})$. The intensity in the image corresponding to point \vec{r} will be described by the function $g(\vec{r})$. Each point in the image has contributions from many points in the sample and mathematically $g(\vec{r}) = f(\vec{r}) \otimes h(\Delta\vec{r})$, i.e. the convolution of $f(\vec{r})$ with point-spread function $h(\vec{r})$ determined by electron optical system. Any function in two dimensions might be represented as a sum of sine waves $g(\vec{r})$ expressed in terms of a combination of the possible values of $G(\vec{k})$, where \vec{k} is the spatial frequency and $G(\vec{k})$ is Fourier transform of $g(\vec{r})$. Convolution in the real space corresponds to multiplication in the reciprocal space; hence Fourier transforms of $g(\vec{r})$, $f(\vec{r})$ and $h(\vec{r})$ are related as

$$G(\vec{k}) = F(\vec{k})H(\vec{k}), \quad (2.10)$$

where $H(\vec{k})$ is the so-called contrast transfer function (CTF) that determines how information (or contrast) in the k -space is transferred to the image. $H(\vec{k})$ is determined as a product of three terms, the aperture function $A(\vec{k})$, the envelope function $E(\vec{k})$, and the aberration function $B(\vec{k})$, as

$$H(\vec{k}) = A(\vec{k})E(\vec{k})B(\vec{k}), \quad (2.11)$$

$A(\vec{k})$ is related to fact that objective aperture cuts off all values of k higher than a selected value. $E(\vec{k})$ manifests the same effect but is a property of the lens itself. $B(\vec{k})$ is usually expressed as $B(\vec{k}) = \exp(i\lambda(\vec{k}))$, where $\lambda(\vec{k})$ is phase-distortion function.

For simplicity, $f(\vec{r})$ in HRTEM can be approximated as

$$f(x, y) = A(x, y)\exp(-i\varphi_t(x, y)), \quad (2.12)$$

where $A(x, y) = 1$ is the amplitude and $\varphi_t(x, y)$ - the phase that depends on the sample thickness t .

In the weak-phase objects approximation (WPOA) the absorption is neglected and the phase change depends only on weak projected potential $V_t(x, y)$ which the electron sees as it passes through the sample:

$$f(x, y) = 1 - \sigma V_t(x, y), \quad (2.13)$$

where σ is the (small) interaction constant. Therefore the electron wave function seen in the image is given by

$$\psi(x, y) = (1 - \sigma V_t(x, y)) \otimes h(x, y), \quad (2.14)$$

and signal intensity is given by

$$I = 1 + 2\sigma V_t(x, y) \otimes \sin(x, y), \quad (2.15)$$

Thus, under WPOA, only the imaginary part of $B(\vec{k})$ contributes to the intensity (because it gives the imaginary part of $h(x, y)$). Typically in HRTEM the intensity distribution of the exit wave function is described by the objective lens transfer function or phase-contrast function [55]

$$T(\vec{k}) = A(\vec{k})E(\vec{k})2\sin\chi(\vec{k}). \quad (2.16)$$

Under WPOA conditions, $T(\vec{k})$ is identical to contrast transfer function (CTF). Appearance of contrast in HRTEM image depends on $T(\vec{k})$ which is an oscillatory function (see Fig. 2.29). The maximum of $T(\vec{k})$ (maximum contrast) appears when phase $\chi(\vec{k})$ takes several odd multiples of $\pm\pi/2$, while zero contrast corresponds to $\chi(\vec{k}) = \pm\pi$. When $T(\vec{k})$ is negative, if diffracted beam which has a phase shift of $-\pi/2$ is further phase shifted by $-\pi/2$, it subtracts amplitude from the direct beam, and atoms appear dark against a bright background (positive phase contrast). If the same beam is phase shifted by $+\pi/2$, it adds amplitude to the direct beam, causing atoms to appear bright (negative contrast). For TEM without C_s corrector, phase-distortion $\chi(\vec{k})$ depends on the spherical aberration coefficient C_s , which is defined by the quality of the lens, the electron wavelength λ defined by the accelerating voltage, the spatial frequency k and the defocus value Δf as follows:

$$\chi(\vec{k}) = \pi\Delta f\lambda k^2 + \frac{1}{2}\pi C_s\lambda^3 k^4. \quad (2.17)$$

Typical behavior of $\sin\chi(\vec{k})$ function for 2 different spherical aberration coefficients is shown in Fig. 2.31. While this function is zero at the origin, it becomes negative for intermediate values of k ; when k is small, Δf term dominates. In this region of k , all information is transferred with positive phase contrast, i.e. atom positions appear dark in the HRTEM image. Function $\sin\chi(\vec{k})$ can continue to oscillate forever but, in practice, $T(\vec{k})$ is modified by envelop functions and damped. The point resolution of TEM is defined as the zero of $\sin\chi(\vec{k})$ for the Δf when the area of negative information transfer is maximally extended towards high k . The resolution of the microscope can be enhanced by either using a very low spherical aberration coefficient C_s (C_s corrected TEM) or small wavelength λ (very high accelerating voltage).

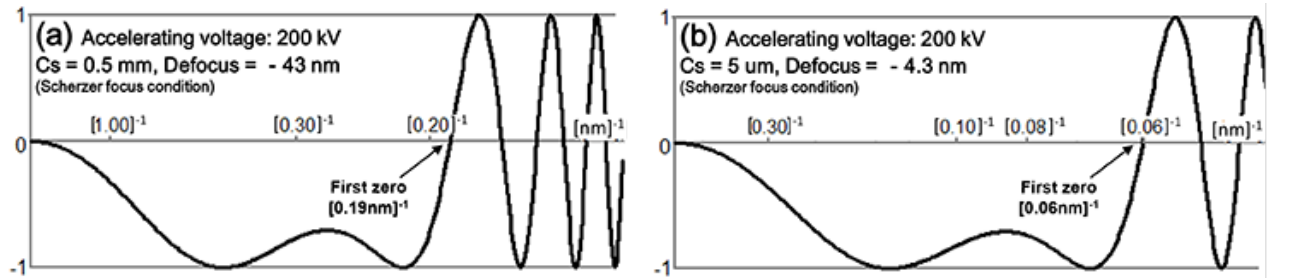


Fig. 2.31. Example of the phase-contrast transfer function ($\sin\chi(\vec{k})$) at an accelerating voltage of 200 kV for: (a) C_s : 0.5 mm and for (b) C_s : 5 mm [119].

HRTEM images are interference patterns formed from the phase relationships of diffracted and transmitted electron waves where maxima and minima of intensity correspond to the periodicity of the crystal. However, due to complexity of image formation, a reliable interpretation of HRTEM images, especially of defects and complex crystal structures, requires comparison of experimental images with simulated images for model structures. In this thesis, HRTEM imaging was performed for the model bilayer $\text{Y}_2\text{O}_3/\text{FeCr}$ system, for which the structure and out-of-plane orientation were characterized by XRD prior to TEM investigations. Therefore, a simplified interpretation of the HRTEM images using Fast

Fourier Transform (FFT) was performed. FFT spot patterns were compared to the simulated diffraction pattern of compounds of cubic *bcc* FeCr and cubic Y₂O₃ obtained using CrystalMaker software.

2.3.2.3.2.6 HAADF imaging

The scattered electrons in STEM mode can be registered by different detectors: Bright-field (BF), dark-field DF, annular dark field (ADF), and high angle annular dark field (HAADF) detectors, which image different angular distribution of the elastic scattering (see Fig. 2.32).

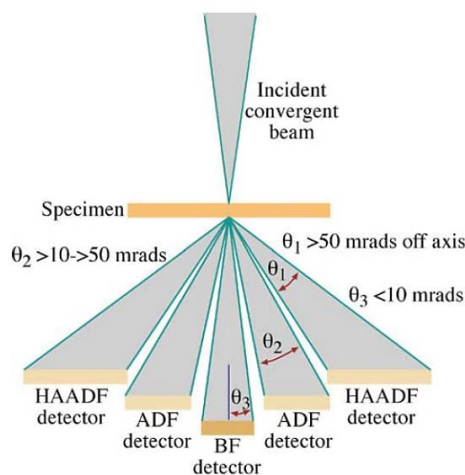


Fig. 2.32. A scheme of the different electron detectors in a STEM along with the range of electron scattering angles gathered by each detector [55].

The BF STEM image represents unscattered or low-angle scattered electrons (similar to direct beam in STEM) while DF, ADF or HAADF images are built up by electrons scattered by a relatively larger angle. HAADF detector is ring-shaped and gathers only electrons scattered at least to the angle corresponding to its inner radius i.e. >50 mrad. With constant sample thickness, the contrast on HAADF STEM images is fully determined by Z and can be directly interpreted in terms of the classical Rutherford scattering differential cross section: light elements will show in dark, whereas heavier elements will be brighter. Like HRTEM, HAADF imaging allows achieving atomic resolution, but it is fundamentally different. HAADF imaging uses coherent optics to form a sub-nanometer probe beam, while scattering from the sample is incoherent. Contrast on HAADF high-resolution images is due to the value of Z and can be interpreted more easily than HRTEM images that typically require simulations for interpretation.

2.3.2.3.3. Energy Dispersive X-ray spectroscopy (EDX)

The Energy Dispersive X-ray (EDX) spectroscopy is a technique of elemental analysis that reveals the presence of elements in the sample based on the measurements of characteristic X-ray energies. Characteristic X-ray generation occurs as a consequence of inner (core) shell electron excitation due to energy transfer from an incident-beam electron. After ionization, atom returns almost to the ground state by filling the hole in the inner shell with an outer shell electron. The excess energy, equal to the difference between the ionization energies of the electrons involved in the transition, is emitted as electromagnetic radiation in the form of X-ray photon. X-ray photon energy is uniquely determined by the atomic number Z of the involved atom and on the quantum numbers (n_i) of energy levels involved in the electron transition [55]. The process of characteristic X-ray emission is shown schematically in Fig. 2.33(a). There exist two notations for characteristic X-ray lines: Siegbahn notation and IUPAC notation. In Siegbahn notation (more frequently used) the name X-ray line which arises e.g. in Fe due to filling a K-shell hole from the L shell is written down as Fe-K _{α} . The first symbol reflects the element involved, and the second indicates the energy level where the hole occurred (K for (n_1), L for (n_2), M for (n_3), etc.). Third symbol (α , β , γ) denotes from which outer shell the hole was filled.

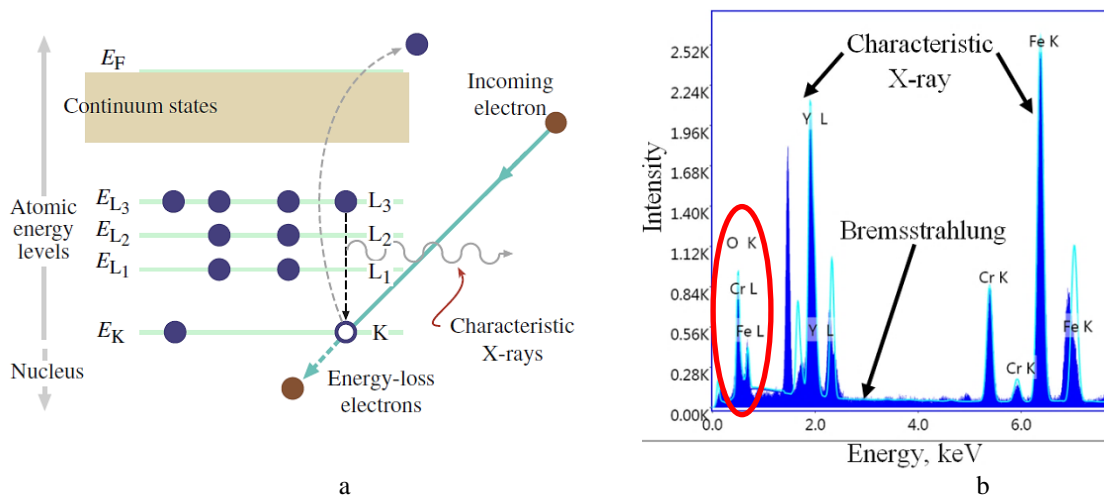


Fig. 2.33. (a) An inner (K) shell electron is ejected from the atom by a high-energy electron. When the hole in the K shell is filled by an electron from the L shell, characteristic (K_{α}) X-ray emission occurs. The beam electron loses energy but continues moving through the sample [55]. (b) Example of an EDX spectrum from the interface of $Y_2O_3/FeCr$ bi-layer system.

The first EDS detector developed for commercial systems was the lithium-drifted silicon or Si(Li) detector, but it is now giving way to the silicon-drift detector or SDD. The EDS detector converts the energy of each individual X-ray photon into a voltage signal of proportional size in three stage process. First, the X-ray photon is converted into charge by ionization of atoms in a semiconductor crystal. Second, the charge is converted into a voltage signal by a preamplifier. Finally, the voltage signal is input into the pulse processor for measurement. The output from the preamplifier is a voltage ‘ramp’ where each X-ray appears as a voltage step on the ramp. EDX both detects X-rays and separates (disperses) them into a spectrum according to their energy. Process actually involves very rapid serial processing of individual X-ray signals, the speed of these processes is such that the spectrum is generated in parallel with the full range of X-ray energies detected simultaneously [55].

EDX spectra are plots of intensity (X-ray counts) versus X-ray energy and basically consist of characteristic X-ray lines superimposed with continuous background produced by Bremsstrahlung emission (see Fig. 2.33 (b)). Characteristic X-rays have discrete energies, but the discrete lines spread into Gaussian peaks in the process of detecting and measuring. The position of a characteristic peak in EDX spectrum, its energy, identifies transfers between individual shells and, consequently, element; the area under the peak is proportional to the number of atoms of the element. Each element contained in the sample gives rise to at least one X-ray peak; high-Z elements show several peaks (K, L, M, etc.). EDX spectroscopy is able to detect elements with $Z > 3$. Hydrogen and helium do not have characteristic X-rays, while Li K X-rays are of too low energy to be detected by EDX. In fact, elements with Z from 4 to 11 are not routinely analyzed by EDX. The opportunity to detect light elements ($Z=4-11$) depends on various factors, e.g. sample thickness, elemental content, detector type, etc.

The spectral resolution of a particular peak in EDX spectrum is defined as the width of the peak measured at the half of the peak height (FWHM). Traditionally the resolution of EDX spectrometers is measured by the FWHM resolution of the Mn- K_{α} peak at 5.9 keV [74]. The best achieved resolution is currently 121 eV. Appearance of several peaks (K, L, M, etc.) for high Z-materials along with relatively low energy resolution (in comparison with EELS) makes peak overlap a frequent problem in EDX. In fact, it becomes especially important for energy levels below 2.5 keV. For samples of $Y_2O_3/FeCr$ investigated in this thesis, the O- K_{α} (525 eV) and Cr- L_{α} (572 eV) peaks overlap (see red marked area in Fig. 2.33 (b)). Therefore it was difficult to confirm the presence of oxygen by EDX in the FeCr part of system, as well as its segregation at the interface. However, the oxygen content determined in Y_2O_3 is reliable since no O- K_{α} peak overlapping with Y- K_{α} (14958 eV) and Y-L (1924 eV) occurs.

For spectra acquisition, the electron beam should be focused to an appropriate size for analysis. Thus, it is essential to use STEM operation mode for the imaging on required sample area. In fact, the spatial resolution of EDX analysis in the TEM is determined by electron probe size, while the depth resolution is governed by the thickness of the sample [74]. The (S)TEM EDX detection limits can be as good as ~0.02-0.1 wt.%. Several acquisition modes are available for STEM EDX analysis: point-line, mapping or spectrum imaging EDX-SI (similar to EELS-SI, see below).

2.3.2.3.4 Electron Energy Loss Spectroscopy (EELS)

Electron Energy Loss Spectroscopy (EELS) is an analytical technique of measuring changes in the energy distribution of electrons after their interaction with the sample and reflects the density of empty states. EELS spectrum represents a histogram of the electron energy distribution, its precise analysis provides chemical and structural information at high spatial resolution.

2.3.2.3.4.1 Principles

EELS instrumentation is based on the magnetic prism which produces uniform magnetic field $B \sim 0.01$ T. After interacting with the sample, the electrons influenced by this field (Lorentz force) travel in a circular trajectory whose radius, R , is given by $R = mv / eB$, where e , v and m are the electron charge, speed and relativistic mass. The electron beam emerges from the magnetic prism being deflected by $\sim 90^\circ$ for convenience. The angular deflection of an electron depends on its velocity within the magnetic field, and consequently on the energy loss. Electrons that have lost energy in the sample have lower velocities and smaller R , leaving the magnet with a slightly larger deflection angle (Fig. 2.34 dash line). Besides introducing bending and dispersion, the magnetic prism also focuses an electron beam. After being focused and dispersed by the magnetic prism, the electrons constitute an EEL spectrum. The quality of EELS spectrum is limited by the electron source spread, the sample thickness (multiple scattering), the delocalized inelastic scattering, as well as aberration of the spectrometer lenses. An angle-limiting aperture is utilized to cut out the portion of the electron beam that contributes to small residual aberrations of the magnetic prism focus and improve spectral resolution. Aperture also reduces the collection semi-angle β and controls intensity during EELS acquisition. Among all electron sources, FEG has the lowest energy spread of ~ 0.3 - 0.7 eV, which can be reduced down to ~ 0.1 eV using installed monochromator [55].

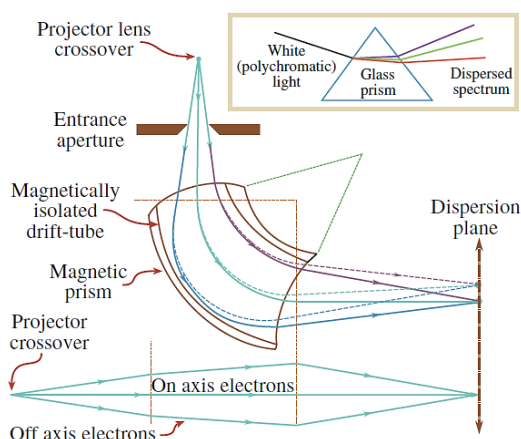


Fig. 2.34. (a) Ray paths through a magnetic prism spectrometer showing the different dispersion and focusing of the no-loss and energy-loss electrons in the dispersion plane of the spectrometer. The inset shows the analogy with the dispersion of white light by a glass prism. (b) The lens focusing action in the plane normal to the spectrometer [55].

The most widely used EELS spectrometers are post-column energy filter by Gatan (GIF) with the parallel recording systems. In these spectrometers all energy channels are recorded simultaneously, with

chosen energy dispersion (eV/channel). The electron's kinetic energy is converted into photons using a scintillator that is optically connected to a charge-coupled device (CCD).

2.3.2.3.4.2 The structure of EEL spectrum

The EEL spectrum is divided into three main parts (Fig. 2.35) which represent different electron-matter interactions: zero-loss peak (ZLP), the low-loss region (LL) and the core-loss (or high-loss) region (CL) [61].

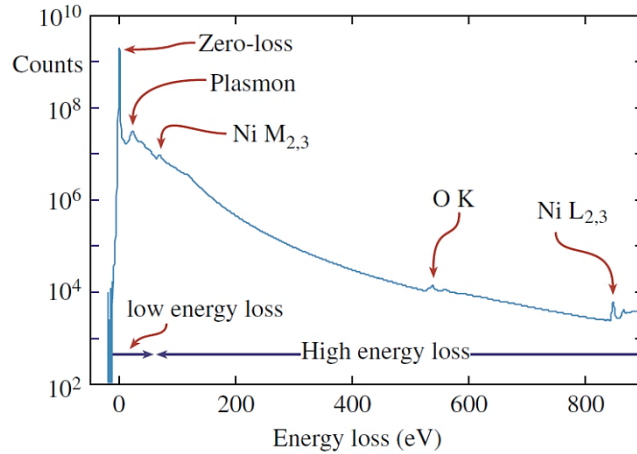


Fig. 2.35. An example of EELS spectrum displayed in logarithmic intensity scale. The zero-loss peak is an order of magnitude more intense than the low energy-loss portion (characterized by the plasmon peak), which is many orders of magnitude more intense than the small ionization edges [55].

The Zero-loss or “elastic” peak

ZLP is formed by electrons transmitted without suffering measurable energy loss, including electrons scattered elastically and those that excite phonon. For ultra-thin TEM sample ZLP holds more than a half of the total signal recorded by the spectrometer. FWHM of the ZLP provides estimation of the energy resolution of the EEL spectrum. ZLP contains little useful information about chemical or electronic structure [55,61].

However, ZLP acquisition is obligatory to perform absolute calibration and quantification, correlation of low-loss signals with core-loss features, as well as thickness measurements. With intensity many orders of magnitude higher than the rest of the spectrum, ZLP easily saturates the CCD detector. Ultra-fast detectors with acquisition time of only several μs per spectrum allow overcoming this problem.

The low loss region

LL region typically extends from hundreds of meV to $\sim 50\text{-}100$ eV. Within this region, the main electron energy-loss mechanism involves excitation of outer shell electrons: the valence electrons or (in metals) conduction electrons. In many solids, a plasmon model provides the best description of valence electron excitation [61]. In addition to exciting “bulk” plasmons, surface plasmons can arise at each exterior surface. In the Drude model [61], assuming that electrons are quasi-free, the energy E_p loss by an electron beam that generates a bulk plasmon with frequency ω_p is given by

$$E_p = \frac{h}{2\pi} \omega_p = \frac{h}{2\pi} \left(\frac{n_e e^2}{\epsilon_0} \right)^{1/2}, \quad (2.18)$$

where h is Planck's constant, e and m are the electron charge and mass, ϵ_0 is the permittivity of free space, and n_e is the free-electron density. For the majority of solids, E_p lies in the range of 5–30 eV. Plasmon energy directly relates to the free electron density and the wide range of material properties.

Bulk plasmon oscillations typically provide the main contribution to the spectrum intensity in the low-loss region. If transmitted electron is inelastically scattered more than once, the total energy loss equals to the sum of individual losses. In the case of plasmon scattering, the result is a series of peaks at multiples of the plasmon energy. The integrated intensity of a bulk plasmon peak can be evaluated as

$$I_n = \frac{I_t t^n}{\eta! \lambda_p^n} \exp(-t / \lambda_p) = \frac{I_0 t^n}{\eta! \lambda_p^n}, \quad (2.19)$$

where I_t , is total integral of the spectrum (ZLP component I_0), λ_p - the plasmon mean free path (MFP), n - the order of the plasmon loss and t - the sample thickness, respectively.

The low-loss spectrum region is used also for band gap measurements and for analysis of light elements, such as helium and hydrogen.

The core-loss region

CL region ranges from ~ 50 eV to several keV and is related to the inner-shell excitations that are relatively high-energy processes. As compared to plasmon excitation, cross sections for ionization events are relatively small. As a result, signal intensity in the CL region is much weaker than in LL region and becomes even smaller as the energy loss increases. Sharp edges superimposed over decreasing power law background, rather than peaks, represent the energy loss due to excitations of inner-shell electrons. The sharp edges on the power-law background occur at the ionization thresholds, whose energy-loss position is approximately the binding energy of the corresponding atomic shell [61]. The inner-shell binding energies depend on the atomic number Z of scattering atom and quantum number of particular electron shell, so that the ionization edges present in an EEL spectrum reveal the element presence in the sample. Most of the ionization edges [55,61], with the exception of light elements such as He and H (energy in the LL region) [75–77] can be found in CL spectrum region. Similar to X-rays, where we have K, L, M, etc., peaks in the spectrum, we get ionization edges from K, L, M, etc., shell electrons. Quantitative elemental analysis is possible by integrating an area under the appropriate ionization edge. Background to a particular ionization edge needs to be extrapolated and subtracted prior quantification because it represents tails of both plasmon peak(s) and previous ionization edges.

EELS is generally used for quantification of elements with ionization edges below 2 keV. Large binding energy of inner-shell electrons in high Z -materials which corresponds to rapid intensity decrease in EEL spectrum makes EDX more appropriate for elemental quantification in such cases. However, EELS spectroscopy provides a unique opportunity for detection of light elements, in particular He and H, along with much better spectral resolution for elements with medium Z .

2.3.2.3.4.3 EELS acquisition modes

In practice, energy-loss data are acquired in the following regimes [61]:

(i) *Energy-loss spectrum* recorded at a particular point on the sample defined by an incident electron beam size (probe) or an area-selecting aperture. Such spectrum might be acquired by means of CTEM or a STEM with stationary probe.

(ii) *Energy- filtered image (EFTEM)* recorded for a given energy loss (or small range of energy loss) using CTEM or STEM techniques.

(iii) *Spectrum image (SI)* obtained by acquiring an energy-loss spectrum at each pixel as a STEM probe is systematically scanned over the sample (STEM-SI see Fig. 2.36(a)). The entire spectrum is stored at each point (EELS data cube) allowing advanced spectral processing to be performed for every pixel in the spectrum image. Using a CTEM fitted with an imaging filter, the same information can be obtained by recording a series of EFTEM images at successive energy losses (EFTEM-SI). This corresponds in Fig. 2.36(b) to acquiring information from successive layers, rather than column by

column as in the STEM method. Due to parallel imaging mode, large areas at high resolution can be studied. Once acquired, the processing is identical to the STEM-SI method.

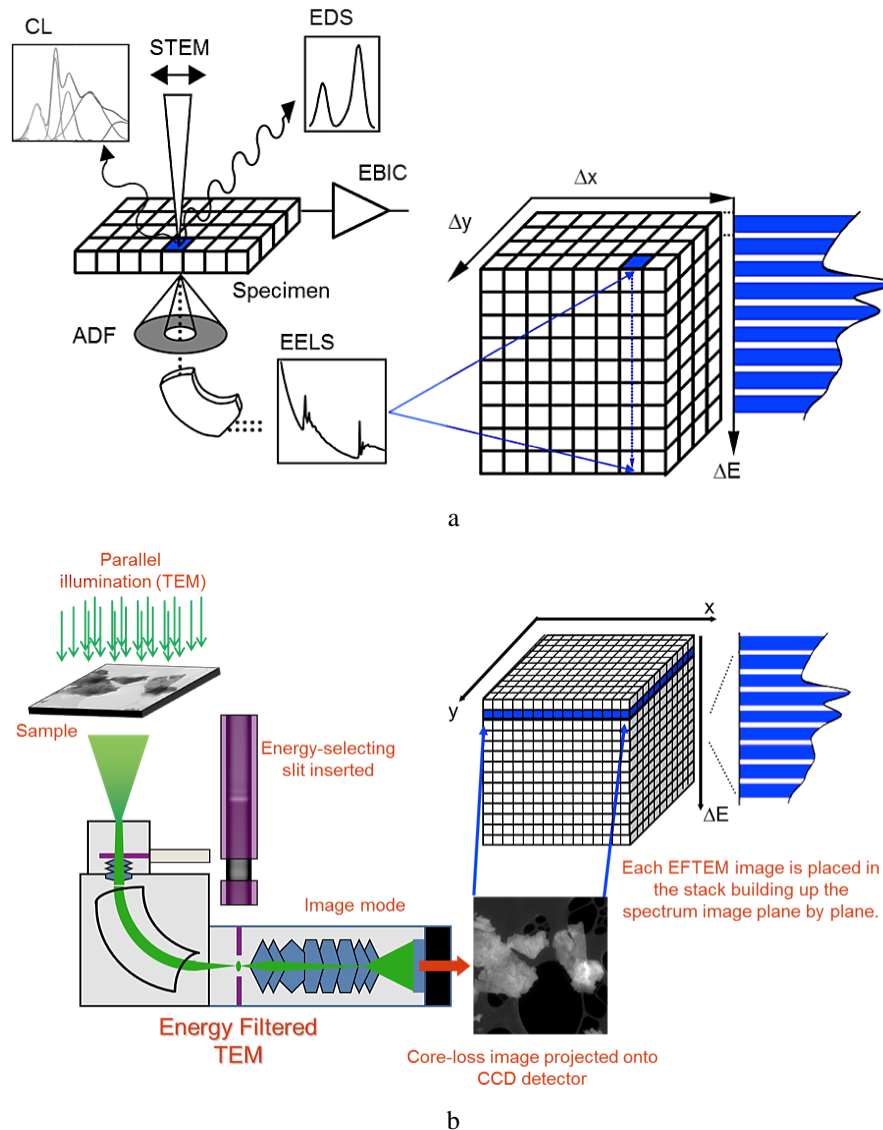


Fig. 2.36. Energy-loss data collection in spectrum imaging acquisition mode. (a) STEM regime; (b) CTEM regime [78].

2.3.2.3.4.4 Dual EELS

The dynamic range of an EELS spectrum is defined as the saturation signal divided by the readout noise. The dynamic range in a spectrum covering the energy loss range of 0–2 keV can exceed 10^6 . A modern CCD detector with a dynamic range of 10^4 cannot record the whole spectrum in a single acquisition run. Practical situations are even more challenging. Data with adequate signal-to-noise ratio required for detailed analysis can only be recorded over an intensity range of 10^2 in a single acquisition. Therefore, the high intensity low-loss region containing the zero loss peak (ZLP) must be recorded separately from the low intensity core-loss region. However, both the low loss and core loss regions acquired from an identical sample area are required to extract maximum information (i.e. perform absolute quantification, correlate low-loss signals with core-loss features, etc.) and allow correction of energy shifts and effects of elastic and multiple inelastic scattering.

Dual EELS mode [79,80] makes it possible to acquire quasi-simultaneously at each probe size two optimized spectra corresponding to two different energy-loss ranges (typically low- and core-loss)

overcoming the large dynamic range encountered in EELS data. In the Dual EELS implementation by Gatan [80], three ultrafast electrostatic deflectors are synchronized to create the final dataset: beam blanking control down to 1 μs (Quantum) and 100 μs (Continuum); energy shift control (up to 2 kV offset with 10 μs switching time); and lateral spectrum shift control to isolate two portions of the spectrum on the detector. The fast switching results in very high collection efficiency.

2.3.2.3.4.5 Sample thickness measurement by EELS

In order to evaluate volume number densities of microstructural components and He-filled cavities, it is mandatory to precisely measure the local thickness of sample. Thickness measurements by EELS rely on the analysis of an experimental spectrum acquired up to ~ 100 eV with included ZLP [61]. The analysis is commonly performed using either the Kramers-Kronig sum or log-ratio methods. Both methods are available as in-built routines in Digital Micrograph software [81].

The most widely used log-ratio method for estimating sample thickness has two modifications, ‘relative’ and ‘absolute’ [61], and is based on measurements of two integrals: I_0 under ZLP and I_t under the whole spectrum. Assuming Poisson statistics of inelastic scattering, the thickness t is given by

$$\frac{t}{\lambda} = \ln\left(\frac{I_t}{I_0}\right), \quad (2.20)$$

where λ is the inelastic mean free path (MFP) of incoming electrons.

Relative thickness in terms of the inelastic MFP obtained directly from this equation is useful to trace thickness variations within a sample of uniform composition (thickness maps). To obtain absolute thickness, a value for MFP is to be known. MFP strongly depends on chemical composition of the sample and measurement conditions (microscope voltage E_0 , convergence semi-angle of the excitation beam α , collection semi-angle β). This dependence has been approximated for parallel beam illumination ($\alpha=0$) and $\beta < 10$ mrad by Malis et. al. [82] on the basis of a dipole formula as

$$\lambda \approx \frac{106FE_0}{E_m \ln(2E_0\beta / E_m)}, \quad (2.21)$$

where F is the relativistic factor (0.618 for $E_0 = 200$ keV), $E_m = 7.6 Z_{eff}^{0.36}$ is the average energy loss, which summarizes material properties, and Z_{eff} is the effective atomic number. For convergent STEM probe and large β angles such approximation underestimates MFP. In this case, a more reliable MFP estimate is better described by an equation relating MFP to the sample density ρ rather than to atomic number [83,84],

$$\lambda \approx \frac{11FE_0}{11\rho^{0.3}} \left/ \ln \left\{ \frac{\alpha^2 + \beta^2 + 2\theta_E^2 + \delta^2}{\alpha^2 + \beta^2 + 2\theta_c^2 + \delta^2} \times \frac{\theta_c^2}{\theta_E^2} \right\} \right., \quad (2.22)$$

where $\delta^2 = |\alpha^2 - \beta^2|$, both α and β are higher than the cut off angle $\theta_c = 20$ mrad, and $\theta_E = 5.5\rho^{0.3}/(FE_0)$ is the characteristic angle.

Both MFP estimations are available as custom scripts [85] in Digital Micrograph software. Accuracy of log-ratio method is controlled by $\sim 10\%$ accuracy of MFP estimation [61,82–84].

In this thesis thickness measurements were used for cavity number density calculations (in chapter 3, section 4.1, and chapter 5) and for the EELS investigation of hydrogen association with He-filled cavities (section 4.3). In the first case, EELS spectra were acquired in TEM EELS mode with $\alpha=2.15$ and $\beta=5.87$ mrad, while in the second case - in STEM EELS-SI mode with $\alpha=28$ mrad and $\beta=56$ mrad (section 4.3). For the TEM EELS measurements MFP was found from equation (2.21) to be 117 nm while for STEM EELS-SI it was estimated as 112 nm using equation (2.22).

2.3.2.3.4.6 Hydrogen association with cavities by EELS

EELS is an efficient tool for studying association of hydrogen with cavities and He bubbles. Two relevant examples are experiments on dual-beam $\text{He}^+ + \text{H}^+$ implantation into SiC [86] and focused ion beam implantation into diamond [87]. In these studies the hydrogen presence was demonstrated based on spectral evidence of the hydrogen K-shell (H-K) ionization edge at ~ 13 eV. By combining very high spatial resolution with spectroscopic information, EELS-SI method allows following changes in position and intensity of possible H and He signals at the same time and thus directly correlating the signals with particular parts of the cavity or He bubble. Recently spatial hydrogen distribution over He bubbles was successfully demonstrated on hydrogen saturated Zircaloy-4 alloy [88], neutron irradiated Be [89] and triple-beam implanted 13%Cr ODS-steel [90] using STEM EELS-SI method.

2.3.2.3.5 Void/bubble imaging

Bubble/void populations associated with different microstructural features, including nano-oxide particles, were studied in this thesis mainly by TEM. This section discusses TEM related methods for bubble/void imaging. For convenience, both bubbles and voids are referred to in this section as cavities, since in most cases, gas filling adds no or minor visible fingerprints on TEM/STEM cavity images.

Cavity imaging is possible in both TEM (BF, HRTEM) and STEM (BF, HAADF and HRSTEM) modes. The choice of a particular technique depends on the research goals, material, cavity size and location. For advanced cavity imaging TEM/STEM related techniques such as 3D electron tomography [91] and electron holography [92] may be applied. When helium filled cavities are attached to precipitates, application of X-Ray [68] or EELS spectrum imaging [93] provides additional benefits for cavity/precipitate differentiation.

Bright field TEM is the most popular technique for cavity imaging, being easy and efficient. Relatively large cavities with diameters in the range of $5 \text{ nm} < d < t/20$ (where t is the sample thickness) are visible in focus in both dynamical and kinematical BF conditions. Similar to disordered or amorphous zones in crystalline matrices [71], cavities imaged by diffraction (structure factor) contrast are best visible in-focus in BF dynamical conditions ($\omega = S\xi_g \approx 0$) at the flanks of low-order thickness fringes: they appear dark at the edge of a bright fringe and bright at the edge of a dark fringe. TEM sample is typically wedge-shaped and large faceted cavities may show thickness fringes at some sample orientations [71]. The increase of sample thickness results in collapse of thickness fringes due to anomalous absorption, the contrast of cavities becomes weaker and they always appear lighter than background. In the literature, large cavities (typically voids) are usually visible like this (see Fig. 2.37). Cavities cannot be seen in in-focus BF images when the ratio of thickness to cavity diameter exceeds ~ 20 [71].

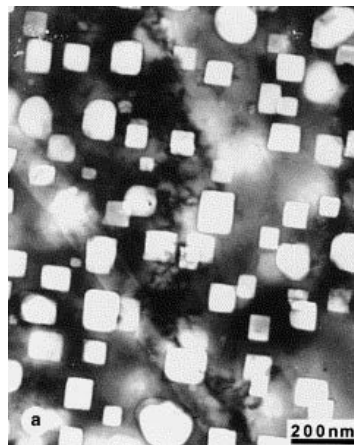


Fig. 2.37. In-focus BF TEM image of vacancy voids in the 16Cr-15Ni-3Mo-0.3Ti steels after irradiation in BN-600 reactor with fast neutrons to 60 dpa at 500°C [94].

The only way to visualize small cavities in BF TEM mode is to use special out-of-focus conditions. In this case the contrast arises from a weak absorption component and a phase-contrast component due to defocus. The phase-contrast component arises from the change in the mean inner potential between the cavity and the matrix as a result of a phase shift between electron waves which pass through the cavity and those passing through the adjacent perfect crystal [71]. The latter gives rise to Fresnel contrast in the form of a series of dark and bright fringes near the edge of the cavity. Typically, only one or two fringes are visible for a thermionic source. The effect is sensitive to the sign and value of defocus of the objective lens. In order to confirm the presence of small cavities, a BF through-focal series should be recorded with the TEM sample oriented sufficiently far from the Bragg condition for all reflections, so that the image loses most of its dynamical diffraction contrast. Under such kinematical conditions, the BF image exhibits a uniform background, cavities appear clearly as white dots surrounded by a dark Fresnel fringe in underfocused images, and contrast is reversed in overfocused images, while no significant contrast is observed close to the exact focus position. Better contrast is usually obtained in underfocused images. An example of such observation is shown in Fig. 2.38. It should be noted that small precipitates such as nano-oxides can provide Fresnel contrast very similar to cavities.

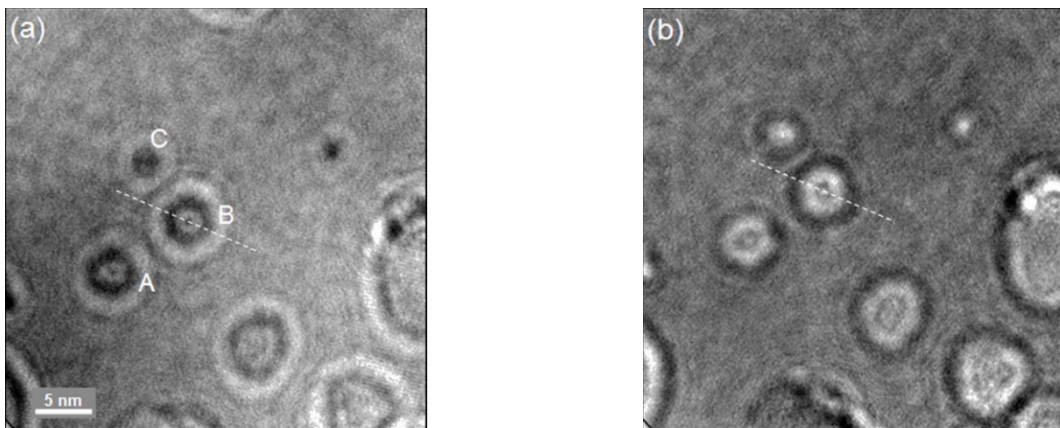


Fig. 2.38. Through-focus TEM bright field micrographs of helium bubbles in Fe-9%Cr alloy after 8 keV He⁺ implantation at 400 °C to 1.1×10^5 appm He. (a) +1 μm overfocused image; (b) -1 μm underfocused image [92].

Cavity sizes are determined based on the location of Fresnel fringes for different values of defocus. In order to accurately quantify cavity size, one needs a relationship between the actual cavity and the diameter of Fresnel fringes formed during out-of-focus imaging. Ideally, detailed simulations of the Fresnel fringe profiles are to be undertaken for such analysis.

Simulations of Fresnel contrast in out-of-focus cavity images using multi-beam Bloch wave under column approximation [72,95] show that for spherical cavities imaged in strong two-beam dynamical conditions the inner diameter of the first dark Fresnel fringe reasonably describe the actual cavity size for cavities with the diameter ≥ 2 nm, being slightly $\sim 10\%$ larger than the actual cavity diameter (see Fig. 2.39). The outer diameter of the first dark Fresnel fringe was found to be much larger than the actual diameter of the cavity. Hence it was recommended to utilize inner diameter of the first dark Fresnel fringe as cavity diameter quantity.

However, there are experimental difficulties in studying cavities near a Bragg condition, because the dislocation and cavity strain fields (if exist) tend to be in strong contrast, so that cavities, especially small ones, are not clearly visible. Also, the ‘inner-diameter of the dark fringe’ criterion produces inconsistencies in the measured and calculated volumes of large faceted cavities determined at various orientations [96].

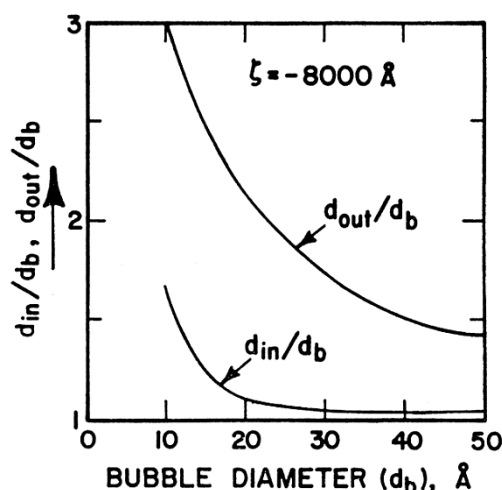


Fig. 2.39. The size correlation between imaged Fresnel rings and the actual bubbles for small spherical voids in thick TEM sample. Dynamical two-beam conditions. The diameters (d_{in}/d_b) and (d_{out}/d_b) of the inner and outer first dark Fresnel fringe are shown as a function of the actual cavity diameter (d_b) for the underfocus of $-0.8 \mu\text{m}$ [71].

The approach adopted in Refs. [72,95] was extended for the case of spherical and faceted cavities imaged under kinematical conditions [96]. For spherical cavities, it predicts the same contrast behavior as before, namely, the first dark fringe in an underfocused image is slightly larger than the actual cavity diameter for cavities $< 5 \text{ nm}$, but tends to decrease down to the actual cavity size for larger cavities (see Fig. 2.40(b)). For faceted cavities, qualitative behavior is the same, but the ratio of the first dark fringe to the actual diameter reduces rapidly and generally notably underestimates the true cavity size. The center of the dark fringe in an underfocused image of faceted cavities taken in kinematical conditions is less sensitive to cavity size increase. Moreover, the center position is mostly insensitive to defocus value for both spherical and faceted cavities. Simulation results of Ref. [96] suggest that the underfocused BF images taken under kinematical conditions provide much better representation of the actual cavity diameter. Note, however, that all calculations [72,95,96] predict that cavities smaller than $\sim 2 \text{ nm}$ in diameter cannot be sized accurately.

New TEMs (with FEG gun) have a resolution of about $1\text{--}3 \text{ \AA}$ or even sub- \AA for C_s -corrected devices and many TEM characterizations require foil thickness noticeably less than 100 nm . Both conditions fall out of the range of input parameters employed for simulations in Refs. [72,95,96]. Recently re-examination of cavity size correlation between imaged Fresnel fringes under kinematical conditions and actual sizes was performed by means of multislice simulation [97], assuming mostly coherent illumination and low foil thickness.

The results of Ref. [97] have confirmed that the actual cavity size (D_0) is generally close to the inner diameter of the first dark Fresnel (D_{in}). However, as shown in Fig. 2.40(a), utilization of FEG ion gun with high coherency and samples with low thickness changes the situation quantitatively for cavities $\geq 3 \text{ nm}$: D_{in} is slightly lower than D_0 for low deviation of illumination semi-angle $\leq 0.5 \text{ mrad}$. With the decrease of coherency, D_{in}/D_0 increases up to ~ 1.1 , similar to the predictions of [72,95,96]. The electron-beam accelerating voltage, cavity size, cavity position and TEM sample thickness were found to have no significant effect on D_{in}/D_0 . The ratio D_{in}/D_0 generally slightly decreases with the increase of the underfocus value up to 20%. In contrast to medium sized cavities, for cavity with diameters $\leq 2 \text{ nm}$ D_{in}/D_0 increases dramatically with the underfocus increase above $\sim 1 \mu\text{m}$ (Fig. 2.40(b)). The results of Ref. [97] suggest that the sizes of cavities with diameters in the range of $1\text{--}2 \text{ nm}$ can be accurately determined on underfocused BF TEM images acquired under kinematical conditions, but underfocus should not exceed $1 \mu\text{m}$. Simulations of Ref. [97] did not reveal notable effect of He filling on the contrast of Fresnel fringes.

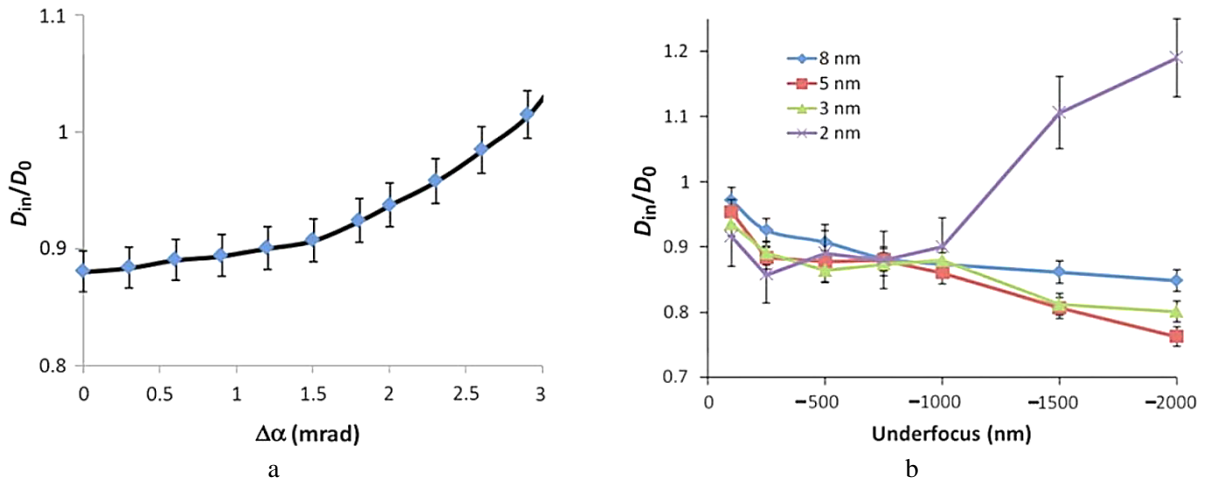


Fig. 2.40. The size correlation between imaged Fresnel fringes and the actual bubbles as a function of the: (a) deviation of illumination semi-angle ($\Delta\alpha$); (b) underfocus for cavities with different sizes [97].

The imaging and quantification of low-sized ~ 2 nm empty or He-filled cavities from BF TEM out-of focus images cavities is quite challenging. He-filled cavities that look round in Fresnel-type BF TEM images can in reality be faceted since the faceted microstructures minimize the interface energies [92]. To reveal size and morphology of such low-sized cavities, electron holography [92] or HRTEM imaging [21,90, 98–102] can be utilized.

STEM HAADF mode is widely used for imaging and sizing of cavities as an alternative to Fresnel-type BF TEM imaging. This technique has obvious advantages. In HAADF images mass-thickness contrast dominates and diffraction/phase contrast effects are avoided. Therefore cavities always (independent of TEM sample orientation) appear with the dark contrast on the relatively bright matrix background due to the lower thickness (matrix background is assumed to have constant thickness). As a consequence, HAADF STEM images of cavities can be interpreted more easily than Fresnel-type BF TEM images. In addition, aberration-corrected STEM HAADF provides more precise sizing of cavities than Fresnel-type BF TEM imaging. However, dark contrast in STEM HAADF images may arise not only from cavities but also from non-matrix lower Z inclusions, such as nano-oxide particles in ODS-steels. Fig. 2.41 shows STEM HAADF image which contains both He-filled cavities and nano-oxides in 14YWT steel implanted with He^+ ions at 400°C .

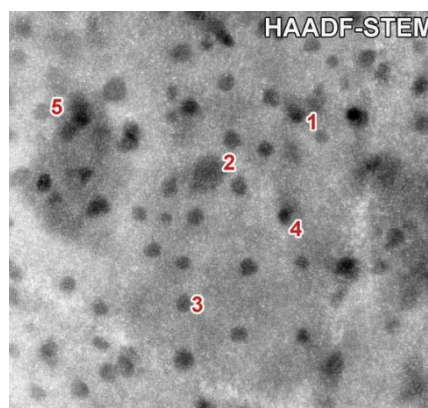
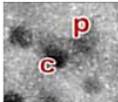
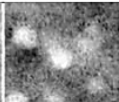
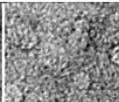
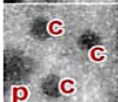
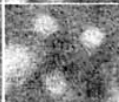
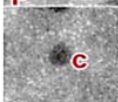
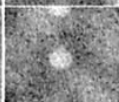
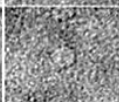
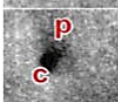
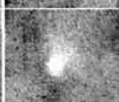
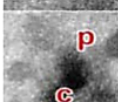
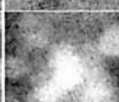
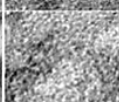


Fig. 2.41. HAADF-STEM image of He-filled cavities and nano-oxides in 14YWT steel implanted with He^+ ions at 400°C [68].

HAADF intensity is related to both mass and thickness, so that a larger inclusion of medium Z might demonstrate a contrast level comparable to a smaller feature of low Z, when both are embedded in a higher-Z matrix [68]. It is obvious that contrast interpretation of the dark features, in terms of precipitates versus cavities, is not straightforward using HAADF images.

Summing up, although STEM HAADF is able to provide appropriate imaging for the cavity size determination and even with higher resolution than Fresnel-type BF TEM (the limit is 1-2 nm, see Fig. 2.40), but the differentiation of cavities from other low Z features is more challenging. It should be noted, that STEM HAADF imaging of cavities is predominantly used when the combined imaging and EELS/EDX spectroscopy is required.

Combination of STEM HAADF and Fresnel-type BF TEM imaging allows more reliable differentiation of cavities and oxide particles, as demonstrated in Fig. 2.42.

Feature	HAADF	BF-STEM	BF-TEM	Contrast	Interpretation
1				HAADF: two dark, several medium; BF-STEM: three bright features; TEM: ringed features	Bubbles on precipitate or NC
2				HAADF: four medium; BF-STEM: all bright feature; TEM: ringed features and large light feature	Bubble near a precipitate
3				HAADF: dark feature; BF-STEM: bright feature; TEM: isolated ringed feature	Isolated bubble
4				HAADF: dark feature with medium contrast nearby; BF-STEM: bright feature with medium contrast nearby; TEM: ringed feature	Bubble on precipitate
5				HAADF: moderate contrast; BF-STEM: moderate contrast; TEM: little contrast	Large precipitate with many bubbles



Labels: c, cavity (void or bubble); p, precipitate or NC.

HAADF, high-angle annular dark field; BF, bright field; STEM, scanning transmission electron microscopy; TEM, transmission electron microscopy; NC, nanocluster.

Fig. 2.42. Qualitative evaluation of contrast in HAADF-STEM, BF-STEM, and BF-TEM images with respect to cavity and nano-oxides in 14YWT steel implanted with He⁺ ions at 400°C [68]. Labels are the same as in Fig. 2.41.

However, as already mentioned, the accuracy of cavity sizing in Fresnel BF TEM mode is limited to ~1-2 nm and in addition, small particles can also demonstrate cavity-like Fresnel contrast. Having in mind these drawbacks, the authors of Ref. [68] suggest that an ideal approach for small cavity/oxide particle differentiation is to combine high-collection-efficiency X-ray spectrum imaging (EDX-SI) followed by multivariate statistical analysis (MVSA) with special Fresnel-type BF STEM imaging. As a consequence of the reciprocity theorem, the contrast in Fresnel-type BF STEM images is equivalent to BF TEM, but much better resolution can be achieved using aberration-corrected microscope. EDX-SI involves HAADF imaging with simultaneous acquisition of characteristic X-Ray signal by EDX detector. Alternatively EELS-SI technique is able to achieve the same goals and has notable advantages in comparison with EDX-SI. EEL spectroscopy demonstrates energy resolution as high as 0.35 eV, whereas only 121 eV is available for EDX. Furthermore, when cavities are filled with a light gas (e.g. He or H) helium distribution can be obtained complementary to elemental mapping within the nano-oxide and matrix regions. In fact, cavity sizes detected by EDX and EELS-SI methods might be even below 1 nm. Although statistically meaningful information on cavity parameters is achievable relatively fast by both EDX and EELS-SI methods, the post-acquisition treatment required for final datasets is time consumable.

In contrast to EDX and EELS, accurate cavity sizing together with reliable cavity/nano-oxide differentiation may be easily obtained by means of HRTEM or HAADF HRSTEM imaging without extended post-acquisition treatment. Typical HRTEM and HAADF HRSTEM images of He-filled cavities affiliated with nano-oxides are shown in Fig. 2.43(a,b). In addition to cavity size, the

crystallographic orientation of particles and/or matrix can be identified. In spite of the absence of long-term post-acquisition treatment, single HRTEM [21,90, 98–102] or HRSTEM [103] images contain only few cavities or/and nano-oxides.

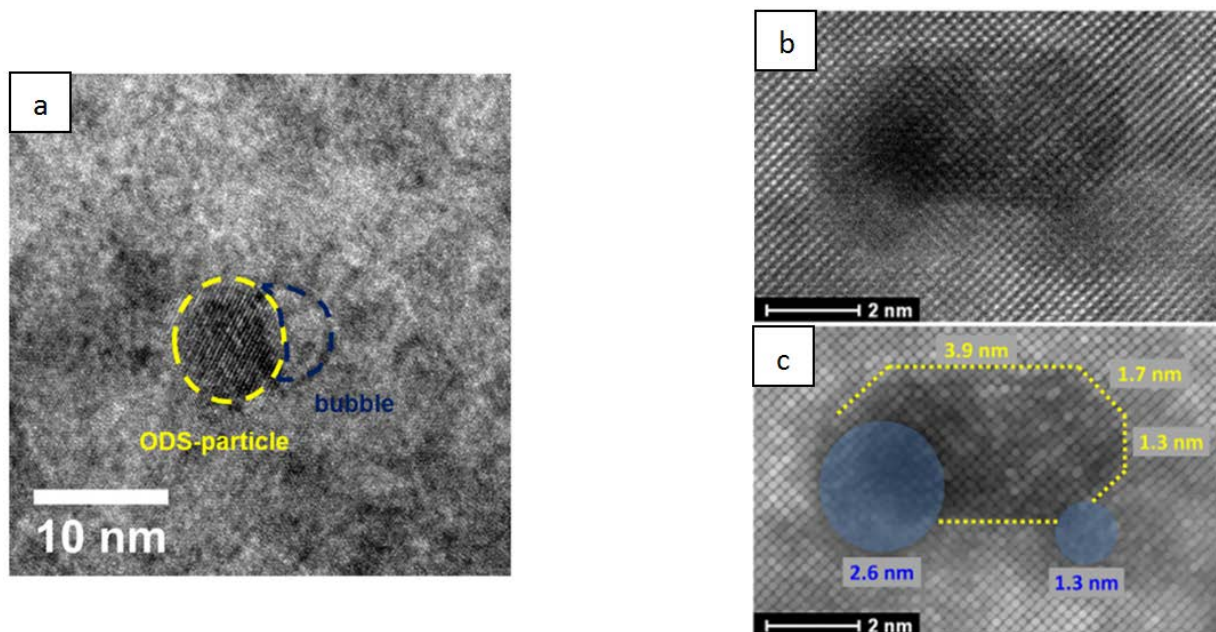


Fig. 2.43. (a) HRTEM image of Y₂O₃-particle with an attached He bubble [90]; (b) and (c) HAADF HRSTEM unprocessed and processed image of Y₂Ti₂O₇ particle with attached He bubbles [103].

Literature data reveal significant benefits of advanced TEM techniques and their combinations as compared to conventional Fresnel BF cavity imaging. However these techniques are, as a rule, time and equipment demanding, thus they do not allow obtaining statistically meaningful information on cavity parameters fast enough. Therefore, the main part of cavity images required in this thesis for the statistical treatment was obtained using conventional BF TEM mode. Because a large number of microstructural features that produce strong strain contrast in all the investigated materials, BF images were acquired in kinematical conditions in order to improve cavity contrast. The samples were oriented sufficiently away from any Bragg condition to suppress dynamical diffraction contrast and through-focus pairs of images in the range of ± 0.3 -2 μm were taken so that clear Fresnel fringes appeared around cavities. Cavities with diameters in the range of 1.2 - 20 nm were detected, but in the majority of images cavities had diameters ~ 3 -5 nm. Images were mainly obtained in the areas with thickness 20-60 nm using FEI Tecnai G² 20 twin with LaB₆ with resolution 0.27 nm and $C_s = 2$ mm. The measurements of cavity size were conducted using underfocused images. Therefore, the ratio of the first dark Fresnel ring (D_{in}) to the actual cavity diameter (d) relevant for our data is expected somewhere between the values 0.9 and 1.1, as estimated in Refs. [95] and [97]. We measure the cavity diameter from the position of the center of the first dark fringe with error bar 10%, as recommended Refs. [34,96].

In order to improve the differentiation between nano-oxide particles and cavities, thin sample areas of 20- 40 nm were used. In most cases it was possible to obtain images of sufficient quality because cavities attached to nano-oxides were relatively large, as shown in chapter 3 below.

In addition to through-focal BF images, additional HRTEM images were obtained using FEI TECNAI G² F20 S-Twin in cases where verification of cavity shape or nano-oxide/cavity affiliation was needed.

EELS-SI analysis used HAADF STEM imaging of cavities at high magnification, where cavities appeared in dark contrast on the matrix background and were well distinguishable from nano-oxides.

2.3.3 Thermal desorption spectroscopy

The thermal desorption spectroscopy (TDS) is a technique dedicated to investigation of adsorption, desorption, and reaction of gas atoms or molecules. TDS measurements involve non-isothermal (temperature ramp) or isothermal sample heating with subsequent monitoring of desorbed gas pressure evolution and/or the desorption flux of molecules or atoms. The collected data is represented as a desorption spectrum that can be correlated to the desorption flux of desired atoms or molecules as a function of time/temperature evolution. The basic idea behind the method is that gas with a higher desorption barrier desorbs at a higher temperature.

TDS was used in this thesis for the measurement of hydrogen release from ODS-EUROFER and EUROFER 97 steel samples after single-beam H^+ and sequential dual-beam $He^+ + H^+$ ion implantations. The analysis of acquired TDS spectra made it possible to evaluate the total amount of hydrogen trapped in a sample and allows to determine the hydrogen trapping capacity of the different microstructural features and defects based on their activation energies [104]. Various types of trapping sites for hydrogen in steels have been suggested in the literature (see Fig. 2.44) including vacancies and certain solute atoms, dislocations, grain boundaries, phase interfaces, triple grain junctions, precipitates, micro- and nanocracks, surface steps, voids/bubbles and surface oxide layers [105–107]. However, no dominant type of trapping site in steels has been reported and, in fact, hydrogen trapping capacity is determined by particular steel microstructure and conditions of hydrogen saturation (H-charging, implantation, etc.).

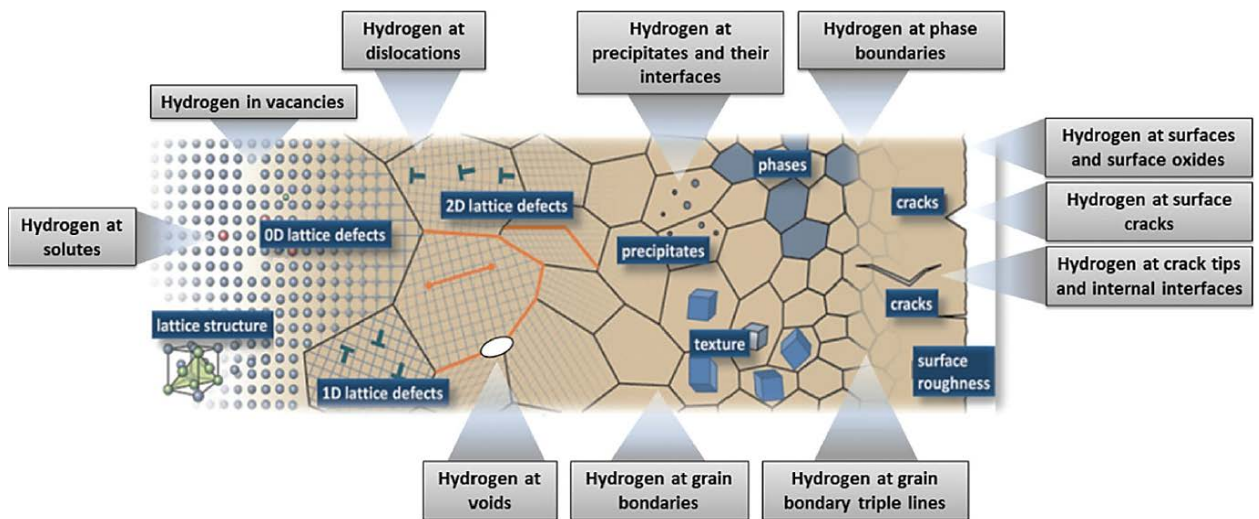


Fig. 2.44. A summary of various hydrogen trapping sites in metallic alloys [106].

Hydrogen release measurements were performed on house-made TDS apparatus in the School of Engineering, Department of Mechanical Engineering of Aalto University (Espoo, Finland). The general view and principal scheme of the TDS setup are shown in Fig. 2.45. TDS setup consists of a UHV-vacuum chamber equipped with a small vacuum furnace, mass-spectrometer (SRS residual gas analyzer RGA100), a pumping system with an effective pumping rate of $6.6 \times 10^{-2} \text{ m}^3/\text{s}$, an air-lock vacuum chamber for sample supply, a sample transportation mechanism and a PC using Lab View based software, which controls the mass spectrometer unit and furnace heating rate.

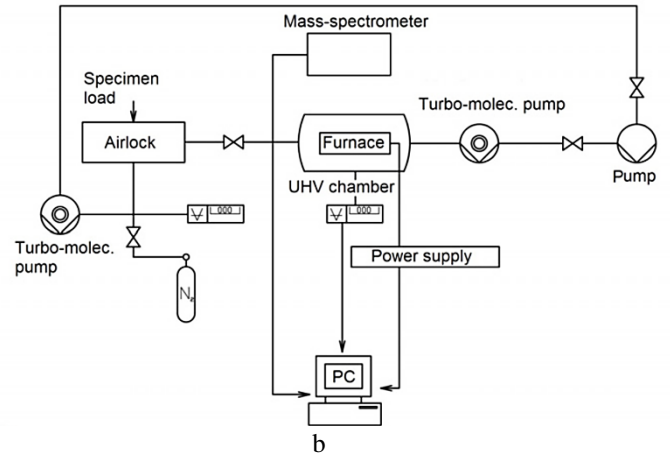


Fig. 2.45. Overview and principle scheme of TDS setup [108].

A typical TDS measurement in the current study involved the following steps:

- Hydrogen implanted samples were loaded into ultra-high vacuum (UHV) chamber with basic vacuum $\sim 1 \times 10^{-7}$ Pa through airlock.
- The heating was performed in the range from RT to 1200 K with a constant heating rate in the range from 3 to 10 K/min. Temperature measurements were done using a thermocouple fixed in contact with a sample as a feedback signal.
- The partial pressure of hydrogen that desorbed from the sample during heating was monitored by mass spectrometer (SRS residual gas analyzer RGA100) in the range from RT to 1200 K. In the mass spectrometer, ionized gas particles were accelerated, separated and detected based on their mass-to-charge ratio.

As a result, plots of hydrogen pressure vs. time/temperature were produced. With fixed volume of UHV chamber and pumping speed, the pressure vs. time dependencies were converted into desorption rate vs. time ones and then the final TDS spectra in the form of desorption rate as a function of sample temperature were obtained applying the employed heating rate.

Typical hydrogen release spectra from three different steels are shown in Fig. 2.46.

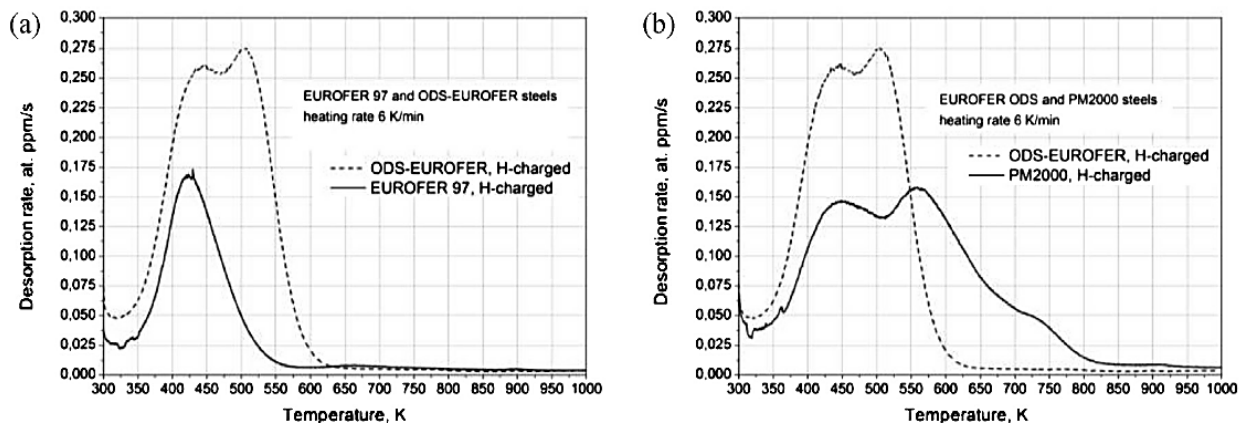


Fig. 2.46. TDS spectra for hydrogen release from: (a) EUROFER 97 and ODS-EUROFER (b) ODS-EUROFER and PM2000 [109].

TDS spectra have typically a complex shape with multiple peaks. The shape of each desorption peak depends on the hydrogen trapping behavior and the amplitude is related to the amount of trapped hydrogen. The area under entire calibrated TDS spectrum equals to the total amount of hydrogen trapped in the sample [110]. The complex shape of TDS spectrum is assumed to be a result of different activation energies for gas de-trapping from various trapping states in the investigated material. This assumption lies

behind numerical models used to determine the de-trapping activation energy of the measured gas species from acquired TDS data.

Analysis of TDS spectrum provides detailed information about hydrogen trapping states based on the determination of the peak temperatures for hydrogen desorption during heating and applying numerical modeling of hydrogen uptake and desorption. Hydrogen transport in the bulk of the metal sample during the heating is a complex process which includes detrapping, diffusion and desorption. A schematic interpretation of different energies involved in hydrogen trapping and diffusion is given in Fig. 2.47. Each trapping site is associated with a certain binding energy, E_b . Untrapped hydrogen is transported in the metal by interstitial diffusion. The activation barrier for hydrogen interstitial diffusion is denoted by E_m . The activation energy E_a required for hydrogen de-trapping is as a sum of diffusion and binding energy of hydrogen.

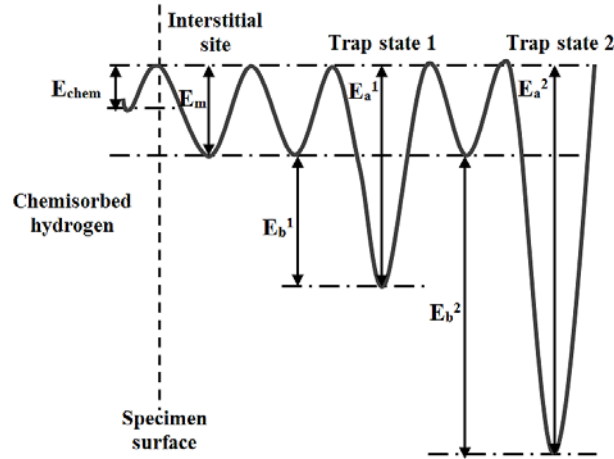


Fig. 2.47. Schematic illustration of different energies involved in hydrogen diffusion and trapping.

A number of methods are used in order to extract information about trapping sites from experimentally measured TDS spectra and to obtain activation energies of hydrogen detrapping from each particular trap. These methods can be subdivided into three classes based on the underlying approaches [104,107]:

(i) Reaction kinetics model [111–114] is based on the kinetics of homogeneous chemical reactions and it does not take into account hydrogen transport in the sample. The model is not applicable for the cases where hydrogen diffusion rather than de-trapping is the limiting step, e.g. for hydrogen desorption from austenite;

(ii) McNabb–Foster trapping–detrapping model that includes the kinetics of trapping and detrapping, the activation energy law and mass conservation;

(c) Oriani model, where a local equilibrium between hydrogen in the traps and in the lattice is assumed.

In *bcc* iron-based alloys, the rate limiting step is de-trapping because hydrogen migration barrier of $E_m \sim 0.04\text{--}0.16$ eV [115,116] is well below the detrapping energies of the majority of trapping sites (summarized in Table 4.8 in chapter 4). Typically hydrogen diffuses out from interstitial sites already at RT. Therefore, the simplified and widely used approach suggested by Choo and Lee [111–114] based on the reaction kinetics model of Kissinger [117] was applied in the thesis to evaluate the activation energies for hydrogen de-trapping from specific traps. According to this approach, desorption kinetics is described by the equation:

$$\frac{\partial X}{\partial t} = A(1 - X) \exp\left(\frac{-E_a}{RT}\right), \quad (2.23)$$

where X is the fraction of hydrogen released, A - an empirical constant, E_a - the de-trapping activation energy, R - the gas constant, and T - the absolute temperature.

For a constant heating rate φ , when a maximum on the desorption rate curve is reached, the first derivative of the l.h.s. in equation (2.23) vanishes and consequently the activation energy for hydrogen de-trapping from the specific trap can be determined as

$$\frac{\partial \ln(\varphi / T_m^2)}{\partial (1/T_m)} = \frac{-E_a}{R}, \quad (2.24)$$

where T_m is the temperature of the peak maximum.

Formally, equation (2.23) is strictly valid only assuming that hydrogen desorption is a first order reaction, while other reaction orders may be possible. Reaction order can be determined from the shape of the TDS peaks: first order reactions produce sigmoidal peak shapes, while second order reactions give Gaussian peaks. In experimental TDS curves (see section 4.2) peaks with Gaussian shape appear. Thus, the desorption of hydrogen from ODS-EUROFER in this thesis is rather of second order. However, calculations of E_a from the plot $\ln(\varphi/T_m^2)$ vs. $1/T_m$ obtained from a series of TDS measurements at different heating rates is not sensitive to the reaction order involved due to the fact that slope of plot is always E_a/R and remains the same for reactions of arbitrary order.

As mentioned above such a complex material as steel contains multiple trap kinds. Together they give rise to many and typically overlapping peaks in TDS spectra. Thus, prior to determining activation energies for hydrogen de-trapping, TDS spectra should be deconvoluted to separate different peaks. The deconvolution procedure can be quite non-trivial because various alternatives are often possible. Illustration of deconvolution complexity and its impact on the results can be found in Ref. [118].

2.4 References

- [1] R. Lindau, A. Moeslang, M. Rieth, M. Klimiankou, E. Materna-Morris, A. Alamo, A.-A. F. Tavassoli, C. Cayron, A.-M. Lancha, P. Fernandez, N. Baluc, R. Schaeublin, E. Diegele, G. Filacchioni, J.W. Rensman, B.v.d. Schaaf, E. Lucon, W. Dietz, “Present development status of EUROFER and ODS-EUROFER for application in blanket concepts,” *Fusion Eng. Des.*, vol. 75–79, pp. 989–996, 2005.
- [2] E. Gaganidze, H.-C. Schneider, B. Dafferner, and J. Aktaa, “High-dose neutron irradiation embrittlement of RAFM steels,” *J. Nucl. Mater.*, vol. 355, no. 1, pp. 83–88, 2006.
- [3] R. Lindau, M. Klimenkov, U. Jäntschi, A. Möslang, and L. Commin, “Mechanical and microstructural characterization of electron beam welded reduced activation oxide dispersion strengthened – Eurofer steel,” *J. Nucl. Mater.*, vol. 416, no. 1, pp. 22–29, 2011.
- [4] M. Klimiankou, R. Lindau, and A. Möslang, “HRTEM Study of yttrium oxide particles in ODS steels for fusion reactor application,” *J. Cryst. Growth*, vol. 249, no. 1, pp. 381–387, 2003.
- [5] M. Klimiankou, R. Lindau, and A. Möslang, “TEM characterization of structure and composition of nanosized ODS particles in reduced activation ferritic–martensitic steels,” *J. Nucl. Mater.*, vol. 329–333, pp. 347–351, 2004.
- [6] D. Brimbal, L. Beck, O. Troeber, E. Gaganidze, P. Trocellier, J. Aktaa, R. Lindau, “Microstructural characterization of Eurofer-97 and Eurofer-ODS steels before and after multi-beam ion irradiations at JANNUS Saclay facility,” *J. Nucl. Mater.*, vol. 465, pp. 236–244, 2015.
- [7] K. D. Zilnyk, V. B. Oliveira, H. R. Z. Sandim, A. Möslang, and D. Raabe, “Martensitic transformation in Eurofer-97 and ODS-Eurofer steels: A comparative study,” *J. Nucl. Mater.*, vol. 462, pp. 360–367, 2015.
- [8] S. Rogozhkin, A. Bogachev, O. Korchuganova, A. Nikitin, N. Orlov, A. Aleev, A. Zaluzhnyi, M. Kozodaev, T. Kulevoy, B. Chalykh, R. Lindau, J. Hoffmann, A. Moeslang, P. Vladimirov, M. Klimenkov, M. Heilmaier, J. Wagner, S. Seils, “Nanostructure evolution in ODS steels under ion irradiation,” *Nucl. Mater. Energy*, vol. 9, pp. 66–74, 2016.
- [9] F. Bergner, G. Hlawacek, and C. Heintze, “Helium-ion microscopy, helium-ion irradiation and nanoindentation of Eurofer 97 and ODS Eurofer,” *J. Nucl. Mater.*, vol. 505, pp. 267–275, 2018.
- [10] A. Das, P. Chekhonin, E. Altstadt, F. Bergner, C. Heintze, and R. Lindau, “Microstructural characterization of inhomogeneity in 9Cr ODS EUROFER steel,” *J. Nucl. Mater.*, vol. 533, p. 152083, 2020.
- [11] Z. Lu, R. G. Faulkner, N. Riddle, F. D. Martino, and K. Yang, “Effect of heat treatment on microstructure and hardness of Eurofer 97, Eurofer ODS and T92 steels,” *J. Nucl. Mater.*, vol. 386–388, pp. 445–448, 2009.
- [12] E. Lucon, A. Leenaers, and W. Vandermeulen, “Post irradiation examination of a thermo-mechanically improved version of EUROFER ODS,” SCK•CEN Open Rep. BLG-1028, Belgium, 2006.
- [13] J. Fu, J. C. Brouwer, R. W. A. Hendrikx, I. M. Richardson, and M. J. M. Hermans, “Microstructure characterisation and mechanical properties of ODS Eurofer steel subject to designed heat treatments,” *Mater. Sci. Eng. A*, vol. 770, p. 138568, 2020.
- [14] R. Schäublin, A. Ramar, N. Baluc, V. de Castro, M. A. Monge, T. Leguey, N. Schmid, C. Bonjour, “Microstructural development under irradiation in European ODS ferritic/martensitic steels,” *J. Nucl. Mater.*, vol. 351, no. 1, pp. 247–260, 2006.

- [15] M. Klimiankou, R. Lindau, and A. Möslang, “Direct correlation between morphology of (Fe,Cr)₂₃C₆ precipitates and impact behavior of ODS steels,” *J. Nucl. Mater.*, vol. 367–370, pp. 173–178, 2007.
- [16] Ch. Ch. Eiselt, M. Klimenkov, R. Lindau, A. Möslang, H. R. Z. Sandim, A. F. Padilha, D. Raabe, “High-resolution transmission electron microscopy and electron backscatter diffraction in nanoscaled ferritic and ferritic–martensitic oxide dispersion strengthened–steels,” *J. Nucl. Mater.*, vol. 385, no. 2, pp. 231–235, 2009.
- [17] M. Klimenkov, R. Lindau, and A. Möslang, “New insights into the structure of ODS particles in the ODS-Eurofer alloy,” *J. Nucl. Mater.*, vol. 386–388, pp. 553–556, 2009.
- [18] H. R. Z. Sandim, R. A. Renzetti, A. F. Padilha, D. Raabe, M. Klimenkov, R. Lindau, A. Moeslang, “Annealing behavior of ferritic-martensitic 9%Cr-ODS-Eurofer steel,” *Mater. Sci. Eng. A*, vol. 527, no. 15, pp. 3602–3608, 2010.
- [19] C. Heintze, F. Bergner, A. Ulbricht, M. Hernández-Mayoral, U. Keiderling, R. Lindau, T. Weissgärber, “Microstructure of oxide dispersion strengthened Eurofer and iron–chromium alloys investigated by means of small-angle neutron scattering and transmission electron microscopy,” *J. Nucl. Mater.*, vol. 416, no. 1, pp. 35–39, 2011.
- [20] H. R. Z. Sandim, R. A. Renzetti, A. F. Padilha, A. Möslang, R. Lindau, and D. Raabe, “Annealing behavior of RAFM ODS-Eurofer steel,” *Fusion Sci. Technol.*, vol. 61, no. 2, pp. 136–140, Feb. 2012.
- [21] A. I. Ryazanov, O. K. Chugunov, S. M. Ivanov, S. T. Latushkin, R. Lindau, A. Möslang, A. A. Nikitina, K. E. Prikhodko, E. V. Semenov, V. N. Unezhev, P. V. Vladimirov, “Tensile properties and microstructure of helium implanted EUROFER ODS,” *J. Nucl. Mater.*, vol. 442, no. 1, Supplement 1, pp. S153–S157, 2013.
- [22] P. Fernández, A. M. Lancha, J. Lapeña, and M. Hernández-Mayoral, “Metallurgical characterization of the reduced activation ferritic/martensitic steel Eurofer’97 on as-received condition,” *Fusion Eng. Des.*, vol. 58–59, pp. 787–792, 2001.
- [23] P. Fernández, A. M. Lancha, J. Lapeña, M. Serrano, and M. Hernández-Mayoral, “Metallurgical properties of reduced activation martensitic steel Eurofer 97’ in the as-received condition and after thermal ageing,” *J. Nucl. Mater.*, vol. 307–311, pp. 495–499, 2002.
- [24] M. Klimenkov, R. Lindau, E. Materna-Morris, and A. Möslang, “TEM characterization of precipitates in EUROFER 97,” *Progress in Nuclear Energy*, vol. 57, pp. 8–13, 2012.
- [25] M. Yamamoto, S. Ukai, S. Hayashi, T. Kaito, and S. Ohtsuka, “Formation of residual ferrite in 9Cr-ODS ferritic steels,” *Mater. Sci. Eng. A*, vol. 527, no. 16, pp. 4418–4423, 2010.
- [26] S. Ohtsuka, S. Ukai, M. Fujiwara, T. Kaito, and T. Narita, “Improvement of 9Cr-ODS martensitic steel properties by controlling excess oxygen and titanium contents,” *J. Nucl. Mater.*, vol. 329–333, pp. 372–376, 2004.
- [27] S. Ukai and S. Ohtsuka, “Nano-mesoscopic structure control in 9Cr–ODS ferritic steels,” *Energy Mater.*, vol. 2, no. 1, pp. 26–35, Mar. 2007.
- [28] X. Zhou, C. Li, L. Yu, H. Li, and Y. Liu, “Effects of Ti addition on microstructure and mechanical property of spark-plasma-sintered transformable 9Cr-ODS steels,” *Fusion Eng. Des.*, vol. 135, pp. 88–94, 2018.
- [29] A. J. Schwartz, M. Kumar, B. L. Adams, and D. P. Field, Eds., *Electron Backscatter Diffraction in Materials Science*. Boston, MA: Springer US, 2009.

- [30] U. F. Kocks, C. N. Tomé, and H.-R. Wenk, *Texture and Anisotropy Preferred Orientations in Polycrystals and their Effect on Materials Properties*. Cambridge University Press, 2000.
- [31] A. A. Aleev, N. A. Iskandarov, M. Klimenkov, R. Lindau, A. Moeslang, A. A. Nikitin, S. V. Rogozhkin, P. Vladimirov, A. G. Zaluzhnyi, “Investigation of oxide particles in unirradiated ODS Eurofer by tomographic atom probe,” *J. Nucl. Mater.*, vol. 409, no. 2, pp. 65–71, 2011.
- [32] J. Ayache, L. Beaunier, J. Boumendil, G. Ehret, and D. Laub, *Sample Preparation Handbook for Transmission Electron Microscopy*. New York, NY: Springer New York, 2010.
- [33] L. A. Giannuzzi and F. A. Stevie, Eds., *Introduction to Focused Ion Beams*. Boston, MA: Springer US, 2005.
- [34] M. Kirk, X. Yi, and M. Jenkins, “Characterization of irradiation defect structures and densities by transmission electron microscopy,” *J. Mater. Res.*, vol. 30, no. 9, pp. 1195–1201, 2015.
- [35] G. Bräuer, “Magnetron Sputtering,” *Compr. Mater. Process.*, pp. 57–73, Jan. 2014.
- [36] M. Henini, Ed., *Molecular Beam Epitaxy*. Elsevier, 2013.
- [37] T. Mitsunaga, “X-Ray Thin-Film Measurement Techniques II. Out-Of-Plane Diffraction Measurements,” *Rigaku J.*, vol. 5, no. 1, pp. 7–12, 2009.
- [38] L. S. Zevin and G. Kimmel, *Quantitative X-Ray Diffractometry*. New York, NY: Springer US, 1995.
- [39] A. Gentils and C. Cabet, “Investigating radiation damage in nuclear energy materials using JANNuS multiple ion beams,” *Nucl. Instruments Methods Phys. Res. Sect. B Beam Interact. with Mater. Atoms*, vol. 447, pp. 107–112, 2019.
- [40] J. Chaumont, F. Lalu, M. Salome, A.-M. Lamoise, and H. Bernas, “A medium energy facility for variable temperature implantation and analysis,” *Nucl. Instruments Methods Phys. Res.*, vol. 189, no. 1, pp. 193–198, 1981.
- [41] C.-O. Bacri, C. Bachelet, C. Baumier, J. Bourçois, L. Delbecq, D. Ledu, N. Pauwels, S. Picard, S. Renouf, C. Tanguy, “SCALP, a platform dedicated to material modifications and characterization under ion beam,” *Nucl. Instruments Methods Phys. Res. Sect. B Beam Interact. with Mater. Atoms*, vol. 406, pp. 48–52, 2017.
- [42] H. Bernas, J. Chaumont, E. Cottureau, R. Meunier, A. Traverse, C. Clerc, O. Kaitasov, F. Lalu, D. Le Du, G. Moroy, M. Salomé, “Progress report on Aramis, the 2 MV tandem at Orsay,” *Nucl. Instruments Methods Phys. Res. Sect. B Beam Interact. with Mater. Atoms*, vol. 62, no. 3, pp. 416–420, 1992.
- [43] E. Cottureau, J. Camplan, J. Chaumont, R. Meunier, and H. Bernas, “ARAMIS: An ambidextrous 2 MV accelerator for IBA and MeV implantation,” *Nucl. Instruments Methods Phys. Res. Sect. B Beam Interact. with Mater. Atoms*, vol. 45, no. 1, pp. 293–295, 1990.
- [44] N. Chauvin, S. Henry, H. Flocard, F. Fortuna, O. Kaitasov, P. Pariset, S. Pellegrino, M.O. Ruault, Y. Serruys, P. Trocelier, “Optics calculations and beam line design for the JANNuS facility in Orsay,” *Nucl. Instruments Methods Phys. Res. Sect. B Beam Interact. with Mater. Atoms*, vol. 261, no. 1, pp. 34–39, 2007.
- [45] J. F. Ziegler, M. D. Ziegler, and J. P. Biersack, “SRIM – The stopping and range of ions in matter (2010),” *Nucl. Instruments Methods Phys. Res. Sect. B Beam Interact. with Mater. Atoms*, vol. 268, no. 11, pp. 1818–1823, 2010.
- [46] *ASTM E521-16, Standard Practice for Investigating the Effects of Neutron Radiation Damage Using Charged-Particle Irradiation*, ASTM International, West Conshohocken, PA, 2016, www.astm.org.

- [47] I. Monnet, T. Van den Berghe, and P. Dubuisson, “A comparison between different oxide dispersion strengthened ferritic steel ongoing in situ oxide dissolution in High Voltage Electron Microscope,” *J. Nucl. Mater.*, vol. 424, no. 1, pp. 204–209, 2012.
- [48] M. P. Short, D. R. Gaston, M. Jin, L. Shao, and F. A. Garner, “Modeling injected interstitial effects on void swelling in self-ion irradiation experiments,” *J. Nucl. Mater.*, vol. 471, pp. 200–207, 2016.
- [49] L. Shao, C.-C. Wei, J. Gigax, A. Aitkaliyeva, D. Chen, B.H. Sencer, F.A. Garner, “Effect of defect imbalance on void swelling distributions produced in pure iron irradiated with 3.5 MeV self-ions,” *J. Nucl. Mater.*, vol. 453, no. 1, pp. 176–181, 2014.
- [50] E. J. Mittemeijer and P. Scardi, Eds., *Diffraction Analysis of the Microstructure of Materials*, vol. 68. Berlin, Heidelberg: Springer Berlin Heidelberg, 2004.
- [51] Y. Waseda, E. Matsubara, and K. Shinoda, *X-Ray Diffraction Crystallography*. Berlin, Heidelberg: Springer Berlin Heidelberg, 2011.
- [52] K. Inaba, “X-ray thin-film measurement techniques I. Overview,” *Rigaku J.*, vol. 24, no. 1, pp. 10–15, 2008.
- [53] S. Kobayashi, “X-ray thin-film measurement techniques IV. In-plane XRD measurement,” *Rigaku J.*, vol. 26, no. 1, pp. 3–11, 2010.
- [54] J. I. Goldstein, D. E. Newbury, J. R. Michael, N. W. M. Ritchie, J. H. J. Scott, D. C. Joy, *Scanning Electron Microscopy and X-ray Microanalysis*. Boston, MA: Springer US, 2003.
- [55] D. B. Williams and C. B. Carter, *Transmission Electron Microscopy*. Boston, MA: Springer US, 2009.
- [56] B. J. Inkson, “2 - Scanning electron microscopy (SEM) and transmission electron microscopy (TEM) for materials characterization,” in *Materials Characterization Using Nondestructive Evaluation (NDE) Methods*, G. Hübschen, I. Altpeter, R. Tschuncky, and H.-G. Herrmann, Eds. Woodhead Publishing, 2016, pp. 17–43.
- [57] L. Reimer, *Scanning Electron Microscopy*, vol. 45. Berlin, Heidelberg: Springer Berlin Heidelberg, 1998.
- [58] H. Koh and L. Reimer, *Transmission Electron Microscopy*, vol. 36. New York, NY: Springer New York, 2008.
- [59] S. J. Pennycook and P. D. Nellist, Eds., *Scanning Transmission Electron Microscopy*. New York, NY: Springer New York, 2011.
- [60] F. Krumeich, *Introduction into transmission and scanning transmission electron microscopy*. Laboratory of Inorganic Chemistry ETH Zürich 8093 Zürich, Switzerland, 2018.
- [61] R. F. Egerton, *Electron Energy-Loss Spectroscopy in the Electron Microscope*. Boston, MA: Springer US, 2011.
- [62] <http://www.ebsd.com/ebsd-explained/10-ebsd-explained>.
- [63] *ASTM E2627-13(2019), Standard Practice for Determining Average Grain Size Using Electron Backscatter Diffraction (EBSD) in Fully Recrystallized Polycrystalline Materials*, ASTM International, West Conshohocken, PA, 2019, www.astm.org.
- [64] <https://www.csns.in2p3.fr/>.
- [65] <https://www.ijclab.in2p3.fr/>.
- [66] <https://www.globalsino.com/EM/>.

- [67] H. Rose and C. F. Kisielowski, “On the Reciprocity of TEM and STEM,” *Microsc. Microanal.*, vol. 11, no. S02, Aug. 2005.
- [68] C. M. Parish and M. K. Miller, “Aberration-corrected X-ray spectrum imaging and fresnel contrast to differentiate nanoclusters and cavities in helium-irradiated alloy 14YWT,” *Microsc. Microanal.*, vol. 20, no. 2, pp. 613–626, 2014.
- [69] C. M. Parish, K. G. Field, A. G. Certain, and J. P. Wharry, “Application of STEM characterization for investigating radiation effects in BCC Fe-based alloys,” *J. Mater. Res.*, vol. 30, no. 9, pp. 1275–1289, 2015.
- [70] F. Krumeich, E. Müller, and R. A. Wepf, “Phase-contrast imaging in aberration-corrected scanning transmission electron microscopy,” *Micron*, vol. 49, pp. 1–14, 2013.
- [71] M. L. Jenkins, *Characterization of radiation damage by transmission electron microscopy*. Bristol ; Institute of Physics Pub, 2001.
- [72] M. R. Rühle, “in ‘Radiation-induced voids in metals’. Proceedings of the 1971 International Conference Held at Albany, New York, June 9-11, 1971.,” U.S. Atomic Energy Commission, Jan. 1972.
- [73] B. Fultz and J. M. Howe. *Transmission Electron Microscopy and Diffractometry of Materials*. Berlin, Heidelberg: Springer Berlin Heidelberg, 2008.
- [74] <https://myscope.training/legacy/analysis/eds/>.
- [75] C. A. Walsh, J. Yuan, and L. M. Brown, “A procedure for measuring the helium density and pressure in nanometre-sized bubbles in irradiated materials using electron-energy-loss spectroscopy,” *Philos. Mag.*, vol. 80, no. 7, pp. 1507–1543, Jul. 2000.
- [76] S. Fréchar, M. Walls, M. Kociak, J. P. Chevalier, J. Henry, and D. Gorse, “Study by EELS of helium bubbles in a martensitic steel,” *J. Nucl. Mater.*, vol. 393, no. 1, pp. 102–107, 2009.
- [77] M.-L. David, F. Pailloux, V. Mauchamp, and L. Pizzagalli, “In situ probing of helium desorption from individual nanobubbles under electron irradiation,” *Appl. Phys. Lett.*, vol. 98, no. 17, p. 171903, Apr. 2011.
- [78] <https://www.gatan.com/techniques/spectrum-imaging>.
- [79] J. Scott, P. J. Thomas, M. MacKenzie, S. McFadzean, J. Wilbrink, A. J. Craven, W. A. P. Nicholson, “Near-simultaneous dual energy range EELS spectrum imaging,” *Ultramicroscopy*, vol. 108, no. 12, pp. 1586–1594, 2008.
- [80] <https://eels.info/about/techniques/dual-eels>.
- [81] “Digital Micrograph™ software by Gatan Inc.”. <https://www.gatan.com/products/tem-analysis/gatan-microscopy-suite-software>.
- [82] T. Malis, S. C. Cheng, and R. F. Egerton, “EELS log-ratio technique for specimen-thickness measurement in the TEM,” *J. Electron Microsc. Tech.*, vol. 8, no. 2, pp. 193–200, Feb. 1988.
- [83] K. Iakoubovskii, K. Mitsuishi, Y. Nakayama, and K. Furuya, “Thickness measurements with electron energy loss spectroscopy,” *Microsc. Res. Tech.*, vol. 71, no. 8, pp. 626–631, Aug. 2008.
- [84] K. Iakoubovskii, K. Mitsuishi, Y. Nakayama, and K. Furuya, “Mean free path of inelastic electron scattering in elemental solids and oxides using transmission electron microscopy: Atomic number dependent oscillatory behavior,” *Phys. Rev. B*, vol. 77, no. 10, p. 104102, Mar. 2008.
- [85] D. R. G. Mitchell, “Dmscripting”. <http://www.dmscripting.com/meanfreepathestimator.html>.

- [86] K. Hojou, S. Furuno, K. N. Kushita, N. Sasajima, and K. Izui, "EELS analysis of SiC crystals under hydrogen and helium dual-ion beam irradiation," *Nucl. Instruments Methods Phys. Res. Sect. B Beam Interact. with Mater. Atoms*, vol. 141, no. 1, pp. 148–153, 1998.
- [87] W. R. McKenzie, M. Z. Quadir, M. H. Gass, and P. R. Munroe, "Focused Ion beam implantation of diamond," *Diam. Relat. Mater.*, vol. 20, no. 8, pp. 1125–1128, 2011.
- [88] M. S. Blackmur, S. Dumbill, I. MacLaren, D. Hernandez-Maldonado, P. D. Styman, M. Gass, R. J. Nicholls, J. M. Hyde, Q. M. Ramasse, K. J. Annand, J. S. Smith, N. Gotham, "The association of hydrogen with nanometre bubbles of helium implanted into zirconium," *Scripta Materialia*, vol. 152, pp. 102–106, 2018.
- [89] M. Klimenkov, P. Vladimirov, J. Hoffmann, N. Zimmer, A. Möslang, and V. Kuksenko, "First simultaneous detection of helium and tritium inside bubbles in beryllium," *Micron*, vol. 127, p. 102754, 2019.
- [90] N. Zimmer, P. Vladimirov, M. Klimenkov, U. Jaentsch, R. Vila, V. Chakin, F. Mota, "Microstructural evolution of three potential fusion candidate steels under ion-irradiation," *J. Nucl. Mater.*, vol. 535, p. 152160, 2020.
- [91] N. R. Catarineu, N. C. Bartelt, J. D. Sugar, S. M. Vitale, K. L. Shanahan, and D. B. Robinson, "Three-dimensional maps of helium nanobubbles to probe the mechanisms of bubble nucleation and growth," *J. Phys. Chem. C*, vol. 123, no. 31, pp. 19142–19152, Aug. 2019.
- [92] E. Snoeck, J. Majimel, M. O. Ruault, and M. J. Hÿtch, "Characterization of helium bubble size and faceting by electron holography," *J. Appl. Phys.*, vol. 100, no. 2, p. 23519, Jul. 2006.
- [93] V. Badjeck, "Electron spectro-microscopy study of damage free and He implanted ODS steels," 2015.
- [94] V. V Sagaradze, S. S. Lapin, M. A. Kirk, and B. N. Goshchitskii, "Influence of high-dose Kr⁺ irradiation on structural evolution and swelling of 16Cr–15Ni–3Mo–1Ti aging steel," *J. Nucl. Mater.*, vol. 274, no. 3, pp. 287–298, 1999.
- [95] M. Ruehle and M. Wilkens, "Defocusing contrast of cavities. I. Theory," *Cryst Lattice Defects*, 1975.
- [96] A. J. E. Foreman, H. S. Von Harrach, and D. K. Saldin, "The TEM contrast of faceted voids," *Philos. Mag.*, vol. 45, no. 4, pp. 625–645, Apr. 1982.
- [97] B. Yao, D. J. Edwards, R. J. Kurtz, G. R. Odette, and T. Yamamoto, "Multislice simulation of transmission electron microscopy imaging of helium bubbles in Fe," *J. Electron Microsc. (Tokyo)*, vol. 61, no. 6, pp. 393–400, 2012.
- [98] P. D. Edmondson, C. M. Parish, Y. Zhang, A. Hallén, and M. K. Miller, "Helium entrapment in a nanostructured ferritic alloy," *Scripta Materialia*, vol. 65, no. 8, pp. 731–734, 2011.
- [99] L. L. Hsiung, "HRTEM study of irradiation-induced cavities in oxide-dispersed ferritic steel," *Metall. Mater. Trans. A*, vol. 44, no. 10, pp. 4496–4504, 2013.
- [100] W. Xu, L. Li, J. A. Valdez, M. Saber, Y. Zhu, C. C. Koch, R. O. Scattergood, "Effect of nano-oxide particle size on radiation resistance of iron-chromium alloys," *J. Nucl. Mater.*, vol. 469, pp. 72–81, 2016.
- [101] L. L. Hsiung, S. J. Tumey, D. T. Hoelzer, and M. J. Fluss, "Nano-oxide-dispersed ferritic steel for fusion energy systems," *MRS Adv.*, vol. 3, no. 31, pp. 1761–1769, Feb. 2018.

- [102] L. L. Hsiung, M. J. Fluss, S. J. Tumeay, B. W. Choi, Y. Serruys, and F. Willaime, "Formation mechanism and the role of nanoparticles in Fe-Cr ODS steels developed for radiation tolerance," *Phys. Rev. B*, vol. 82, p. 184103, 2010.
- [103] T. Stan, Y. Wu, J. Ciston, T. Yamamoto, and G. R. Odette, "Characterization of polyhedral nano-oxides and helium bubbles in an annealed nanostructured ferritic alloy," *Acta Mater.*, vol. 183, pp. 484–492, 2020.
- [104] K. Verbeken, "2 - Analysing hydrogen in metals: bulk thermal desorption spectroscopy (TDS) methods," in *Woodhead Publishing Series in Metals and Surface Engineering*, vol. 1, R. P. Gangloff and B. P. Somerday, Eds. Woodhead Publishing, 2012, pp. 27–55.
- [105] S. M. Myers, M. I. Baskes, H. K. Birnbaum, J. W. Corbett, G. G. DeLeo, S. K. Estreicher, E. E. Haller, P. Jena, N. M. Johnson, R. Kirchheim, S. J. Pearton, and M. J. Stavola, "Hydrogen interactions with defects in crystalline solids," *Rev. Mod. Phys.*, vol. 64, no. 2, pp. 559–617, Apr. 1992.
- [106] M. Koyama, M. Rohwerder, C. C. Tasan, A. Bashir, E. Akiyama, K. Takai, D. Raabe, and K. Tsuzaki, "Recent progress in microstructural hydrogen mapping in steels: quantification, kinetic analysis, and multi-scale characterisation," *Mater. Sci. Technol.*, vol. 33, no. 13, pp. 1481–1496, Sep. 2017.
- [107] O. Barrera, D. Bombac, Y. Chen, T. D. Daff, E. Galindo-Nava, P. Gong, D. Haley, R. Horton, I. Katzarov, J. R. Kermode, C. Liverani, M. Stopher, and F. Sweeney, "Understanding and mitigating hydrogen embrittlement of steels: a review of experimental, modelling and design progress from atomistic to continuum," *J. Mater. Sci.*, vol. 53, no. 9, pp. 6251–6290, 2018.
- [108] E. Malitckii, "Hydrogen and helium effects on reduced activation Fe-Cr ferritemartensite and ODS steel," 2015.
- [109] E. Malitckii, Y. Yagodzinskyy, M. Ganchenkova, S. Binyukova, H. Hänninen, R. Lindau, P. Vladimirov, A. Moeslang, "Comparative study of hydrogen uptake and diffusion in ODS steels," *Fusion Eng. Des.*, vol. 88, no. 9, pp. 2607–2610, 2013.
- [110] G.-W. Hong and J.-Y. Lee, "The measurement of the trap binding energy by the thermal analysis technique," *Scripta Metallurgica*, vol. 17, no. 7, pp. 823–826, 1983.
- [111] J.-Y. Lee and S. M. Lee, "Hydrogen trapping phenomena in metals with B.C.C. and F.C.C. crystals structures by the desorption thermal analysis technique," *Surf. Coatings Technol.*, vol. 28, no. 3, pp. 301–314, 1986.
- [112] S.-M. Lee and J.-Y. Lee, "The trapping and transport phenomena of hydrogen in nickel," *Metall. Trans. A*, vol. 17, no. 2, pp. 181–187, 1986.
- [113] J. L. Lee and J. Y. Lee, "Hydrogen trapping in AISI 4340 steel," *Met. Sci.*, vol. 17, no. 9, pp. 426–432, Sep. 1983.
- [114] W. Y. Choo and J. Y. Lee, "Thermal analysis of trapped hydrogen in pure iron," *Metall. Trans. A*, vol. 13, no. 1, pp. 135–140, 1982.
- [115] T. Michler and M. P. Balogh, "Hydrogen environment embrittlement of an ODS RAF steel – Role of irreversible hydrogen trap sites," *Int. J. Hydrogen Energy*, vol. 35, no. 18, pp. 9746–9754, 2010.
- [116] S. Frappart, A. Oudriss, X. Feaugas, J. Creus, J. Bouhattate, F. Thébault, L. Delattre, H. Marchebois, "Hydrogen trapping in martensitic steel investigated using electrochemical permeation and thermal desorption spectroscopy," *Scripta Materialia*, vol. 65, no. 10, pp. 859–862, 2011.
- [117] H. E. Kissinger, "Reaction kinetics in differential thermal analysis," *Anal. Chem.*, vol. 29, no. 11, pp. 1702–1706, Nov. 1957.

[118] F. G. Wei and K. Tsuzaki, “Quantitative analysis on hydrogen trapping of TiC particles in steel,” *Metall. Mater. Trans. A*, vol. 37, no. 2, pp. 331–353, 2006.

[119] <https://www.jeol.co.jp/en/words/emterms/>.

Chapter 3 Helium effects on the microstructure evolution of ODS-EUROFER steel

According to the state of the art presented in section 1 of this manuscript, ODS steels manifest high radiation tolerance in modern nuclear facilities and, in particular, low void swelling. However, the future fission (Generation IV) and fusion facilities are expected to accumulate much higher helium/hydrogen concentrations at much higher rate. For example, for DEMO fusion reactor blanket system, ~10 appm He/dpa and 40 appm H/dpa are expected [1]. Helium accumulation negatively influences radiation resistance of structural materials by decreasing the swelling incubation dose. Another complication for the performance of advanced nuclear facilities will be high operation temperature (ranging within 723-923 K), which can be risky in terms of high temperature helium embrittlement (HTIE). It is currently expected that nanosized oxide particles in ODS steel should be beneficial for decreasing both swelling and high temperature embrittlement, providing additional trapping sites for point defects and He at the oxide particle/matrix interfaces and thus preventing excessive helium accumulation at the grain boundaries [2–7].

However, ODS steels are very complex materials and it is not only oxide nanoparticles embedded in Fe-Cr matrix that compete for point defects and helium atoms. ODS-EUROFER, in particular, contains high densities of dislocations, grain boundaries and second phase precipitates ($M_{23}C_6$ type carbides), see section 2.1.1. It is not *a priori* obvious how efficient are Y_2O_3 nanoparticles as point defect/secondary gas trapping centers in comparison to the other structural defects. Neither is it guaranteed that strong helium accumulation on oxide nanoparticles would not lead to any undesirable effects in terms of ODS-steel radiation tolerance.

Thus the research described in this chapter aims to achieve two primary objectives:

- To investigate the efficiency of Y_2O_3 nanoparticles as helium trapping sites in ODS-EUROFER under implantation with either single He^+ ion beam or simultaneously with He^+ and heavy ions (with a strongly different He/dpa ratio).
- To demonstrate potential risks associated with using oxide nanoparticles in conditions of ODS steel operation in a high He/dpa ratio environment.

The chapter covers 4 topics:

- (1) Microstructure development in ODS-EUROFER steel during single-beam helium ion implantation.
- (2) Microstructure development in ODS-EUROFER steel during dual-beam irradiation with helium and gold ions.
- (3) The role of oxide nanoparticles in bubble-to-void transition.
- (4) Discussion.

Each section is further divided in subsections; in the beginning of each subsection the relevant methodology of analysis is described.

The chapter deals only with the TEM investigation results and their analysis. For the relevant ion implantation conditions see sections 2.2.3.3-2.2.3.3.

3.1 Microstructure development in ODS-EUROFER steel during single-beam He⁺ ion implantation

In order to clarify the relative contribution to helium accumulation and swelling from oxide nanoparticles as a part of the complex microstructure of ODS-EUROFER, the impact of all microstructural defects should be estimated quantitatively. This section covers experimental and statistical analysis results on microstructure development in ODS-EUROFER steel during single-beam helium implantation under different conditions. Transmission electron microscopy investigations in this section focus on parameters of helium filled cavities (bubbles) themselves (size and number density). Parameters of the helium bubble ensembles associated with different defect types (grain boundaries, dislocations, M₂₃C₆ carbides and Y₂O₃ particles) and bubbles located in the grain bulk interior will be quantitatively evaluated depending on the helium ion fluence, flux and temperature variation, including room temperature implantation regime followed by post-implantation annealing (PIA). Based on these data, swelling and the fraction of helium accumulated in visible bubbles will be calculated utilizing indirect approach for combining contributions of helium bubbles associated with different features of the microstructure, taking into account the geometry and volume density of these microstructural defects in the material volume. The results of statistical analysis of bubble population parameters and the estimates of swelling and helium fraction accumulated in the bubbles obtained for ODS-EUROFER steel under fixed implantation conditions will be compared with the oxide-free reference material, i.e. EUROFER 97 steel.

3.1.1 General description of microstructural evolution

Let us start with a general characterization of the microstructural evolution in ODS-EUROFER, which will serve as a background for the later sections of this chapter, where the results of statistical and comparative analysis will be presented.

Generally, two types of samples could be utilized for the investigation of microstructural evolution after helium ion implantation by means of TEM technique, namely planar view samples (see sections 2.1.1.2, 2.1.1.3 and 2.1.2.3) prepared either by Ar ion milling or backside electropolishing, or cross-sectional samples prepared by FIB lift-out technique or by Ar ion milling. According to Ref. [8], the best samples for investigation of bubbles population parameters are samples produced by electropolishing due to the absence of ion induced artifacts. In contrast, preparation of specimens by means of FIB or Ar polishing may well introduce near-surface voids and other surface features, which could be mistaken for bubbles/voids produced during ion implantation/irradiation. Thus planar view TEM samples prepared by backside electropolishing seem to be a reasonable choice for current investigations. However, planar view TEM samples can be utilized for the evaluation of the bubble parameters only when the size distribution of bubbles is uniform along the ion implantation range. Bubble number density in that case could be re-estimated using local thickness of TEM thin foil measured by EELS log-ratio approach. Therefore, the uniformity of bubble size distribution with respect to ion concentration profile has been checked before the utilization of planar view samples. For that purpose, cross-sectional FIB lift-out samples were used in the beginning of section 3.1.1.1.

Cavity images in TEM are often produced using the through-focal series method in a conventional TEM without scanning [9]. Under kinematical conditions, cavities look as white objects surrounded by dark Fresnel fringes in underfocus images, and as dark objects surrounded by bright fringes in overfocus images. Another common methods use STEM or bright-field (BF STEM) and annular dark-field (ADF or HAADF) [7,8] or Aberration-Corrected X-Ray Spectrum Imaging [7] to detect and measure cavity densities and sizes. For the main part of TEM data presented in this section, the BF TEM through-focal series method was used as the most straightforward one that allows rapid processing of large data arrays.

3.1.1.1 Distribution of bubbles vs. implantation depth

The general problem of ion implantation is the variation of bubble/cavity size along the ion/vacancy implantation profiles. If size variation turns out to be notable, the interpretation of planar view TEM images becomes quite challenging. Large bubbles/cavities corresponding to projection range depth (where the highest implanted ion concentration is achieved) can be incorrectly interpreted as e.g. bubbles attached to a microstructural defect, such as a grain boundary. In order to cope with the problem, incident ion energies and sample thickness should be appropriately selected.

Fig. 3.1 compares the results for two different implantations with 10 and 40 keV He⁺ ions. Bright field TEM (BF TEM) underfocused images are taken from the zone located near the relevant projected ranges, R_p , of He⁺ ions.

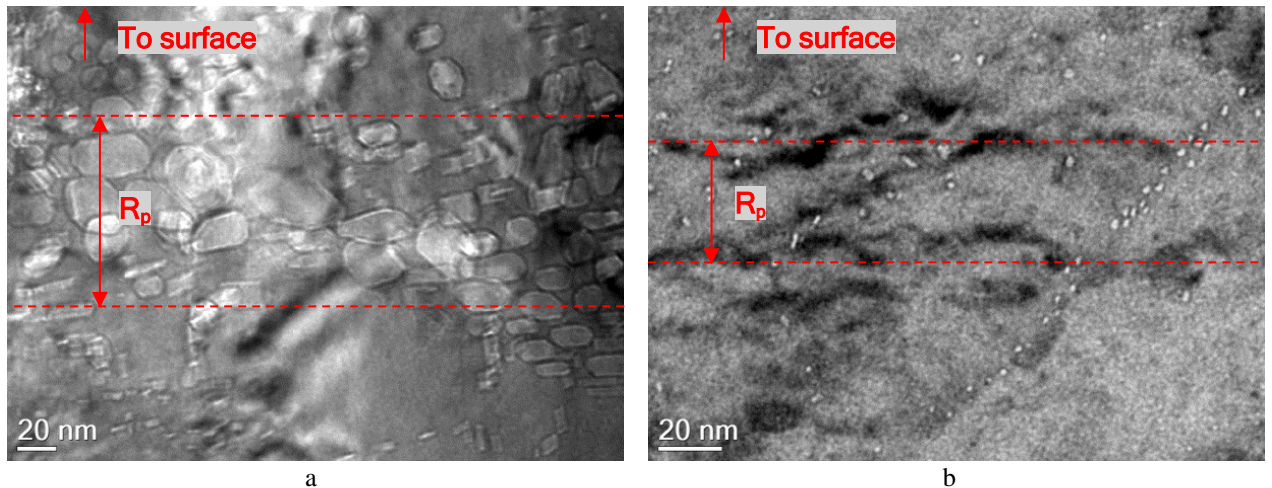


Fig. 3.1. FIB cross-section of ODS-EUROFER steel implanted with 40 keV He⁺ ions to the fluence of $5 \times 10^{16} \text{ cm}^{-2}$ at 923 K (a) and with 10 keV He⁺ ions to the fluence of $5 \times 10^{15} \text{ cm}^{-2}$ at 823 K (b). BF TEM imaging conditions: $\sim 1 \mu\text{m}$ underfocus. Dash lines show projection range zone (with the highest He content).

The implantation with 40 keV He⁺ ions results in non-uniform distribution in both bubble density and size as a function of depth from the implanted surface (Fig. 3.1(a)). The highest size of bubbles is observed in the zone corresponding to the projected range R_p of He⁺ ions. In contrast, the implantation with 10 keV helium ions results in a relatively uniform bubble distribution as a function of depth, leading to no preferential bubble growth at the He projection range (see Fig. 3.1(b)). Therefore, such ion energy is more suitable for the investigations of He effects expected in the bulk of ODS-EUROFER steel under neutron irradiation because the parameters of He bubble ensembles are sensitive to the microstructural defects distribution rather than the ion/vacancy variations along the implantation profile. Minor heterogeneity of bubble density with respect to ion implantation profile could be simply re-evaluated for any implantation depth by means of precise control of local sample thickness by EELS log-ratio technique. For this reason, the He⁺ ion energy was selected equal to 10 keV for all implantations in this study.

In order to confirm the relative uniformity of bubble distribution in the 10 keV He⁺ implanted samples, a more detailed analysis was performed using cross-sectional FIB samples. TEM micrographs of ODS-EUROFER steel after ion implantation with 10 keV He⁺ beam obtained under different magnifications are shown in Fig. 3.2(a-c) in a through-focus pair of BF TEM images acquired in $-1 \mu\text{m}$ underfocus and $+1 \mu\text{m}$ overfocus conditions.

The ensembles of He bubbles are clearly visible by the characteristic change in Fresnel contrast from the overfocus to underfocus conditions. He bubbles appear at depths from 5-7 to 100 nm from implanted surface. A narrow denuded zone with the thickness of $\sim 5 \text{ nm}$ was observed in near surface region. Also, the formation of a $\sim 2-5 \text{ nm}$ thick surface oxide layer was detected. The maximum depth of He bubble band correlates well with helium ion implanted and defect production profiles predicted by

SRIM code based calculation (see section 2.2.3.2). The He bubbles distribution in the implanted volume is non-uniform; many bubbles clearly decorate microstructural defects - grain boundaries, dislocations and precipitates.

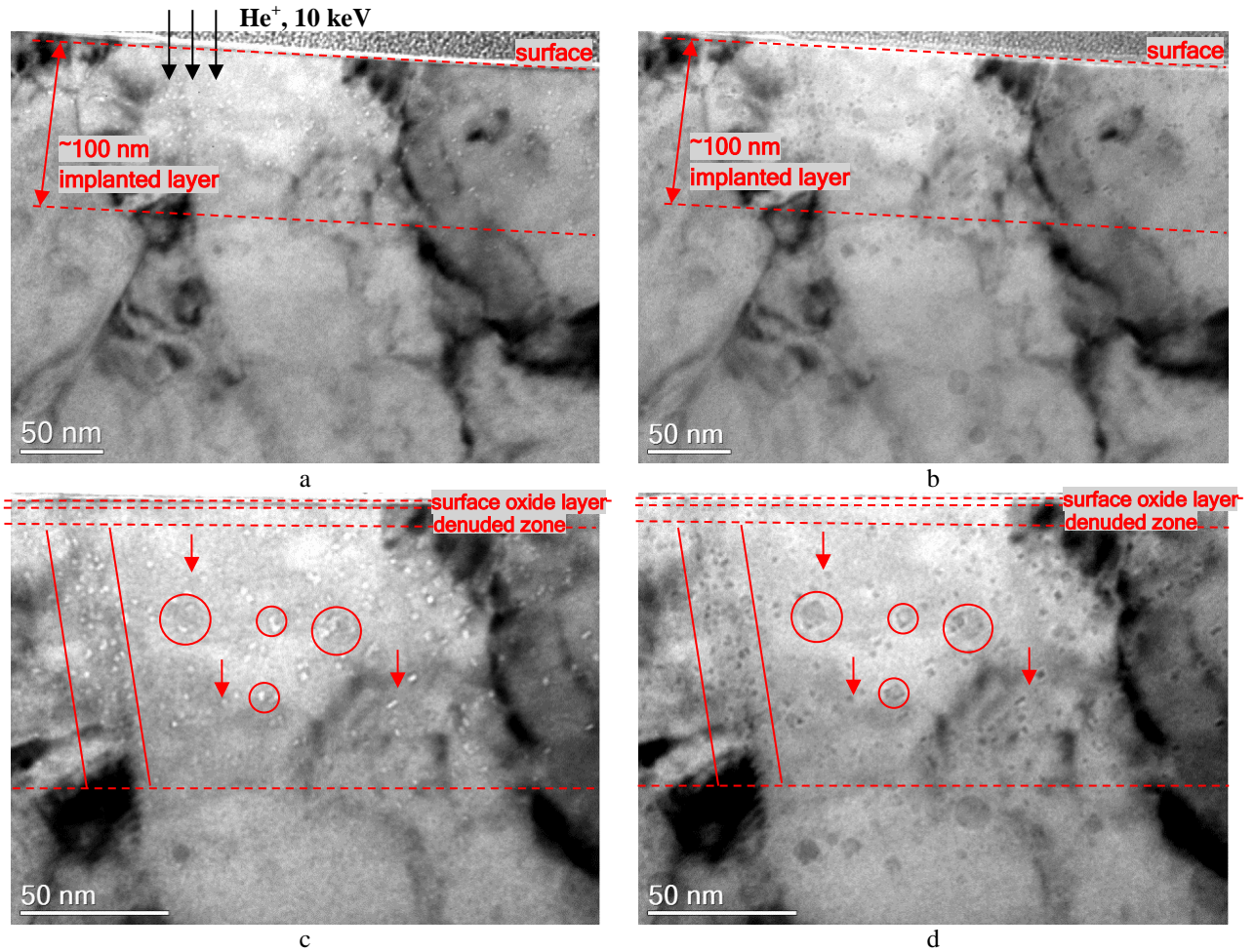


Fig. 3.2. FIB cross-section of ODS-EUROFER steel implanted with 10 keV He⁺ ions to the fluence of $5 \times 10^{15} \text{ cm}^{-2}$ at 823 K with at the flux of $5 \times 10^{11} \text{ cm}^{-2} \text{ s}^{-1}$. BF TEM imaging conditions: (a,c) $\sim 1 \mu\text{m}$ underfocus and (b,d) $\sim 1 \mu\text{m}$ overfocus. Dash lines show limit the described zones, solid lines mark structural defects decorated with He bubbles.

In Fig. 3.3, the results of statistical analysis of He bubble parameters, i.e. number density and mean size, are presented as a function of the distance from the sample surface.

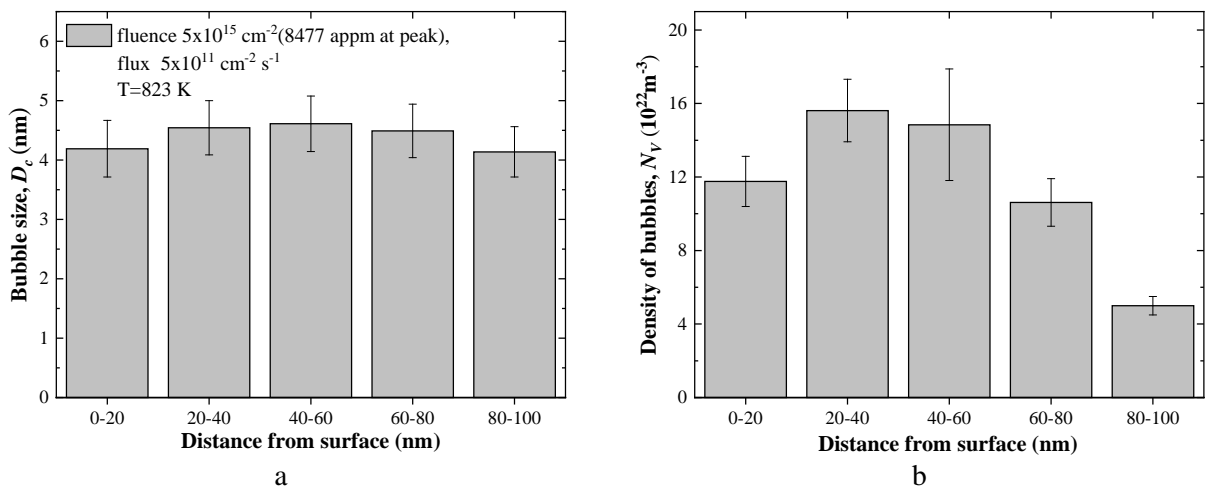


Fig. 3.3. He bubble size (a) and density (b) distribution with respect to distance from implanted surface in ODS-EUROFER steel implanted with 10 keV He⁺ ions at T=823 K with the flux of $5 \times 10^{11} \text{ cm}^{-2} \text{ s}^{-1}$ to the fluence of $5 \times 10^{15} \text{ cm}^{-2}$.

The mean bubble size is found to be practically insensitive to the observation depth and equal to $\sim 4.4 \pm 0.3$ nm, showing no correlation to the helium implantation and vacancy production profiles along the whole ion implanted range. In contrast, the bubble number density follows ion/vacancy generation profile predicted by SRIM. The highest bubble density of $(1.6 \pm 0.2) \times 10^{23} \text{ m}^{-3}$ appeared at the depths of 20-40 nm from the implanted surface. The depth uniformity of bubble size distribution justifies the use of planar view observations in order to estimate the spatial distribution of bubbles using the whole surface of implanted sample.

Fig. 3.4 shows typical through-focus pair of BF TEM images obtained from planar view sample of ODS-EUROFER implanted in the same regime as the FIB cross-sectional sample in Fig. 3.1(b) and Fig. 3.2.

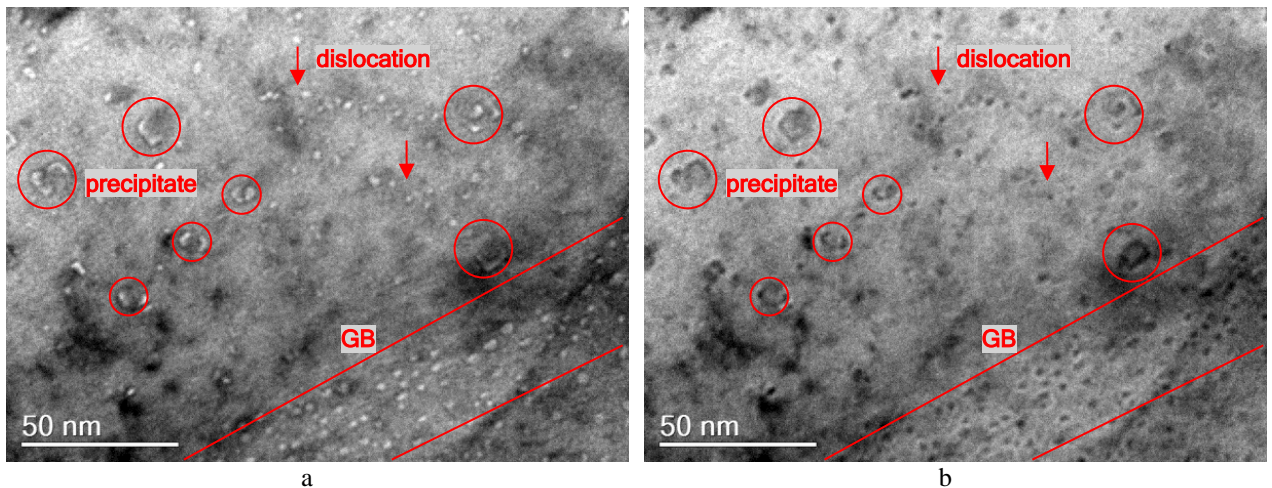


Fig. 3.4. Planar view of the sample of ODS-EUROFER steel implanted with 10 keV He^+ ions to the fluence of $5 \times 10^{15} \text{ cm}^{-2}$ at 823 K with at the flux of $5 \times 10^{15} \text{ cm}^{-2} \text{ s}^{-1}$. Sample thickness is ~ 40 nm. BF TEM imaging conditions are: (a) $\sim 1 \mu\text{m}$ underfocus and (b) $\sim 1 \mu\text{m}$ overfocus.

The general trend in bubble spatial distribution is similar to that visible on the cross-sectional samples; the bubbles clearly decorate grain boundaries, dislocations and precipitates. The overall number of bubbles visible in a single TEM image is, however, notably higher because now there are no restrictions by the narrow thickness (~ 100 nm) of the ion implantation zone. Also, the quality of images is better due to the absence of a thin amorphous layer which is always present at the surface of FIB prepared samples.

The results of this section lead us to the conclusion that 10 keV ion implantation is a suitable regime for the observation of the evolution of He bubbles. The low sensitivity of the evolved microstructure to the depth variation allows us to reliably trace correlations between helium bubbles and various microstructural defects, such as grain boundaries, dislocations and precipitates, in planar view using different observation zones. Correspondingly, the planar view TEM samples (prepared by one-side jet electrochemical polishing) were selected as the most promising approach for the estimation of parameters of bubble populations associated with different microstructural components because:

- FIB preparation artefacts are absent;
- relatively thin samples without surface amorphization can be used, which improves the measurement accuracy of bubble sizes;
- relatively large observation area is available, which improves statistics on bubble population parameters.

Correspondingly, planar view samples were primarily used in this study for the measurements of He bubble size and density, while cross-sectional samples were used mostly for data verification when required. Prior to TEM analysis, the surface oxide layer and ~ 5 -10 nm wide surface zone below it, both affected by the surface effects, were removed by low energy ion polishing. Finally, in order to obtain

relatively large statistics with the high accuracy of bubble size determination, the area from 10 to 40 nm from surface was chosen for analysis.

3.1.1.2 Distribution of bubbles over defect types

According to the results presented in section 2.1.1.1 of this manuscript, four major types of microstructural defects present in ODS-EUROFER steel may act as trapping sites for He atoms and serve as nucleation sites for bubble formation. In this section, qualitative analysis of typical behavior of He bubbles ensembles is performed with respect to high- and low-angle grain boundaries, dislocations, $M_{23}C_6$ and Y_2O_3 precipitates. All TEM data described in this section are obtained in the same experimental conditions, namely 10 keV He^+ implantation to the fluence of $5 \times 10^{15} \text{ cm}^{-2}$ with a flux of $5 \times 10^{11} \text{ cm}^{-2} \text{ s}^{-1}$ at 823 K.

Fig. 3.5 shows typical BF TEM trough-focused pairs of images for areas containing dislocations and either a high-angle grain boundary (see Fig. 3.5(a,b)), or a low-angle grain boundary (see Fig. 3.5(c,d)).

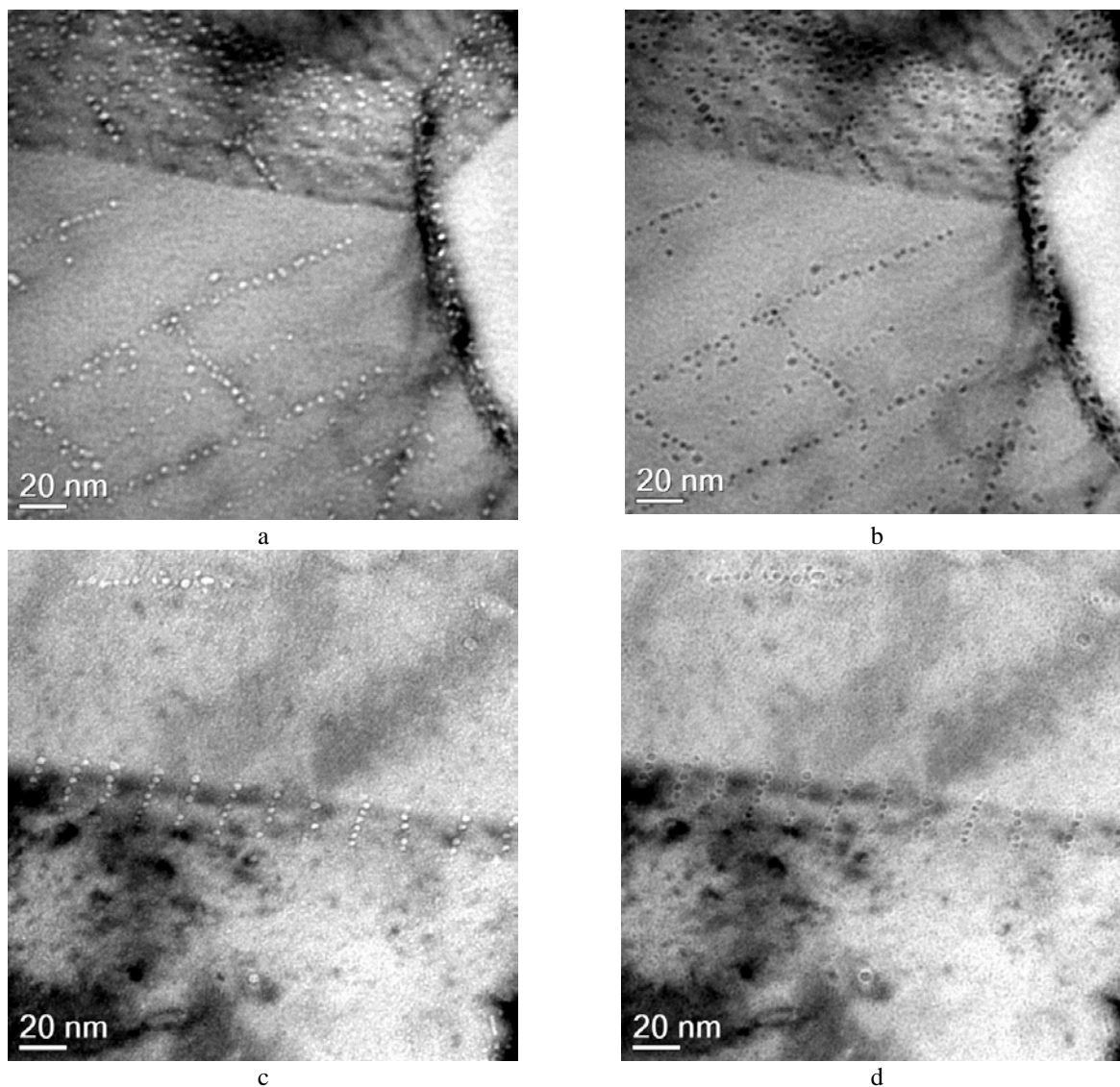


Fig. 3.5. Typical trough-focus images of high-angle grain boundaries and dislocations (a-b) and low-angle grain boundaries and dislocations (c-d) in ODS-EUROFER steel implanted with 10 keV He^+ ions to the fluence of $5 \times 10^{15} \text{ cm}^{-2}$ at 823 K with the flux of $5 \times 10^{11} \text{ cm}^{-2} \text{ s}^{-1}$. BF TEM imaging conditions are: (a,c) $\sim 0.5 \mu\text{m}$ underfocus and (b,d) $\sim 0.5 \mu\text{m}$ overfocus.

It is clearly seen that helium efficiently accumulates in small size He bubbles with high density at both types of grain boundaries and at dislocations. Low-angle grain boundaries in ODS-EUROFER (see Fig. 3.5(c,d)) appear to be dislocation walls. Hence, for bubble number density and swelling estimations, only high-angle grain boundaries were considered. Since low-angle grain boundaries are decorated by the bubbles similar to dislocations, they are not treated explicitly during the subsequent statistical analysis because the density of dislocations contained in low-angle grain boundaries is two orders of magnitude lower than dislocation density inside the grain bulk (see section 2.1.1.1). The typical sizes of He bubbles associated with both types of grain boundaries are similar to sizes of bubbles at dislocations and within the defect-free grain space. In contrast to austenitic steels, where helium bubbles at grain boundaries at the studied temperature tend to coalesce and promote high-temperature helium embrittlement [10], we have noticed no bubble coalescence at the grain boundaries ODS-EUROFER. Preliminary TEM examinations show that in the discussed regime the number density of bubbles in the defect-free grain space is low (see for example Fig. 3.5). However this result should be confirmed with quantitative analysis which will consider local thickness of thin foil.

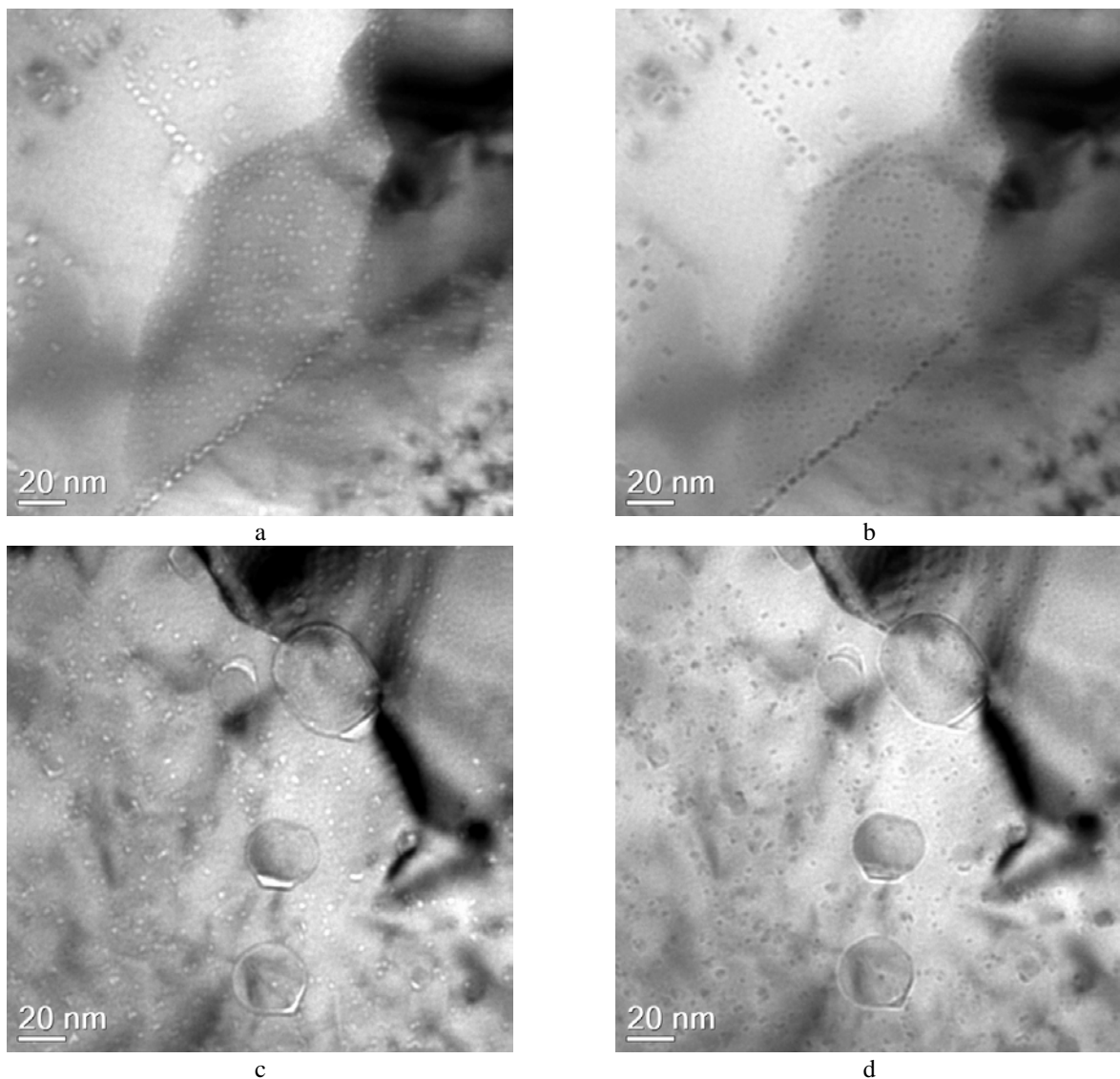


Fig. 3.6. Typical trough-focus images of $M_{23}C_6$ carbide precipitates (a-b) and Y_2O_3 nanosized precipitates (c-d) in ODS-EUROFER steel implanted with 10 keV He^+ ions to the fluence of $5 \times 10^{15} \text{ cm}^{-2}$ at 823 K with the flux of $5 \times 10^{11} \text{ cm}^{-2} \text{ s}^{-1}$. BF TEM imaging conditions: (a,c) $\sim 0.5 \mu\text{m}$ underfocus and (b,d) $\sim 0.5 \mu\text{m}$ overfocus.

Typical BF TEM trough-focus micrographs of a globular $M_{23}C_6$ carbide precipitate ($\sim 100 \text{ nm}$) at the grain boundary and several Y_2O_3 nano-oxide precipitates ($\sim 7\text{-}30 \text{ nm}$) in defect-free grain bulk of

ODS-EUROFER sample are shown in Figs. 3.6(a,b) and 3.6(c,d), respectively. As can be seen in Fig. 3.6(a-b), He is collected at $M_{23}C_6$ precipitate/matrix interface in an array of relatively small equiaxial (spherical or faceted) He bubbles (slightly smaller than those in the surrounding matrix). In contrast, Y_2O_3 nanoparticles host in the same implantation conditions single (rarely two) relatively large bubbles with notably larger size than the typical size of bubbles in the matrix (see Fig. 3.6(c,d)). He bubbles attached to Y_2O_3 particles demonstrate specific lens shape.

Clearly, helium in ODS-EUROFER steel shows notably different behavior at the yttria/matrix and carbide/matrix interfaces. The difference in helium behavior at the investigated interfaces indicates different mechanisms of formation and growth of helium bubbles.

All Y_2O_3 nanoparticles observed, regardless of the size, hosted He bubbles. This is similar to the results of Ref. [11], where practically all oxide nanoparticles were covered with He bubbles. It should be kept in mind, however, that the oxide-bubble association is not universal. For example, in very different implantation conditions the share of particles covered with bubbles could be as low as 30-40% [12] or there could be no particles covered with bubbles at all [13].

An interesting observation is the definite correlation of bubble sizes with the sizes of host oxide particles. With the increase of the nanoparticle size, the size of attached bubble also increases. This is illustrated in Fig. 3.7, showing through-focus BF TEM images with bubbles on different size Y_2O_3 nanoparticles in helium implanted ODS-EUROFER steel.

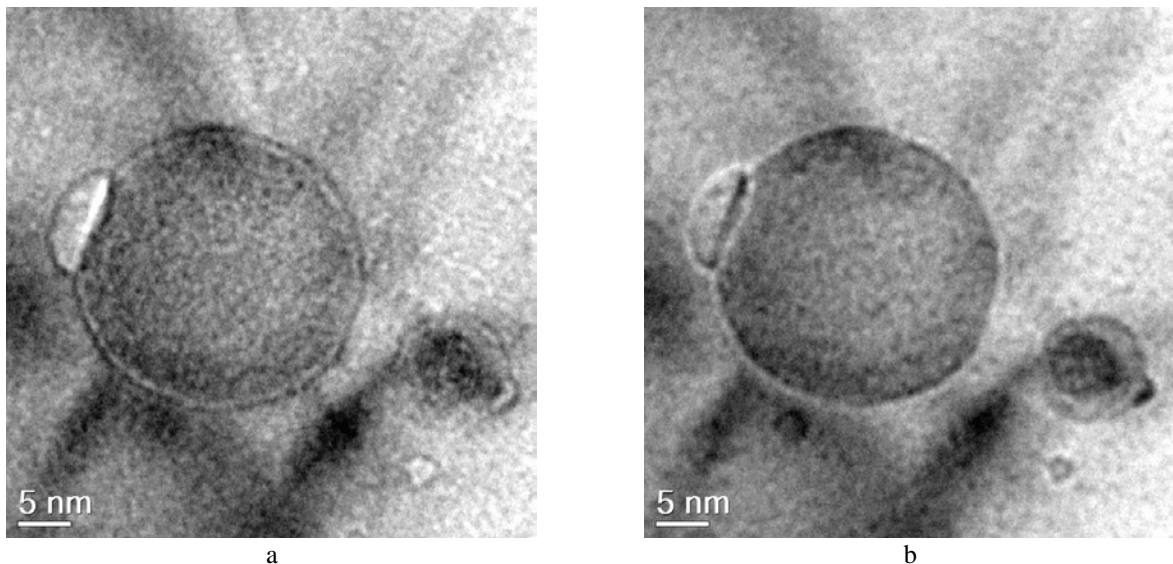


Fig. 3.7. Typical through-focus images of Y_2O_3 nano-oxide precipitates in ODS-EUROFER steel implanted with 10 keV He^+ ions to the fluence of $5 \times 10^{15} \text{ cm}^{-2}$ at 823 K with a flux of $5 \times 10^{11} \text{ cm}^{-2} \text{ s}^{-1}$. BF TEM imaging conditions: (a) $\sim 0.4 \mu\text{m}$ underfocus and (b) $\sim 0.4 \mu\text{m}$ overfocus.

3.1.2 The relative importance of different defect microstructure components for helium accumulation depending on ion implantation conditions (temperature, ion flux, fluence)

As mentioned earlier, the estimation of material swelling based on TEM data requires the knowledge of bubble volumes and number densities (i.e. number of bubbles per unit volume). These parameters for the case of single He^+ implantation of ODS-EUROFER depend on:

- the helium implantation parameters used, and
- the densities of microstructural defects that promote He bubble formation.

Thus to elucidate the He bubble nucleation and growth kinetics, He bubble distributions at all microstructural features, as well as in the bulk of grains, were characterized as a function of helium implantation fluence, flux and temperature.

3.1.2.1 Methodology of statistical analysis of bubble populations visible in TEM micrographs

The preliminary analysis of TEM images has revealed remarkable variability of He bubble size and number density distributions in different TEM observation zones of individual samples. Therefore, in order to acquire representative statistics, quantitative analysis of bubble array parameters for each implantation regime was performed using 5 different zones with at least 100 bubbles and 2 individual grains inside each zone. Bubble sizes and number densities were calculated separately for the defect-free internal grain space and for all microstructural defects hosting He bubbles, including grain boundaries, dislocations, $M_{23}C_6$ carbides and Y_2O_3 nano-oxides.

Having in mind that bubbles visible in TEM are often non-spherical (e.g. elongated and/or faceted), it is necessary first of all to define what is meant below by bubble ‘size’. In this study, we treat the size of an individual bubble in terms of its effective diameter, estimated as:

$$D_c^k = \frac{D_{\max}^k + D_{\min}^k}{2},$$

where D_{\max}^k and D_{\min}^k are the maximum and the minimum Feret diameters obtained by approximating a real bubble with an inscribed ellipse centered on the center of the first Fresnel fringe on underfocused image, k indicates the bubble association type (e.g. $k = V$ for bubbles in the defect-free grain interior and $k = D, GB, C$ and P for bubbles on dislocations (D), grain boundaries (GB), carbide (C) and oxide particles (P), respectively). The mean bubble diameter associated with individual defect type additionally averaged over all 5 investigated zones is denoted as $\langle D_c^k \rangle$.

The only exception in this approach was the determination of parameters for bubbles associated with carbide particles. Inhomogeneous distribution and low density of large $M_{23}C_6$ type carbides make statistical analysis of bubble population associated with this defect type very complicated. Often electron transparent zones on TEM thin foil do not contain carbides at all or a zone containing carbide particle(s) is not suitable for the determination of bubble parameters associated with other defect types. Therefore, where possible, only one zone under each implantation regime was used for the estimation of bubble parameters on carbides.

As shown in section 3.1.1.2, D_c^p of He bubbles attached to Y_2O_3 nanoparticles correlate with the sizes of nanoparticles, D_p . Thus, D_c^p for each implantation regime was obtained through the following procedure. First, the experimental dependence $D_c^p(D_p)$ was derived and fitted with a power law $D_c^p(D_p) = a \cdot D_p^b$, where a and b were fitting parameters. Power b is kept constant for varying fluence, flux and temperature conditions assuming the same bubble growth law. In the subsequent section 3.2, parameter b is treated as a variable. The resulting $\langle D_c^p \rangle$ value was determined as the size of the bubble, corresponding to the mean size of Y_2O_3 nanoparticles (that is, $D_p = 12$ nm, see section 2.1.1.1).

The procedure for the determination of bubble number densities is somewhat more sophisticated. Indeed, in the standard approach of the bubble number density determination based on TEM micrographs, the cavity number density is normalized either per unit image area, or, where the local sample thickness is known, per unit volume. Such an approach is directly applicable to bubbles in the bulk of the sample (that is, those not associated with any microstructural defect), with the volume number density determined as:

$$N_c^V = \frac{n}{V}, (\text{m}^{-3}),$$

where n is the counted bubble number in the observation region of the TEM thin foil and $V = S_a t$ is its volume, while S_a and t are its area and thickness.

However, the application of this approach to bubbles on structural defects meets problems. When bubbles are associated with extended defects, such as dislocations, grain boundaries and large precipitates that locally collect multiple bubbles, the standard approach may fail to give a reliable measure of bubble relative contribution to the bubble volume density. Indeed, in all ion implantation conditions applied in this study the bubbles are mostly quite small and their observation demands the use of high TEM magnifications so that the observation area is relatively small. The parts of extended defects visible in different TEM images can strongly vary from image to image and are usually not representative of the average volume density of extended defects in the investigated material.

In this situation it was considered more reasonable to introduce for the bubbles associated with extended microstructural defects the concept of ‘specific’ number density N_c^k (k has the same meaning as for the D_c^k), which is normalized per characteristic unit of corresponding microstructural defect, e.g. per unit dislocation length or per unit surface of a two-dimensional defect. Thus defined specific number densities of bubbles on various microstructural defects allow direct comparison for bubbles associated with particular defects on different TEM micrographs, while the averages over different zones for the same implantation regime, $\langle N_c^k \rangle$, make it possible to follow the bubble evolution depending on the variations in implantation regimes. In turn, the volume number densities of bubbles, $\langle N_v^k (\text{m}^{-3}) \rangle$, required e.g. for the estimation of bubble contributions to swelling, can be determined as a product of the ‘specific’ number densities by the average volumetric densities of the relevant extended defects.

In this study, the local bubble number densities N_c^k for different extended microstructural defects are determined as follows:

- for grain boundaries:

$$N_c^{GB} = \frac{n}{l_{GB} \sqrt{h_{GB}^2 + t^2}}, (\text{m}^{-2}),$$

where n is the counted bubble number at a grain boundary, l_{GB} and h_{GB} are the visible length and width of the grain boundary, t is the local thickness of TEM thin foil measured by EELS log ratio method.

- for dislocations:

$$N_c^D = \frac{n}{\sum_i l_d^i}, (\text{m}^{-1}),$$

where n is the counted bubble number at all visible dislocations in a given area and $\sum_i l_d^i$ - the total length of all dislocations in the same area.

- for M_{23}C_6 carbide precipitates:

$$N_c^c = \frac{n}{S_{carbide}}, (\text{m}^{-2}),$$

where n is the counted bubble number at carbide/matrix interface and $S_{carbide}$ - the surface area of globular shaped carbide in the counting region.

Finally, the number density of bubbles on Y_2O_3 nanoparticles is predetermined by the observation that typically each oxide particle hosts only one He bubble. Consequently, the volume number density of bubbles on oxide particles can be set equal to that of oxide particles themselves:

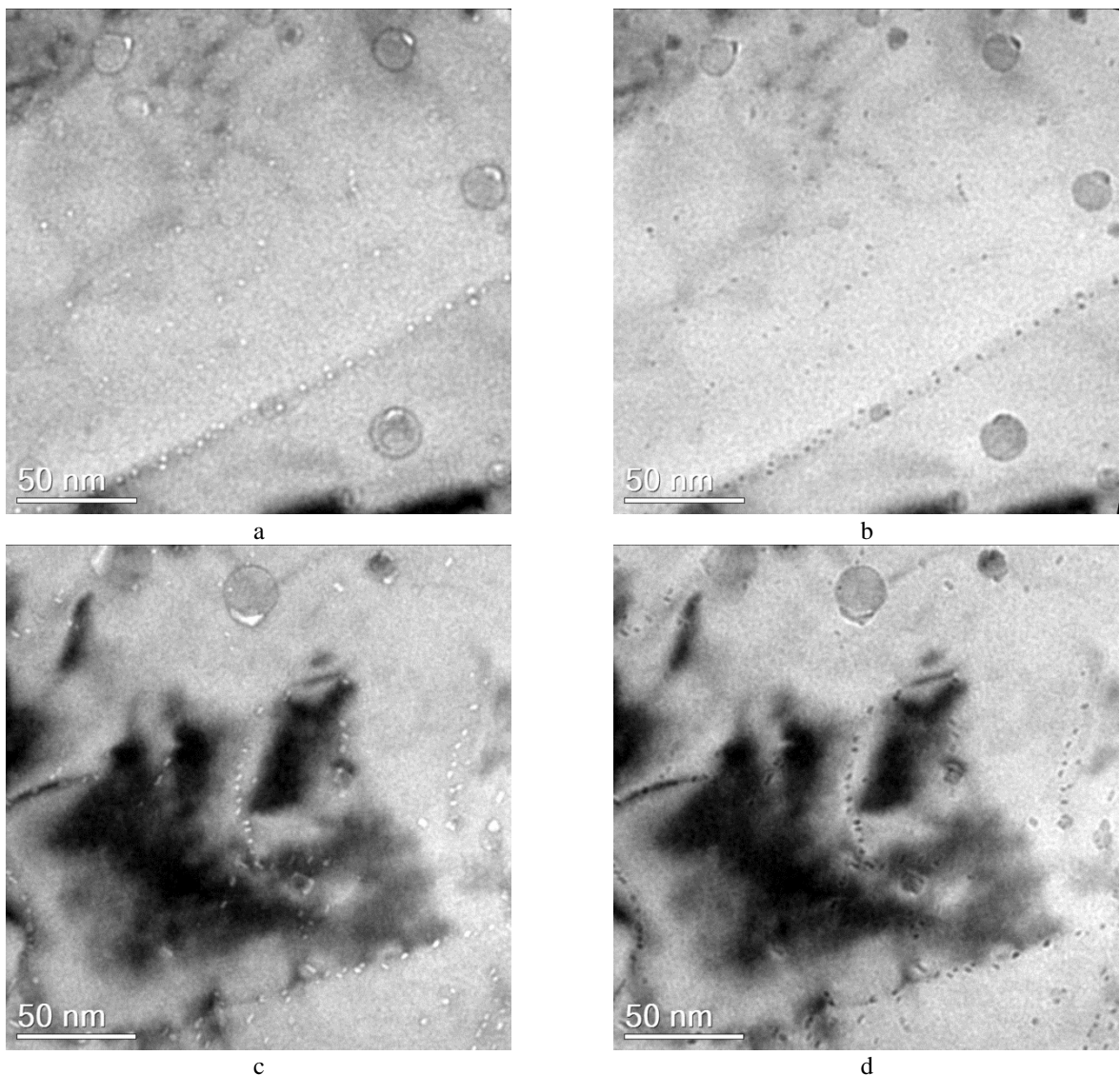
$$N_c^p = N_{\text{Y}_2\text{O}_3}, (\text{m}^{-3}),$$

where $N_{\text{Y}_2\text{O}_3}$ is the nanoparticles number density (see section 2.1.1.1).

3.1.2.2 Variation of helium bubble parameters as a function of He⁺ ion implantation fluence

In order to systematically study the effect of various experimental parameters on the kinetics of bubble ensembles in ODS-EUROFER, several series of experiments were performed, where only one of the implantation parameters was changed with the other being fixed. This section discusses the bubble evolution in samples implanted with He⁺ ions at 823 K to fluencies $1 \times 10^{15} \text{ cm}^{-2}$, $5 \times 10^{15} \text{ cm}^{-2}$, and $1 \times 10^{16} \text{ cm}^{-2}$ at the constant flux of $5 \times 10^{11} \text{ cm}^{-2} \text{ s}^{-1}$. The accumulated He concentrations at these fluencies were, respectively, 1.25×10^3 , 6.3×10^3 and 1.25×10^3 appm in the region of interest (see section 2.2.3.2).

Typical BF TEM through-focus images of ODS-EUROFER implanted at 823 K to different fluences are shown in Fig. 3.8. For all three fluences, the partitioning of implanted He between different microstructural defects and the bulk is observed: He bubbles decorate grain boundaries, dislocations and precipitates. As can be seen, with the increase of helium implantation fluence the size of the bubbles also increases.



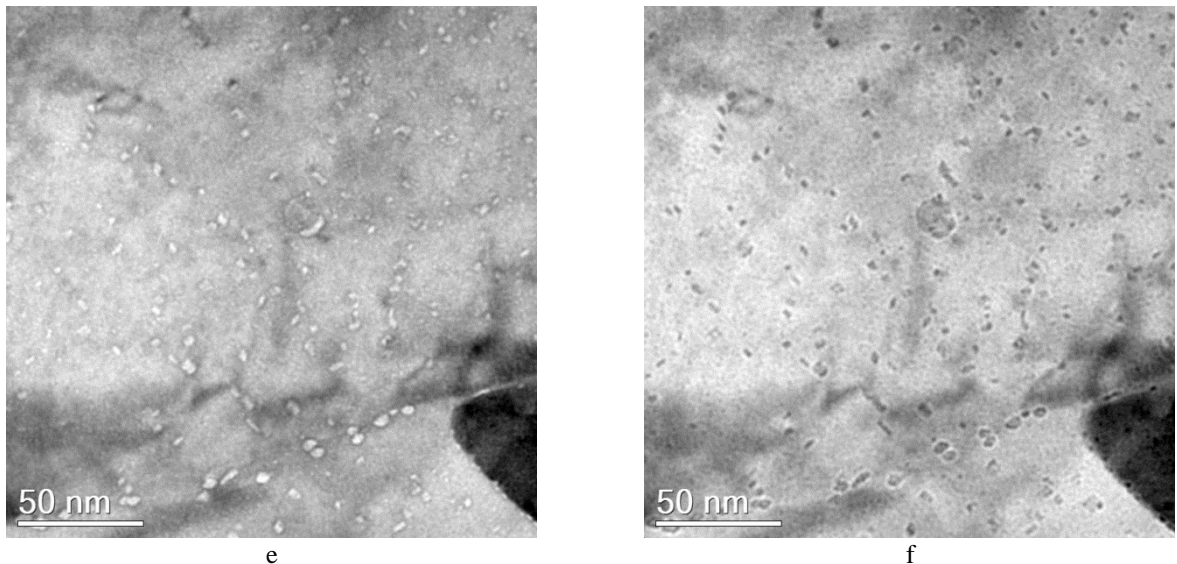


Fig. 3.8. Microstructure of ODS-EUROFER steel implanted with 10 keV He^+ ions at 823 K with flux of the $5 \times 10^{11} \text{ cm}^{-2} \text{ s}^{-1}$ to different fluencies: (a,b) $1 \times 10^{15} \text{ cm}^{-2}$; (c,d) $5 \times 10^{15} \text{ cm}^{-2}$; (e,f) $1 \times 10^{16} \text{ cm}^{-2}$. BF TEM imaging conditions: (a,c,e) $\sim 1 \mu\text{m}$ underfocus and (b,d,f) $\sim 1 \mu\text{m}$ overfocus.

The shape of He bubbles changes from more rounded at the lowest fluence to faceted at higher fluencies, which is common for both voids and He bubbles in *bcc* Fe and FeCr alloys [14,15]. Typical trough-focus images of faceted cavities obtained at the highest fluence of $1 \times 10^{16} \text{ cm}^{-2}$ are shown in Fig. 3.9.

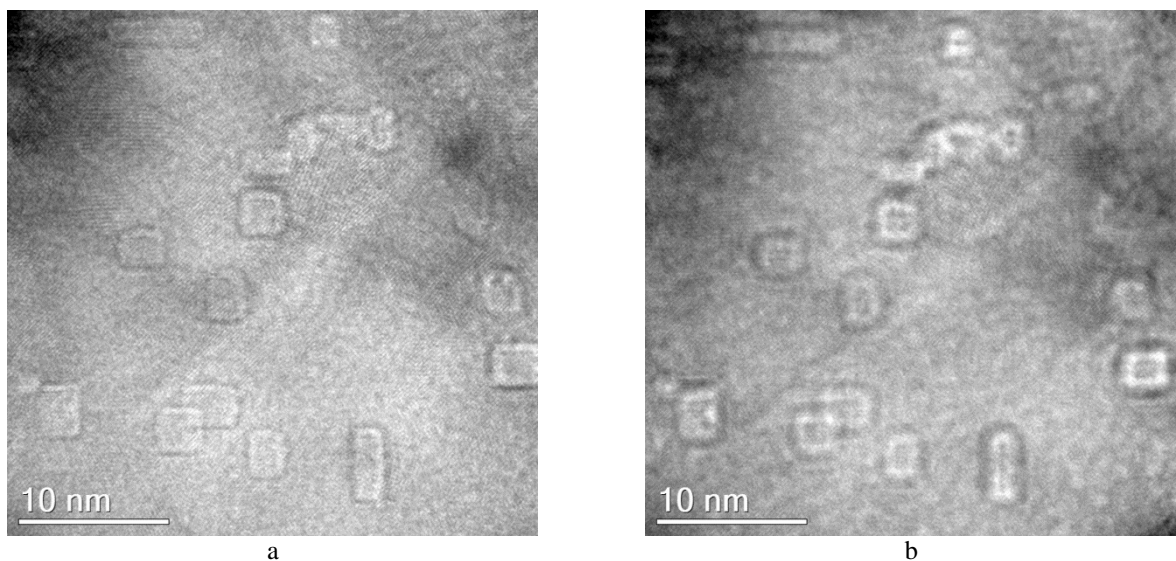


Fig. 3.9. He bubbles inside grain bulk interior of ODS-EUROFER steel implanted with 10 keV He^+ ions at 823 K with the flux of $5 \times 10^{11} \text{ cm}^{-2} \text{ s}^{-1}$ to the fluence of $1 \times 10^{16} \text{ cm}^{-2}$; BF TEM imaging conditions are: (a) $\sim 0.4 \mu\text{m}$ underfocus; (b) $\sim 0.4 \mu\text{m}$ overfocus.

A characteristic feature of bubble microstructure at all three fluencies is the remarkably larger size of bubbles associated with oxide particles as compared to bubbles associated with other microstructural defects or bubbles in the bulk. At the highest fluence, the bubbles attached to oxide particles often reach sizes similar to or even larger than the size of the host particle itself (see Fig. 3.10(a)). As a result, the particles smaller than approximately 10 nm are largely enveloped by the bubbles, leaving only minor neck connecting particle to the matrix. A similar effect was found under the $1 \times 10^{15} \text{ cm}^{-2}$ and $5 \times 10^{15} \text{ cm}^{-2}$ implantation regimes as well, but the fraction of particles swallowed by bubbles was relatively small.

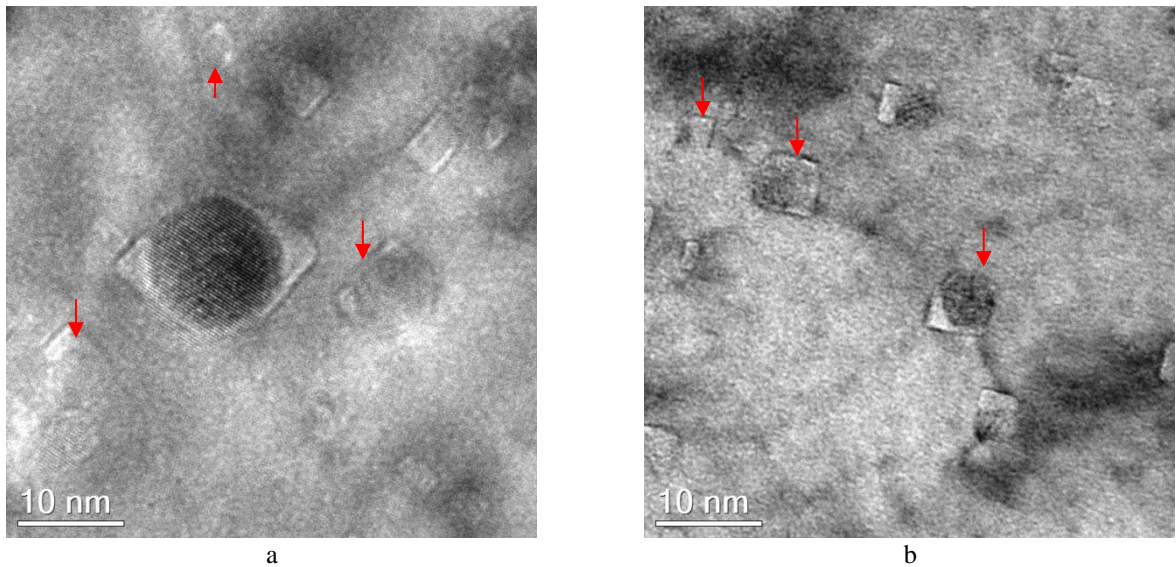


Fig. 3.10. Association of He bubbles with Y_2O_3 nanoparticles of different size in ODS-EUROFER steel implanted with 10 keV He^+ ions at 823 K with the flux of $5 \times 10^{11} \text{ cm}^{-2} \text{ s}^{-1}$ to the fluence of $1 \times 10^{16} \text{ cm}^{-2}$. Oxide particles completely enveloped by He bubbles are marked by arrows. BF TEM imaging conditions: $\sim 0.4 \mu\text{m}$ underfocus.

Now let us describe the variation of bubble parameters with the increase of fluence in quantitative terms. Analysis starts with the bubbles associated with oxide nanoparticles, which require a special treatment, as explained in section 3.1.2.1. In order to determine the average size of bubbles associated with yttria nanoparticles, $\langle D_c^p \rangle$, we need to know the relation between the bubble size and the size of the host particle. The observed bubble sizes as a function of the host particle sizes are plotted in Fig. 3.11. For all three fluencies one can see clear trends in the dependence $D_c^p(D_p)$ that can be conveniently described by power trend lines. The best fit trend lines using the power law $D_c^p(D_p) = a \cdot D_p^b$ with the fitting parameters summarized in Table 3.1 are also shown in Fig. 3.11. Using the derived trend lines, we can determine the average effective diameter of bubbles on oxide particles, as described in section 3.1.2.1; these values are given in the last column of Table 3.1.

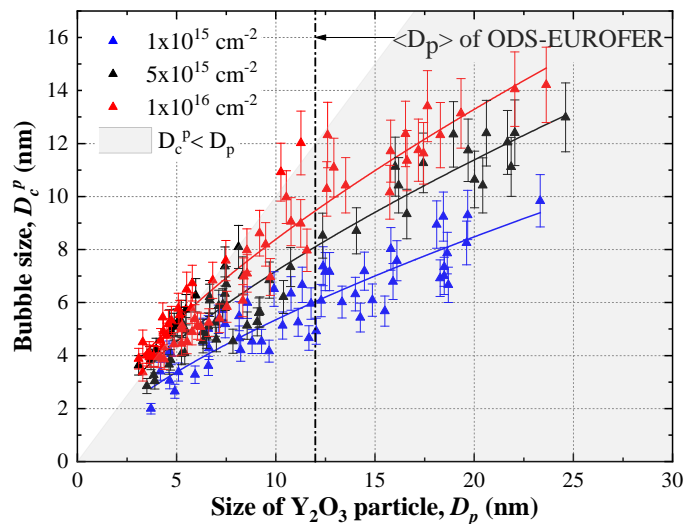


Fig. 3.11. Bubble size on yttria nanoparticles vs. particle size for the ODS-EUROFER steel implanted with 10 keV He^+ ions at 823 K with the flux of $5 \times 10^{11} \text{ cm}^{-2} \text{ s}^{-1}$ to the fluences of 1×10^{15} ; 5×10^{15} ; and $1 \times 10^{16} \text{ cm}^{-2}$. Solid lines are best fits for each fluence. The grey marked area corresponds to the bubbles with the size smaller than that of the particle. Error bars are 10% uncertainties associated with the size of the first Fresnel fringe on bubble observed in underfocused images [9,16].

Table 3.1. Parameters for the power law fitting used in Fig. 3.11.

He ion implantation regime	b	a	$\langle D_c^p \rangle$, nm
$1 \times 10^{15} \text{ cm}^{-2}$ (1253 appm)	0.66	1.16	6.04
$5 \times 10^{15} \text{ cm}^{-2}$ (6267 appm)	0.66	1.56	8.11
$1 \times 10^{16} \text{ cm}^{-2}$ (12533 appm)	0.66	1.82	9.46

As can be seen, the average size $\langle D_c^p \rangle$ for bubbles on oxide particles increases from ~6 nm to ~9.5 nm with the increase of He^+ ion fluence from $1 \times 10^{15} \text{ cm}^{-2}$ to $1 \times 10^{16} \text{ cm}^{-2}$. At the same time, within the fixed fluence, $\langle D_c^p \rangle$ increases as nanoparticle size increases, for instance from 4 nm to 14 nm with nanoparticle size increase from 3 to 23 nm at the fluence of $1 \times 10^{16} \text{ cm}^{-2}$. It can be concluded that the average size of bubbles associated with yttria nanoparticles only weakly depends on the He fluence in the studied range and is mostly affected by the size of the host nanoparticle. It can be also noticed that at the smallest fluence all bubbles are smaller than their host particles, while already at the intermediate fluence one can notice some particles with the sizes close to 5 nm that host bubbles of comparable or larger size (falling in the white background zone in Fig. 3.11). At the highest fluence value of $1 \times 10^{16} \text{ cm}^{-2}$ the relation $D_c^p \geq D_p$ is commonly met for the smaller (less than, roughly, 7 nm) particles, but sometimes the bubbles envelope particles as large as 12 nm in diameter.

Statistical analysis of bubble parameters for the bubbles in the bulk and bubbles associated with extended microstructural defects follows the approach described in section 3.1.2.1. The results for different fluences are given in Table 3.2. The average effective diameter and the specific bubble number densities N_c^k for bubbles located in the bulk and associated with grain boundaries, dislocations, carbide and oxide precipitates are given for 10 grains (5 TEM observation zones) for each fluence. The uncertainty of N_c^k is determined as a superposition of the standard error and the error corresponding to local thickness measurements of TEM foil by EELS log-ratio technique (10%) [17,18]. The uncertainties provided for D_c^k are obtained combining the standard error and the error associated with bubble effective diameter measurement from the center of the first Fresnel fringe on underfocused BF TEM image [9,16].

As can be concluded from the data in Table 3.2, at each particular fluence there is little difference in size between bubbles in the bulk and bubbles on dislocations and grain boundaries, the latter being ~10% larger than the others. The bubbles on carbides are typically somewhat smaller, while those on oxide particles are noticeably larger. The increase of He fluence results in the increase of the bubble size for all bubbles, whatever the defect type they are associated with.

The increase of the ion implantation fluence and the total content of implanted He in the matrix leads to the growth of all bubble types, including those in the bulk and on all microstructural features. The highest size growth (by ~2 times) between the fluencies of 1×10^{15} and $1 \times 10^{16} \text{ cm}^{-2}$ was observed for bubbles on grain boundaries and in the grain matrix. Slightly lower growth, by around 1.8 times, was detected for dislocations. Both types of precipitates, i.e. M_{23}C_6 carbides and Y_2O_3 oxides, provide the lowest bubble growth rate. Thus, bubbles associated with yttria nanoparticles are 2.2 times larger than bubbles in the bulk at the fluence of $1 \times 10^{15} \text{ cm}^{-2}$, while at the fluences of 5×10^{15} and $1 \times 10^{16} \text{ cm}^{-2}$, this ratio decreases to 1.75 and 1.66, respectively. Similarly, at the lowest fluence, bubbles on M_{23}C_6 particles have the same size as bubbles in the bulk, while at 5×10^{15} and $1 \times 10^{16} \text{ cm}^{-2}$ the bubbles attached to carbides have 0.83 and 0.74 times smaller size than bubbles in the bulk.

Table 3.2. Statistical analysis of specific number densities and average diameters of bubbles in ODS-EUROFER steel implanted with 10 keV He⁺ ions at the flux of 5×10¹¹ cm⁻²s⁻¹ to different fluencies at T=823 K, for several zones.

Fluence cm ⁻²	Zones	Volume		Grain boundaries		Dislocations		Carbides		Y ₂ O ₃ nano-oxides	
		N _c ^V (10 ²² m ⁻³)	D _c ^V (nm)	N _c ^{GB} (10 ¹⁵ ,m ⁻²)	D _c ^{GB} (nm)	N _c ^D (10 ⁸ m ⁻¹)	D _c ^D (nm)	N _c ^C (10 ¹⁶ m ⁻²)	D _c ^C (nm)	N _c ^P (10 ²² m ⁻³)	D _c ^P (nm)
1×10¹⁵ 1253 appm	1	1.76	2.65	2.66	3.02	1.76	2.82				
	2	1.76	3.09	4.31	3.21	1.55	3.10				
	3	1.81	2.57	4.33	3.32	1.15	2.81				
	4	2.01	2.42	7.32	2.58	1.52	2.59				
	5	2.25	2.70	5.00	3.04	1.52	2.68				
	Average	1.92	2.68	4.72	3.04	1.50	2.80	1.99	2.72	1.00	6.04
	Error	0.22	0.20	0.97	0.23	0.19	0.17	0.20	0.27	0.10	0.60
5×10¹⁵ 6267 appm	1	1.78	4.33	5.45	5.06	1.83	4.66				
	2	2.72	4.27	5.22	4.51	1.51	4.74				
	3	2.76	4.47	5.36	4.54	1.45	4.68				
	4	3.80	4.35	5.38	4.95	1.51	4.73				
	5	2.99	4.35	13.10	4.89	1.41	4.65				
	Average	2.81	4.36	6.90	4.79	1.54	4.69	2.31	3.55	1.00	8.11
	Error	0.46	0.23	1.87	0.35	0.18	0.24	0.23	0.36	0.10	0.81
1×10¹⁶ 12533 appm	1	3.79	4.86	7.91	6.12	1.53	5.60				
	2	6.45	5.22	6.49	6.38	1.50	5.44				
	3	2.36	6.99	7.19	5.78	1.49	5.64				
	4	6.70	4.74	6.62	5.66	1.60	4.26				
	5	7.69	5.02	7.16	6.33	1.56	5.21				
	Average	5.40	5.37	7.07	6.05	1.54	5.23	2.40	3.96	1.00	9.46
	Error	1.24	0.75	0.76	0.53	0.16	0.56	0.24	0.40	0.10	0.95

As explained in the previous section, the calculated specific number densities of bubbles $\langle N_c^k \rangle$ at different extended sinks and at oxide particles cannot be compared directly. Therefore, only the evolution of $\langle N_c^k \rangle$ with the ion implantation fluence is discussed below separately for each microstructural defect type.

The most pronounced increase between the lowest and the highest achieved fluence (by a factor of 2.8) was detected for the number density of bubbles in the grain matrix. In contrast, the increase of $\langle N_c^k \rangle$ for grain boundaries and carbides was relatively weak, by factors of 1.5 and 1.2, respectively. For bubbles associated with dislocations, the linear number density $\langle N_c^d \rangle$ did not change at all (cf. $\langle N_c^d \rangle$ values of 1.50 and 1.54 m^{-1} for the fluences 1×10^{15} and $1 \times 10^{16} \text{ cm}^{-2}$, respectively), reaching saturation already at the lowest fluence. The yttria particles are all associated with helium bubbles already at the lowest fluence, so that the number density of these bubbles also does not change with fluence.

A remarkable feature of the observed bubble growth kinetics is that the bubbles on extended defects grow at approximately the same rate as bubbles in the matrix. Though the bubbles on the grain boundaries are slightly larger than those in the bulk, no grain boundary bubble coalescence resulting in the formation of huge bubbles was observed even at the highest achieved He content of 1.25×10^3 appm. Neither the formation of bi-modal cavity distribution indicating the onset of bubble-to-void transition was noticed even at the highest fluence achieved. Both observations evidence high resistivity of ODS-EUROFER steel to swelling and high-temperature intergranular embrittlement at the studied temperature.

3.1.2.3 Variation of helium bubble parameters with He^+ ion implantation flux

Another series of experiments was performed at the same temperature of 823 K in order to clarify the sensitivity of evolving bubble ensembles to the rate of helium introduction into the steel matrix. For this purpose, He^+ implantations with three different fluxes, 5×10^{11} , 1×10^{12} , and $5 \times 10^{12} \text{ cm}^{-2}\text{s}^{-1}$, were performed to achieve the same fluence of $5 \times 10^{15} \text{ cm}^{-2}$, corresponding to the total accumulated He concentration of 6.3×10^3 appm.

Typical BF TEM through-focus images of ODS-EUROFER steel implanted using different fluxes are shown in Fig. 3.12. The common trend of helium bubble partitioning between the grain bulk and the microstructural defects is observed in all cases. It can be noticed that the bubble sizes tend to decrease slightly with the increase of helium implantation flux. It also looks like the number density of bubbles in the bulk tends to increase as the flux increases. However, more decisive conclusions require quantitative processing of TEM observations.

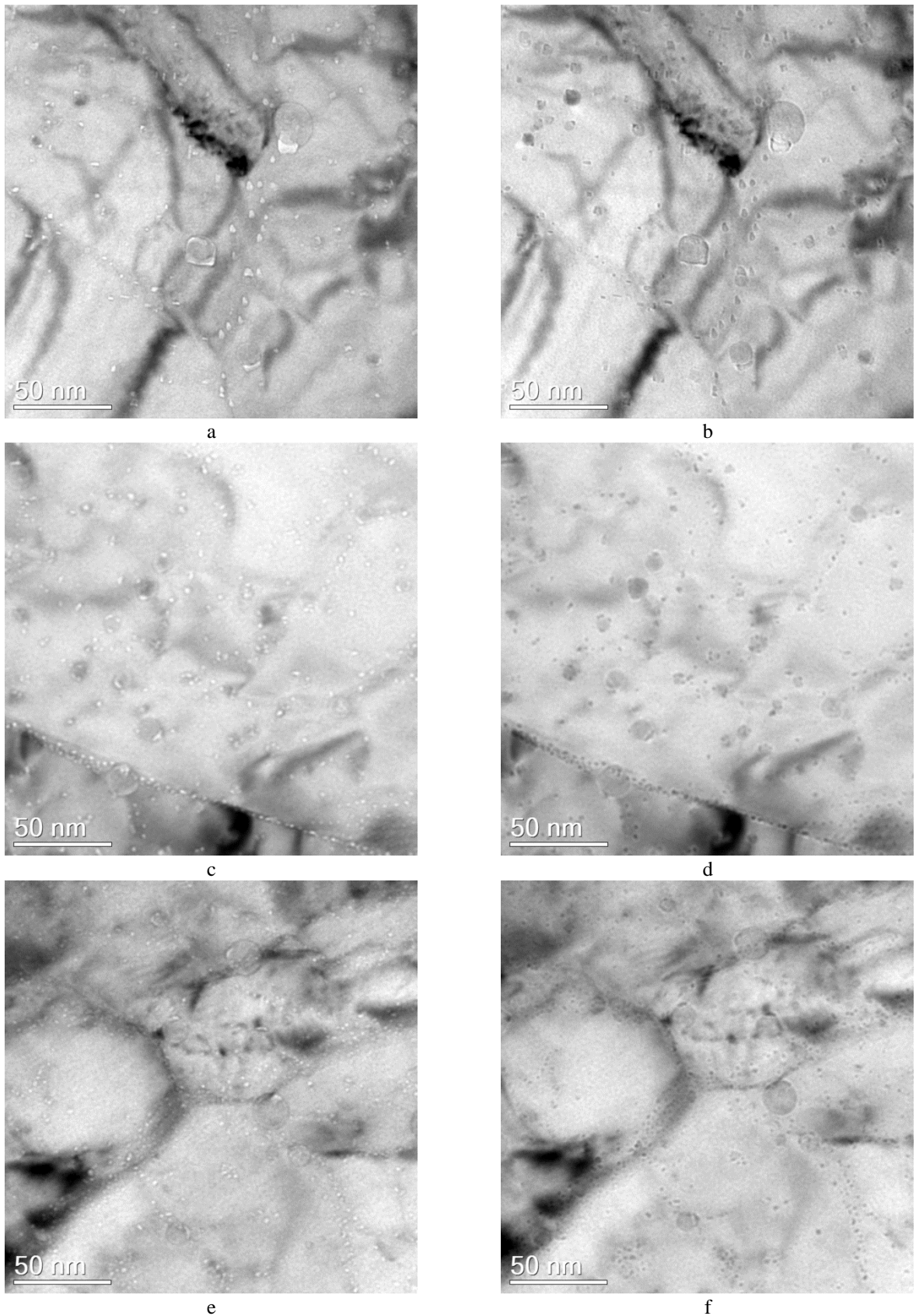


Fig. 3.12. Microstructure of ODS-EUROFER steel implanted with 10 keV He^+ ions at 823 K to the fluence of $5 \times 10^{15} \text{ cm}^{-2}$ with different fluxes: (a,b) $5 \times 10^{11} \text{ cm}^{-2} \text{ s}^{-1}$; (c,d) $1 \times 10^{12} \text{ cm}^{-2} \text{ s}^{-1}$; (e,f) $5 \times 10^{12} \text{ cm}^{-2} \text{ s}^{-1}$. BF TEM imaging conditions are: (a,c,e) $\sim 1 \mu\text{m}$ underfocus and (b,d,f) $\sim 1 \mu\text{m}$ overfocus.

Similar to section 3.1.1.2, we start with studying the bubbles attached to the Y_2O_3 nanoparticles. For all fluxes used one observes correlation between the sizes of the bubbles and the host nanoparticles. In order to estimate the average bubble size, the trend lines $D_c^p(D_p)$ were determined for each flux from the plot of bubble versus particle sizes, as shown in Fig. 3.13. The best fit parameters for the trend lines and the derived average bubble sizes $\langle D_c^p \rangle$ are collected in Table 3.3.

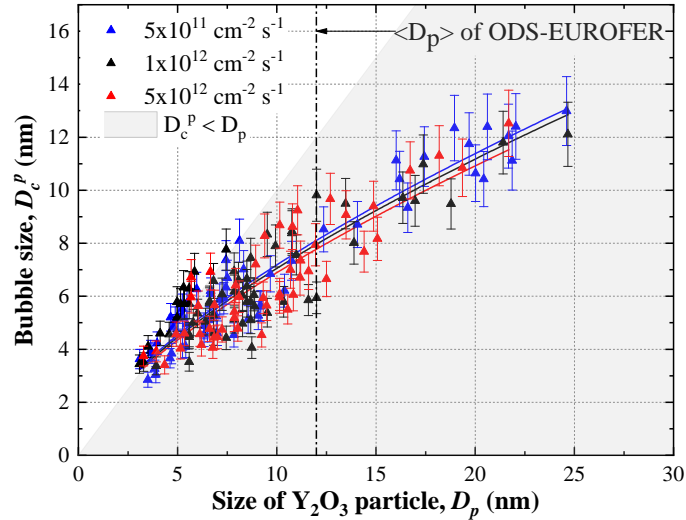


Fig. 3.13. Bubble size on yttria nanoparticles vs. particle size for the ODS-EUROFER steel implanted with 10 keV He^+ ions at 823 K with the fluxes varying from 5×10^{11} to $5 \times 10^{12} \text{ cm}^{-2} \text{ s}^{-1}$ to the fluence of $5 \times 10^{15} \text{ cm}^{-2}$. Solid lines are best fits for each flux. The grey marked area corresponds to the bubbles with the size smaller than that of the particle. Error bars are 10% uncertainties associated with the size of the first Fresnel fringe on bubble observed in underfocused images [9,16].

Table 3.3. Parameters for the power law fitting used in Fig. 3.13.

He implantation flux	b	a	$\langle D_c^p \rangle$, nm
$5 \times 10^{11} \text{ cm}^{-2} \text{ s}^{-1}$	0.66	1.56	8.11
$1 \times 10^{12} \text{ cm}^{-2} \text{ s}^{-1}$	0.66	1.53	7.96
$5 \times 10^{12} \text{ cm}^{-2} \text{ s}^{-1}$	0.66	1.49	7.78

As can be seen, the trend lines indicate only a slight decrease of bubble sizes on oxide particles when the flux increases by an order of magnitude, while $\langle D_c^p \rangle$ remains almost unchanged. Similar to the case of fluence variation at the fixed flux of $5 \times 10^{11} \text{ cm}^{-2} \text{ s}^{-1}$, the bubble sizes are more sensitive to the size of the associated nanoparticle than to the ion implantation condition variation. For all fluxes used, one can notice oxide particles with bubbles larger than the particle itself. Such oxide particles fall in the size range of 3 to ~ 7 nm and this range is not sensitive to the flux variation, in contrast to the case of fluence variation.

Results of statistical analysis of He bubble parameters in the grain matrix, on dislocations and on grain boundaries in samples implanted with different fluxes are given in Table 3.4. The parameters of bubbles on $M_{23}C_6$ carbide particles could not be determined at the fluxes of 1×10^{12} and $5 \times 10^{12} \text{ cm}^{-2} \text{ s}^{-1}$ because electron transparent zones in these samples contained no carbides. However, for the purpose of subsequent comparison of contributions to swelling from bubbles on different defects (see section 3.1.2.2 below), one can roughly estimate them using the knowledge acquired during the implantations with different fluencies described in the previous section.

Table 3.4. Statistical analysis of specific number densities and average diameters of bubbles in ODS-EUROFER steel implanted with 10 keV He⁺ ions at different fluxes to the fluence of 5×10¹⁵ cm⁻² at T=823 K, for several zones.

Flux cm ⁻² s ⁻¹	Zones	Volume		Grain boundaries		Dislocations		Carbides		Y ₂ O ₃ nano-oxides	
		N _c ^V (10 ²² m ⁻³)	D _c ^V (nm)	N _c ^{GB} (10 ¹⁵ , m ⁻²)	D _c ^{GB} (nm)	N _c ^D (10 ⁸ m ⁻¹)	D _c ^D (nm)	N _c ^C (10 ¹⁶ m ⁻²)	D _c ^C (nm)	N _c ^P (10 ²² m ⁻³)	D _c ^P (nm)
5×10 ¹¹	1	1.78	4.33	5.45	5.06	1.83	4.66				
	2	2.72	4.27	5.22	4.51	1.51	4.74				
	3	2.76	4.47	5.36	4.54	1.45	4.68				
	4	3.80	4.35	5.38	4.95	1.51	4.73				
	5	2.99	4.35	13.10	4.89	1.41	4.65				
	Average	2.81	4.36	6.90	4.79	1.54	4.69	2.31	3.55	1.00	8.11
	Error	0.46	0.23	1.87	0.35	0.175	0.24	0.23	0.36	0.10	0.81
1×10 ¹²	1	10.41	3.31	7.52	3.67	2.08	3.23				
	2	1.20	2.90	8.78	2.96	2.57	2.68				
	3	9.88	3.34	9.56	3.67	1.83	3.79				
	4	14.65	3.24	12.70	3.09	2.07	3.02				
	5	7.87	3.60	9.69	3.46	1.58	3.89				
	Average	8.80	3.28	9.65	3.37	2.03	3.32	2.31*	2.66*	1.00	7.96
	Error	2.61	0.23	1.36	0.28	0.27	0.37	0.23*	0.27*	0.10	0.80
5×10 ¹²	1	14.33	2.56	11.75	2.36	2.41	2.20				
	2	19.32	2.74	11.53	2.43	2.48	2.44				
	3	53.14	2.40	15.54	2.35	2.33	2.22				
	4	14.84	2.66	11.77	2.51	2.26	2.51				
	5	6.63	2.86	7.25	2.92	1.40	3.16				
	Average	21.65	2.65	11.56	2.51	2.18	2.51	2.31*	2.04*	1.00	7.78
	Error	9.35	0.16	1.87	0.18	0.31	0.26	0.23*	0.20*	0.10	0.78

* Approximately estimated values

In particular, the specific number density of bubbles (per unit surface of carbide particles) practically saturates by the fluence of $5 \times 10^{15} \text{ cm}^{-2}$, while the average size of bubbles on carbides, D_c^c , correlates with the average size of bubbles in the bulk. Hence for subsequent swelling estimates at different fluxes we will assume the same specific number density of bubbles on the carbide surface, $N_c^c = 2.3 \text{ m}^{-2}$, while the bubble diameters for the fluxes in the range $1 \times 10^{12} - 5 \times 10^{12} \text{ cm}^{-2}\text{s}^{-1}$ will be estimated from the diameters of bubbles in the grain matrix, D_c^V , using the relation:

$$D_c^c(1 \times 10^{12} - 5 \times 10^{12}) = A \cdot D_c^V,$$

where $A = D_c^c / D_c^V$ is the ratio of corresponding average bubble diameters at the flux of $5 \times 10^{11} \text{ cm}^{-2}\text{s}^{-1}$, for which carbides were observed. Corresponding estimates are also added to Table 3.4. Finally, the data for bubbles on oxide particles, as estimated above, is added to Table 3.4 for completeness.

As can be judged from the table, at each particular flux there is little difference between the average sizes of bubbles in the bulk and on extended defects. Similarly, whatever the flux, bubbles associated with Y_2O_3 nano-particles are the largest.

A common trend for bubbles in the bulk, on dislocations and on grain boundaries is the increase of the bubble specific number density $\langle N_c^k \rangle$ accompanied with the decrease of the average bubble size D_c^k as the implantation flux grows. The most impressive number density increase (by a factor of more than 7) between the lowest and the highest implantation flux used is observed for bubbles in the grain matrix. The increase of the specific bubble number densities on grain boundaries and dislocations is, in contrast, relatively modest, by factors of 1.68 and 1.41, respectively. At the same time, bubble sizes in the bulk and on extended defects fall between the lowest and the highest ion implantation fluxes in a similar way, approximately twice (slightly less for bubbles in the bulk as compared to bubbles on extended defects). In contrast, the average size of bubbles on oxide particles decreases only slightly with the increase of flux, so that the ratio of the average sizes of bubbles on oxide particles and in the bulk increases, constituting approximately 1.9, 2.4, and 2.9 for the fluxes of 5×10^{11} , 1×10^{12} , and $5 \times 10^{12} \text{ cm}^{-2}\text{s}^{-1}$, respectively. The bubbles on oxide particles are in one-to-one relation with Y_2O_3 precipitates and thus their number densities are insensitive to flux variations.

The evolution of bubbles associated with M_{23}C_6 carbides is not discussed in this section due to the absence of relevant statistical information.

3.1.2.4 Variation of helium bubble parameters with ion implantation temperature

The third set of experiments involved variation of ion implantation temperature while keeping fixed implantation flux and fluence. In this set of experiments, several samples were implanted at temperatures 723 K, 823 K, and 923 K with 10 keV He^+ ions to the fluence of $5 \times 10^{15} \text{ cm}^{-2}$ (introducing 6.3×10^3 appm He into the implanted region) using the flux of $5 \times 10^{11} \text{ cm}^{-2}\text{s}^{-1}$.

Typical BF TEM through-focus images of ODS-EUROFER implanted at temperatures 723 K, 823 K, and 923 K are shown in Fig. 3.14. In agreement with the other experiments, He bubbles extensively decorate grain boundaries, dislocations and precipitates. The sizes of bubbles on yttria nanoparticles are at all temperatures notably different from those on the other microstructural defects. Pronounced bubble size increase with the increasing temperature can be easily noticed.

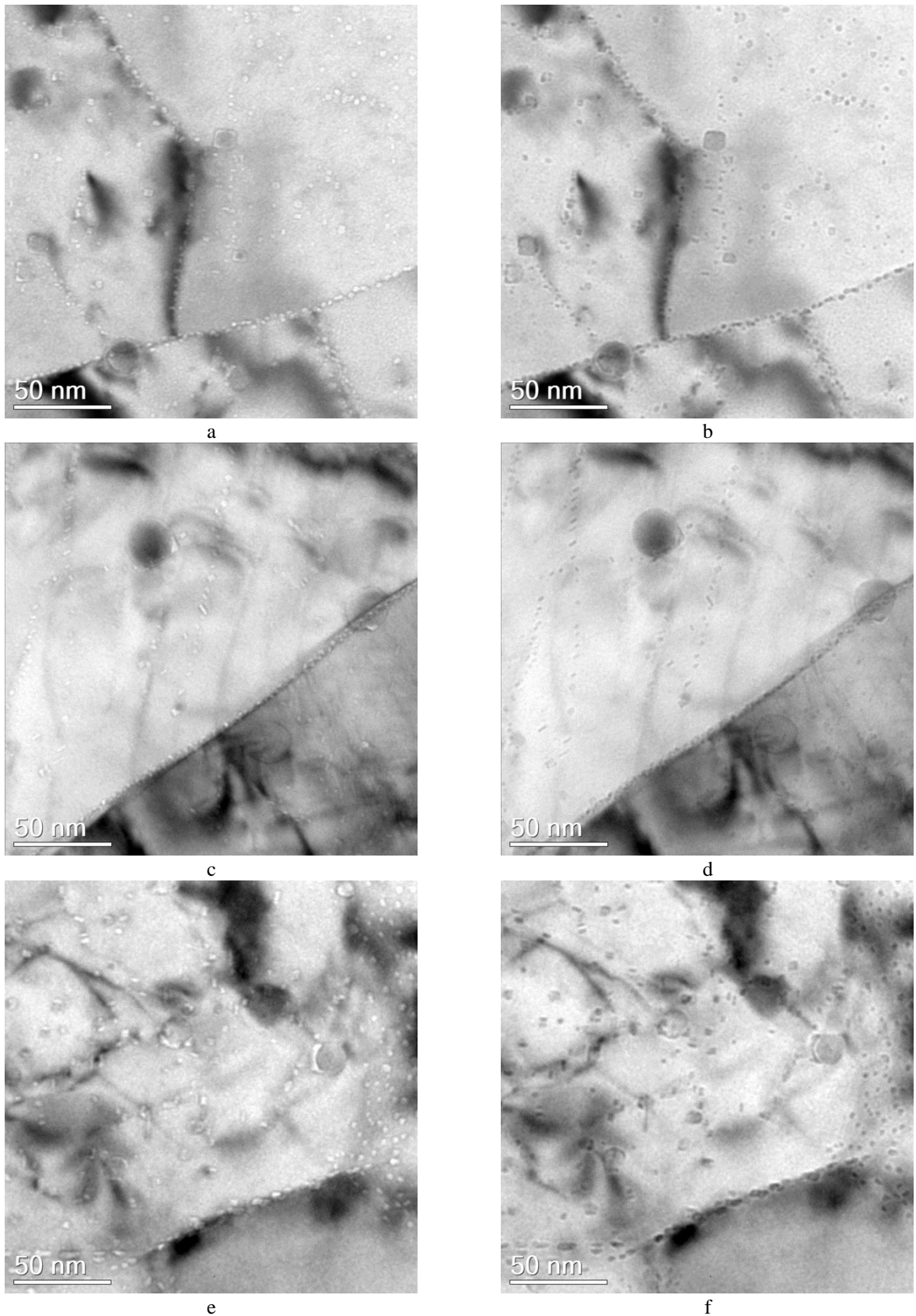


Fig. 3.14. Microstructure of ODS-EUROFER steel implanted with 10 keV He⁺ ions with the flux of $5 \times 10^{11} \text{ cm}^{-2} \text{ s}^{-1}$ to fluence $5 \times 10^{15} \text{ cm}^{-2}$ at different temperatures: (a,b) 723 K; (c,d) 823 K; (e,f) 923 K. BF TEM imaging conditions: (a,c,e) $\sim 1 \mu\text{m}$ underfocus and (b,d,f) $\sim 1 \mu\text{m}$ overfocus.

The qualitative analysis of bubble array parameters starts with the determination of the average size of bubbles attached to oxide nanoparticles. In order to determine it, we plot the experimentally measured bubble diameters versus the sizes of hosting oxide particles for each studied temperature and approximate them with power law trend lines $D_c^p(D_p)$, as shown in Fig. 3.15. The best fit parameters and the resulting average bubble sizes $\langle D_c^p \rangle$ for the studied temperatures are collected in Table 3.5.

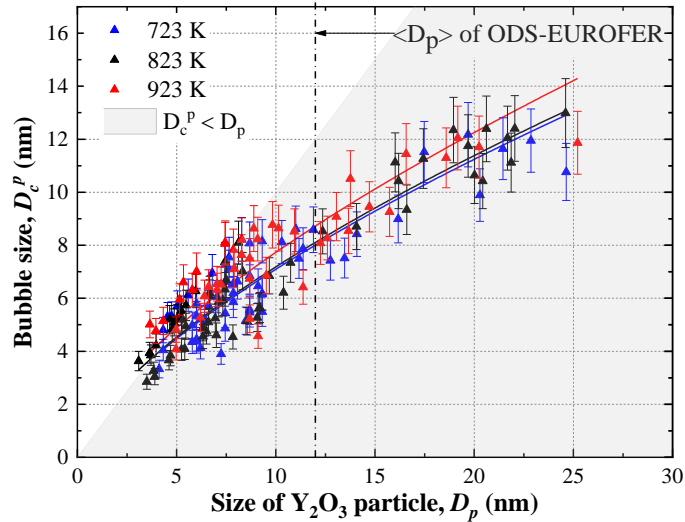


Fig. 3.15. Bubble size on yttria nanoparticles vs. particle size for the ODS-EUROFER steel implanted with 10 keV He⁺ ions at temperatures 723, 823, and 923 K with the flux of $5 \times 10^{11} \text{ cm}^{-2} \text{ s}^{-1}$ to the fluence of $5 \times 10^{15} \text{ cm}^{-2}$. Solid lines are best fits for each temperature. The grey marked area corresponds to the bubbles with the size smaller than that of the particle. Error bars are 10% uncertainties associated with the size of the first Fresnel fringe on bubble observed in underfocused images [9,16].

Table 3.5. Parameters for the power law fitting used in Fig. 3.15.

He implantation regime	b	a	$\langle D_c^p \rangle$, nm
T=723 K	0.66	1.54	8.01
T=823 K	0.66	1.56	8.11
T=923 K	0.66	1.67	8.73

According to the estimates above, $\langle D_c^p \rangle$ is not much sensitive to temperature variation in the studied range, increasing from ~ 8.0 nm to ~ 8.7 nm as the temperature increases from 723 to 923 K. Similar to observations for fluence and flux variation, the sizes of the bubbles associated with yttria particles are stronger affected by the sizes of nanoparticles than by the ion implantation conditions used. At all studied temperatures one observes particles with bubbles larger than the particle itself (such bubbles are represented by points falling in the white area in Fig. 3.15). At the lowest studied temperature, the particles that are nearly completely enveloped by associated bubbles have sizes not larger than 4 nm, but at the highest temperature of 923 K the bubbles can nearly completely envelope particles as large as 7-8 nm.

The results of statistical analysis of He bubble parameters in the grain matrix and on extended defects are collected in Table 3.6 for ODS-EUROFER steel samples implanted at different temperatures. For bubbles on the $M_{23}C_6$ carbides the experimental data is available only for the sample implanted at 823 K because no carbide particles were found on TEM images for samples implanted at 723 K and 923 K. So, similar to the flux variation regime, the bubble parameters for these temperatures in Table 3.6 are evaluated using the measured values for 823 K and following the procedure described in section 3.1.2.3.

Table 3.6. Statistical analysis of specific number densities and average diameters of bubbles in ODS-EUROFER steel implanted with 10 keV He⁺ ions at the flux of 5×10¹¹ cm⁻²s⁻¹ to the fluence of 5×10¹⁵ cm⁻² at different temperatures, for several zones.

T, K	Zones	Volume		Grain boundaries		Dislocations		Carbides		Y ₂ O ₃ nano-oxides	
		$N_c^V (10^{22} \text{ m}^{-3})$	D_c^V (nm)	$N_c^{GB} (10^{15}, \text{ m}^{-2})$	D_c^{GB} (nm)	$N_c^D (10^8 \text{ m}^{-1})$	D_c^D (nm)	$N_c^C (10^{16} \text{ m}^{-2})$	D_c^C (nm)	$N_c^P (10^{22} \text{ m}^{-3})$	D_c^P (nm)
723	1	5.65	4.12	13.55	3.78	1.91	3.92				
	2	6.99	3.81	9.81	3.60	2.32	3.41				
	3	5.03	3.16	10.36	3.62	1.72	3.15				
	4	5.06	2.83	7.42	3.47	1.62	3.45				
	5	7.20	3.00	8.16	3.64	1.97	3.53				
	Average	5.99	3.38	9.86	3.62	1.91	3.49	2.31*	2.80*	1.00	8.01
	Error	0.80	0.39	0.16	0.19	0.23	0.26	0.23*	0.28*	0.10	0.80
823	1	1.78	4.33	5.45	5.06	1.83	4.66				
	2	2.7	4.27	5.22	4.51	1.51	4.74				
	3	2.76	4.47	5.36	4.54	1.45	4.68				
	4	3.80	4.35	5.38	4.95	1.51	4.73				
	5	2.99	4.35	13.10	4.89	1.41	4.65				
	Average	2.81	4.36	6.90	4.79	1.54	4.69	2.31	3.55	1.00	8.11
	Error	0.46	0.23	0.19	0.35	0.18	0.24	0.23	0.36	0.10	0.81
923	1	1.98	4.94	7.38	5.49	1.27	4.97				
	2	1.73	4.92	6.51	5.73	1.25	5.44				
	3	1.84	4.88	6.15	5.56	1.78	4.86				
	4	1.22	5.81	7.06	5.22	1.32	5.36				
	5	3.00	4.29	5.29	4.99	2.01	4.64				
	Average	1.95	4.97	6.48	5.40	1.52	5.05	2.31*	4.11*	1.00	8.73
	Error	0.38	0.52	0.77	0.44	0.23	0.42	0.23*	0.41*	0.10	0.87

* Approximately estimated values

At each particular studied temperature, the average sizes of bubbles in the bulk, on dislocations and on grain boundaries are quite similar, though bubbles on grain boundaries are typically slightly (by ~10%) larger than the others, whereas the bubbles associated with Y_2O_3 nanoparticles are visibly larger than on other microstructural features.

The general trends for the bubble parameter variation with temperature are the same for bubbles in the bulk and on extended defects, namely, the bubble number density decreases and the bubble mean size increases with the increase of temperature. The strongest decrease is demonstrated by bubbles in the bulk, whose number density at 923 K is only roughly one third of that at 723 K. The decrease of specific number densities of bubbles on dislocations and on grain boundaries is noticeably less pronounced, by ~25% and ~35%, respectively. The average sizes of bubbles in the bulk and on extended defects increase roughly by a factor of 1.5 between 723 K and 923 K. Correspondingly, since the average size of bubbles on oxide particles weakly depends on temperature, the size difference between bubbles associated with oxide particles and with other microstructural features becomes less pronounced as the ion implantation temperature grows. For example, the ratio of average sizes of bubbles on oxide particles and in the bulk constitutes roughly 2.4, 1.9 and 1.8 for temperatures 723, 823 and 923 K, respectively. The mean bubble size of bubbles at the nano-oxide/matrix interface in samples implanted at 923 K appears to be 8.7 nm while grain boundary, dislocation, and the bulk demonstrate lower values of 5.4, 5.1 and 5.0 nm, respectively.

Summing up the results of statistical analysis presented in sections 3.1.2.2 – 3.1.2.4, one can conclude that

(i) All Y_2O_3 nanoparticles are decorated with single (very rarely – two) He bubbles and the sizes of these bubbles are visibly larger than for the bubbles in the bulk and on extended defects regardless of the ion implantation conditions applied.

(ii) The sizes of bubbles attached to yttria nanoparticles correlate with the sizes of host particles, demonstrating a trend that the larger particles tend to host larger bubbles; this trend remains valid for all ion implantation conditions used.

(iii) Bubbles located in the grain matrix and associated with extended defects (grain boundaries, dislocations) follow the common general trend, where the average bubble size grows with increasing temperature and fluence (He content) and decreases with increasing flux.

(iv) The number density of bubbles in the grain matrix and, especially, the specific bubble densities on extended defects, tend to saturate with the increase of ion implantation fluence. With respect to variation of implantation flux and temperature, only very moderate variations of specific number densities of bubbles on extended defects were observed. In contrast, the number density of bubbles in the grain matrix was very sensitive to ion implantation condition variations. For instance, an order of magnitude increase of the implantation flux results in more than 7-fold increase of the bubble number density in the bulk, whereas the specific number densities of bubbles on dislocations and grain boundaries increase only by ~70% and ~40%, respectively.

3.1.2.5 Contributions of bubbles on different microstructural components to the total swelling and helium inventory

3.1.2.5.1 Methodology of swelling estimation

Transmission electron microscopy is a well-established technique for the swelling estimation through the evolution of cavity/bubble population parameters. In the approach prescribed by ASTM standard [19], the swelling is defined in terms of the cumulative volume $\sum_i V_{ci}$ of all cavities in the visible area, irrespective to their association with that or other microstructural feature,

$$S_{ASTM} (\%) = \left\langle \sum_i V_{ci} / V \right\rangle \times 100\% , \quad (3.1)$$

where V is the volume of the visible area.

Unfortunately, this recipe doesn't allow to figure out the contributions of various microstructural components to the cumulative swelling, as well as the contributions to helium accumulation from bubbles associated with particular defects. As shown in sections 3.1.1 and 3.1.2.2-3.1.2.4, ion implantation under all applied experimental conditions results in different He bubble families related to microstructural features of ODS-EUROFER steel. Taking this into account, we consider it reasonable to evaluate cumulative swelling by indirect approach as follows:

$$S = \sum_k S_k , \quad (3.2)$$

where $S_k = V_c^k \cdot N_c^k \cdot 100\%$ is the swelling value associated with particular defect type, index k denotes different bubble families, in the same way as in section 3.1.2.1, $V_c^k (\text{m}^3)$ and N_c^k are the average volume and the number density of bubbles associated with the k -th type of microstructural defects.

The average bubble volume for the bubbles associated with grain boundaries, carbides and cavities in the grain matrix is calculated as:

$$V_c^k = \frac{\pi}{6} \cdot \langle D_c^k \rangle^3 , \quad (3.3)$$

where $\langle D_c^k \rangle$ is the effective bubble diameter obtained from statistical analysis for the bubbles associated with each microstructural component (see Tables 3.2, 3.4, and 3.6).

As reported in sections 3.1.1 and 3.1.2.2-3.1.2.4, bubbles attached to Y_2O_3 nanoparticles have a specific lens-like shape and so their volumes can be noticeably less than that predicted by the previous equation (see Fig. 3.16 illustrating a spherical segment of a cavity attached to either flat or spherical particle surface).

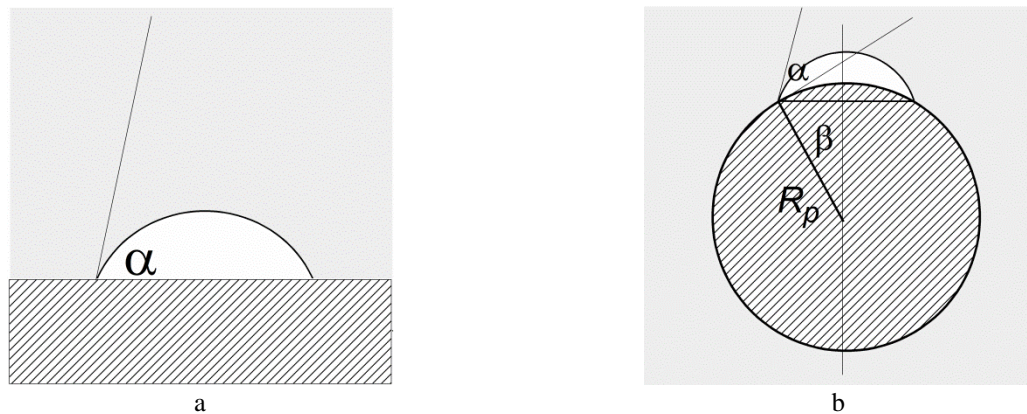


Fig. 3.16. Approximation of the lens-shaped bubbles attached to a flat (a) or spherical surface (b) of the Y_2O_3 nanoparticle.

In the case of a flat substrate surface, bubble volume can be calculated as:

$$V_c^p = \int_x^R \pi(r^2 - x^2)dx = \pi \left(\frac{2}{3}R^3 - R^2x - \frac{1}{3}x^3 \right) = \frac{\pi}{3}R^3(\cos\alpha + 2)(\cos\alpha - 1)^2, \quad (3.4)$$

where α is the contact angle, as shown in Fig. 3.16. For bubbles on yttria particle the contact angle $\alpha = 48 \pm 5^\circ$ was estimated by direct measurements on TEM images and found to be insensitive to either the nanoparticle size or implantation conditions used.

For the curved surface bubble volume was calculated as:

$$V_c^p = V_1 - V_2 = \frac{\pi}{3} \left[R^3(2 + \cos(\alpha + \beta))(1 - \cos(\alpha + \beta))^2 - R_p^3(2 + \cos\beta)(1 - \cos\beta)^2 \right], \quad (3.5)$$

where R_p is the Y_2O_3 nanoparticle radius, $\cos(\alpha + \beta)$ and $\cos\beta$ are represented as:

$$\cos\beta = \frac{(R_p - R\cos\alpha)}{\sqrt{R_p^2 - 2R R_p \cos\alpha + R^2}}; \quad \cos(\alpha + \beta) = \frac{(R_p \cos\alpha - R)}{\sqrt{R_p^2 - 2R R_p \cos\alpha + R^2}}. \quad (3.6)$$

An example of the bubble volume dependence on the size of the host oxide particle is shown in Fig. 3.17 in the nanoparticle size range from 0.2 to 100 nm. The bubble radius of $R_c^p = 4.05$ nm used in the example is a typical value observed for implantation to the fluence of $5 \times 10^{15} \text{ cm}^{-2}$ at 823 K with the flux of $5 \times 10^{11} \text{ cm}^{-2}\text{s}^{-1}$. For comparison, the volumes of bubbles with the same radius in the bulk and on a flat interface are shown.

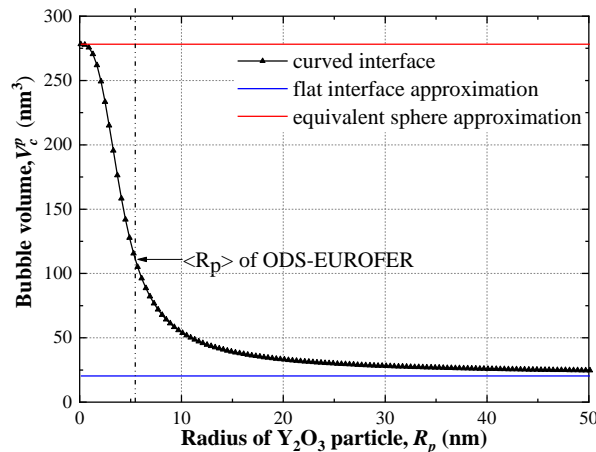


Fig. 3.17. Bubble volume calculated for curved surface, flat interface and equivalent sphere approximation; for $R=4.05$ nm and $\alpha = 48^\circ$.

It is seen in Fig. 3.17 that the bubble volume is well approximated by equation (3.3) only when the bubble is noticeably larger than the host particle. In the opposite limiting case of a small bubble on a large particle the volume of the bubble can be an order of magnitude smaller (for the example in the Fig. 3.17 this happens for nanoparticles larger than 50 nm). For the realistic value of the mean nanoparticle radius value of ~ 6 nm of ODS-EUROFER steel, neither limiting case is valid. Therefore, the processing of TEM micrographs the volumes V_c^p for bubbles associated with oxide particles were calculated using equation (3.5).

In order to calculate the contributions to swelling from different families of bubbles, one has to know their number densities per unit volume. As discussed in section 3.1.2.1, only the number density of bubbles in the grain matrix can be estimated directly from statistical analysis of TEM images. For bubbles on extended defects only specific bubble number densities $\langle N_c^k \rangle$ allow reliable estimation. These values for different experimental conditions were summarized in Tables 3.2, 3.4, and 3.6. In order to convert these specific number densities into those normalized per unit sample volume, we use the relations

$$N_V^k = \langle N_c^k \rangle \cdot N_k, \quad (3.7)$$

where N_k is the density of extended defects per unit material volume typical for the studied material (see section 2.1.1.1). Similarly, for bubbles on the oxide particles their number density is taken equal to the typical number density of oxide particles in ODS-EUROFER. The total bubble number density can then be obtained by simple summation, $N_V = \sum_k N_V^k$.

The fractions of implanted He accumulated in bubbles associated with that or another component of defect microstructure were estimated as:

$$F_{He}^k (\%) = \frac{V_c^k \cdot n_{He}^k \cdot N_V^k}{\langle N_{TRIM} \rangle}, \quad (3.8)$$

where n_{He}^k (m^{-3}) is the average number density of He atoms inside bubbles associated with the k -th structural feature and $\langle N_{TRIM} \rangle$ is the average content of implanted element in the entire region of interest calculated by TRIM. The cumulative helium fraction $F_{He} = \sum_k F_{He}^k$ in all bubbles was calculated by simple summation overall microstructural defect arrays.

The unknown value of the number densities of He atoms in the bubbles could be estimated from the He pressure in the bubble, p , by using suitable equation of state (EOS) [20–22]. The relation between the helium volume density and pressure predicted by different EOS at $T=825$ K is shown in Fig. 3.18.

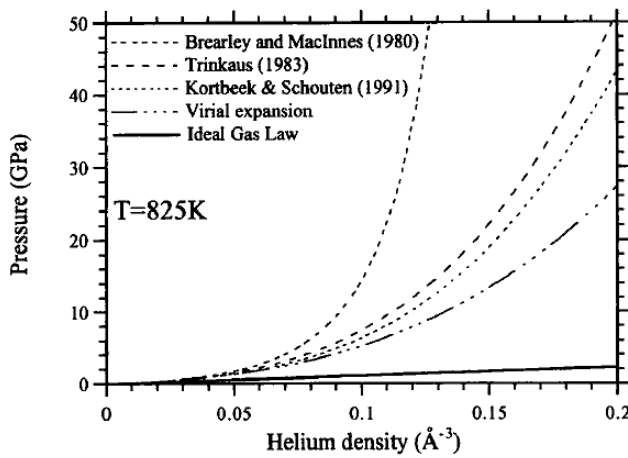


Fig. 3.18. Various EOSs for He at $T = 825$ K [21].

formed in our implantation conditions in the bulk and on microstructural defects vary in the range from 2 to 7 nm; it corresponds to the pressure range from 4 to 1.2 GPa. As can be noticed in Fig. 3.18, at these pressure levels all the shown EOS (excluding the ideal gas) predict roughly the same pressures. Hence, for the estimates of the He content in the bubbles one can select any of them. To be specific, we have used the hard sphere equation of state known as Carnahan-Starling (or Brearley and MacInnes) EOS:

$$p_{He} (Pa) = n_{He} \cdot k \cdot T \cdot \frac{1 + y + y^2 - y^3}{(1 - y)^3}, \quad (3.9)$$

where T is the temperature, k – the Boltzmann constant, $y = \frac{\pi \cdot n_{He} \cdot d_0^3}{6}$, and d_0 is the hard sphere diameter. Here we have used $d_0 = 2.18 \times 10^{-10}$ m as suggested in Ref. [21] based on fitting the experimental data on helium density measurements by EELS.

The errors of evaluated swelling and He fraction values are estimated as a combination for the bubble number density and size errors.

As will be shown below, the estimated amount of He atoms in the bubbles is often less than that implanted, implying that a part of implanted He is captured in small helium-vacancy clusters invisible by TEM. Having in mind that implantation creates equal numbers of vacancies and interstitial atoms, the immobilization of vacancies in He-V clusters means that an equal number of uncompensated interstitials is captured by point defect sinks, thus contributing to swelling. Assuming for simplicity that all ‘invisible’ He atoms are simply captured in substitutional positions, the total swelling rate could be evaluated as follows:

$$S_{total} = (F_{He_total}(\text{appm}) - F_{He}(\text{appm})) \cdot 10^{-4} + S, \quad (3.10)$$

where $F_{He_total}(\text{appm})$ is the average concentration of implanted helium in the entire region of interest calculated by TRIM, and S is the swelling estimated via TEM image processing.

The proposed indirect approach makes it possible to reconcile the locality of TEM analysis with the necessity to estimate separate contributions to the swelling and helium inventory for bubble families associated with different microstructural features. The discussion below addresses only the kinetics of swelling and captured helium fraction, evaluated using the experimental data given in sections 3.1.2.2-3.1.2.4.

3.1.2.5.2 Fluence dependent variation of contributions from different bubble families to swelling and helium inventory

Table 3.7 and Fig. 3.19 summarize the results for the bubble number density N_v^k , swelling contribution S_k , the average ratio of vacancies to He atom number in the bubbles (V/He), and the fraction of accumulated helium F_{He}^k separately for each bubble family at three different fluences.

Fluence dependent variations of bubble number densities are sensitive to the nature of the bubble family. The most favorable location for bubbles at all fluences is on grain boundaries. The evaluated bubble number density on grain boundaries increases with fluence, but quite moderately, from $N_v^{GB} = 3.6 \times 10^{22} \text{ m}^{-3}$ to $N_v^{GB} = 5.5 \times 10^{22} \text{ m}^{-3}$. Even less pronounced dynamics of number density is demonstrated by bubble families associated with the other extended defects - dislocations and carbide precipitates, remaining at the level of $2.0 \times 10^{22} \text{ m}^{-3}$. The number density of bubbles associated with oxide nanoparticles is uniquely determined by the number density of nanoparticles, $N_v^p = 1.0 \times 10^{22} \text{ m}^{-3}$ and also does not change as the fluence increases. In contrast, the number density of bubbles in the bulk continuously grows. While at the lowest studied fluence it is comparable to that of bubbles on dislocations and carbides, by the highest accumulated He fluence it becomes essentially the same as that of grain boundary bubbles. But in spite of the sharp increase of the number density of bubbles in the bulk, the total bubble number density grows with the implantation fluence relatively modestly, from $N_v \approx 10 \times 10^{22} \text{ m}^{-3}$ to $N_v \approx 16 \times 10^{22} \text{ m}^{-3}$.

The overall increase of number densities of visible He bubbles with the fluence increase is accompanied with the increase of swelling, but the contributions to swelling vary depending on the particular bubble family. The largest contribution for all fluences comes from grain boundary bubbles. It changes from $S_{GB} = 0.05 \%$ to $S_{GB} = 0.63 \%$ between the lowest and the highest fluences achieved. However, in terms of swelling rate, the most notable swelling increase (by more than a factor of 20, from $S_v = 0.02 \%$ at the fluence of $1 \times 10^{15} \text{ cm}^{-2}$ to $S_v = 0.44 \%$ at $1 \times 10^{16} \text{ cm}^{-2}$) is provided by the bubble population in the bulk. Individual swelling contributions of bubble populations attached to other extended defects and oxide nanoparticles are smaller than that of grain boundary bubbles and demonstrate slower dynamics (increasing by a factor of ~ 6 for bubbles on dislocations and oxide particles and ~ 3.5 for bubbles on carbides).

The modes of swelling increase with fluence also depend on the particular bubble population. Thus, bubbles on grain boundaries and carbides contribute to swelling due to both bubble size and bubble number density increase. The swelling contribution from bubbles on Y_2O_3 particles and dislocations is due exclusively to bubble growth. In contrast, the increase of swelling provided by bubbles in the bulk is mainly promoted by sharply growing bubble number density. But, in spite of pronounced differences in the kinetics of individual bubble families, the total swelling shows nearly linear variation with the fluence, from 0.14 % to 1.5 % as the fluence grows from $1 \times 10^{15} \text{ cm}^{-2}$ to $1 \times 10^{16} \text{ cm}^{-2}$.

In addition to He accumulated in the bubbles visible in TEM images, a certain fraction of He can be retained in invisible He-vacancy clusters and also contribute to swelling. Hence, an important parameter to estimate is the fraction of implanted He that is captured in the bubbles at different fluences. It can be expected that with the growth of bubbles during ion implantation the relative content of He captured in them (per unit sample volume) would decrease. A convenient measure of this effect is the ratio of the number of vacancies contained in a bubble to the number of He atoms it contains, or the V/He ratio. It can be noticed in Table 3.7 that the V/He ratio indeed increases with the fluence for all bubble families. The lowest He concentrations are observed in the bubbles attached to oxide nanoparticles, which are generally larger than the bubbles in the bulk or on extended defects.

The largest estimated fraction of accumulated helium at the lowest studied fluence ($F_{He}^{GB} \approx 28\%$ of the total implanted amount) is captured in the grain boundary bubble population, while bubbles on dislocations, carbide and oxides precipitates, and in the bulk contain similar shares of accumulated helium at the level of $\sim 11-12\%$ each. Fluence increase up to $1 \times 10^{16} \text{ m}^{-2}$ leads to noticeable increase of the implanted He share accumulated in the bubbles in the bulk (up to $F_{He}^V \approx 18\%$) and causes only a slight decrease of helium fraction in bubbles on grain boundaries (down to $F_{He}^{GB} \approx 25\%$). So, despite the decrease, the grain boundary cavities remain the most important accumulators of implanted helium. At the same time, the shares of He accumulated in bubbles on dislocations, carbides, and nano-oxides significantly decrease, down to $F_{He}^d = 6.3\%$, $F_{He}^c = 3.4\%$ and $F_{He}^p = 6.0\%$, respectively, at the highest implantation fluence.

The cumulative helium fraction captured in all visible bubbles, when expressed in absolute numbers, increases from ~ 920 appm to ~ 7400 appm when the implantation fluence increases from the lowest to the highest accumulated value. However, the relative accumulated helium fraction demonstrates the decrease from $\sim 73\%$ down to $\sim 60\%$ with fluence increase. In other words, a very noticeable fraction of implanted He atoms in this experiment is dissolved in the matrix.

Summing up, the following trends characterize swelling and He inventory kinetics as a function of implantation fluence in our experiments:

(i) The most important contributor to both swelling and He inventory is the population of bubbles on grain boundaries. The increase of fluence increases the relative importance of bubbles in the bulk, which become competitive with the grain boundary bubbles by the highest fluence achieved. While the helium capture efficiency in bubbles on extended defects and second phase precipitates tends to saturate with fluence, growing from $1 \times 10^{15} \text{ cm}^{-2}$ to $1 \times 10^{16} \text{ cm}^{-2}$, bubbles in the bulk become more and more important as sinks for helium introduced by ion implantation.

(ii) Bubbles on dislocations and second phase particles (carbides and oxides) provide relatively modest individual contributions to either swelling, or He inventory. However, when put together, these bubble families provide the contribution comparable to the joint contribution of bubbles on grain boundaries and in the bulk, though with the increase of fluence the importance of this contribution tends to decrease.

(iii) The relatively modest contribution of Y_2O_3 nanoparticles to the helium inventory is primarily due to the low number density of nanoparticles. As a result, even noticeably larger bubbles attached to oxide nanoparticles are unable to compete for helium atoms with the grain boundary bubbles.

Table 3.7. The average sizes and volume number densities of bubbles, swelling, V/He ratio and retained He fraction associated with different bubble populations in ODS-EUROFER steel implanted with He⁺ ions at the flux of 5×10¹¹ cm⁻²s⁻¹ to different fluencies at T=823 K.

1×10¹⁵ cm⁻², 1.25×10³ appm	D_c^k (10⁻⁹ m)	N_V^k (10²² m⁻³)	S_k (%)	V/He_k	F_{He}^k (appm)	F_{He}^k (%)
Grain boundaries	3.04±0.23	3.64±0.75	0.053±0.013	1.52	355±88	28.3±7.0
Dislocations	2.80±0.17	1.95±0.24	0.022±0.004	1.47	153±25	12.2±2.0
Carbides	2.72±0.27	1.84±0.18	0.019±0.006	1.46	134±42	10.7±3.4
Y₂O₃	6.04±0.60	1.00±0.10	0.028±0.009	2.03	141±44	11.2±3.5
Volume	2.68±0.20	1.92±0.22	0.019±0.003	1.45	134±24	10.7±1.9
Total		10.35± 2.12	0.143± 0.045		917±290	73.1±23.1
5×10¹⁵ cm⁻², 6.25×10³ appm	D_c^k (10⁻⁹ m)	N_V^k (10²² m⁻³)	S_k (%)	V/He_k	F_{He}^k (appm)	F_{He}^k (%)
Grain boundaries	4.79±0.35	5.32±1.44	0.306±0.086	1.83	1686±474	26.9±7.6
Dislocations	4.69±0.24	2.00±0.23	0.108±0.012	1.81	602±69	9.6±1.1
Carbides	3.55±0.36	2.13±0.21	0.050±0.016	1.61	313±99	5.0±1.6
Y₂O₃	8.11±0.81	1.00±0.10	0.098±0.031	2.35	422±133	6.7±2.1
Volume	4.36±0.23	2.81±0.46	0.122±0.020	1.76	699±115	11.2±1.8
Total		13.26±3.59	0.684± 0.216		3722±1177	59.4± 18.8
1×10¹⁶ cm⁻², 12.5×10³ appm	D_c^k (10⁻⁹ m)	N_V^k (10²² m⁻³)	S_k (%)	V/He_k	F_{He}^k (appm)	F_{He}^k (%)
Grain boundaries	6.05±0.53	5.45±0.59	0.632±0.085	2.03	3132±420	25.0±3.4
Dislocations	5.23±0.56	2.00±0.20	0.149±0.029	1.90	793±152	6.3±1.2
Carbides	3.96±0.40	2.21±0.22	0.072±0.023	1.69	429±136	3.4±1.1
Y₂O₃	9.46±0.95	1.00±0.10	0.192±0.061	2.55	758±240	6.0±1.9
Volume	5.37±0.75	5.40±1.24	0.437±0.151	1.92	2289±790	18.3±6.3
Total		16.06± 3.68	1.482± 0.484		7401±2340	59.0±18.7

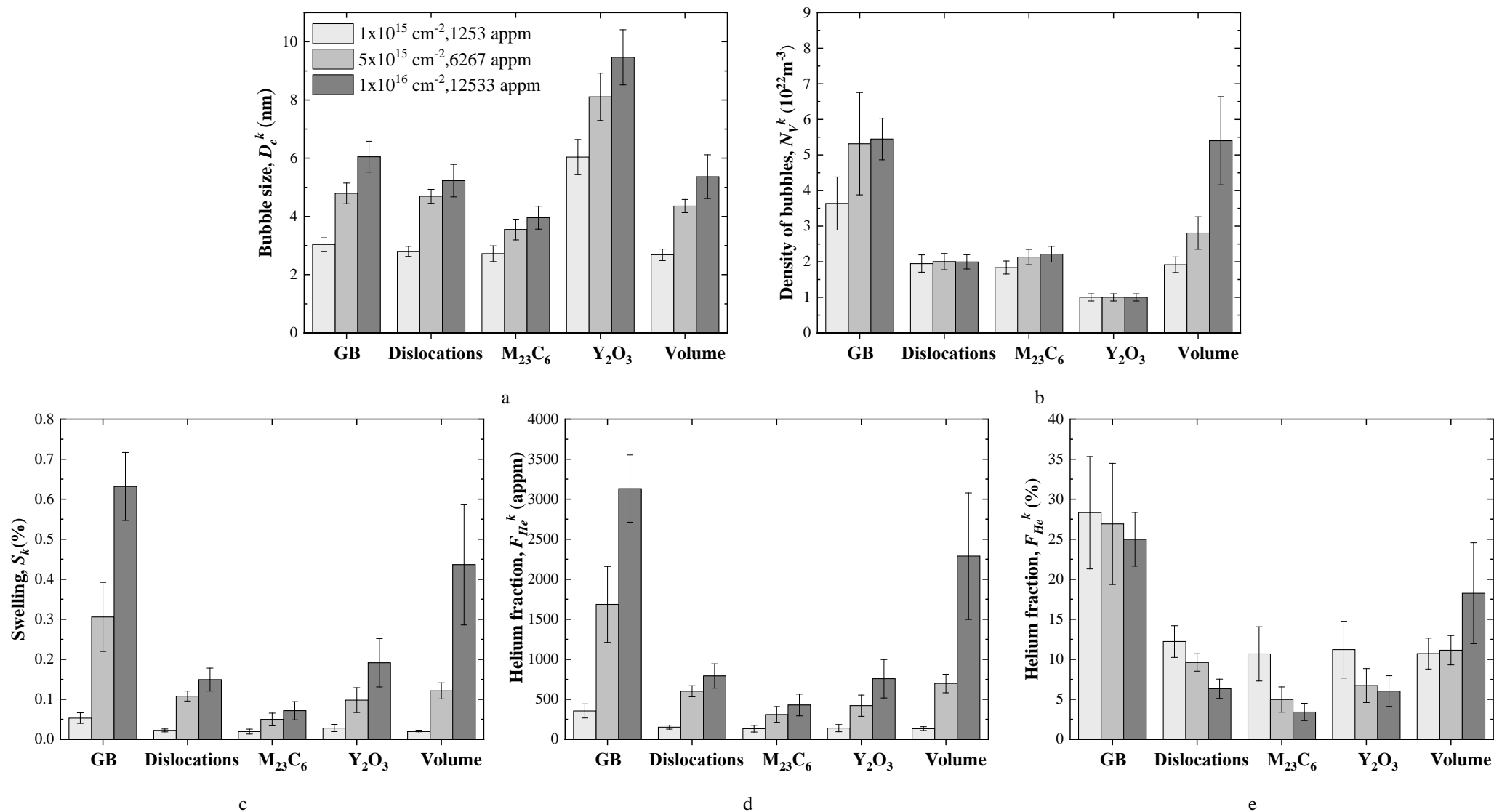


Fig. 3.19. Graphical representation of the data from Table 3.7. Shades of grey used to differentiate between the data for different fluences are explained in the legend located in panel (a).

3.1.2.5.3 Flux dependence of contributions from different bubble families to swelling and helium inventory

Table 3.8 and Fig. 3.20 summarize the results for the bubble number density N_V^k , swelling contribution S_k , the average ratio of vacancies to He atoms in the bubbles (V/He), and the fraction of accumulated helium F_{He}^k separately for each bubble family at three different fluxes.

As can be concluded from the obtained data, the increase of the flux is accompanied with the decrease of the average bubble size and the increase of bubble number density for all families of bubbles. While the size decrease is in all cases quite moderate, the sensitivity of bubble number density to flux variation depends on the bubble location. The number densities of bubbles on grain boundaries and dislocations demonstrate less than 2-fold increase, whereas the number density of bubbles in the bulk increases by a factor of ~ 8 . As a result, the overall picture of bubble distribution visibly changes upon transition from the lowest to the highest flux. While at the lowest flux the bubbles are preferentially located on structural defects (grain boundaries and dislocations), bubbles in the bulk dominate at the highest one. One can also notice overall increase of the bubble number density, which grows from $N_V \approx 13 \times 10^{22} \text{ m}^{-3}$ to $N_V \approx 37 \times 10^{22} \text{ m}^{-3}$ with flux variation from the lowest to the highest value used.

Following the observed variations of the bubble microstructure, the increase of implantation flux results in the suppression of the overall swelling from $\sim 0.7\%$ down to $\sim 0.4\%$ with the flux increase from $5 \times 10^{11} \text{ cm}^{-2}\text{s}^{-1}$ to $5 \times 10^{12} \text{ cm}^{-2}\text{s}^{-1}$. When considered individually for each bubble family, the swelling contributions from bubbles associated with microstructural defects decrease with the increasing flux. The swelling caused by the grain boundary bubbles falls down most pronouncedly, from $S_{GB} = 0.31\%$ down to 0.07% . Swelling contributions from bubbles on dislocations and carbide precipitates fall down to $\sim 0.02\%$ from, respectively, $\sim 0.1\%$ and $\sim 0.05\%$. The contribution from bubble population on oxide particles remains practically unchanged at the level of 0.1% . In contrast, swelling from the bubbles in the bulk increases with the flux increase from $S_V = 0.12\%$ to 0.21% . As a result, variation of flux noticeably changes the relative importance of bubble families in terms of their importance for swelling. While at the lowest flux the largest contribution to swelling is due to grain boundary bubbles, the strongest contributors at the highest flux become bubbles in the bulk.

The difference in the swelling contribution variation with the implantation flux for different bubble populations reflects the competition between the trends for bubble size decrease and the number density decrease. The notable increase of swelling contribution for bubbles in the bulk is mainly due to the sharp increase of their number density with the increase of the flux. Swelling contribution from bubbles attached to nanoparticles changes only slightly because the number density is independent of the flux, while the average size demonstrates only a minor reduction with increasing implantation flux (see Fig. 3.12). For the other bubble families, the trend for size reduction dominates, resulting in the swelling contribution decrease.

The trends for the average V/He ratio variation follow those for bubble sizes. The largest value of V/He ~ 2.30 is estimated for bubbles on oxide particles, which remain the largest whatever the flux. Bubbles associated with the other microstructural components and bubbles in the bulk demonstrate the decrease of V/He ratio (by a factor of 1.4) with flux increase.

At the lowest flux used, the maximal share of helium ($\sim 27\%$) is accumulated in grain boundary bubbles. Bubbles on dislocations and in the bulk accumulate $\sim 10\%$ of all the implanted helium each. Bubbles on carbides and Y_2O_3 nanoparticles accumulate, respectively $\sim 5.0\%$ and $\sim 6.7\%$ of implanted He. The increase of flux significantly decreases the share of implanted helium accumulated in bubbles on grain boundaries (down to $\sim 8.5\%$ at the highest flux) and on dislocations and carbides (down to $\sim 2-1\%$ each). At the same time, the share of implanted He captured by bubbles in the bulk increases with the implantation flux, reaching at the highest flux $\sim 23\%$. However, this increase does not compensate for the

reduction in He inventory in the other bubble populations and the total estimated share of implanted helium accumulated in bubbles visible in TEM decreases from ~59% at the lowest flux to ~41% at the highest one.

The observed trends in swelling and helium redistribution accompanying the variation of implantation flux can be summarized as follows:

(i) The increase of the implantation flux results in the increase of number density and the decrease of the average size of all bubble populations, both in the bulk and on structural defects. As a result, the total swelling and the relative share of implanted helium accumulated in the bubbles decrease as the flux grows.

(ii) At the microstructural level, the increase of implantation flux is manifested in the transition from preferential He accumulation in bubbles associated with structural defects to bubbles in the grain bulk. While at the lowest used flux of $5 \times 10^{11} \text{ cm}^{-2} \text{ s}^{-1}$ the largest contribution to swelling and the largest share of accumulated helium are provided by the bubbles on grain boundaries, at the highest fluence of $5 \times 10^{12} \text{ cm}^{-2}$ both swelling and helium accumulation are largely controlled by bubbles in the grain bulk.

(iii) The contributions to swelling and helium accumulation from bubbles attached to Y_2O_3 nanoparticles are relatively minor and not too sensitive to the flux variation. For all the studied fluxes this bubble population provides swelling of ~0.1% and captures ~6% of all the accumulated He at the achieved fluence of $5 \times 10^{15} \text{ cm}^{-2}$.

(iv) The efficiency of He capture in bubbles tends to decrease with increasing flux. Thus, the share of implanted He captured in invisible sinks grows from ~40% to ~60% between the lowest and the highest fluxes achieved.

Table 3.8. The average sizes and volume number densities of bubbles, swelling, V/He ratio and retained He fraction associated with different bubble populations in ODS-EUROFER steel implanted with He⁺ ions at three different fluxes to the fluence of 5×10¹⁵ cm⁻² at T=823 K.

5×10¹¹ cm⁻²s⁻¹,6.25×10³ appm	D_c^k (10⁻⁹ m)	N_V^k (10²² m⁻³)	S_k (%)	V/He_k	F_{He}^k (appm)	F_{He}^k (%)
Grain boundaries	4.79±0.35	5.32±1.44	0.306±0.086	1.83	1686±474	26.9±7.6
Dislocations	4.69±0.24	2.00±0.23	0.108±0.012	1.81	602±69	9.6±1.1
Carbide	3.55±0.36	2.13±0.21	0.050±0.016	1.61	313±99	5.0±1.6
Y₂O₃	8.11±0.81	1.00±0.10	0.098±0.031	2.35	422±133	6.7±2.1
Volume	4.36±0.23	2.81±0.46	0.122±0.020	1.76	699±115	11.2±1.8
Total		13.26±3.59	0.684± 0.216		3722±1177	59.4± 18.8
1×10¹² cm⁻²s⁻¹,6.25×10³ appm	D_c^k (10⁻⁹ m)	N_V^k (10²² m⁻³)	S_k (%)	V/He_k	F_{He}^k (appm)	F_{He}^k (%)
Grain boundaries	3.37±0.28	7.43±1.04	0.149±0.030	1.58	948±193	15.1±3.1
Dislocations	3.32±0.37	2.64±0.36	0.051±0.014	1.57	324±87	5.2±1.4
Carbide	2.66±0.27*	2.13±0.21*	0.021±0.007*	1.44*	146±46*	2.3±0.7*
Y₂O₃	7.96±0.80	1.00±0.10	0.091±0.029	2.33	395±125	6.3±2.0
Volume	3.28±0.23	8.80±2.61	0.162±0.052	1.56	1047±333	16.7±5.3
Total		22.0±6.53	0.474±0.151		2860±910	45.6±14.5
5×10¹² cm⁻²s⁻¹,6.25×10³ appm	D_c^k (10⁻⁹ m)	N_V^k (10²² m⁻³)	S_k (%)	V/He_k	F_{He}^k (appm)	F_{He}^k (%)
Grain boundaries	2.51±0.18	8.91±1.44	0.074±0.016	1.42	531±114	8.5±1.8
Dislocations	2.51±0.26	2.83±0.40	0.023±0.006	1.41	165±45	2.6±0.7
Carbide	2.04±0.20*	2.13±0.21*	0.010±0.003*	1.32*	73±23*	1.2±0.4*
Y₂O₃	7.78±0.78	1.00±0.10	0.083±0.026	2.30	362±114	5.8±1.8
Volume	2.65±0.16	21.65±9.35	0.210±0.093	1.44	1459±646	23.3±10.3
Total		36.52±15.76	0.400±0.177		2590±1147	41.4±18.3

* Approximately estimated values

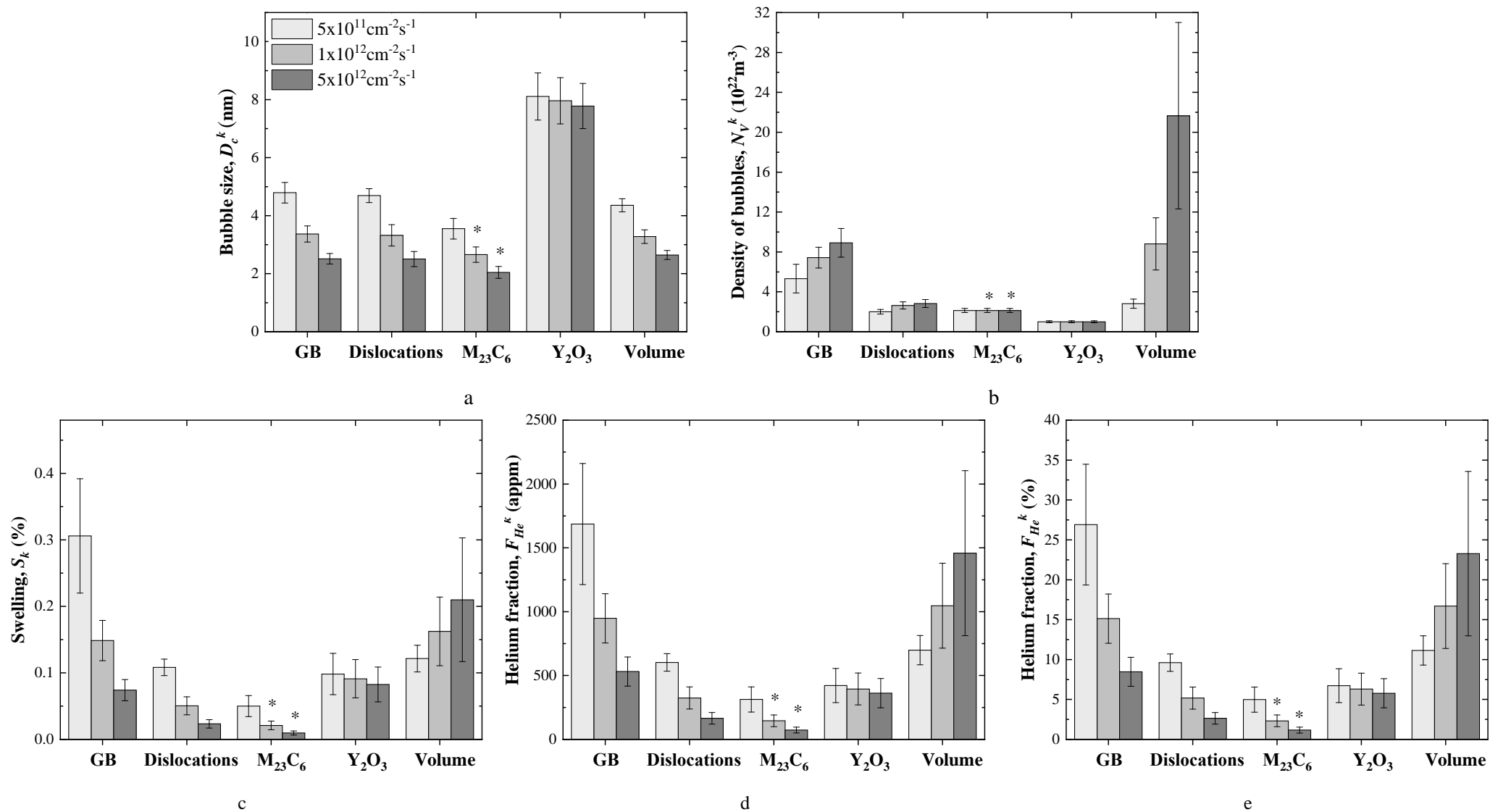


Fig. 3.20. Graphical representation of the data from Table 3.8. Shades of grey used to differentiate between the data for different fluxes are explained in the legend located in panel (a).

3.1.2.5.4 Temperature dependence of contributions from different bubble families to swelling and helium inventory

Table 3.9 and Fig. 3.21 summarize the results for the bubble number density N_v^k , swelling contribution S_k , the average ratio of vacancies to He atoms in the bubbles, and the fraction of accumulated helium F_{He}^k separately for each bubble family at temperatures of 723, 823 and 923 K.

The general trends observed for all bubble families with the increase of temperature are the increase of the average bubble size and the decrease the bubble number densities. Since the bubble size variation with the implantation temperature has already been discussed in section 3.1.2.4, here we consider only the number density variations.

The total bubble volumetric number density decreases from $N_v \approx 19 \times 10^{22} \text{ m}^{-3}$ down to $N_v \approx 12 \times 10^{22} \text{ m}^{-3}$ as the temperature increases from 723 to 923 K. The largest contribution to the total bubble number density at all the studied temperatures comes from bubbles on grain boundaries; their number density moderately decreases from $\sim 7.6 \times 10^{22} \text{ m}^{-3}$ down to $\sim 5.0 \times 10^{22} \text{ m}^{-3}$ as the temperature increases within the studied temperature range. The number density of bubbles associated with dislocations is weakly sensitive to temperature, decreasing from $\sim 2.5 \times 10^{22} \text{ m}^{-3}$ down to $\sim 2.0 \times 10^{22} \text{ m}^{-3}$ in the same temperature range. The most pronounced is the number density decrease for bubbles in the bulk, from $\sim 6.0 \times 10^{22} \text{ m}^{-3}$ down to $\sim 2.0 \times 10^{22} \text{ m}^{-3}$. Due to the lack of experimental data for both border temperatures, no trend could be obtained for the number density of bubbles on carbide particles, but it is expected that it does not differ much from that found at 823 K, that is, $\sim 2.0 \times 10^{22} \text{ m}^{-3}$.

The estimated total swelling induced by all bubbles grows with the temperature in the studied temperature range, changing from $\sim 0.5\%$ at 723 K to $\sim 0.9\%$ at 923 K. The same trend is demonstrated by all bubble populations, associated with microstructural defects. The main contribution to swelling comes from bubbles on grain boundaries; it grows from $\sim 0.2\%$ to $\sim 0.4\%$ between the lowest and the highest studied temperatures. At somewhat faster rate increase contributions to swelling from bubbles on dislocations (from $\sim 0.06\%$ to $\sim 0.13\%$), oxide particles (from $\sim 0.1\%$ to $\sim 0.13\%$) and carbide precipitates (from $\sim 0.02\%$ to $\sim 0.08\%$). Only bubbles in the bulk demonstrate the inverse trend of slightly decreasing swelling contribution with temperature increase. As a result, while at 723 K the swelling from bubbles in the bulk ($\sim 0.12\%$) is comparable to that from bubbles on grain boundaries, at 923 K it decreases down to the level typical for other bubble populations, $\sim 0.1\%$.

At the lowest T=723 K, similar contribution to swelling is provided by bubbles associated with grain boundaries $S_{CB} = 0.19\%$ and grain bulk $S_v = 0.12\%$. Slightly lower value of swelling at the same temperature is reported for the bubbles at the oxide nanoparticle/matrix interfaces $S_p = 0.09\%$. The lowest swelling values are found for the bubble population associated with dislocations $S_d \approx 0.06\%$ and carbides $S_c \approx 0.02\%$.

Swelling increase for bubbles on extended defects and oxide particles results from the noticeable growth of bubble average sizes. In contrast, for bubbles in the bulk the growth of average size is counterbalanced by the decreasing number density and thus the contribution of this bubble population to swelling remains weakly sensitive to temperature variation.

The ratio V/He is the highest for bubbles associated with nanoparticles (V/He=2.19 at T=723 K and V/He=2.59 at T=923 K), which is quite natural having in mind that these bubbles are noticeably larger than those of all other bubble populations, whatever the temperature. However, for all other bubble families the ratio V/He also increases with temperature due to the average bubble size growth.

Similar to swelling, the temperature increase from 723 to 923 K results in notable increase (from $\sim 48\%$ to $\sim 69\%$) for the estimated share of implanted He atoms that is accumulated in the visible bubbles. The largest part of He atoms is always captured in grain boundary bubbles, which accommodate from

~20% of all He at 723 K to ~33% at 923 K. Bubbles on dislocations and precipitates accumulate noticeably less implanted He atoms, but the captured He share also increases with temperature increase, namely, from ~6% to ~11% for bubbles on dislocations, from ~7% to ~8.5% for bubbles on oxide nanoparticles and from ~3% to ~7% for bubbles on carbides. In contrast, the share of helium captured within bubbles in the bulk somewhat decreases from ~13% down to ~10% when implantation temperature grows from 723 K to 923 K.

The observed trends in swelling and helium redistribution over different bubble families in reply to the variation of implantation temperature in the studied range of 723-923 K can be summarized as follows:

(i) Both swelling and helium inventory in the bubbles noticeably grow in reply to the implantation temperature increase.

(ii) For all temperatures, the grain boundary bubbles give the largest contributions to both the swelling and the helium inventory, which grow with the increase of temperature. A similar trend is observed for bubbles on other extended defects and nanoparticles, though their individual contributions are remarkably lower than those from grain boundary bubbles.

(iii) The competing trend of growing bubble average size against the bubble density decrease with the increase of temperature results in relatively weak temperature sensitivity of contributions to both swelling and helium inventory from bubbles in the bulk. Nonetheless, both contributions decrease with the temperature increase, contrary to the overall trend.

(iv) Though bubbles on oxide particles are pronouncedly larger than bubbles of other populations, their contribution to swelling and He accumulation remains well below that from grain boundary bubbles and comparable to that from all other bubble families. The reason for that is the relatively low number density of bubbles, which is determined by the concentration of oxide particles. Temperature increase decreases the relative importance of oxide nanoparticles in helium accumulation and swelling.

Table 3.9. The average sizes and volume number densities of bubbles, swelling, V/He ratio and retained He fraction associated with different bubble populations in ODS-EUROFER steel implanted with He⁺ ions at the flux of 5×10¹¹ cm⁻²s⁻¹ to the fluence of 5×10¹⁵ cm⁻² at different temperatures.

723 K, 6.25×10³ appm	D_c^k (10 ⁻⁹ m)	N_V^k (10 ²² m ⁻³)	S_k (%)	V/He _k	F_{He}^k (appm)	F_{He}^k (%)
Grain boundaries	3.62±0.19	7.59±1.19	0.188±0.031	1.55	1230±201	19.6±3.2
Dislocations	3.49±0.26	2.48±0.30	0.055±0.009	1.53	368±63	5.9±1.0
Carbide	2.80±0.28*	2.13±0.21*	0.024±0.008*	1.39*	166±53*	2.7±0.8*
Y₂O₃	8.01±0.80	1.00±0.10	0.093±0.029	2.19	429±136	6.9±2.2
Volume	3.38±0.39	5.99±0.80	0.122±0.034	1.51	809±226	12.9±3.6
Total		19.19±3.01	0.482±0.153		3002±950	48.0±15.2
823 K, 6.25×10³ appm	D_c^k (10 ⁻⁹ m)	N_V^k (10 ²² m ⁻³)	S_k (%)	V/He _k	F_{He}^k (appm)	F_{He}^k (%)
Grain boundaries	4.79±0.35	5.32±1.44	0.306±0.086	1.83	1686±474	26.9±7.6
Dislocations	4.69±0.24	2.00±0.23	0.108±0.012	1.81	602±69	9.6±1.1
Carbide	3.55±0.36	2.13±0.21	0.050±0.016	1.61	313±99	5.0±1.6
Y₂O₃	8.11±0.81	1.00±0.10	0.098±0.031	2.35	422±133	6.7±2.1
Volume	4.36±0.23	2.81±0.46	0.121±0.020	1.76	699±115	11.2±1.8
Total		13.26±3.59	0.684±0.216		3722±1177	59.4±18.8
923 K, 6.25×10³ appm	D_c^k (10 ⁻⁹ m)	N_V^k (10 ²² m ⁻³)	S_k (%)	V/He _k	F_{He}^k (appm)	F_{He}^k (%)
Grain boundaries	5.40±0.44	4.99±0.59	0.411±0.059	2.03	2037±292	32.5±4.7
Dislocations	5.05±0.42	1.98±0.30	0.134±0.024	1.97	686±124	11.0±2.0
Carbide	4.11±0.41*	2.13±0.21*	0.078±0.025*	1.80*	437±138*	7.0±2.2*
Y₂O₃	8.73±0.87	1.00±0.10	0.135±0.043	2.59	524±166	8.4±2.6
Volume	4.97±0.52	1.96±0.38	0.125±0.032	1.96	644±164	10.3±2.6
Total		12.06±2.34	0.883±0.279		4328±1369	69.2±21.8

* Approximately estimated values

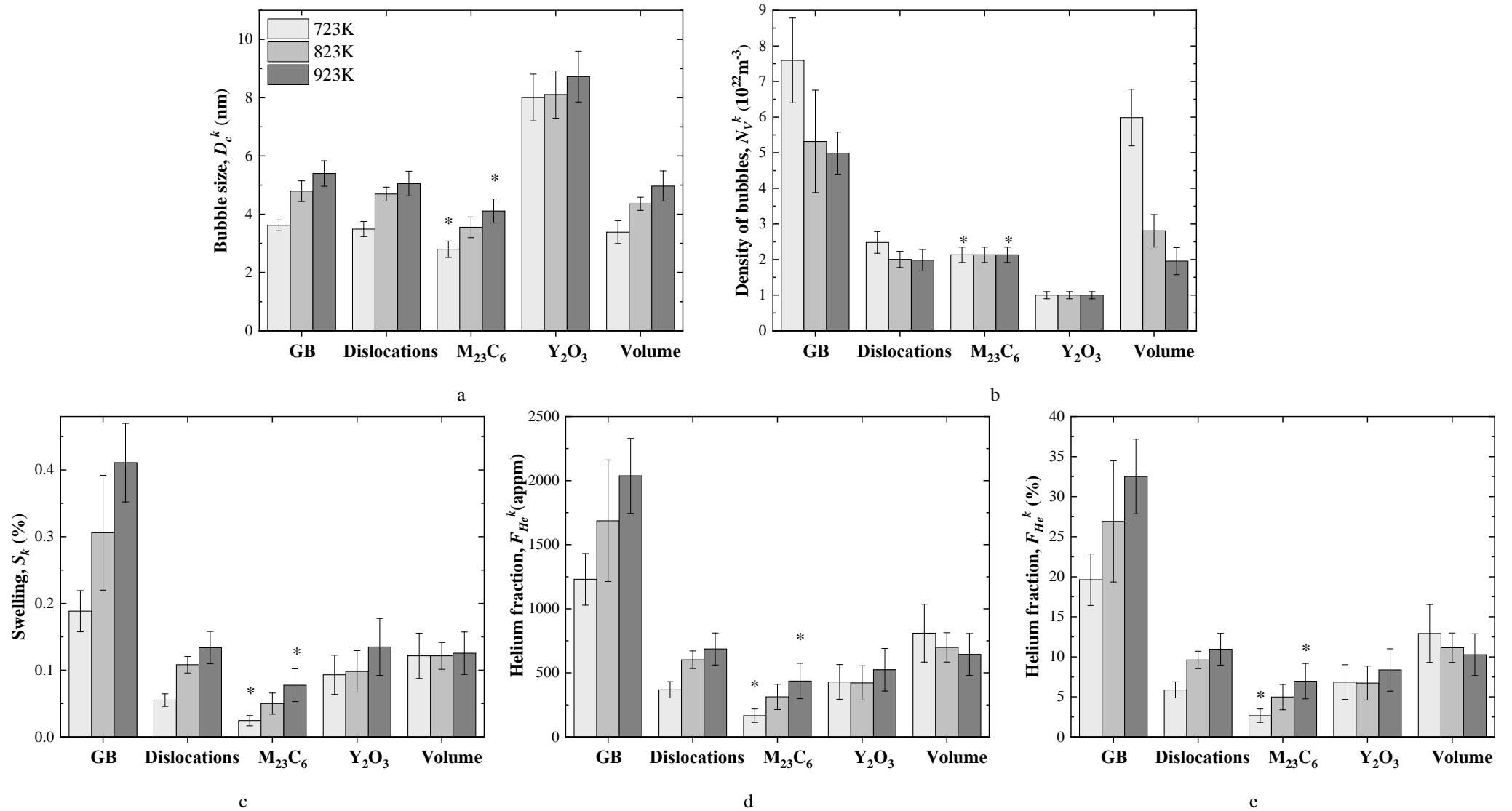


Fig. 3.21. Graphical representation of the data from Table 3.9. Shades of grey used to differentiate between the data for different temperatures are explained in the legend in panel (a).

3.1.2.5.5 General trends of swelling and helium inventory variations in reply to implantation condition variations

Swelling is one of the main reasons of dimensional instability of irradiated solids and, as such, is observed for very different irradiation conditions and can be due to very different reasons. The most typical for power plant reactors is the so-called void swelling, which is manifested at the microstructural level in the growth of empty cavities (voids). In this case, the total increase of the material volume can be shown to be practically coincident with the total volume of all voids. Correspondingly, the swelling estimation approach based on the evaluation of the void average size and number density from TEM data gives quite reliable estimate for the microscopic swelling in spite of the fact that TEM is able to resolve only cavities larger than a certain threshold size of, typically, ~ 1 nm. The situation sharply changes, when the radiation damage production by fast particles is accompanied with the efficient accumulation of noble gas (most often – helium) atoms, either created in transmutation reactions, or directly introduced by implantation (as is the case in this study). In many void swelling resistant metals, including ferritic-martensitic steels, the accumulation of helium under irradiation is accompanied with its precipitation in small cavities that are filled with gas atoms. In contrast to voids that grow due to the preferential accumulation of vacancies created by irradiation, the growth of gas-filled cavities (bubbles) is controlled by the number of gas atoms captured by the bubble. The bubble sizes are seldom very much larger than the TEM observation threshold and there always exists a certain amount of gas atoms captured in small gas-vacancy clusters invisible in TEM. When the number of gas atom contained in the ‘invisible’ clusters is comparable to that accumulated in the visible bubbles, a straightforward evaluation of the total cavity volume can introduce non-negligible underestimation of the true volume expansion of the material.

The estimates of helium fraction accumulated by bubbles, as given in Tables 3.7-3.9, indicate that none of the applied implantation regimes provides close to 100 % capture of implanted helium by the whole bubble population and so a noticeable share of implanted He atom should be located in small He-vacancy clusters invisible by TEM. The fact that some amount of helium remains inside ODS-EUROFER in some features invisible by TEM technique does not look surprising, taking into account the results of Ref. [23], where helium desorption from polycrystalline *bcc* iron implanted with 10 keV He⁺ ions started only at T=1073 K. In some implantation regimes, for instance, for the helium implantation with high flux 5×10^{12} cm⁻²s⁻¹ or at the temperature of 723 K, the share of implanted helium that is accumulated by all bubbles was estimated to be even less than 50% of the implanted amount. The swelling contribution from the small He-vacancy clusters was not reflected in the numbers given for the total swelling in Tables 3.7-3.9. In order to give a feeling for the level of this underestimation, the total swelling values that include contributions from both bubbles and He-vacancy clusters were calculated for all implantation regimes used. In the calculations we assumed that He atoms captured in small He-vacancy clusters occupy on the average one vacancy, which is a very conservative estimate. Cumulative values of V/He ratio, He fraction corresponding to bubbles, swelling estimated by TEM data (bubbles) and total swelling including the contribution from helium atoms captured in small vacancy clusters are shown in Table 3.10. Fig. 3.22 gives a visual presentation allowing to get a feeling of the relative importance of visible bubbles and invisible He-vacancy clusters in the total swelling.

As can be concluded based on the estimates, the relative contribution of invisible clusters to swelling changes only weakly with increasing fluence (remaining at the level of 20-25%) at the fixed implantation flux and temperature, but is quite sensitive to flux and temperature variations, increasing from $\sim 25\%$ to $\sim 50\%$ with the increase of implantation flux and decreasing from $\sim 30\%$ down to $\sim 20\%$ with the increase of implantation temperature within the ranges studied. In all considered cases, the swelling underestimation due to the neglect of helium dissolved in small vacancy clusters is non-negligible. As a general trend, one can expect that the application of the TEM image-based estimates of bubble parameters can be quite inaccurate in any experimental studies performed at low temperatures and using too high rates of He production/introduction in the matrix.

Table 3.10. Cumulative values of V/He ratio, retained He fraction, swelling estimated by TEM data and total swelling that includes contribution from helium dissolved in small He-vacancy clusters.

Fluence variation	$\langle V/He \rangle$	F_{He} (appm)	F_{He} (%)	S_{TEM} (%)	S_{total} (%)
$1 \times 10^{15} \text{ cm}^{-2}$, $F_{He_total} = 1.25 \times 10^3$ appm	1.59	917 ± 290	73.1 ± 23.1	0.143 ± 0.045	0.176 ± 0.056
$5 \times 10^{15} \text{ cm}^{-2}$, $F_{He_total} = 6.25 \times 10^3$ appm	1.87	3722 ± 1177	59.4 ± 18.8	0.684 ± 0.216	0.938 ± 0.297
$1 \times 10^{16} \text{ cm}^{-2}$, $F_{He_total} = 12.5 \times 10^3$ appm	2.02	7401 ± 2340	59.0 ± 18.7	1.482 ± 0.484	1.995 ± 0.689
Flux variation					
$5 \times 10^{11} \text{ cm}^{-2} \text{ s}^{-1}$, $F_{He_total} = 6.25 \times 10^3$ appm	1.87	3722 ± 1177	59.4 ± 18.8	0.684 ± 0.216	0.938 ± 0.297
$1 \times 10^{12} \text{ cm}^{-2} \text{ s}^{-1}$, $F_{He_total} = 6.25 \times 10^3$ appm	1.70	2860 ± 910	45.6 ± 14.5	0.474 ± 0.151	0.814 ± 0.259
$5 \times 10^{12} \text{ cm}^{-2} \text{ s}^{-1}$, $F_{He_total} = 6.25 \times 10^3$ appm	1.58	2590 ± 1147	41.4 ± 18.3	0.400 ± 0.177	0.767 ± 0.340
Temperature variation					
723 K, $F_{He_total} = 6.25 \times 10^3$ appm	1.63	3002 ± 950	48.0 ± 15.2	0.482 ± 0.153	0.808 ± 0.256
823 K, $F_{He_total} = 6.25 \times 10^3$ appm	1.87	3722 ± 1177	59.4 ± 18.8	0.684 ± 0.216	0.938 ± 0.297
923 K, $F_{He_total} = 6.25 \times 10^3$ appm	2.07	4328 ± 1369	69.2 ± 21.8	0.883 ± 0.279	1.077 ± 0.340

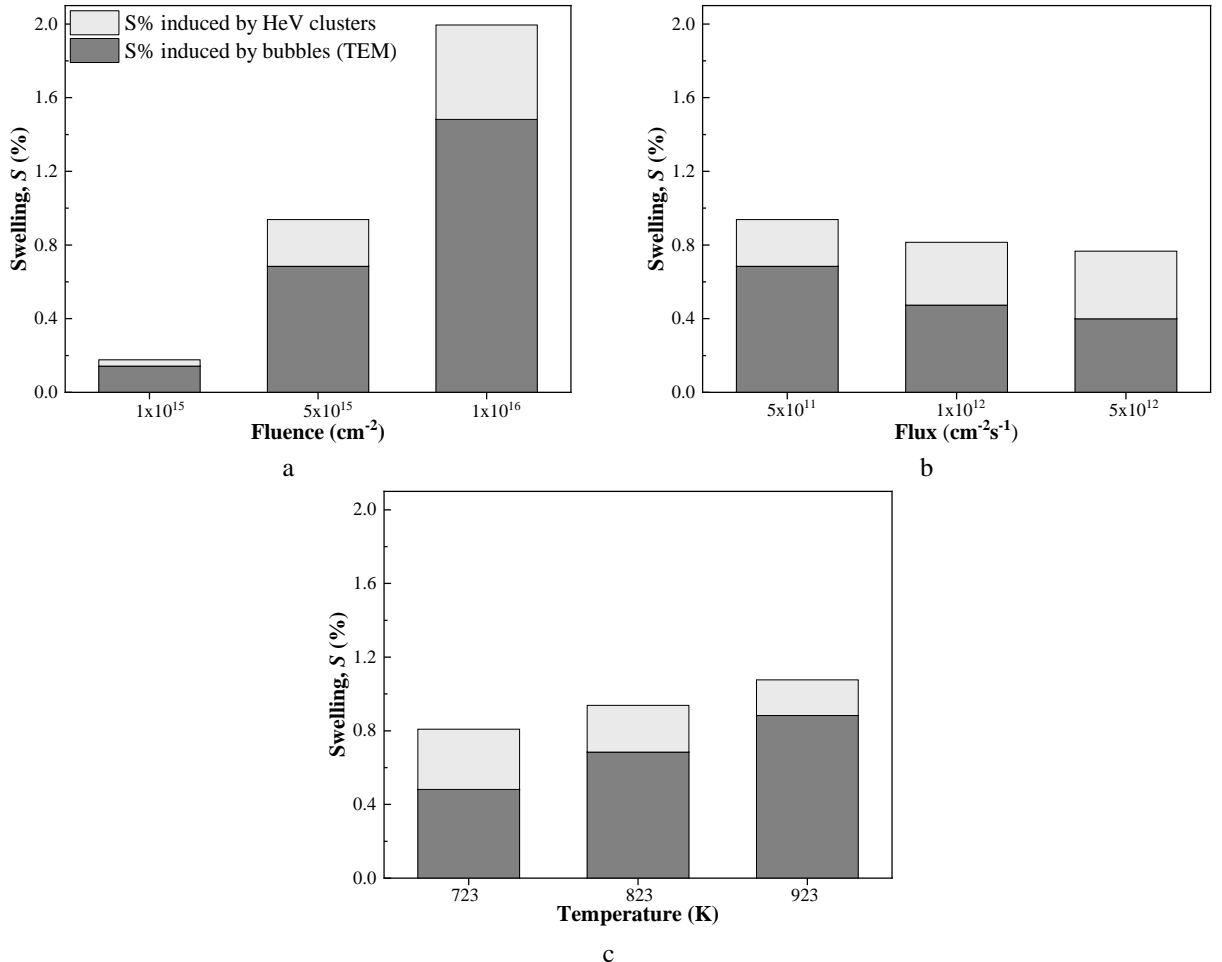


Fig. 3.22. Relative contributions to total swelling from bubbles and HeV clusters for (a) fluence, (b) flux, and (c) temperature variation conditions.

3.1.2.6 Swelling and helium inventory in ODS-EUROFER steel after post-implantation annealing

Helium pre-implantation at room temperature followed by post-implantation annealing (PIA) is a common way to simulate He accumulation in radiation materials science. However, it is not evident that this approach is suitable in the case of such complex material as ODS-EUROFER steel. That is, the bubble populations developed after a two-stage treatment including room temperature He⁺ implantation followed by PIA is not necessarily representative of the bubble structures developed during high-temperature He⁺ implantation. The goal of this section is to compare the general trends of microstructural evolution in ODS-EUROFER steel during high temperature He⁺ implantation with the results of an experiment performed using a combination of room temperature He⁺ pre-implantation and PIA (referred below as low T implantation regime followed by PIA). Similarly to the preceding discussion, the data analysis will address different bubble families separately.

Post implantation annealing of ODS-EUROFER samples pre-implanted at RT with He⁺ ions to the fluence of $5 \times 10^{15} \text{ cm}^{-2}$ was performed in vacuum for 90 minutes at 823 K. Results of bubble population analysis, as well as calculated swelling and helium fraction values, are compared for low T implantation regime followed by PIA and high temperature implantation regime ($T=823 \text{ K}$, flux $1 \times 10^{12} \text{ cm}^{-2}\text{s}^{-1}$, fluence $5 \times 10^{15} \text{ cm}^{-2}$). Typical BF TEM through-focus images of ODS-EUROFER samples after low T implantation followed by PIA are shown in Fig. 3.23.

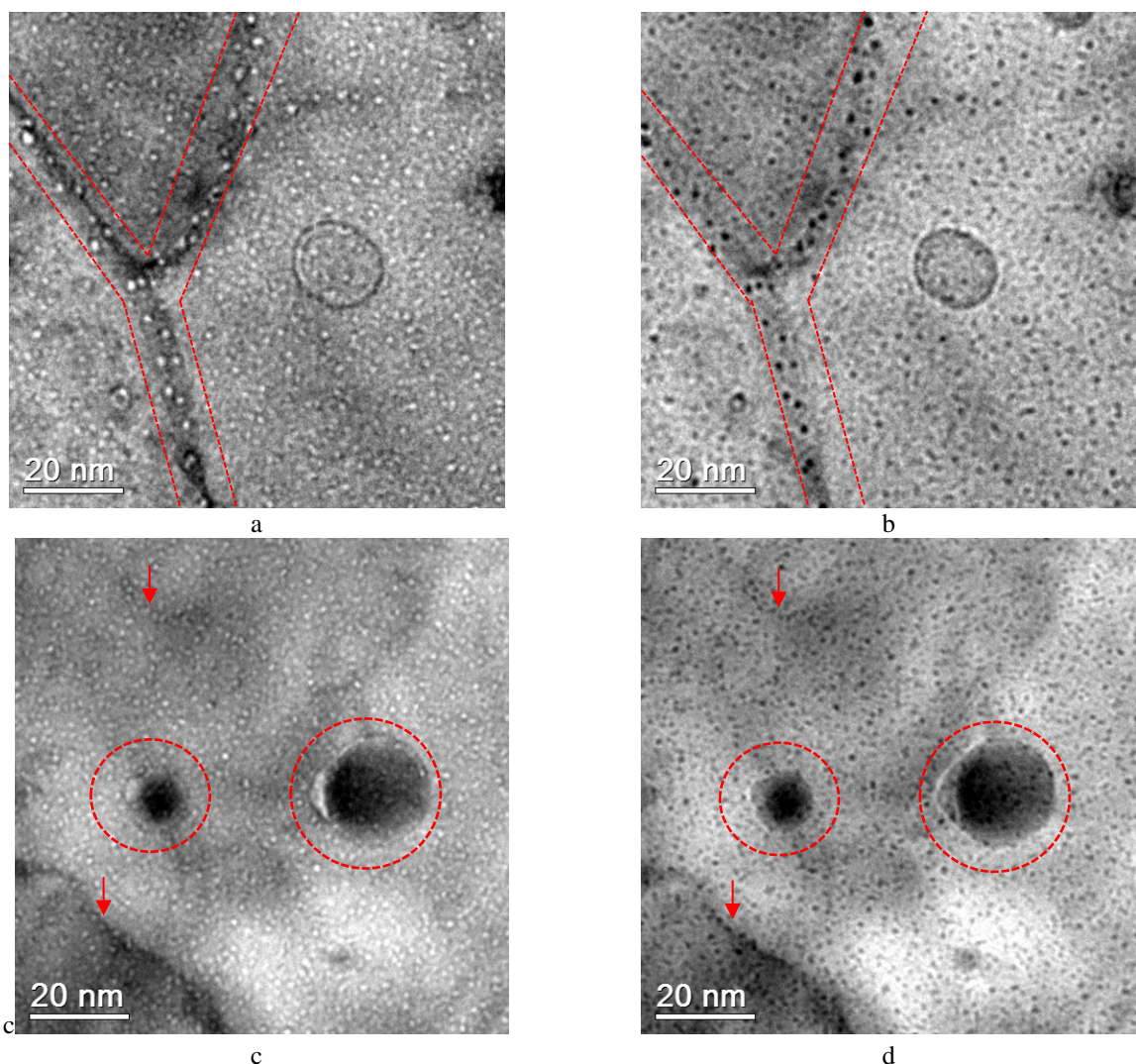


Fig. 3.23. Microstructure of ODS-EUROFER steel implanted with 10 keV He⁺ ions with a flux of $5 \times 10^{11} \text{ cm}^{-2}\text{s}^{-1}$ to the fluence of $5 \times 10^{15} \text{ cm}^{-2}$ at room temperature and subsequently annealed at 823 K for 90 minutes. BF TEM imaging conditions: (a,c) $\sim 0.8 \mu\text{m}$ underfocus and (b,d) $\sim 0.8 \mu\text{m}$ overfocus.

Like in the high-temperature implantation case, the implanted He is trapped in the bubbles decorating different microstructural defects (grain boundaries, see Fig. 3.23(a,b), dislocations and precipitates, see Fig. 3.23(c,d)), as well as in the bubbles in the grain bulk. As can be seen in Fig. 3.23(a,b), bubbles associated with grain boundaries look, on the average, slightly larger than those in the bulk and on dislocations. Fig. 3.23(c,d) evidences that, similar to high-temperature implantation, bubbles attached to nano-oxides are noticeably larger than those belonging to all other bubble populations and the bubble sizes seem to correlate with the sizes of the host nano-oxide particles. But, as compared to TEM images obtained after high temperature implantation, much higher density of tiny bubbles in the bulk can be immediately noticed.

In order to extract quantitative information from the TEM data, we use the same approach as described in section 3.1.2.1. Like before, we start with bubbles associated with nano-oxides and determine their average size $\langle D_c^p \rangle$ from the measured dependence $D_c^p(D_p)$ shown in Fig. 3.24. The figure shows also the power law fitting of the observed set of points $D_c^p(D_p)$ and the reference value $\langle D_c^p \rangle$. In addition, the $D_c^p(D_p)$ fitting curve from Fig. 3.13 obtained for the relevant high temperature implantation regime ($T=823$ K, flux 1×10^{12} cm $^{-2}$ s $^{-1}$, fluence 5×10^{15} cm $^{-2}$) is plotted for comparison.

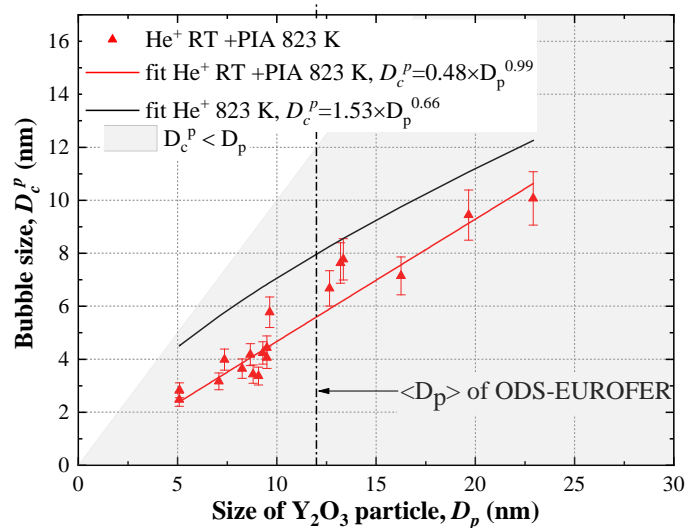


Fig. 3.24. Bubble size on yttria nanoparticles vs. particle size for the ODS-EUROFER steel samples implanted at RT with He $^+$ ions at the flux of 5×10^{11} cm $^{-2}$ s $^{-1}$ to the fluence of 5×10^{15} cm $^{-2}$ and annealed at $T=823$ K. Red solid line fits current dataset, black solid line is the fit for He $^+$ implantation at 823 K. The grey marked area corresponds to the bubbles with the size smaller than that of the particle. Error bars are 10% uncertainties associated with the size of the first Fresnel fringe on bubble observed in underfocused images [9,16].

As seen in Fig. 3.24, D_c^p increases from ~ 3 nm to ~ 10 nm as nanoparticle size increases from 5 to 23 nm, demonstrating the same qualitative trend as that observed after high temperature implantation. In comparison with the high temperature implantations, the bubbles on oxide particles are consistently smaller for the same particle size and no particles strongly enveloped by bubbles were found. Accordingly, the estimated average size for bubbles on oxide particles for the low temperature implantation regime, $\langle D_c^p \rangle \approx 5.6$ nm, is lower than that found for high temperature implantation, $\langle D_c^p \rangle \approx 8$ nm.

The results of statistical analysis of He bubbles in ODS-EUROFER steel implanted with He $^+$ ions at RT and subsequently annealed at 823 K are collected in Table 3.11. The average size (diameter) and specific number densities N_c^k for bubbles in the bulk and bubbles associated with grain boundaries, dislocations, and oxide precipitates are given for 10 grains (5 zones). The table contains no data for

bubbles on carbide particles because no $M_{23}C_6$ carbides were met in electron transparent zones of TEM samples implanted in this regime. However, according to the results of statistical analysis presented in sections 3.1.2.2 and 3.1.2.5.2 for fluence variation condition, carbides provide only minor contributions to cumulative bubble number density, swelling and helium inventory. Therefore, the lack of the data for bubbles attached to carbides is not expected to seriously affect the trends described below.

Table 3.11. Statistical analysis of specific number densities and average diameters of bubbles in ODS-EUROFER steel implanted with 10 keV He^+ ions at the flux of $5 \times 10^{11} \text{ cm}^{-2} \text{ s}^{-1}$ to the fluence of $5 \times 10^{15} \text{ cm}^{-2}$ at RT after annealing at 823 K, for several zones.

Zones	Volume		Grain boundaries		Dislocations		Y_2O_3 nano-oxides	
	N_c^V (10^{22} m^{-3})	D_c^V (nm)	N_c^{GB} ($10^{15}, \text{ m}^{-2}$)	D_c^{GB} (nm)	N_c^D (10^8 m^{-1})	D_c^D (nm)	N_c^P (10^{22} m^{-3})	D_c^P (nm)
1	229.62	1.68	16.17	2.25	4.73	1.58		
2	162.30	1.56	24.12	1.98	3.86	1.70		
3	169.12	1.69	14.77	2.40	2.10	1.87		
4	145.16	1.93	18.04	2.21	3.55	1.86		
5	238.86	1.49	26.85	1.68	4.34	1.60		
Average	189.02	1.65	19.99	2.10	3.72	1.72	1.00	5.62
Error	28.38	0.11	3.30	0.18	0.63	0.10	0.10	0.56

*Uncertainties for bubble number densities and sizes are estimated in the same way as in Tables 3.2, 3.4 and 3.6.

Populations of He bubbles associated with dislocations and located in the bulk demonstrate roughly the same mean sizes D_c^k . Bubbles associated with grain boundaries appear to be ~ 1.3 times larger than those associated with dislocations and the grain bulk. In agreement with qualitative analysis of TEM images, the largest average bubble size, $D_c^k \approx 5.6 \text{ nm}$ is observed for bubbles attached to Y_2O_3 nano-particles. As explained earlier in section 3.1.2.1, the calculated specific number density of bubbles $\langle N_c^k \rangle$ at different extended defects and at oxide particles cannot be compared directly. To make the comparison meaningful, we convert all specific densities into the number densities per unit volume of the sample, $\langle N_V^k \rangle$, using the indirect approach described in section 3.1.2.5.1.

Table 3.12 collects a summary of calculated bubble parameters for different microstructural features in ODS-EUROFER steel sample after RT implantation and PIA, including the average bubble diameters D_c^k , volumetric bubble density N_V^k , swelling associated with bubbles S_k , V/He ratio, and the fraction of accumulated helium F_{He}^k .

Table 3.12. The average sizes and volume number densities of bubbles, swelling, V/He ratio and retained He fraction associated with different bubble populations in ODS-EUROFER steel implanted at RT with He^+ ions at the flux of $5 \times 10^{11} \text{ cm}^{-2} \text{ s}^{-1}$ to the fluence of $5 \times 10^{15} \text{ cm}^{-2}$ followed by PIA at 823 K

	D_c^k (10^{-9} m)	N_V^k (10^{22} m^{-3})	S_k (%)	V/He	F_{He}^k (appm)	F_{He}^k (%)
Grain boundaries	2.10±0.18	15.39±2.54	0.075±0.02	1.33	566±146	9.0±2.3
Dislocations	1.72±0.10	4.83±0.82	0.013±0.003	1.24	104±22	1.7±0.3
Y_2O_3	5.62±0.56	1.00±0.01	0.0211±0.007	1.97	108±34	1.7±0.5
Volume	1.65±0.11	189.02±28.38	0.444±0.096	1.23	3647±789	58.2±12.6
Total		210.24±35.50	0.553±0.175		4425±1399	70.6±22.3

As can be noticed, the bubble population is dominated by bubbles in the grain bulk, with the estimated number density $\langle N_V^V \rangle \approx 190 \times 10^{22} \text{ m}^{-3}$. The number density of bubbles on grain boundaries is

more than an order magnitude lower than in the bulk, while the number densities of bubbles on dislocation and oxide particles are even less.

As a result of the very high number density, bubbles in the bulk provide the main contributions to overall swelling, $\langle S_V \rangle \approx 0.44\%$, and the fraction of accumulated helium, $\langle F_{He}^V \rangle \approx 58\%$, even though these bubbles have smaller average size than bubbles associated with extended defects and particles. Contributions to swelling and helium inventory from all other bubble populations are relatively minor.

Comparison of bubble parameters between the low temperature implantation regime followed by PIA and high temperature implantation regime is given in Fig. 3.25 separately for each bubble population.

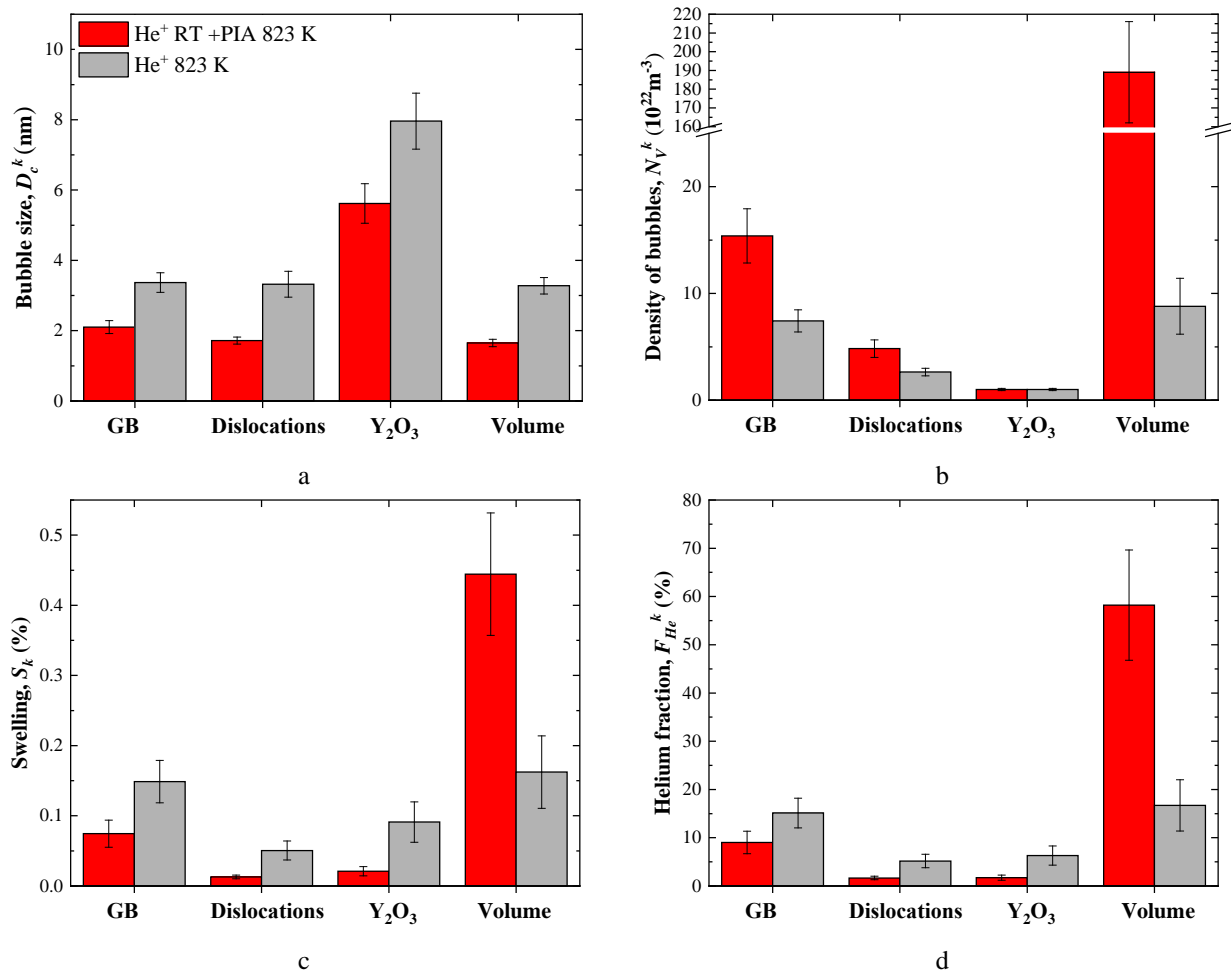


Fig. 3.25. Comparative statistical analysis of bubble mean size, volume density of bubbles, swelling and retained He fraction associated with different bubble populations in ODS-EUROFER implanted with He⁺ ions at the flux of $5 \times 10^{11} \text{ cm}^{-2}\text{s}^{-1}$ to the fluence of $5 \times 10^{15} \text{ cm}^{-2}$ at RT followed by 90 minutes PIA at 823 K (red bars) and at 823 K with the flux of $1 \times 10^{12} \text{ cm}^{-2}\text{s}^{-1}$ to the fluence of $5 \times 10^{15} \text{ cm}^{-2}$ (grey bars). Color references provided in panel (a) are valid for all panels. Data for high-temperature regime are adapted from Table 3.8.

Despite very similar values of cumulative swelling, $S = 0.55\%$ and $S = 0.48\%$ for the low temperature and high temperature implantation regimes (excluding impact of carbides), respectively, bubble parameters at different microstructural components and contributions of different bubble populations to swelling and helium inventory differ considerably. In general, bubbles formed in the low temperature implantation regime followed by PIA are smaller than bubbles formed after high temperature implantation by roughly a factor of 2. More precisely, the averages sizes of bubbles at grain boundaries, at dislocations and in the bulk constitute, respectively, 0.62, 0.52 and 0.50 of the average sizes of bubbles formed during the high temperature implantation (see Fig. 3.24 (a)). Only for bubbles attached to nano-oxide particles the difference in sizes is found to be relatively small. The bubble number densities show the opposite trend (see Fig. 3.24(b)); those at the low temperature followed by PIA regime are always

higher than after implantation at high temperature. The number density increase for bubbles at the grain boundaries and dislocations is not very pronounced, by factors of 2.07 and 1.83, respectively. But the number density of bubbles in the grain bulk increases drastically (nearly by a factor of 20) and they constitute the majority of the whole bubble population. This results in a significant re-distribution of bubble population impacts on the swelling and helium inventory. While under the high-temperature implantation regime bubbles at grain boundaries and in the bulk contribute to swelling and the accumulated helium fraction in similar shares, swelling and helium inventory after low temperature implantation + PIA are dominated by bubbles in the bulk, whereas the contributions of grain boundaries, dislocations and yttria nanoparticles fall down roughly by a factor of 2. Finally, it can be noticed that low temperature implantation + PIA enables overall more efficient He clustering in the visible bubbles, which collect ~71% of all implanted He; for the high temperature implantation the share of He collected in the visible bubbles is only ~43%.

Summing up, the analysis of the data collected in Table 3.8 (high temperature regime) and 3.12 (low temperature implantation +PIA) and presented in Fig. 3.25 demonstrates that the low temperature implantation+PIA regime does not reproduce microstructural development in ODS-EUROFER steel observed during high temperature implantation with similar parameters. Even though the cumulative swelling in both implantation regimes is similar, the roles of bubble populations in the bulk and on structural defects differ significantly. Only nano-oxides demonstrate very similar potential for helium storage during both implantation regimes. The significant difference between He bubble populations after low and high temperature implantations indicates that the resulting gas-driven microstructure is primarily determined by the helium re-distribution at the implantation stage and not much affected by helium mobility at the annealing stage.

3.1.2.7 Sensitivity of the obtained data to the uncertainties in input parameters

The indirect approach to the estimation of the swelling and helium inventory shares from individual microstructural features has certain limitation because of the necessity to know the average volume densities, N_k , for all the relevant features. Thus, the derived results, such as individual swelling contributions, cumulative swelling values and accumulated helium amounts are sensitive to the accuracy of the used densities N_k . In addition, one should keep in mind that the densities of microstructural defects that host He bubbles (e.g. dislocation density) can themselves change during ion implantation and/or high-temperature annealing. In this section we would like to estimate the sensitivity of predictions to the uncertainty of the determination of microstructural defect number densities using as an example Y_2O_3 nanoparticles, which are in the focus of the current study. Let us consider how much the predicted values of swelling and the accumulated He fraction vary in response to variation of the Y_2O_3 nanoparticle number density N_p within reasonable limits.

The literature sources (e.g. [3,24–28]) report quite different number densities of Y_2O_3 nanoparticles even for the same batch of ODS-EUROFER. The reasons for such a discrepancy are multiple, e.g. inhomogeneous particle distribution over the volume of ODS-EUROFER steel, different particle density from one TEM sample to another, low contrast of particle on both BF TEM and HAADF STEM images that makes particle identification uncertain, etc. When making estimates in sections 3.1.2.2-3.1.2.6 we used the mean particle number density derived from the literature data. As the lower limit for the oxide particle number density variation range we apply here the lowest number found in the literature, namely $N_p = 5 \times 10^{21} \text{ m}^{-3}$ [26]. The upper limit for the number density range can be obtained from the following reasoning. A typical weight content of Y_2O_3 in ODS-EUROFER steel is 0.3 wt. %. Let's assume that all oxide powder is transformed into nanoparticles during alloy compaction and heat treatment. For the typical mean nanoparticle diameter of $D_p = 12 \text{ nm}$ the mass conservation law gives

then the number density of $N_p = 17 \times 10^{21} \text{ m}^{-3}$, which will be used below as the upper bound for nanoparticle number density.

Figs. 3.26(a) and 3.26(b) illustrate the influence of oxide nanoparticle number density N_p variation on the contribution of bubbles associated with nanoparticles to swelling and helium fraction, as well as on the cumulative swelling and helium inventory, respectively.

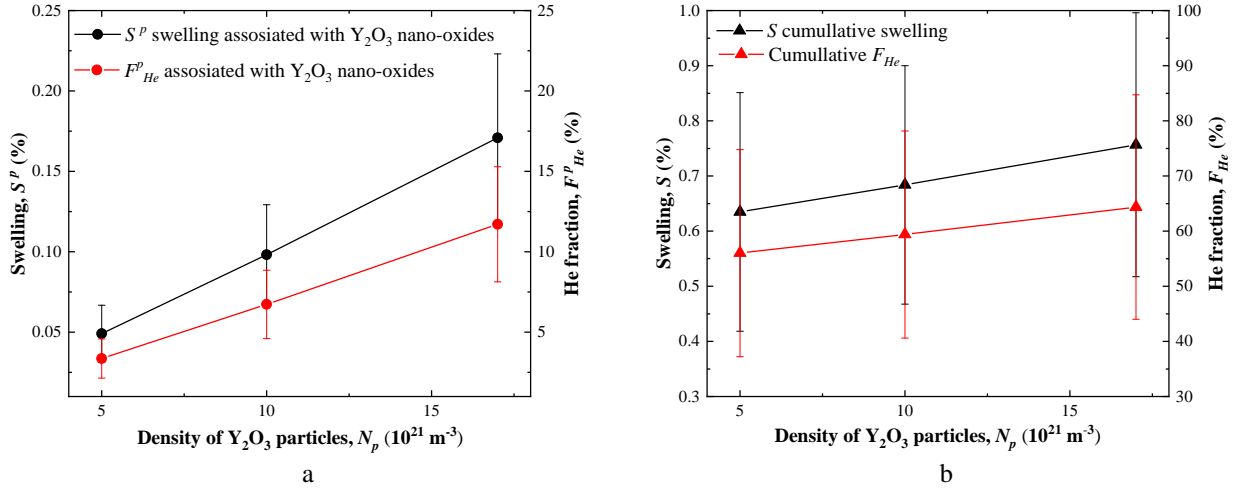


Fig. 3.26. The effect of nanoparticle number density N_p variation on (a) the particle-associated bubble contributions to swelling S_p and the captured helium fraction F_{He}^p and (b) on the cumulative swelling S and helium fraction F_{He} in all visible bubbles.

The increase of nanoparticle density from $5 \times 10^{21} \text{ m}^{-3}$ to $17 \times 10^{21} \text{ m}^{-3}$ results in proportional growth of both swelling S_p and corresponding helium fraction provided by bubbles associated with nanoparticles F_{He}^p . In this way, the growth of Y_2O_3 particle density up to $17 \times 10^{21} \text{ m}^{-3}$ leads to the complete change of particle role in cumulative swelling. That is, bubbles attached to nanoparticles become the main contributors to swelling among all microstructural components, contributing even slightly more than bubbles in the bulk, $S_v = 0.16$. With respect to accumulated helium fraction, even the highest particle number density doesn't allow to overcome the other structural components. For example, corresponding values for the grain boundaries, $F_{He}^{GB} = 15.1\%$, and in the bulk, $F_{He}^V = 16.7\%$, remain still higher.

Despite pronounced growth of the absolute values of swelling and helium inventory shares provided by bubbles on oxide nanoparticles as a result of nanoparticle number density variation, the cumulative values of swelling and helium fraction show only moderate change (see Fig. 3.26(b)) because the contribution of particle-associated bubbles to both of these parameters is relatively minor as compared to those from bubble populations on other microstructural features.

3.1.3 The analysis of helium partitioning between bubbles at different microstructural defects and the estimation of cumulative swelling in EUROFER 97 in comparison to ODS-EUROFER

In order to clearer understand the relative role of yttria nanoparticles in the helium accumulation kinetics in ODS-EUROFER steel, it is instructive to compare the general trends of ODS-EUROFER microstructural evolution under helium implantation with those in oxide particle free material with similar composition, that is EUROFER 97 steel. This section summarizes the results of TEM investigations of EUROFER 97 steel implanted with helium in experimental setup similar to that used for ODS-EUROFER. As shown in section 2.1.1, the elemental content and phase composition of ODS-EUROFER and EUROFER 97 are similar; the main difference is in the grain structure. To the best of our knowledge, there is no detailed database quantitatively characterizing microstructure of EUROFER 97 steel, including e.g. the relative densities of grain boundaries of various kinds (prior austenite / packet / block / lath), or carbide precipitates ($M_{23}C_6$ and MX). The lack of such data precludes the estimation of helium partitioning between different microstructural features and the estimation of their contribution to swelling in EUROFER 97 involving the technique suggested in sections 3.1.2.1 and 3.1.2.5.1. Therefore, in this section we restrict ourselves to the direct comparison of bubble sizes and specific number densities on different types of microstructural features in EUROFER 97 and ODS-EUROFER, while for the comparison of swelling rate and the fraction of helium accumulated in the bubbles only cumulative value estimates will be used.

The typical microstructure of EUROFER 97 implanted with He^+ ions to the fluence of 1×10^{16} cm^{-2} at 823 K is shown in a through-focus pair of BF TEM images in Fig. 3.27. The population of He-filled bubbles is clearly identified by the characteristic change in Fresnel contrast from the overfocus-to-underfocus conditions. Many bubbles are associated with various microstructural features. As a result, the bubbles are non-uniformly spatially distributed following local variations in associated microstructure. He bubbles decorate grain boundaries, dislocations, and second phase precipitates and appear to be similar in size to the bubbles in the grain bulk interior.

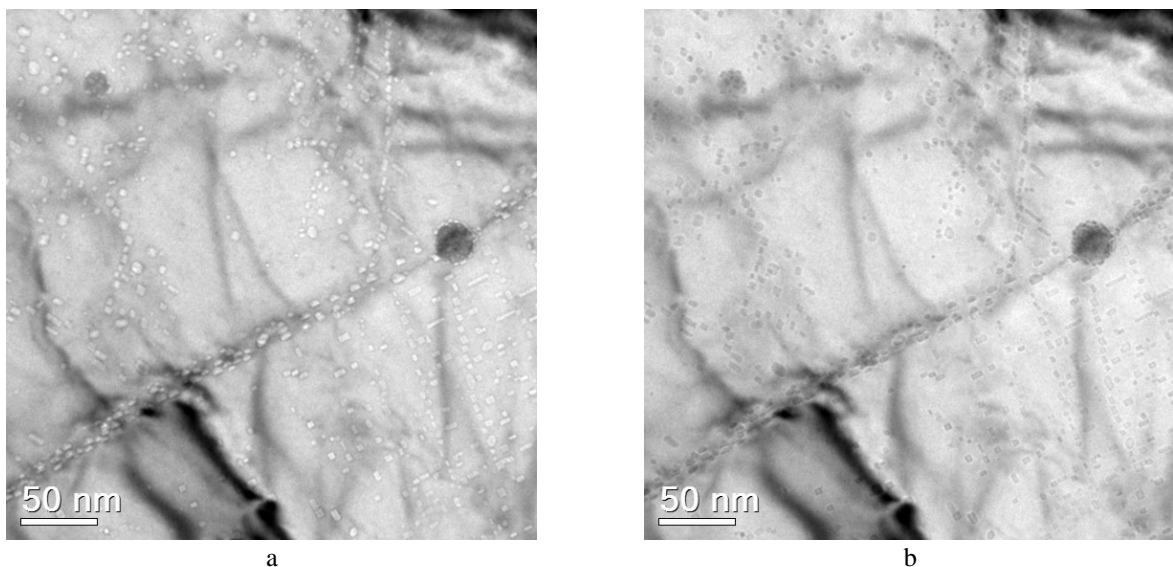


Fig. 3.27. Typical microstructure of EUROFER 97 implanted with He^+ ions to the fluence of 1×10^{16} cm^{-2} at 823 K. BF TEM imaging conditions: (a) ~ 1 μm underfocus and (b) ~ 1 μm overfocus.

Fig. 3.28 shows regions containing grain boundary $M_{23}C_6$ carbides (Fig. 3.28(a)) and intragranular carbonitride MX precipitates (Fig. 3.28(b)) characteristic for EUROFER 97 steel. Both types of precipitates are heavily decorated with large numbers of relatively small bubbles. The sizes of bubbles attached to both types of carbides look similar.

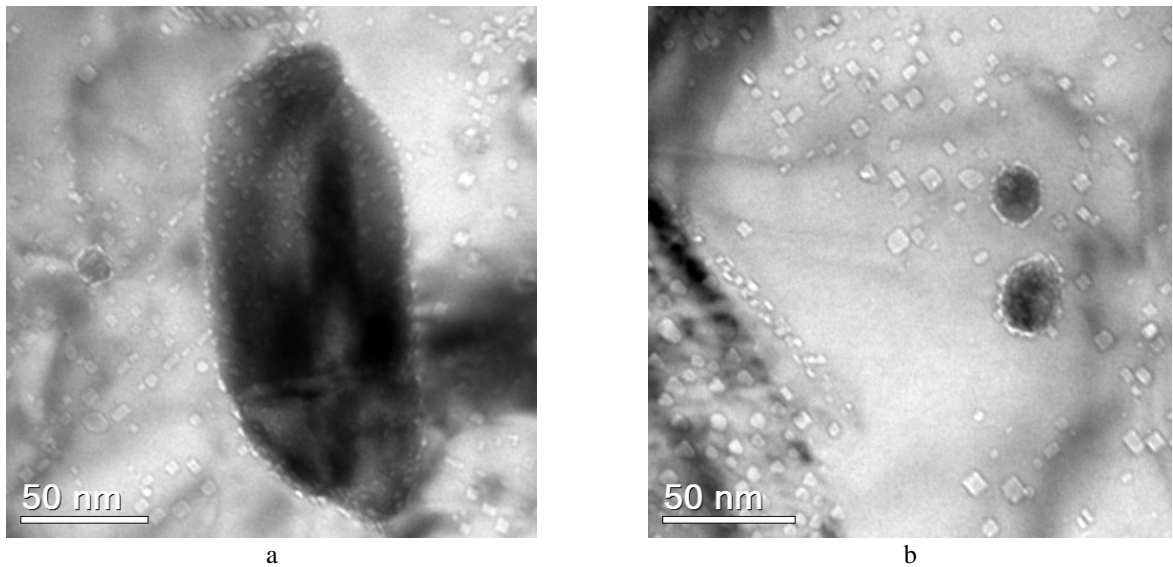


Fig. 3.28. Carbide precipitates in EUROFER 97 implanted at 823 K with He^+ ions to the fluence of $1 \times 10^{16} \text{ cm}^{-2}$ (12.5×10^3 appm): (a) MC carbide; (b) M_{23}C_6 carbide. BF TEM imaging conditions: $\sim 0.5 \mu\text{m}$ underfocus.

Typical TEM images of EUROFER 97 and ODS-EUROFER samples implanted under the same conditions are compared in Fig. 3.29. Judging from Figs. 3.27-3.29, the general trends of microstructure development in ODS-EUROFER and its non-ODS counterpart look qualitatively very similar: He bubbles with similar sizes are distributed between structural defects. In order to obtain a basis for more detailed comparison, the parameters of bubble ensembles related to each microstructural defect type in both materials were estimated quantitatively, as described below.

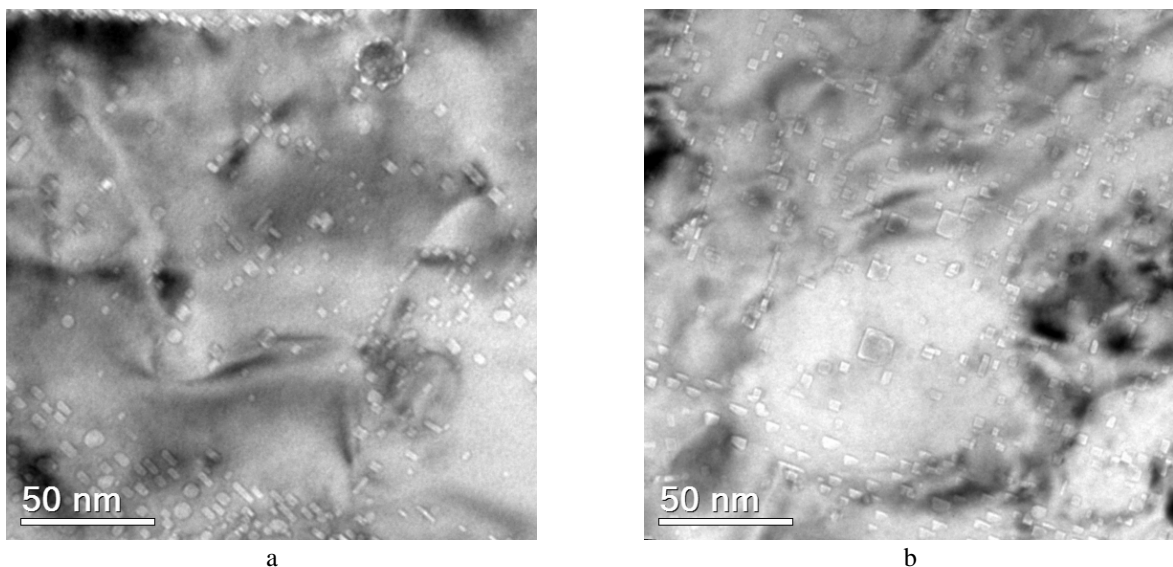


Fig. 3.29. Microstructure of EUROFER 97 (a) and ODS-EUROFER (b) implanted at 823 K with He^+ ions to the fluence of $1 \times 10^{16} \text{ cm}^{-2}$ (12.5×10^3 appm). BF TEM imaging condition $\sim 0.8 \mu\text{m}$ underfocus.

As demonstrated in sections 3.1.1-3.1.2, helium in ODS-EUROFER steel shows notably different behavior at the yttria/matrix and carbide/matrix interfaces. Typically, the surface of carbides is covered by multiple small bubbles, while oxide precipitates host one (rarely two) relatively large bubbles. However a straightforward comparison of these precipitate types in ODS-EUROFER steel was not quite fair because of very different size of M_{23}C_6 carbides ($\sim 100 \text{ nm}$) and Y_2O_3 ($\sim 12 \text{ nm}$) oxide precipitates. In contrast, in EUROFER 97 steel various types of carbonitride MX precipitates (including (Ta,V)C, TaC and VN) with the mean size ($\sim 20 \text{ nm}$) comparable to that of yttria nanoparticles in ODS-EUROFER are present. Having in mind similar sizes of carbonitride precipitates in EUROFER 97 and oxide particles in

ODS-EUROFER, it is instructive to compare helium trapping on such precipitates under the same implantation conditions. Figs. 3.30(a) and 3.30(b) show BF TEM micrographs of MX precipitate in EUROFER 97 and Y_2O_3 precipitate in ODS-EUROFER, respectively, after implantation with He^+ ions to the fluence of $1 \times 10^{16} \text{ cm}^{-2}$ at 823 K. As can be seen in Fig. 3.30(a), the MX precipitate ($\sim 15 \text{ nm}$) in EUROFER 97 steel is decorated with multiple relatively small He bubbles (slightly smaller than those in the surrounding matrix), similar to large $M_{23}C_6$ carbides in both materials. In contrast, under the same implantation conditions He at the Y_2O_3 nanoparticle/matrix interface is collected in a single bubble with notably larger size than the typical size of bubbles in the matrix (Fig. 3.30(b)).

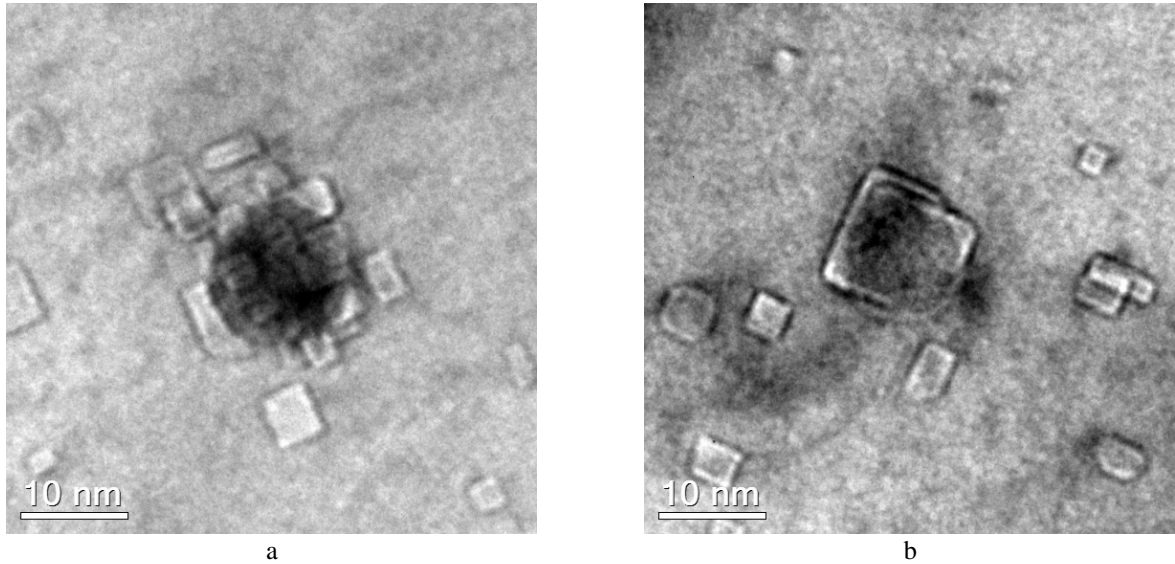


Fig. 3.30. MX precipitate in EUROFER 97 (a) and yttria precipitate in ODS-EUROFER (b) steels implanted with He^+ ions to the fluence of $1 \times 10^{16} \text{ cm}^{-2}$ ($12.5 \times 10^3 \text{ appm}$) at 823 K. BF TEM imaging conditions: $\sim 0.5 \mu\text{m}$ underfocus.

The data of comparative statistical analysis of specific number densities (per defect) and average sizes of helium bubbles associated with different microstructural features in EUROFER 97 and ODS-EUROFER steels are summarized in Table 3.13 and in Fig. 3.31.

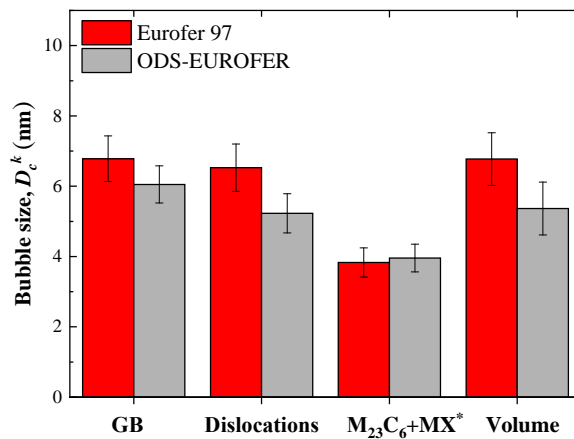


Fig. 3.31. The average sizes of He bubbles associated with different microstructural defects in EUROFER 97 and ODS-EUROFER implanted to the fluence of $1 \times 10^{16} \text{ cm}^{-2}$ ($12.5 \times 10^3 \text{ appm}$) at $T= 823 \text{ K}$ with a flux $5 \times 10^{11} \text{ cm}^{-2}\text{s}^{-1}$. *MX precipitates are observed only in EUROFER 97.

Bubbles in EUROFER 97 steel are slightly larger than in ODS-EUROFER, no matter whether they are located in the bulk or on microstructural defects, except carbide precipitates. The average sizes of bubbles in the grain interior and at dislocations are a factor of about 1.25 higher for EUROFER 97 than for ODS-EUROFER. The average sizes of bubbles at carbides are the same in both materials.

A similar trend is found for the density of helium bubbles (per defect). In general, all calculated number densities are higher for EUROFER 97, excluding bubbles on dislocations. The ratio of bubble number densities in EUROFER 97 to ODS-EUROFER is about 1.35 in the grain interior and on carbides; for grain boundaries it is about 1.1. Bubble number densities at dislocations (per unit length of dislocation) are practically the same.

Table 3.13. Comparative statistical analysis of specific number densities and average diameters of bubbles in the bulk and at different microstructural defect for EUROFER 97 and ODS-EUROFER steels implanted with 10 keV He⁺ ions.

fluence $1 \times 10^{16} \text{ cm}^{-2}$, flux $5 \times 10^{11} \text{ cm}^{-2} \text{ s}^{-1}$, T=823 K		Volume		Grain boundaries		Dislocations		Carbides	
		N_c^V (10^{22} m^{-3})	D_c^V (nm)	N_c^{GB} (10^{15} m^{-2})	D_c^{GB} (nm)	N_c^D (10^8 m^{-1})	D_c^D (nm)	N_c^C (10^{16} m^{-2})	D_c^C (nm)
EUROFER 97	Zones								
	1	12.82	6.93	10.43	6.36	1.55	5.84	4.06	3.61
	2	5.55	7.25	7.40	6.76	1.54	6.59	2.53	3.47
	3	5.52	7.23	6.86	6.99	1.39	6.99	4.66	3.27
	4	6.60	5.84	7.03	6.49	1.69	6.25	2.46	4.31
	5	6.14	6.60	7.62	7.31	1.53	6.97	3.05	4.49
	Average	7.32	6.77	7.87	6.78	1.54	6.53	3.35	3.83
	Error	1.72	0.75	1.08	0.65	0.16	0.67	0.59	0.41
ODS-EUROFER	Average	5.40	5.37	7.07	6.05	1.54	5.23	2.40	3.96
	Error	1.24	0.75	0.76	0.53	0.16	0.56	0.24	0.40

Data on EUROFER 97 include detailed information over 5 different zones of the sample; data for ODS-EUROFER are copied from Table 3.2.

The detailed comparison of expected swelling and of helium fraction captured in the bubbles following the approach suggested in section 3.1.2.5.1 and used for ODS-EUROFER is currently impossible due to the lack of the necessary microstructural data for EUROFER 97, as already explained at the beginning of the section. Hence, two simplified approaches were used to roughly estimate the expected swelling in EUROFER 97, namely – the standard ASTM approach (see section 3.1.2.5.1) and the indirect approach, somewhat resembling that used for ODS-EUROFER (the swelling estimates will be referred to below as S_{ASTM} and $S_{indirect}$, respectively).

In the indirect approach, the swelling was estimated as,

$$S_{indirect} (\%) = \langle V_c \rangle \cdot \langle \sum N_v \rangle \cdot 100\% ,$$

where $\langle V_c \rangle$ is the volume of a single bubble averaged over all microstructural defect types in each investigated area and additionally averaged over 5 investigated areas, while $\langle \sum N_v \rangle$ is the total bubble number density in all studied areas.

Helium fraction $\langle F_{He} \rangle$ was calculated in the same way as for ODS-EUROFER from the visible bubble volumes, taking into account volume density of all visible helium bubbles $\sum N_v$ and the average bubble volume $\langle V_c \rangle$.

Calculated values of swelling, V/He ratio and helium fraction are presented in Table 3.14 and in Fig.3.32.

Table 3.14. Cumulative values of helium bubble number density, V/He ratio, swelling estimated by TEM data and retained He fraction for EUROFER 97 and ODS-EUROFER steels.

$1 \times 10^{16} \text{ (cm}^{-2}\text{)},$ $F_{\text{He}_{total}} =$ 12533 appm	$N_V \text{ (} 10^{23} \text{ m}^{-3}\text{)}$	$S_{\text{indirect}} \text{ (\%)}$	$S_{\text{ASTM}} \text{ (\%)}$	$\langle V/\text{He} \rangle$	$F_{\text{He}} \text{ (appm)}$	$F_{\text{He}} \text{ (\%)}$
EUROFER 97	1.93 ± 0.21	2.22 ± 0.44	2.35 ± 0.40	2.03	11019 ± 2174	87.9 ± 17.3
ODS-EUROFER	1.61 ± 0.37	1.48 ± 0.48	-	2.02	7401 ± 2340	59.0 ± 18.7

As might be expected from the larger sizes and densities of helium bubbles in EUROFER 97, higher values of swelling and accumulated helium fraction are predicted for EUROFER 97 in comparison with ODS-EUROFER. The increase in swelling is expected to be 1.5 or 1.6, depending on the approach (standard or indirect) used for swelling estimation in EUROFER 97. The average V/He ratio in the bubbles is practically the same for both steels. Around 90% of implanted helium in EUROFER 97 is estimated to be captured in the bubbles in contrast with ODS-EUROFER, where the captured fraction is only around 60% of the implanted He amount.

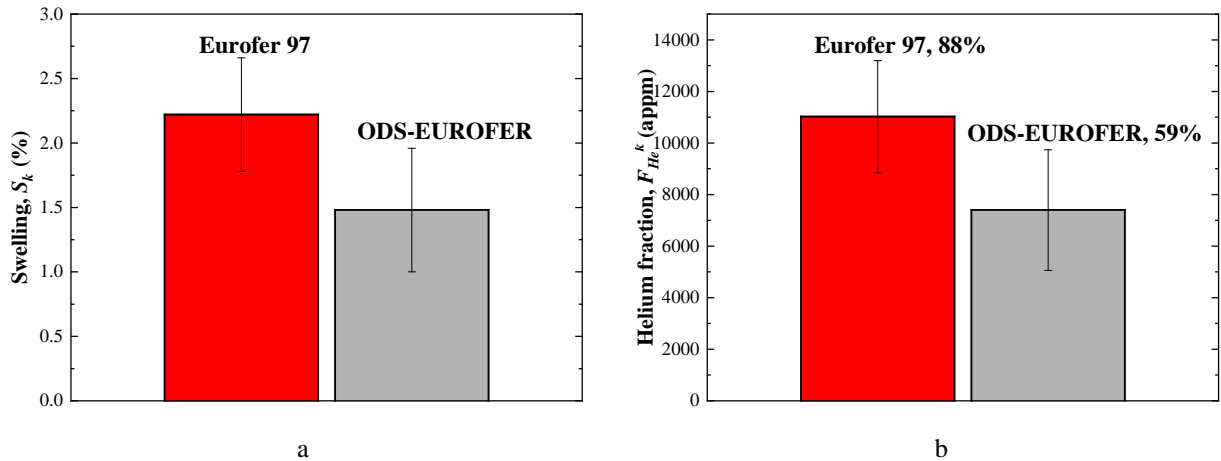


Fig. 3.32. Cumulative swelling (a) and fraction of implanted helium (b) in EUROFER 97 (red bars) and ODS-EUROFER (grey bars) implanted to fluence $1 \times 10^{16} \text{ cm}^{-2}$ (12.5×10^3 appm) at the $T = 823 \text{ K}$ with the flux of $5 \times 10^{11} \text{ cm}^{-2} \text{ s}^{-1}$.

Higher values of accumulated helium fraction and swelling for EUROFER 97 steel in comparison with ODS-EUROFER could be associated with both the higher grain size of EUROFER 97 and the absence of Y_2O_3 nanoparticles.

3.2 Microstructural evolution of ODS-EUROFER steel during dual-beam He⁺+Au²⁺ irradiation

In section 3.1, a detailed analysis of microstructural development in ODS-EUROFER steel as a result of single-beam helium implantation was presented. It is known, however, that fusion reactor environment is characterized not only by high concentrations of accumulated helium, but by a notable level of radiation damage as well. The accumulation in the steel of very high vacancy concentrations has potential risk of promoting conversion of gas bubbles into voids and transition to non-saturable swelling. The results of section 3.1 evidence that the relatively moderate point defect production rate during single-beam He⁺ implantation is insufficient to create large enough concentration of vacancies that might promote the bubble-to-void transition. It remains an open question whether such transition can be enabled when the rate of radiation damage generation is substantially higher than that accompanying helium implantation.

The aim of this section is to investigate synergetic effect of helium accumulation and irradiation damage in conditions, when radiation damage production is decoupled from the gas implantation. This was achieved by using dual-beam irradiation, where the 10 keV He⁺ implantation into ODS-EUROFER steel samples was accompanied with irradiation with 4 MeV Au²⁺ ions. Two different dual-beam irradiation regimes were used:

- Sequential dual-beam irradiation i.e. *ex situ* implantation with 10 keV He⁺ ions to the fluence of $5 \times 10^{15} \text{ cm}^{-2}$ at room temperature followed by *in situ* irradiation with 4 MeV Au²⁺ at 823 K to the fluence of $4.5 \times 10^{15} \text{ cm}^{-2}$ (section 3.2.1).
- Simultaneous *in situ* dual-beam irradiation at 823 K with 10 keV He⁺ ions to the fluence of $5 \times 10^{15} \text{ cm}^{-2}$ and 4 MeV Au²⁺ ions to the fluence of $4.5 \times 10^{15} \text{ cm}^{-2}$ (section 3.2.2).

Additional details about implantation and sample preparation can be found in sections 2.2.3.3 and 2.1.1.2-2.1.1.3, respectively.

The parameters of helium bubbles correlated with microstructural defects (grain boundaries, dislocations and precipitates) are estimated by means of indirect approach described in sections 3.1.2.1 and 3.1.2.5.1. Having in mind that bubbles attached to yttria nanoparticles are always noticeably larger than bubbles in the bulk or bubbles associated with other structural defects, our attention here will be mostly focused on this bubble population as the most probable candidate for bubble-to-void transition observation. The results of statistical analysis of bubble population parameters and the estimates of swelling and helium fraction accumulated in the bubbles are compared below with similar results for single-beam helium implantation.

3.2.1 Microstructural evolution of helium pre-implanted ODS-EUROFER steel during 4 MeV Au²⁺ irradiation

In order to investigate the effects of helium accumulation and irradiation damage we used, first of all, sequential dual-beam irradiation. The sample was first *ex situ* implanted with 10 keV He⁺ ions and then electropolished from the backside to obtain a TEM sample for subsequent *in situ* 4 MeV Au²⁺ irradiation. Preliminary TEM investigation revealed no visible He bubbles after He⁺ implantation. The *in situ* irradiation with Au²⁺ ions at 823 K was done with the gold ion flux of $4 \times 10^{11} \text{ cm}^{-2} \text{ s}^{-1}$, corresponding to damage production rate of $2.2 \times 10^{-3} \text{ dpa/s}$, while the cumulative dose provided by both He⁺ and Au²⁺ beams was estimated to be $\sim 22.5 \text{ dpa}$ using SRIM program. High-temperature Au²⁺ irradiation was accompanied with the formation of $\sim 7\text{-}10 \text{ nm}$ thick amorphous surface oxide that was cleaned by 0.5 keV Ar⁺ ion beam. The final He concentration inside the investigated region is estimated to be $\sim 6300 \text{ appm}$. The irradiated sample was studied in TEM to extract statistical data on parameters of bubble population associated with different microstructural components.

Typical BF TEM trough-focus images of ODS-EUROFER after sequential dual-beam irradiation are shown in Fig. 3.33.

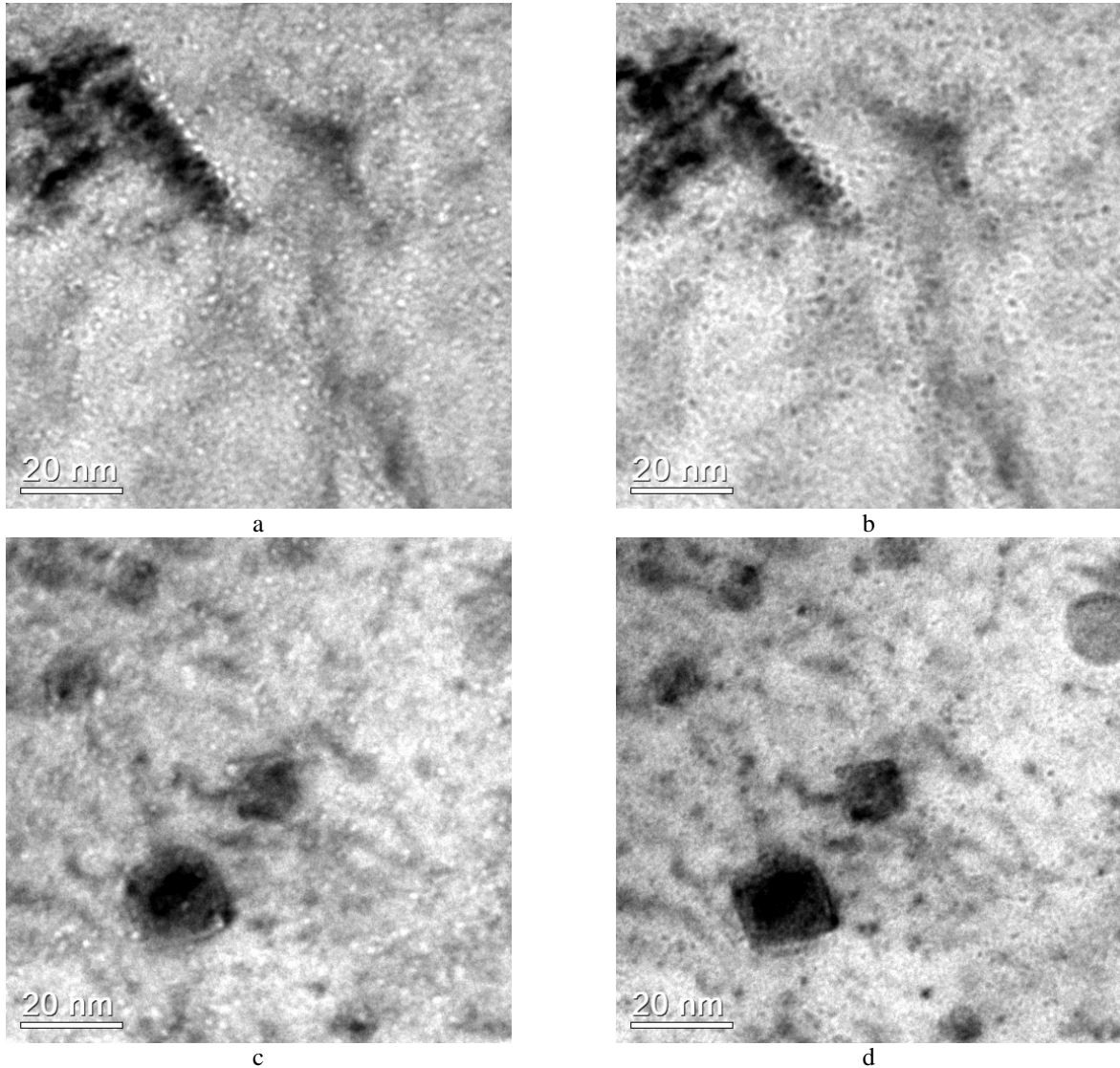


Fig. 3.33. Microstructure of ODS-EUROFER steel implanted at RT with 10 keV He^+ ions at the flux of $5 \times 10^{11} \text{ cm}^{-2} \text{ s}^{-1}$ to the fluence of $5 \times 10^{15} \text{ cm}^{-2}$ and then *in situ* irradiated at 823 K with 4 MeV Au^{2+} at the flux of $4 \times 10^{11} \text{ cm}^{-2} \text{ s}^{-1}$ to the fluence of $4.5 \times 10^{15} \text{ cm}^{-2}$. BF TEM imaging conditions: (a,c) $\sim 0.8 \mu\text{m}$ underfocus and (b,d) $\sim 0.8 \mu\text{m}$ overfocus.

Sequential irradiation of ODS-EUROFER samples with He^+ and Au^{2+} ions resulted in high density of tiny bubbles. The partitioning of implanted He between the bulk and different microstructural features (grain boundaries, dislocations and precipitates) took place similar to the case of single-beam helium implantation. Helium bubbles decorating the grain boundaries and dislocations can be seen in Fig. 3.33(a,b), while bubbles decorating precipitates can be noticed in Fig. 3.33(c,d). The sizes of bubbles decorating grain boundaries and dislocations are mostly the same as for the bubbles in the bulk. Similar to single-beam helium implantation case, each yttria particle hosts only one helium bubble with the size typically larger than those in other bubble populations. The sizes of the bubbles associated with nanoparticles are sensitive to the host particle size.

The statistical description of the observed data is started, as before, with the estimation of the average size of the bubbles associated with yttria nanoparticles $\langle D_c^p \rangle$ based on the fitting of experimental dependence $D_c^p(D_p)$ shown in Fig. 3.34. The best fit parameters for the dependence $D_c^p(D_p)$ and the estimated value of $\langle D_c^p \rangle$ are presented in Fig. 3.34 and in Table 3.15, respectively.

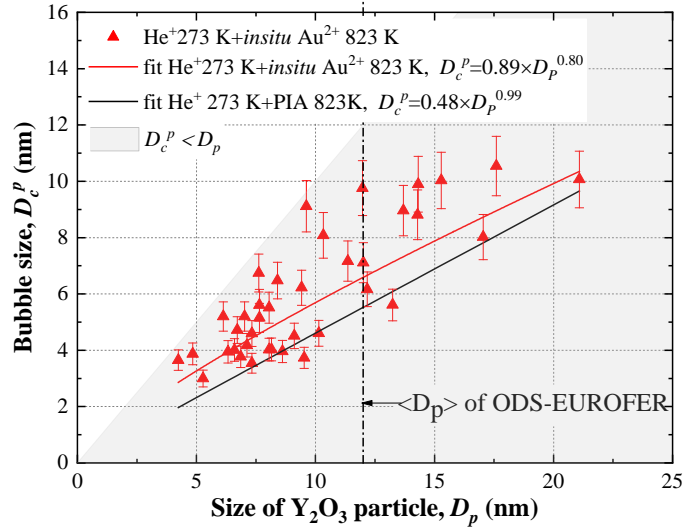


Fig. 3.34. Bubble size on yttria nanoparticles vs. particle size for the ODS-EUROFER steel implanted at RT with 10 keV He^+ ions at the flux of $5 \times 10^{11} \text{ cm}^{-2} \text{ s}^{-1}$ to the fluence of $5 \times 10^{15} \text{ cm}^{-2}$ and then *in situ* irradiated at 823 K with 4 MeV Au^{2+} ions at the flux of $4 \times 10^{11} \text{ cm}^{-2} \text{ s}^{-1}$ to the fluence of $4.5 \times 10^{15} \text{ cm}^{-2}$. Red solid line fits the current dataset, black solid line is the fit for single-beam He^+ implantation at RT followed by PIA at 823 K. The grey marked area corresponds to the bubbles with the size smaller than that of the particle. Error bars are 10% uncertainties associated with the size of the first Fresnel fringe on bubble observed in underfocused images [9,16].

Having in mind that the discussed experiment used helium pre-implantation at RT, it is reasonable to compare the obtained dependence $D_c^p(D_p)$ with a similar data fit for single-beam He^+ implantation to the same fluence of $5 \times 10^{15} \text{ cm}^{-2}$ at RT followed by PIA at $T = 823 \text{ K}$ (shown as a black line in Fig. 3.34). According to the data presented in plot 3.34, D_c^p increases from $\sim 3.7 \text{ nm}$ to $\sim 10 \text{ nm}$ with nanoparticle size increase from 4 to 21 nm. The trend is qualitatively similar to the case of single-beam helium implantation. However, the estimated value of $\langle D_c^p \rangle \approx 6.6 \text{ nm}$ for sequential dual-beam irradiation with He^+ and Au^{2+} ions is found to be larger than $\langle D_c^p \rangle \approx 5.7 \text{ nm}$ under the single He^+ implantation regime followed by PIA. No yttria particles completely enveloped by bubbles were found.

The results of statistical analysis for different He bubble populations are collected in Table 3.15.

Table 3.15. Statistical analysis of specific number densities and average diameters of bubbles in ODS-EUROFER steel implanted with 10 keV He^+ ions at the flux of $5 \times 10^{11} \text{ cm}^{-2} \text{ s}^{-1}$ to the fluence of $5 \times 10^{15} \text{ cm}^{-2}$ at RT and then irradiated *in situ* with 4 MeV Au^{2+} ions at the flux of $4 \times 10^{11} \text{ cm}^{-2} \text{ s}^{-1}$ to the fluence of $4.5 \times 10^{15} \text{ cm}^{-2}$ at 823 K.

Zones	Volume		Grain boundaries		Dislocations		Y_2O_3 nano-oxides	
	N_c^V (10^{23} m^{-3})	D_c^V (nm)	N_c^{GB} (10^{15} m^{-2})	D_c^{GB} (nm)	N_c^D (10^8 m^{-1})	D_c^D (nm)	N_c^P (10^{22} m^{-3})	D_c^P (nm)
1	13.70	1.99	14.90	2.47	3.84	1.77		
2	24.20	1.65	26.60	1.78	4.60	1.65		
3	21.80	1.74	19.90	1.98	3.48	1.74		
4	15.40	1.97	15.90	2.36	2.62	1.82		
5	16.30	1.88	15.40	2.39	2.20	2.05		
Average	18.28	1.85	18.54	2.20	3.35	1.81	1.00	6.57
Error	2.90	0.11	3.08	0.20	0.59	0.11	0.10	0.66

The average size and specific bubble number densities N_c^k presented in Table 3.15 for bubble populations in the bulk, at grain boundaries and on dislocations were collected for 10 grains (5 zones). Error bars shown for N_c^k (k -defect type) and D_c^k have the same meaning as in Tables 3.2, 3.4 and 3.6. As

in previous sections, electron transparent zones on the studied TEM sample subjected to sequential dual-beam irradiation contained no $M_{23}C_6$ carbides, so no data for bubbles on carbide precipitates are available.

The analysis of bubble population parameters shows that helium bubbles associated with dislocations and located in the bulk have similar average sizes D_c^k . Bubbles at grain boundaries appear to be ~20% larger than in the bulk. The bubbles attached to yttria particles are the largest, with an average size $D_c^p = 6.6$ nm. The specific number densities of bubbles $\langle N_c^k \rangle$ at different extended defects and oxide particles in Table 3.15 allow no direct comparison; it requires the conversion to volumetric number densities $\langle N_V^k \rangle$ in terms of the indirect approach.

The recalculated volumetric bubble density N_V^k , swelling associated with bubbles S_k , V/He ratio and fraction of accumulated helium F_{He}^k for different bubble population in ODS-EUROFER steel after sequential irradiation with He^+ and Au^{2+} ions are collected in Table 3.16.

Table 3.16. The average sizes and volume number densities of bubbles, swelling, V/He ratio and retained He fraction associated with different bubble populations in the ODS-EUROFER steel implanted at RT with 10 keV He^+ ions at the flux of $5 \times 10^{11} \text{ cm}^{-2} \text{ s}^{-1}$ to the fluence of $5 \times 10^{15} \text{ cm}^{-2}$ and then irradiated *in situ* at 823 K with 4 MeV Au^{2+} ions at the flux of $4 \times 10^{11} \text{ cm}^{-2} \text{ s}^{-1}$ to the fluence of $4.5 \times 10^{15} \text{ cm}^{-2}$.

	D_c^k (10^{-9} m)	N_V^k (10^{22} m^{-3})	S_k (%)	V/He	F_{He}^k (appm)	F_{He}^k (%)
Grain boundaries	2.20±0.20	14.28±2.37	0.079±0.021	1.35	595±157	9.5±2.5
Dislocations	1.81±0.11	4.35±0.76	0.013±0.003	1.26	107±23	1.7±0.4
Y₂O₃	6.57±0.66	1.00±0.10	0.041±0.013	2.12	193±61	3.1±1.0
Volume	1.85±0.11	182.80±28.46	0.602±0.118	1.27	4770±937	76.1±14.9
Total		202.43±33.64	0.735±0.232		5665± 1791	90.4±28.6

As can be seen in Table 3.16, the major contribution to bubble number density comes from bubbles in the grain bulk, $\langle N_V^V \rangle \approx 180 \times 10^{22} \text{ m}^{-3}$. Significantly lower bubble number densities of $\langle N_V^{GB} \rangle \approx 14 \times 10^{22} \text{ m}^{-3}$ and $\langle N_V^d \rangle = 4 \times 10^{22} \text{ m}^{-3}$ are found for bubbles on grain boundaries and dislocations. The lowest volume number density corresponds to bubbles at yttria /matrix interfaces.

The highest number density of bubbles in the bulk results in their dominance in the swelling, $\langle S_V \rangle = 0.6\%$, and the fraction of accumulated helium, $\langle F_{He}^V \rangle \approx 76\%$. The contributions to swelling and helium inventory from bubble populations associated with grain boundaries and oxide nanoparticles are nearly an order of magnitude smaller, $\langle S_{GB} \rangle = 0.08\%$ / $\langle F_{He}^{GB} \rangle = 9.5\%$ and $\langle S_p \rangle = 0.04\%$ / $\langle F_{He}^p \rangle = 3.1\%$, respectively. The role of dislocations in swelling and helium storage is found to be minor. Remarkably, in contrast to previously reported data for single-beam helium implantation, up to 90% of implanted helium is found to be trapped in the bubbles.

The comparison of sequential dual-beam He^+ and Au^{2+} irradiation and implantation with a single He^+ beam followed by PIA is shown in Fig. 3.35 for average bubble sizes, bubble number densities, swelling and retained helium fractions corresponding to different bubble populations.

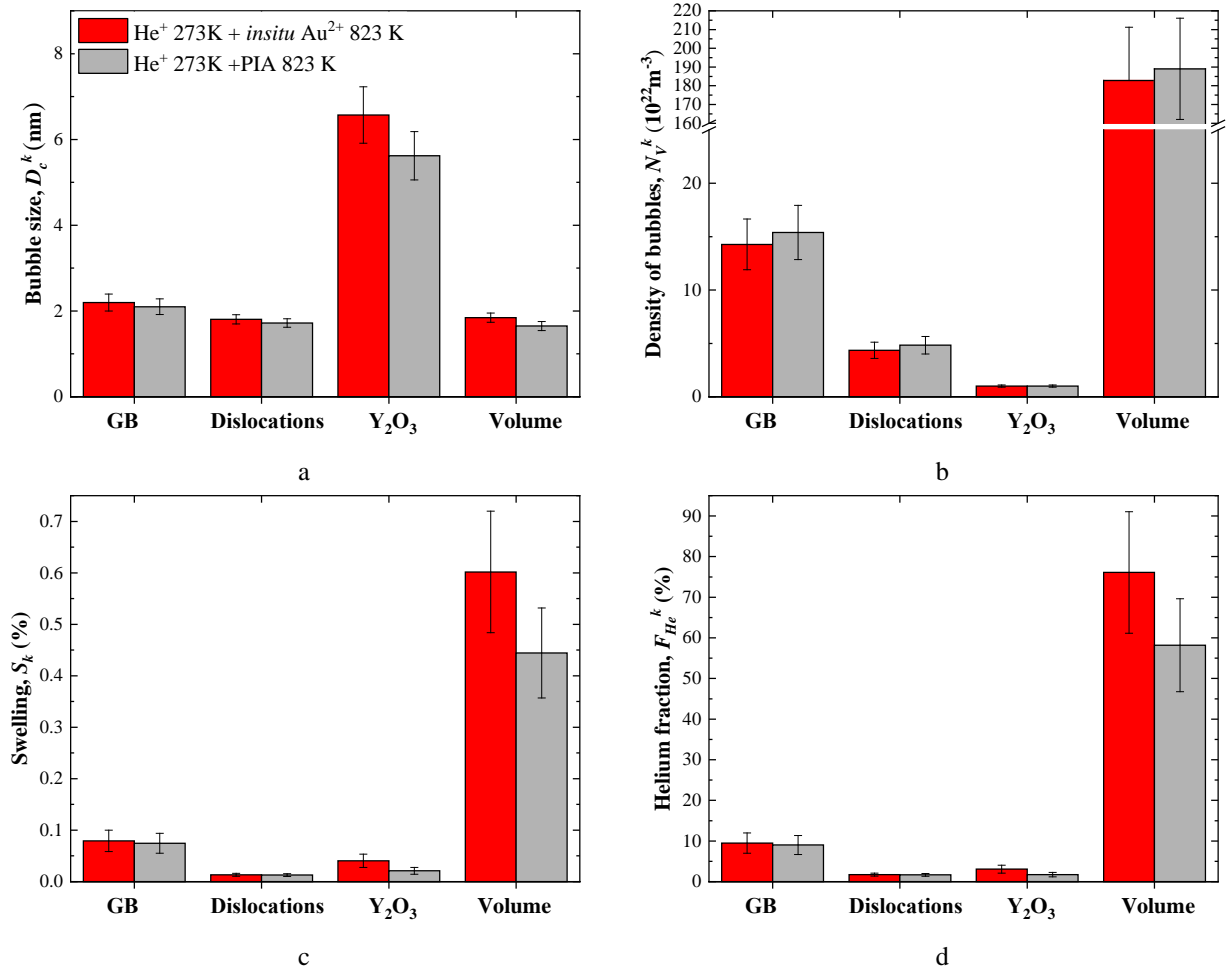


Fig. 3.35. Comparative statistical analysis of bubble mean size, the volume density of bubbles, swelling and retained He fraction associated with different bubble populations in ODS-EUROFER steel either sequentially dual-beam irradiated with 10 keV He⁺ at RT and 4 MeV Au²⁺ ions at 823 K (red bars), or single-beam implanted with 10 keV He⁺ ions at RT followed by 90 minutes PIA at 823 K (grey bars). Color references provided in panel (a) are valid for all panels. Data for He⁺ single beam implantation is from Table 3.12.

As can be easily noticed, for both the sequential dual-beam He⁺+Au²⁺ irradiation and single-beam He⁺ implantation followed by PIA the trends for bubble size, the partitioning of bubbles over microstructural components, as well as impacts of different bubble populations on swelling and helium retention are very similar. Taking into account error bars, only minor size increase is observed for bubble populations associated with grain boundaries and dislocations as well as located in the grain bulk (see Fig. 3.35(a)). Bubbles attached to nanoparticles are found to be slightly more sensitive to the synergetic influence of helium accumulation and damage. The mean size of bubbles attached to nanoparticles under sequential dual-beam He⁺ and Au²⁺ irradiation is ~16% larger than the size of the same bubble type under single-beam He⁺ implantation. In general, sequential dual-beam He⁺ and Au²⁺ irradiation results in lower volumetric number densities of bubbles associated with all microstructural components as compared to single-beam He⁺ implantation regime. Despite the reduction of volumetric bubble number densities, the calculated swelling S_k and retained helium fraction F_{He}^k values at all microstructural components are found to be higher for the sequential dual-beam regime. In terms of S_k and F_{He}^k , the most pronounced differences between single- and dual-beam regimes are found for bubbles associated with nano-oxides and, to less extent, for bubbles in the bulk. Thus, the contributions to swelling S_p and fraction of accumulated helium F_{He}^p from the bubbles on oxide particles in the case of sequential He⁺ and Au²⁺ irradiation are by factors of ~1.9 and ~1.8 larger than for single He⁺ implantation. The same factors for bubbles in the bulk are ~1.35 and 1.31. The total swelling and the

helium fraction retained in all bubbles are also larger for sequential He⁺ and Au²⁺ irradiation compared to single-beam He⁺ regime, $S \sim 0.74\%$ vs. $\sim 0.55\%$ and $F_{\text{He}} \sim 90\%$ vs. $\sim 71\%$, respectively.

Summing up, the comparison of the bubble evolution in ODS-EUROFER samples subjected to high-temperature processing either with, or without additional damage production by MeV gold ions, demonstrates little difference in bubble populations formed either in the grain bulk, or at such structural defects as grain boundaries and dislocations. Only for bubbles associated with yttria nanoparticles one can observe a certain increase in the bubble size due to the additional damage production with gold ions, but the increase is quite modest and does not lead to qualitative changes, such as bubble-to void transition or complete particle absorption inside growing bubbles. This means that the observed gas-driven microstructure is mostly determined by helium re-distribution during He⁺ implantation at room temperature, while the high temperature processing, which forces helium bubble coarsening and makes them visible in TEM, is not really sensitive to the additional damage production by heavy ion irradiation.

3.2.2 Microstructural evolution of ODS-EUROFER steel during simultaneous dual-beam He⁺+Au²⁺ irradiation

As an alternative to the sequential introduction of helium and radiation damage, as discussed in the previous section, simultaneous dual-beam He⁺+ Au²⁺ irradiation experiment at high temperature was performed. In this experiment, ODS-EUROFER sample was implanted *in situ* at 823 K with 10 keV He⁺ ions to the fluence of $5 \times 10^{15} \text{ cm}^{-2}$ with the flux $5 \times 10^{11} \text{ cm}^{-2}\text{s}^{-1}$ and, at the same time, irradiated with 4 MeV Au²⁺ ions with the flux of $4 \times 10^{11} \text{ cm}^{-2}\text{s}^{-1}$, which eventually corresponded to the fluence of $4.5 \times 10^{15} \text{ cm}^{-2}$. Prior to implantation, the samples were checked in order to confirm nano-oxide presence in the investigated regions. Due to the expected growth of quite thick surface oxide during *in situ* implantation at this temperature, the depth region of interest (sample thickness) was expanded up to 60 nm from sample surface. Therefore, zones with nano-oxides observed prior to *in situ* irradiation were not useful for the TEM examinations after irradiation. So, new zones with higher thickness and similar nanoparticle size and spatial distributions were chosen for TEM analysis of irradiated samples. Helium concentration inside the investigated region was calculated to be ~ 7100 appm and cumulative dose from both He⁺ and Au²⁺ ions was ~ 24.6 dpa. The statistical analysis of bubble populations was done using indirect approach for each microstructural component. The obtained bubble population parameters, as well as the derived swelling and accumulated helium contributions for each microstructural component were compared with the data obtained for single-beam He⁺ implantation at 823 K with the same fluence of $5 \times 10^{15} \text{ cm}^{-2}$.

Typical BF TEM through-focus images of different zones on ODS-EUROFER steel sample subjected to simultaneous *in situ* He⁺ and Au²⁺ irradiation at 823 K to 22.4 dpa are shown in Fig. 3.36.

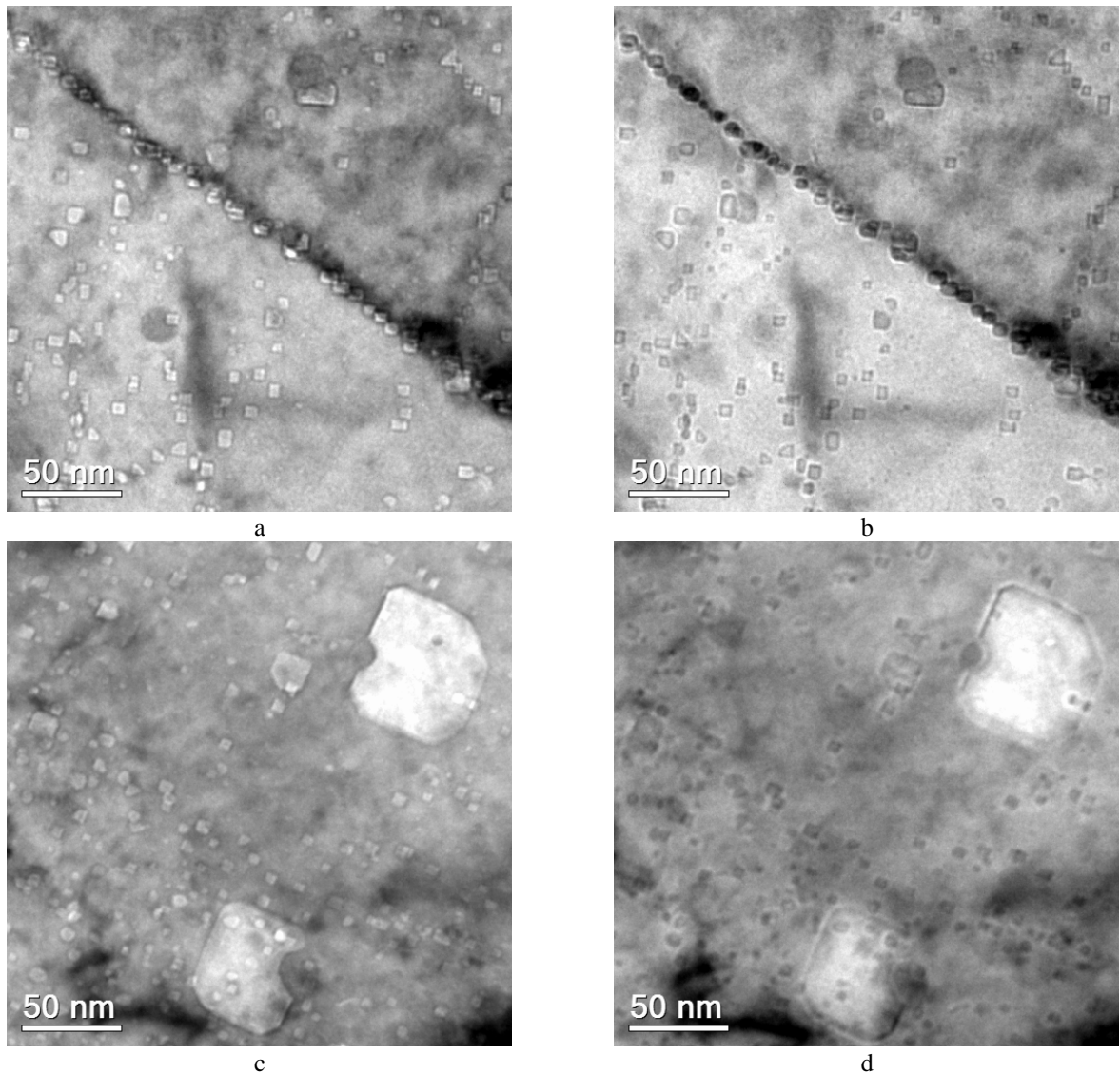


Fig. 3.36. Microstructure of ODS-EUROFER steel after simultaneous dual-beam *in situ* irradiation at 823 K with 10 keV He^+ ions at the flux of $5 \times 10^{11} \text{ cm}^{-2} \text{ s}^{-1}$ to the fluence of $5 \times 10^{15} \text{ cm}^{-2}$ and 4 MeV Au^{2+} ions with the flux of $4 \times 10^{11} \text{ cm}^{-2} \text{ s}^{-1}$ to the fluence of $4.5 \times 10^{15} \text{ cm}^{-2}$. BF TEM imaging conditions are: (a,c) $\sim 0.8 \mu\text{m}$ underfocus and (b,d) $\sim 0.8 \mu\text{m}$ overfocus.

As in the case of single-beam He^+ implantation, bubbles are generally associated with various microstructural features. As a result, the bubbles are non-uniformly spatially distributed following local variations in associated microstructure. He bubbles decorate grain boundaries, dislocations, and yttria nanoparticles. Populations of bubbles located in the grain bulk and associated with grain boundaries and dislocations demonstrate similar bubble sizes. At the same time, the bubbles attached to nano-oxides are notably larger. As can be noticed in Fig. 3.36(c,d), some Y_2O_3 nanoparticles are associated with cavities roughly 10 times larger than the bubbles associated with the other microstructural components. For a clearer view of bubble size difference, BF TEM images of helium bubbles attached to nano-oxides are shown in Fig. 3.37 at a higher magnification. It can be noticed that cavities on yttria particles fall into two different classes. For the most part, the cavities on particles are smaller or comparable in size to the host precipitates and look similar to bubbles observed in the case of single-beam He^+ implantation at the same temperature. But one can also notice large cavities with the size much larger than that of hosting nanoparticles. The larger cavities keep faceted cuboidal shape corresponding to the cubic lattice of the steel matrix.

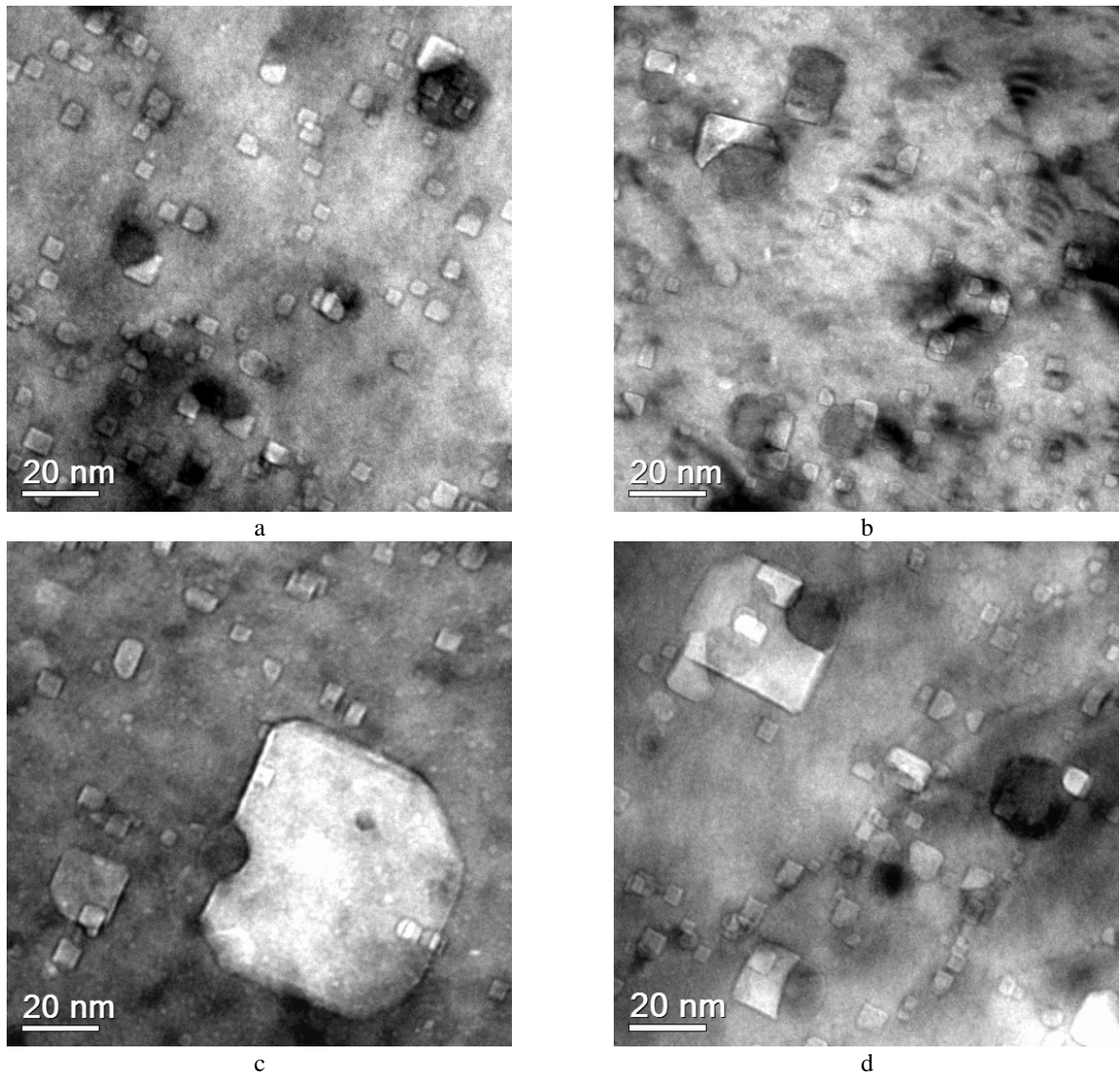


Fig. 3.37. Association of helium bubbles/voids with Y_2O_3 nanoparticles in ODS-EUROFER steel after simultaneous dual-beam *in situ* irradiation at 823 K with 10 keV He^+ ions at the flux of $5 \times 10^{11} \text{ cm}^{-2} \text{ s}^{-1}$ to the fluence of $5 \times 10^{15} \text{ cm}^{-2}$ and 4 MeV Au^{2+} ions with the flux of $4 \times 10^{11} \text{ cm}^{-2} \text{ s}^{-1}$ to the fluence of $4.5 \times 10^{15} \text{ cm}^{-2}$: (a,b) bubbles attached to particles and (c,d) large cavities attached to particles. BF TEM imaging conditions: $\sim 0.5 \mu\text{m}$ underfocus.

One thus observes a typical bi-modal cavity size distribution. Such kind of size distribution is not uncommon for steels irradiated in conditions with high He/dpa ratio and is usually interpreted as a result of the so called bubble-to-void transition [29]. This means that the bubbles that have accumulated a certain critical number of gas atoms do not need more gas in order to grow and increase their size in a void-like mode by direct accumulation of radiation-generated vacancies. Usually only a small part of the whole bubble population undergoes the bubble-to-void transition, while the majority of the bubbles remain in the bubble form. If we accept this point of view, the large cavities can be treated as ‘voids’ in the sense that their sizes are no more related to the number of gas atoms they contain, but is determined by the level of radiation damage created by all irradiating particles. Judging from images presented in Fig. 3.37, smaller yttria nanoparticles host relatively small bubbles, whereas large cavities are affiliated with larger nanoparticles. This is consistent with the assumption of bubble-to-void transition because, as we have already noticed in the case of single-beam He^+ implantation, the larger particles tend to host larger bubbles and thus are the most probable locations for possible transition to voids.

If, however, we exclude from consideration the large cavities, the remaining bubbles demonstrate the trends that are qualitatively very similar to the picture observed in the case of single-beam He^+ implantation using the same fluence and temperature. The bubbles with comparable sizes are distributed

between the bulk and various structural defects. In order to obtain the grounds for detailed comparison, the parameters of different bubble populations were estimated quantitatively.

In a usual manner adopted in this thesis, we start with the determination of the average size of bubbles on oxide particles, which is evaluated quantitatively in terms of the dependence $D_c^p(D_p)$. The measured bubble diameters D_c^p for simultaneous *in situ* dual-beam $\text{He}^+ + \text{Au}^{2+}$ irradiation are plotted versus their host particle diameters D_p in Fig. 3.38(a). The same figure shows for comparison the trend line for bubbles on yttria particles derived for single-beam He^+ implantation at the same temperature and helium dose.

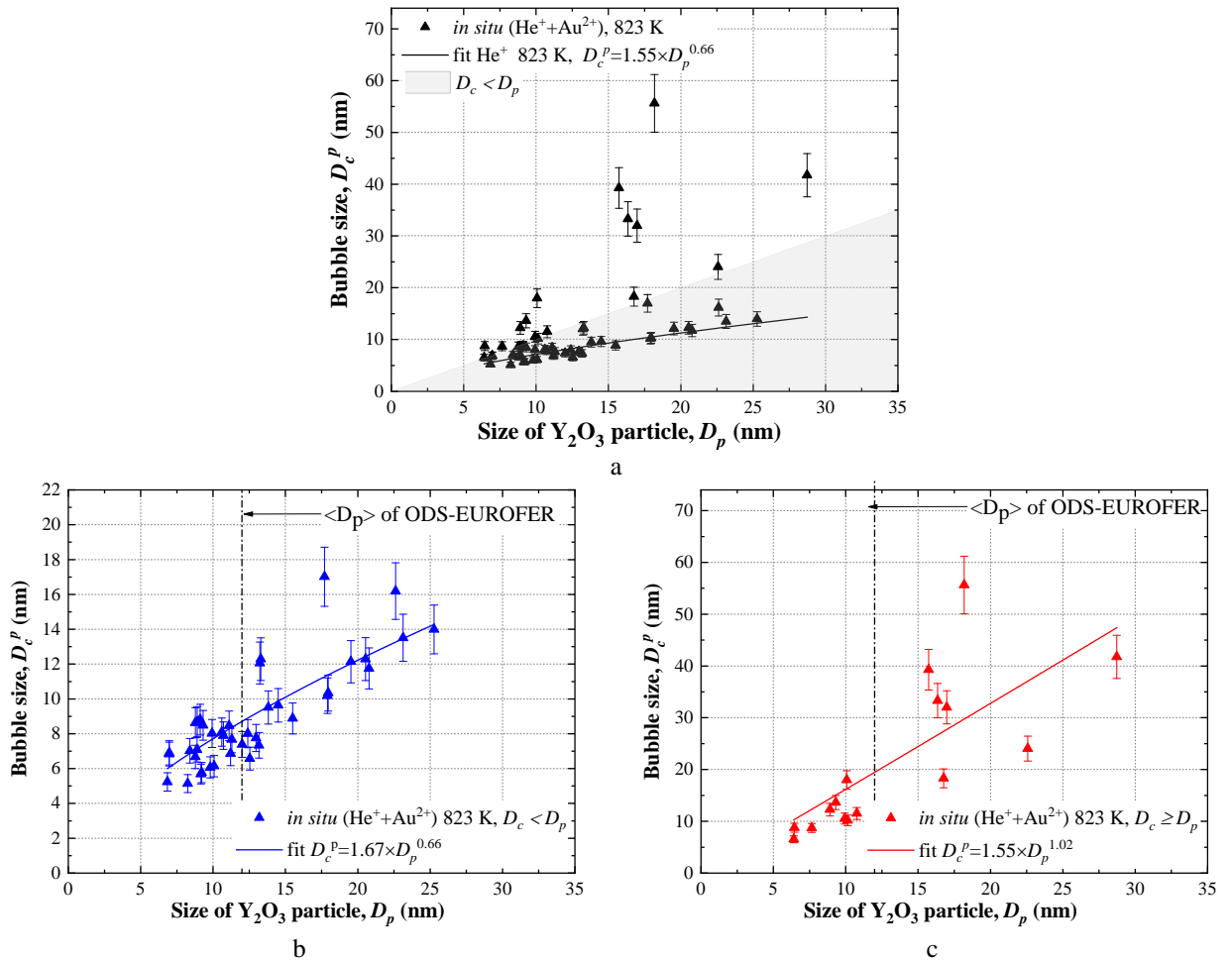


Fig. 3.38. Bubble size on yttria nanoparticles vs. particle size for the ODS-EUROFER steel simultaneously *in situ* irradiated at 823 K with 10 keV He^+ ions at the flux of $5 \times 10^{11} \text{ cm}^{-2} \text{ s}^{-1}$ to the fluence of $5 \times 10^{15} \text{ cm}^{-2}$ and 4 MeV Au^{2+} ions at the flux of $4 \times 10^{11} \text{ cm}^{-2} \text{ s}^{-1}$ to the fluence of $4.5 \times 10^{15} \text{ cm}^{-2}$. (a) Black dots are full current data set. Black solid line is the fit for single-beam He^+ implantation. The grey marked area corresponds to the bubbles with the size smaller than that of the particle. (b) Data subset for “bubble” population satisfying the condition $D_c^p \leq D_p$; blue solid line is the data fit for single-beam He^+ implantation. (c) Data subset for “void” population satisfying the condition $D_c^p > D_p$; red solid line is the best data fit. Error bars are 10% uncertainties associated with the size of the first Fresnel fringe on bubble observed in underfocused images [9,16].

The general trend that larger particles host, as a rule, larger cavities is observed both in the case of the dual-beam $\text{He}^+ + \text{Au}^{2+}$ irradiation and in the case of single He^+ beam regime. However it is also clearly visible that only a part of all the data points for the dual-beam regime (roughly, those satisfying the condition $D_c^p \leq D_p$ and falling in the grey shaded area in Fig. 3.38(a)) follows closely the trend line for the single-beam He^+ implantation. But there is also a group of points (falling well outside of the grey shaded area) that strongly deviate from the single-beam trend line and correspond rather to the population

of large cavities (voids). In order to take into account this observation, the full set of data points for the simultaneous dual-beam irradiation was subdivided into two subsets, corresponding to the “bubble” population, which is arbitrarily defined as bubbles satisfying the condition $D_c^p \leq D_p$, and “void” population, which satisfies the opposite condition. These data subsets are shown separately in Figs. 3.38(b) and 3.38(c), respectively, and were fitted independently by power laws of the form $D_c^p(D_p) = a \cdot D_p^b$ in order to obtain the required average cavity sizes $\langle D_c^p \rangle$ for each population. For the “bubble” population, the power value in the fitting law was taken equal to that obtained when fitting $D_c^p(D_p)$ for the single He⁺ beam regime, assuming the same bubble growth law. In contrast, for the “void” population both fitting constants, a and b , were adjusted to obtain the best data fit. The final fitting parameters are given in Fig. 3.38(b,c), while the expected average sizes $\langle D_c^p \rangle$ are collected in Table 3.17. Note that the average size for the “bubble” population formed during the simultaneous dual-beam He⁺+Au²⁺ irradiation, $\langle D_c^p \rangle = 8.7$ nm, is not so different from the value of $\langle D_c^p \rangle = 8.1$ nm for the single-beam He⁺ implantation.

The average bubble sizes D_c^k and specific number densities N_c^k for the simultaneous dual He⁺+Au²⁺ beam irradiation regime are presented in Table 3.17 for different bubble populations in 10 grains (5 zones). Errors shown for N_c^k and D_c^k have the same meaning as in Tables 3.2, 3.4 and 3.6. The electron transparent zones on the TEM samples simultaneously irradiated with dual He⁺ and Au²⁺ beam contained no visible M₂₃C₆ carbides, so no data on bubbles located on carbide precipitates is available.

Table 3.17. Statistical analysis of specific number densities and average diameters of bubbles/cavities in the ODS-EUROFER steel after simultaneous *in situ* dual-beam irradiation with 10 keV He⁺ ions at the flux of 5×10^{11} cm⁻²s⁻¹ to the fluence of 5×10^{15} cm⁻² and 4 MeV Au²⁺ ions at the flux of 4×10^{11} cm⁻²s⁻¹ to the fluence of 4.5×10^{15} cm⁻² at 823 K.

7.1×10 ⁻³ appm He, 27.4 dpa 2.20×10 ⁻³ dpa/s	Volume		Grain boundaries		Dislocations		Y ₂ O ₃ nano-oxides	
	N_c^V (10 ²³ m ⁻³)	D_c^V (nm)	N_c^{GB} (10 ¹⁵ m ⁻²)	D_c^{GB} (nm)	N_c^D (10 ⁸ m ⁻¹)	D_c^D (nm)	N_c^P (10 ²² m ⁻³)	D_c^P (nm)
1	2.46	5.96	3.01	8.15	1.06	6.65	-	-
2	4.27	5.51	2.50	6.22	1.21	4.91	-	-
3	1.42	7.15	2.14	8.28	1.03	6.89	-	-
4	1.68	5.65	4.83	6.21	1.57	5.72	-	-
5	1.48	7.07	3.01	6.86	0.952	6.77	-	-
Average	2.26	6.27	3.10	7.14	1.16	6.19	1.00	8.70*/19.55**
Error	0.640	0.79	0.60	1.02	0.178	0.81	0.10	0.87*/1.95**

*For the nano-oxide associated bubbles with that belong to the “bubble” population

**For the nano-oxide associated bubbles with that belong to the “void” population

Quantitative analysis of bubble ensemble parameters shows that helium bubbles in the grain bulk and on dislocations have similar mean sizes D_c^k . Bubbles at the grain boundaries are ~10% larger than bubbles in the bulk. The largest are the cavities on yttria particles, with the average sizes $\langle D_c^p \rangle = 8.7$ nm and $\langle D_c^p \rangle = 19.6$ nm for “bubble” and “void” populations, respectively. The specific number densities of bubbles $\langle N_c^k \rangle$ at different extended defects and oxide particles in Table 3.17 allow no direct comparison;

it is done below after the conversion to volumetric number densities $\langle N_V^k \rangle$ in terms of the indirect approach.

The recalculated volumetric bubble density N_V^k , swelling associated with bubbles S_k , V/He ratio and fraction of accumulated helium F_{He}^k for different bubble population in ODS-EUROFER steel after simultaneous *in situ* dual He⁺+Au²⁺ beam irradiation are shown in Table 3.18. Unfortunately, the presence of two cavity populations on yttria particles makes the estimates of their contributions to swelling uncertain because of the poor statistics of large cavities and impossibility to find which share of bubbles has undergone bubble-to-void transition. Therefore, in further analysis the swelling values associated with nanoparticles, S_p , are calculated for two limiting cases, either completely neglecting the larger cavities, or assuming that all bubbles on oxide particles undergo the bubble-to-void transition. The latter assumption in our conditions is evidently non-realistic; it is used only to estimate the upper bound for swelling related to cavities on oxide particles. As far as the fraction of retained helium and the V/He ratios in bubbles are concerned, these are calculated only for the “bubble” population, completely neglecting the presence of large cavities, since there is no way to extract the He content in the larger cavities from their sizes.

Table 3.18. The average sizes and volume number densities of bubbles, swelling, V/He ratio and retained He fraction associated with different bubble populations in the ODS-EUROFER steel after simultaneous *in situ* dual-beam irradiation at 823 K with 10 keV He⁺ ions at the flux of $5 \times 10^{11} \text{ cm}^{-2}\text{s}^{-1}$ to the fluence of $5 \times 10^{15} \text{ cm}^{-2}$ and 4 MeV Au²⁺ ions with the flux of $4 \times 10^{11} \text{ cm}^{-2}\text{s}^{-1}$ to the fluence of $4.5 \times 10^{15} \text{ cm}^{-2}$.

7.1×10⁻³ appm He, 27.4 dpa 2.20x10⁻³dpa/s	D_c^k (10 ⁻⁹ m)	N_V^k (10 ²² m ⁻³)	S_k (%)	V/He	F_{He}^k (appm)	F_{He}^k (%)
Grain boundaries	7.14±1.02	2.39±0.47	0.455±0.132	2.20	2080±274	29.4±3.9
Dislocations	6.19±0.81	1.51±0.22	0.188±0.047	2.05	915±43	12.9±0.6
Y₂O₃	8.70±0.87 19.55±1.95*	1.00±0.10	0.134±0.042 3.284±1.039*	2.44	553±23	7.8±0.3
Volume	6.27±0.79	2.26±0.64	0.292±0.099	2.07	1422±141	20.1±2.0
Total		7.16±2.03	1.068±0.3631 4.219±1.44*		4970± 1690	70.2± 23.9

*Assuming that all cavities associated with nano-oxides would constitute “void” population

The largest shares of the whole bubble set constitute bubbles in the bulk and at grain boundaries, with nearly equal volume number densities of $\sim 2.3 \times 10^{22} \text{ m}^{-3}$. Dislocations and nano-oxides provide somewhat lower contributions, with cavity number densities of $N_V^d = 1.5 \times 10^{22} \text{ m}^{-3}$ and $N_V^p = 1.0 \times 10^{22} \text{ m}^{-3}$, respectively.

If we completely neglect the large cavities associated with the oxide particles, then the highest contribution to swelling, $S_{GB} = 0.46\%$, comes from the bubbles located on the grain boundaries. Slightly lower, but comparable contribution to swelling, $S_V = 0.29\%$, is provided by bubbles in the bulk. Contributions to swelling from bubble ensembles on dislocations and nano-oxides, $S_d = 0.19\%$ and, $S_p = 0.13\%$, are lower, but non-negligible. Overall, one can conclude that all bubble populations contribute to the overall swelling in comparable shares. Completely different situation is expected, if all the bubbles attached to Y₂O₃ nanoparticles would undergo bubble-to-void transition. In that case large cavities formed at the yttria nanoparticle/matrix interfaces would dominate in the swelling behavior of steel. Under this assumption, the calculated swelling value corresponding to voids attached to nano-oxides would be $S_p = 3.3\%$, that is at least 4 times larger than that obtained neglecting large cavities. And

one can expect that at larger irradiation doses the difference will only increase, because the growth of voids is no longer limited by the amount of accumulated helium in the steel matrix.

Due to the larger average size of bubbles on oxide particles, even neglecting the large cavities, these bubbles demonstrate the largest ratio $V/He=2.44$. The V/He ratios for bubble populations on dislocations and in the grain bulk are slightly lower, at the level of $V/He=2.05$. Bubbles on grain boundaries exhibit the intermediate value of $V/He=2.02$.

The main traps for helium that capture $\sim 29\%$ of all the implanted helium under simultaneous *in situ* dual-beam $He^+ + Au^{2+}$ irradiation turn out to be grain boundary bubbles. Bubbles in the bulk accumulate comparable share of implanted helium, $F_{He}^V \sim 20\%$. Bubbles on dislocations and nano-oxides are notably less efficient as He traps, capturing lower shares of the implanted helium, $\sim 13\%$ and $\sim 8\%$, respectively. When put together, all bubbles contain $\sim 70\%$ of implanted helium, implying that, in spite of the high irradiation temperature, a noticeable share of He remains captured in small He-vacancy clusters invisible in TEM.

It is instructive to compare bubble population parameters, as well as contributions to estimated swelling and helium fraction obtained in the case of simultaneous *in situ* dual-beam irradiation with He^+ and Au^{2+} ions with similar parameters observed for the case of single-beam He^+ implantation at the same temperature and helium fluence. This comparison is presented in Fig. 3.39.

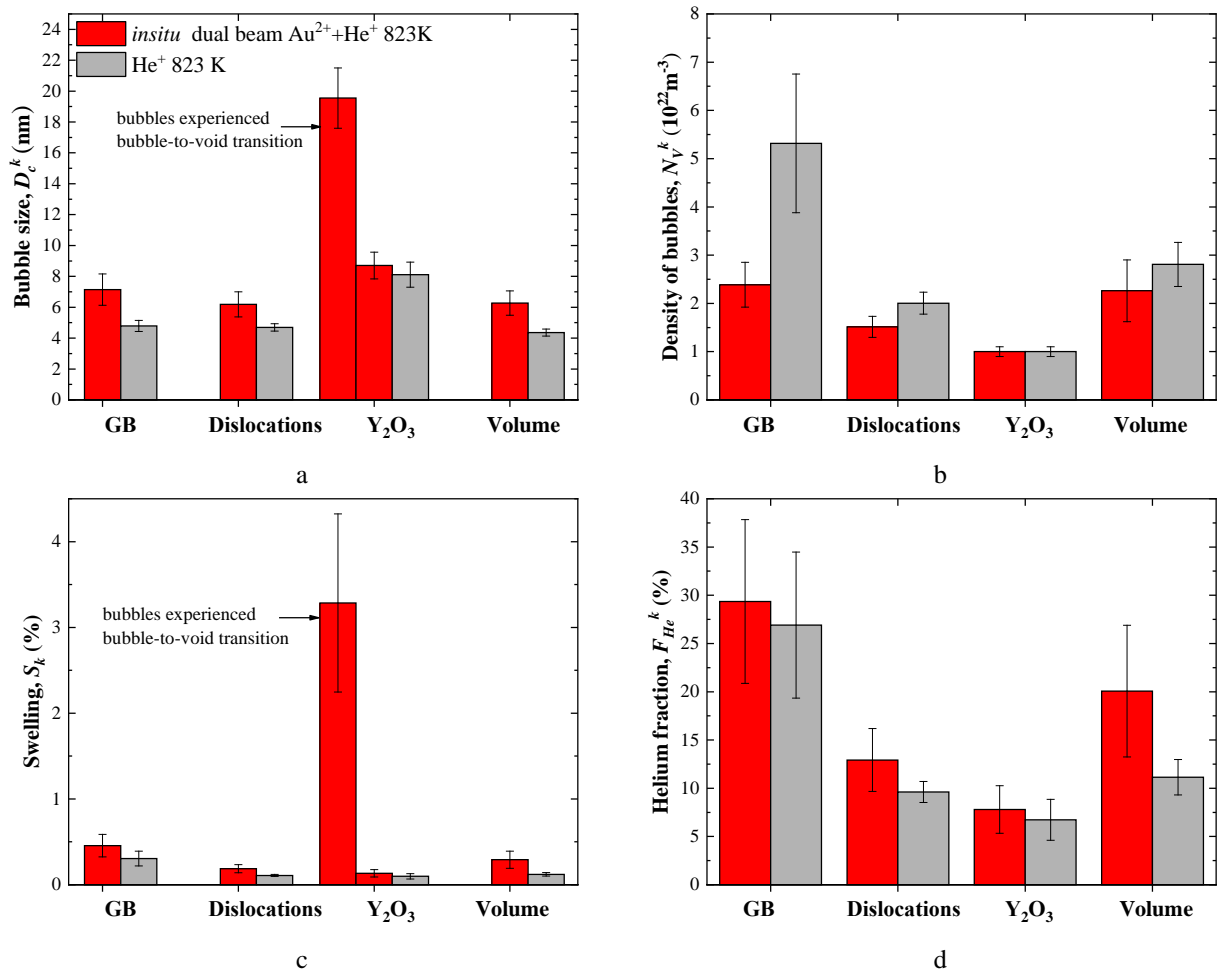


Fig. 3.39. Comparative statistical analysis of bubble mean size, the volume density of bubbles, swelling and retained He fraction associated with different bubble populations in ODS-EUROFER steel either simultaneously dual-beam irradiated with 10 keV $He^+ + 4$ MeV Au^{2+} ions at 823 K (red bars), or single-beam implanted with 10 keV He^+ ions at 823 K (grey bars). Color references provided in panel (a) are valid for all panels. Data for single-beam He^+ implantation are from Table 3.7.

As can be noticed in Fig. 3.39, additional damage production by 4 MeV Au²⁺ ions systematically reduces the number density and increases the average sizes of the bubbles both in the grain bulk and on extended defects. However, if one does not take into account the large cavities on oxide particles, the differences between the dual-beam and single He⁺ beam irradiations are quite moderate. The most strongly affected are grain boundaries, where the additional damage production results in the increase of the average bubble size to $\langle D_c^{GB} \rangle = 7.1$ nm, as compared to $\langle D_c^{GB} \rangle = 4.8$ nm in the single-beam implantation regime. In fact, only the appearance of large cavities on yttria particles constitutes a qualitative difference between the dual-beam irradiation and single-beam He⁺ implantation. The average size of large cavities promoted by the increased damage production, $\langle D_c^p \rangle = 19.6$ nm, is more than twice larger than the average size of bubbles on oxide particles for single He⁺ beam regime, $\langle D_c^p \rangle = 8.1$ nm.

In terms of swelling and helium inventory, the addition of a secondary MeV heavy ion beam increases contributions to both swelling and He retention for all bubble populations, either in the bulk, or on microstructural defects. The magnitude of the increase is not very large, however, if one does not consider large cavities on oxide particles. The strongest effect is observed for bubbles in the bulk; their contributions to both swelling S_V and the fraction of retained helium F_{He}^V increase approximately twice. Correspondingly, the total share of implanted He that is captured in the bubbles increases under synergetic action of helium accumulation and damage acceleration up to $F_{He} \sim 70\%$, whereas in the single-beam He⁺ regime only $F_{He} \sim 54\%$, that is slightly more than a half of all implanted He, was captured in the visible bubbles. Overall, if large cavities on oxide particles are not taken into account, the effect of accelerated damage on swelling and helium retention is only moderate and, among the microstructural defects, the largest contribution is provided by grain boundary bubble population, just as was the case under single helium implantation regime.

But the creation of large cavities on oxide nanoparticles, if it is indeed the result of the bubble-to-void-transition, changes the situation with swelling drastically, as illustrated in Fig. 3.40.

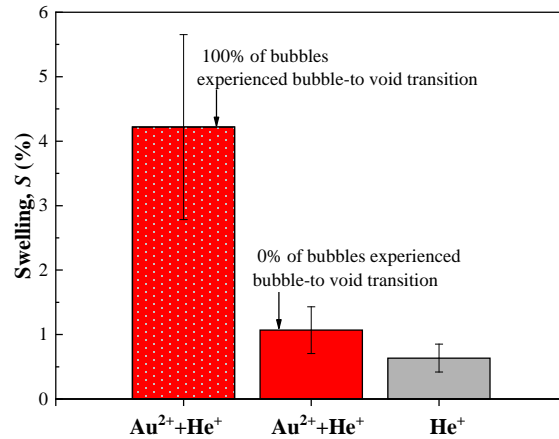


Fig. 3.40. Cumulative swelling in ODS-EUROFER irradiated at T= 823 K either simultaneously with a dual-beam of 10 keV He⁺ ions with the flux of 5×10^{11} cm⁻²s⁻¹ to the fluence of 5×10^{15} cm⁻² and 4 MeV Au²⁺ ions with the flux of 4×10^{11} cm⁻²s⁻¹ to the fluence of 4.5×10^{15} cm⁻² (red bars) or by single-beam 10 keV He⁺ ions with the flux of 5×10^{11} cm⁻²s⁻¹ to the fluence of 5×10^{15} cm⁻² (grey bar). Data for He⁺ single-beam implantation are taken from Table 3.7.

As can be noticed, neglecting the contribution of large cavities, swelling in the dual-beam irradiation case is only 1.7 times higher than in the case of single-beam helium impanation. On the other hand, if all bubbles associated with nanoparticles would undergo such a transition, then, with the estimated above average size of 19.6 nm, their contribution to swelling would increase by an order of magnitude, up to $\langle S_p \rangle = 3.3\%$, well above the contribution of grain boundary or any other bubble

population. The expected cumulative swelling would then be higher than the single-beam He⁺ implantation value already by a factor of 6.65. In reality, the true swelling value for dual-beam irradiation is somewhere between the two limiting values. But one should not forget that with the increase of irradiation dose the swelling contribution from the large cavities will grow much faster than could be provided by all the other bubble populations because the growth of large cavities is no longer controlled by the amount of helium they retain. Therefore it is clear that bubble-to-void transition has qualitatively changed the steel resistivity to swelling.

Summing up, the detailed analysis of experimental results presented in this section leads us to the following conclusions:

(i) The only important qualitative effect caused by strong acceleration of damage production in He-implanted sample of ODS-EUROFER steel by a simultaneously applied 4 MeV heavy ion (Au²⁺) beam is found to be the formation of large cavities on some oxide particles. The effect is interpreted as a manifestation of the bubble-to-void transition caused by the increase of the efficient vacancy supersaturation in the matrix as a result of irradiation with energetic gold ions. The fact that the effect is observed only on the oxide particles seems natural because the largest bubbles in ODS steel were found to always decorate the oxide particles. Bubble-to-void transition, even though taking place on a minor part of oxide particles, bears potential risk of accelerating swelling. In addition, the nearly complete embedding of oxide particles in large voids can decrease the particle efficiency as dislocation pinning centers.

(ii) Otherwise, the bubble formation pattern under the simultaneous dual-beam irradiation with He⁺ and Au²⁺ ions at T=823 K is only weakly sensitive to the strong increase of radiation damage production. Similar to the case of single He⁺ beam implantation at the same temperature, one observes partitioning of the bubbles between the bulk and various microstructural defects. It is worth mentioning that the increase of the damage generation rate is commonly expected to be equivalent to the effective temperature shift towards higher temperatures. Hence, it was natural to expect that the dual-beam irradiation would result in the decrease of bubble number density and the increase of their average size, which was indeed observed for all bubble populations, with the only exception of bubbles on oxide particles, whose number density is predetermined by the number density of particles.

(iii) The estimated swelling and helium retention in visible He bubbles are both increased in the dual-beam He⁺ + Au²⁺ irradiation case as compared to single He⁺ beam implantation, but, not taking into account the impact of large cavities associated oxide particles, the increase is quite moderate and can be rationalized in terms of the effective temperature shift associated with the increased damage production by the gold ion beam. It should be emphasized that, in spite of a certain increase of swelling contribution from grain boundary bubbles, no indications of bubble coalescence on grain boundaries that might lead to high-temperature helium embrittlement in of ODS-EUROFER steel could be observed under the dual-beam He⁺ + Au²⁺ irradiation regime.

3.2.3 The mechanism of bubble-to-void transition acceleration by oxide nanoparticles

The results of simultaneous dual-beam $\text{He}^+ + \text{Au}^{2+}$ irradiation (section 3.2.2) demonstrate that steel saturation with ODS oxide particles results in the creation of large cavities that are not observed in the case of single-beam He^+ implantation. Having in mind that the main difference between these regimes is the much higher dpa/He introduction ratio in the case of simultaneous dual-beam irradiation, it has been assumed that the appearance of large cavities resulted from bubble-to-void transition, which is known to be simplified by the increase of vacancy supersaturation in the irradiated material [30]. A specific feature of the observed large cavities was their attachment to oxide nanoparticles, which indicates that oxide particles might trigger the bubble-to-void transition. The physical reasons for this may be twofold. First of all, a cavity-associated bubble has smaller volume as compared to a bubble of the same size in the bulk and thus requires less gas atoms to reach the pressure, needed for the transition. Second, it was experimentally observed that the effective diameters of bubbles on oxide particles are generally larger than those of bubbles in the bulk or bubbles associated with extended microstructural defects, such as dislocations or grain boundaries. This might also accelerate the achievement of a critical size for the bubble-to-void transition, provided the critical transition size for bubbles on particles is not too different from that for bubbles in the bulk. In this section we suggest a simple quantitative description of the bubble-to-void transition for He bubbles associated with spherical particles. Having in mind the experimental picture, we assume that a particle hosts only a single bubble. In addition, we assume that the cavity is formed on the matrix side of the particle/matrix interface and has approximately spherical form. The latter is not exactly true for the experimental observation above (the voids are typically faceted), but can be considered as a reasonable approximation to simplify the calculations without strongly distorting the expected trends.

3.2.3.1 The basics of bubble-to-void transition theory

Theoretical description of large-scale irradiation-induced effects in structural materials (such as swelling and irradiation creep) is commonly done in the framework of the so called kinetic rate theory [31,32], which is a version of the mean-field statistical description of a many body problem, involving multiple point defect sinks (voids and/or gas bubbles, precipitates, dislocations, grain boundaries) interacting via diffusional transport of point defects (vacancies and self-interstitials) created in materials by irradiation [33]. Within this formalism, the equation of cavity growth rate (that is the rate of cavity volume, V , change with time t) is commonly written down in the form [34],

$$\frac{dV}{dt} = [Y_v D_v (C_v - C_v^{th}) - Y_i D_i C_i], \quad (3.11)$$

where D_m and C_m are the diffusion coefficients and the mean-field ('average') concentrations of point defects of type m ($m = v$ or i for vacancies or interstitials, respectively), C_v^{th} is the equilibrium vacancy concentration at the cavity surface and Y_m are numerical coefficients, commonly referred to as 'bias factors'. By definition, bias factors of point-defect sinks are properties of sinks and are insensitive to the mean-field point defect concentrations [33]. In turn, the mean-field point defect concentrations are not sensitive to properties of individual point defect sinks, being determined by the balance between the efficiency of point defect generation by irradiation and the full point defect loss efficiency on the whole ensemble of point defect sinks present in the material.

In the simplest case of a spherical cavity with radius R in the bulk, the cavity bias factors have a simple form, $Y_i = Y_v = 4\pi R$ [31], but in more general cases, they can be quite complicated functions of both cavity size and additional parameters (see e.g. Ref. [35] and references therein). For example, when cavities contain noticeable amount of captured gas atoms, such additional parameters can include internal gas pressure and the elastic properties of point defects and material itself. When cavities are associated

with other microstructural defects, such as dislocations, grain boundaries, or precipitates, the cavity bias factors can be additionally modified by the host structural defect assistance to the point defect transport to cavities and thus be very different for vacancies and interstitials. However, in order to explain the reasons for the bubble-to-void transition, it is sufficient to restrict ourselves to the simplest form of bias factors, as suggested in the original paper [30] that has introduced the concept of bubble-to-void transition.

Equation (3.11) can be rewritten alternatively as

$$\frac{dV}{dt} = Y_v D_v C_{v0}^{th} (\Delta - \Delta_v^{th}), \quad (3.12)$$

where Δ is the effective vacancy supersaturation, defined as

$$\Delta = \frac{Y_v D_v C_v - Y_i D_i C_i}{Y_v D_v C_{v0}^{th}}, \quad (3.13)$$

$\Delta_v^{th} = C_v^{th} / C_{v0}^{th}$, $C_{v0}^{th} = \exp(-E_v^f / k_B T)$ is the vacancy concentration in equilibrium with a flat material surface, E_v^f - the vacancy formation energy in the bulk, k_B - the Boltzmann constant and T - the absolute temperature. The growth or shrinkage of an individual cavity is thus determined by the relation between the effective vacancy supersaturation and Δ_v^{th} .

For the simplest case of a cavity without internal gas (i.e. void) it is generally true that its growth rate remains negative for all void sizes smaller than a certain critical value. For a spherical void, this statement can be reformulated so that, in order for a void to grow, its radius R should exceed a certain critical value, R_c . Then the void grows permanently, provided Δ does not fall down with time. In order to demonstrate this, let us set $Y_i = Y_v$, so that the effective vacancy supersaturation does not depend on void size, while Δ_v^{th} is described by the Gibbs-Thomson equation,

$$\Delta_v^{th} = \exp\left(\frac{2\gamma\Omega}{kTR}\right), \quad (3.14)$$

where Ω is the atomic volume in the matrix and σ_0 is the surface traction that can be expressed in terms of specific free surface energy (surface tension), γ , as

$$\sigma_0 = -\frac{2\gamma}{R}. \quad (3.15)$$

It can be easily verified, that the difference $\Delta - \Delta_v^{th}$ monotonically increases as a function of R and is positive only provided

$$R > R_c = R_s / s, \quad (3.16)$$

where $R_s = 2\gamma\Omega/k_B T$ and $s = \ln\Delta$. The case of $R = R_c$ corresponds to an equilibrium (the void neither shrinks, no grows), but the equilibrium is an unstable one.

A more complicated situation is met, when the material accumulates during irradiation a certain amount of gas (typically, helium) that is poorly soluble in the matrix and precipitates in the available empty spaces, including vacancies and small cavities (vacancy clusters). When helium is accumulated in a cavity, it prevents complete cavity dissolution. Hence, a gas-containing cavity (gas bubble) should have, in addition to R_c , one more equilibrium size, R_g , which answers the situation where the cavity surface tension is approximately counterbalanced by the gas pressure inside the bubble.

The expression for the equilibrium radius R_c in the case of gas bubbles is given by a more complicated relation than equation (3.16), because the surface traction in equation (3.14) is now described as

$$\sigma_0 = P - \frac{2\gamma}{R}, \quad (3.17)$$

where P is the internal gas pressure in the cavity, which is also sensitive to the bubble size. For a bubble containing a fixed number of gas atoms, n_g , one has to use an appropriate equation of state (EOS) in order to relate pressure to the bubble volume. A typical equation of state can be written down as

$$P = \xi k_B T F(\xi V_g), \quad (3.18)$$

where $\xi = n_g/V$ is the gas density in the cavity, V_g - the gas atom 'volume', and F - some function of the gas density, which tends to unity, when $\xi \rightarrow 0$. In the latter case, the equation of state transforms into the ideal gas equation. Assuming it for simplicity (in spite of the fact that for small gas bubbles the ideal gas approximation works poorly), the equation for the equilibrium bubble radii can be written down in the form

$$Q(R, n_g) = 0, \quad (3.19)$$

where we have introduced the notation

$$Q(R, n_g) = \frac{3n_g \Omega}{4\pi R^3} - \frac{R_s}{R} + s. \quad (3.20)$$

When treated as a function of R at a fixed value of n_g , Q has a unique minimum at the void size

$$R_{\min} = \sqrt{\frac{9n_g \Omega}{4\pi R_s}}, \quad (3.21)$$

while the value of function Q in the minimum is

$$Q(R_{\min}) = s - \frac{2 R_s}{3 R_{\min}}. \quad (3.22)$$

It is seen that equation (3.19) can be satisfied only provided $Q(R_{\min}) \leq 0$, or

$$s \leq \frac{2 R_s}{3 R_{\min}}. \quad (3.23)$$

Otherwise, Q is positive for all R , meaning that bubbles of all sizes tend to grow. The limiting case for the existence of positive roots of Q corresponds to exact equality, when

$$R_{\min} = R^* = \frac{2 R_s}{3 s}, \quad (3.24)$$

and the number of gas atoms in such cavity, according to eq. (3.21), equals to

$$n_g^* = \frac{16\pi}{81s^2\Omega} R_s^3. \quad (3.25)$$

It is convenient to use these R^* and n_g^* values in order to introduce non-dimensional variables $\rho = R/R^*$ and $\eta_g = n_g/n_g^*$ as normalized bubble radius and normalized gas content in the bubble, respectively. In these variables, Q can be expressed in a very simple form,

$$Q(\rho, \eta) = \frac{3}{2} s \left[\frac{1}{3} \frac{\eta_g}{\rho^3} - \frac{1}{\rho} + \frac{2}{3} \right]. \quad (3.26)$$

Finally, when expressed in the dimensionless variables, equations (3.21) and (3.22) are reduced to

$$\rho_{\min} = \sqrt{\eta_g} \quad \text{and} \quad Q(\rho_{\min}) = \frac{s}{\rho_{\min}} (\rho_{\min} - 1). \quad (3.27)$$

The plot of Q as a function of normalized bubble radius ρ at different values of η_g is shown in Fig. 3.41.

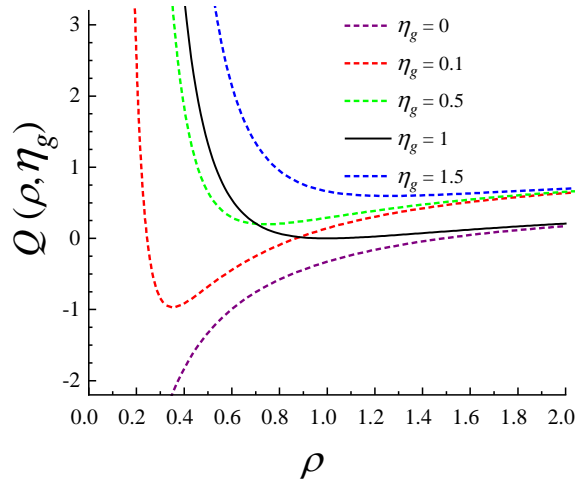


Fig. 3.41. The dependence of function Q on normalized cavity radius ρ at different values of normalized gas content in the cavity η_g . (a) $\eta_g = 0$; (b) $\eta_g = 0.1$; (c) $\eta_g = 0.5$; (d) $\eta_g = 1.0$; (e) $\eta_g = 1.5$.

As can be seen, $Q(\rho, \eta_g)$ has two roots for $\eta_g < 1$. The smaller one corresponds to stable equilibrium size R_g and the larger one – to the critical size for unlimited cavity growth, R_u . In practice, when insoluble gas is introduced into the matrix gradually, during either irradiation (e.g. via transmutation reactions) or ion implantation, the growth of cavities initially is only possible due to gas atom accumulation in vacancy clusters. Typically, in irradiation/implantation conditions the rate of vacancy production in metals is much higher than that of helium accumulation and the experimental temperatures are high enough to guarantee vacancy mobility. So, when a cavity captures a gas atom, its volume can accommodate to the new gas content, corresponding to the lower root of Q . However, this process continues only while the gas atom number in the cavity remains smaller than n_g^* . When this limit is exceeded, the cavity does not need more gas atoms in order to grow and grows in a void-like mode, not caring about further accumulation of gas atoms (even if it continues). For this reason, n_g^* is usually referred to as the critical number of gas atoms for the bubble-to-void transition and R^* - as the bubble-to-void transition radius.

3.2.3.2 Gas bubble growth on second-phase particles

When a growing bubble is associated with a second-phase particle, the model description becomes more complicated. For simplicity, it is assumed that vacancies are insoluble in the substrate, so that the interface between the cavity and the substrate is not affected by vacancy accumulation in the cavity. Moreover, we assume that, independent of the cavity size, the cavity surface facing the matrix always remains spherical, while the wetting angle α (see Fig. 3.42) remains constant and is uniquely determined by the relation

$$\cos \alpha = \frac{\gamma_{sm} - \gamma_{sc}}{\gamma}, \quad (3.28)$$

where γ_{sm} and γ_{sc} stand for the specific surface energies of substrate interfaces with the matrix and the vacuum, respectively. The surface tension for the cavity-matrix interface is denoted, as before, by γ .

Let us consider now a spherical bubble that grows on a spherical second-phase particle and thus has a shape shown in Fig. 3.42(b). The cavity growth law can still be described by equation (3.12), but the cavity bias factors are now given by more complicated expressions than for a cavity in the bulk. However, as far as there is no substantial difference between Y_v and Y_i , this is not important for the problem we consider. It is also not *a priori* evident how the expression for the factor Δ_v^{th} should look like, but it can be easily shown that equation (3.14) remains applicable for a spherical cavity segment on a spherical substrate.

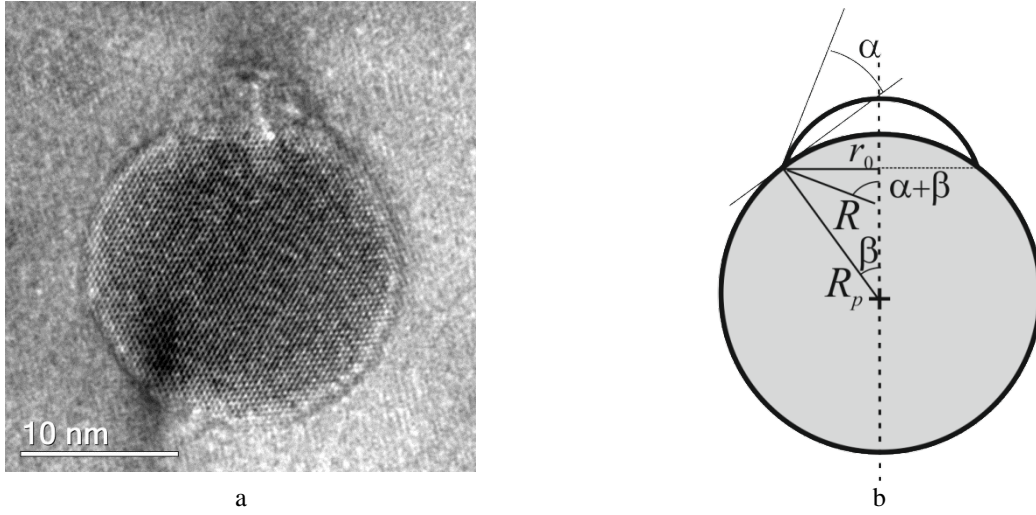


Fig. 3.42. (a) HRTEM image of a He-filled cavity attached to yttria nanoparticle in ODS-EUROFER steel irradiated with a single He^+ ion beam to $\sim 8.5 \times 10^3$ appm He (peak value). HRTEM imaging conditions: $\sim 0.3 \mu\text{m}$ underfocus. (b) Schematic representation of a lens-shaped cavity attached to spherical nanoparticle.

Indeed, when the surface tension can differ on different segments of the cavity surface, S , the equilibrium vacancy concentration C_v^{th} at the cavity/matrix interface can be obtained from the general requirement that the system free energy should be at minimum when the cavity is in equilibrium with a solution of vacancies in the environment. The change of the system free energy, dF , on adding one vacancy (i.e. a small volume $dV = \Omega$) to the cavity can be written down as

$$dF = -PdV + d\left(\int_S \gamma dS\right) - \mu, \quad (3.29)$$

where μ is the chemical potential (per vacancy) of vacancies in the bulk and integration of surface tension is over the whole cavity surface. Having in mind that the average vacancy concentration in the bulk is extremely low even in the ion implantation conditions (simple estimates indicate that in our experimental conditions it does not exceed 10^{-9} , one can use for μ the dilute solution approximation, namely [36]

$$\mu = E_v^f + k_B T \ln C_v.$$

In equilibrium one has $dF = 0$, which immediately gives for the equilibrium concentration the relation

$$C_v^{th} = C_{v0}^{th} \exp\left(-\frac{\Omega}{k_B T} \left(P - \frac{d}{dV} \left(\int_{S_c} \gamma dS\right)\right)\right). \quad (3.30)$$

Since we assume that the cavity shape at a small change of the cavity volume quickly accommodates itself to the equilibrium one, being always represented by two spherical interfaces (one with the substrate and another with the matrix), then

$$\Delta_v^{th} \equiv \exp\left(-\left[P - \gamma \frac{dS_c}{dV_c} - (\gamma_{sc} - \gamma_{sm}) \frac{dS_{sc}}{dV_c}\right] \frac{\Omega}{k_B T}\right), \quad (3.31)$$

where V_c is the volume of the cavity, S_c – the area of the cavity-matrix surface, and S_{sc} – the area of the cavity-substrate interface. Taking into account equation (3.28), this is reduced to

$$\Delta_v^{th} \equiv \exp\left(-\left[P - \gamma \frac{d\Delta S_c}{dV_c}\right] \frac{\Omega}{k_B T}\right), \quad (3.32)$$

where $\Delta S_c = S_c - S_{sc} \cos \alpha$.

In order to calculate the derivative $d\Delta S_c/dV_c$, one needs explicit equations for the volume and surface area of a cavity that lies on a spherical particle with radius R_p . The volume is given by equation (3.5), while the segment surface areas are

$$S_c = 2\pi R^2(1 - \cos(\alpha + \beta)) \quad \text{and} \quad S_{sc} = 2\pi R_p^2(1 - \cos \beta), \quad (3.33)$$

where angles α and β are as defined in Fig. 3.41(b). Having in mind equation (3.6), the cosines in equation (3.33) can be written down in a compact form as

$$\cos(\alpha + \beta) = \frac{a}{\mathfrak{R}} \quad \text{and} \quad \cos \beta = \frac{b}{\mathfrak{R}},$$

where we have introduced new variables $a = \cos \alpha - \zeta$, $b = 1 - \zeta \cos \alpha$, $\mathfrak{R} = \sqrt{1 - 2\zeta \cos \alpha + \zeta^2}$, and $\zeta = R/R_p$. With these variables, one can write

$$\Delta S_c = S_c - \cos \alpha S_{sc} = 2\pi R_p^2 \left[\zeta^2 \left(1 - \frac{a}{\mathfrak{R}} \right) - \cos \alpha \left(1 - \frac{b}{\mathfrak{R}} \right) \right] \quad (3.34)$$

and

$$V_c = \frac{\pi}{3} R_p^3 \zeta^3 \left[\left(2 - 3 \frac{a}{\mathfrak{R}} + \frac{a^3}{\mathfrak{R}^3} \right) - \left(2 - 3 \frac{b}{\mathfrak{R}} + \frac{b^3}{\mathfrak{R}^3} \right) \right], \quad (3.35)$$

so that the derivative $d\Delta S_c/dV_c$, can be calculated as

$$\frac{d\Delta S_c}{dV_c} = \frac{d\Delta S_c}{d\zeta} / \frac{dV_c}{d\zeta},$$

The derivatives over ζ are obtained straightforwardly,

$$\frac{d\Delta S_c}{d\zeta} = 2\pi R_p R \left(2 - 2 \frac{a}{\mathfrak{R}} - \frac{a \sin^2 \alpha}{\mathfrak{R}^3} \right) \quad \text{and} \quad \frac{dV_c}{d\zeta} = \pi R_p R^2 \left(2 - 2 \frac{a}{\mathfrak{R}} - \frac{a \sin^2 \alpha}{\mathfrak{R}^3} \right),$$

and hence

$$\frac{d\Delta S_c}{dV_c} = \frac{2}{R}, \quad (3.36)$$

which has exactly the same form as for a cavity in the bulk. Thus, equation (3.32) is reduced to equation (3.14).

The equation for the equilibrium bubble radii can then be written down in the form identical to equation (3.19), where function Q has the form (assuming the ideal gas law for the gas pressure in the cavity),

$$Q(R, n_g) = \frac{n_g \Omega}{V_c} - \frac{R_s}{R} + s. \quad (3.37)$$

The only difference of equation (3.37) from equation (3.20) is that the volume of the cavity is now smaller than that for the cavity in the bulk.

In a special case considered in Ref. [37], where cavity lies on a flat matrix-substrate interface ($\beta=0$), the equation for the equilibrium bubble radii can be written down in terms of non-dimensional void radius and gas content as

$$Q(R, n_g) = \frac{3s}{2} \left[\frac{4}{3(2 + \cos \alpha)(1 - \cos \alpha)^2} \frac{\eta_g}{\rho^3} - \frac{1}{\rho} + \frac{2}{3} \right] = 0. \quad (3.38)$$

The minimum of Q lies at the relative void size ρ_{\min} , defined by equation

$$\rho_{\min} = \sqrt{\frac{4}{(1 - \cos \alpha)[2 - \cos \alpha - \cos^2 \alpha]}} \eta_g, \quad (3.39)$$

while the function value at $\rho = \rho_{\min}$ is

$$Q(\rho_{\min}, n_g) = \frac{s}{\rho_{\min}} [\rho_{\min} - 1]. \quad (3.40)$$

The bubble-to-void transition occurs when $Q(\rho_{\min}) = 0$, that is at $\rho_{\min} = 1$, exactly the same as for the bubble in the bulk. However, the critical number of gas atoms required to reach the transition radius differs, being equal to

$$n_{gl}^* = \frac{(1 - \cos \alpha)^2 [2 + \cos \alpha]}{4} n_g^* \equiv f_l n_g^*. \quad (3.41)$$

Depending on α , the factor $f_l(\alpha)$ varies as shown in Fig. 3.43, never exceeding unity. So in this particular limiting case the bubble-to-void transition radius R^* for a spherical bubble segment does not change as compared to the bubble in the bulk, but the critical number of gas atoms decreases for all wetting angles α .

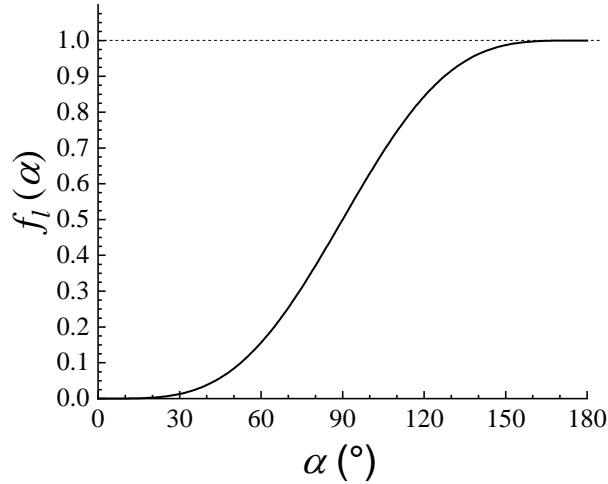


Fig. 3.43. Variation of the factor $f_l = n_{gl}^* / n_g^*$ as a function of wetting angle α .

Now let us consider a cavity located on a spherical particle with radius R_p . As can be noticed in equation (3.35), the cavity volume in this case is a function of the ratio $\zeta = R/R_p$. The plot of normalized cavity volume $v_c = 3V_c / (4\pi R^3)$ as a function of ζ is shown in Fig. 3.44 for different values of wetting angle α .

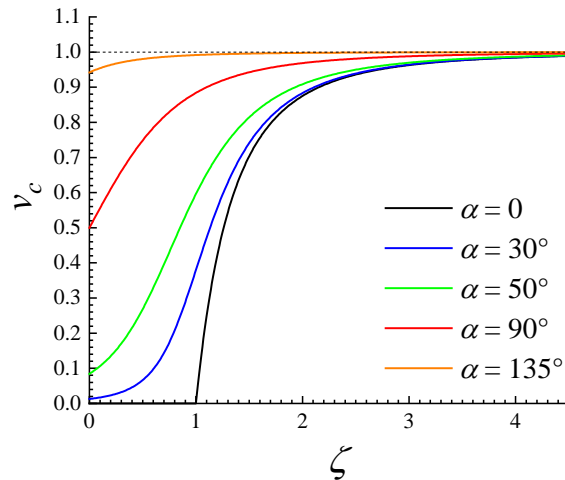


Fig. 3.44. The normalized bubble volume as a function of the cavity to particle size ratio ζ . Different curve colors correspond to different wetting angles as specified in the legend.

In non-dimensional variables ρ and η_g , the equation for equilibrium cavity radii is reduced to

$$Q(R, n_g) = \frac{3s}{2} \left[\frac{1}{3v_c(\rho)} \frac{\eta_g}{\rho^3} - \frac{1}{\rho} + \frac{2}{3} \right] = 0. \quad (3.42)$$

The location of the minimum of this function can be found from equation

$$\eta_g = v_c(\rho_{\min})(1 - 2\chi(\zeta_p^* \rho_{\min}, \alpha)) \rho_{\min}^2, \quad (3.43)$$

while the value of the function in the minimum point is

$$Q(\rho_{\min}) = \frac{S}{\rho_{\min}} \left[\rho_{\min} - 1 - \chi(\zeta_p^* \rho_{\min}, \alpha) \right], \quad (3.44)$$

where $\zeta_p^* = R^* / R_p$ and

$$\chi(\zeta, \alpha) = \frac{(2 + \cos \beta)(1 - \cos \beta)^2}{2\zeta^3 (2 + \cos(\alpha + \beta))(1 - \cos(\alpha + \beta))^2}. \quad (3.45)$$

It is worth mentioning that the minimum value of Q in the ideal gas approximation is insensitive to the number of gas atoms in the bubble.

The dependence of χ on the void to particle radii ratio ζ is shown in Fig. 3.45 for different values of the wetting angle. In the limiting cases of small and large ζ it is described, respectively, by the relations

$$\chi(\zeta, \alpha) \approx \frac{3(1 + \cos \alpha)^2}{8(2 + \cos \alpha)} \zeta \quad \text{and} \quad \chi(\zeta, \alpha) \approx \frac{(2 - \cos \alpha)(1 + \cos \alpha)^2}{8\zeta^3}.$$

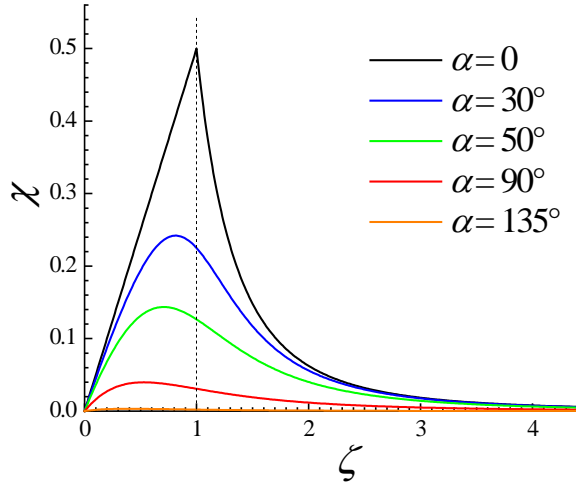


Fig. 3.45. The dependence of χ on the cavity to particle size ratio ζ . Different curve colors correspond to different wetting angles as specified in the legend.

An implicit equation for the bubble-to-void transition radius ρ_p^* is obtained by equating $Q(\rho_p^*)$ to zero, which gives

$$\rho_p^* = 1 + \chi(\zeta_p^* \rho_p^*, \alpha), \quad (3.46)$$

Since χ is a positive function for all possible arguments, the bubble-to-void transition radius for a cavity on a spherical particle is larger than for similar size bubbles in the bulk or on a flat substrate. But the increase of ρ_p^* is relatively small for all particle sizes, especially when the wetting angle is not too close to zero. In a zero-order approximation we can get an analytical parametric dependence of ρ_p^* on the relative bubble size by setting $\rho_p^* = 1$ in the r.h.s. of equation (3.46),

$$\rho_{pa}^* = 1 + \tilde{\chi}(\zeta_p^*, \alpha). \quad (3.47)$$

The difference between the exact values of ρ_p^* and the approximate ones obtained using this simplification is shown in Fig. 3.46(a).

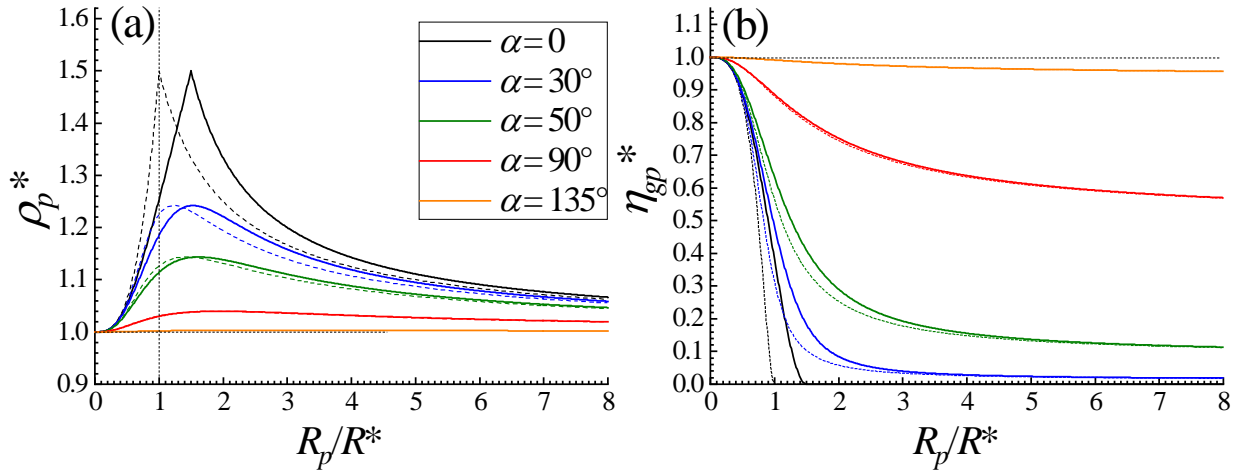


Fig. 3.46. The comparison of exact (solid lines) and approximate (dashed lines) values of (a) ρ_p^* and (b) η_{gp}^* as a function of the normalized particle size R_p/R^* at different α . Curve colors in both panels are specified in the legend.

Substituting ρ_p^* into equation (3.44), one obtains the equation for the critical number of gas atoms, η_{gp}^* , required to reach the bubble-to-void transition size,

$$\eta_{gp}^* = v_c(\zeta_p^*, \alpha)(1 - 2\chi(\zeta_p^*, \alpha))\rho_p^{*2}. \quad (3.48)$$

The dependence of η_{gp}^* on the normalized particle size R_p/R^* is shown in Fig. 3.46(b). The same figure shows also the approximate analytical dependences obtained by setting $\rho_p^* = 1$ in the first two terms in the r.h.s. of equation (3.48), namely

$$\eta_{gp}^* \approx v_c(\zeta_p^*, \alpha)(1 - 2\chi(\zeta_p^*, \alpha))\rho_{pa}^{*2}. \quad (3.49)$$

It can be seen that eq. (3.49) gives a reasonable approximation of the critical gas content in the bubble for wetting angles exceeding roughly 45° .

Finally, let us discuss how the predictions for the critical bubble size and gas content will change if we discard the ideal gas approximation. In this case the relation between the gas pressure and the gas density in the bubble is given by relation (3.18). Correspondingly, the equation determining the equilibrium bubble radii has the form

$$Q(R, n_g) = \frac{3s}{2} \left[\frac{1}{3v_c(\rho)} \frac{\eta_g}{\rho^3} F\left(\theta \frac{\eta_g}{v_c(\rho)\rho^3} - \frac{1}{\rho} + \frac{2}{3}\right) \right] = 0, \quad (3.50)$$

which can be rewritten in an equivalent form as

$$n_g z F(\theta n_g z) = \left(\frac{3}{\rho} - 2\right), \quad (3.51)$$

where

$$\theta = \frac{sV_g}{2\Omega} \quad (3.52)$$

and

$$z = \frac{1}{\rho^3 v_c(\rho)}. \quad (3.53)$$

The value ρ_{\min} of cavity radius in the minimum of function Q is determined by the requirement of vanishing derivative of Q at ρ_{\min} , which is equivalent to

$$z \frac{d}{dz} \left[\eta_g z F(\theta \eta_g z) \right]_{z=z(\rho_{\min})} = \frac{(1 - 2\chi(\zeta_p \rho_{\min}, \alpha))}{\rho_{\min}}. \quad (3.54)$$

Using now the fact that for a critical bubble both equations (3.51) and (3.54) should be satisfied simultaneously, the equations for the critical gas atom number η_{gp}^* and critical radius ρ_p^* can be written down in the form closely resembling equations (3.43) and (3.46),

$$\eta_{gp}^* = \frac{F_1(\theta\eta_{gp}^*z(\rho_p^*))}{F(\theta\eta_{gp}^*z(\rho_p^*))}(1-2\chi(\zeta_p\rho_p^*,\alpha))\rho_p^{*3}v_c(\rho_p^*) \quad (3.55)$$

and

$$\rho_p^* = \frac{3}{2} - \frac{1}{2}F_1(\theta\eta_{gp}^*z(\rho_p^*))\left[1-2\chi(\zeta_p\rho_p^*,\alpha)\right], \quad (3.56)$$

where

$$F_1(y) = \frac{1}{\left[1+y\frac{d}{dy}[\ln F(y)]\right]}. \quad (3.57)$$

These relations lead to some general conclusions even without specifying a particular form of EOS. First of all, whatever is the equation of state, one has $F(0) = F_1(0) = 1$. Second, when the argument y (proportional to the number of gas atoms in the cavity) increases, the function $F(y)$ grows monotonically, tending to infinity as $y \rightarrow 1$. Correspondingly, $F_1(y \rightarrow 1) \rightarrow 0$. Thus, both $F_1(y)$ and F_1/F vary within the interval $[0,1]$. Since $1-2\chi$ also varies within the same limits (see Fig. 3.45), the account of EOS deviation from the ideal gas law results in the shift of critical bubble-to-void radius from 1 closer to 1.5. For the critical number of gas atoms the trend is less clear and requires knowledge of the particular equation of state.

Let us consider, for example, hard-sphere equation of state (HSEOS) in the Carnahan-Starling approximation [38], which has the form of equation (3.18) with

$$F(y) = \frac{1+y+y^2-y^3}{(1-y)^3}. \quad (3.58)$$

In the case when the cavity filling gas is helium, the gas atom 'volume' V_g can be taken equal to 5.42 \AA^3 [21]. Equations (3.55), (3.56) become now coupled and allow only numerical solution that depends on three parameters, namely α , R_p , and θ . The latter is defined in equation (3.52) and is directly proportional to the efficient vacancy supersaturation, $\theta \cong 0.23s$, where we have used the above-mentioned value of V_g and $\Omega = 11.8 \text{ \AA}^3$ for the atomic volume of iron. The calculated plots of η_{gp}^* and ρ_p^* as functions of the particle radius are shown in Fig. 3.47 for different values of s and α .

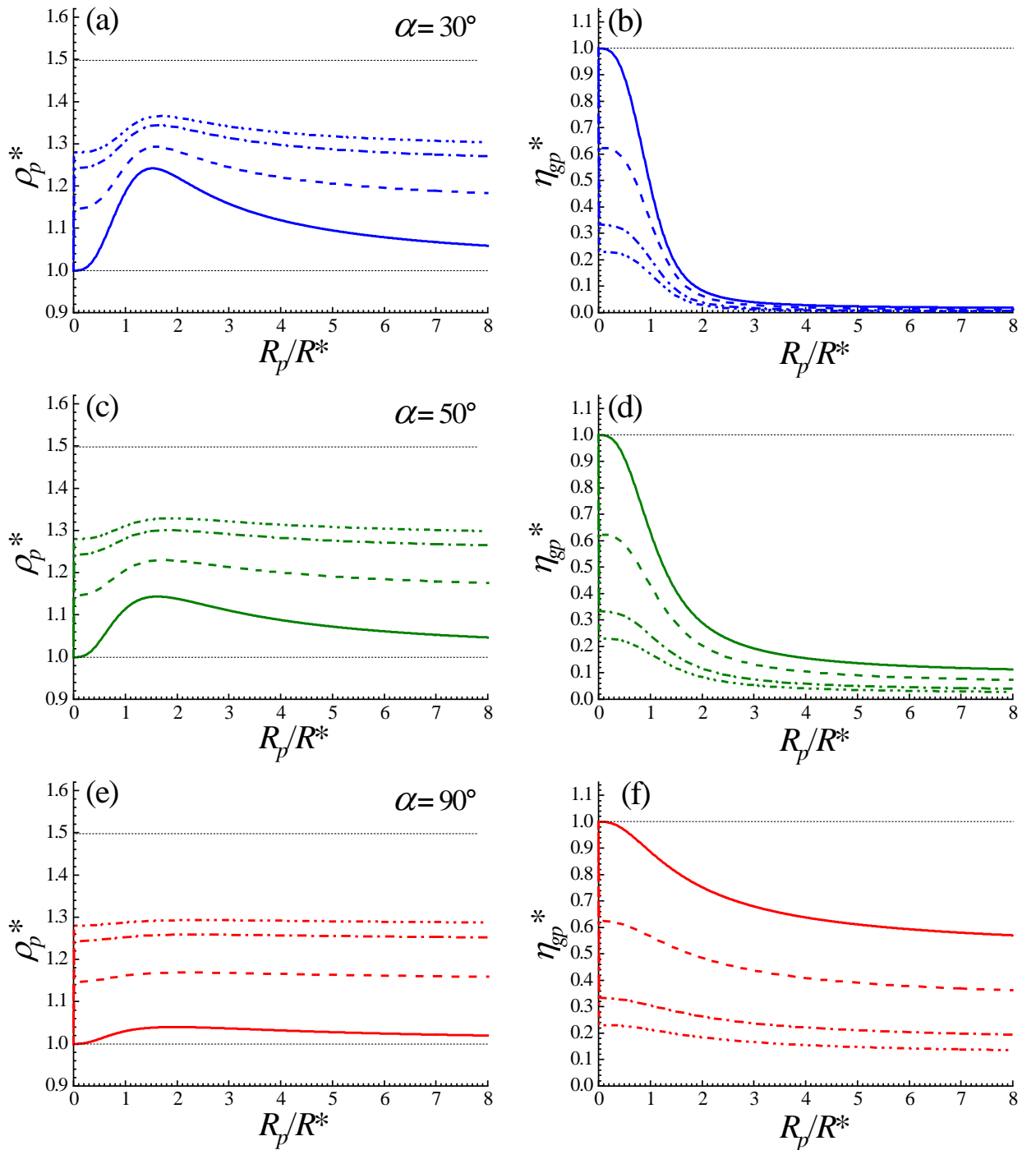


Fig. 3.47. The critical parameters ρ_p^* (left column) and η_{gp}^* (right column) as a function of the normalized particle size R_p/R^* at different α (as indicated in the legends). Curves within each panel correspond either to the ideal gas law (solid) or to HSEOS with $s = 1$ (dash), 5 (das-dot) and 10 (dash-dot-dot).

As can be seen, the normalized critical radii are predicted to be always larger than the corresponding values for the ideal gas approximation, while the normalized gas density in the bubble is lower. It is worth mentioning that the trend remains valid in the limiting case $\alpha \rightarrow 180^\circ$, when the solution becomes formally equivalent to that for a spherical gas bubble in the bulk. The latter case was considered earlier in Ref. [39], where, having in mind the corrected presentation of calculated results given later in Ref. [29], exactly the same trend was predicted.

3.2.3.3 Discussion

As follows from the theoretical considerations in section 3.2.3.2, helium bubbles that grow on oxide particles require less gas atoms for the bubble-to-void transition as compared to bubbles in the bulk, in spite of slightly larger critical radius. Hence it is quite reasonable that the oxide particles serve as triggers for the bubble-to-void-transition. It is interesting to estimate, however, how good the model can perform in describing the effect of dpa/He ratio increase on the onset of bubble-to-void transition in quantitative terms.

According to equation (3.24), the critical radius R^* for the bubble-to-void transition is inversely proportional to the efficient vacancy supersaturation, which relates, in turn, to the average point defect concentrations in the matrix that are determined by the balance of point defect generation rate by irradiation, G , and the strengths of internal sinks for point defects, k_v^2 and k_i^2 , as

$$D_m C_m = \frac{G}{k_m^2}.$$

Using these relations, one can re-write s as

$$s = \ln \left(\frac{k_i^2 - k_v^2}{k_i^2 k_v^2} \frac{G}{D_v C_{v0}^{th}} \right), \quad (3.59)$$

The sink strengths in this equation are total sink strengths that are calculated as the sums of strengths of all point defect sinks available in the material [40],

$$k_m^2 = \sum_j k_{mj}^2,$$

where j runs over all possible sinks. Four major groups of sinks are present in ODS-EUROFER steel, namely dislocations, grain boundaries, oxide particles and cavities, some of which are located in the bulk and some are attached to other structural defects. When estimating the sink strengths, we assume that the presence of cavities on dislocations and grain boundaries does not affect much the sink strengths of extended defects and estimate them according to standard relations. In particular, for dislocations we assume [40]:

$$k_{md}^2 = Z_m \rho_d,$$

where ρ_d is the dislocation density and Z_m - the dislocation bias factors, determined as

$$Z_m = \frac{4\pi}{\ln(1/\pi\rho_d R_{dm}^2)},$$

where R_{dm} are the dislocation capture radii for point defects of type m . For numerical estimates the latter can be taken equal to $R_{di} = 10b$ and $R_{dv} = 4b$, where b is the dislocation Burgers vector [41].

The grain boundary sink strength can be estimated as [42]

$$k_{mg}^2 = \frac{15}{(d_g/2)^2},$$

where d_g is the effective grain diameter, which was estimated for the elongated grains of ODS-EUROFER steel as the average of the mean grain length and width. Sink strength of He-filled cavities in the bulk is calculated as [40]

$$k_{mc}^2 = 4\pi r_c N_c,$$

where r_c and N_c are the average cavity radius and number density in the grain bulk. Finally, having in mind that all Y_2O_3 particles are covered with single cavities with the size comparable to that of the particle, the sink strength of such particle-bubble complexes can be roughly estimated as

$$k_{mp}^2 = 4\pi r_c^{eff} N_p,$$

where $r_c^{eff} = \sqrt{(r_c^p)^2 + (r_p)^2}$ is the effective radius of the oxide-cavity complex, r_p and r_c^p are the average radii of oxide nanoparticles and the associated cavities, respectively, and N_p is the particle number density.

For a relevant quantitative estimation of the effect of dpa/He ratio increase on the onset of bubble-to-void transition, let us compare critical bubble radii for single and dual-beam irradiations performed at the same temperature and with identical He⁺ ion beam parameters, but differing in the efficiency of radiation damage production and, thus, the dpa/He introduction ratio, i.e.

(1) Dual-beam regime: 10 keV He⁺ ions with the flux of $5 \times 10^{11} \text{ cm}^{-2}\text{s}^{-1}$ to the fluence of $5 \times 10^{15} \text{ cm}^{-2}$, and 4 MeV Au²⁺ ions with the flux of $4 \times 10^{11} \text{ cm}^{-2}\text{s}^{-1}$ to the fluence of $4.5 \times 10^{15} \text{ cm}^{-2}$;

(2) Single-beam regime: 10 keV He⁺ ions with the flux of $5 \times 10^{11} \text{ cm}^{-2}\text{s}^{-1}$ to the fluence of $5 \times 10^{15} \text{ cm}^{-2}$.

Most of the input parameters necessary for the estimation of sink strengths can be found in Tables 3.19 and 3.20, while the resulting sink strengths are collected in Table 3.21 for both irradiation regimes. Taking the self-diffusion coefficient equal to $D_v C_v^{th} = 2.76 \exp(-3.0 \text{ eV} / k_B T) \text{ cm}^2/\text{c}$ [43] and assuming the temperature of 823 K, we get $s \cong 1.7$ for the single-beam helium implantation case ($G = 4 \times 10^{-5} \text{ dpa/s}$) and $s \cong 5.9$ for the dual-beam irradiation ($G = 2.4 \times 10^{-3} \text{ dpa/s}$). In other words, the critical radius of bubble-to-void transition in the dual-beam irradiation case should be more than three times lower than in the case of single-beam implantation, even if we take into account the correction due to the non-ideal helium EOS in the bubbles. Qualitatively, this can explain the experimental observation that the bubble-to-void transition has occurred only in the dual-beam irradiated sample.

Table 3.19. Typical microstructural parameters of ODS-EUROFER steel in tempered state.

Microstructural component	Parameters	Values	Ref.
Grain boundaries	Mean grain length	0.7 μm	
	Means grain width	0.3 μm	
	Volume density	$7.7 \times 10^{-6} \text{ m}^{-1}$	
Dislocations	Density	$1.3 \times 10^{14} \text{ m}^{-2}$	[26, 44]
Oxide nanoparticles	Average diameter	12.0 nm	[3]
	Number density	$10.0 \times 10^{21} \text{ m}^{-3}$	[45]

Table 3.20. Comparison of average sizes and volume number densities of cavities and swelling contributions for different cavity populations in the ODS-EUROFER steel sample after dual-beam He⁺+Au²⁺ irradiation and single-beam He⁺ implantation. Data are adapted from Tables 3.7 and 3.18.

Structural component	Dual-beam He ⁺ +Au ²⁺ irradiation			Single-beam He ⁺ implantation		
	$D_c^k, \text{ nm}$	$N_V^k, 10^{22} \text{ m}^{-3}$	$S_k, \%$	$D_c^k, \text{ nm}$	$N_V^k, 10^{22} \text{ m}^{-3}$	$S_k, \%$
Grain boundaries	7.1±1.0	2.4±0.5	0.46±0.13	4.8±0.4	5.3±1.4	0.31±0.09
Dislocations	6.2±0.8	1.5±0.2	0.19±0.05	4.7±0.2	2.0±0.2	0.11±0.01
Y₂O₃ particles	8.7±0.9	1.0±0.1	0.13±0.04	8.1±0.8	1.0±0.1	0.10 ±0.03
Volume	19.6±2.0*		3.28±1.04*			
Total	6.3±0.8	2.3±0.6	0.29±0.10	4.4±0.2	2.8±0.5	0.12±0.02
		7.2±2.0	1.07±0.36		11.1±3.0	0.63±0.22
			4.22±1.44*			

* Assuming that all the cavities associated with nano-oxides would constitute “void” population

Table 3.21. Estimated sink strengths for ODS-EUROFER steel samples after dual-beam He⁺+Au²⁺ irradiation and single-beam He⁺ implantation. For cavities on oxide particles, the calculated effective diameters are also included.

Sink type	Parameter	Estimated values	
		in single-beam implanted sample	in dual-beam irradiated sample
Grain boundaries	Sink Strength, 10 ¹⁴ m ⁻²	2.6	2.6
Dislocations	Sink Strength, 10 ¹⁴ m ⁻²	2.1/2.7 ^a	2.1/2.7 ^a
Cavities in the bulk	Sink Strength, 10 ¹⁴ m ⁻²	5.8	6.7
Cavities on Y₂O₃ particles	Effective diameter, nm	14.5	14.8 (22.9 ^b)
	Sink Strength, 10 ¹⁴ m ⁻²	9.10	9.3 (14.4 ^b)
Total sink strengths, 10 ¹⁴ m ⁻²		19.61 / 20.2 ^a	20.7/ 21.4 ^a ; 25.8 / 26.5 ^{a,b}

^a The first number stands for vacancies and the second one - for interstitial atoms

^b In a case where all of the cavities associated with nano-oxides would transform into voids

At the same time, the critical radii predicted by the theory are definitely too small. For the typical values $\gamma = 2 \text{ J/m}^2$ and $\Omega = 11.8 \text{ \AA}^3$, we get $R_c = 4.2 \text{ nm}$, which would mean the critical cavity diameter of 3.3 nm for single-beam implantation, while for the dual-beam case it would be only $\sim 1 \text{ nm}$. The account of the non-ideal helium behavior in the bubbles increases these estimates, but no more than by 20-30 %. In reality it should be at least an order of magnitude larger because, judging from Fig. 3.38, the transition starts from the bubble diameter $\sim 10 \text{ nm}$. It should be kept in mind, however, that a discrepancy in quantitative estimates of critical cavity size is quite common in the literature and can be due, in particular, to the neglect of the cavity size dependence of cavity bias factors, which is non-negligible for cavities in the nanometer size range [35].

Finally, it is worth mentioning that, as can be noticed in Fig. 3.46(b), small particles (with $R_p/R^* < 1$) weakly affect the critical gas content η_{gp}^* in particle-associated cavities, whatever is the wetting angle. Only particles with the size comparable or larger than the critical one in the bulk remarkably decrease the critical gas content in the bubble. In practical terms, this means that only sufficiently large second phase particles can be efficient triggers for the bubble-to-void transition, promoting the void swelling onset. This prediction is in agreement with both the current experimental results and the earlier findings [11,46,47]. The effect is especially pronounced for moderate wetting angles, including that typical for cavities on yttria particles.

Summing up, the developed model of bubble-to-void transition for gas bubbles on second-phase particles predicts that the critical radius for bubble-to-void transition for such bubbles increases (up to 50 %, depending on the bubble and particle parameters) as compared to that for bubbles in the bulk, but the critical number of gas atoms promoting the transition decreases. The effect is most pronounced for relatively large host particles, which are thus the most probable candidates to launch the bubble-to-void transition, which agrees well with the available experimental observations.

3.3 Summary and Discussion

The main objective of chapter 3 is the clarification of the relative importance of Y_2O_3 nanoparticles as helium trapping sites in ODS-EUROFER and estimation of potential risks associated with oxide nanoparticles in conditions of ODS steel operation in a high He/dpa ratio environment. Having in mind these objectives, let us discuss the results of ODS-EUROFER steel characterization after single-beam He^+ implantation (section 3.1.2) and dual-beam $He^+ + Au^{2+}$ irradiation (section 3.2.2) along with the theoretical description of bubble-to-void transition for gas bubbles on oxide particles (section 3.2.3).

A summary of TEM based estimates of helium fraction and swelling in ODS-EUROFER steel implanted with single He^+ beam in different regimes is given in Figs. 3.48-3.50.

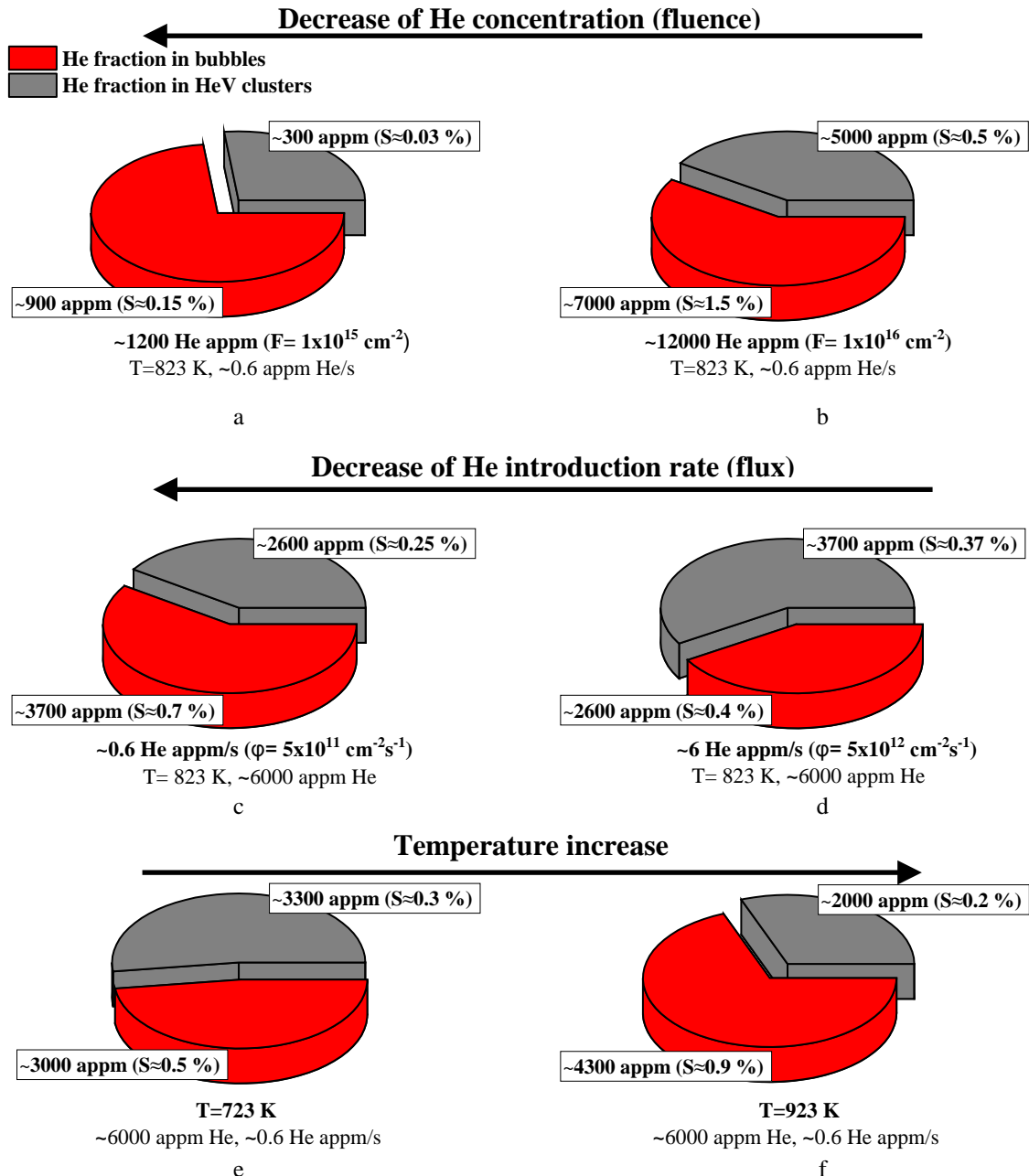


Fig. 3.48. Relative contributions to retained He fraction and total swelling from bubbles and He-V clusters in ODS-EUROFER steel implanted with He^+ ions: (a,b) as a function of fluence in the range $1 \times 10^{15} - 1 \times 10^{16} \text{ cm}^{-2}$ for the flux of $5 \times 10^{11} \text{ cm}^{-2} \text{ s}^{-1}$ at $T=823 \text{ K}$; (c,d) as a function of flux in the range of $5 \times 10^{11} - 5 \times 10^{12} \text{ cm}^{-2} \text{ s}^{-1}$ with the fluence of $5 \times 10^{15} \text{ cm}^{-2}$ at $T=823 \text{ K}$; (e,f) as a function of temperature in the range of 723-823 K to the fluence of $5 \times 10^{15} \text{ cm}^{-2}$ with the flux of $5 \times 10^{11} \text{ cm}^{-2} \text{ s}^{-1}$. Colors differentiate the data for bubbles and HeV clusters, as explained in the legend located in panel (a). The depicted helium shares are normalized to the total implanted helium concentrations. Presentation is based on the data collected in Table 3.10.

As a general trend, the estimates of helium fraction accumulated by bubbles (Fig. 3.48) based on TEM observations indicate that none of the applied single-beam implantation regimes provides complete capture of implanted helium by the whole bubble population and a noticeable share of implanted He atom remains trapped in He-vacancy clusters invisible by TEM. Hence, a straightforward evaluation of swelling based on the size and number density of visible bubbles underestimates the true swelling of ODS-EUROFER in our experimental conditions. Helium partitioning between bubbles and He-V clusters is found to be sensitive to fluence, flux and temperature variations. As can be noticed in Fig. 3.48, the amount of helium captured in small He-V clusters increases with the increase of implantation fluence (i.e. the achieved helium content) and flux (helium accumulation rate) but decreases with the increase of implantation temperature. The relative contribution of invisible clusters to helium inventory is more sensitive to fluence and temperature than to flux variation within the ranges studied. At the same time, the relative contribution of invisible clusters to swelling changes only weakly with increasing fluence (remaining at the level of 20-25%), but is quite sensitive to flux and temperature variations, increasing from ~25% to ~50% with the increase of implantation flux and decreasing from ~30% down to ~20% with the increase of implantation temperature. Summing up, one can expect that the estimates of swelling and captured He fraction based on the summary volume of visible bubbles in TEM images can be very inaccurate in experimental studies performed at low temperatures, high He concentrations and high rates of He production/introduction.

A remarkable feature of the observed bubble growth kinetics in all studied implantation regimes is the formation of different bubble families that grow not only in the grain bulk but also on microstructural defects, such as extended defects (dislocations, grain boundaries) and second-phase particles (carbides and oxides). Restricting below to helium fraction and swelling associated with the bubbles, let's discuss in more detail the relative contributions of different bubble populations to these values in different single He⁺ implantation regimes (see Fig. 3.49 for helium inventory and Fig. 3.50 for swelling). It can be easily noted that the kinetics of bubbles on oxide particles is notably different from that for all other bubble populations. In these bubble populations bubble size and density depend strongly on the implantation conditions, but within each fixed implantation regime bubbles on grain boundaries, dislocations and carbides grow at approximately the same rate as the bubbles in grain bulk. Correspondingly, relative contributions of these bubble families to helium inventory and swelling are primarily controlled by their volumetric number densities, which are sensitive to particular irradiation conditions. In contrast, the number density of bubbles on Y₂O₃ nanoparticles is predetermined by the number density of oxide particles that typically host a single He bubble per particle and is thus not affected by implantation conditions. Bubbles on oxide particles are pronouncedly larger than bubbles of other populations and the sizes of bubbles associated with yttria nanoparticles are less sensitive to variations of implantation conditions in the studied ranges than to the sizes of host nanoparticles.

In the majority of studied implantation regimes both swelling and He inventory are largely controlled by bubble populations on structural defects (particles, dislocations and grain boundaries), while bubbles in the grain bulk provide relatively minor contribution. In quantitative terms, the relative contributions to helium accumulation and consequently swelling from bubbles on structural defects and in the grain bulk are mostly sensitive to variations of implantation flux. As the implantation flux increases, the relative role of bubbles in the bulk becomes stronger and at the highest flux of 6 appm He/s this bubble population provides roughly the same contribution to swelling and helium inventory as bubbles on structural defects. With the increase of implantation fluence (helium concentration) and the decrease of temperature the relative contribution of bubbles in the grain bulk also increases, but for fluence and temperature variations within the studied ranges remains well below that from bubbles on structural defects.

■ Y_2O_3 particles
 ■ Grain boundaries
 ■ Dislocations
 ■ Volume
 M_{23}C_6 carbides

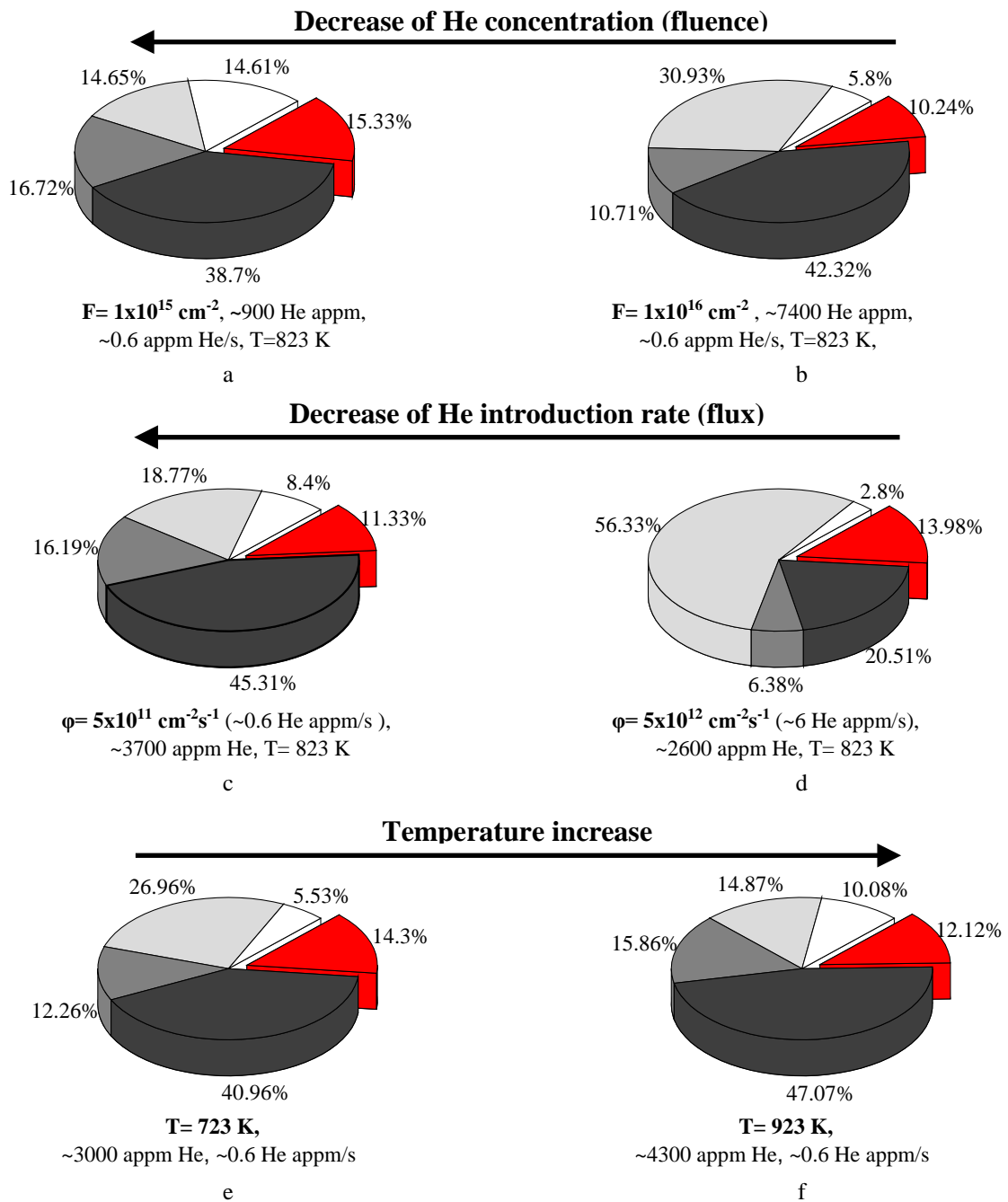


Fig. 3.49. Contributions of bubbles associated with different microstructural features to retained He fraction in ODS-EUROFER steel implanted with He^+ ions: (a,b) as a function of fluence in the range 1×10^{15} - 1×10^{16} cm^{-2} with the flux of 5×10^{11} $\text{cm}^{-2}\text{s}^{-1}$ at $T=823$ K; (c,d) as a function of flux in the range of 5×10^{11} - 5×10^{12} $\text{cm}^{-2}\text{s}^{-1}$ to the fluence of 5×10^{15} cm^{-2} at $T=823$ K; (e,f) as a function of temperature in the range of 723-823 K to the fluence of 5×10^{15} cm^{-2} with the flux of 5×10^{11} $\text{cm}^{-2}\text{s}^{-1}$. Colors differentiate between bubble populations, as explained in the legend located on top of the figure. The depicted helium shares are normalized to the total helium concentration contained in all bubbles. Presentation is based on the data collected in Tables 3.7-3.9.

Among the bubble populations associated with structural defects, the most important contributors to both swelling and He inventory are bubbles located on grain boundaries. Only bubbles in the grain bulk can serve as serious competitors in certain cases, mainly at high He fluxes and, to less extent, at high helium fluences. As compared to bubbles in the grain bulk, on dislocations and carbide precipitates, the average size of bubbles on grain boundaries is typically larger, but only moderately. Even at the highest achieved He content of ~ 12000 appm we have observed no grain boundary bubble coalescence that might

lead to the formation of huge bubbles and promote high-temperature helium embrittlement. The strong contribution of grain boundaries to helium inventory and swelling in the single-beam irradiation regimes used in this study results mainly from the low grain size of ODS-EUROFER and consequently high density of grain boundaries and the associated bubbles. This contribution slightly grows with the increase of temperature and fluence. On the contrary, with the increase of helium flux the contributions of grain boundary to helium inventory and swelling significantly decrease (by factors of 2 and 2.5, respectively, within the studied range).

■ Y_2O_3 particles
 ■ Grain boundaries
 ■ Dislocations
 ■ Volume
 ■ M_{23}C_6 carbides

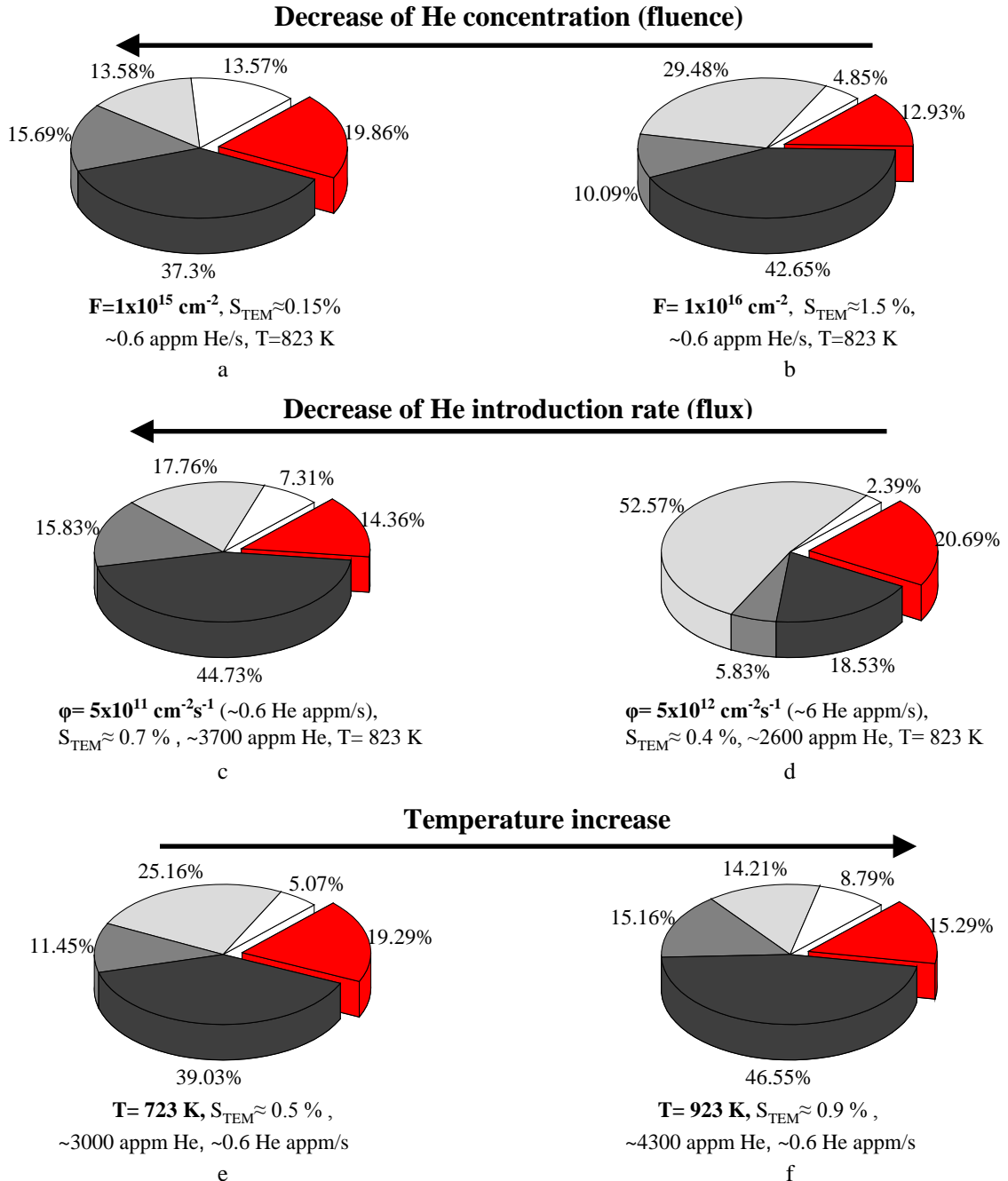


Fig. 3.50. Contributions to swelling from bubbles associated with different microstructural features in ODS-EUROFER implanted with He^+ ions: (a,b) as a function of fluence in the range 1×10^{15} - $1 \times 10^{16} \text{ cm}^{-2}$ with the flux of $5 \times 10^{11} \text{ cm}^{-2}\text{s}^{-1}$ at $T=823 \text{ K}$; (c,d) as a function of flux in the range of 5×10^{11} - $5 \times 10^{12} \text{ cm}^{-2}\text{s}^{-1}$ to the fluence of $5 \times 10^{15} \text{ cm}^{-2}$ at $T=823 \text{ K}$ with the; (e,f) as a function of temperature in the range of 723-823 K to the fluence of $5 \times 10^{15} \text{ cm}^{-2}$ with the flux of $5 \times 10^{11} \text{ cm}^{-2}\text{s}^{-1}$. Colors differentiate between bubble populations, as explained in the legend located on top of the figure. Presentation is based on the data collected in Tables 3.7-3.9.

In spite of being pronouncedly larger than bubbles of all other populations in all single-beam implantation regimes used, bubbles on oxide particles contribute to helium accumulation and swelling by only less than 15% and 21%, respectively. The relatively minor role of Y_2O_3 nanoparticles in helium inventory and swelling is primarily due to the low number density of nanoparticles in ODS-EUROFER steel. Since the size of bubbles attached to Y_2O_3 nanoparticles is weakly affected by implantation conditions and the bubble number density coincides with that of oxide particles, the contribution of these bubbles to swelling and helium accumulation are also not too sensitive to fluence, flux and temperature variations in the studied ranges; both contributions increase by only a few percent with the decrease of implantation fluence or temperature and with the increase of implantation flux. Contributions of bubbles on oxide particles to both swelling and He inventory remain well below those from grain boundary bubbles but are comparable to those from all other bubble families in most implantation regimes, with the only exception of the high flux regime, where they considerably subside also to bubbles in the grain bulk.

Having in mind that ODS steels in reactor service environment will be subject to intense radiation damage by fast neutrons, the effect of enhanced dpa/He appm ratio on swelling and helium inventory in ODS-EUROFER was studied in this thesis by means of simultaneous *in situ* dual-beam irradiation with He^+ and Au^{2+} ions. The estimated helium partitioning and swelling contributions from different bubble families are compared for the dual-beam $He^+ + Au^{2+}$ irradiation and single-beam He^+ implantation at the same temperature and helium flux in Figs. 3.51 and 3.52, respectively. The diagrams do not include contributions from bubbles on carbide particles because no $M_{23}C_6$ carbides were encountered in electron transparent zones of TEM samples irradiated in the dual-beam regime. However, this should not seriously distort the shown trends because, as demonstrated in the single-beam implantation experiment, bubbles on carbide precipitates provide only minor contributions to swelling and helium inventory.

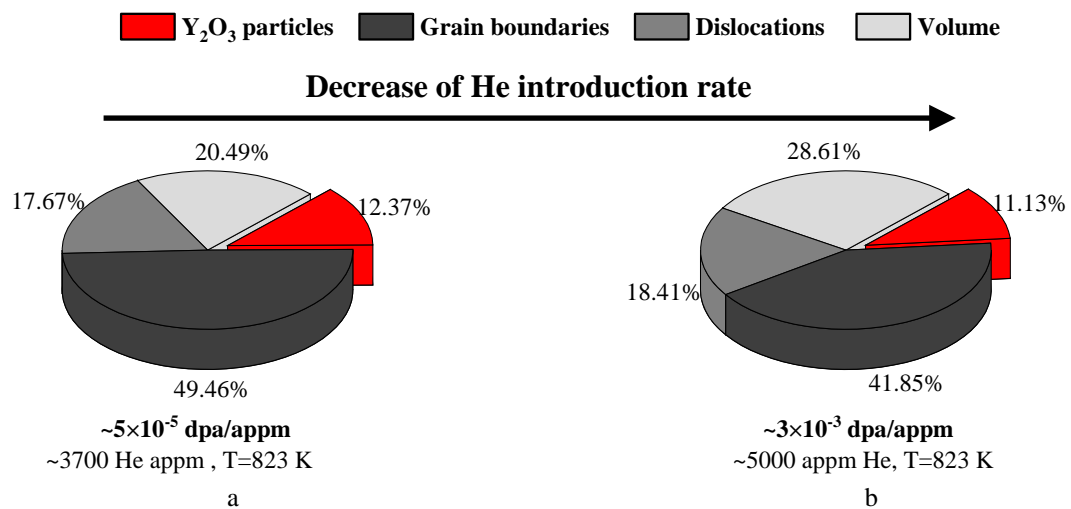


Fig. 3.51. Contributions of bubbles associated with different microstructural features to retained He fraction in ODS-EUROFER steel implanted at 823 K with He^+ ions with the flux of $5 \times 10^{11} \text{ cm}^{-2} \text{ s}^{-1}$ to the fluence of $5 \times 10^{15} \text{ cm}^{-2}$: (a) in a single-beam regime; (b) simultaneously with Au^{2+} ion beam with the flux of $4 \times 10^{11} \text{ cm}^{-2} \text{ s}^{-1}$ to the fluence of $4.5 \times 10^{15} \text{ cm}^{-2}$. Colors differentiate between bubble populations, as explained in the legend located on top of the figure. The depicted helium shares are normalized to the total helium concentration contained in all bubbles. Presentation is based on the data collected in Tables 3.7 and 3.18.

In terms helium inventory (see Fig. 3.51), the enhanced dpa/He appm ratio increases to retention He contributions for all bubble populations, either in the bulk, or on microstructural defects. The strongest effect is observed for bubbles in the bulk; their contribution to the fraction of retained helium increases approximately twice. Correspondingly, the total share of implanted He that is captured in the bubbles increases under synergetic action of helium accumulation and damage acceleration up to $\sim 70\%$, whereas in the single-beam He^+ regime it constitutes only $\sim 54\%$, that is only slightly more than a half of all implanted He was captured in the visible bubbles. Overall, the effect of accelerated damage on helium

retention is relatively moderate and, among the microstructural defects, the largest contribution is provided by grain boundary bubbles, just as it was the case in single-beam helium implantation regime.

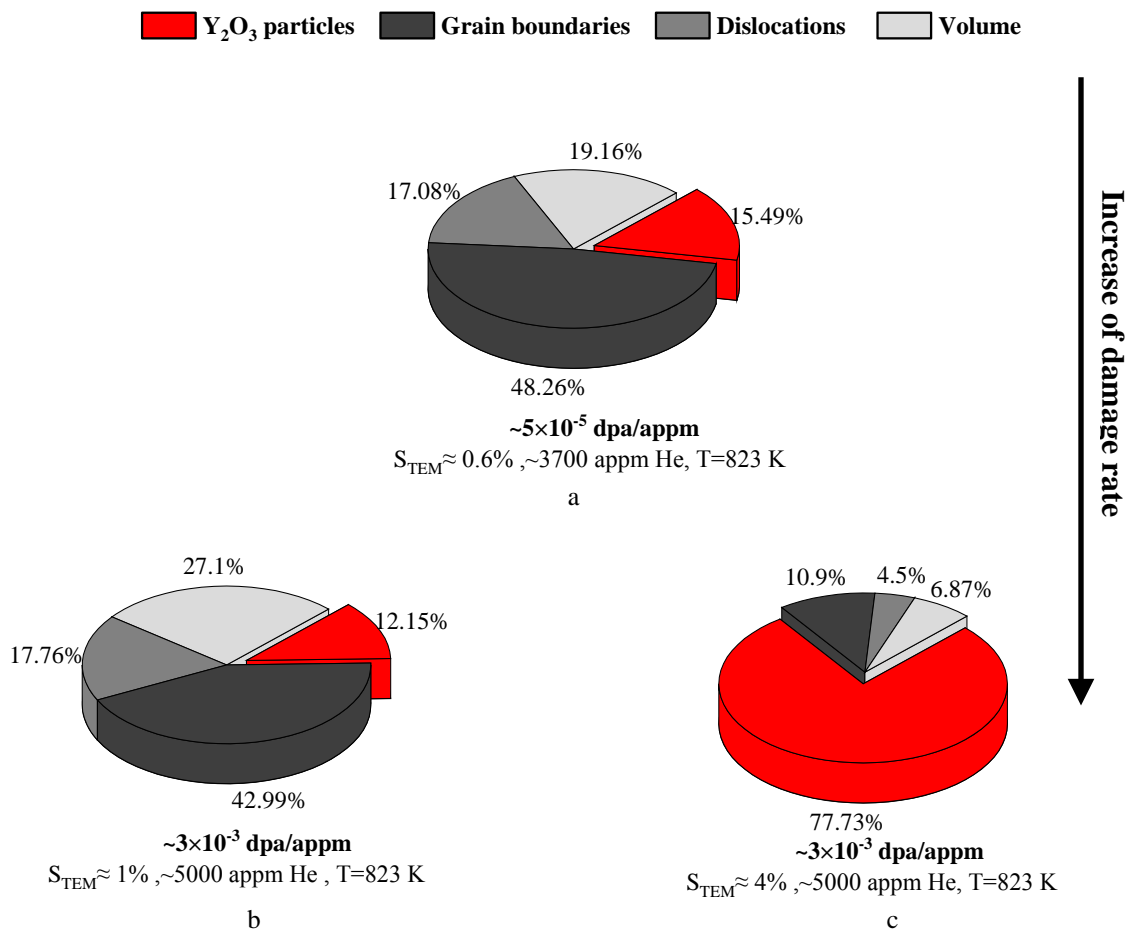


Fig. 3.52. The influence of dpa/appm ratio on swelling contributions from bubbles on different microstructural defects. Colors differentiate between bubble populations, as explained in the legend located on top of the figure. Presentation is based on the data collected in Tables 3.7 and 3.18.

An important qualitative effect caused by the strong acceleration of damage production in He-implanted sample of ODS-EUROFER steel by a simultaneously applied Au²⁺ beam was the formation of large cavities on some oxide particles. The effect is interpreted as a manifestation of the bubble-to-void transition caused by the increase of the efficient vacancy supersaturation in the matrix as a result of irradiation with energetic Au²⁺ ions. In the literature one can find only a couple of reports [46,47] mentioning bubble-to-void transition in bubble population associated with nanoparticles in ODS alloys that had accumulated more than a thousand appm He after neutron irradiation to >20 dpa at 773 K. The fact that the transition occurs only on the oxide particles seems natural because the largest bubbles in ODS steel were found to always decorate oxide particles. In this thesis, the bubble-to-void transition triggering by oxide nanoparticles was explained in terms of a theoretical model that predicts that the critical number of gas atoms required to promote the bubble-to-void transition for a helium bubble located on a particle is noticeably lower than for a critical bubble in the bulk. Note that according to both the theoretical model and the experimental observations the transition is triggered by sufficiently large host particles.

The creation of large cavities on oxide nanoparticles strongly affects swelling, as illustrated in Fig. 3.52. As can be noticed, if one neglects the contribution of large cavities (Fig. 3.52(b)), swelling in the dual-beam irradiation case is only 1.7 times larger than that for single-beam helium implantation (Fig. 3.52(a)). This moderate increase can be rationalized in terms of the so-called ‘temperature shift’ effect associated with the increased damage production by the Au²⁺ ion beam. It should be emphasized

that, in spite of a certain increase of swelling contribution from grain boundary bubbles in the dual-beam $\text{He}^+ + \text{Au}^{2+}$ irradiation regime, there is still no bubble coalescence on grain boundaries that might lead to high-temperature helium embrittlement in ODS-EUROFER steel. If, however, all bubbles associated with nanoparticles would undergo such a transition, their contribution to swelling would increase up to 78 %, i.e. nearly by an order of magnitude, (Fig. 3.52(c)), largely exceeding the contributions of grain boundary or any other bubble population. The expected cumulative swelling would then be higher than the single-beam He^+ implantation value already by a factor of 6.65. In reality, the true swelling value for dual-beam irradiation should fall somewhere between the two limiting values. But one should not forget that with the increase of irradiation dose the swelling contribution from the large cavities will eventually become much larger than could be provided by all the other bubble populations because the growth of large cavities is no longer controlled by the amount of helium they retain. Therefore it is clear that bubble-to-void transition bears the risk of qualitatively changing steel resistivity to swelling.

Summing up, the results of single-beam implantation and dual-beam irradiation indicate that

(i) The contribution to He inventory from bubbles associated with oxide particles is minor in all investigated regimes due to moderate number density of Y_2O_3 particles in ODS-EUROFER steel. Thus, our results do not support the widespread idea that helium trapping in bubbles on oxide nanoparticles can efficiently suppress helium accumulation on grain boundaries and thus reduce the risk of high-temperature intergranular embrittlement. However, the formation of bubbles on grain boundaries, even though not strongly affected by the presence of oxide nanoparticles, even at the highest fluence (12000 appm) and temperature (923 K) did not lead to bubble coalescence either in single-beam implantation or in the dual-beam irradiation regime with enhanced damage production. Therefore, the high-temperature intergranular embrittlement seems not to be a lifetime restrictive phenomenon for the ODS-EUROFER steel in high He/dpa ratio environment.

(ii) Swelling estimated from the volume of the entire visible bubble population did not exceed 1.5 % even at the highest achieved fluence of 12000 appm in single-beam implantation conditions and no indication of bubble-to-void transition was found. This evidences high resistance of ODS-EUROFER steel to swelling during helium accumulation.

(iii) Bubble-to-void transition observed in the dual-beam regime, even though taking place on a minor part of oxide particles, bears potential risk of accelerating swelling.

One should not forget that the single-beam implantation and dual-beam irradiation regimes used in this thesis are very different from the conditions expected in fusion or spallation reactor environments, where gas accumulation rates are expected to be few orders of magnitude lower, while the damage rate - notably higher than in our experiments [1]. Therefore, quantitative estimates of swelling and helium partitioning between different bubble families obtained for ODS-EUROFER steel in this study are not directly relevant for fusion or spallation reactors. However, the qualitative trends in helium partitioning between bubble families and their swelling contributions in ODS-EUROFER steel can be extrapolated on the reactor in-service conditions. To improve visibility, Figs. 3.48-3.52 are supplemented with arrows indicating the extrapolation direction to fusion and spallation conditions. According to our results, TEM based estimates of swelling in fusion and spallation conditions should not lead to significant underestimation since the contribution of small He-V clusters decreases with the decrease of He concentration, He introduction rate and damage rate, as well as with the temperature increase. Provided no bubble-to-void transition occurs in the bubble population associated with Y_2O_3 nanoparticles in ODS-EUROFER steel, these bubbles, similar to bubbles on dislocations and carbides will provide only a minor contribution to both He inventory and swelling in the reactor operation conditions. Due to quite low grain size in ODS-EUROFER steel and high temperatures expected in fusion and spallation reactors, the main contribution to both swelling and helium inventory will most probably come from grain-boundary bubbles. Even though bubbles in the grain bulk were found in this study to be competitive with grain-boundary bubbles in certain regimes (high helium flux of fluence), these regimes (especially high flux

that promotes dense bubble arrays in the bulk) are not relevant for the expected reactor operation conditions. The only serious risk of severe swelling might be related to the occurrence of bubble-to-void transition, which can be accelerated by the presence of oxide particles. Even if bubble-to-void transition will take place on a minor part of oxide particles, the total swelling of ODS-EUROFER will be eventually controlled by this bubble population, no matter who is the main contributor to helium inventory, and so it makes sense to briefly discuss how to prevent this undesirable effect.

Judging from the obtained results, the most efficient way of precluding bubble-to-void transition acceleration by oxide particles is the limitation of oxide size. Indeed, since the bubble sizes are proportional to the sizes of particles themselves, keeping particle sizes at the level of ~10 nm, would not allow the particle-associated bubbles to exceed the critical size. An additional benefit of having oxide particles possibly small comes from the fact that, as far as the volume fraction of oxide in steel remains constant, the efficiency of particles as sinks of point defects increases as the average particle size decreases. As a result, the total sink strength increases as well, while the efficient vacancy supersaturation falls down. Having in mind that the critical bubble size for the bubble-to-void transition is inversely proportional to the effective vacancy supersaturation in the material [30], the increase of oxide nanoparticle number density at the expense of the decrease of particle size contributes to the increase of the critical transition size. At the same time, the oxide particles should not be too small because small ($\leq 4-5$ nm) particle eventually become nearly completely incorporated inside the bubbles and can lose their ability to serve as dislocation pinning centers, which is the principal objective of steel matrix strengthening with nano-oxides. Hence, the particle size range of 5-10 nm seems to optimal in order to avoid both launching the bubble-to-void transition and possible decrease the high-temperature hardness of the steel.

3.4 References

- [1] P. Vladimirov and A. Möslang, “Comparison of material irradiation conditions for fusion, spallation, stripping and fission neutron sources,” *J. Nucl. Mater.*, vol. 329–333, no. Part A, pp. 233–237, 2004.
- [2] P. D. Edmondson, C. M. Parish, Y. Zhang, A. Hallén, and M. K. Miller, “Helium bubble distributions in a nanostructured ferritic alloy,” *J. Nucl. Mater.*, vol. 434, no. 1, pp. 210–216, 2013.
- [3] A. I. Ryazanov, O. K. Chugunov, S. M. Ivanov, S. T. Latushkin, R. Lindau, A. Möslang, A. A. Nikitina, K. E. Prikhodko, E. V. Semenov, V. N. Unezhev, P. V. Vladimirov, “Tensile properties and microstructure of helium implanted EUROFER ODS,” *J. Nucl. Mater.*, vol. 442, no. 1, Supplement 1, pp. S153–S157, 2013.
- [4] G. R. Odette and D. T. Hoelzer, “Irradiation-tolerant nanostructured ferritic alloys: Transforming helium from a liability to an asset,” *JOM*, vol. 62, no. 9, pp. 84–92, Sep. 2010.
- [5] T. Chen, H. Kim, J. G. Gigax, D. Chen, C.-C. Wei, F. A. Garner, L. Shao, “Radiation response of oxide-dispersion-strengthened alloy MA956 after self-ion irradiation,” *Nucl. Instruments Methods Phys. Res. Sect. B Beam Interact. with Mater. Atoms*, vol. 409, pp. 259–263, 2017.
- [6] Q. Li, C. M. Parish, K. A. Powers, and M. K. Miller, “Helium solubility and bubble formation in a nanostructured ferritic alloy,” *J. Nucl. Mater.*, vol. 445, no. 1, pp. 165–174, 2014.
- [7] C. M. Parish and M. K. Miller, “Aberration-corrected X-ray spectrum imaging and fresnel contrast to differentiate nanoclusters and cavities in helium-irradiated alloy 14YWT,” *Microsc. Microanal.*, vol. 20, no. 2, pp. 613–626, 2014.
- [8] M. Kirk, X. Yi, and M. Jenkins, “Characterization of irradiation defect structures and densities by transmission electron microscopy,” *J. Mater. Res.*, vol. 30, no. 9, pp. 1195–1201, 2015.
- [9] M. L. Jenkins, *Characterization of radiation damage by transmission electron microscopy*. Bristol ; Institute of Physics Pub, 2001.
- [10] S. J. Zinkle and J. T. Busby, “Structural materials for fission & fusion energy,” *Mater. Today*, vol. 12, no. 11, pp. 12–19, 2009.
- [11] L. L. Hsiung, M. J. Fluss, S. J. Tumey, B. W. Choi, Y. Serruys, and F. Willaime, “Formation mechanism and the role of nanoparticles in Fe-Cr ODS steels developed for radiation tolerance,” *Phys. Rev. B*, vol. 82, p. 184103, 2010.
- [12] C. M. Parish, K. A. Unocic, L. Tan, S. J. Zinkle, S. Kondo, L. L. Snead, D. T. Hoelzer, Y. Katoh, “Helium sequestration at nanoparticle-matrix interfaces in helium + heavy ion irradiated nanostructured ferritic alloys,” *J. Nucl. Mater.*, vol. 483, pp. 21–34, 2017.
- [13] M. Roldán, P. Fernández, J. Rams, D. Jiménez-Rey, E. Materna-Morris, and M. Klimenkov, “Comparative study of helium effects on EU-ODS EUROFER and EUROFER97 by nanoindentation and TEM,” *J. Nucl. Mater.*, vol. 460, pp. 226–234, 2015.
- [14] A. Bhattacharya, E. Meslin, J. Henry, B. Décamps, and A. Barbu, “Dramatic reduction of void swelling by helium in ion-irradiated high purity α -iron,” *Mater. Res. Lett.*, vol. 6, no. 7, pp. 372–377, Jul. 2018.
- [15] D. Brimbal, E. Meslin, J. Henry, B. Décamps, and A. Barbu, “He and Cr effects on radiation damage formation in ion-irradiated pure iron and Fe–5.40wt.% Cr: A transmission electron microscopy study,” *Acta Mater.*, vol. 61, no. 13, pp. 4757–4764, 2013.

- [16] B. Yao, D. J. Edwards, R. J. Kurtz, G. R. Odette, and T. Yamamoto, "Multislice simulation of transmission electron microscopy imaging of helium bubbles in Fe," *Microscopy*, vol. 61, no. 6, pp. 393–400, 2012.
- [17] T. Malis, S. C. Cheng, and R. F. Egerton, "EELS log-ratio technique for specimen-thickness measurement in the TEM," *J. Electron Microsc. Tech.*, vol. 8, no. 2, pp. 193–200, Feb. 1988.
- [18] K. Iakoubovskii, K. Mitsuishi, Y. Nakayama, and K. Furuya, "Thickness measurements with electron energy loss spectroscopy," *Microsc. Res. Tech.*, vol. 71, no. 8, pp. 626–631, Aug. 2008.
- [19] *ASTM E521-16, Standard Practice for Investigating the Effects of Neutron Radiation Damage Using Charged-Particle Irradiation*, ASTM International, West Conshohocken, PA, 2016, www.astm.org.
- [20] S. E. Donnelly, "The density and pressure of helium in bubbles in implanted metals: A critical review," *Radiation Effects*, vol. 90, no. 1–2, pp. 1–47, Jan. 1985.
- [21] C. A. Walsh, J. Yuan, and L. M. Brown, "A procedure for measuring the helium density and pressure in nanometre-sized bubbles in irradiated materials using electron-energy-loss spectroscopy," *Philos. Mag.*, vol. 80, no. 7, pp. 1507–1543, 2000.
- [22] S. Fréchar, M. Walls, M. Kociak, J. P. Chevalier, J. Henry, and D. Gorse, "Study by EELS of helium bubbles in a martensitic steel," *J. Nucl. Mater.*, vol. 393, no. 1, pp. 102–107, 2009.
- [23] D. Xu and B. D. Wirth, "Post-implantation thermal desorption of helium from poly- and single-crystalline iron," *J. Nucl. Mater.*, vol. 386–388, no. C, pp. 395–399, 2009.
- [24] Ch. Ch. Eiselt, M. Klimenkov, R. Lindau, A. Möslang, H. R. Z. Sandim, A. F. Padilha, D. Raabe, "High-resolution transmission electron microscopy and electron backscatter diffraction in nanoscaled ferritic and ferritic–martensitic oxide dispersion strengthened–steels," *J. Nucl. Mater.*, vol. 385, no. 2, pp. 231–235, 2009.
- [25] R. Schäublin, A. Ramar, N. Baluc, V. de Castro, M.A. Monge, T. Leguey, N. Schmid, C. Bonjour, "Microstructural development under irradiation in European ODS ferritic/martensitic steels," *J. Nucl. Mater.*, vol. 351, no. 1, pp. 247–260, 2006.
- [26] S. Rogozhkin, A. Bogachev, O. Korchuganova, A. Nikitin, N. Orlov, A. Aleev, A. Zaluzhnyi, M. Kozodaev, T. Kulevoy, B. Chalykh, R. Lindau, J. Hoffmann, A. Moeslang, P. Vladimirov, M. Klimenkov, M. Heilmaier, J. Wagner, S. Seils, "Nanostructure evolution in ODS steels under ion irradiation," *Nucl. Mater. Energy*, vol. 9, pp. 66–74, 2016.
- [27] C. Heintze, F. Bergner, A. Ulbricht, M. Hernández-Mayoral, U. Keiderling, R. Lindau, T. Weissgärber, "Microstructure of oxide dispersion strengthened Eurofer and iron–chromium alloys investigated by means of small-angle neutron scattering and transmission electron microscopy," *J. Nucl. Mater.*, vol. 416, no. 1, pp. 35–39, 2011.
- [28] F. Bergner, G. Hlawacek, and C. Heintze, "Helium-ion microscopy, helium-ion irradiation and nanoindentation of Eurofer 97 and ODS Eurofer," *J. Nucl. Mater.*, vol. 505, pp. 267–275, 2018.
- [29] Y. Dai, G. R. Odette, and T. Yamamoto, "The effects of helium in irradiated structural alloys," in *Comprehensive Nuclear Materials*, vol. 1, Elsevier Inc., 2012, pp. 141–193.
- [30] L. K. Mansur and W. A. Coghlan, "Mechanisms of helium interaction with radiation effects in metals and alloys: a review," *J. Nucl. Mater. 119*, vol. 119, pp. 1–25, 1983.
- [31] A. D. Brailsford and R. Bullough, "The rate theory of swelling due to void growth in irradiated metals," *J. Nucl. Mater.*, vol. 44, no. 2, pp. 121–135, 1972.
- [32] A. D. Brailsford and R. Bullough, "The theory of sink strength," *Philos. Trans. R. Soc. London. Ser. A, Math. Phys. Sci.*, vol. 302, pp. 88–136, 1981.

- [33] V. A. Borodin, “Generalized rate theory for spatially inhomogeneous systems of point defect sinks,” *Physica A: Statistical Mechanics and its Applications*, vol. 211, no. 2–3, pp. 279–316, Nov. 1994.
- [34] V. A. Borodin, “Radiation induced swelling,” *State-of-the-art Report on Structural Materials Modelling, Report NEA/NSC/R(2016)5, OECD*, pp. 165–225, 2016.
- [35] V. I. Dubinko, “New insight on bubble-void transition effects in irradiated materials,” *J. Nucl. Mater.*, vol. 206, no. 1, pp. 1–21, Nov. 1993.
- [36] N. W. Ashcroft and N. D. Mermin, *Solid State Physics*. Cengage Learning, 2011.
- [37] R. E. Stoller and G. R. Odette, “The effect of helium on swelling in stainless steel: influence of cavity density and morphology,” *Eleventh International Symposium on the Effects of Irradiation on Materials, ASTM STP 782; ASTM*, pp. 275–294, 1982.
- [38] N. F. Carnahan and K. E. Starling, “Equation of state for nonattracting rigid spheres,” *J. Chem. Phys.*, vol. 51, no. 2, pp. 635–636, 1969.
- [39] R. E. Stoller and G. R. Odette, “Analytical solutions for helium bubble and critical radius parameters using a hard sphere equation of state,” *J. Nucl. Mater.*, vol. 131, no. 2–3, pp. 118–125, Apr. 1985.
- [40] G. S. Was, “Radiation-enhanced diffusion and defect reaction rate theory,” in *Fundamentals of Radiation Materials Science: Metals and Alloys*, New York, NY: Springer New York, 2017, pp. 207–252.
- [41] E. Kuramoto and T. Tsutsumi, “Computer simulation of the bias factor in void swelling in metals,” *J. Nucl. Mater.*, vol. 212–215, pp. 175–178, 1994.
- [42] S. I. Golubov, A. V. Barashev, and R. E. Stoller, “1.13 - Radiation damage theory,” in *Comprehensive Nuclear Materials*, R. J. M. Konings, Ed. Oxford: Elsevier, 2012, pp. 357–391.
- [43] Y. Iijima, K. Kimura, and K. Hirano, “Self-diffusion and isotope effect in α -iron,” *Acta Metall.*, vol. 36, no. 10, pp. 2811–2820, 1988.
- [44] D. Brimbal, L. Beck, O. Troeber, E. Gaganidze, P. Trocellier, J. Aktaa, R. Lindau, “Microstructural characterization of Eurofer-97 and Eurofer-ODS steels before and after multi-beam ion irradiations at JANNUS Saclay facility,” *J. Nucl. Mater.*, vol. 465, pp. 236–244, 2015.
- [45] H. R. Z. Sandim, R. A. Renzetti, A. F. Padilha, D. Raabe, M. Klimenkov, R. Lindau, A. Moeslang, “Annealing behavior of ferritic-martensitic 9%Cr-ODS-Eurofer steel,” *Mater. Sci. Eng. A*, vol. 527, no. 15, pp. 3602–3608, 2010.
- [46] B. Yao, D. J. Edwards, R. J. Kurtz, G. R. Odette, and T. Yamamoto, “Microstructure characterization of neutron irradiated and helium injected PM2000, 14YW, and modified F82H Alloys,” *Fusion Mater. Semiannul Prog. Rep. June 2012*, vol. DOE-ER-031, p. 26, 2012.
- [47] H. J. Jung, D. J. Edwards, R. J. Kurtz, G. R. Odette, Y. Wu, and T. Yamamoto, “Microstructural summary of ODS ferritic alloys (14YW, 14YWT, 12YWT, MA957FR, PM2000) and RAFM Steels (F82H Mod.3-CW, Eurofer97) from JP27 in-situ He injection (ISHI) experiment at 500°C,” *Fusion Mater. Semiannul Prog. Rep. June 2015*, vol. DOE-ER-031, p. 55, 2015.

Chapter 4 Synergetic effects of helium and hydrogen accumulation on the microstructural evolution of ODS-EUROFER steel

As already mentioned in the beginning of chapters 1 and 3, considerable experimental and modeling experience concerning simultaneous influence of damage production and He accumulation on ferritic-martensitic steel performance in the current generation of fission reactors has been accumulated by now. However, considerably more severe conditions for structural material operation are expected in Generation IV fission reactors and in the future fusion reactors. Not only the dpa and He accumulation rates should be one to two orders of magnitude larger, but also simultaneous production of H in transmutation nuclear reactions introduces a new variable. The understanding of hydrogen effects on the microstructural stability of ODS steels remains at present insufficient and is a topic of active modern experimental and modeling research.

Hydrogen is a fast diffuser in steels and it is commonly assumed that in typical high-temperature reactor operation conditions it should not be retained at high concentrations. However, recent investigations [1,2] have shown that during electrochemical charging ODS steel can accumulate more hydrogen in comparison with its non-ODS counterpart. Moreover, there is a growing body of evidence that the development of dense helium-filled cavity ensembles in steels considerably modifies steel ability to retain hydrogen and that displacement damage, helium, and hydrogen are able to act in a synergistic manner on the development of irradiation-induced defect microstructure [3–10]. For example, the presence of hydrogen in triple-beam (heavy ion + He + H) implantation experiments promoted the development of bi-modal cavity size distribution that notably increased swelling in the temperature range of 723-743 K [4–6,10], though no such effect was observed in similar implantation conditions without hydrogen beam. The mechanisms of such strong effect of hydrogen remain uncertain, especially having in mind that post-implantation chemical analysis in one of these studies [5] revealed no hydrogen in the samples implanted at high temperatures. One can mention also some other unusual results of triple-ion beam implantation, such as the detection of hydrogen in molecular form in ODS steel after room-temperature implantation [9] or the formation of hydroxide phase HFe_5O_8 with a hexagonal structure even at 898 K [7].

In such complicated experiments, the simultaneous action of multiple effects makes it hard to elucidate particular roles of each transmutation product in material microstructure development and their contributions to swelling behavior. Due to non-trivial interaction of damage production with helium and hydrogen accumulation it is also not easy to separate the roles of individual microstructural components, in particular - oxide nanoparticles, in hydrogen accumulation.

Therefore the research described in this chapter addresses two primary objectives:

- To investigate the role of hydrogen in the evolution of different cavity populations in ODS steel in a high H/dpa ratio environment and the resulting hydrogen effects on swelling;
- To study hydrogen retention in ODS-EUROFER steel after single-beam H^+ and sequential dual-beam $\text{He}^+ + \text{H}^+$ ion implantations at both low and high temperatures with particular attention on the role of Y_2O_3 nanoparticles in hydrogen trapping.

The chapter covers three topics:

- (1) Microstructural evolution in helium pre-implanted ODS-EUROFER steel after hydrogen ion implantation at room and elevated temperatures.
- (2) Hydrogen trapping and uptake in ODS-EUROFER steel implanted both solely with hydrogen and sequentially with helium and hydrogen ions.
- (3) Association of hydrogen with He-filled cavities.

The research methodology in this chapter includes conventional TEM, thermal desorption (TDS) and electron energy loss spectroscopy (EELS) investigations of ion implanted samples. For the details of ion implantation and sample preparation see sections 2.2.3.4 and 2.1.1.2- 2.1.1.3, respectively.

4.1 Microstructural response of ODS-EUROFER steel to sequential dual-beam He⁺+H⁺ ion implantation

This section covers experimental and statistical analysis results on microstructure development in ODS-EUROFER steel after sequential dual-beam implantation with 10 keV He⁺ and 5 keV H⁺ ions under different temperature regimes, i.e.:

- He⁺ implantation to the fluence of $5 \times 10^{15} \text{ cm}^{-2}$ at 823 K followed by H⁺ implantation to the fluence of $1 \times 10^{17} \text{ cm}^{-2}$ at 823 K (see section 4.1.1).
- He⁺ implantation to the fluence of $5 \times 10^{15} \text{ cm}^{-2}$ at RT followed by H⁺ implantation to the fluence of $1 \times 10^{17} \text{ cm}^{-2}$ at RT (see section 4.1.2.1); a part of the samples implanted in this regime was subjected to the post-implantation annealing (PIA) similar to single-beam helium implanted samples investigated in section 3.1.2.6, that is for 90 minutes at 823 K.
- He⁺ implantation to the fluence of $1 \times 10^{16} \text{ cm}^{-2}$ at 823 K followed by H⁺ implantation to the fluence of $1 \times 10^{17} \text{ cm}^{-2}$ at RT (see section 4.1.2.2).

It is commonly assumed that hydrogen itself does not create bubble or void arrays inside the metallic materials, in contrast to helium. As shown below in this chapter, the final microstructure after sequential implantation with He⁺ and H⁺ ions is indeed pre-determined by the He⁺ implantation stage. Therefore transmission electron microscopy investigations in this section focus on evolution of parameters of helium bubbles (size, number density and shape, if relevant) caused by H⁺ implantation. Because no formation of new bubbles due to hydrogen implantation is expected, helium filled cavities formed at the He⁺ implantation stage are treated as markers for any microstructural changes occurred during H⁺ implantation. Contributions of these helium bubbles to the total swelling and helium inventory depending on bubble association with different microstructural components (grain boundaries, dislocations and the grain bulk) have already been presented in detail in chapter 3 and are not discussed in this section. Taking into account that bubbles attached to yttria nanoparticles are always noticeably larger than bubbles in the bulk or bubbles associated with other structural defects, only this bubble population is analyzed in detail in the current section. Cumulative swelling is estimated by means of indirect approach described in sections in 3.1.2.1 and 3.1.2.5.1. In order to visualize the possible synergy between helium and hydrogen, the results of statistical analysis of bubble parameters and the estimates of swelling after sequential dual-beam implantation with He⁺ and H⁺ ions are compared with similar results for single-beam He⁺ implantation.

4.1.1 Microstructural evolution of ODS-EUROFER steel pre-implanted with He⁺ ions after H⁺ ion implantation at elevated temperature

In order to investigate possible synergy between helium and hydrogen at elevated temperatures, sequential implantation at 823 K was used. ODS-EUROFER samples were first implanted with 10 keV He⁺ ions with the flux of $1 \times 10^{12} \text{ cm}^{-2}\text{s}^{-1}$ to the fluence of $5 \times 10^{15} \text{ cm}^{-2}$ (leading to accumulation of $\sim 6.3 \times 10^3$ appm He in the region extending at 10-40 nm from sample surface) and then with 5 keV H⁺ ions with the flux of $7 \times 10^{12} \text{ cm}^{-2}\text{s}^{-1}$ to the fluence of $1 \times 10^{17} \text{ cm}^{-2}$ (that is ~ 15.3 at. % H in the same region).

The estimates of helium fraction accumulated by bubbles summarized in Table 3.10 of the previous chapter indicate that in the applied He⁺ implantation regime a noticeable share of implanted He atoms is located in small He-vacancy clusters invisible for TEM. The damage caused by the subsequent H⁺ implantation at elevated temperature can force these small He-vacancy clusters to move and to be captured by the visible bubbles and promote their growth. Hence, one should be cautious to interpret possible swelling increase at the H⁺ implantation stage in terms of synergetic influence of helium and hydrogen. Therefore results of TEM observations on ODS-EUROFER samples after sequential implantation with He⁺ and H⁺ ion beams are compared with the data obtained both for the case of single-beam He⁺ implantation followed by tempering at 823 K (which took place during the same H⁺

implantation in samples with screened H^+ beam), and for the case of single-beam He^+ implantation without tempering.

A typical through-focus pair of BF TEM images obtained on cross-sectional FIB-cut samples of ODS-EUROFER implanted at temperature 823 K sequentially with He^+ ions to the fluence of $5 \times 10^{15} \text{ cm}^{-2}$ and H^+ ions to the fluence of $1 \times 10^{17} \text{ cm}^{-2}$ is shown in Fig. 4.1(a,b). Similar TEM micrographs for ODS-EUROFER steel after single-beam He^+ implantation to the same fluence followed by tempering are given in Fig. 4.1(c,d).

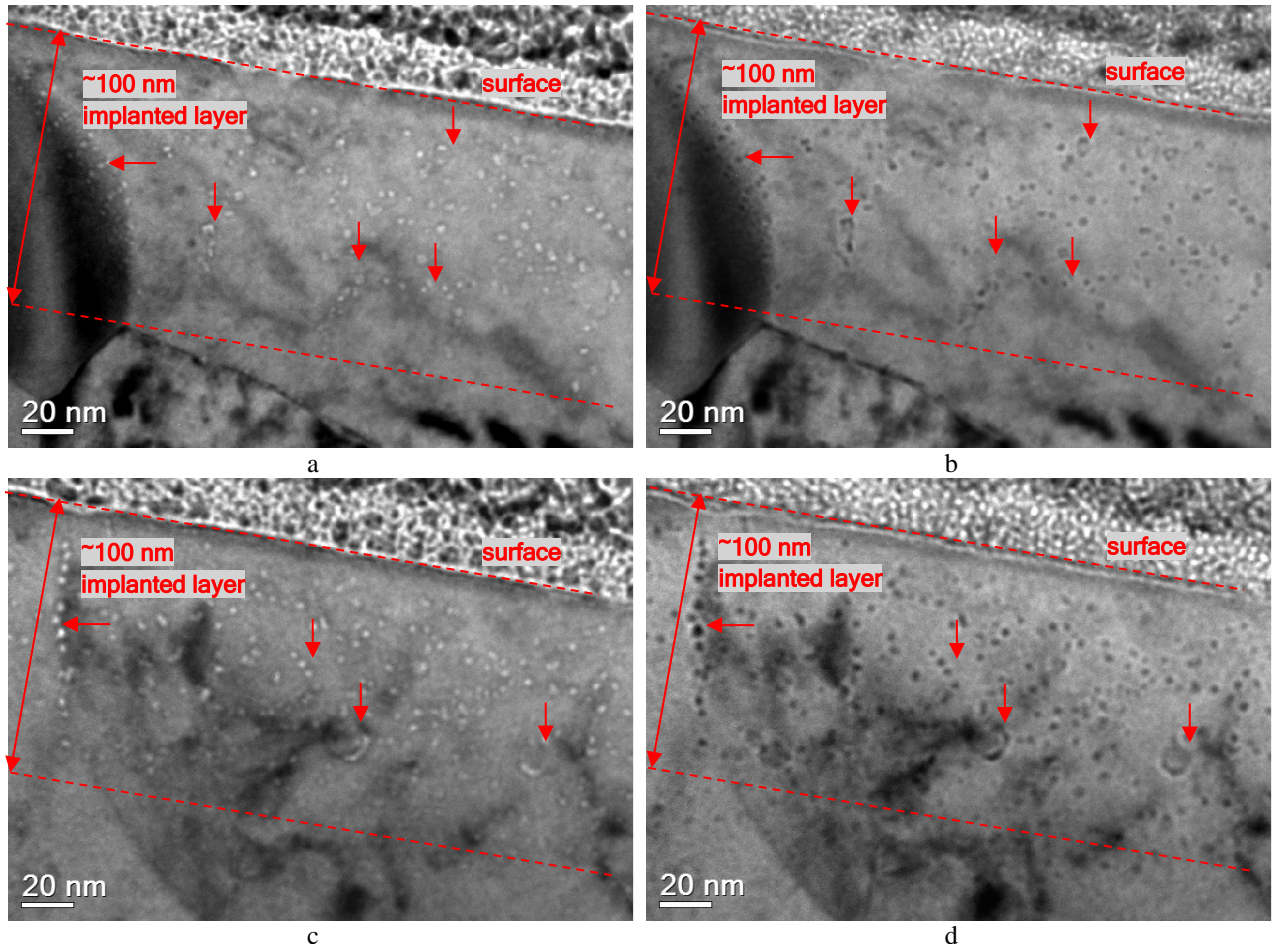


Fig. 4.1. Microstructure of ODS-EUROFER steel (FIB-cut cross-section): (a,b) after sequential implantation with He^+ ions at the flux of $1 \times 10^{12} \text{ cm}^{-2} \text{ s}^{-1}$ to the fluence of $5 \times 10^{15} \text{ cm}^{-2}$ and H^+ ions at the flux of $7 \times 10^{12} \text{ cm}^{-2} \text{ s}^{-1}$ to the fluence of $1 \times 10^{17} \text{ cm}^{-2}$ and (c,d) after single-beam He^+ implantation in the same conditions followed by tempering for the same duration of H^+ implantation. BF TEM imaging conditions: (a,c) $\sim 1 \mu\text{m}$ underfocus and (b,d) $\sim 1 \mu\text{m}$ overfocus. Dash lines show implanted zone, arrows mark structural defects decorated by bubbles.

Before and after H^+ implantation, bubbles appear at depths from 7-10 to 110 nm from the ion beam-facing surface. A narrow denuded zone with the thickness of $\sim 7 \text{ nm}$ was found in near surface region. The maximum depth of bubble bands correlates well with the profiles of implanted helium/hydrogen ions and defect production as predicted by SRIM-based calculations (see section 2.2.3.4). In agreement with the data for single-beam He^+ implantation, bubbles efficiently decorate grain boundaries, dislocations and precipitates in both implantation regimes. Judging from Figs. 4.1(a,b) and 4.1(c,d), bubble sizes and number densities at all distances from the sample surface look qualitatively very similar for the sequential implantation regime with $He^+ + H^+$ ions and for the single He^+ beam followed by tempering. However, more decisive conclusions require quantitative processing of TEM observations.

To start with, let's compare the bubble parameters for sequential implantation regime with He^+ and H^+ ions and implantation with He^+ ions followed by the tempering. Fig. 4.2 presents mean bubbles size and number density for both regimes as a function of the distance from the sample surface. In both

cases, the bubble number density follows ion/vacancy profiles predicted by SRIM. The highest bubble densities of $\sim 2.4 \times 10^{23} \text{ m}^{-3}$ and $\sim 2.3 \times 10^{23} \text{ m}^{-3}$ appeared at the distances 20-40 nm from the implanted surface for the sequential dual-beam implantation and single-beam implantation followed by tempering, respectively. In contrast, bubble average sizes vary little with the depth from the surface. After the sequential implantation with He^+ and H^+ ions, the mean bubble size is found to fall in the range from 3.9 to 4.4 nm, while after He^+ implantation followed by tempering it varies within 3.9-4.3 nm. In general, the average sizes of bubbles after dual-beam implantation are slightly (by 2-5%) larger than after single-beam He^+ implantation with tempering.

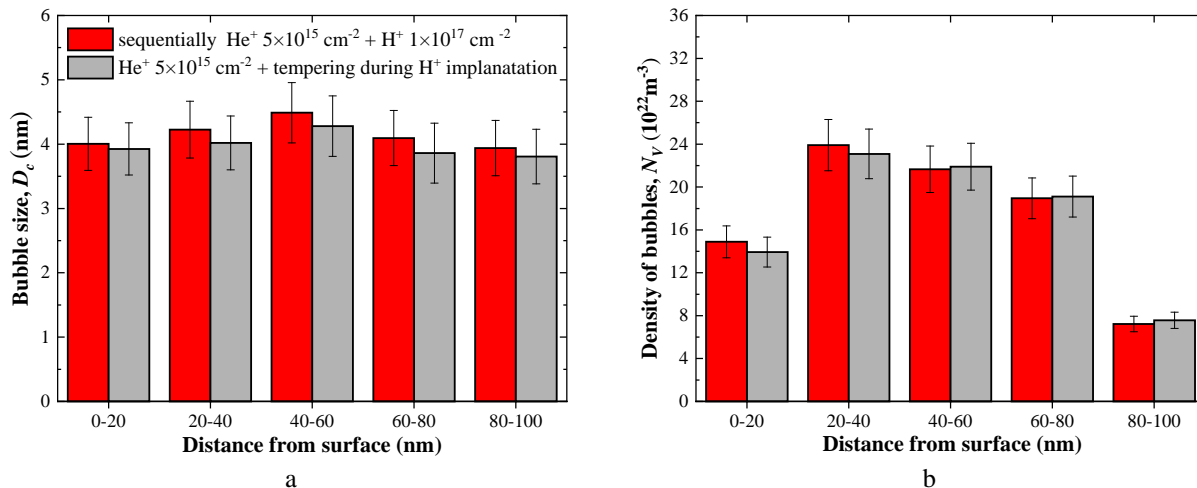


Fig. 4.2. The distribution of He bubble mean sizes (a) and number densities (b) depending on the distance from the implanted surface in ODS-EUROFER steel samples after either sequential dual-beam implantation with He^+ and H^+ ions or single-beam He^+ implantation at 823 K. The colors of data bars correspond to different implantation regimes as indicated in the legend located in panel (a).

Due to the fact that bubbles attached to yttria nanoparticles are notably larger than bubbles in all the other bubble populations, it makes sense to discuss their parameters in more detail. Figs. 4.3(a) and 4.3(b) show BF TEM micrographs of similar sized ($\sim 15 \text{ nm}$) Y_2O_3 nano-oxide precipitates in ODS-EUROFER, after sequential implantation with He^+ and H^+ ions and after single-beam He^+ followed by tempering, respectively. As can be seen, in both implantation conditions the nano-oxide particles are decorated with bubbles of similar size.

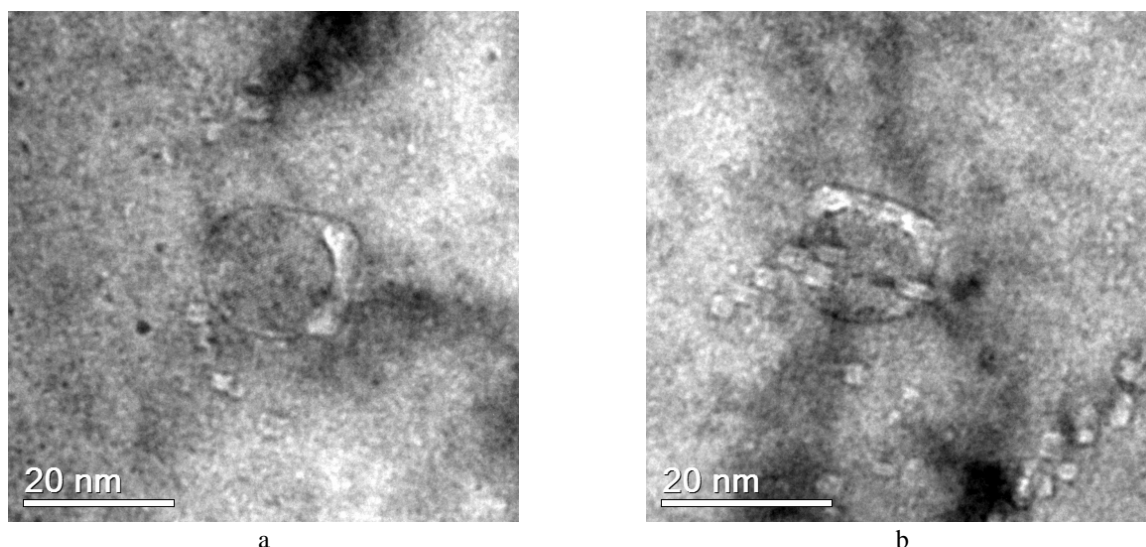


Fig. 4.3. Typical images of Y_2O_3 nano-precipitates in ODS-EUROFER steel implanted (a) sequentially with He^+ ions with the flux of $1 \times 10^{12} \text{ cm}^{-2} \text{ s}^{-1}$ to the fluence of $5 \times 10^{15} \text{ cm}^{-2}$ and H^+ ions with the flux of $7 \times 10^{12} \text{ cm}^{-2} \text{ s}^{-1}$ to the fluence of $1 \times 10^{17} \text{ cm}^{-2}$, and (b) after single-beam He^+ implantation in the same conditions followed by tempering for the same duration of H^+ implantation. BF TEM imaging conditions: $\sim 0.8 \mu\text{m}$ underfocus.

In a usual manner adopted in this thesis (see section 3.1.2.5.1), bubble population parameters, swelling and the fraction of helium accumulated by the whole bubble population were calculated for the layer extending from 10 to 40 nm from the sample surface. The statistical description of the observed data starts, as before, with the estimation of the average size of bubbles on oxide particles in terms of the dependence $D_c^p(D_p)$. The experimentally measured bubble diameters versus the sizes of hosting oxide particles are shown in Fig. 4.4 for both ion implantation regimes discussed in this section together with the fitted trend lines. The best fit parameters and the resulting average bubble sizes $\langle D_c^p \rangle$ are collected in Table 4.1. For comparison, Fig. 4.4 contains also a similar fit for single-beam He^+ implantation without tempering (a black line).

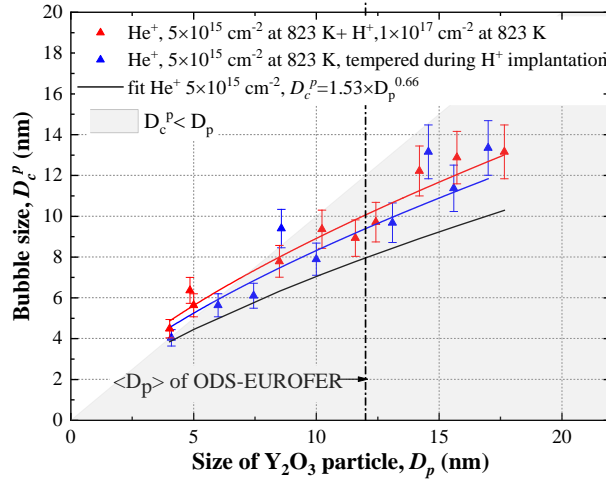


Fig. 4.4. Bubble size on yttria nanoparticles vs. particle size for the ODS-EUROFER steel implanted at 823 K either sequentially with He^+ and H^+ ions (red dots) or with single He^+ beam followed by tempering during H^+ implantation. Red and blue lines fit data sets for sequential dual-beam He^+ + H^+ and single-beam He^+ +tempering regimes, respectively. Black line is the fit for single-beam He^+ implantation without tempering. The grey marked area corresponds to the bubbles with the size smaller than that of the particle. Error bars are 10% uncertainties associated with the size of the first Fresnel fringe on bubble observed in underfocused images [11,12].

According to the data presented in Fig. 4.4, D_c^p increases from ~ 4.5 nm to ~ 13 nm with nanoparticle size increase from ~ 4 to 17 nm for both sequential dual-beam implantation with He^+ and H^+ ions and for single-beam He^+ implantation followed by tempering. As can be seen yttria particles enveloped by bubbles were found to be attached to the particles smaller than 6 nm in diameter in both discussed implantation regimes.

Table 4.1. Parameters for the power law fitting used in Fig. 4.3.

Ion implantation regime	b	a	$\langle D_c^p \rangle$, nm
$\text{He}^+, 5 \times 10^{15} \text{ cm}^{-2} + \text{H}^+, 1 \times 10^{17} \text{ cm}^{-2}$	0.66	1.93	10.06
$\text{He}^+, 5 \times 10^{15} \text{ cm}^{-2} + \text{tempering during H}^+ \text{ implantation}$	0.66	1.80	9.38
$\text{He}^+, 5 \times 10^{15} \text{ cm}^{-2}$, without tempering*	0.66	1.53	7.96

* Data for He^+ single-beam implantation without tempering are copied from Table 3.3

The estimated values of average bubble sizes attached to nanoparticles are found to be $\langle D_c^p \rangle = 10.06$ nm vs. $\langle D_c^p \rangle = 9.38$ nm for sequential dual-beam implantation with He^+ and H^+ ions and for single He^+ implantation followed by tempering, respectively. Despite qualitative similarity of both trends

to the case of single-beam helium implantation without tempering, the estimated values of $\langle D_c^p \rangle$ are found to be larger than $\langle D_c^p \rangle \approx 7.9$ nm under single He⁺ implantation without tempering.

Table 4.2 collects a summary of calculated bubble parameters in the ODS-EUROFER steel samples after sequential dual-beam implantation and after single helium implantation followed by tempering, including the average bubble diameters D_c^k , volumetric bubble number density N_V^k , swelling associated with bubbles S_k , and the fraction of accumulated helium F_{He}^k . Also included are the data for single helium implantation without tempering from Table 3.8. Comparison of bubble parameters for all discussed regimes is given in Fig. 4.5 separately for bubbles associated with all defects including bubbles in the bulk and for bubble population associated with nanoparticles.

Table 4.2. The average sizes and volume number densities of bubbles, swelling, V/He ratio and retained He fraction associated with different bubble populations in the ODS-EUROFER steel implanted at 823 K both sequentially with He⁺ ions at the flux of 1×10^{12} cm⁻² to the fluence of 5×10^{15} cm⁻² and H⁺ ions at the flux of 7×10^{12} cm⁻²s⁻¹ to the fluence of 1×10^{17} cm⁻², and with single He⁺ beam at the flux of 1×10^{12} cm⁻²s⁻¹ to the fluence of 5×10^{15} cm⁻² with and without subsequent tempering.

Implantation regime		D_c^k (10 ⁻⁹ m)	N_V^k (10 ²² m ⁻³)	S_k (%)	F_{He}^k (appm)	F_{He}^k (%)
He⁺+H⁺	Y ₂ O ₃	10.06±1.00	1.00±0.01	0.249±0.079	953±302	15.2±4.8
	Dislocations, Grain boundaries, Volume	4.12±0.41	19.40±1.94	0.707±0.224	4175±1320	66.6±21.1
	Total		20.40±2.00	0.957±0.303	5129±1622	81.8±25.9
He⁺, tempered	Y ₂ O ₃	9.38±0.94	1.00±0.01	0.185±0.058	734±232	11.7±3.7
	Dislocations, Grain boundaries, Volume	3.97±0.40	18.51±1.85	0.607±0.192	3739±1182	59.7±18.9
	Total		19.51±1.95	0.792±0.250	4473±1415	71.4±22.6
He⁺, without tempering*	Y ₂ O ₃	7.96±0.80	1.00±0.01	0.091±0.029	395±125	6.3±2.00
	Dislocations, Grain boundaries, Volume	3.32±0.33	21.0±6.23	0.383±0.121	2465±784	39.3±12.5
	Total		22.00±6.52	0.474±0.151	5821±1852	45.6±14.5

*Data for He⁺ single-beam implantation without tempering are borrowed from Table 3.8.

Taking into account error bars, practically no size increase is observed for bubble populations associated with grain boundaries, dislocations and located in the bulk as a result of H⁺ implantation. Bubbles attached to nanoparticles are found to be more sensitive to the synergetic influence of helium and hydrogen implantation. The average size of bubbles attached to nanoparticles after sequential dual-beam He⁺ and H⁺ implantation is ~7 % larger in comparison with the same bubble type after single-beam He⁺ implantation followed by tempering. At the same time, bubbles sizes detected under both sequential dual-beam He⁺ and H⁺ implantation and single-beam He⁺ implantation with tempering are found to be ~26 % larger for bubbles attached to yttria nano-particles and ~24 % larger for other bubble populations as compared to the single-beam He⁺ implantation without tempering.

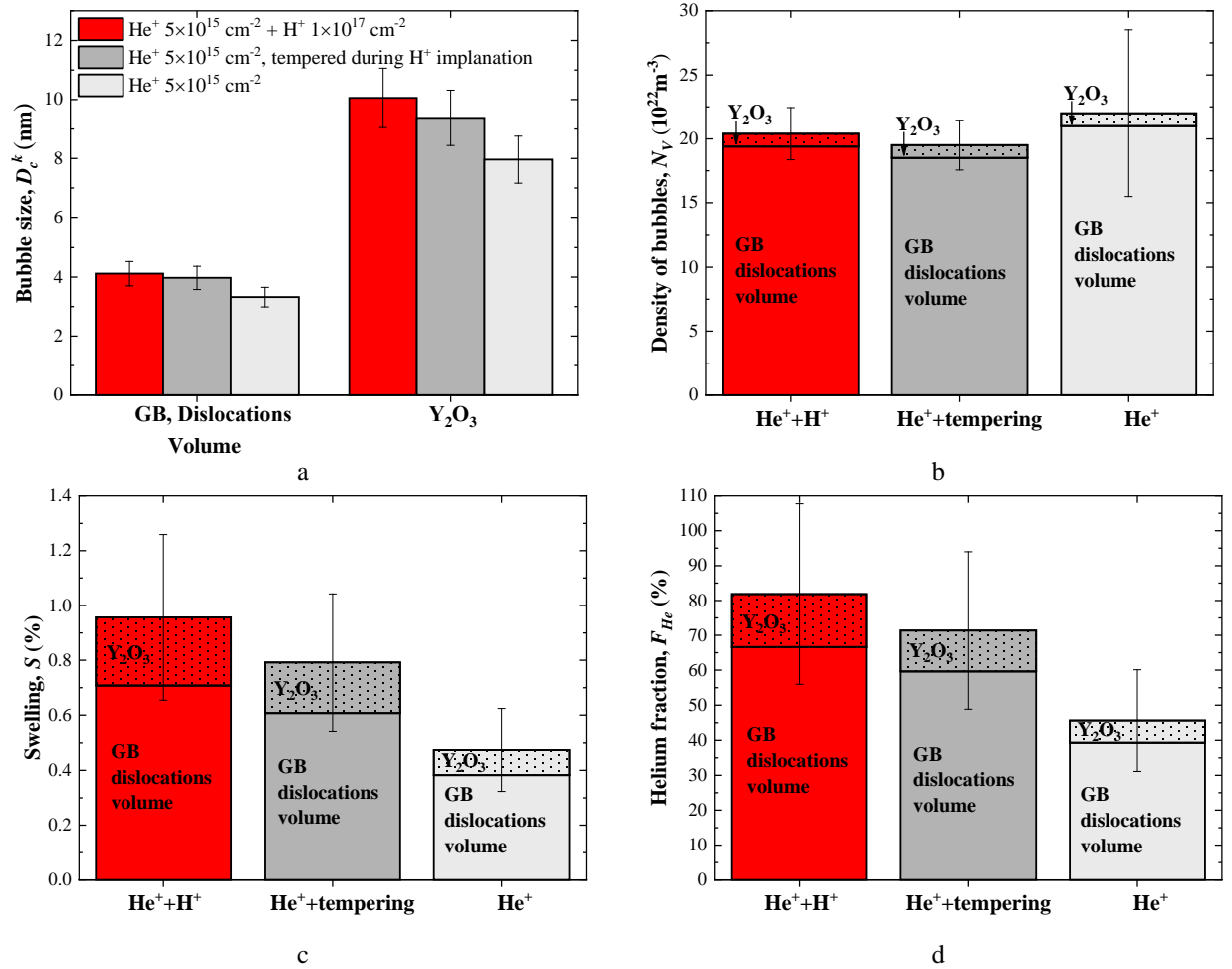


Fig. 4.5. Comparative statistical analysis of bubble average sizes, volume densities of bubbles, swelling and retained He fraction associated with bubbles in ODS-EUROFER steel implanted at 823 K sequentially with He⁺ ions at the flux of 1 × 10¹² cm⁻²s⁻¹ to the fluence of 5 × 10¹⁵ cm⁻² and H⁺ ions at the flux of 7 × 10¹² cm⁻²s⁻¹ to the fluence of 1 × 10¹⁷ cm⁻² (red bars), and with single He⁺ beam at the flux of 1 × 10¹² cm⁻²s⁻¹ to the fluence of 5 × 10¹⁵ cm⁻² with and without tempering during H⁺ implantation (grey bars). Color references provided in panel (a) are valid for all panels. Data for single He⁺ beam implantation without tempering are borrowed from Table 3.8.

In contrast to bubble sizes, the volumetric number densities of bubbles associated with all microstructural components are not affected either by tempering or H⁺ implantation.

In terms of S_k and F_{He}^k , only minor differences between two implantation regimes are found for all bubbles families. Thus, contribution of bubbles associated with nano-oxides to both swelling S_p and the fraction of retained helium F_{He}^p increase approximately by a factor of ~1.3 as compared to single He⁺ implantation followed by tempering. Similar factors for other bubbles families are found to be ~1.17 and 1.12, which is even lower than for bubbles attached to nanoparticles. The total swelling and the helium fraction retained in all bubbles are also slightly larger for sequential He⁺ and H⁺ implantation as compared to the single-beam He⁺ regime with tempering, $S \sim 0.96\%$ vs. $\sim 0.79\%$ and $F_{He} \sim 82\%$ vs. $\sim 71\%$, respectively. It is clear from these numbers that sequential implantation with He⁺ and H⁺ ion beams leads, within the calculated error bars, to no bubble size or swelling increase as compared to single-beam He⁺ with tempering.

On the other hand, notable difference in contributions to swelling S_k and the fraction of accumulated helium F_{He}^k are detected between sequential dual He⁺ and H⁺ beam implantation and single-beam He⁺ implantation without tempering for all bubble types. For example, contributions to swelling S_p and the fraction of retained helium F_{He}^p from bubbles attached to nanoparticles increased approximately

by a factor of ~ 2.4 when He^+ implantation was followed by H^+ implantation. For other bubbles families the increase factor was ~ 1.7 .

Summing up, the bubbles formed after the initial He^+ implantation continue to grow during subsequent hold at 823 K in samples implanted and not implanted with H^+ ions leading to measurable increase of swelling associated with the bubbles located both in the grain bulk and on structural defects, especially on oxide nanoparticles. However, the presence or absence of hydrogen implantation results in only minor differences in bubble population parameters. Only for bubbles associated with yttria nanoparticles one can observe some increase in the bubble size due to H^+ implantation, but the increase is quite modest. This means that the observed microstructural changes should be mostly attributed to helium re-distribution during the high temperature processing, rather than to the effect of hydrogen on bubble growth.

4.1.2 Microstructural evolution of ODS-EUROFER steel pre-implanted with He^+ ions after H^+ ion implantation at room temperature

The results of section 4.1.1 imply that at the elevated temperature the implanted hydrogen has *per se* little impact on the evolution of bubble ensembles developed at the helium implantation stage. One evident reason for that is that hydrogen is a relatively fast diffuser in steel and as such can quickly escape from quite thin TEM samples into the environment already during the high-temperature implantation. Even if some part of implanted hydrogen is retained in some traps, its concentration can be too low to result in any changes that can be detected by TEM. If this is the case, one can expect to increase the possible hydrogen effects on ODS-EUROFER microstructural evolution by playing with the temperature in order to control hydrogen diffusivity and hydrogen retention in the material. With this consideration in mind, three targeted experiments at room temperature were performed:

- H^+ implantation into ODS-EUROFER steel samples pre-implanted with He^+ ions at RT, which contains almost no bubbles visible by TEM.
- PIA at 823 K of a part of samples implanted consecutively with He^+ and H^+ ions.
- H^+ implantation into ODS-EUROFER steel samples pre-implanted with He^+ ions at 823 K, which contain well-developed bubble population.

Bubble parameters estimated on sequentially implanted with helium and hydrogen samples are compared with parameters observed on samples after single RT helium implantation followed by PIA at 823 K.

4.1.2.1 Combination of room temperature implantation regimes

In this experiment ODS-EUROFER samples were first saturated with He without creating TEM visible bubble structures using He^+ pre-implantation at RT with the flux of $5 \times 10^{11} \text{ cm}^{-2} \text{ s}^{-1}$ to the fluence of $5 \times 10^{15} \text{ cm}^{-2}$. Subsequent implantation with H^+ ions with the flux of $7 \times 10^{12} \text{ cm}^{-2} \text{ s}^{-1}$ to the fluence of $1 \times 10^{17} \text{ cm}^{-2}$ was also performed at RT. After hydrogen implantation, the samples were annealed at 823 K for 90 minutes, similar to single-beam He implanted samples investigated in section 3.1.2.6.

Typical BF TEM through-focus images of ODS-EUROFER samples after single-beam He^+ implantation at RT, after subsequent implantation with H^+ ions at RT, and the finishing post implantation annealing (PIA) at 823 K are shown in Figs. 4.6(a,b), 4.6(c,d) and 4.6(e,f), respectively. As can be seen in Fig. 4.6(a,b), no bubbles on grain boundaries or in grain bulk are found after RT He^+ implantation. In contrast, subsequent sample implantation with H^+ ions results in a high density of tiny bubbles (see Fig. 4.6(c,d)). The bubbles form both in the grain bulk and on various microstructural defects, such as grain boundaries and dislocations. The sizes of bubbles in all populations are roughly the same. The final high-temperature annealing of samples sequentially implanted with He^+ and H^+ ions only slightly increases the bubble sizes both in the grains and on grain boundaries, cf. Figs. 4.6(c,d) and 4.6(e,f).

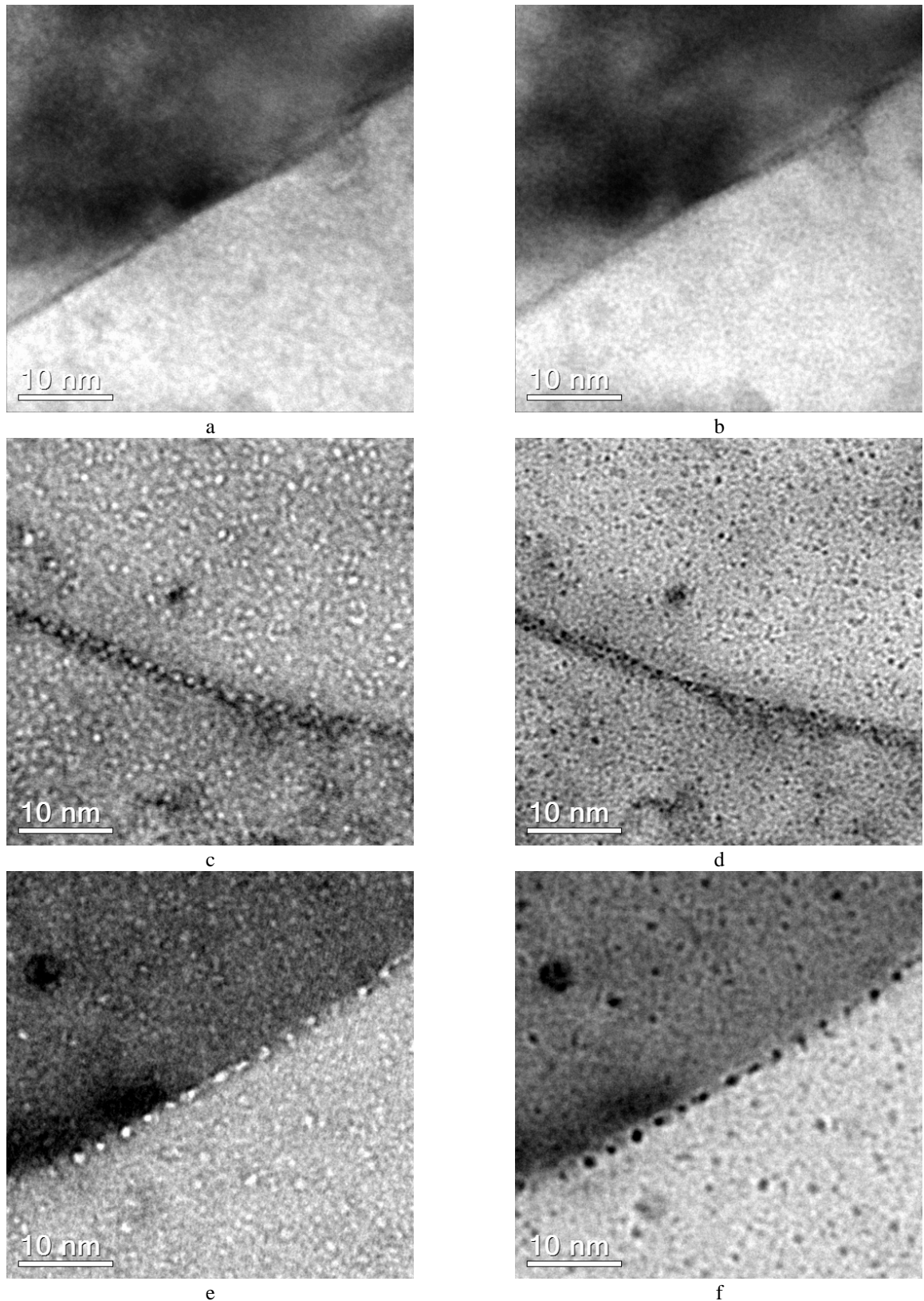


Fig. 4.6. Microstructure of ODS-EUROFER steel implanted at RT: (a,b) with single He^+ beam at the flux of $5 \times 10^{11} \text{ cm}^{-2} \text{ s}^{-1}$ to the fluence of $5 \times 10^{15} \text{ cm}^{-2}$; (c,d) after subsequent implantation with H^+ ions at the flux of $7 \times 10^{12} \text{ cm}^{-2} \text{ s}^{-1}$ to the fluence of $1 \times 10^{17} \text{ cm}^{-2}$; and (e,f) sequentially with He^+ and H^+ ions followed by PIA at 823 K; BF TEM imaging conditions: (a,c,e) $\sim 0.3 \mu\text{m}$ underfocus and (b,d,f) $\sim 0.3 \mu\text{m}$ overfocus.

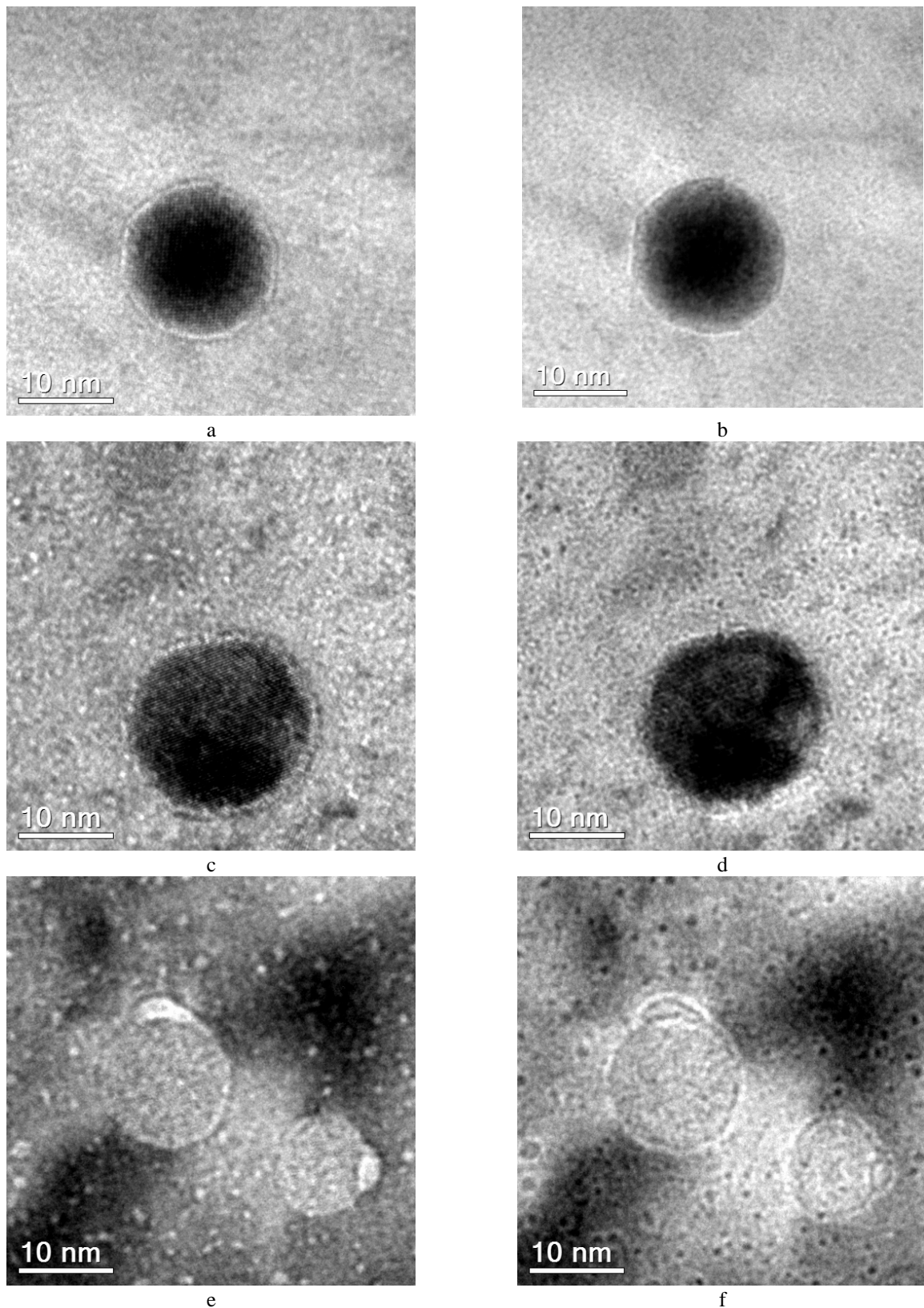


Fig. 4.7. Typical images of Y_2O_3 nano-oxide precipitates in ODS-EUROFER steel implanted at RT: (a,b) with single He^+ beam at the flux of $5 \times 10^{11} \text{ cm}^{-2} \text{ s}^{-1}$ to the fluence of $5 \times 10^{15} \text{ cm}^{-2}$; (c,d) after subsequent implantation with H^+ ions at the flux of $7 \times 10^{12} \text{ cm}^{-2} \text{ s}^{-1}$ to the fluence of $1 \times 10^{17} \text{ cm}^{-2}$; and (e,f) sequentially with He^+ and H^+ ions followed by PIA at 823 K; BF TEM imaging conditions: (a,c,e) $\sim 0.3 \mu\text{m}$ underfocus and (b,d,f) $\sim 0.3 \mu\text{m}$ overfocus.

Having in mind the earlier observation of preferential bubble growth on yttria nanoparticles, the affiliation of bubbles with oxide nano-particles was investigated thoroughly. Figs. 4.7(a,b), 4.7(c,b) and 4.7(e,f) show BF TEM micrographs of similar sized nano-oxide precipitates in ODS-EUROFER, after

single-beam He⁺ implantation at RT, subsequent implantation with H⁺ ions at RT, and final PIA at 823 K, respectively. Although the earlier reported results of experiments on He⁺ implantation convincingly evidence that oxide nanoparticles are preferential nucleation sites for helium bubbles, the RT He⁺ implantation does not lead to the formation of visible bubbles at oxide/matrix interfaces (see Fig. 4.7(a,b)). H⁺ injection at RT into He pre-implanted ODS-EUROFER samples promotes bubble formation not only at grain boundaries and in the bulk, but also at nano-oxides. As can be concluded from the comparison of Figs. 4.7(c,d) and 4.6(c,d), after H⁺ implantation at RT, in contrast to all previously obtained data, yttria nanoparticles are decorated by high density of bubbles with the same size as for the bubble populations in the bulk and on grain boundaries. However precise estimation of the number of bubbles attached to yttria oxides is impeded due to the small size of the bubbles and the fact that some bubbles situated inside the bulk could be mistakenly interpreted as bubbles at the nanoparticle/matrix interfaces. Annealing at 823 K of samples sequentially implanted with He⁺ and H⁺ completely changes the situation with bubble family at the nanoparticle matrix/interface; one observes a usual pattern where each oxide nanoparticle hosts a single lens-shaped bubble with the size typically notably larger than the average size of bubbles associated with other microstructural components.

The analysis of TEM images evidences that bubbles on nanoparticles are larger than the bubble in other populations only if sequential implantation with He⁺ and H⁺ ions at RT is followed by an annealing at 823 K. For this case, the average size of the bubbles associated with yttria nano-particles $\langle D_c^p \rangle$ is determined from fitting the experimental dependence $D_c^p(D_p)$ shown in Fig. 4.8. The best fit parameters for the dependence $D_c^p(D_p)$ and the estimated value of $\langle D_c^p \rangle$ are presented in Fig. 4.8 and in Table 4.3, respectively.

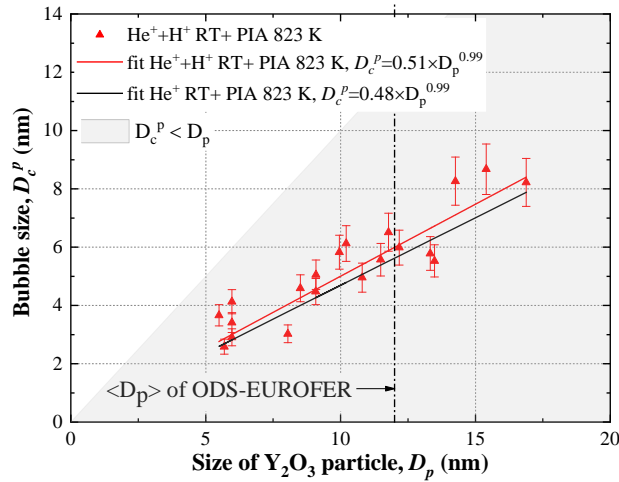


Fig. 4.8. Bubble size on yttria nanoparticles vs. particle size for the ODS-EUROFER steel sequentially implanted at RT with He⁺ ions at the flux of $1 \times 10^{12} \text{ cm}^{-2} \text{ s}^{-1}$ to the fluence of $5 \times 10^{15} \text{ cm}^{-2}$ and H⁺ ions at the flux of $7 \times 10^{12} \text{ cm}^{-2} \text{ s}^{-1}$ to the fluence of $1 \times 10^{17} \text{ cm}^{-2}$, followed by PIA at 823 K. Red solid line fits the current data set. Black solid line is the fit for single-beam He⁺ implantation at RT followed by PIA at 823 K. The grey marked area corresponds to the bubbles with the size smaller than that of the particle. Error bars are 10% uncertainties associated with the size of the first Fresnel fringe on bubble observed in underfocused images [11,12].

As can be seen in Fig. 4.8, D_c^p increases from ~4 nm to ~8 nm with nanoparticle size increase from 6 to 17 nm for the sequential implantation with He⁺ and H⁺ ions at RT followed by PIA at 823 K regime. Taking into account that the discussed experiment involved He⁺ pre-implantation at RT prior to H⁺ implantation and PIA, it is reasonable to compare the obtained dependence $D_c^p(D_p)$ with a similar fit for single-beam He⁺ implantation at RT to the same fluence followed by PIA at the same temperature (black line in Fig. 4.8). It can be noticed that in both cases the trend is qualitatively similar. The estimated value of $\langle D_c^p \rangle \approx 6.0 \text{ nm}$ for sequential dual-beam implantation with He⁺ and H⁺ ions after PIA is found to

be slightly larger than $\langle D_c^p \rangle \approx 5.6$ nm under single-beam He⁺ implantation followed by PIA. No yttria particles strongly enveloped by bubbles were found in both cases.

The calculated values of the average bubble diameters D_c^k , volumetric bubble number density N_V^k , swelling associated with bubbles S_k , and the fraction of accumulated helium F_{He}^k , as well as cumulative values of these parameters in the ODS-EUROFER sample after sequential dual-beam implantation with He⁺ and H⁺ ions before and after PIA at 823 K are summarized in Table 4.3. For the purpose of comparison, the Table includes also the data for single He⁺ implantation followed by PIA from Table 3.12. In addition, bubble parameters for all discussed regimes are compared in Fig. 4.9 for bubbles associated with all defects including bubbles in the bulk and bubbles on nanoparticles.

Table 4.3. The average sizes and volume number densities of bubbles, swelling, V/He ratio and retained He fraction associated with different bubble populations in the ODS-EUROFER steel implanted at RT both sequentially with He⁺ ions at the flux of 5×10^{11} cm⁻²s⁻¹ to the fluence of 5×10^{15} cm⁻² and H⁺ ions with the flux of 7×10^{12} cm⁻²s⁻¹ to the fluence of 1×10^{17} cm⁻²s⁻¹ before and after PIA at 823 K, and with single He⁺ beam with the same parameters after PIA at 823 K.

Implantation regime		D_c^k (10 ⁻⁹ m)	N_V^k (10 ²² m ⁻³)	S_k (%)	F_{He}^k (appm)	F_{He}^k (%)
He ⁺ +H ⁺	Total (Y ₂ O ₃ Dislocations, Grain boundaries, Volume)	1.20±0.12	249.16±38.98	0.251±0.085	2035±689	32.5±11.0
	Y ₂ O ₃	5.96±0.60	1.00±0.01	0.027±0.08	134±42	2.1±0.7
He ⁺ +H ⁺ , annealed	Dislocations, Grain boundaries, Volume	2.03±0.29	233.36±39.10	0.662±0.213	5301±1705	84.6±27.2
	Total		234.36±39.26	0.689±0.221	5435±1748	86.7±24.9
He ⁺ , annealed *	Y ₂ O ₃	5.62±0.56	1.00±0.01	0.021±0.07	108±34	1.7±0.5
	Dislocations, Grain boundaries, Volume	1.82±0.25	209.24±35.33	0.532±0.168	4317±1365	68.9±21.8
	Total		210.24±35.50	0.553±0.175	4425±1399	70.6±22.3

*Data for single-beam He⁺ implantation are borrowed from Table 3.12.

As can be seen in Table 4.3, a combination of the high bubble density $N_V \approx 250 \times 10^{22}$ m⁻³ with very small bubble size of ~1.2 nm leads to a moderate cumulative swelling, $S \approx 0.25\%$ after sequential dual-beam implantation at room temperature with He⁺ and H⁺ ions. The fraction of helium trapped by all bubble populations is estimated as ~33%. The subsequent annealing of the samples regime at 823 K has resulted in bubble growth for all bubble families. However, while in as-implanted condition bubbles of all families had similar sizes, the annealing has led to more pronounced growth of the bubbles associated with oxide nanoparticles, which increased in size by a factor of 5, in contrast to the factor of 2 for all other bubble populations. The total bubble number density in samples sequentially implanted with He⁺ and H⁺ ions was practically unaffected by the annealing. As a result of bubble growth, the cumulative swelling S and the helium fraction F_{He} retained in the bubble have increased after the annealing, by a factor of ~2.7.

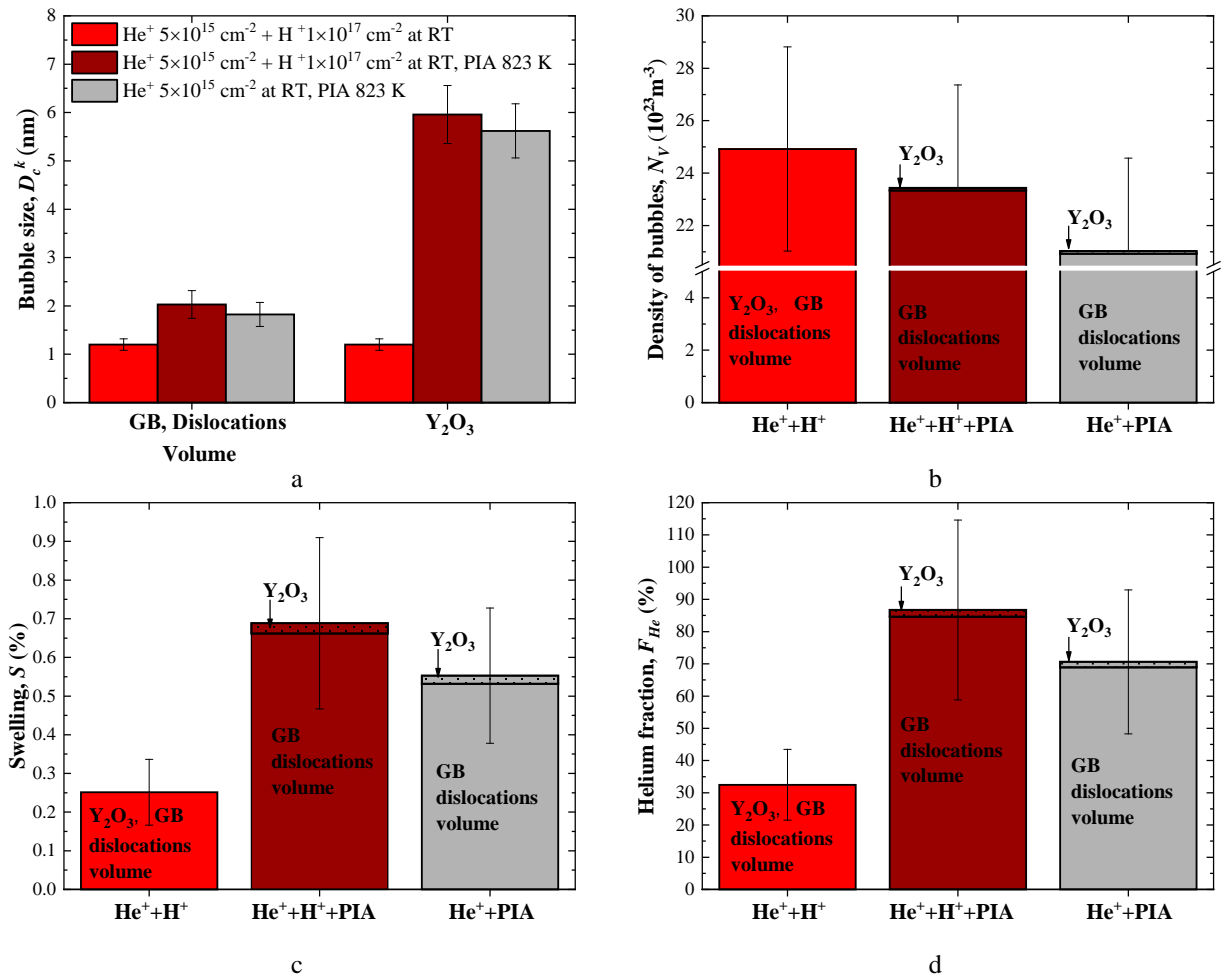


Fig. 4.9. Comparative statistical analysis of bubble average sizes, volume densities of bubbles, swelling and retained He fraction associated with bubbles in ODS-EUROFER steel implanted at RT sequentially with He^+ ions with the flux of $5 \times 10^{11} \text{ cm}^{-2} \text{ s}^{-1}$ to the fluence of $5 \times 10^{15} \text{ cm}^{-2}$ and H^+ ions with the flux of $7 \times 10^{12} \text{ cm}^{-2} \text{ s}^{-1}$ to the fluence of $1 \times 10^{17} \text{ cm}^{-2}$ before and after PIA at 823 K (red bars), and with single He^+ beam with the same parameters and PIA at 823 K (grey bars). Color references provided in panel (a) are valid for all panels. Data for single He^+ beam implantation are from Table 3.12.

In order to clarify the role of hydrogen in swelling increase during the annealing, it is instructive to compare parameters of bubble populations for sequential dual-beam and single-beam regimes. Comparison of average bubble sizes after the annealing demonstrates that the addition of secondary H^+ beam results in slightly larger bubbles (by $\sim 6\%$ for the bubbles attached to nano-oxides and $\sim 12\%$ for other bubble families) than after single-beam He^+ implantation. The cumulative bubble number density demonstrates a similar trend of moderate (by $\sim 6\%$) increase after dual-beam implantation. In terms of S_k and F_{He}^k , only minor differences between two implantation regimes are observed after annealing for all bubble populations. Thus, the contributions to swelling S_p and the fraction of accumulated helium F_{He}^p from bubbles on oxide particles in the case of sequential He^+ and H^+ implantation are by factors of ~ 1.29 and ~ 1.24 larger than for single He^+ implantation. For all other bubble families these factors are ~ 1.24 and 1.23 . The cumulative swelling and the helium fraction retained in all bubbles after annealing are also higher for sequential He^+ and H^+ implantation as compared the single-beam He^+ implantation regime, $S \sim 0.69\%$ vs. $\sim 0.55\%$ and $F_{\text{He}} \sim 87\%$ vs. $\sim 69\%$, respectively.

Summing up,

(i) H⁺ implantation into He pre-implanted ODS-EUROFER at room temperature promotes nucleation of bubbles with the size of ~1 nm. The bubbles are formed both in the bulk and on structural defects, but no preferential bubble size growth on oxide nanoparticle/matrix interfaces occurs. It cannot be definitely said whether the bubble appearance is due simply to the additional damage accumulation during hydrogen implantation or is somehow related to the introduction of H atoms in the matrix with a pre-existing defect structure.

(ii) The 823 K annealing of samples sequentially implanted with He⁺ and H⁺ ions promotes noticeable bubble size increase in all bubble populations but has little effect on the bubble number densities, which remain practically unchanged. The most pronounced bubble growth after annealing (up to ~5 times) is detected for the bubbles attached to nano-oxides. Cumulative swelling significantly increases after annealing as compared to just-implanted samples. The estimated fraction of helium retained in bubbles also increases after annealing from 33 % to 87 %. This results suggests that, similar to sequential dual-beam implantation at 823 K (see section 4.1.1), the large share of He after the He⁺ implantation stage is retained in the matrix in the form of substitutional He and/or small He_nV_m clusters, which are able to diffuse during high-temperature processing into the visible He-filled cavities and lead to their growth and the increase of estimate swelling value.

(iii) Comparison of the bubble evolution in ODS-EUROFER samples subjected to high-temperature processing either with or without additional H⁺ injection, demonstrates little size difference in all bubble populations formed, though after sequential dual-beam implantation bubbles are found to be systematically slightly larger. But the differences are minor and do not lead to significant effects such as notable swelling increase or complete particle absorption inside growing bubbles as a result of additional H⁺ injection. This confirms our earlier conclusion that the observed microstructural changes at elevated temperatures are determined rather by helium re-distribution than by hydrogen accumulation.

4.1.2.2 Combination of different temperature regimes

The effects of H⁺ implantation on He pre-implanted ODS-EUROFER reported in sections 4.1.1 and 4.1.2.1 are found to be minor in samples treated at elevated temperatures, implying no significant synergetic effects as a result of sequential helium and hydrogen implantation. However, some effects were observed when He⁺ and H⁺ implantation was performed at room temperature. In the low temperature regime used in section 4.1.2.1, no bubbles were detected after single-beam He⁺ implantation, and additional H⁺ injection promotes the nucleation of tiny bubbles. It remained an open question, however, whether hydrogen itself plays any role in the development of the He bubble ensemble. Thus, the aim of this section is to investigate possible microstructural changes in ODS-EUROFER steel with well-developed bubble population. In particular, we have consider the implantation regime that consisted of He⁺ pre-implantation at 823 K followed by H⁺ implantation at room temperature. As demonstrated in chapter 3, high temperature He⁺ implantation promotes the formation of He-filled cavities with relatively large sizes, while low temperature H⁺ injection allows one to decrease hydrogen diffusion rate and suppress hydrogen desorption from the sample, which might be among the reasons for the lack of observable hydrogen effects.

The sample was first implanted with 10 keV He⁺ ions to the fluence of 1×10^{16} cm⁻² and then electropolished from the back-side to obtain a TEM sample for subsequent H⁺ implantation to the fluence of 1×10^{17} cm⁻². Prior to H⁺ implantation, electron transparent area was investigated by means of TEM in order to determine parameters of particular bubble ensemble. After that, H⁺ implantation was performed on TEM thin foil sample followed by subsequent TEM observation of the same transparent area. This approach does not allow acquiring ample statistics but allows following directly any modifications of bubble ensemble by H⁺ implantation. Correspondingly, only qualitative analysis of bubble parameters is presented in this section.

Typical BF TEM underfocused images of ODS-EUROFER sample after single-beam He⁺ implantation at 823 K and after subsequent implantation with H⁺ ions at RT are shown in Figs. 4.10(a) and 4.10(b), respectively.

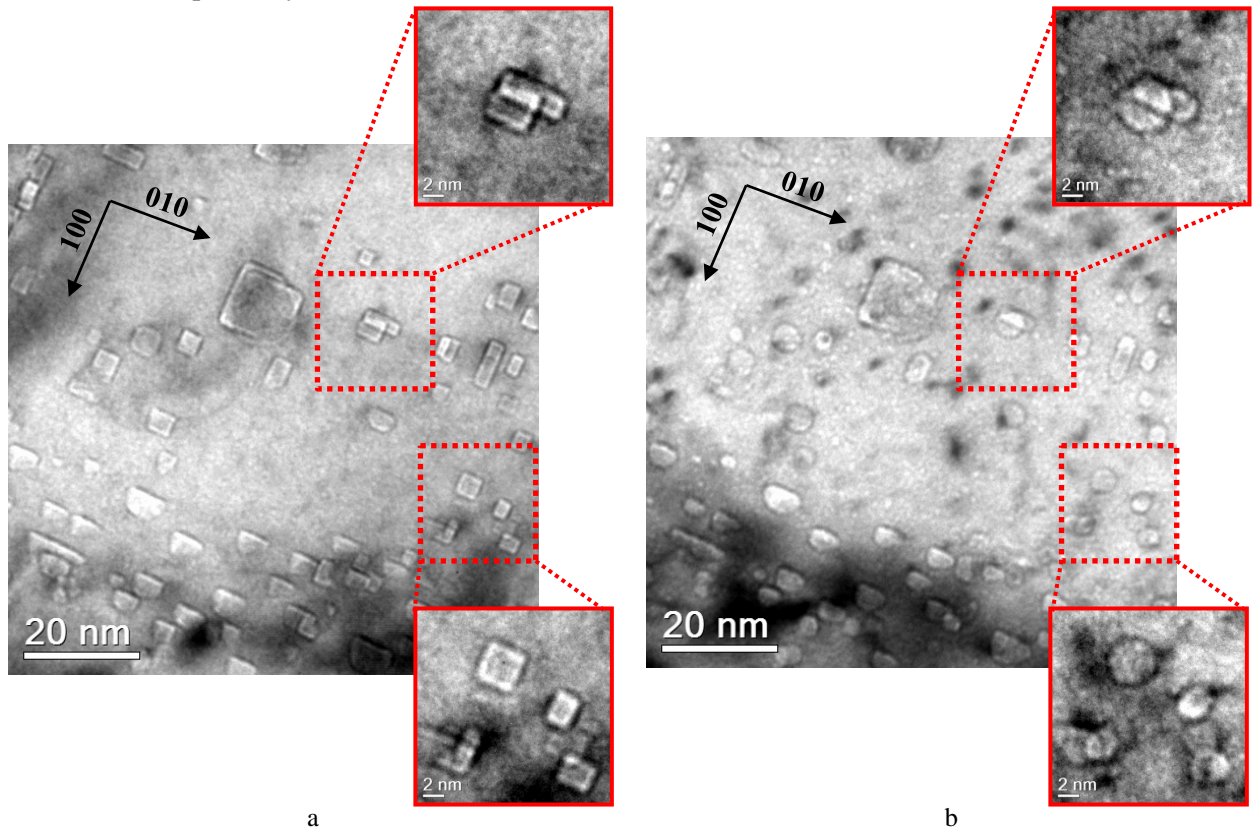


Fig. 4.10. Microstructure of ODS-EUROFER steel implanted (a) with single He⁺ beam at the flux of $5 \times 10^{11} \text{ cm}^{-2} \text{ s}^{-1}$ to the fluence of $1 \times 10^{16} \text{ cm}^{-2}$ at 823 K; (b) sequentially with He⁺ ions and then with H⁺ with the flux of $7 \times 10^{12} \text{ cm}^{-2} \text{ s}^{-1}$ to the fluence of $1 \times 10^{17} \text{ cm}^{-2}$ at RT. BF TEM imaging condition $\sim 0.5 \mu\text{m}$ underfocus.

As can be noticed, He⁺ implantation results in the formation of well-defined bubble population; with bubbles in the investigated area located at a grain boundary, on nano-oxides and inside the defect free grain space. Bubble sizes mostly fall in the range $\sim 3.5 - 6 \text{ nm}$; only a single bubble with the larger size of $\sim 12 \text{ nm}$ at the nano-oxide particle can be noticed in central part of Fig. 4.10(a). The images taken close to (001) zone axis show that the bubbles are faceted with facets parallel to (100) planes.

Comparison of Figs. 4.10(a) and 4.10(b) reveals that H⁺ implantation at room temperature doesn't change the size of pre-created bubbles in all bubble populations. At the same time, sharp faceted bubble shapes observed prior to H⁺ implantation become strongly smoothed after H⁺ implantation. The effect of shape change is more pronounced for relatively small bubbles, so that cuboidal He bubbles $\sim 3.5\text{-}4 \text{ nm}$ in size look spherical after H⁺ injection (see insets). The observed changes of bubble shape might be tentatively explained by hydrogen trapping at the cavity surfaces that results in the modification of surface energy. In the framework of this hypothesis, the bubble size sensitivity of bubble "rounding" could be naturally explained by the lower hydrogen concentration at the surface of larger bubbles.

Fig. 4.11 presents BF TEM through-focus images of ODS-EUROFER steel samples taken at high magnification after sequential implantation with He⁺ at 823 K and H⁺ at RT.

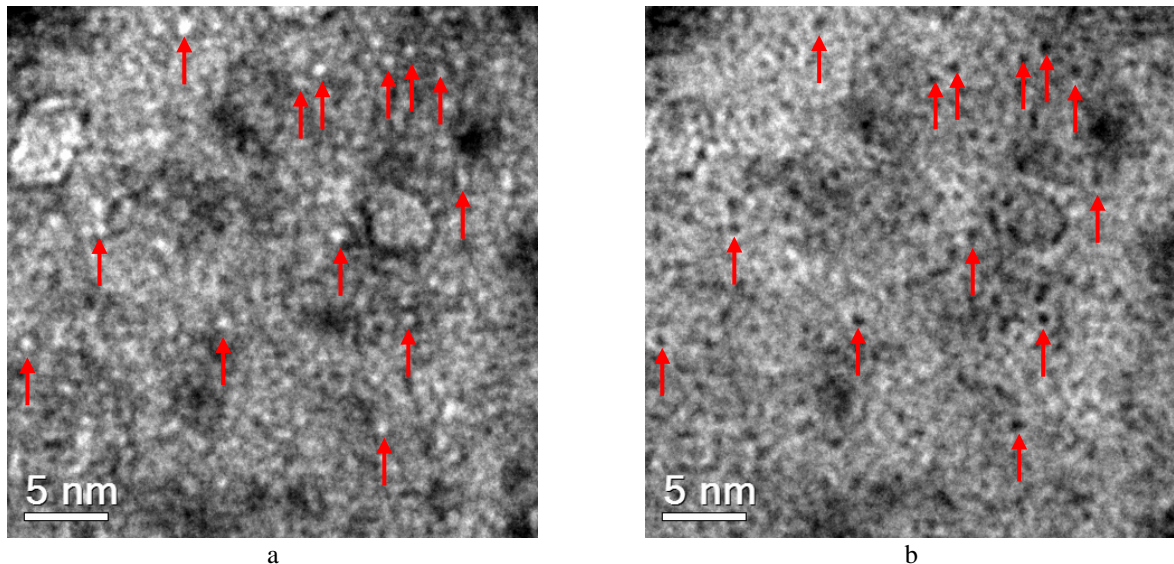


Fig. 4.11. Microstructure of ODS-EUROFER steel implanted sequentially with He^+ ions at the flux of $5 \times 10^{11} \text{ cm}^{-2} \text{ s}^{-1}$ to the fluence of $1 \times 10^{16} \text{ cm}^{-2}$ at 823 K and then with H^+ ions with the flux of $7 \times 10^{12} \text{ cm}^{-2} \text{ s}^{-1}$ to the fluence of $1 \times 10^{17} \text{ cm}^{-2}$ at RT. BF TEM imaging conditions: (a) $\sim 0.3 \mu\text{m}$ underfocus, (b) $\sim 0.3 \mu\text{m}$ overfocus.

Characteristic change in Fresnel contrast from the overfocus-to-underfocus conditions indicates that the H^+ implantation leads to the formation of some objects with high density and typical size $\leq 1 \text{ nm}$ in the grain matrix. It is difficult to make definite conclusion regarding the nature of observed features due to their small size and low contrast on TEM BF images. However, having in mind typical change of Fresnel contrast of these features when coming from under- to overfocus imaging conditions, it strongly suggests that these features constitute an additional bubble population promoted by H^+ implantation. This interpretation is supported by the observation of the development of tiny bubble ensemble due to RT H^+ implantation in the experiment described in section 4.1.2.1. Prior to H^+ injection, nearly 40% of implanted helium is dissolved in the ODS-EUROFER matrix in the form of small He-vacancy clusters invisible by TEM (cf. Table 3.7) and its collection into a new bubble population with high number density and sub-nanometer size might be promoted by radiation-enhanced diffusion at low irradiation temperature.

Summing up, the results presented in this section evidence that H^+ implantation into ODS-EUROFER samples pre-implanted with He^+ ions at 823 K changes neither the size, nor the number density of pre-existing He bubbles. However, hydrogen implantation is also accompanied with the clear rounding of bubble shapes, which is hard to explain in terms of radiation damage effects and should be rather considered as the direct effect of hydrogen. Also, the nucleation of high density of tiny cavities similar to those observed after sequential dual-beam $\text{He}^+ + \text{H}^+$ implantation was observed, but, based on the obtained data, it is hard to decide, whether this observation is due the direct effect of hydrogen accumulation or the radiation-promoted diffusion of He retained in small He-V clusters at the low irradiation temperature, or both.

4.1.3 Conclusions

Summing up the results of TEM analysis presented in sections 4.1.1 – 4.1.2, one can conclude that:

(i) After sequential implantation with He^+ and H^+ ions at 823 K the implanted hydrogen is found to have little effect on bubble populations formed after the helium implantation. The observed increase in the bubbles sizes of all bubble populations (in the bulk and on structural defects) after hydrogen implantation should be attributed rather to temperature and irradiation accelerated diffusion of point defects and small He-V clusters invisible in TEM.

(ii) H^+ implantation of He pre-implanted ODS-EUROFER steel samples at RT promotes the appearance of ~1 nm large bubbles and the suppression of bubble faceting. However, no major influence of implanted hydrogen on bubble population evolution and overall swelling was noticed.

(iii) However performed TEM investigations do not allow to directly confirm or deny the presence of hydrogen inside of the ODS-EUROFER steel under all implantation conditions used; the bubble change reported in section 4.1.2.2 suggests that at least some amount of hydrogen should be trapped near the surface of He-filled cavities.

4.2. Uptake and trapping of hydrogen in ODS-EUROFER steel

This section is focused on presentation and analysis of thermal desorption spectroscopy (TDS) measurements in ODS-EUROFER steel after sequential implantation with 10 keV He^+ and 5 keV H^+ ions in regimes similar to those used for the TEM investigations in section 4.1.2, i.e.

- He^+ implantation with the flux of $5 \times 10^{11} \text{ cm}^{-2}\text{s}^{-1}$ to the fluence of $5 \times 10^{15} \text{ cm}^{-2}$ at RT followed by H^+ implantation with the flux of $7 \times 10^{12} \text{ cm}^{-2}\text{s}^{-1}$ to the fluence of $1 \times 10^{17} \text{ cm}^{-2}$ at RT (regime D);
- He^+ implantation with the flux of $5 \times 10^{11} \text{ cm}^{-2}\text{s}^{-1}$ to the fluence of $1 \times 10^{16} \text{ cm}^{-2}$ at 823 K followed by H^+ implantation with the flux of $7 \times 10^{12} \text{ cm}^{-2}\text{s}^{-1}$ to the fluence of $1 \times 10^{17} \text{ cm}^{-2}$ at RT (regime II).

Hydrogen release measurements on samples of ODS-EUROFER and EUROFER 97 steels were performed on TDS apparatus in the School of Engineering, Department of Mechanical Engineering (Aalto University, Finland) by Dr. Yuriy Yagodzhinsky. The release curves were obtained by means of mass-spectrometry measurement of hydrogen desorption from the studied specimens in ultra-high vacuum (UHV) chamber ($\sim 10^{-8}$ mbar) under constant heating rate in the temperature range from ambient to 1200 K.

The TDS outcome is discussed here in conjunction with TEM results reported in sections 4.1.2.1 and 4.1.2.2 in order to support previous findings regarding the helium and hydrogen synergetic influence on microstructure development of the studied ODS steel. To investigate the role of hydrogen in the microstructure evolution in ODS-EUROFER samples pre-implanted with He^+ ions, the retained hydrogen content is quantified through TDS measurements and compared to that in the He-free samples. In order to clearer understand the possible role of yttria nanoparticles in the hydrogen accumulation, the general trends in hydrogen uptake and trapping in ODS-EUROFER are compared with those in EUROFER 97 steel, which has a similar composition but no oxide particles.

TDS measurements for ODS-EUROFER steel after sequential dual-beam implantation with He^+ and H^+ ions were conducted at different heating rates, which made it possible to determine the activation energies of H de-trapping from various microstructural components. This has allowed us to tentatively associate different TDS peaks with particular types of microstructure components (or lattice defects) based on their characteristic trapping energies reported in the literature.

4.2.1 Hydrogen trapping in helium-free ODS-EUROFER and EUROFER 97 steels

Hydrogen release curves from ODS-EUROFER and EUROFER 97 steel samples implanted at room temperature with a single hydrogen beam to the fluence of $1 \times 10^{17} \text{ cm}^{-2}$ are shown in Fig 4.12(a,b). The samples were heated up at the rate of 6 K/min. Fig. 4.12(a) shows the raw measured signal, while Fig. 4.12(b) presents the same data after filtering and background subtraction performed using Origin Pro 2018 software. Data filtering was done by means of Adjacent-Averaging method and background was

subtracted using double exponential function with offset (ExpDecay2). Later on, only such processed TDS curves will be shown.

TDS spectra measured on ODS-EUROFER and EUROFER 97 samples after single-beam hydrogen implantation exhibit three peaks located at the temperatures of about 450 K (peak 1), 650 K (peak 2) and 800 K (peak 3). The observation of three peaks on desorption curves indicates the presence of at least three types of hydrogen trapping sites [13] available in both ODS-EUROFER and EUROFER 97 steels. The relative intensities of peaks on experimental desorption curves, indicative of the relative amount of hydrogen accumulated in corresponding trapping sites, are different for different steels. In ODS-EUROFER, the peak at ~450 K is notably higher than those at ~650 K and ~800 K. Hence, the major part of hydrogen in ODS-EUROFER is accumulated by trapping sites with relatively low binding energy. All peaks on the desorption curve for EUROFER 97 steel have similar heights. Comparison between ODS-EUROFER and EUROFER 97 demonstrates much stronger peak 1 at ~450 K for ODS-EUROFER, whereas the amplitudes of peaks 2 and 3 are rather similar. Thus, ODS-EUROFER steel accumulates hydrogen more efficiently than its non-ODS counterpart as a result of hydrogen capture at relatively weak trapping sites.

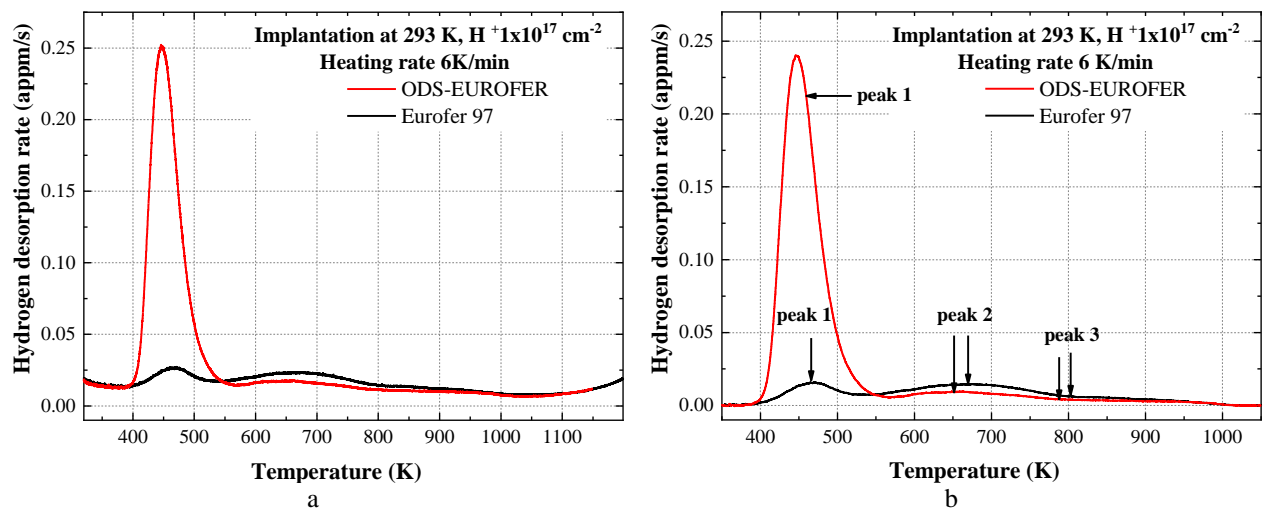


Fig. 4.12. TDS curves of hydrogen release from ODS-EUROFER and EUROFER 97 steel samples implanted with H^+ ions at the flux of $7 \times 10^{12} \text{ cm}^{-2} \text{ s}^{-1}$ to the fluence of $1 \times 10^{17} \text{ cm}^{-2}$ at RT: (a) raw data; (b) spectra after filtering and background subtraction.

In order to quantitatively estimate the ability of both steels to accumulate hydrogen, its content was calculated assuming that the area under the TDS curve is equivalent to the trapped hydrogen concentration [14]. It should be kept in mind, however, that as-supplied (prior to hydrogen implantation) samples of both materials can contain some amount of hydrogen trapped from the atmosphere. Therefore, the ability of steels to accumulate hydrogen should be studied by comparison of thermal desorption spectra from hydrogen-implanted and as-supplied samples. In this thesis the TDS measurements for the as-supplied samples were not performed. Instead, the values of 5.96 appm and 4.07 appm for hydrogen concentration in as-supplied ODS-EUROFER and EUROFER 97 steel samples measured in Ref. [15] were used, having in mind that exactly the same materials with the same heat treatment and sample preparation route were studied there. Table 4.4 presents the calculated hydrogen content in ODS-EUROFER and EUROFER 97 samples implanted with H^+ ions at room temperature, both with and without the initial hydrogen content.

Table 4.4. Estimated desorbed hydrogen content in ODS- EUROFER and EUROFER 97 steels implanted at room temperature with 5 keV H⁺ ions with the flux of 7×10¹² cm⁻²s⁻¹ to the fluence of 1×10¹⁷ cm⁻².

Material	Total hydrogen concentration (appm)	Hydrogen concentration accumulated as a result of implantation (appm)*
ODS-EUROFER	165.7	159.7
EUROFER 97	50.6	46.7

* Assuming the initial hydrogen content in ODS-EUROFER and EUROFER 97 from Ref. [15]

According to the estimates above, the ODS-EUROFER steel accumulates 3.4 times more hydrogen than its non-ODS counterpart. Since the chemical compositions of both steels are almost the same, it is tempting to assign significantly stronger hydrogen uptake by ODS-EUROFER steel to hydrogen trapping at features specific for ODS-EUROFER, such as yttria nanoparticles. However, the microstructural analysis of investigated materials given in section 2.1.1.1 evidences that the densities of various microstructural defects in both steels are also quite different. The dislocation density in ODS-EUROFER steel is higher than in EUROFER 97, while the grain size is notably lower, and consequently, the grain boundary density is higher. These factors might also result in the enhanced hydrogen uptake in ODS-EUROFER steel in comparison to the oxide-free material.

4.2.2 Hydrogen trapping in helium pre-implanted ODS-EUROFER and EUROFER 97 steels

4.2.2.1 Hydrogen trapping in ODS-EUROFER and EUROFER 97 steels pre-implanted with He⁺ ions at room temperature

Thermal desorption curves of hydrogen release at the constant heating rate of 6 K/min obtained for ODS-EUROFER and EUROFER 97 steels after sequential He⁺ and H⁺ implantation in regime I are shown in Figs. 4.13(a) and 4.13(b), respectively. For comparison, TDS curves after single-beam implantation from Fig. 4.12 are also depicted.

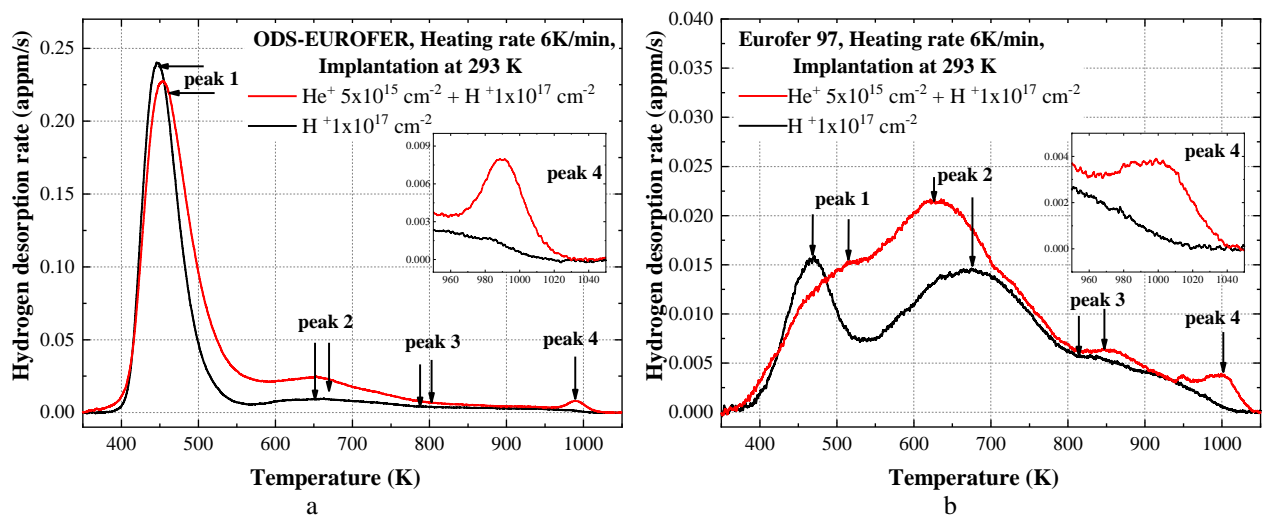


Fig. 4.13. TDS spectra of hydrogen release from samples sequentially implanted at RT with He⁺ ions at the flux of 5×10¹¹ cm⁻²s⁻¹ to the fluence of 5×10¹⁵ cm⁻² and H⁺ ions at the flux of 7×10¹² cm⁻²s⁻¹ to the fluence of 1×10¹⁷ cm⁻²: (a) ODS-EUROFER; (b) EUROFER 97. For comparison, the data obtained for single-beam H⁺ implantation are shown as black curves.

As can be seen in Fig. 4.13(a), the experimental desorption curve for ODS-EUROFER sequentially implanted at RT with He⁺ and H⁺ ions manifests four hydrogen release peaks located at the temperatures of about 450 K, 650 K, 800 K and 1000 K, which indicates the presence of at least four

trapping sites with different binding energies. Except for the high-temperature peak at around 1000 K, the release peaks are similar to those observed in ODS-EUROFER steel after single-beam H⁺ implantation. In other words, He⁺ pre-implantation has relatively little effect on hydrogen trapping in ODS-EUROFER because the major part of hydrogen after sequential dual-beam ion implantation is accumulated in the same traps as after the single H⁺ beam regime. The peak at ~450 K after sequential He⁺ + H⁺ implantation at RT shows minor decrease, while the peak at ~650 K slightly grows as compared to single-beam H⁺ implantation. Only the appearance of an additional high-temperature peak indicates the creation during sequential implantation of new hydrogen traps that did not exist after single-beam H⁺ implantation. The observed behavior indicates that sequential implantation with He⁺ and H⁺ ions tends to re-distribute some hydrogen to traps with higher binding energies as compared to single H⁺ beam implantation. The total amount of hydrogen desorbed from ODS-EUROFER steel after sequential implantation also seems larger than after single-beam H⁺ implantation, which will be confirmed below by quantitative analysis.

Similar to ODS-EUROFER, sequential implantation of EUROFER 97 with He⁺ and H⁺ ions in regime I leaves unchanged the positions of lower-temperature hydrogen release peaks in the TDS spectrum as compared to the single-beam H⁺ implantation and results in the appearance of an additional high temperature peak at around 1000 K, see Fig. 4.13(b). The peak height at ~450 K decreases and the peak height at ~650 K increases. So, like in the case of ODS-EUROFER, sequential He⁺ + H⁺ implantation of EUROFER 97 results in the re-location of some hydrogen to traps with higher binding energies. The areas under the TDS curves after sequential He⁺ + H⁺ in regime I and after single-beam H⁺ implantation of EUROFER 97 look similar, so that it is hard to conclude on the influence of helium pre-implantation on the total hydrogen uptake in EUROFER 97 steel without quantitative processing of TDS data.

A comparison of TDS spectra between ODS-EUROFER and EUROFER 97 steel samples shows that the peak location temperatures in both materials are similar, but not the peak heights. The first peak at ~450 K is several times higher in ODS-EUROFER as compared to EUROFER 97, while the heights of peaks 2 and 3 are comparable. Hence, ODS-EUROFER steel accumulates hydrogen more efficiently than its non-ODS counterpart due to enhanced hydrogen capture at some relatively weak trapping sites. Overall, the trends observed in both investigated steels after sequential implantation are very similar to those reported after single-beam H⁺ implantation.

In order to extract quantitative information from TDS data, we use the same approach as that applied to TDS data after single-beam H⁺ implantation. The quantitative estimates of the accumulated hydrogen content in ODS-EUROFER and EUROFER 97 steel samples sequentially implanted with He⁺ and H⁺ ions at room temperature are collected in Table 4.5.

Table 4.5. Estimated desorbed hydrogen content in ODS- EUROFER and EUROFER 97 steels sequentially implanted at room temperature with He⁺ ions at the flux of $5 \times 10^{11} \text{ cm}^{-2}\text{s}^{-1}$ to the fluence of $5 \times 10^{15} \text{ cm}^{-2}$ and H⁺ ions at the flux of $7 \times 10^{12} \text{ cm}^{-2}\text{s}^{-1}$ to the fluence of $1 \times 10^{17} \text{ cm}^{-2}$.

Material	Total hydrogen concentration (appm)	Hydrogen concentration accumulated as a result of implantation (appm)*
ODS-EUROFER	227.23	221.27
EUROFER 97	68.55	64.48

* Assuming the initial hydrogen content in ODS-EUROFER and EUROFER 97 from Ref. [15]

Quantitative estimates of hydrogen content in ODS-EUROFER and EUROFER 97 after sequential implantation show that ODS-EUROFER steel sample has accumulated ~3.4 times more hydrogen than EUROFER 97. The same difference in hydrogen uptake in ODS-EUROFER and EUROFER 97 was found after single-beam H⁺ implantation.

It is instructive to compare the calculated total hydrogen content for both steels after sequential implantation with He⁺ and H⁺ ion beams in regime I and after single-beam H⁺ implantation. The total

accumulated hydrogen contents in ODS-EUROFER and EUROFER 97 steels for these regimes are compared in Fig. 4.14.

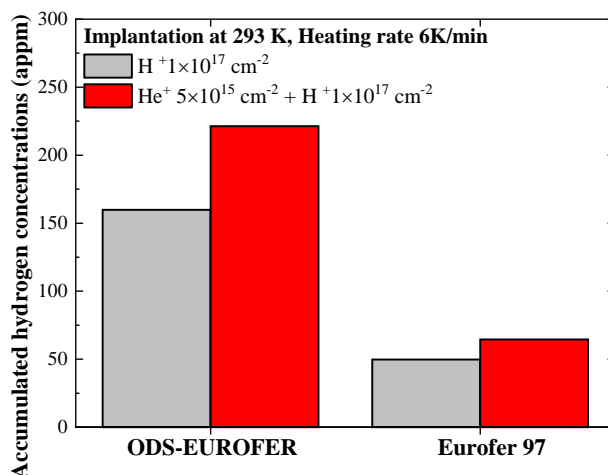


Fig. 4.14. Comparison of accumulated hydrogen concentrations measured by TDS analysis in samples of ODS-EUROFER and EUROFER 97 steels implanted at RT sequentially with He⁺ ions at the flux of $5 \times 10^{11} \text{ cm}^{-2} \text{ s}^{-1}$ to the fluence of $5 \times 10^{15} \text{ cm}^{-2}$ and H⁺ ions at the flux of $7 \times 10^{12} \text{ cm}^{-2} \text{ s}^{-1}$ to the fluence of $1 \times 10^{17} \text{ cm}^{-2}$ (red bars) and in the samples implanted with single H⁺ ion beam (grey bars).

As can be concluded from the data in Tables 4.4-4.5 and from Fig. 4.14, after sequential implantation with He⁺ and H⁺ ions in regime I, the total accumulated hydrogen concentration in both ODS-EUROFER and EUROFER 97 is ~40% higher than after implantation with H⁺ ions only. The desorption curves in Fig. 4.13 show no increase of release peak heights at either ~450 K or ~800 K for ODS-EUROFER and EUROFER 97 steels. The heights of additional release peaks at ~1000 K observed for both steels only after sequential implantation is quite low. Thus, the detected increase of total accumulated hydrogen concentration under sequential regime I is associated mainly with the peak at around 650 K and its corresponding trapping sites. Having in mind the observations in section 4.1.2.1, namely, the nucleation of tiny bubbles in He pre-implanted ODS-EUROFER after H⁺ implantation, it seems reasonable to associate the major traps responsible for additional hydrogen accumulation in peak 2 at ~650 K with He-filled cavities or He-V clusters which were formed at the first implantation stage.

4.2.2.2 Hydrogen trapping in ODS-EUROFER steel pre-implanted with He⁺ ions at 823 K

A separate set of TDS measurements was undertaken on hydrogen implanted ODS-EUROFER samples that were preliminary implanted with He⁺ ions at 823 K (regime II) rather than at room temperature, where quite different gas bubble microstructure was created by helium pre-implantation. The implantation regime was exactly the same as that used for TEM investigations reported in section 4.1.2.2. While room-temperature helium implantation produces essentially no visible bubbles ('bubble-free' material), implantation at 823 K creates a well-developed bubble structure ('bubble-saturated' material). Correspondingly, the microstructures evolving in ODS-EUROFER steel samples after subsequent room temperature H⁺ injection are sensitive to the regime of helium pre-implantation, see section 4.1.2.2. In samples pre-implanted with He⁺ ions at 823 K one observes not only the nucleation of high density of tiny cavities similar to those observed for 'bubble-free' material, but also clear rounding of bubbles created at the helium implantation stage. The suppression of bubble faceting suggests that at least some amount of hydrogen is trapped in these He-filled cavities, thus affecting the total hydrogen uptake.

Thermal desorption spectrum of hydrogen release from ODS-EUROFER steel after sequential He⁺ + H⁺ implantation in regime II obtained at a constant heating rate of 6 K/min is shown in Fig. 4.15

together with the spectrum for single-beam H⁺ implantation at RT at the same ion flux and to the same fluence.

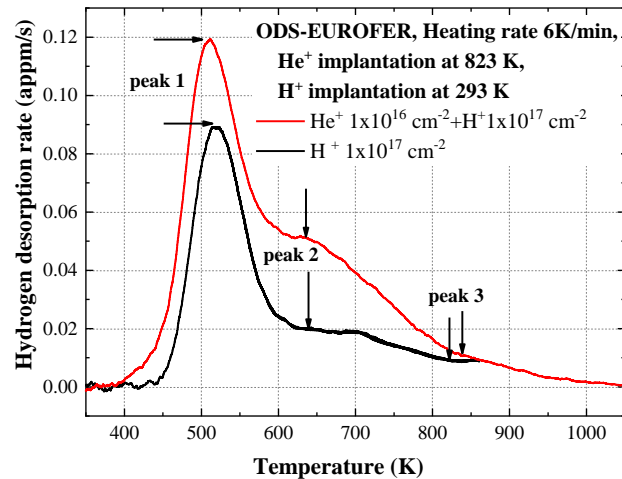


Fig. 4.15. TDS spectra of hydrogen release from ODS-EUROFER steel samples sequentially implanted with He⁺ ions at the flux of $5 \times 10^{11} \text{ cm}^{-2} \text{ s}^{-1}$ to the fluence of $1 \times 10^{16} \text{ cm}^{-2}$ at 823 K and with H⁺ ions at the flux of $7 \times 10^{12} \text{ cm}^{-2} \text{ s}^{-1}$ to the fluence of $1 \times 10^{17} \text{ cm}^{-2}$ at RT (red curve), and after single-beam H⁺ implantation with the flux of $7 \times 10^{12} \text{ cm}^{-2} \text{ s}^{-1}$ to the fluence of $1 \times 10^{17} \text{ cm}^{-2}$ at RT (black curve).

As can be seen in Fig. 4.15, both TDS spectra measured for ODS-EUROFER steel after sequential He⁺ and H⁺ implantation in “bubble-saturated” regime and single-beam H⁺ implantation demonstrate three release peaks located at the temperatures around 520 K, 650 K and 850 K. Therefore, at least three types of trapping sites with different binding energies are available in ODS-EUROFER steel sequentially implanted with He⁺ at 823 K and H⁺ at room temperature. As compared to single-beam H⁺ implantation of ODS-EUROFER, a moderate height increase of peak 1 at 450 K and more pronounced increase of peak 2 at 650 K were detected after sequential He⁺ + H⁺ implantation. Even though the desorption curve for single-beam H⁺ implantation was measured, due to experimental limitations, only up to 850 K, the peak intensities at ~850 K seem similar for H⁺ implantation into ‘bubble-saturated’ and pristine material.

The experimental desorption curves evidence a clear enhancement of the total hydrogen uptake in the hydrogen implanted ODS-EUROFER steel sample after helium pre-implantation in regime II as compared to single-beam H⁺ implantation. The quantitative results of total hydrogen content calculations for ODS-EUROFER steel samples implanted with and without preliminary He⁺ implantation are compared in Table 4.6. In order to make the estimates comparable, the integration of both desorption curves was performed up to 850 K, that is the upper measured value for single-beam hydrogen implanted ODS-EUROFER samples.

Table 4.6. The estimated content of hydrogen in ODS-EUROFER steel implanted at RT with H⁺ ions at the flux of $7 \times 10^{12} \text{ cm}^{-2} \text{ s}^{-1}$ to the fluence of $1 \times 10^{17} \text{ cm}^{-2}$ into pristine samples and into samples preliminary implanted with He⁺ ions at the flux of $5 \times 10^{11} \text{ cm}^{-2} \text{ s}^{-1}$ to the fluence of $1 \times 10^{16} \text{ cm}^{-2}$ at 823 K.

Implantation regime	Total hydrogen concentration (appm)	Hydrogen concentration accumulated as a result of implantation (appm)*
Single-beam H ⁺	116.96	110.73
Sequential He ⁺ +H ⁺	203.74	197.78

* Assuming the initial hydrogen content in ODS-EUROFER from Ref. [15]

Judging from the data in Table 4.6, the preliminary implantation with He⁺ ions that results in the sample saturation with helium bubbles promotes nearly 80% stronger hydrogen uptake after subsequent H⁺ implantation, as compared to similar hydrogen implantation into pristine ODS-EUROFER samples. The increase of total hydrogen uptake is mainly provided by the increase of peak 2 at ~650 K.

Prior to comparing the results of hydrogen desorption from ODS-EUROFER samples pre-implanted with He⁺ ions at 823 K with those obtained for RT He⁺ pre-implantation, it should be emphasized that direct quantitative comparison would be risky. Weakly trapped hydrogen is known to release from *bcc* iron-based alloys even at room temperature within days. Therefore, hydrogen release spectra from samples that were implanted with H⁺ ions in similar regimes but spent different time between implantation and TDS measurements are prone to uncontrolled variations, including the change in contained hydrogen content, minor changes of peak intensity or peak shifts to lower or higher temperature [16]. While all TDS measurements in section 4.2.2.1 were conducted on the samples from the same implantation set, TDS measurements on ODS-EUROFER samples implanted with H⁺ ions after He⁺ pre-implantation at 823 K were performed separately. Hence, only the general trends of hydrogen desorption from ODS-EUROFER steel after room temperature H⁺ injection into ‘bubble-free’ (He⁺ pre-implantation at RT) and ‘bubble-saturated’ (He⁺ pre-implantation at 823 K) samples are compared below.

The comparison of TDS spectra for ODS-EUROFER in Fig. 4.13(a) and 4.15 immediately shows that the temperatures and relative heights of peak 1 at ~450-500 K and peak 3 at ~800-850 K detected for sequentially implanted samples in regimes I and II are similar. Therefore, the hydrogen storage ability of trapping sites corresponding to these peaks should be also similar in both regimes. The high temperature peak at ~1000 K visible in ODS-EUROFER samples implanted sequentially in the ‘bubble-free’ regime was not detected when hydrogen was implanted into ‘bubble-saturated’ material. The most remarkable difference is, however, related to peak 2 at ~650 K, which is notably higher in the case of hydrogen implantation into ‘bubble-saturated’ material. As suggested in section 4.2.2.1, hydrogen traps responsible for the release peak at ~650 K might be He-filled cavities or He-V clusters formed at the helium implantation stage. After H⁺ injection into ‘bubble-free’ ODS-EUROFER only a single population of tiny bubbles was formed, whereas two bubble population were observed in “bubble-saturated” material, that is tiny bubbles with diameters less than 1 nm and facet-rounded bubbles with the average size of ~5 nm. The higher cumulative number density of bubbles in the latter case suggests that they might be responsible for the higher amount of hydrogen retained in traps associated with the peak at ~650 K in ODS-EUROFER samples sequentially implanted with He⁺ at 823 K and H⁺ at room temperature.

4.2.2.3 Activation analysis

The results presented up to now do not allow drawing reliable conclusion about the origin of trapping sites (microstructural components or defects) responsible for hydrogen retention. In order to distinguish properly the trapping sites associated with TDS hydrogen release peaks from ion implanted ODS-EUROFER steel, the hydrogen release activation analysis has been performed. The samples of ODS-EUROFER steel after sequential room temperature implantation with He⁺ and H⁺ ions were used for activation analysis because TDS spectra for these samples demonstrate the largest number of release peaks and, consequently, involve the largest number of possible hydrogen trapping sites. Taking into account similar quantitative behavior of release peaks at ~450 K, ~650 K and ~800 K after sequential implantation with He⁺ and H⁺ ions and after single-beam H⁺ implantation, the results of activation analysis received below are believed to be valid for both implantation conditions.

A special run of thermal desorption measurements using ODS-EUROFER samples sequentially implanted at room temperature with He⁺ ions with the flux of $5 \times 10^{11} \text{ cm}^{-2} \text{ s}^{-1}$ to the fluence of $1 \times 10^{16} \text{ cm}^{-2}$ and H⁺ ions with the flux of $7 \times 10^{12} \text{ cm}^{-2} \text{ s}^{-1}$ to the fluence of $1 \times 10^{17} \text{ cm}^{-2}$ (similar to regime I discussed above) was performed to extract the activation energies of possible hydrogen trapping sites and to identify their nature. TDS measurements were conducted using three different heating rates, namely 3 K/min, 6 K/min and 10 K/min.

Thermal desorption spectra of hydrogen release obtained on ODS-EUROFER samples after sequential room temperature He⁺ + H⁺ implantation using different heating rates are shown in Figs. 4.16(a) and 4.16(b) before and after filtering and background subtraction, respectively.

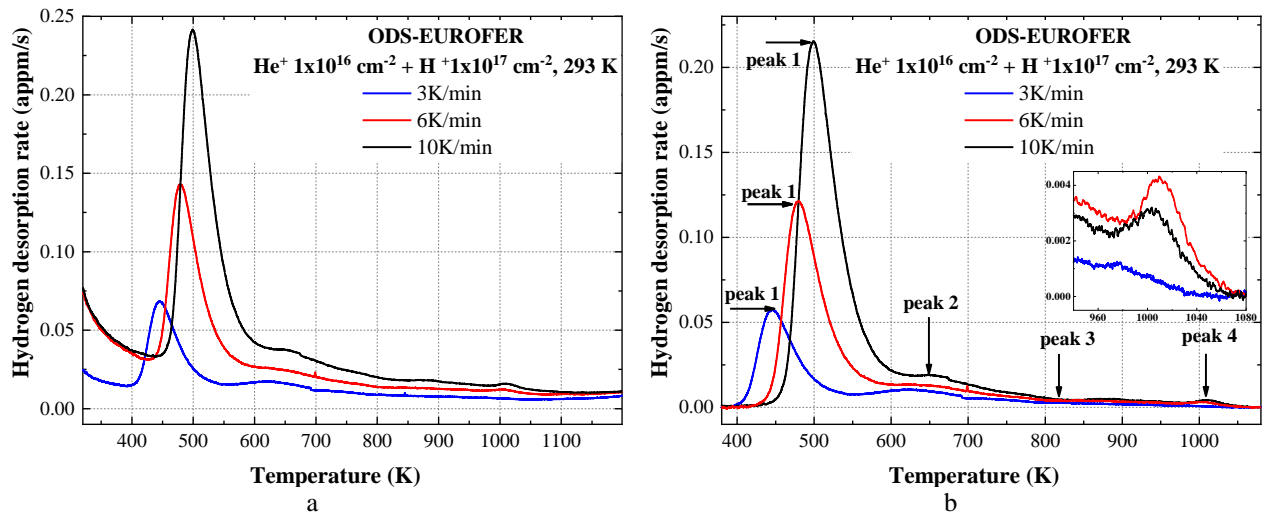


Fig. 4.16. TDS curves of hydrogen release obtained from samples of ODS-EUROFER sequentially implanted at RT with He^+ ions at the flux of $5 \times 10^{11} \text{ cm}^{-2} \text{ s}^{-1}$ to the fluence of $1 \times 10^{16} \text{ cm}^{-2}$ and H^+ ions at the flux of $7 \times 10^{12} \text{ cm}^{-2} \text{ s}^{-1}$ to the fluence of $1 \times 10^{17} \text{ cm}^{-2}$. The curves corresponding to heating rates of 3K/min, 6K/min and 10 K/min are colored blue, red, and black, respectively: (a) raw spectra; (b) spectra after filtering and background subtraction. The inset in panel (b) shows a magnified portion of the curves in the region of peak 4.

According to the Kissinger-Akahira-Sunose (KAS) model-free-kinetics method [17] for the analysis of TDS spectra, the heating rate correlates with the peak temperature location. The peak temperature for a particular hydrogen trap (at a particular temperature, i.e. peak 1, peak 2 and etc.) tends to shift to higher temperatures with the increase of the heating rate in TDS tests. This trend is clearly visible in Fig. 4.16 for peaks 1-3. Although peak 4 (at the highest temperature) has very low intensity, which causes some scatter in the TDS measurements, the same tendency of peak shift with the increase of heating rate is clear in this case too, as demonstrated in the inset of Fig. 4.16(b).

In order to determine the activation energies (E_a) of hydrogen traps related to the peaks observed in the TDS spectra, we use the relation suggested by Lee et al. [18–20], namely:

$$\frac{\partial \left(\frac{\partial T / \partial t}{T_m^2} \right)}{\partial (1/T_m)} = - \frac{E_a}{R}. \quad (4.1)$$

Equation (4.1) is a simplified form of the original Kissinger equation [21], where dT/dt is the heating rate (K/min), T_m (K) - the maximum TDS peak temperature, E_a (eV) - the activation energy of de-trapping for the specific hydrogen trap associated with T_m , and R ($\text{eV} \times \text{K}^{-1}$) - the Boltzmann constant. TDS curves obtained in measurements with different heating rates were smoothed, the background was subtracted following the same approach as in the previous sections, the spectra were deconvoluted into similar sets of Gaussian peaks, and the corresponding peak maximum temperatures were determined. Plotting $\ln \left(\frac{\partial T / \partial t}{T_m^2} \right)$ vs. $(1/T_m)$ for each peak makes it possible to obtain the activation energy of hydrogen de-trapping E_a from trapping sites corresponding to that specific peak.

It is important to note that although in previous sections the low-temperature peak (peak 1) was treated as a single peak, its shape is not Gaussian and it should be deconvoluted into more than one Gaussian peak. An example of such deconvolution procedure and its complexity has been given by Wei and Tsuzaki [22], who deconvoluted the low temperature peak into several peaks and emphasized that the number of peaks actually remains an arbitrary choice. In this section, as shown in Fig. 4.17 for the heating rate of 6 K/min, the low temperature peak was deconvoluted into three Gaussian peaks (sub-peaks 1.1, 1.2, and 1.3, respectively), which is the minimum number providing a smooth fit, while the higher temperature peaks 2 to 4 were treated as single peaks. After the number of peaks had been fixed, all TDS curves at different heating rates were deconvoluted in a similar way.

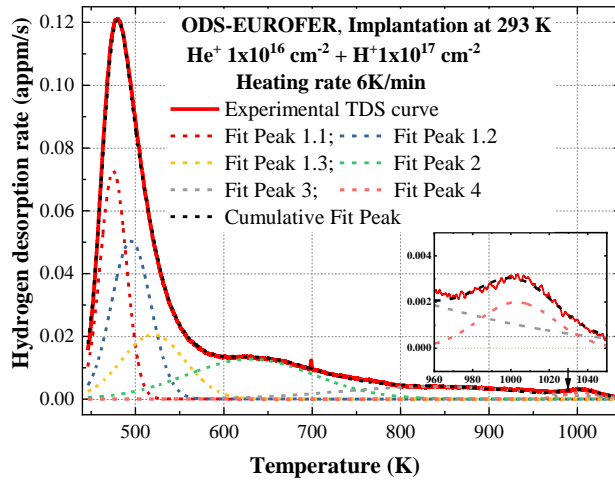


Fig. 4.17. An example of deconvolution of the TDS spectrum for ODS-EUROFER sample sequentially implanted at RT with He⁺ ions at the flux of $5 \times 10^{11} \text{ cm}^{-2} \text{ s}^{-1}$ to the fluence of $1 \times 10^{16} \text{ cm}^{-2}$ and H⁺ ions at the flux of $7 \times 10^{12} \text{ cm}^{-2} \text{ s}^{-1}$ to the fluence of $1 \times 10^{17} \text{ cm}^{-2}$. The heating rate is 6 K/min. The color coding for each deconvolution peak is explained in the legend.

The dependencies of $\ln((\partial T/\partial t)/T_m^2)$ on the inverse peak temperatures ($1/T_m$) extracted from TDS curve deconvolution for heating rates 3 K/min, 6 K/min, and 10K/min are shown in Fig. 4.18. The activation energies of hydrogen detrapping from different traps were determined from the linear fit to the sets of points for different peaks are summarized in Table 4.7. The errors in Table 4.7 are the standard errors of the slope determination for $\ln((\partial T/\partial t)/T_m^2)$ vs. ($1/T_m$).

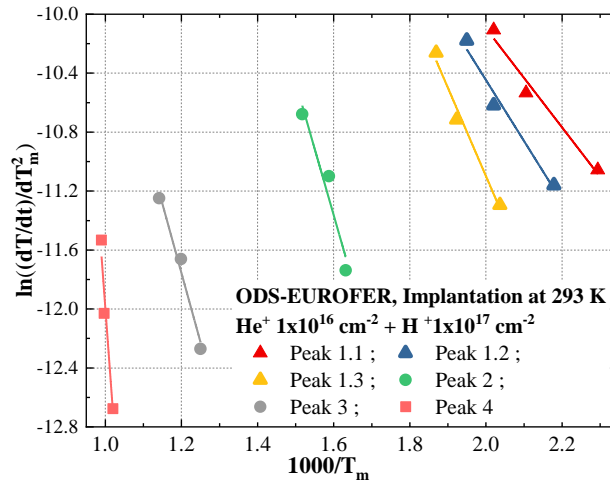


Fig. 4.18. Dependence of $\ln((\partial T/\partial t)/T_m^2)$ on ($1/T_m$) for ODS-EUROFER samples sequentially implanted at RT with He⁺ ions at the flux of $5 \times 10^{11} \text{ cm}^{-2} \text{ s}^{-1}$ to the fluence of $1 \times 10^{16} \text{ cm}^{-2}$ and H⁺ ions at the flux of $7 \times 10^{12} \text{ cm}^{-2} \text{ s}^{-1}$ to the fluence of $1 \times 10^{17} \text{ cm}^{-2}$. The curve color coding is explained in Fig. 4.17.

Table 4.7. Summary of maximum peak temperatures and activation energies corresponding to the deconvoluted peaks of TDS spectra for ODS-EUROFER samples sequentially implanted at RT with He⁺ ions at the flux of $5 \times 10^{11} \text{ cm}^{-2} \text{ s}^{-1}$ to the fluence of $1 \times 10^{16} \text{ cm}^{-2}$ and H⁺ ions at the flux of $7 \times 10^{12} \text{ cm}^{-2} \text{ s}^{-1}$ to the fluence of $1 \times 10^{17} \text{ cm}^{-2}$.

Parameters		Peak 1					Peak 2	Peak 3	Peak 4
		Sub-peak 1.1	Sub-peak 1.2	Sub-peak 1.3					
Temperature of H release peak, T_m (K)	3 K/min	436	459	491		613	800	980	
	6K/min	475	495	520		630	834	1003	
	10K/min	495	513	535		659	876	1010	
Activation energy, E_a (eV)		0.29 ± 0.05	0.36 ± 0.06	0.52 ± 0.07		0.78 ± 0.20	0.81 ± 0.12	3.02 ± 0.65	

In thermal desorption spectroscopy, it is a common practice to divide hydrogen isotope trapping sites into two classes depending on the temperature at which hydrogen release from these sites occurs. Hydrogen that desorbs at sufficiently low temperatures is weakly bound to traps and corresponding trapping sites are called reversible traps because the capture of hydrogen in these sites is counterbalanced by sufficiently easy de-trapping. The more strongly trapped hydrogen is only released at high temperatures; corresponding trapping sites are called irreversible traps. The release of hydrogen atoms from irreversible traps is difficult. Irreversible hydrogen traps, due to their high binding energies, are able to capture hydrogen until they become fully saturated. In more quantitative terms, the division of traps into two classes can be done referring to the magnitude of their binding energy with the traps. Traps with a binding energy less than ~ 0.6 eV are usually referred to as reversible, while those with binding energies higher than ~ 0.6 eV are referred to as irreversible ones [23]. In terms of this classification, hydrogen traps associated with peaks 1.1-1.3 are reversible and those associated with peaks 2 to 4 - irreversible. Correspondingly, the enhanced hydrogen trapping in ODS-EUROFER steel as compared to EUROFER 97, originates from hydrogen accumulation in reversible traps, while the increased amount of retained hydrogen after dual-beam $\text{He}^+ + \text{H}^+$ implantation as compared to the single-beam H^+ regime is due to hydrogen accumulation in irreversible traps.

4.2.2.4 Tentative identification of hydrogen traps

The activation energies obtained above can be used to identify hydrogen traps responsible for that or another peak based on both the acquired knowledge about microstructural features present in ODS-EUROFER steel after sequential room temperature $\text{He}^+ + \text{H}^+$ implantation (see section 4.1.2) and the available literature data on the characteristic binding energies of hydrogen with different components of steel microstructure and radiation defects.

Table 4.8. Published data on trapping (activation) energies E_a for hydrogen isotopes in *bcc* iron-based alloys. Notice that the main part of the data in the references is compiled from secondary sources.

Trapping sites	Activation energy (eV)	References
Interstitial sites	0.04-0.08	[24]
	0.16	[25]
Dislocation strain field	0.24-0.29	[23–27]
Dislocation core	0.62	[26]
Grain boundaries	0.19-0.55	[24]
	0.28-0.31	[28]
	0.33	[26]
Martensitic lath grain boundaries	0.34-0.36	[29]
	0.17-0.38	[30]
Cr-based carbides	0.69	[27]
	0.52-0.57	[28]
Y_2O_3 interfaces	0.73	[24,27]
	0.35	[1,15]
Monovacancies	0.5-0.81	[26]
	0.53	[31]
Vacancy clusters	0.71	[31]
Microvoids	0.37-0.42	[27]
	0.5	[26]
	0.73-0.99	[23]
Microbubbles (with He)	0.78	[31]
H_2 molecule, bonding energy	4.54-4.91	[32]

ODS-EUROFER steel has quite complex microstructure, which even in as-supplied state includes such microstructural components as grain boundaries, dislocations, M_{23}C_6 and Y_2O_3 particles. All these

microstructural features are potentially able to serve as hydrogen trapping sites. After implantation, also gas bubbles, gas-vacancy clusters and implantation-induced vacancies should be included in the list of possible traps. In order to estimate the relative role of these microstructural features in the overall hydrogen trapping, one can use the published literature data on the binding/activation energies (E_a) associated with different hydrogen traps in *bcc* iron and iron-based alloys, which are listed in Table 4.8.

In agreement with the common classification of hydrogen traps, the analysis below starts with the discussion on the possible origin of reversible traps in ODS-EUROFER steel and then addresses irreversible trapping sites, which seem to be more important in practical terms. Indeed, having in mind that ODS-EUROFER is mainly intended for applications related to Gen. IV and fusion reactors with the temperatures in the range of 773-973 K, only irreversible trapping sites will determine swelling resistance of the steel under the expected operation conditions.

4.2.2.4.1 Hydrogen trapping mechanisms associated with peaks 1.1-1.3 at ~435-535 K (reversible traps)

The ODS-EUROFER steel manifests higher hydrogen retention than EUROFER 97 under all applied implantation regimes as follows from the height increase of release peak 1 on TDS curves. This peak was deconvoluted into three peaks that might be associated with different trapping sites with somewhat different activation energies.

The lowest activation energy for the first de-convoluted peak 1.1 has been estimated as 0.29 eV. This energy is too high to be associated with hydrogen trapping in interstitial positions of *bcc* Fe lattice, cf. Table 4.8. In other words, the hydrogen that was dissolved in the interstitial positions in iron lattice either desorbed from the sample or was re-distributed to stronger traps before the TDS measurements were started. The hydrogen traps with the next higher binding energies are dislocations and grain boundaries. Judging from the data collected in Table 4.8, the most appropriate candidates for hydrogen traps corresponding to sub-peak 1.1 are dislocations with the reported hydrogen binding energy in the range of 0.24 to 0.29 eV and possibly some grain boundaries. Tempered ferritic-martensitic steels have a four-level hierarchy of grain-boundary morphology, including prior austenite grain, packet, block, and lath boundaries, which is reflected in a relatively broad spread of the reported hydrogen binding energies to grain boundaries, which falls within 0.18 to 0.55 eV. However, the majority of the reference values correspond to either sub-peak 1.1, or, where martensitic lath boundaries are concerned, to sub-peak 1.2. The association of sub-peaks 1.1 and 1.2, which give the main contribution to peak 1, with dislocations and grain boundaries provides a ready explanation to the observation of noticeably higher peak 1 in ODS-EUROFER steel as compared to EUROFER 97. Indeed, the number of hydrogen traps captured in any particular trap type is proportional to the volume density of traps, see e.g. Ref. [33]. In ODS-EUROFER steel, both dislocation and grain boundary densities are higher than in EUROFER 97.

The third de-convoluted sub-peak 1.3 has activation energy of 0.52 eV and, based on the data in Table 4.8, can be associated with either $M_{23}C_6$ carbides present in as-supplied ODS-EUROFER steel or with implantation-induced vacancies. However, the association of sub-peak 1.3 with carbides seems less probable. Indeed, $M_{23}C_6$ precipitates larger than 100 nm practically do not capture hydrogen [34], while the density of $M_{23}C_6$ carbides with the sizes below 100 nm in ODS-EUROFER steel is quite moderate, especially in comparison with carbide densities reported in [28] for the other ferritic-martensitic steels. At the same time, the amplitude of peak 1.3 in ODS-EUROFER TDS curve is quite notable. The calculated activation energy of ~0.52 eV also favorably compares to the hydrogen binding energy in single vacancies. The peak 1.3, together with peaks 1.1-1.2, also contributes to the increase of hydrogen retention in ODS-EUROFER as compared to EUROFER 97 under both single-beam and sequential dual-beam $He^+ + H^+$ implantation regimes applied. Putting together these facts, we tend to associate peak 1.3 with the activation energy of ~0.52 eV with hydrogen trapping in vacancies.

The possibility of hydrogen trapping at Y_2O_3/Fe interfaces remains uncertain. Two remarkably different hydrogen binding energies were reported for such trapping mode in the literature, namely ~ 0.35 eV [1,15] and ~ 0.73 eV [24,27]. The second one is too high to be associated with peak 1 and would correspond rather to peak 2. However, we have observed no notable increase of hydrogen uptake at higher temperatures in ODS-EUROFER steel as compared to its non-ODS counterpart in this study, so the binding energy of ~ 0.73 eV is not relevant for the hydrogen trapping at Y_2O_3/Fe interfaces in ODS-EUROFER steel. However, with the lower binding energy of 0.35 eV the oxide particle surfaces could contribute to sub-peak 1.2, thus increasing the height of peak 1 in ODS-EUROFER steel as compared to EUROFER-97. The accumulation of hydrogen inside the oxide particles is not very probable because of the bad hydrogen solubility in yttria [35].

Summing up, the results of activation analysis indicate that implantation induced vacancies, dislocations, grain boundaries and possibly Y_2O_3 nanoparticle interfaces constitute the reversible hydrogen trapping sites in ODS-EUROFER after single-beam and sequential hydrogen implantation at room temperature. Nearly three times lower capture of hydrogen in reversible traps in the EUROFER 97 steel as compared to ODS-EUROFER is attributed to the lower concentration or absence of the relevant microstructural features in EUROFER 97.

4.2.2.4.2 Hydrogen trapping mechanisms associated with peaks 2 and 3 at ~ 610 -800 K (irreversible traps)

The calculated activation energies for peak 2 and peak 3 are 0.78 eV and 0.81 eV, respectively, but both peaks are quite broad, which is usually associated with a large variety of different traps with close binding energies. Such picture would be expected for hydrogen trapping by microvoids or He-filled micro-bubbles that are characterized in the literature with a broad range of binding energies (0.37-0.99 eV) and so it is tempting to associate peaks 2 and 3 with hydrogen de-trapping from these microstructural features. Some reasons in support of this identification are suggested below.

As shown earlier in this section, hydrogen implantation after helium pre-implantation results in both studied steels in the increased hydrogen retention in traps associated with peak 2 as compared to implantation with hydrogen only. A similar effect of enhanced hydrogen trapping after sequential implantation with helium and hydrogen (or deuterium) ions was observed also in some other ferritic-martensitic steels [36,37], as well as in pure *bcc* iron [38] and austenitic steels [39,40]. For some other ferritic-martensitic steels the preliminary He^+ implantation resulted after subsequent H^+ implantation in no peak 1 at all, with all hydrogen being trapped in irreversible traps that release hydrogen at temperatures (in the range of 600-900 K) roughly similar to those of peaks 2 and 3 [41,42]. The numerical modeling of hydrogen desorption from sequentially implanted steel samples in Ref. [42] has led the authors to conclusion that the dominate traps are helium bubbles with hydrogen binding energy of 0.8 ± 0.1 eV, the value very close to that obtained in this work.

Several mechanisms responsible for hydrogen trapping by He bubbles were proposed in the literature. The most probable seems to be hydrogen trapping at the walls of He bubbles, as suggested in Ref. [31]. The binding energy associated with such trapping, 0.78 eV for bubbles in iron [31], is in excellent agreement with our estimate for peak 2. However, also alternative suggestions can be found in the literature. For example, hydrogen isotope trapping in the vicinity of helium bubbles has been suggested as a possible mechanism of hydrogen retention under sequential dual-beam $He^+ + H^+$ implantation [41]. However, this mechanism is not relevant in the current context because it was suggested to explain a relatively small shift (by 30 K) of peak 1 due to He^+ pre-implantation rather than the nature of the high temperature peak. One more possible mechanism of hydrogen trapping by He bubbles, namely the formation of H_2 molecules inside bubbles or voids [39], though not impossible, as discussed in the next section, can hardly be associated with peaks 2 or 3. Indeed, because of strong chemical bonding of hydrogen atoms in a molecule [32], hydrogen cannot escape from cavities at

moderate temperatures and thus peak 2 with the activation energy of less than 1 eV cannot result from direct hydrogen molecules dissociation and escape into the steel matrix from He bubbles. The only possibility for the desorption of H₂ molecules captured within bubbles might be through the migration of such bubbles to sample surface or some hydrogen diffusion shortcuts (e.g. grain boundaries). However, in our experiments, this was definitely not the case. First of all, no indications of bubble mobility were noticed during the annealing of ODS-EUROFER samples sequentially implanted with He⁺ and H⁺ ions at temperature even higher than that of release peak 2 (see section 4.1.2.1). Second, the release of hydrogen due to the bubble migration to the surface would be manifested in simultaneous release of hydrogen and helium, which was also not observed. A control TDS measurement of He release from one of sequentially He+H implanted samples fixed the first noticeable He peak only at ~1250 K, far above the peak 2 temperature.

Summing up, the experimental results analyzed above in combination with the published literature data indicate that hydrogen release peaks 2 and 3 with the activation energies 0.78 eV and 0.81 eV observed in ODS-EUROFER after sequential He⁺+H⁺ implantation at room temperature are associated with hydrogen trapping in helium bubbles, most probably at bubble walls through the mechanism similar to chemisorption.

4.2.2.4.3 Hydrogen trapping mechanisms associated with peak 4 at ~1000 K (irreversible traps)

The high-temperature peak appears only in specific implantation conditions (namely only after He⁺ pre-implantation), but is observed in both ODS-EUROFER and EUROFER 97, implying that its appearance is not directly related to the presence or absence of oxide particles, but is rather due to some microstructural features that evolve as a result of He⁺ implantation. At the same time, the calculated activation energy of peak 4, ~3 eV, is much larger than hydrogen de-trapping energies reported in the literature for defects in iron-based *bcc* alloys (see Table 4.8), even considering rather high uncertainty (exceeding 0.5 eV) in the determination of the activation energy value. Therefore, this hydrogen release peak cannot be explained by de-trapping and desorption of atomic hydrogen, but may be tentatively associated with the dissociation of molecular hydrogen trapped in sufficiently large cavities. Indeed, according to first-principals calculations, hydrogen molecules in iron cannot exist as an entity in either single vacancies [43,44], or small vacancy clusters [45]. The preferential location for hydrogen is in atomic form on the cavity walls. Only when the cavity is large enough and the walls are already covered with hydrogen atoms, hydrogen molecules inside the cavity are able to withstand dissociation. Correspondingly, when the implanted hydrogen is captured in cavities, it covers initially the cavity walls (this stage is referred to in Ref. [45] as undersaturated regime). However, as the amount of captured hydrogen increases and its surface density reaches sufficiently high level to force interaction between neighboring hydrogen atoms on the surface, hydrogen pairs can be released into the inner space of cavities and can stay in molecular form for a long time because the reverse process of molecule dissociation requires high energy and cannot be catalyzed by the cavity walls, which are nearly completely covered with hydrogen. This situation is referred to as saturated stage [45]. Indirect evidence in favor of this interpretation is the above-mentioned hydrogen induced rounding of bubbles with several nanometer size formed at the He⁺ pre-implantation stage, which can be due to the increase of gas pressure in the bubbles as a result of molecular hydrogen creation in the cavity inner space in addition to He atoms. Summing up, the formation of hydrogen molecules in cavities is generally possible, but requires two conditions to be satisfied, namely sufficiently high concentrations of hydrogen in the steel matrix in order to saturate cavity surfaces and sufficiently large cavity size in order to have enough place to accommodate hydrogen molecules in the cavity interior.

In addition to theoretical considerations, there exist some experimental studies justifying the assumption of molecular hydrogen formation in steel samples containing cavities and saturated with high

concentrations of hydrogen. For example, in recent experiments on room temperature hydrogen implantation into Fe-12%wt.Cr-ODS steel [9] in a variety of regimes, including single-beam H^+ , dual-beam He^+/H^+ and Fe^+/H^+ , and triple-beam $Fe^+/He^+/H^+$ modes, the presence of hydrogen molecules in the hydrogen saturated samples was found using Raman spectroscopy only in multi-beam irradiation regimes that included He^+ implantation, although atomic hydrogen was found after implantation in all samples. For this reason, the authors of Ref. [9] associate the presence of molecular hydrogen with the cavities promoted by helium atoms. In a number of other studies, the formation of hydrogen molecules inside the cavities was suggested as a possible reason of swelling increase caused by synergetic effect of helium and hydrogen, e.g. in triple-beam irradiation experiments in ferritic alloys [5–7] or as an explanation for a large amount of retained hydrogen in neutron irradiated austenitic steels [39].

Results presented earlier in section 4.2 of the thesis demonstrate the presence of hydrogen desorption peak at ~ 1000 K in both ODS-EUROFER and EUROFER 97 steels only in samples pre-implanted with He^+ ions (see red curves in Figs. 4.13(a) and 4.13(b)). This behavior resembles that observed in Ref. [9] and gives certain confidence to the association of the release peak at ~ 1000 K with molecular hydrogen captured in helium-filled cavities and de-trapped as a result of hydrogen molecule dissociation, even in spite of the fact that the dissociation energy of hydrogen molecule in vacuum, 4.5–4.9 eV, is notably higher than the peak 4 activation energy. Indeed, at the temperatures relevant for peak 4 all hydrogen chemisorbed on cavity walls is expected to have been completely desorbed in peaks 2 and/or 3, so that the dissociation of hydrogen molecules could be catalyzed by hydrogen-free cavity walls.

It might look strange, at first glance, that the release peak 4 was observed in He pre-implanted samples only provided pre-implantation was done at room temperature, whereas in samples pre-implanted with He^+ ions at 823 K the peak was absent. This different behavior can, however, be rationalized in terms of the difference in the cavity microstructures observed after H^+ implantation into samples pre-implanted with helium at room and elevated temperatures. Namely, two cavity populations were observed after sequential $He^+(823\text{ K})+H^+$ implantation, while after $He^+(RT)+H^+$ implantation only a single population of tiny cavities could be identified. The total bubble surface estimated based on the obtained cavity parameters in both cases turns out to be at least $\sim 20\%$ larger in the case of high-temperature He^+ pre-irradiation thanks to the cavity population formed already at the helium pre-implantation stage. Taking into account that the same hydrogen fluence ($1 \times 10^{17} \text{ cm}^{-2}$) was used in both implantation regimes and recalling that prior to hydrogen molecule formation the cavity surfaces have to be saturated with atomic hydrogen [45], it is natural to expect that the total number of created hydrogen molecules will be larger in the sample with the smaller cumulative bubble surface, that is pre-implanted with helium at RT. Note that even in this case the height of peak 4 is quite low; an additional suppression of molecular hydrogen formation makes it indistinguishable.

4.2.3 Conclusions

Summing up the results of TDS analysis in sections 4.2.1 – 4.2.2, it can be concluded that

(i) ODS-EUROFER steel manifests ~ 3 times stronger hydrogen uptake as compared to the ODS-free EUROFER 97 steel under single-beam H^+ and sequential dual-beam He^++H^+ implantations at room temperature. The high hydrogen trapping ability of ODS steel is consistent with results obtained earlier for ODS-EUROFER steel [1,2,15], ODS 9-16 Cr steel [46], and 14YWT steel [47]. The analysis of experimental results in conjunction with available literature data shows that the stronger hydrogen retention in ODS-EUROFER steel as compared to EUROFER 97 originates from hydrogen trapping in reversible traps such as dislocations, grain boundaries, single vacancies and oxide nanoparticle surfaces.

(ii) In both ODS-EUROFER and EUROFER 97 steels, sequential implantation with He^+ and H^+ ion beams increases total hydrogen retention as compared to single-beam H^+ implantation. This is consistent with literature data for pure *bcc* iron [38] and ferritic-martensitic steels [36,37]. The performed activation analysis shows that the increase of total hydrogen retention is due to hydrogen accumulation in

irreversible traps with the de-trapping energies of 0.78-0.81 eV, which were tentatively identified as He-filled cavities that accumulate hydrogen atoms on the cavity walls.

(iii) A high temperature peak at ~1000 K with the activation energy of ~3 eV was detected in samples of ODS-EUROFER and EUROFER 97 sequentially implanted with He⁺ and H⁺ ions at room temperature. Having in mind the high de-trapping energy, the very low peak height as compared to other peaks, as well as the absence of the peak in samples not pre-implanted with helium, it was tentatively identified as being due to dissociation of molecular hydrogen captured in the He-filled cavities.

4.3 Electron energy loss spectroscopy investigation of hydrogen association with helium bubbles in ODS-EUROFER steel

The results of TEM analysis presented in section 4.1 show that H⁺ implantation into He pre-implanted samples of ODS-EUROFER has only minor effect on bubble population evolution and swelling. In particular, hydrogen implantation promotes the development of ~1 nm large bubbles and the suppression of bubble faceting. The bubble shape change (section 4.1.2.2) suggests that at least some amount of hydrogen might be trapped at the walls of He bubbles. The activation analysis of TDS data shows that some hydrogen accumulates in irreversible traps with the de-trapping energies of ~0.78-0.81 eV and ~3 eV. These traps were tentatively associated with hydrogen atom capture at bubble walls and, in molecular form, hydrogen inside the bubbles, respectively.

Summing up, both TEM and TDS analyses confirm the retention of hydrogen in the studied ODS-steel after sequential dual-beam implantation and moderate synergetic influence of helium and hydrogen on microstructure development in ODS-EUROFER steel. However, combination of conventional techniques does not provide a direct confirmation of hydrogen association with helium bubbles. An additional experimental technique should be applied to investigate the spatial distribution of hydrogen in the investigated material as well as to confirm the hydrogen trapping mechanism in helium bubbles.

In order to acquire more direct evidences of hydrogen association with helium bubbles, we have applied the Electron Energy-Loss Spectroscopy (EELS) technique in spectrum imaging (SI) acquisition mode. EELS-SI measurements were done on ODS-EUROFER samples sequentially implanted with He⁺ and H⁺ ions in the same regime as those used for the conventional TEM (section 4.1.2.2) and TDS measurements (section 4.2.2.2), that is

- 10 keV He⁺ ion implantation to the fluence of 1×10^{16} cm⁻² at 823 K followed by 5 keV H⁺ ion implantation to the fluence of 1×10^{17} cm⁻² at room temperature.

This section covers EELS-SI experimental results, data treatment and analysis of possible hydrogen signal within individual He bubbles in ODS-EUROFER steel. The extraction of H-K and He-K signals has been performed using spectral difference method on individual EEL spectra and the entire EELS-SI dataset. Raw EELS data pre-processing prior to the spectral difference analysis included background subtraction and plural scattering removal. The procedure of hydrogen signal extraction from the superposition of various contributions in the same energy-loss range is considered in details.

4.3.1 Analysis of raw EELS-SI data

The EELS-SI measurements on samples of ODS-EUROFER steel sequentially implanted with He⁺ and H⁺ ions were performed by Dr. Katia March on a probe-corrected JEOL ARM-200F scanning transmission electron microscope equipped with a Gatan Enfium dual energy electron loss spectrometer at the Eyring Materials Center (Arizona State University, Tempe, USA). The equipment operated at 200 kV and had a Zero-Loss Peak (ZLP) Full-Width at Half-Maximum (FWHM) of ~0.7 eV. The convergence and collection semi-angles were 28 and 56 mrad, respectively. The energy dispersion was set at 0.050 eV/channel. Since the He-K and H-K signals were expected at 21.2 eV for atomic He [48] and at 12.5 eV for molecular H [48], EELS-SI datasets were acquired in the low-loss (LL) region of EEL

spectrum to detect He and H segregations. In order to extract the maximum information, to perform correction of energy drift (arising from the beam instability) and to remove effects of elastic and plural inelastic scattering, the recording of LL EEL spectrum region including zero-loss peak (ZLP) was required. To deal with the large difference of signal intensity of the ZLP peak and LL spectrum the SI signals were recorded in the Dual EELS acquisition mode [49,50]. A pair of EELS-SI datasets, namely, the zero-loss SI (ZL SI) from ~ 9 to 90 eV and the low-loss SI (LL SI) from ~ 3 to 100 eV, was acquired in rapid succession at each probe position using different integration times. The camera integration time $t_{LL} = 240 \mu\text{s}$ was set to give the desired signal level for LL SI, while $t_{ZL} = 2 \mu\text{s}$ was set to limit the top of the most intense ZLP below the saturation level of the CCD detector for ZL SI.

Fig. 4.19(a) shows the High-Angle Annular Dark Field (HAADF) STEM survey image used for the acquisition of EELS-SI data. EELS-SI datasets were taken from two zones marked with red boxes. HAADF images recorded simultaneously with the EELS-SI datasets of zone 1 and zone 2 are shown in Fig. 4.19(b) and 4.19(c), respectively. The investigated zone 1 contains an Y_2O_3 particle ~ 15 nm in diameter with attached He bubble and a He bubble with low contrast in the grain bulk, while zone 2 contains two He bubbles with diameters ~ 5 nm in the grain bulk.

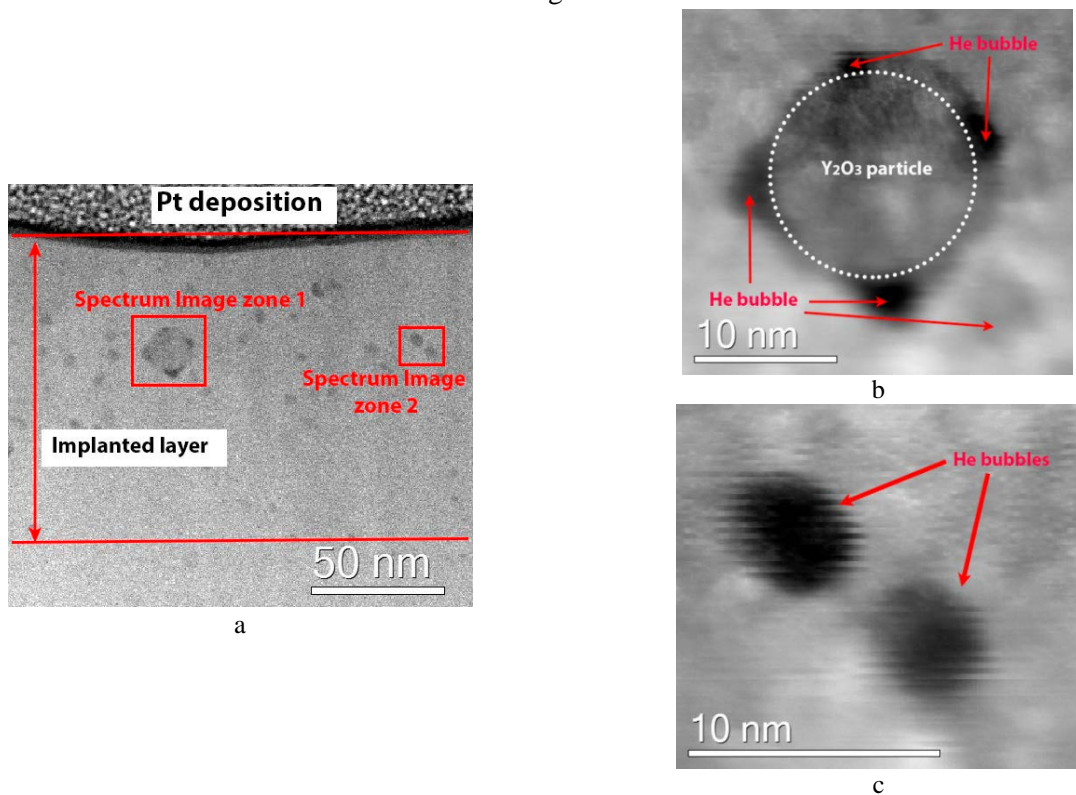


Fig. 4.19. High-angle annular dark-field image of ODS-EUROFER steel sequentially implanted with He^+ ions with the flux of $5 \times 10^{11} \text{ cm}^{-2}\text{s}^{-1}$ to the fluence of $1 \times 10^{16} \text{ cm}^{-2}$ at 823 K and H^+ ions with the flux of $7 \times 10^{12} \text{ cm}^{-2}\text{s}^{-1}$ to the fluence of $1 \times 10^{17} \text{ cm}^{-2}$ at RT: (a) HAADF survey image showing the regions from which SIs were recorded; (b) HAADF image recorded simultaneously with the SI dataset of zone 1 with He bubble attached to Y_2O_3 particle; (c) HAADF image recorded simultaneously with the SI dataset of zone 2 with two He bubbles in the grain bulk.

Post-processing of the EELS-SI datasets was performed in Digital Micrograph 3.4 (GMS) [51] using a combination of in-built routines and custom scripts (including SI Tools plugin [52]). As the first processing step, X-ray spikes caused by spurious external radiation were removed from ZL and LL SI parts of datasets using the in-built function of GMS “Volume \rightarrow Remove X-rays”. After the removal of X-ray spikes, the energy drift was corrected on pixel-to-pixel basis using ZLP position in entire ZL SI applying GMS routine “SI \rightarrow Align SI by Peak”. Since the LL SI was recorded in a rapid succession to the ZL SI at each probe position in the Dual EELS acquisition mode, it was assumed that the shift required for the LL SI is the same as that for the ZL at the same pixel. Thus, it was not necessary to splice

the data before correcting the energy position. The energy drift on LL SI was corrected using the peak shift map obtained during the ZL SI energy drift correction procedure.

As the next processing step, the initial signals were de-noised. The reduction of random noise was performed by means of the Principal Component Analysis (PCA) [53] routine using the Hyperspy software [54] separately for ZL and LL SI datasets. The de-noised spectra were checked to ensure that there were no artifacts from missing components. Across all the analyzed experimental SI signals, the number of kept principal components varied between 8 and 12.

Fig. 4.20 presents representative low-loss EEL spectra extracted from the matrix, He bubble and Y_2O_3 particle on LL and ZL SI after PCA de-noising and energy drift correction. The areas for signal extraction are specified in Fig. 4.20(a). To improve the visibility, the signals subtracted from the Y_2O_3 particle, the matrix, and He bubble are scaled with respect to ZL spectra by 50x, 100x and 120x, respectively.

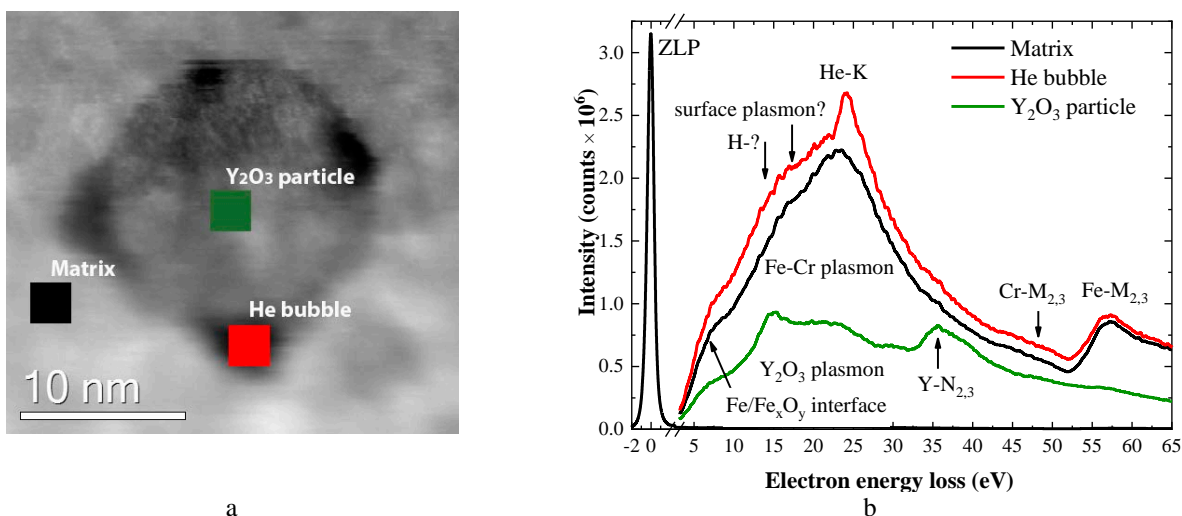


Fig. 4.20. (a) HAADF image of zone 1 showing the regions from which the summed spectra were extracted. (b) Representative low-loss EEL spectra extracted at selected positions of the ODS-EUROFER steel sample sequentially implanted with He^+ ions with the flux of $5 \times 10^{11} \text{ cm}^{-2} \text{ s}^{-1}$ to the fluence of $1 \times 10^{16} \text{ cm}^{-2}$ at 823 K and H^+ ions with the flux of $7 \times 10^{12} \text{ cm}^{-2} \text{ s}^{-1}$ to the fluence of $1 \times 10^{17} \text{ cm}^{-2}$ at RT. Black, red, and green curves correspond to the matrix, He bubble, and Y_2O_3 particle, respectively.

In the matrix and He bubble spectra, two most prominent signals are the Fe-Cr bulk plasmon oscillation peak with the maximum at 23.4 eV and $Fe-M_{2,3}$ shell ionization edge at $\sim 55-58$ eV. The component at $\sim 6.5-8.5$ eV in both matrix and He bubble spectra might represent surface plasmon excitation (SP) due to the presence of natural oxide layer Fe_xO_y [48] on the surface of the studied sample, similar to those observed at the Si/SiO₂ [55] and Al/Al₂O₃ [56,57] interfaces. For the spectrum extracted from He bubble, two additional components appear at the left and right shoulders of Fe-Cr bulk plasmon peak. The sharp peak at the right plasmon shoulder in the energy range of 24-26 eV with the maximum at ~ 25 eV is apparently He-K ionization edge [10,58,59]. Another signal is visible as a shoulder to the left of the Fe-Cr bulk plasmon peak with the maximum at $\sim 10-18$ eV. The signal is broad and it is challenging to locate the exact peak position from the raw EELS data. The broad peak might indicate that the signal arises from several superimposed sources falling in this energy range, including, in particular, bubble surface plasmon oscillation (BSP) and H-K ionization edge. In the framework of the Drude model, an electron beam at a glancing incidence can excite near an empty sphere (void) in metal a number of plasmon modes with different intensities. Using the energy of bulk Fe-Cr plasmon, 23.4 eV, the Drude model predicts BSP energy changing from 19.1 down to 16.6 eV as the angular momentum quantum number of the excited mode changes from 1 to ∞ . According to EELS atlas [48], the H-K ionization edge has a peak at 12.5 eV, but for hydrogen dissolved in metals the reported measured positions of the signal are usually somewhat higher, e.g. ~ 13 eV for Be [60] and ODS-steel [10], and ~ 13.5 eV for Zircaloy-

4 [61]. The LL spectrum region can contain also low energy M- and N-edges of transition metals. In particular, weak traces of Cr-M_{2,3} at ~42-47 eV and Y-N_{2,3} at ~36 eV are visible in the matrix and He bubble spectra. Since the thickness of the Y₂O₃ particle in the investigated region is comparable to the matrix thickness, the Fe-Cr bulk plasmon peak and Fe-M_{2,3} edge have low intensities in the spectrum extracted from the nanoparticle region. Two additional signals are detected in the spectrum extracted from the nanoparticle region; that at ~14-16 eV is due to the Y₂O₃ bulk plasmon oscillation [48] and another is a pronounced Y-N_{2,3} edge at ~36 eV.

Data treatment presented below in 4.3.1 section is provisional and serves only as guideline for analysis in section 4.3.2.

For the observed energy ranges, the spatial intensity distribution of spectral signatures was visualized by simple signal integration in few eV energy-selected windows using de-noised and drift corrected LL EELS-SI signals from zone 1 (Fig. 4.21) and zone 2 (Fig. 4.22).

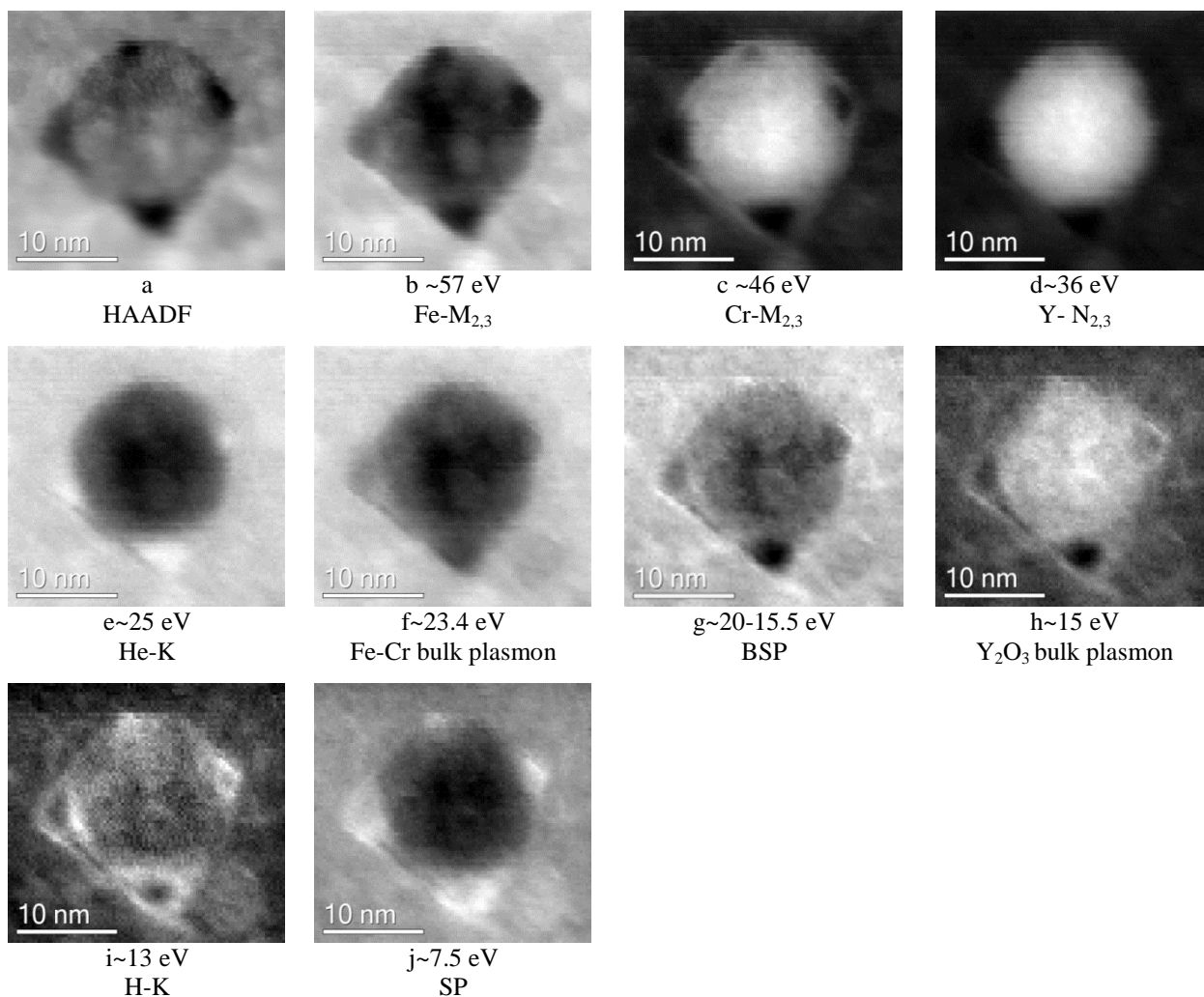


Fig. 4.21. The spatial distribution of components identified on raw LL EELS-SI data acquired from zone 1: (a) HAADF image; (b)-(j) EELS energy-selected window images associated with possible signals at (b) ~55–58 eV (Fe-M_{2,3}); (c) ~45–47 eV (Cr-M_{2,3}); (d) ~35–37 eV (Y- N_{2,3}); (e) ~24–26 eV (He-K); (f) ~22–24 eV (Fe-Cr bulk plasmon); (g) ~15.5–20.1 eV (bubble surface plasmon-BSP); (h) ~14–16 eV (Y₂O₃ bulk plasmon); (i) ~12–14 eV (H-K); (j) ~6.5–8.5 eV (surface oxide plasmon-SP).

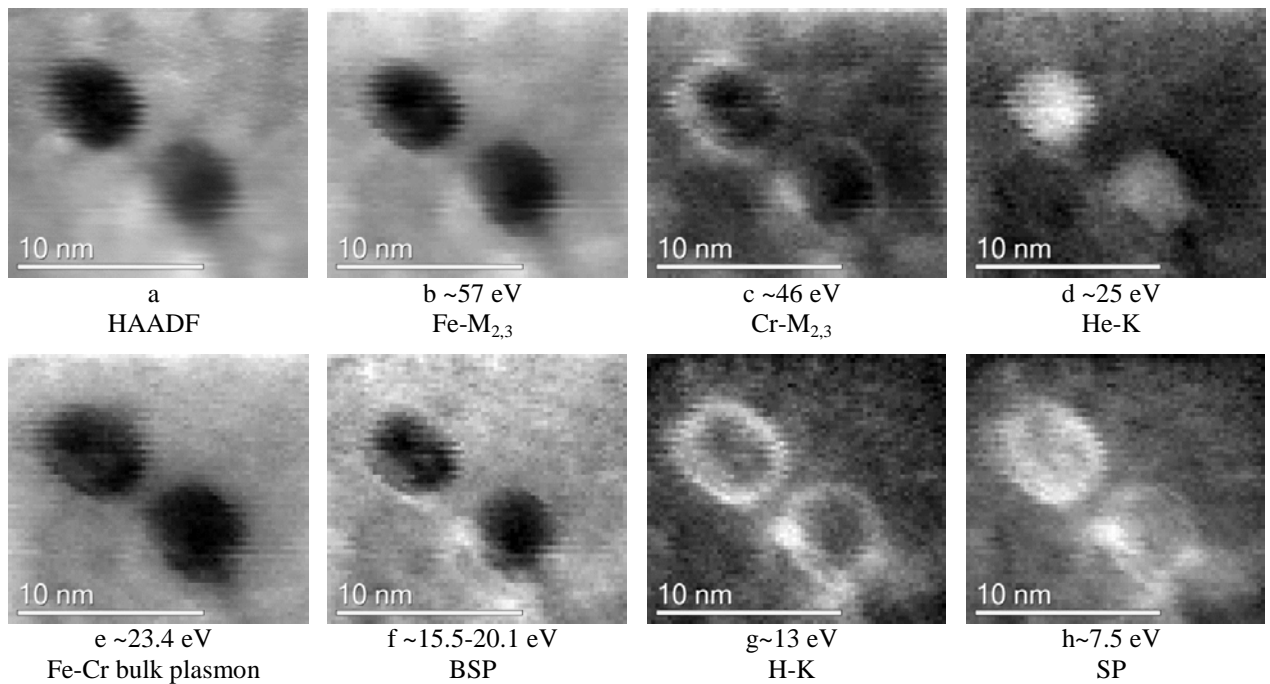


Fig. 4.22. The spatial distribution of components identified from raw LL EELS-SI data acquired from zone 2: (a) HAADF image; (b)-(h) EELS energy-selected window images associated with possible signals at (b) $\sim 55\text{--}58$ eV (Fe-M_{2,3}); (c) $\sim 45\text{--}47$ eV (Cr-M_{2,3}); (d) $\sim 24\text{--}26$ eV (He-K); (e) $\sim 22\text{--}24$ eV (Fe-Cr bulk plasmon); (f) $\sim 15.5\text{--}20.1$ eV (bubble surface plasmon-BSP); (g) $\sim 12\text{--}14$ eV (H-K); (h) $\sim 6.5\text{--}8.5$ eV (surface oxide plasmon-SP).

As can be seen in Figs. 4.21(b,f) and 4.22(b,e), in both investigated zones the Fe-M_{2,3} signal at ~ 57 eV and Fe-Cr bulk plasmon signal at ~ 23.4 eV manifest intensity drop at the positions of He bubbles and Y₂O₃ nanoparticle. In the energy range of Y-N_{2,3} (~ 36 eV) and Y₂O₃ bulk plasmon (~ 15 eV) one observes circular regions of increased intensity (see Figs 4.21(d) and 4.21(h)) that nicely match the typical morphology of Y₂O₃ nanoparticles (cf. BF TEM images in section 4.1). The brighter regions visible in Fig. 4.21(h) outside the nanoparticle area arise from superposition of Y₂O₃ bulk plasmon with other signals in the same energy range, including the left shoulder of the bulk Fe-Cr plasmon, a possible H-K ionisation edge and BSP oscillation (as discussed in detail below). The signal in the energy range of Cr-M_{2,3} ($\sim 45\text{--}47$ eV) is weak and visible only at the peripheries of bubbles in both zones and in Y₂O₃ particle interior in zone 1, see Figs. 4.21(c) and 4.22(c). It is hard to say which effects are responsible for the observed spatial distribution of this weak signal in the range of Cr-M_{2,3}. Figs. 4.20(e) and 4.21(d), corresponding to the energy window at $\sim 24\text{--}26$ eV where the He-K edge signal is expected, demonstrate a moderate intensity increase visible in the bubble interior for both investigated zones. This is in agreement with the presence of He-K peak in Fig. 4.20(a). However, this peak is located close the maximum of wide Fe-Cr plasmon peak at ~ 23.4 eV, which interferes with the signal from He and is responsible, in particular, for significant signal contribution observed in the area outside the bubbles. The image for BSP energy window of 15.5-20.1 eV demonstrates sharp rings of increased signal intensity at the periphery of bubbles in both investigated zones (see Figs. 4.21(g) and 4.22(f)). The non-vanishing signal in the matrix in both zones is due to superposition of BSP signal with the left shoulder of bulk Fe-Cr plasmon. Less sharp, but more intense rings of increased intensity around the peripheries of bubbles are observed also in the images for the energy window around ~ 13 eV (see Figs. 4.21(i) and 4.22(h)), indicating that H-K signal is located in the same spatial area as BSP signal. The non-vanishing signal intensity visible in this energy window in the matrix and inside Y₂O₃ nanoparticle is due to the left shoulder of the bulk Fe-Cr plasmon and the Y₂O₃ signal, respectively. Very close energy ranges and similar spatial locations of expected H-K (~ 13 eV) and BSP ($\sim 16.6\text{--}19.1$ eV) signals invoke uncertainties in the interpretation of observed intensity rings at the peripheries of bubbles in terms of BSP or H-K signals. Finally, images in the energy window of the surface oxide plasmon (SP) at ~ 7.5 eV demonstrate signal increase in the

bubble location areas in both investigated zones, most probably due to the lower matrix thickness in the bubble areas, which enhances the relative intensity of interfacial effects.

In order to make the spatial location of spectral component possibly associated with H-K signal at ~ 13 eV clearer, the images for this energy window in both investigated zones (Figs. 4.21(i) and 4.22(g)) were superimposed onto the images of for energy windows at ~ 25 eV (He-K) and ~ 16.6 - 19.1 eV (BSP) to produce composite color maps shown in Figs. 4.23 and 4.24 for zones 1 and 2, respectively.

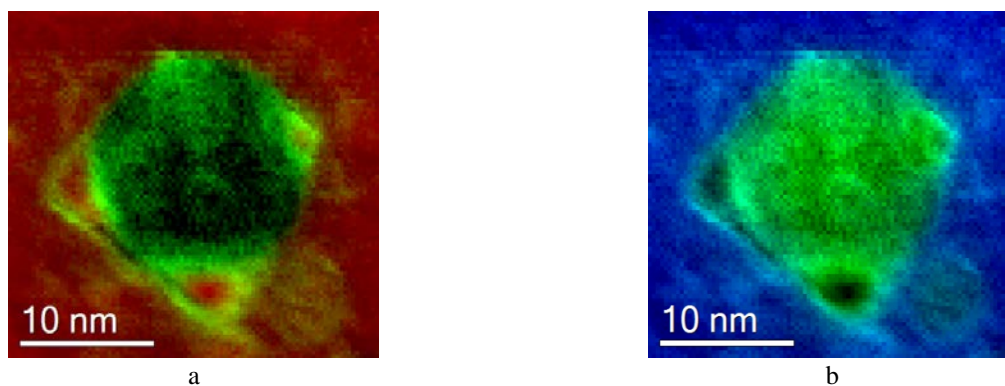


Fig. 4.23. Composite color maps of EELS-SI of energy-selected window 12-14 eV (H-K, green) from Fig. 4.20(i) combined with either (a) the image for energy-selected window 24-26 eV (He-K, red), or (b) the image for energy-selected window 15.5-20 eV (bubble surface plasmon, blue).

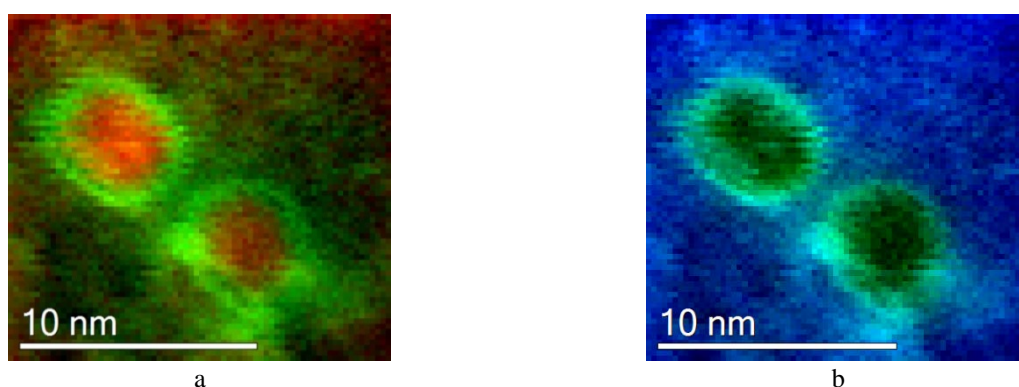


Fig. 4.24. Composite color maps of EELS-SI of energy-selected window 12-14 eV (H-K, green) from Fig. 4.21(g) combined with either (a) the image for energy-selected window 24-26 eV (He-K, red), or (b) the image for energy-selected window 15.5-20 eV (bubble surface plasmon, blue).

As can be noticed in Figs. 4.23(a) and 4.24(a), the signal at the H-K energy of ~ 13 eV is visible as rings of intensity at the peripheries of bubbles, whereas the signal at the He-K energy of ~ 25 eV is concentrated in the central part of bubble area. The interrelation between the signals in the H-K energy window at ~ 13 eV and in the BSP window of ~ 16.6 - 19.1 eV, as shown in Fig. 4.23(b) and 4.24(b), is more complicated. Both signals largely overlap at the bubble periphery, but the possible H-K signal is visible not only at the bubble periphery but also extends into the bubble interior, though with decreasing intensity. This indicates that hydrogen might be present throughout the entire bubble (or bubble surface), though possibly with increased density at bubble's periphery. However, the reliability of this interpretation is diminished by the fact that the signal intensities in both energy windows are affected by the of Fe-Cr bulk plasmon, which is evidenced by non-vanishing signal intensity visible in all composite color maps in the areas far from the bubbles.

Summing up, a simplistic treatment of the raw SI datasets, as presented in this section, does not allow drawing robust conclusions concerning either hydrogen association with He bubbles, or hydrogen location at the periphery or in the interior of bubbles. Moreover, the Y_2O_3 particle in the LL SI dataset recorded in zone 1 contributes an additional intense signal at ~ 14 - 16 eV (Y_2O_3 bulk plasmon), just a few eV apart from the positions of BSP and H-K signals. To avoid this additional complication, the treatment

below deals only with the EELS-SI dataset recorded in zone 2, where just 2 bubbles in the grain bulk are observed.

4.3.2 Data processing using spectral difference method

In order to analyze He-K and H-K signals associated with He bubbles in more detail, a deconvolution treatment using spectral difference method [58,62,63] has been applied. This method is commonly used to extract small signals presented in a single EEL spectrum or entire EELS-SI. The spectral difference procedure for the treatment of SI dataset includes two steps: (i) scaling matrix and bubble signals to compensate thickness variation at each pixel and (ii) subtraction of the matrix signal from that of the bubble, yielding the spectral difference. In the ideal case, the spectral difference SI should only contain information about the bubble. However, the presence of surface oxide and possibly the amorphous carbon contamination at the sample surface can provide spurious contributions to the spectral difference.

Prior to the application of spectral difference method it is advisable to eliminate plural scattering effects that result in the LL spectrum shape changes (both at the edges and at the background) in reply to local variations in the sample thickness or composition. After the removal of multiple scattering effects, the shape of the signal from the matrix should be the same in all “matrix” pixels, which simplifies scaling and subtracting the matrix contribution from the bubble region. In order to remove the effects of plural scattering, the Fourier-log deconvolution method is commonly used [64]. The presence of the ZLP in the LL spectrum is mandatory for application of Fourier-log deconvolution. Therefore, the drift corrected and de-noised ZL and LL SI signals recorded in zone 2 should be merged in a single dataset. Doing this, one should take into account a difference in the spectrum integration times between ZL and LL datasets, which results in different spectral intensity at the same energy range in ZL and LL spectra. During the splicing procedure the scaling factor (splice ratio) should be applied to compensate the difference in spectral intensity on each spectrum of either ZL or LL dataset. Ideally, in the overlapped region of ZL and LL spectra, the splice ratio should equal to the data acquisition time ratio [50,65]. In order to verify that this time ratio is the correct scaling factor, the spectrum extracted from ZL SI is compared in Fig. 4.25(a) with the spectrum of LL SI scaled in same energy region by the signal acquisition time ratio, which equals to 120 for the SI datasets recorded in zone 2. Fig. 4.25(b) gives the comparison of the same spectrum of ZL SI with the spectrum of LL SI normalized using the slope between ZLP and plasmon peak (spectrum region used during splicing routine in GMS). To reduce the noise and represent the average shape of curve, the shown spectra are summed over all spatial pixels in each SI.

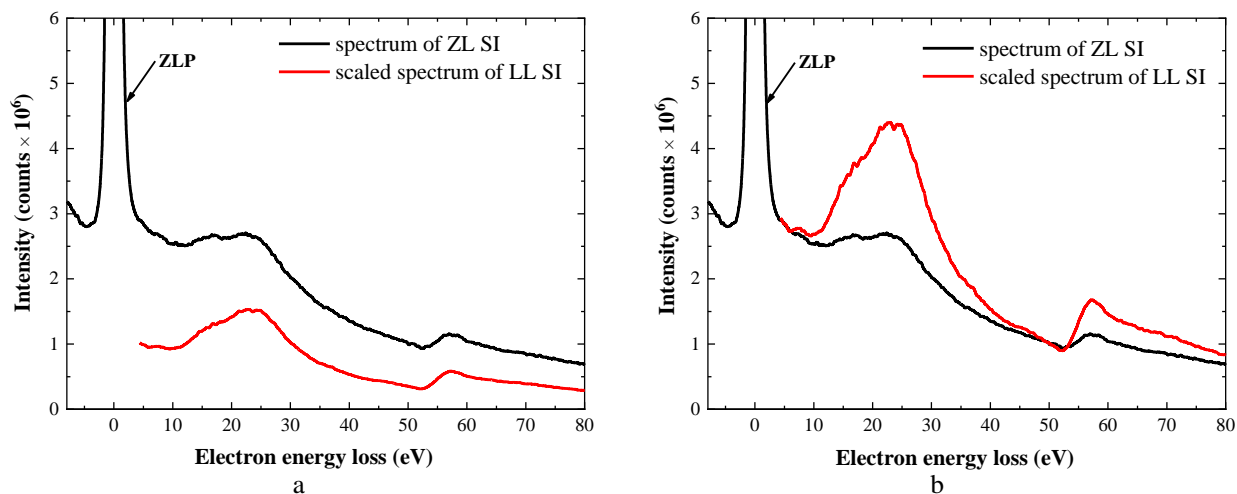


Fig. 4.25. A comparison of the EEL spectrum extracted from ZL SI and the scaled spectrum from LL SI: (a) using time ratio as scaling factor and (b) using the ratio of intensities at the slope between ZLP and plasmon.

The comparison of ZL and LL spectra demonstrates the presence of a spurious background under the ZL spectrum that affects the slope between ZLP and bulk plasmon peak. Therefore, neither the scaling through the time ratio, nor the standard splicing routine in GMS can be applied directly.

The spurious background under the ZL spectrum is a result of multiple backscattering of electrons within the spectrometer detector chamber, not simply from misalignment of the beam trap. This kind of “bleed-through” between the core-loss spectrum and the low-loss spectrum was reported in Refs. [50,65]. The authors of Ref. [50] state that “bleed-through” often affects the low-loss SI containing ZLP in Dual EELS datasets and suggest an empirical procedure of “bleed-through” artifact correction. Following this procedure, the spectra from all spatial pixels in the ZL SI were summed up and the summary spectrum was calibrated to be at an energy range that results in a suitable fit of the power law function at the left side of ZLP. This background represents the average shape of the “bleed-through” contribution. The background was scaled to match the intensity below ZLP and subtracted from ZL SI. A typical spectrum extracted from 100 pixel area in “bleed-through” corrected ZL SI is shown in Fig. 4.26(a). Fig. 4.26(b) compares the same “bleed-through” corrected spectrum of ZL SI with the LL SI spectrum extracted from the same spatial region and scaled by the time ratio 1:120.

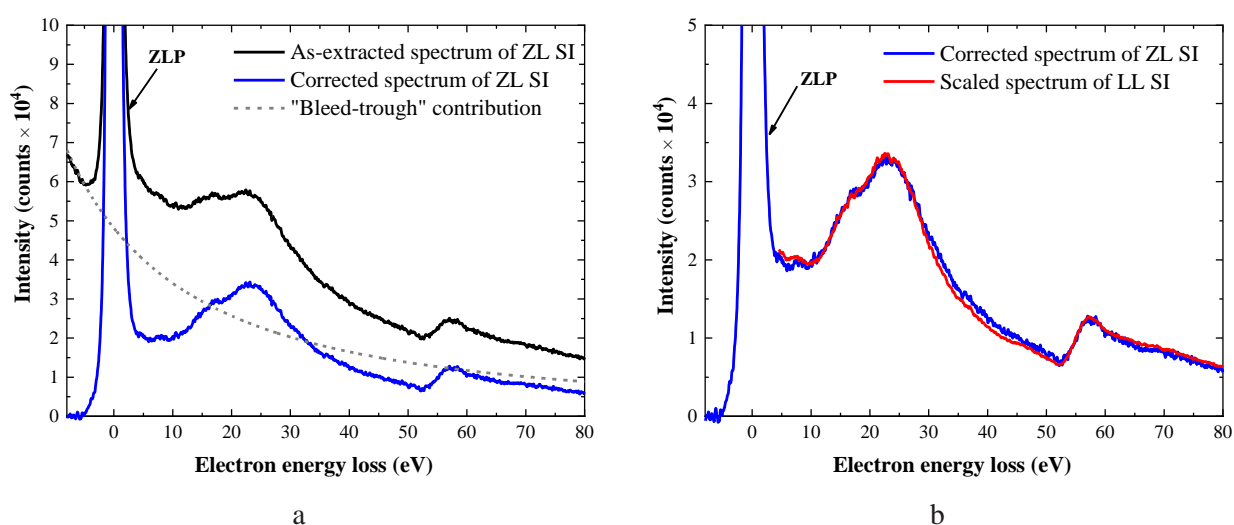


Fig. 4.26. (a) The effect of the “bleed-through” between ZL and LL signals on the ZL spectrum. (b) Comparison of the corrected EEL spectrum from ZL SI and the spectrum from LL SI scaled by the time ratio 1:120.

As can be seen, after the background suppression and LL signal scaling by the time ratio ZL and LL datasets demonstrate excellent match, justifying the applicability of the approach suggested in Ref. [50] to our datasets.

In order to merge the processed ZL and LL SI datasets, the standard splice routine “Spectrum →Splice” in GMS was used with a 20 channel overlap. Once the splicing had been performed, it was possible to deconvolve the effects of plural scattering from the SI using Fourier-log method applying the in-built GMS function “EELS→ Remove the plural scattering → Fourier-log”. Fitted logarithm model was used for ZLP extraction. As a result, a deconvoluted SI dataset was obtained.

Fig. 4.27(a) shows the EEL spectra subtracted from deconvoluted SI of zone 2 using areas in the matrix close to the center of He bubble and at He bubble edge (periphery), as indicated in panel 4.27(c). As already mentioned at the beginning of this section, the EEL spectrum extracted from He bubbles demonstrates two most prominent signals, namely the Fe-Cr bulk plasmon oscillation and Fe- $M_{2,3}$ shell ionization edge. Other possible signals such as SP oscillation, H-K edge, BSP oscillation, He-K, Y- $N_{2,3}$, and Cr- $M_{2,3}$ are weak and located at the shoulders or close to the maximum of Fe-Cr bulk plasmon peak. As suggested in Ref. [66], in order to better recognize weak peaks on EEL spectrum it helps to use the second differential curve of the signal. Such second differential curve obtained from the spectra shown in Fig. 4.27(a) is given in Fig. 4.27(b).

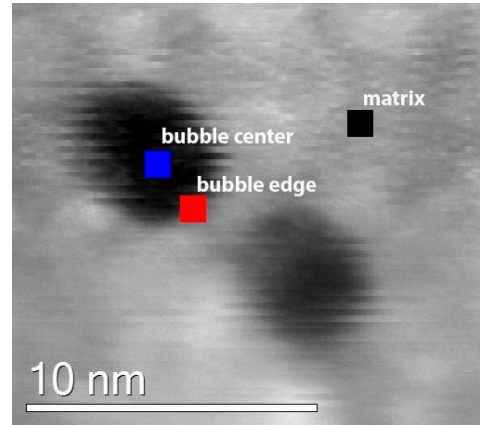
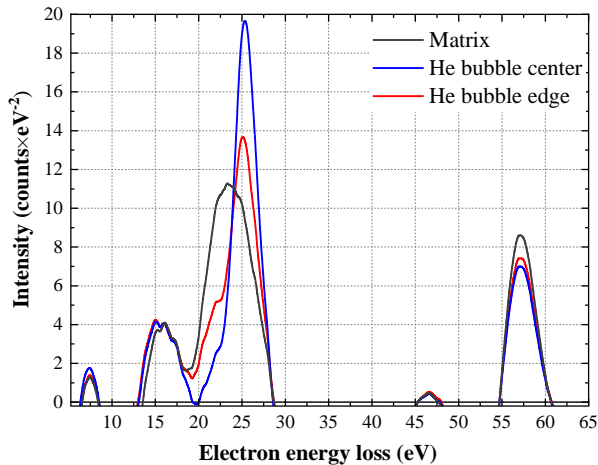
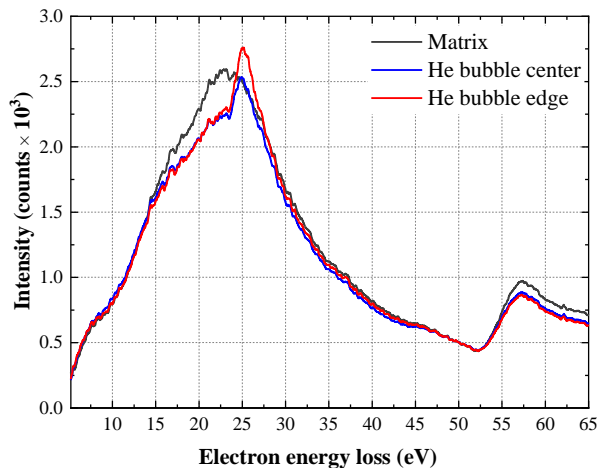


Fig. 4.27. (a) EEL spectra extracted from deconvoluted SI using 3x3 pixel areas in the matrix, close to He bubble center and at the He bubble edge (periphery). (b) The second differential curve of the EEL spectra shown in panel (a). (c) HAADF image of zone 2 showing the regions from which the spectra were extracted.

Judging from the differential curves, the EEL spectra of the matrix and He bubble have 5 and 6 peaks, respectively. In all differential curves, isolated peaks at ~ 57 eV, ~ 47 eV and ~ 7.5 eV represent Fe- $M_{2,3}$, Cr- $M_{2,3}$ and surface oxide/matrix interface signals, respectively. The Y- $N_{2,3}$ is not visible due to the lack of oxide particles. The positions of isolated peaks as well as the peaks widths at the intersection with the abscissa axis are the same for the matrix, He bubble center and He bubble edge differential curves. This indicates that in as-extracted spectra Fe- $M_{2,3}$, Cr $M_{2,3}$ and interfacial surface oxide signals the peak position and full widths at the half maximum (FWHM) are also the same for the matrix, He bubble center and He bubble edge. In addition to these peaks, one can notice in the as-extracted EEL spectra the signatures of two other peaks at ~ 16 eV and at ~ 23.4 - 25 eV (Fig. 4.27(b)). The positions of these peaks and their width at the intersection with the abscissa axis differ for the matrix, He bubble center and He bubble edge differential curves. The matrix curve has only a single peak at ~ 23.4 eV. In the bubble center and at the bubble edge along with peak at ~ 23.4 eV, additional peak appears due to He-K signal with the maximum at ~ 25 eV. The peak at ~ 16 eV corresponds to the left shoulder of Fe-Cr plasmon with superposed signals. The increase of peak width at the lower energy side is visible in both differential curves for the He bubble as compared to the matrix curve. The observed change indicates the shift of complex peak ~ 16 eV in as-extracted He bubble EEL spectra and suggests the existence of an additional signal at the lower energy range. Since SP is represented by an isolated peak at ~ 7.5 eV and BSP energy is estimated to fall in the window 16.6 - 19.1 eV, the H-K signal ~ 13 eV remains the most probable reason for the detected changes at the left shoulder of Fe-Cr plasmon.

To obtain spectral difference SI with only the bubble signature, the scaling of matrix and bubble signals to account for thickness differences should be performed prior to the subtraction of matrix contribution from bubble spectra. Different energy windows for such scaling have been proposed in the literature. In particular, the normalization of matrix to bubble signal was performed in Ref. [63] in a ~ 6 eV wide window at the Fe-Cr plasmon pre-edge in order to extract the He-K edge intensity from bubbles in ODS-steel, whereas the normalization of signals at the high energy shoulder of Zr-N_{2,3} edge was used to extract He-K and H-K peak intensity from bubbles in Zr alloy [61]. However, the scaling approaches suggested in the literature are not applicable for our dataset. Signals of H-K and BSP (Fig. 4.27(a)) are not directly recognizable in the spectra as-extracted from He bubble, while the He-K signal is clearly visible as semi-isolated sub-peak at the top of Fe-Cr bulk plasmon. Having in mind that He concentration in Fe-Cr matrix is below the detection limit (~ 0.5 at.%), one can expect that the subtraction of scaled matrix contribution from bubble spectrum does not decrease the intensity of He-K edge. From the comparison of matrix and bubble spectra it is obvious that scaling at either Fe-Cr plasmon pre-edge or at the high energy shoulder of Fe-M_{2,3} edge will result in the overestimation of matrix intensity at the maximum of Fe-Cr bulk plasmon peak and in corresponding underestimation of He-K edge intensity. Taking into account the positions, shape and intensity of He-K and Fe-Cr plasmon peaks in our in case, we have selected the scaling windows of 20-22 eV.

Figs. 4.28(a) and 4.28(b) compare EEL spectra at bubble center and bubble edge, both scaled to account for thickness differences, with the spectrum of the matrix, while Fig. 4.28(c) compares the resulting spectral differences at bubble center and bubble edge positions.

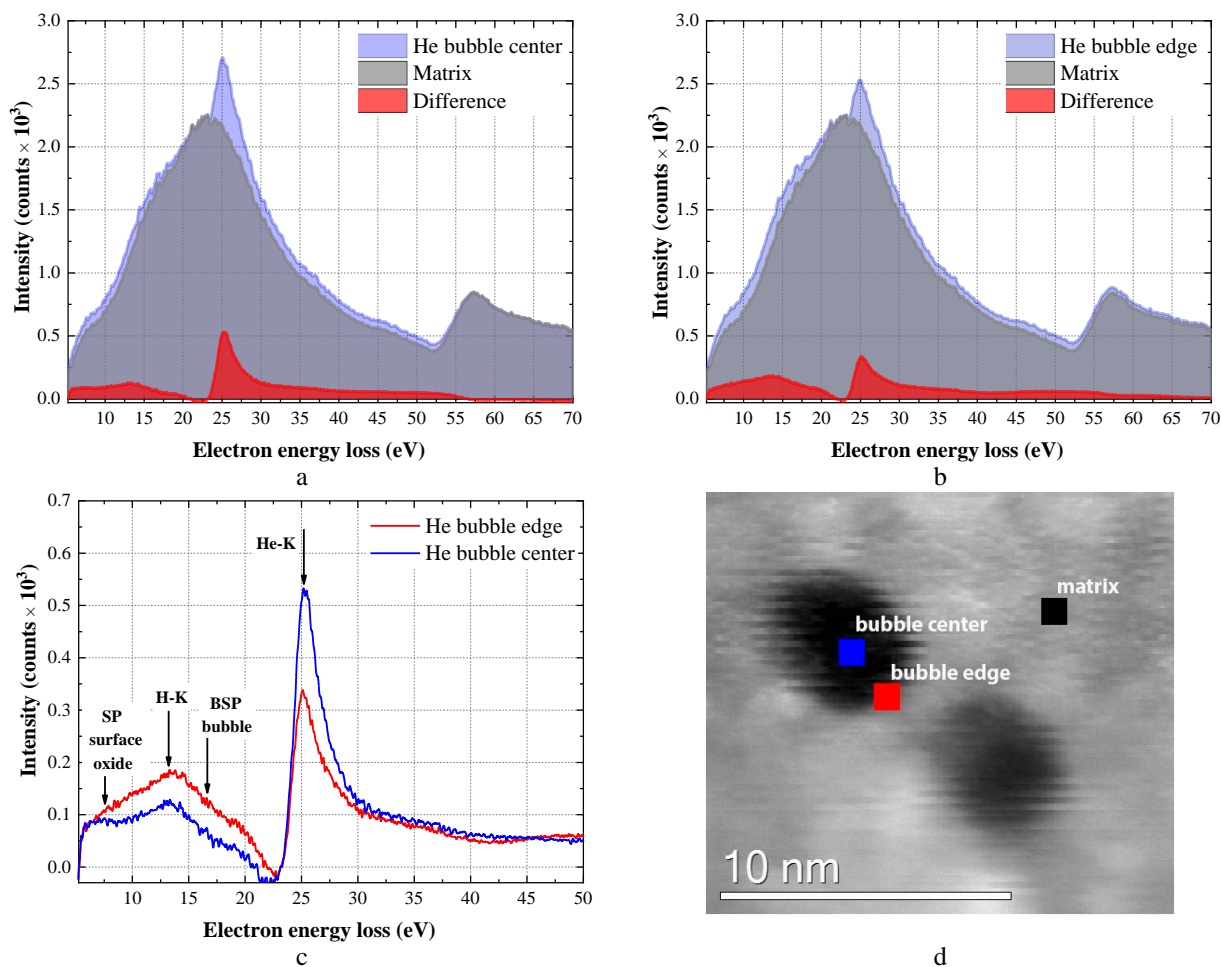


Fig. 4.28. (a,b) EEL spectra subtracted from deconvoluted SI using 3×3 pixel areas and scaled to account for thickness differences: (a) close to He bubble center vs. the matrix; (b) close to He bubble edge vs. the matrix; (c) comparison of spectral differences in bubble center and bubble edge areas; (d) HAADF image of zone 2 showing the regions from which the spectra were extracted. He K-edge at ~ 25 eV and wide peak with a maximum at ~ 13.2 eV which is a result of superposed BSP (~ 16.6 eV-19.1), H-K edge (~ 13 eV) and SP (~ 7.5 eV) signals.

The spectral differences shown in Fig. 4.28(c) include a sharp peak at ~25 eV that can be unequivocally identified as He K-shell ionization edge, despite the fact that this energy does not exactly match the 1s→2p energy transition of 21.2 eV for atomic He. It is known that He-K peak shifts towards higher energies because He confined in bubbles is not in the state of a dilute gas. The shift of the He 1s→2p transition with respect to the free He atom value, known as “blue shift”, has been reported on many occasions in the literature, not only for steels [10,58,59], but also e.g. for Pd [67], Zr [61], Be [60], and Si [55,68]. The observed He-K peak energy of ~25 eV is slightly higher than that reported earlier for ferritic-martensitic steels [10,59]. This might be due to the higher He density in bubbles as a consequence of high He⁺ implantation fluence used in this study.

One more peak arises in the spectral difference curve at the left shoulder of Fe-Cr bulk plasmon. This spectral signature with an apparent maximum at ~13.2 eV is broad and has lower intensity than He-K edge signal. The peak position is close to that reported for the H-K shell ionization edge of ~12.5-13.5 eV ([10,48,60,61,66,69]). The morphology of this spectral signature is different from relatively sharp H-K signal typically reported for H-K ionization edge [10,60,66,69] but agrees well with that reported for H-K signal associated with He bubbles in Zr alloy [61]. As specified in the beginning of this section, two signals at ~7.5 eV (SP) and within ~16.6-19.1 eV (BSP) are located in close proximity of H-K at the left shoulder of Fe-Cr bulk plasmon. Since the spectral signature with the maximum at ~13.2 eV is wide and asymmetric, it is reasonable to assume that it results from superposition of H-K signal with SP and BSP signals. Comparison of spectral differences for bubble center and bubble periphery shows that the intensity of the signal at 13.2 eV is slightly higher at the bubble periphery, whereas the intensity of He-K signal is higher close to the bubble center.

At this junction, it was possible to estimate and subtract the matrix contribution from the entire deconvolved SI, producing a final extracted SI with spectral difference information from bubbles only. First of all, the spectra from 900 spatial pixels in the matrix area were summed up and divided by the number of pixels; this signal was assumed to represent the average shape of matrix contribution at each pixel. Then the spectrum at each spatial pixel was scaled to match the intensity in the 20-22 eV energy window (prior to the Fe-Cr bulk plasmon peak) and subtracted using the GMS plugin SI tools “SI tools →Substract spectrum”.

To gain insight into He-K, H-K, SP, and BSP signal spatial distribution, the areas under spectral difference curve were then determined for entire SI by simple window integration on pixel-to-pixel basis between 6-10 eV, 11-15 eV, 16-20 eV and 22.5-26.5 eV for SP, H-K, BSP and He-K signals, respectively. The intensity maps integrated over 4 eV energy range for each signal are shown in Fig. 4.29.

The signal at the energy range of SP ~7.2 eV is uniformly spatially distributed over the bubble location area. Most probably, it is due to lower matrix thickness in the bubble area which enhances the relative intensity of oxide interfacial effects. The signal in the energy range of BSP ~16.6-19.1 eV is distributed throughout the entire bubble with pronounced rings of increases intensity at the bubble periphery. A similar intensity distribution is demonstrated by the signal in the H-K energy window, though the increase of intensity at the periphery of bubbles is less pronounced than for BSP signal. The He-K signal at ~25 eV is mostly uniformly distributed in the bubble interior. The area of increased He-K signal intensity is smaller and situated closer to bubble center as compared to possible BSP and H-K signals. A non-vanishing signal intensity in the matrix is visible in all maps. Moreover, the BSP signal which should be associated mainly with bubbles periphery (at glancing incidence) appears with lower intensity also in the areas close to bubble centers. This implies that we deal with a superimposed signal that could not be properly deconvoluted by application of spectral difference method only.

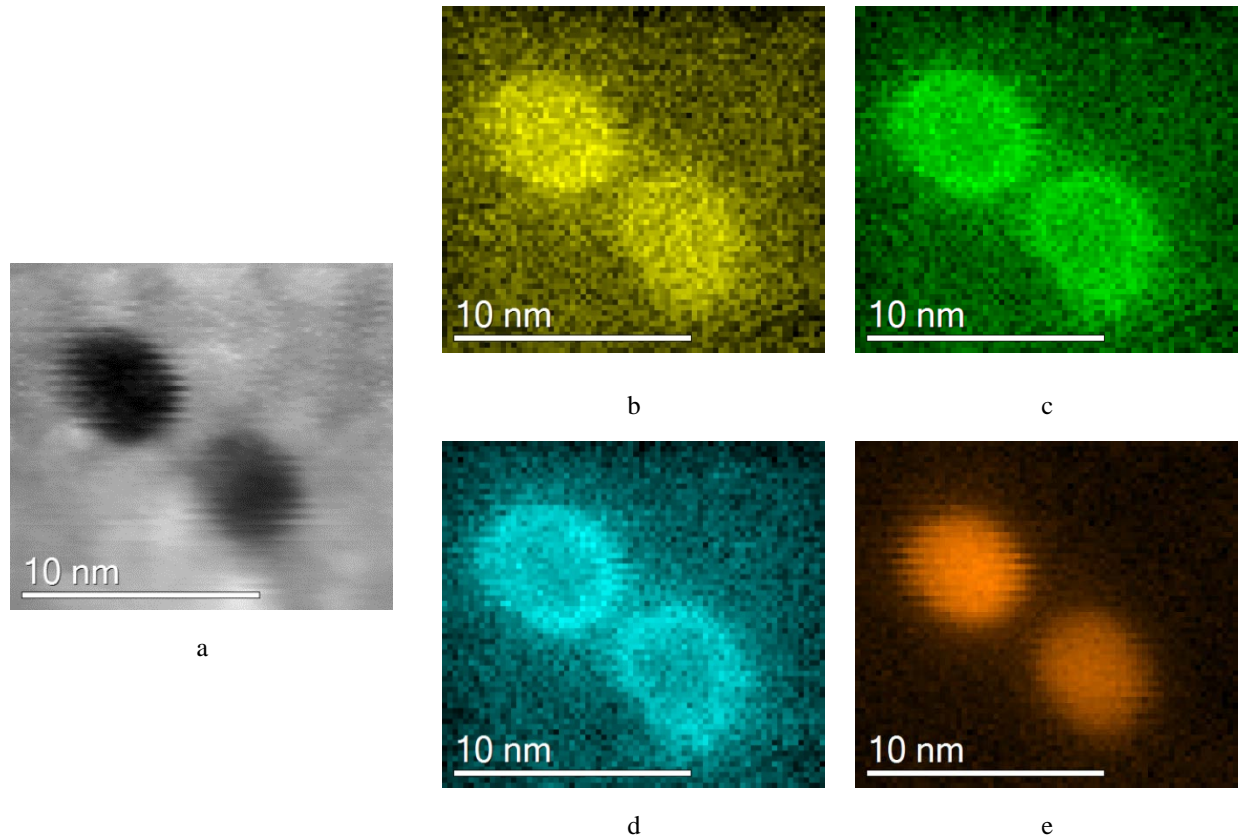


Fig. 4.29. (a) HAADF image of zone 2. Intensity maps of components identified in spectral difference SI of zone 2 generated by application of 4 eV integration windows: (b) 6-10eV (SP from surface oxide); (c) 11-15 eV (H-K); (d) ~16-20 eV (BSP from bubble); (e) ~22.5-26.5 eV (He-K).

As shown in Fig. 4.28(c), the cumulative peak at ~13.2 eV that represents possible superposition of SP, H-K and BSP signals is broad and asymmetric. In order to verify the possible association of H-K with He bubbles it is necessary to properly differentiate between H-K and BSP contributions, which is a challenging task considering similar energy and spatial distribution of possible H-K and BSP signals. To obtain a clear intensity map of each signal it is helpful to fit the spectrum difference SI with a predefined model. The shape of the broad peak at ~13.2 eV in Fig. 4.28(c) suggests that it can be adjusted by a superposition of at least three Gaussians. As a zero order approximation it can be assumed that these Gaussians are centered on the known peak positions of SP, H-K and BSP signals, while He-K edge might be temporarily omitted and fitted separately later on. To obtain suitable parameters for the model, EEL spectra extracted with 3×3 pixels from the bubble central area and bubble periphery were first fitted in Origin Pro 2018 software in the energy range from 5 to 21 eV and then applied as an initial guess for fitting the entire SI spectrum difference with the help of GMS.

A crucial point for the fitting is the selection of the Gaussian position for BSP because in the case of bubbles with high density of helium it can be red-shifted (i.e. to lower frequencies) with respect to the range of 16.6-19.1 eV estimated within the classical Drude model approximation for an empty sphere in metal [70] and thus there is a risk to mistakenly interpret it as H-K contribution. Therefore, prior to curve fitting, it makes sense to discuss the possible reasons of BSP signal shifts and to estimate corresponding shift values.

For a sharp-surface spherical void surrounded by a metal matrix modelled with the Drude dielectric function, the classical dispersion relation for the frequency ω_l of the l -th surface plasmon mode is [70]

$$\omega_l = \frac{\omega_p}{\sqrt{(2l+1)/(l+1)}}, \quad (4.2)$$

where ω_p and l are the bulk plasmon frequency and the angular momentum quantum number (mode polarity), respectively.

With the experimental Fe-Cr bulk plasmon energy of 23.4 eV, the energy of a void surface plasmon can vary from $E_{l=1}=19.1$ eV for dipolar mode to $E_{l=\infty}=16.6$ eV for the infinite order mode. In the classical treatment, the energies (frequencies) of the excited surface plasmon modes with different polarities (l) are insensitive to the void radius and the equation (4.2) is the model-independent large void limit for all non-retarded dispersion relation calculations.

There exist also a number of more sophisticated semi-classical and quantum mechanical approaches to describe the properties of surface plasmon oscillations near voids and bubbles, such as a hydrodynamical model [71,72], fluid dynamical approach with variational scheme [73,74], density functional theory in a local density approximation [75] and a sum-rule-based method [76].

Calculations with a semi-classical hydrodynamic model [71] predict that the structure of EEL spectrum in the region of plasmon excitations depends notably on the size of the void. For each l -mode there is a minimum void radius which can withstand the induced polarization charge because positive and negative charges in strong Coulomb interaction cannot be separated by less than a certain limit. Estimates according to [71,76] show that for a typical bubble radius of 2.5 nm in our dataset, surface plasmon modes with polarities from $l=2$ to $l=29-35$ can be excited. However, the excitation probability of modes with different polarity varies significantly. According to [71], the void radius affects the excitation probability of plasmonic modes so that the polarity of the mode dominating in the energy absorption increases with the increase of void radius. For voids with relatively small radii (e.g. $R \leq 10$ nm in Al) most of the energy is lost in the excitation of the dipolar ($l=1$) mode. Since bulk plasmon oscillation frequency for Al is lower than for Fe-Cr alloy, the void radius for which the dipole mode dominates in the energy absorption is roughly estimated to be ≤ 6 nm in Fe-Cr alloy. Hence, in our case, where bubble radius doesn't exceed ~ 2.5 nm, the impact of BSP modes with $l > 1$ to the EELS signal should be negligible. Indeed, the dipolar mode excitation at ~ 19.1 eV is a proper candidate to describe the right-hand part of signal ($\sim 16-20$ eV) in the experimental EELS signals (blue and red curves in Fig. 4.28(c)). Even if we have overestimated the upper void radius required for the dipole mode domination and modes with higher polarity would provide some contribution to cumulative BSP signal, the peak at ~ 13.2 eV (central part of the experimental peak in the window $\sim 11-15$ eV) remains still too low in energy to be associated with the BSP contribution from high mode excitation at ~ 16.6 eV.

When void radius falls below 1 nm, semi-classical [71–74] and quantum mechanical [75,76] calculations predict the “blue-shift” of surface plasmon energy relative to the classical case. Both semi-classical and quantum mechanical calculations provide qualitatively similar result but the magnitude of the calculated “blue-shift” varies in different approaches. The “blue-shift” of surface plasmon energy was indeed demonstrated for Ag nanoparticles and found to be ~ 0.5 eV as the particle radius decreased from 10 nm to below 1 nm [77]. However, to the best of our knowledge, no experimental data has been published so far for the inverse problem of isolated void in metal matrix. According to calculation in Ref. [76], an approximate upper bound for surface plasmon frequency obtained using a step electronic density is

$$\omega_l = \sqrt{\frac{2}{3}(l+2)(2l+1)\frac{\beta_F^2}{R^2} + \omega_p^2 \frac{l+1}{2l+1}}, \quad (4.3)$$

where $\beta_F = \sqrt{\frac{3}{5}}V_F$, V_F is the Fermi velocity, R - the void radius, and ω_p and l have the same meaning as in equation (4.2).

With $R = 2.5$ nm in our experimental dataset and assuming no gas inside the cavity, the “blue-shift” for dipolar mode calculated through equation (4.3) is ~ 0.03 eV with respect to the classical case (19.1 eV). For the modes with high polarity “blue-shift” becomes more pronounced (up to 1.22 eV for $l=35$), so that energy positions corresponding to modes with high polarity tend to be located even higher

than the dipolar mode. Summing up, theoretical predictions concerning the excitation probability and “blue shift” of surface plasmon signal for a void along with the experimental shape of EEL spectrum imply that for our experimental dataset it is sufficient to consider only dipolar mode contribution to BSP signal. Hence, the subsequent analysis deals with the dipolar excitation mode only.

As can be seen in Fig. 4.29(a), zone 2 contains two He bubbles that can electromagnetically interact if the separation between them is smaller than the critical decay length of the electric field [70,78–80]. Coupling of individual bubbles might lead to hybridization of plasmonic modes with subsequent shifts of individual component plasmon frequencies [70]. It was predicted for a pair of particles [81]/voids [79,80] and experimentally demonstrated for particles that hybridization of modes with $l > 1$ gives rise to two energy split modes: the lower energy antisymmetric or “bonding” plasmon and the higher energy symmetric or “antibonding” plasmon. If both voids have the same radius, R , the dispersion relation for the energy split dipole modes ($l = 1$) can be expressed in terms of the ratio R/D , where D is the distance between void centers, as [79]

$$\omega_{+/-} = \omega_p \sqrt{\frac{2}{3} \left(1 \pm \frac{R^3}{D^3}\right)}, \text{ for the polar momentum number } m=0 \quad (4.4)$$

and

$$\omega_{+/-} = \omega_p \sqrt{\frac{2}{3} \left(1 \pm \frac{R^3}{2D^3}\right)}, \text{ for the polar momentum number } m = \pm 1, \quad (4.5)$$

where only the terms up to the third order in R/D are retained.

The bubble radii in our case can be directly measured on HAADF images with an error less than ~10%. However, the distance between bubble centers D is uncertain due to unknown depth location of bubble centers with respect to TEM film surface. So we consider two limiting cases, either where bubbles are located at the same depth or where bubbles are located just under two opposite surfaces. In the first case, the distance between bubbles is $D = 7.3$ nm, which gives the energy shift $\Delta E_{\max} = \pm 0.39$ eV for $l=1$ and $m=0$. In the second case the distance is $D = 12.4$ nm and the energy shift is $\Delta E_{\min} = \pm 0.08$ eV. In other words, in our experimental conditions the estimated shifts of split modes are minor and result in the broadening of cumulative BSP signal rather than in visible shifts to lower and higher energy with respect to the energy for an individual bubble. Thus, the dipole interaction between the bubbles should not affect significantly the BSP energy position and can be neglected in the case of our dataset.

Thus, assuming empty bubble as one of the limiting cases, the BSP signal from bubbles with the radius of ~2.5 nm is dominated by the dipole mode and the “blue-shift” of the signal for the dominant dipole mode is negligible, being lower than the accuracy of our measurements. The account of high polarity modes and hybridization effects in our study can only broaden cumulative BSP signal at the dipole mode excitation energy range but does not decrease its energy and does not lead to strong overlapping of BSP contribution with H-K signal. Hence, there seems to be no reasons for the “red-shift” of BSP signal with respect to the classical case for an individual bubble.

Finally, let us consider the BSP shift related to the presence of helium inside the bubbles, so that the dielectric constant ε of the medium inside the bubbles differs from unity. In our case the size and hybridization effects on the BSP energy (frequency) are moderate and so the frequency of BSP mode for an isolated bubble filled with helium might be estimated according to the semi-classical Natta equation as

$$\omega_l = \omega_p \sqrt{\frac{l+1}{l(\varepsilon_{He} + 1)} + 1}, \quad (4.6)$$

where $\varepsilon_{He}(\omega)$ is the frequency dependent dielectric constant of dense He gas that can be calculated using the Clausius-Mossotti formula [82]

$$\varepsilon_{He}(\omega) = 1 + \frac{4\pi n\alpha(\omega)}{1 - (4\pi n\alpha(\omega)/3)}, \quad (4.7)$$

n is the gas concentration inside the bubble, and $\alpha(\omega)$ - the frequency dependent electronic polarizability of medium in the bubble. The latter can be approximated by Lorentz ansatz [56]

$$\alpha(\omega) = \frac{\alpha_0 \omega_0^2}{(\omega_0^2 - \omega^2 - i\gamma\omega)}, \quad (4.8)$$

where α_0 is the atomic electronic polarizability of He and the He resonance at $h\omega = 21.23$ eV is damped by a constant γ . Damping was neglected for the present evaluation. In the case of He-filled bubbles α_0 is pressure-dependent [56,75]. The upper limit of α_0 was estimated in the same way as in Ref. [56]. Helium density n used for the estimation of α_0 and $\varepsilon_{He}(\omega)$ was calculated using the He-K “blue shift” value according to the Ref. [59] as:

$$n = \frac{\Delta E - 0.39}{0.036}. \quad (4.9)$$

In our dataset, the experimental value of He-K “blue shift” is $\Delta E = 3.7$ eV and the corresponding He density calculated using (4.9) is 94 at/nm^3 . Using equation (4.7) we obtain the frequency-dependent dielectric constant $\varepsilon_{He}(\omega_1) = 1.68$ for the dipole BSP mode. Finally, the position of BSP for a bubble filled with 94 at/nm^3 of helium is calculated to be at 17.3 eV. As can be seen, the presence of He inside the bubble results in the red shift of the BSP frequency indeed. However, even considering this energy shift, the BSP peak position remains well above the low-energy peak maximum visible in Fig. 4.28(c).

Let us revert now to the fitting of the EEL spectra extracted from spectral difference SI in the bubble central area and at the bubble periphery, as shown in Fig. 4.28(c). First of all, the low-energy peak maximum visible in Fig. 4.28(a) was fitted using Origin Pro 2018. Fig. 4.30(a) shows the three Gaussian fitting of the data with the BSP peak position fixed at ~ 19.1 eV. The cumulative fit obtained through the superposition of SP, H-K and BSP signals matches the experimental signal perfectly. The SP signals at ~ 7.2 eV have the same intensity in spectra extracted from areas close to the bubble center and bubble periphery, whereas the intensities of H-K peak at ~ 13.5 eV and BSP peak at ~ 19.1 eV are higher for the spectrum obtained at the bubble periphery.

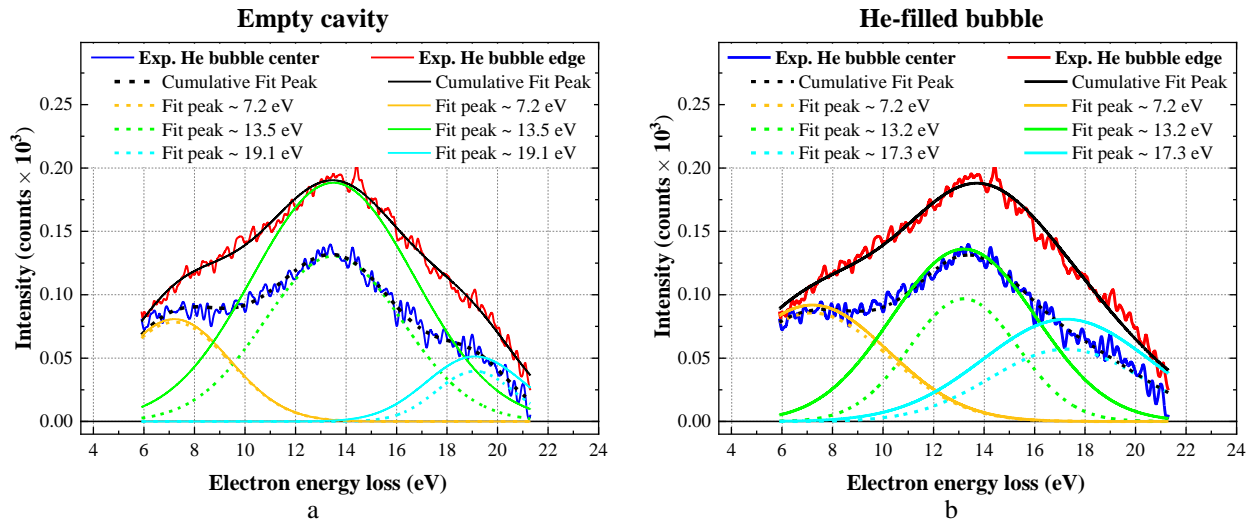


Fig. 4.30. Curve fitting of the superposed signals at the left shoulder of Fe-Cr bulk plasmon extracted from 3×3 pixel areas at bubble center and bubble periphery in spectral difference SI of zone 2. Fit peaks at ~ 7.2 eV, and 13.2 - 13.5 eV represent SP and H-K signals, respectively. (a) BSP peak position at 19.1 eV, as estimated for an empty cavity; (b) BSP peak position at 17.3 eV, as for a He-filled bubble with He density 94 at/nm^3 . The color model of the fit corresponds to that applied in Fig. 4.29.

Fig. 4.30(b) shows fitting of the same experimental EEL spectra, assuming that BSP peak is located at ~ 17.3 eV. The shift of BSP energy position from 19.1 to 17.3 eV does not lead to qualitative

changes: the SP peak at ~ 7.2 eV demonstrates the same intensity close to the bubble center and bubble periphery, while the intensities of H-K peak at ~ 13.2 eV and BSP peak at ~ 17.3 eV are higher at bubble periphery. However, the relative intensities are slightly different. Contribution of BSP signal is higher and that of H-K is lower when BSP signal is fitted using the 17.3 eV energy position (filled bubble). Calculation of He density through the “blue-shift” might provide the overestimation [58,59], hence the values of frequency-dependent dielectric constant and BSP energy might be slightly overestimated as well. Therefore, the exact BSP energy position is expected somewhere between the energy calculated for empty and He-filled cavities. For further evaluation we use both BSP energies of 19.1 and 17.3 eV as two limiting cases.

Using the Gaussian parameters obtained during the fitting of single EEL spectrum in Origin Pro, two fitting models with BSP positions at 19.1 and 17.3 eV were build using non-linear least squares (NLLS) fitting routine in GMS. The fitting model included four Gaussians to describe the signals of SP (at 7.2 eV), H-K (at 13.2 or 13.5 eV), BSP (at 17.3 or 19.1 eV), and He-K ($1s \rightarrow 2p$) at ~ 25 eV. The rest of the signal at the right hand side of He-K might be associated with He $1s \rightarrow 3p$ transition as reported in Ref. [60]. However, in our case this signal is represented by quite smooth tail up ~ 40 eV rather than a peak. Hence it was treated as a background arising from non-ideal matrix subtraction and was fitted with a shaped step function as implemented in GMS. Examples of single EEL spectrum fits using GMS are provided in Fig. 4.31(a-d).

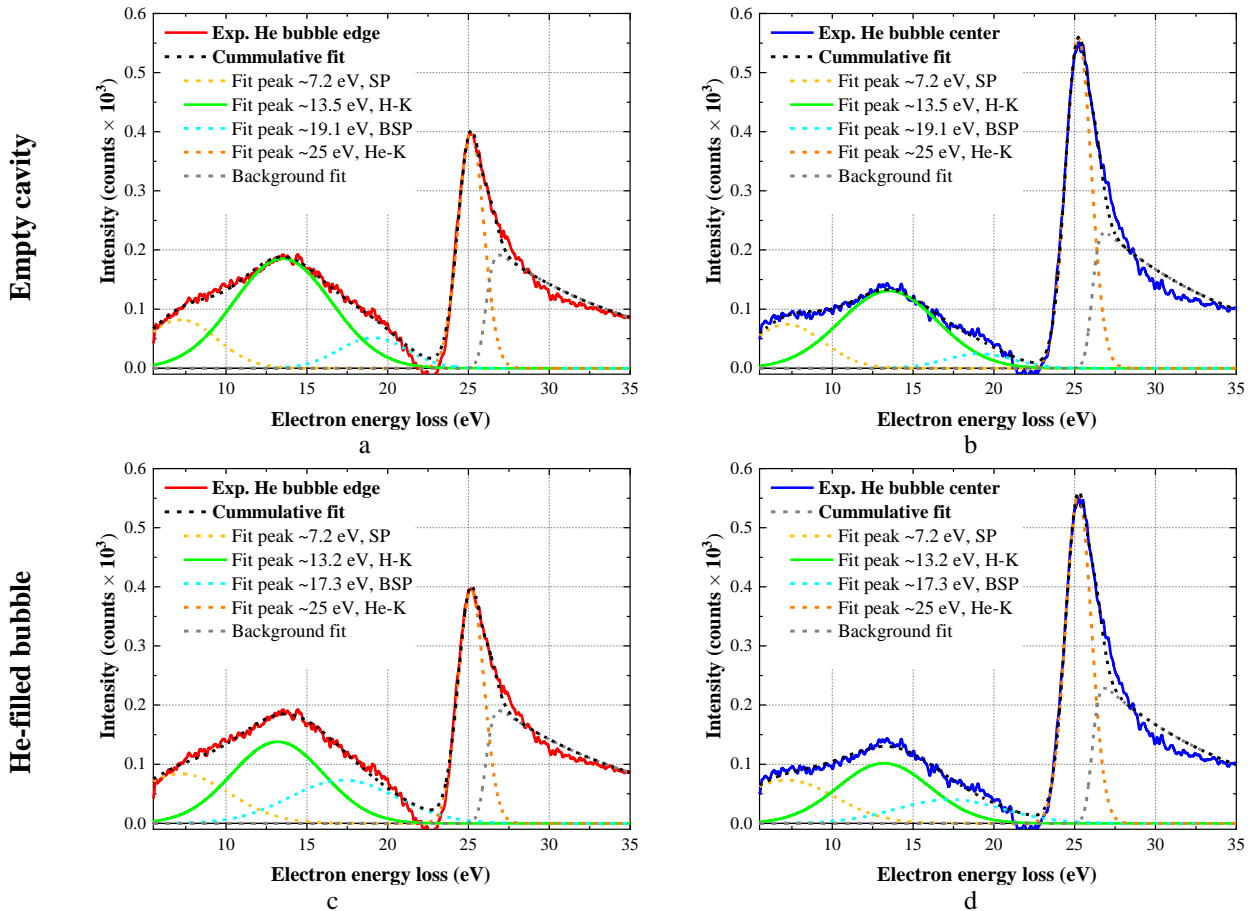


Fig. 4.31. Curve fitting using NLLS fitting GMS routine of the superposed signals extracted from 3×3 pixel areas at bubble center and bubble periphery in spectral difference SI of zone 2. Fit peaks at ~ 7.2 , 13.2-13.5, 17.3-19.1 and 25 eV represent SP, H-K, BSP and He-K signals, respectively. (a) Bubble periphery, BSP energy $l=1$ estimated for empty bubble; (b) bubble center, BSP energy $l=1$ estimated for empty bubble; (c) bubble periphery, BSP energy $l=1$ estimated for bubble filled with He density 94 at./nm^3 ; (d) bubble center, BSP energy $l=1$ estimated for bubble filled with He density 94 at./nm^3 .

The constructed fit models were applied to the entire spectral difference SI of zone 2. Figs. 4.32 and 4.33 provide the resulting maps of SP, BSP, H-K and He-K signal intensity using the models with BSP positions at 19.1 (empty bubble) and 17.3 eV (filled bubble), respectively. The maps are generated by simple integration of individual Gaussian fits in their entire energy range. The color model for signal maps corresponds to that in Figs. 4.30-4.31.

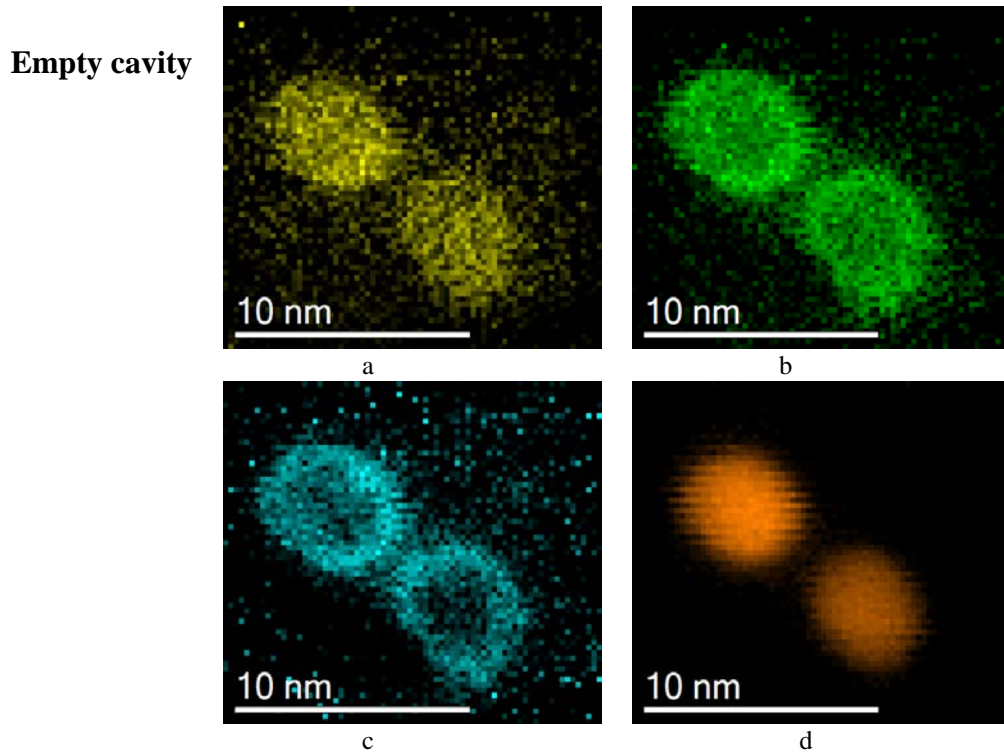


Fig. 4.32. Intensity maps obtained by NLLS Gaussian fitting of components identified in spectral difference SI of zone 2: (a) ~ 7.2 eV (SP of surface oxide interface); (b) ~ 13.5 eV (H-K); (c) ~ 19.1 eV (BSP of empty bubble); (d) ~ 25 eV (He-K).

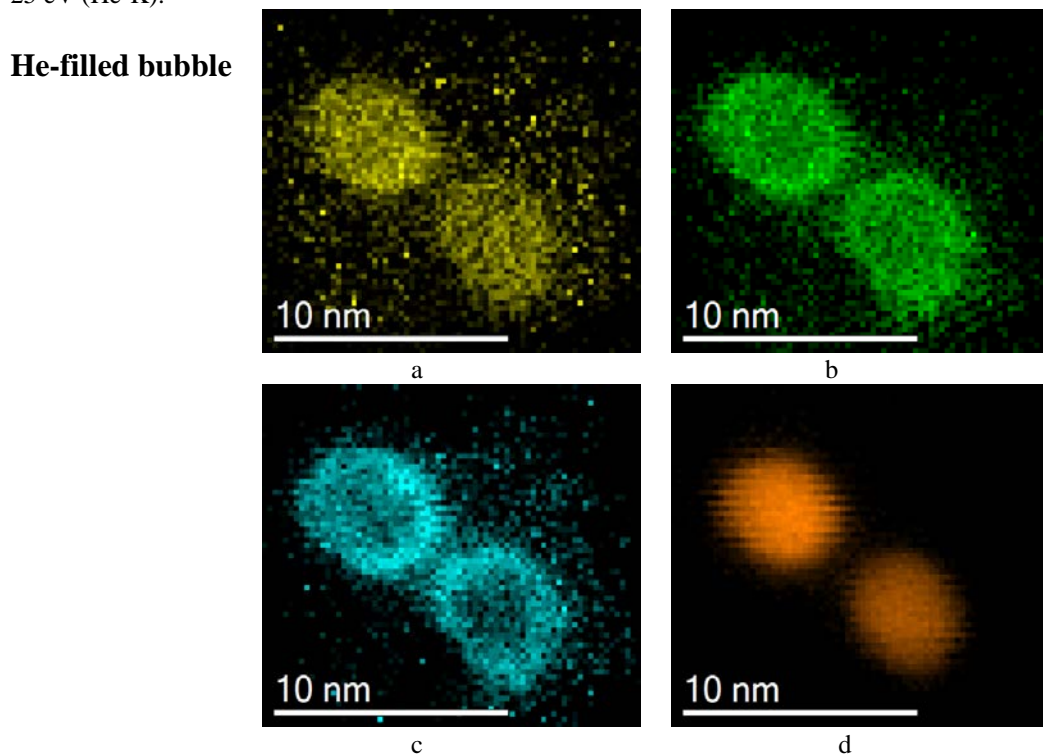


Fig. 4.33. Intensity maps obtained by NLLS Gaussian fitting of components identified in spectral difference SI of zone 2: (a) ~ 7.2 eV (SP of surface oxide interface); (b) ~ 13.2 eV (H-K); (c) ~ 17.3 eV (BSP of filled bubble); (d) ~ 25 eV (He-K).

Whatever BSP position used for the fitting, visual comparison of signal maps evidences the same spatial intensity distribution of all signals. Some minor spots of artificial intensity are present outside the bubble regions in SP, BSP and H-K signal maps, which appear probably because the FWHMs of Gaussians used for the fitting of SP, BSP and H-K signals were broader than they should be. This Gaussian broadening might be a consequence of amorphous carbon contamination which is not considered in the applied fitting model. The SP signal from surface oxide at 7.2 eV is visible over the entire area of both bubbles, possibly because the lower matrix thickness in the bubbles area enhances the intensity of oxide interfacial effects. In contrast to Fig. 4.29(d), BSP signal is visible as rings at the peripheries of bubbles. H-K signal is clearly presented at both central and peripheral areas of bubbles. Thus, the applied curve fitting routine allows to spatially separate contribution from BSP and H-K signals.

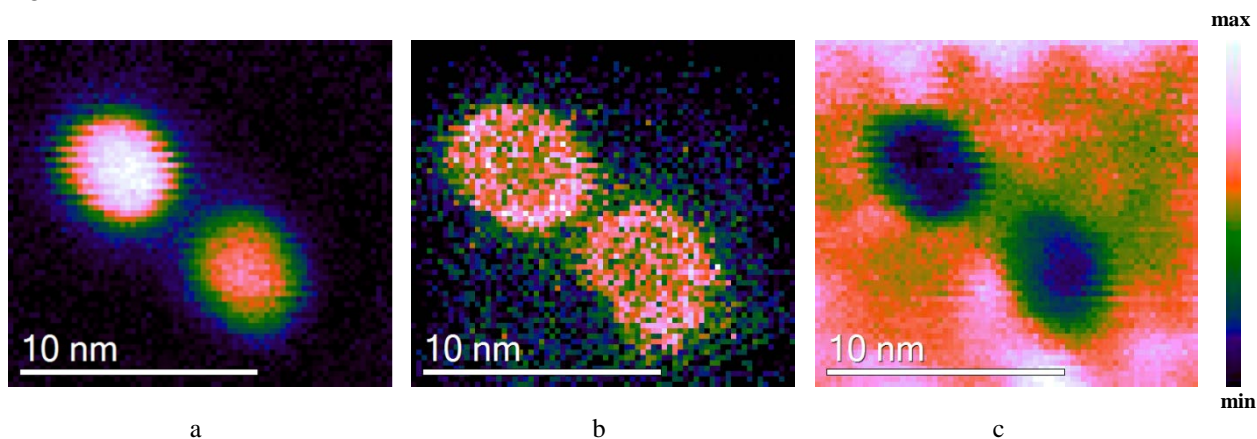


Fig. 4.34. Intensity maps obtained by NLLS Gaussian fitting from spectral difference SI of zone 2: (a) ~25 eV (He-K); (b) ~13.2 eV H-K; (c) thickness map. For better visibility, the target H-K and He-K maps for the fitting results with BSP position of filled bubble are presented using color model different from that in Figs. 4.32-4.33.

As it can be seen in Figs. 4.32(b, d) and 4.33(b, d), both helium and hydrogen are present over the entire bubble areas. However, the intensity of He-K and H-K signals differs between the central part of the bubble and the bubble periphery (Fig. 4.34(a, b)). Helium signal clearly has the maximum of intensity at the bubble centers. The spatial helium distribution reflects the variation of bubble thickness: the maximum of He-K intensity corresponds to the largest bubble thickness region and, respectively, to the highest measured gas volume. In contrast, hydrogen signal is mostly uniformly distributed and demonstrates intensity increase only at the bubble periphery, not following the variation of bubble thickness. So, one can conclude that hydrogen in helium bubbles is not in the form of molecular gas. The observed signal distribution is more consistent with either the absorption of hydrogen at bubble walls or hydrogen trapping in a close vicinity of helium bubbles.

4.3.3 Discussion and conclusions

The results of EELS-SI analysis suggest that the hydrogen trapping by He bubbles most probably occurs at bubble walls. Even the presence of H-K signal at the centers of bubbles in Fig. 4.34 does not contradict to this conclusion because it can be due to hydrogen captured at the top and bottom bubble surfaces. The results of TDS analysis (sections 4.2.2.3-4.2.2.3) strongly support this interpretation. Based on helium and hydrogen spatial distribution observed by EELS-SI method in conjunction with TDS results and literature data, the spatial distribution of gas atoms in the bubbles can be interpreted in terms of a “core-shell” structure, where the core of helium is surrounded by a shell of hydrogen atoms. This picture is in a good agreement with the density functional theory calculations for helium bubbles in iron reported in Ref. [83] which indicates that hydrogen is attracted to He bubble walls and forms a shell around the bubbles.

Similar results concerning helium and hydrogen distribution in helium bubbles were reported for neutron irradiated beryllium [60] and ion irradiated zirconium [61]. The presence of hydrogen inside bubbles and its absorption on bubble walls were demonstrated by EELS-SI analysis in flat hexagonal bubbles with ~100 nm diameter formed on basal planes of beryllium under neutron irradiation. The reported H-K signal was remarkably stronger than in our case, most probably due to notably larger bubble size. The authors of Ref. [60] postulated the presence of hydrogen inside bubbles. The intensity increase of H-K signal on bubbles walls was interpreted as either preferential absorption of hydrogen or the formation of Be hydride at the bubble walls, coupled with surface plasmon contribution.

In Ref. [61] hydrogen association with spherical faceted He bubbles 7–10 nm in size was reported for Zircaloy-4. The intensity and shape of detected H-K signal at ~13.5 eV was similar to that detected in our study. However, the signal intensity was distributed mainly as a halo around the periphery of the bubbles, similar to the pattern observed in our raw data treatment (Figs. 4.21(i) and 4.22(g)). As it has been pointed out above, such data without thorough analysis cannot be considered as a reliable evidence of hydrogen trapping at the bubble walls because bubble surface plasmon produces a similar signal in a very close energy range. For example, a similar intensity pattern at ~12.3–13.3 eV around helium bubbles in silicon was attributed in Ref. [55] to bubble plasmon oscillations. However, in opinion of the authors of Ref. [61], the contribution from hydrogen covering bubble walls cannot be excluded even in this case because it is difficult to produce silicon samples without hydrogen and the empty bubbles in silicon which are expected to yield a surface plasmon had no associated halo in the energy range of ~12.3–13.3 eV [68]. Eventually, hydrogen adsorption on bubble surface and Zr-H bond formation as a possible mechanism of hydrogen trapping by helium bubbles were justified in Ref. [61] by supplementing conventional EELS with Ultra-High-Resolution (UHR) EELS (vibrational spectroscopy).

It should be mentioned that a reliable differentiation between H-K and bubble surface plasmon (BSP) peaks in beryllium, zirconium and silicon is challenging because the bulk plasmon peak in these materials lies at the energies of 18.9, 16.6 and 17.4 eV, respectively, so that the BSP energies are close to ~13 eV. The iron-based ODS-EUROFER alloy is more beneficial from this point of view because the energy of bulk plasmon peak is larger (~23.4 eV) and thus the bubble surface plasmon is better separated from the hydrogen signal location. Considering the bubble size, even the coupling of close-lying bubbles and the helium filling effects resulting in the “blue” and “red” shifts of BSP energy do not suggest full superposition of bubble surface plasmon and hydrogen signals in ODS-EUROFER.

The hydrogen association with He bubbles was reported very recently also in triple-beam implanted 13%Cr ODS-steel by means of EELS-SI technique [10]. The intensity of reported H-K signal is there higher than in our case, possibly due to the larger bubble size. Spatially hydrogen is distributed throughout entire bubble with intensity maximum at the lowest sample thickness. No intensity increase of H-K signal was detected in Ref. [10] at helium bubble periphery. The different hydrogen distribution reported in Ref. [10] possibly indicates a different mechanism of hydrogen trapping in helium bubbles as compared to that observed in our study. The authors of Ref. [10] do not specify an exact mechanism of hydrogen accumulation in bubbles. However, the reported maximum of EELS signal on H-K map that matches the lowest sample thickness, that is, the highest measured gas volume, suggests that hydrogen inside the bubbles might accumulate in molecular form. The reasons for this difference to our study might be in very different irradiation/implantation conditions. ODS alloy in Ref. [10] was irradiated at an elevated temperature and an additional high-energy beam of few MeV Fe^{3+} was involved in the irradiation process.

Summing up the results of EELS- SI investigation in sections 4.3.1 – 4.3.2, it can be concluded that

(i) The subtraction of the matrix contribution from corresponding bubble spectra yields spectral differences that clearly include two contributions, that is a broad signal at ~6.5-20 eV with the maximum at ~13 eV and a sharp peak with the maximum at ~25 eV.

(ii) The signal at ~25 eV was identified as He 1s \rightarrow 2p transition. The density of He at the central part of bubbles calculated through the “blue-shift” value is estimated to be ~94 at/nm³. This value is in good agreement with that reported earlier for Fe-based alloys [10,59].

(iii) The broad signal at ~6.5-20 eV with the maximum at ~13 eV was fitted with the superposition of three Gaussians with predefined peak positions. As a result, the cumulative broad signal was interpreted as a superposition of contributions from the surface oxide plasmon (at ~7.2 eV), H-K (at ~13.2-13.5 eV) and bubble surface plasmon (at either ~17.3 eV (corresponding to He-filled bubble) or ~19.1 eV (corresponding to an empty bubble)).

(iv) Similar energy and signal shape of the H-K and bubble surface plasmon signals in ODS-EUROFER steel make it hard to clearly differentiate between them. The possibility of bubble surface plasmon and H-K signals overlapping was discussed in details. Considering the possible shifts of bubble surface plasmon energy due the bubble size, coupling of two bubbles and the helium filling effect, the possibility of entire overlapping of bubble surface plasmon and hydrogen peaks was excluded.

(v) Based on NLLS fitting routine in GMS, hydrogen and helium signal intensity maps were obtained. Helium signal has the maximum intensity at the bubble centers suggesting that helium uniformly fills bubble interior. In contrast, the extracted hydrogen signal is distributed mostly uniformly over the bubble areas, demonstrating definite intensity increase only at the bubble periphery, which should be expected rather for bubble wall coverage by hydrogen. The observed helium and hydrogen distributions are in agreement with TDS finding that in the applied implantation conditions hydrogen is most probably trapped at bubble walls via a mechanism similar to chemisorption.

4.4 Summary and discussion

4.4.1 The effects of helium and hydrogen interplay observed in the sequential dual-beam He⁺+H⁺ ion implantations

The main objective of chapter 4 is to study possible helium and hydrogen synergetic effects on swelling through the monitoring of bubble population parameters in ODS-EUROFER steel and investigation of helium influence on hydrogen retention in well-controlled conditions of sequential dual-beam implantation. Having in mind this objective, let's summarize the results of ODS-EUROFER steel characterization after sequential implantation with He⁺ and H⁺ ions obtained by different experimental techniques. A summary of experimentally observed hydrogen effects on ODS-EUROFER steel pre-implanted with helium is given in Table 4.9. TEM and TDS results for the sequentially implanted samples are compared to single-beam He⁺ and single-beam H⁺ implantation results, respectively.

Table 4.9. Summary of hydrogen effects on ODS-EUROFER steel samples pre-implanted with helium ions.

	Conventional TEM	TDS	EELS-SI
<p>He⁺ F=5×10¹⁵ - 1×10¹⁶ cm⁻² at RT + H⁺ F= 1×10¹⁷ cm⁻² at RT</p>	<ul style="list-style-type: none"> • Nucleation of bubbles with low size and high number density; • The increase of bubble size after annealing at 823 K by ~6 % for bubbles on Y₂O₃ particles and by ~12 % for bubbles in the bulk and on other structural defects; • No changes in the number density of bubbles after annealing at 823 K; • A minor increase of swelling by 25 % after additional annealing at 823 K. 	<ul style="list-style-type: none"> • The increase of total H retention by 40% due to hydrogen accumulation in irreversible traps with the de-trapping energies of 0.78-0.81 eV; • Weak signal from strong hydrogen traps with de-trapping energy of ~3 eV. 	Not investigated
<p>He⁺ F=1×10¹⁶ cm⁻² at 823 K + H⁺ F= 1×10¹⁷ cm⁻² at RT</p>	<ul style="list-style-type: none"> • Suppression of bubble faceting; • Nucleation of bubbles with sub-nanometer size and high number density; • Swelling modification below detection limit. 	<ul style="list-style-type: none"> • The increase of total H retention by 80% due to hydrogen accumulation in irreversible traps with the de-trapping energies of 0.78-0.81 eV. 	H signal is associated with He bubbles. The signal is spatially distributed over the entire bubble area with moderate enhancement at the bubble periphery.
<p>He⁺ F=5×10¹⁵ cm⁻² at 823 K + H⁺ F= 1×10¹⁷ cm⁻² at 823 K</p>	<ul style="list-style-type: none"> • The bubbles attached to Y₂O₃ particles grow by ~7 %; while bubbles associated to other defects and located in the grain bulk remain unchanged; • No changes in the number density of bubbles ; • The increase of cumulative swelling by 21 %. 	Not investigated	Not investigated

Conventional TEM data indicate relatively minor influence of implanted hydrogen on overall swelling for all sequential implantation regimes used. Hydrogen implantation increases cumulative swelling by less than 25% as compared to that observed after single-beam He⁺ implantation. The visible bubble microstructure in ODS-EUROFER is mainly determined by the achieved helium concentration and the conditions of helium implantation or/and high-temperature processing. For high temperature experimental conditions used, bubble number density is affected weakly by H⁺ implantation. Comparison of the bubble evolution in ODS-EUROFER samples subjected to high-temperature He⁺ ion pre-implantation or post-implantation annealing at the 823 K reveals that after sequential dual-beam He⁺+H⁺ implantation the observed bubbles are systematically slightly larger than after single-beam He⁺ implantation. However, a notable share of helium atoms after the He⁺ implantation stage is retained in the

matrix in the form of substitutional He atoms and/or small He_nV_m clusters. Diffusion of He atoms and/or He_nV_m clusters to He bubbles during high-temperature hydrogen implantation or post-implantation annealing leads to bubble growth and increases the estimated swelling value. It looks like the observed microstructural changes at the elevated temperature (823 K) are determined rather by helium redistribution due to acceleration of defects mobility and additional radiation damage created by H^+ beam than by hydrogen accumulation. This conclusion is supported by the estimates of helium fraction retained in bubbles after annealing and by TDS measurements of hydrogen release. In dual-beam implanted samples the fraction of helium retained in bubbles increases after annealing from 33% to 87 % (see section 4.1.2), while the major part of hydrogen is released at temperatures below 750 K (see section 4.2.2).

While hydrogen implantation plays little role in microstructural development after implantation at elevated temperature or post-implantation annealing, some hydrogen effects on the bubble population were detected when room temperature hydrogen implantation was used. H^+ implantation into ODS-EUROFER steel pre-implanted with helium either at RT (section 4.1.2.1) or at 823 K (section 4.1.2.2) has promoted nucleation of bubbles with high number density and size of $\sim 0.5\text{-}1$ nm. The observed bubble nucleation can be due either to additional stabilization of vacancy cluster by trapped hydrogen atoms or to the enhanced diffusion of He retained in small He-V clusters as a result of additional damage production by hydrogen beam. In addition, for ODS-EUROFER samples sequentially implanted with He^+ at 823 K and H^+ at RT (section 4.1.2.2) one observes a clear rounding of faceted bubbles developed at the He^+ pre-implantation stage. The suppression of bubble faceting is hard to explain in terms of radiation damage effects and is more probably due to hydrogen accumulation at the walls of helium bubbles via chemisorption-like mechanism. The trapping of hydrogen at helium bubbles is supported also by TDS and EELS-SI observations. As shown in section 4.2.1-4.2.2, implantation of He^+ at RT or 823 K followed by H^+ implantation at RT increases total hydrogen retention in ODS-EUROFER by, respectively, 40% or 80% as compared to single-beam H^+ implantation. The increased hydrogen retention results from hydrogen accumulation in irreversible traps with the de-trapping energies of 0.78-0.81 eV, which are commonly associated in the literature with hydrogen binding to bubble surfaces. Helium and hydrogen spatial distribution obtained by EELS-SI technique on samples sequentially implanted with He^+ at 823 K and H^+ at RT strongly supports this tentative identification. As reported in section 4.3, helium signal (He-K) has the maximum intensity at the bubble center suggesting that helium uniformly fills bubble volume. In contrast, the extracted hydrogen signal is distributed mostly uniformly over the bubble areas with a definite intensity increase at the bubble periphery, which should be expected rather for bubble surface coverage by hydrogen. The spatial distribution of gas atoms in the bubbles after sequential implantation with He^+ ions at 823 K and H^+ at RT can be interpreted in terms of a “core-shell” structure, where the helium core inside the cavity is surrounded by a shell of hydrogen atoms at cavity walls. The presence of molecular hydrogen in bubbles nucleated after sequential implantation with both He^+ and H^+ ions at RT is suggested by the results of TDS analysis, but the share of hydrogen retained in molecular form is extremely small.

An important objective of chapter 4 was to investigate the role of Y_2O_3 nanoparticles in hydrogen accumulation in ODS-EUROFER steel. As reported in section 4.2, ODS-EUROFER steel manifests ~ 3 times stronger hydrogen uptake as compared to ODS-free EUROFER 97 steel under single-beam H^+ implantation and sequential dual-beam He^++H^+ implantations at room temperature. However, the analysis of experimental results in conjunction with available literature data indicates that the stronger hydrogen retention in ODS-EUROFER steel as compared to EUROFER 97 cannot be attributed exclusively to the presence of oxide nanoparticles and should be related rather to differences in the volume densities of other trapping sites, such as dislocations, grain boundaries and single vacancies. The direct accumulation of hydrogen inside the oxide particles is not very probable because of the low hydrogen solubility in yttria [35], but it cannot be excluded that hydrogen accumulates either at nanoparticle surfaces or at bubbles associated with nanoparticles. Considering the estimated hydrogen binding energy to oxide

particle/matrix interfaces of 0.36 eV, hydrogen trapping at nanoparticle/matrix interfaces can hardly affect swelling, even if the effects on mechanical properties of ODS-EUROFER steel might be expected [2,16]. The influence of hydrogen on bubble population associated with yttria nanoparticles was also found to be minor in all implantation conditions used in this thesis. After sequential implantation with He⁺ and H⁺ at RT, bubbles were formed both in the bulk and on structural defects but no preferential bubble size increase on oxide nanoparticle/matrix interfaces occurred. After high-temperature (823 K) H⁺ implantation or post-implantation annealing of samples pre-implanted with helium at RT, bubbles associated with Y₂O₃ nanoparticles were larger than in the grain bulk or on other structural defects. However, similar to other bubble populations, bubbles attached to nanoparticles have demonstrated low sensitivity to H⁺ implantation; their average size has increased by less than 7 % in comparison with that observed after single-beam He⁺ implantation. Since hydrogen desorption from bubbles occurs mostly at temperatures below 750 K, this minor bubble growth should be related rather to helium re-distribution than to hydrogen accumulation in bubbles.

Summing up, under experimental conditions used in this thesis hydrogen injection into ODS-EUROFER steel pre-implanted with helium did not reveal any potential hazards of notable swelling increase, in contrast to additional damage production which is able to trigger bubble-to-void transition in bubble population associated with Y₂O₃ nanoparticles (see section 3.3). The specific chemisorption-like mechanism of hydrogen trapping at helium bubble walls is suggested to play the main role in hydrogen accumulation under investigated experimental conditions.

4.4.2 The impact of results on the interpretation of triple-beam experiments used for modelling fusion and spallation environment

Although the implantation conditions used in this study are very different from those in fusion or spallation reactor environments (our gas accumulation rates are few orders of magnitude higher and the damage rate is notably lower), the obtained results can contribute to better understanding of the synergy of hydrogen and helium in the microstructure development and are useful for the interpretation of mechanisms of swelling excess previously reported in multi-beam irradiations intended to simulate fusion and spallation operational conditions.

Pronounced swelling increase was reported by several research groups for *bcc* iron [84] and conventional ferritic/ferritic-martensitic steels [4–6,10] under simultaneous action of damage production and helium and hydrogen accumulation. It should be noted that, according to the majority of reported triple-beam data [6,10,85], swelling detected in commercial ODS-steels was quite limited. Notable swelling under triple-beam conditions was reported only in Refs. [7] and [10] for K3-ODS and HIP-13Cr-ODS (material after hiping without heat treatment), respectively. The exact mechanisms of hydrogen influence on helium-driven swelling remain unclear, but, in general terms, hydrogen can be involved in either cavity nucleation, or cavity growth, or both.

Let us consider first possible hydrogen effects on cavity nucleation. It is known that when irradiation of metals is accompanied with sufficiently fast accumulation of helium, the development of cavities is mainly driven by stabilization of small vacancy clusters with helium atoms that prevent cluster dissociation [86–89]. In this case, hydrogen effect on cavity nucleation can be related to additional stabilization of small vacancy clusters by trapped hydrogen atoms that are also able to be captured in small vacancy-hydrogen clusters in steel matrix [45,90,91]. However, based on the available literature data on the efficiency of He and H atom binding in small gas-vacancy clusters, it can be expected that the relative importance of hydrogen assistance to helium in the stabilization of small vacancy clusters at the cavity nucleation stage is strongly temperature dependent.

Indeed, according to first-principles calculations, hydrogen is less strongly bound to small vacancy clusters in *bcc* iron than helium and the gas capture pattern is considerably different. Helium is

known to be badly solvable in iron matrix and is trapped inside a cavity. For a single helium trapped in a single vacancy, the helium binding energy is estimated to vary within 2.3-3.7 eV [86–89]. For small He_nV_m clusters, the binding energy depends on helium-to-vacancy ratio and decreases from ~ 3.7 eV as n/m increases, but does not fall below 1.8 eV even for unrealistically high ratio of $n/m = 4$ [88]. In contrast, hydrogen is trapped at the periphery of a vacancy cluster and the binding energy of hydrogen atom to a monovacancy is only 0.56-0.6 eV [44,45,91], additionally decreasing down to 0.39 eV as the hydrogen-to vacancy ratio in H_nV_m clusters increases up to 6 [45,91]. The decrease in the gas atom binding to clusters becomes notable only for sufficiently high gas-to-vacancy ratios, exceeding ~ 2 for He_nV_m clusters and ~ 4 for H_nV_m .

When He and H are injected into steel simultaneously, the situation becomes more complicated due to possible formation of mixed $\text{He}_n\text{H}_m\text{V}_k$ clusters, but the binding of gas atoms in such clusters follows the same trends as for binary gas-vacancy clusters, as demonstrated by first principles [92] and classical molecular dynamics (MD) simulations [83,93]. That is, hydrogen atoms have positive binding energies to triple $\text{He}_n\text{H}_m\text{V}_k$ clusters, but are bound less strongly than helium and the binding of both helium and hydrogen weakens with the increase of gas inventory. The spatial distribution of helium and hydrogen atoms in small vacancy clusters follows the patterns appropriate for binary clusters, that is, helium fills the interior of the cluster, while hydrogen decorates the cluster walls [83]. Having in mind that the direct interaction between He and H atoms is extremely weak [83,92], variations of gas atom binding energies to triple clusters as compared to similar binary clusters are due mostly to elastic deformation of iron matrix in the immediate vicinity of the cluster and thus should not be extremely strong. The strongest synergy in the helium and hydrogen interaction with vacancies can be expected at relatively high n/k and/or m/k ratios. For example, when a helium atom is placed into a single-vacancy based cluster $\text{He}_n\text{H}_m\text{V}$ ($n=1-2$, $m=1-3$) in *bcc* iron, the hydrogen binding energy decreases by ~ 0.1 eV [92]. The attractive interaction of a helium atom in the same triple cluster is also decreased by tenths of eV when hydrogen atoms are present. Calculations of binding energies for $\text{He}_n\text{H}_m\text{V}_6$ with up to 30 He and H atoms [83] shows the same trend in H binding, while He binding is less sensitive to H presence.

A very strong difference in the binding efficiency suggests an explanation why the effects of hydrogen on cavity nucleation have been observed in our room temperature experiments (see sections 4.1.2.1 and 4.1.2.2) and not in the experiments where cavity populations developed at elevated temperatures, that is during high-temperature He^+ pre-implantation or post-implantation annealing at 823 K (see sections 4.1.1 and 4.1.2.1). It is clear that at the temperature of 823 K, the growing small He-V clusters are unable to trap hydrogen atoms for the time sufficient to noticeably contribute to cluster stabilization. In contrast, the hydrogen binding energy of ~ 0.6 eV is high enough to provide efficient hydrogen trapping in triple He-H-V clusters at room temperature and to assist in the cavity formation, provided hydrogen is introduced in the matrix simultaneously with helium, or as in our case, when the pre-implantation with He^+ ions is done at RT and the cluster nucleation stage is not over by the end of He^+ implantation (as can be judged from the absence of visible cavities after single-beam He^+ implantation in similar conditions). As a result, one may expect that hydrogen involvement in small vacancy cluster stabilization leads to an increase of cavity number density, as was indeed observed.

One more factor that influences the cavity nucleation is the production of additional radiation damage by hydrogen beam because it increases the relative number of clusters He_nV_m with $n = 1-2$ and $m = 3-4$, which are expected to be highly mobile [94] and promote He transport to larger immobile He_nV_m clusters, resulting in the growth of the latter. As a result, those small clusters that remain below visibility limit after He^+ pre-implantation stage develop into visible clusters after hydrogen implantation.

The observation of no visible hydrogen effect on cluster number density in high temperature experiments is in excellent agreement with the available data that indicate no hydrogen influence on cavity nucleation in triple-beam experiment at relatively high temperatures. For example, early TEM observations after single-beam Fe^+ , dual-beam Fe^+He^+ and triple-beam $\text{Fe}^+\text{He}^+\text{D}^+$ irradiations (to

100 dpa from Fe ions, with 10 appm He/dpa and 40 appm D/dpa introduction ratios) at 673-873 K [3] have demonstrated that the presence of a helium beam (both with and without additional deuterium beam) increases cavity number density as compared to heavy ion irradiation alone for the same damage dose, but this increase was insensitive to the presence or absence of deuterium beam [3]. Later studies in a similar temperature range [4–7,10,84] also came to conclusion that the presence of hydrogen does not increase cavity number density in triple-beam experiments.

This conclusion is also indirectly supported by the data from F82H steel samples irradiated with a triple-beam simulating spallation environment [5], where the hydrogen inventory remaining in the sample one week after the irradiation was measured using $^1\text{H}(^{15}\text{N},\alpha\gamma)^{12}\text{C}$ resonance nuclear reaction. Hydrogen concentrations in the samples irradiated at 353 K and 743 K were found to be ~0.5 at. % and below the detection limit (of 0.13 at. %), respectively. That is, the concentration of hydrogen retained in the matrix after irradiation at the high temperature was too low to expect efficient hydrogen trapping at cavities that might substantially contribute to cavity nucleation.

Since hydrogen influence on cavity density at elevated temperature seems is insubstantial, swelling enhancement in triple-beam experiments should be mainly related to variations in cavity size distribution. Indeed, the comparison of literature data on double- and triple-beam irradiation experiments shows that hydrogen co-implantation can lead to up to 10-fold increase in cavity diameters [4–8]. The data on cavity size reported for ferritic, ferritic-martensitic and ODS-steels after triple-beam experiments are summarized in Table 4.10.

Table 4.10. Average cavity sizes $\langle d \rangle$ detected in commercial ferritic, ferritic-martensitic and ODS-steels after triple-beam irradiations simulating fusion conditions.

Ref.	[4,5]			[6]	[6]			[10]			[7,95]
Material	F82H steel			9 Cr	12 Cr			EUROFER 97			K3-ODS
Irradiation conditions	50 dpa, 900 appm He, 3500 appm H			50 dpa, 500 appm He, 2000 appm H	50 dpa, 500 appm He, 2000 appm H			40 dpa, 500 appm He, 2000 appm H			30 -40 dpa, 450-640 appm He, 1200-1600 appm H
Temperature, K *	743	783	873	783	743	783	873	603/623	673/723	773/823	873 /898
$\langle d \rangle$ nm, Fe+He	6.7	5.2	6.1	5	-	15	-	1.3	1.2	2	-
$\langle d \rangle$ nm, Fe+He+H	11.2	8.6-6	8.0-7.5	50	17	50	5	1.9	4.8	4.2	14 (7-20)
Diameter increase factor	~1.7	~1.5	~1.3	~10	-	~3	-	~1.5	~4	~2	-

* Temperatures where bi-modal cavity distributions were observed are marked bold

As can be noticed in Table 4.10, after triple-beam irradiation the cavities were larger than after dual-beam irradiation at comparable temperatures. However, both below 723 K and above 783 K the average cavity size increases modestly. Such moderate increase is in agreement with rate theory simulations [7,92] that predict ~50-15% increase of the mean cavity/cluster size due to the presence of triple clusters $\text{H}_n\text{H}_m\text{V}_k$ when both H and He simultaneously participate in cavity nucleation at 723-743 K. However, this trend is violated in a narrow temperature range of less than 100 K width around roughly 753 K, where one observes cavity size increase by a factor of 2-10. The notable increase of cavity size and swelling in triple-beam experiments [4–6,10] in the temperature window of 723 K-783 K (data marked in bold in Table 4.10) was always accompanied by the development of bi-modal cavity distribution, whereas only unimodal cavity distribution was found in dual-beam irradiated samples at the same temperature and helium concentration. The bi-modal cavity size distribution in K3-ODS was observed also in Refs. [7,95] at temperatures 873 /898 K, where no dual-beam data were available for

comparison. The bi-modal size distribution is usually indicative of the transition from helium-driven to bias-driven cavity growth and strongly suggests that hydrogen beam in triple-beam experiments somehow facilitates the bubble-to-void transition, decreasing the critical transition size.

Strictly speaking, the onset of bias-driven swelling in triple-beam experiment may be related not to the introduction of hydrogen, but simply to the increase of vacancy supersaturation due to additional damage produced by H⁺ beam. The increase of peak swelling in triple-beam experiments is essentially in the narrow temperature range typical for swelling of Fe-based alloys irradiated with self-ions [96]. At lower temperatures the bias-driven cavity growth is suppressed by insufficient vacancy mobility, while at higher temperatures cavity growth is prevented by too easy vacancy emission from void-like (underpressurized) cavities. If the reasons for enhanced swelling under triple-beam are indeed related to variations in the efficient vacancy supersaturation, one can expect that swelling temperature window and peak temperature may vary not only with dose, dose rate and He/H injection range but also with material microstructure and elemental content. The latter effect was indeed noticed by the authors of Ref. [7] and gives a ready explanation why notable swelling increase under triple-beam conditions has not been reported so far for ODS-EUROFER steel, which has excellent swelling resistance due to high sink strength in this material.

Yet, one cannot exclude also the direct effect of hydrogen on the critical bubble-to-void transition size. The most evident ways of such direct influence are the trapping of hydrogen on cavity walls, which might change the surface energy and thus the efficiency of thermal vacancy emission, and the accumulation of hydrogen inside cavities in molecular form that would increase the internal gas pressure. Let us discuss possible impact of these factors on bubble-to-void transition at 723 K-783 K in triple-beam experiments.

As already discussed, hydrogen can be trapped on the walls helium-filled cavities with hydrogen binding energy varying within 0.8 - 0.25 eV [83] depending on He/V and H/V ratio. Typical diameters of bubbles undergoing transition to bias-driven regime are of the order of 10 nm. Bubbles of this size have typically relatively low He/V ratio. For example, the optimal He/V ratios predicted by modelling for equilibrium bubbles in *bcc* iron are ~0.5-1 [97,98], while experimentally observed values in Fe-based alloys are even lower, in the range of 0.2-0.85 [59,99]. In this study, an estimate using the hard sphere EOS has given He/V ratio ranging from 0.4 to 0.8 (see section 3.1.2.5). These relatively low He/V ratios only weakly affect the hydrogen binding to cavity walls. Hence, one can expect that the binding of hydrogen to cavity walls should be strong enough, at the level of 0.8 eV. TDS and EELS data of our study (see sections 4.2.2 and 4.3) lead to a similar conclusion that hydrogen binds to the surface of helium filled cavities in ODS-EUROFER with the energy of 0.78-0.81 eV. Having in mind these TDS data, one can conclude that efficient trapping of hydrogen on cavity walls is possible at temperature below roughly 750 K. Let us recall also that after triple-beam irradiation at 743 K [5] the concentration of hydrogen was below detection limit. That means that hydrogen trapping at cavity walls as a mechanism of critical bubble-to-void transition size decrease should not be operative at temperatures noticeably exceeding 750 K. In particular for triple-beam experiments listed in Table 4.10, this mechanism might contribute to bubble-to-void transitions observed in Refs. [4,5,10], but not for the higher temperature experiments [6,7,95].

Such temperature limitations are not restrictive for hydrogen trapped inside cavities in molecular form. The binding energy of a hydrogen molecule is very high, ~4.54-4.91 eV [32]. Though it may decrease due to the interaction of hydrogen molecules with cavity walls, TDS results in this study (see section 4.2.2) indicate that it is still ~3 eV, if the high-temperature desorption peak can be associated with molecular hydrogen desorption from ~1 nm diameter bubbles through the dissociation mechanism. Judging from so strong binding, molecular hydrogen can contribute to gas pressure in small cavities up to temperatures notably higher than those used in triple-beam experiments. An open question remains, however, the reason for hydrogen molecule accumulation in the cavity interior. In any case, the chances to form hydrogen molecules from atomic hydrogen trapped at cavity walls seem poor. Our TDS results

indicate that the relative share of hydrogen captured in the strongest sinks with 3 eV binding energy is extremely low and even if the peak is indeed related to molecular hydrogen trapped in cavities, its contribution to gas pressure in the bubbles is hardly substantial. The nuclear reaction based analysis of hydrogen retained in F82H steel after triple-beam irradiation at 743 K [5] has also demonstrated no measurable amount of hydrogen that might be left inside cavities in molecular state.

Summing up, we expect that synergetic effect of helium and hydrogen on strong cavity growth and noticeably enhanced swelling in ferritic-martensitic steels can be an issue only for experiments conducted close to the 690-750 K. At higher temperatures interstitial hydrogen atoms are no more trapped by cavity walls, while molecular hydrogen contribution to gas pressure inside cavities can't be all together excluded.

Thus, even though the experiments performed in well-controlled conditions of sequential dual-beam implantation do not directly reproduce fusion or spallation environments, the analysis of their results provides valuable insights on the possible synergy in helium and hydrogen behavior in ODS steels, which might contribute to the development of computational models that accurately predict ODS steel in-service behavior.

4.5 References

- [1] E. Malitckii, Y. Yagodzinskyy, M. Ganchenkova, S. Binyukova, H. Hänninen, R. Lindau, P. Vladimirov, A. Moeslang, “Comparative study of hydrogen uptake and diffusion in ODS steels,” *Fusion Eng. Des.*, vol. 88, no. 9, pp. 2607–2610, 2013.
- [2] Y. Yagodzinskyy, E. Malitckii, M. Ganchenkova, S. Binyukova, O. Emelyanova, T. Saukkonen, H. Hänninen, R. Lindau, P. Vladimirov, A. Moeslang, “Hydrogen effects on tensile properties of EUROFER 97 and ODS-EUROFER steels,” *J. Nucl. Mater.*, vol. 444, no. 1, pp. 435–440, 2014.
- [3] K. Farrell and E.H. Lee, “Ion damage in a Fe-10Cr-6Mo-0.5Nb ferritic steel,” *Radiation-Induced Changes in Microstructure: 13th International Symposium (Part I)*, vol. STP 955, pp. 498–507, Jan. 1987.
- [4] E. Wakai, T. Sawai, K. Furuya, A. Naito, T. Aruga, K. Kikuchi, S. Yamashita, S. Ohnuki, S. Yamamoto, H. Naramoto, S. Jistukawa, “Effect of triple ion beams in ferritic/martensitic steel on swelling behavior,” *J. Nucl. Mater.*, vol. 307–311, pp. 278–282, 2002.
- [5] E. Wakai, K. Kikuchi, S. Yamamoto, T. Aruga, M. Ando, H. Tanigawa, T. Taguchi, T. Sawai, K. Oka, S. Ohnuki, “Swelling behavior of F82H steel irradiated by triple/dual ion beams,” *J. Nucl. Mater.*, vol. 318, pp. 267–273, 2003.
- [6] T. Tanaka, K. Oka, S. Ohnuki, S. Yamashita, T. Suda, S. Watanabe, E. Wakai, “Synergistic effect of helium and hydrogen for defect evolution under multi-ion irradiation of Fe–Cr ferritic alloys,” *J. Nucl. Mater.*, vol. 329–333, pp. 294–298, 2004.
- [7] J. Marian, T. Hoang, M. Fluss, and L. L. Hsiung, “A review of helium–hydrogen synergistic effects in radiation damage observed in fusion energy steels and an interaction model to guide future understanding,” *J. Nucl. Mater.*, vol. 462, pp. 409–421, 2015.
- [8] Y. E. Kupriyanova, V. V. Bryk, O. V. Borodin, A. S. Kalchenko, V. N. Voyevodin, G. D. Tolstolutskaia, F. A. Garner, “Use of double and triple-ion irradiation to study the influence of high levels of helium and hydrogen on void swelling of 8–12% Cr ferritic-martensitic steels,” *J. Nucl. Mater.*, vol. 468, pp. 264–273, 2016.
- [9] D. Brimbal, L. Beck, M. Payet, and F. Jomard, “The synergistic effect of hydrogen and helium implantations in forming H₂ molecules in a Fe-12 wt.%Cr-ODS steel characterized by Raman spectroscopy and SIMS,” *Nucl. Instruments Methods Phys. Res. Sect. B Beam Interact. with Mater. Atoms*, vol. 461, pp. 191–196, 2019.
- [10] N. Zimmer, P. Vladimirov, M. Klimenkov, U. Jaentsch, R. Vila, V. Chakin, F. Mota, “Microstructural evolution of three potential fusion candidate steels under ion-irradiation,” *J. Nucl. Mater.*, vol. 535, p. 152160, 2020.
- [11] M. L. Jenkins, *Characterization of radiation damage by transmission electron microscopy*. Bristol ; Institute of Physics Pub, 2001.
- [12] B. Yao, D. J. Edwards, R. J. Kurtz, G. R. Odette, and T. Yamamoto, “Multislice simulation of transmission electron microscopy imaging of helium bubbles in Fe,” *Microscopy*, vol. 61, no. 6, pp. 393–400, 2012.
- [13] W. Y. Choo and J. Y. Lee, “Thermal analysis of trapped hydrogen in pure iron,” *Metall. Trans. A*, vol. 13, no. 1, pp. 135–140, 1982.
- [14] G.-W. Hong and J.-Y. Lee, “The measurement of the trap binding energy by the thermal analysis technique,” *Scripta Metallurgica*, vol. 17, no. 7, pp. 823–826, 1983.

- [15] Evgenii Malitckii, “Hydrogen and helium effects on reduced activation Fe-Cr ferritemartensite and ODS steel,” 2015.
- [16] E. Malitckii, Y. Yagodzinskyy, M. Ganchenkova, T. Saukkonen, H. Hänninen, R. Lindau, P. Vladimirov, A. Moeslang, “Hydrogen uptake and its effect on mechanical properties of Eurofer 97-2 and ODS-Eurofer steels,” in *SMiRT 22 - San Francisco, USA. August 18-23, 2013*, 2013.
- [17] B. Janković, B. Adnađević, and S. Mentus, “The kinetic study of temperature-programmed reduction of nickel oxide in hydrogen atmosphere,” *Chem. Eng. Sci.*, vol. 63, no. 3, pp. 567–575, 2008.
- [18] J. L. Lee and J. Y. Lee, “Hydrogen trapping in AISI 4340 steel,” *Met. Sci.*, vol. 17, no. 9, pp. 426–432, Sep. 1983.
- [19] J.-Y. Lee and S. M. Lee, “Hydrogen trapping phenomena in metals with B.C.C. and F.C.C. crystals structures by the desorption thermal analysis technique,” *Surf. Coatings Technol.*, vol. 28, no. 3, pp. 301–314, 1986.
- [20] S.-M. Lee and J.-Y. Lee, “The trapping and transport phenomena of hydrogen in nickel,” *Metall. Trans. A*, vol. 17, no. 2, pp. 181–187, 1986.
- [21] H. E. Kissinger, “Reaction kinetics in differential thermal analysis,” *Anal. Chem.*, vol. 29, no. 11, pp. 1702–1706, Nov. 1957.
- [22] F. G. Wei and K. Tsuzaki, “Quantitative analysis on hydrogen trapping of TiC particles in steel,” *Metall. Mater. Trans. A*, vol. 37, no. 2, pp. 331–353, 2006.
- [23] I. Maroef, D. L. Olson, M. Eberhart, and G. R. Edwards, “Hydrogen trapping in ferritic steel weld metal,” *Int. Mater. Rev.*, vol. 47, no. 4, pp. 191–223, Aug. 2002.
- [24] T. Michler and M. P. Balogh, “Hydrogen environment embrittlement of an ODS RAF steel – Role of irreversible hydrogen trap sites,” *Int. J. Hydrogen Energy*, vol. 35, no. 18, pp. 9746–9754, 2010.
- [25] S. Frappart, A. Oudriss, X. Feaugas, J. Creus, J. Bouhattate, F. Thébault, L. Delattre, H. Marchebois, “Hydrogen trapping in martensitic steel investigated using electrochemical permeation and thermal desorption spectroscopy,” *Scripta Materialia*, vol. 65, no. 10, pp. 859–862, 2011.
- [26] H. K. D. H. Bhadeshia, “Prevention of hydrogen embrittlement in steels,” *ISIJ Int.*, vol. 56, no. 1, pp. 24–36, 2016.
- [27] S. K. Dwivedi and M. Vishwakarma, “Effect of hydrogen in advanced high strength steel materials,” *Int. J. Hydrogen Energy*, vol. 44, no. 51, pp. 28007–28030, 2019.
- [28] T. Depover and K. Verbeken, “Hydrogen trapping and hydrogen induced mechanical degradation in lab cast Fe-C-Cr alloys,” *Mater. Sci. Eng. A*, vol. 669, pp. 134–149, 2016.
- [29] D. Pérez Escobar, T. Depover, E. Wallaert, L. Duprez, M. Verhaege, and K. Verbeken, “Thermal desorption spectroscopy study of the interaction between hydrogen and different microstructural constituents in lab cast Fe-C alloys,” *Corros. Sci.*, vol. 65, pp. 199–208, 2012.
- [30] A. Nagao, M. Dadfarnia, B. P. Somerday, P. Sofronis, and R. O. Ritchie, “Hydrogen-enhanced-plasticity mediated decohesion for hydrogen-induced intergranular and ‘quasi-cleavage’ fracture of lath martensitic steels,” *J. Mech. Phys. Solids*, vol. 112, pp. 403–430, 2018.
- [31] S. M. Myers, D. M. Follstaedt, F. Besenbacher, and J. Boettiger, “Trapping and surface permeation of deuterium in He-implanted Fe,” *J. Appl. Phys.*, vol. 53, no. 12, pp. 8734–8744, Dec. 1982.
- [32] D. C. Patton, D. V Porezag, and M. R. Pederson, “Simplified generalized-gradient approximation and anharmonicity: Benchmark calculations on molecules,” *Phys. Rev. B*, vol. 55, no. 12, pp. 7454–7459, Mar. 1997.

- [33] M. Dadfarnia, P. Sofronis, and T. Neeraj, "Hydrogen interaction with multiple traps: Can it be used to mitigate embrittlement?," *Int. J. Hydrogen Energy*, vol. 36, no. 16, pp. 10141–10148, 2011.
- [34] T. Depover and K. Verbeken, "The detrimental effect of hydrogen at dislocations on the hydrogen embrittlement susceptibility of Fe-C-X alloys: An experimental proof of the HELP mechanism," *Int. J. Hydrogen Energy*, vol. 43, no. 5, pp. 3050–3061, 2018.
- [35] D. Sun, J. Ding, Y. Yang, P. Zhang, and J. Zhao, "First-principles investigation of hydrogen behavior in different oxides in ODS steels," *Int. J. Hydrogen Energy*, vol. 44, no. 31, pp. 17105–17113, 2019.
- [36] Y. Yamauchi, K. Gotoh, Y. Nobuta, T. Hino, S. Suzuki, and M. Akiba, "Deuterium retention and desorption behavior of reduced activated ferritic steel with surface damage due to high energy helium ion irradiation," *Fusion Eng. Des.*, vol. 85, no. 10, pp. 1838–1840, 2010.
- [37] Y.-P. Xu, T. Lu, X.-C. Li, F. Liu, H.-D. Liu, J. Wang, Z.-Q. An, F. Ding, S.-H. Hong, H.-S. Zhou, G.-N. Luo, "Influence of He ions irradiation on the deuterium permeation and retention behavior in the CLF-1 steel," *Nucl. Instruments Methods Phys. Res. Sect. B Beam Interact. with Mater. Atoms*, vol. 388, pp. 5–8, 2016.
- [38] Q. Xu and J. Zhang, "Effects of He, D interaction on thermal desorption of He and D₂ and microstructural evolution in pure Fe," *J. Nucl. Mater.*, vol. 479, pp. 255–259, 2016.
- [39] F.A. Garner, E.P. Simonen, B.M. Oliver, L.R. Greenwood, M.L. Grossbeck, W.G. Wolfer, P.M. Scott, "Retention of hydrogen in fcc metals irradiated at temperatures leading to high densities of bubbles or voids," *J. Nucl. Mater.*, vol. 356, no. 1, pp. 122–135, 2006.
- [40] D. J. Edwards, F. A. Garner, S. M. Bruemmer, and P. Efsing, "Nano-cavities observed in a 316SS PWR flux thimble tube irradiated to 33 and 70dpa," *J. Nucl. Mater.*, vol. 384, no. 3, pp. 249–255, 2009.
- [41] D. Hamaguchi, H. Iwakiri, T. Kawamura, H. Abe, T. Iwai, K. Kikuchi, N. Yoshida, "The trapping behavior of deuterium in F82H ferritic/martensitic steel," *J. Nucl. Mater.*, vol. 386–388, pp. 375–378, 2009.
- [42] G. D. Tolstolutskaia, V. V Ruzhytskyi, V. N. Voyevodin, I. E. Kopanets, S. A. Karpov, and A. V Nikitin, "The role of radiation damage on retention and temperature intervals of helium and hydrogen detrapping in structural materials," *J. Nucl. Mater.*, vol. 442, no. 1, Supplement 1, pp. S710–S714, 2013.
- [43] D. A. Mirzaev, A. A. Mirzoev, K. Y. Okishev, and A. V Verkhovyykh, "Hydrogen–vacancy interaction in bcc iron: ab initio calculations and thermodynamics," *Molecular Physics*, vol. 112, no. 13, pp. 1745–1754, Jul. 2014.
- [44] Y. Tateyama and T. Ohno, "Stability and clusterization of hydrogen-vacancy complexes in alpha-Fe: An ab initio study," *Phys. Rev. B*, vol. 67, no. 17, p. 174105, May 2003.
- [45] E. Hayward and C.-C. Fu, "Interplay between hydrogen and vacancies in α -Fe," *Phys. Rev. B*, vol. 87, no. 17, p. 174103, May 2013.
- [46] O. V Ogorodnikova, Z. Zhou, K. Sugiyama, M. Balden, Y. Gasparyan, and V. Efimov, "Surface modification and deuterium retention in reduced-activation steels under low-energy deuterium plasma exposure. Part I: undamaged steels," *Nucl. Fusion*, vol. 57, no. 3, p. 36010, 2016.
- [47] X. Hu, L. Tan, K. Wang, C. P. Massey, D. T. Hoelzer, and Y. Katoh, "Deuterium retention in advanced steels for fusion reactor structural application," *J. Nucl. Mater.*, vol. 516, pp. 144–151, 2019.
- [48] C. C. Ahn, Ed., *Transmission Electron Energy Loss Spectrometry in Materials Science and The EELS Atlas*, Second Edi. Wiley, 2004.

- [49] J. Scott, P. J. Thomas, M. MacKenzie, S. McFadzean, J. Wilbrink, A.J. Craven, W. A. P. Nicholson, “Near-simultaneous dual energy range EELS spectrum imaging,” *Ultramicroscopy*, vol. 108, no. 12, pp. 1586–1594, 2008.
- [50] J. Bobynko, I. MacLaren, and A. J. Craven, “Spectrum imaging of complex nanostructures using DualEELS: I. digital extraction replicas,” *Ultramicroscopy*, vol. 149, pp. 9–20, 2015.
- [51] “Digital Micrograph™ software by Gatan Inc.” <https://www.gatan.com/products/tem-analysis/gatan-microscopy-suite-software>.
- [52] D. R. G. Mitchell, “SI tools version:20160903, v4.0.” <http://www.dmscripting.com/sitools.html>.
- [53] I. T. Jolliffe, *Principal Component Analysis*. New York: Springer-Verlag, 2002.
- [54] Francisco de la Peña; Eric Prestat; Vidar Tonaas Fauske; Pierre Burdet; Petras Jokubauskas; Magnus Nord; Tomas Ostasevicius; Katherine E. MacArthur; Mike Sarahan; Duncan N. Johnstone; Joshua Taillon; Jonas Lähnemann; Vadim Migunov; Alberto Eljarrat; Jan C, “HyperSpy: multi-dimensional data analysis”. <https://doi.org/10.5281/zenodo.3352341>.
- [55] M.-L. David, F. Pailloux, V. Mauchamp, and L. Pizzagalli, “In situ probing of helium desorption from individual nanobubbles under electron irradiation,” *Appl. Phys. Lett.*, vol. 98, no. 17, p. 171903, Apr. 2011.
- [56] R. Manzke, G. Creelius, and J. Fink, “Excitation of Surface Plasmons on He-Filled Cavities in Al,” *Phys. Rev. Lett.*, vol. 51, no. 12, pp. 1095–1098, Sep. 1983.
- [57] J.-T. Li, J. Parisi, Z.-B. Wang, and Y.-K. Pu, “The energy evolution of surface plasmons on an oxidized aluminum surface: the role of the atomic polarizability of oxygen adsorbates and the thickness of the oxide layer,” *J. Phys. D: Appl. Phys.*, vol. 47, no. 42, p. 425304, 2014.
- [58] C. A. Walsh, J. Yuan, and L. M. Brown, “A procedure for measuring the helium density and pressure in nanometre-sized bubbles in irradiated materials using electron-energy-loss spectroscopy,” *Philos. Mag.*, vol. 80, no. 7, pp. 1507–1543, Jul. 2000.
- [59] S. Fréchar, M. Walls, M. Kociak, J. P. Chevalier, J. Henry, and D. Gorse, “Study by EELS of helium bubbles in a martensitic steel,” *J. Nucl. Mater.*, vol. 393, no. 1, pp. 102–107, Aug. 2009.
- [60] M. Klimenkov, P. Vladimirov, J. Hoffmann, N. Zimmer, A. Möslang, and V. Kuksenko, “First simultaneous detection of helium and tritium inside bubbles in beryllium,” *Micron*, vol. 127, p. 102754, 2019.
- [61] M. S. Blackmur, S. Dumbill, I. MacLaren, D. Hernandez-Maldonado, P. D. Styman, M. Gass, R. J. Nicholls, J. M. Hyde, Q. M. Ramasse, K. J. Annand, J. S. Smith, N. Gotham, “The association of hydrogen with nanometre bubbles of helium implanted into zirconium,” *Scripta Materialia*, vol. 152, pp. 102–106, 2018.
- [62] J. Bruley, “Detection of nitrogen at {100} platelets in a type IaA/B diamond,” *Philos. Mag. Lett.*, vol. 66, no. 1, pp. 47–56, Jul. 1992.
- [63] V. Badjeck, “Electron spectro-microscopy study of damage free and He implanted ODS steels,” 2015.
- [64] R. F. Egerton, *Electron Energy-Loss Spectroscopy in the Electron Microscope*. Boston, MA: Springer US, 2011.
- [65] A. J. Craven, J. Bobynko, B. Sala, and I. MacLaren, “Accurate measurement of absolute experimental inelastic mean free paths and EELS differential cross-sections,” *Ultramicroscopy*, vol. 170, pp. 113–127, 2016.

- [66] K. Hojou, S. Furuno, K. N. Kushita, N. Sasajima, and K. Izui, “EELS analysis of SiC crystals under hydrogen and helium dual-ion beam irradiation,” *Nucl. Instruments Methods Phys. Res. Sect. B Beam Interact. with Mater. Atoms*, vol. 141, no. 1, pp. 148–153, 1998.
- [67] D. Taverna, M. Kociak, O. Stéphan, A. Fabre, E. Finot, B. Décamps, and C. Colliex, “Probing physical properties of confined fluids within individual nanobubbles,” *Phys. Rev. Lett.*, vol. 100, no. 3, p. 35301, Jan. 2008.
- [68] K. Alix, M.-L. David, G. Lucas, D. T. L. Alexander, F. Pailloux, C. Hébert, L. Pizzagalli, “Gentle quantitative measurement of helium density in nanobubbles in silicon by spectrum imaging,” *Micron*, vol. 77, pp. 57–65, 2015.
- [69] W. R. McKenzie, M. Z. Quadir, M. H. Gass, and P. R. Munroe, “Focused Ion beam implantation of diamond,” *Diam. Relat. Mater.*, vol. 20, no. 8, pp. 1125–1128, 2011.
- [70] C. Colliex, M. Kociak, and O. Stéphan, “Electron Energy Loss Spectroscopy imaging of surface plasmons at the nanometer scale,” *Ultramicroscopy*, vol. 162, pp. A1–A24, 2016.
- [71] N. Barberan and J. Bausells, “Plasmon excitation in cavities,” *Solid State Commun.*, vol. 73, no. 9, pp. 651–655, 1990.
- [72] R. v. Baltz, M. Mensch, and H. Zohm, “Longitudinal electric response and loss-function of metallic microspheres and voids,” *Zeitschrift für Phys. B Condens. Matter*, vol. 98, no. 2, pp. 151–161, 1995.
- [73] R. de Haro and J. da Providência, “Excited states in metal voids,” *Phys. Rev. B*, vol. 54, no. 11, pp. 7823–7829, Sep. 1996.
- [74] J. da Providência, “Surface modes in metal clusters and cavities,” *J. Phys. Condens. Matter*, vol. 9, no. 14, pp. 2931–2946, 1997.
- [75] K.-S. D. Wu and D. E. Beck, “Electronic structure and plasma excitations at the surface of small voids in jellium,” *Phys. Rev. B*, vol. 36, no. 2, pp. 998–1006, Jul. 1987.
- [76] L. Serra, F. Garcías, J. Navarro, N. Barberán, M. Barranco, and M. Pi, “Electronic surface excitations of cavities in metals,” *Phys. Rev. B*, vol. 46, no. 15, pp. 9369–9379, Oct. 1992.
- [77] J. A. Scholl, A. L. Koh, and J. A. Dionne, “Quantum plasmon resonances of individual metallic nanoparticles,” *Nature*, vol. 483, no. 7390, pp. 421–427, 2012.
- [78] E. Prodan, C. Radloff, N. J. Halas, and P. Nordlander, “A Hybridization Model for the Plasmon Response of Complex Nanostructures,” *Science (80-.)*, vol. 302, no. 5644, pp. 419 LP – 422, Oct. 2003.
- [79] A. A. Lucas, A. Ronveaux, M. Schmeits, and F. Delanaye, “Van der Waals energy between voids in dielectrics,” *Phys. Rev. B*, vol. 12, no. 12, pp. 5372–5380, Dec. 1975.
- [80] A. A. Lucas, “Plasmon Cohesive Energy of Voids and Void Lattices in Irradiated Metals,” *Phys. Rev. B*, vol. 7, no. 8, pp. 3527–3537, Apr. 1973.
- [81] A. L. Koh, K. Bao, I. Khan, W. E. Smith, G. Kothleitner, P. Nordlander, S. A. Maier, and D. W. McComb, “Electron energy-loss spectroscopy (EELS) of surface plasmons in single silver nanoparticles and dimers: Influence of beam damage and mapping of dark modes,” *ACS Nano*, vol. 3, no. 10, pp. 3015–3022, Oct. 2009.
- [82] N. W. Ashcroft and N. D. Mermin, *Solid State Physics*. Cengage Learning, 2011.
- [83] E. Hayward and C. Deo, “Synergistic effects in hydrogen–helium bubbles,” *J. Phys. Condens. Matter*, vol. 24, no. 26, p. 265402, 2012.

- [84] M. Roldán, P. Fernández, R. Vila, A. Gómez-Herrero, and F. J. Sánchez, “The effect of triple ion beam irradiation on cavity formation on pure EFDA iron,” *J. Nucl. Mater.*, vol. 479, pp. 100–111, 2016.
- [85] D. Brimbal, L. Beck, O. Troeber, E. Gaganidze, P. Trocellier, J. Aktaa, R. Lindau, “Microstructural characterization of Eurofer-97 and Eurofer-ODS steels before and after multi-beam ion irradiations at JANNUS Saclay facility,” *J. Nucl. Mater.*, vol. 465, pp. 236–244, 2015.
- [86] K. Morishita, R. Sugano, and B. D. Wirth, “MD and KMC modeling of the growth and shrinkage mechanisms of helium–vacancy clusters in Fe,” *J. Nucl. Mater.*, vol. 323, no. 2, pp. 243–250, 2003.
- [87] K. Morishita, R. Sugano, B. D. Wirth, and T. Diaz de la Rubia, “Thermal stability of helium–vacancy clusters in iron,” *Nucl. Instruments Methods Phys. Res. Sect. B Beam Interact. with Mater. Atoms*, vol. 202, pp. 76–81, 2003.
- [88] C.-C. Fu and F. Willaime, “Ab initio study of helium in alpha-Fe: Dissolution, migration, and clustering with vacancies,” *Phys. Rev. B*, vol. 72, no. 6, p. 64117, Aug. 2005.
- [89] G. Lucas and R. Schäublin, “Stability of helium bubbles in alpha-iron: A molecular dynamics study,” *J. Nucl. Mater.*, vol. 386–388, pp. 360–362, 2009.
- [90] B. Irigoyen, R. Ferullo, N. Castellani, and A. Juan, “The interaction of hydrogen with an Fe vacancy: a molecular orbital simulation,” *J. Phys. D. Appl. Phys.*, vol. 29, no. 5, pp. 1306–1309, 1996.
- [91] E. Hayward and C. Deo, “Energetics of small hydrogen–vacancy clusters in bcc iron,” *J. Phys. Condens. Matter*, vol. 23, no. 42, p. 425402, 2011.
- [92] C. J. Ortiz, R. Vila, and J. M. Pruneda, “Ab initio study of helium and hydrogen interactions in alpha-Fe,” *arXiv:1205.6374v2 [cond-mat.mtrl-sci]*, 2012.
- [93] V. V Kirsanov, M. V Musina, and V. V Rybin, “The influence of hydrogen on the formation of helium vacancy voids in metal,” *J. Nucl. Mater.*, vol. 191–194, pp. 1318–1322, 1992.
- [94] V. A. Borodin and P. V Vladimirov, “Diffusion coefficients and thermal stability of small helium–vacancy clusters in iron,” *J. Nucl. Mater.*, vol. 362, no. 2, pp. 161–166, 2007.
- [95] M. J. Fluss, L. L. Hsiung, and J. Marian, “Dual and Triple Ion-Beam Irradiations of Fe, Fe(Cr) and Fe(Cr)-ODS Final Report: IAEA SMORE CRP,” United States, 2011.
- [96] G. S. Was, *Fundamentals of Radiation Materials Science*. New York, NY: Springer New York, 2017.
- [97] R. E. Stoller and Y. N. Osetsky, “An atomistic assessment of helium behavior in iron,” *J. Nucl. Mater.*, vol. 455, no. 1, pp. 258–262, 2014.
- [98] A. Caro, J. Hetherly, A. Stukowski, M. Caro, E. Martinez, S. Srivilliputhur, L. Zepeda-Ruiz, M. Nastasi, “Properties of helium bubbles in Fe and FeCr alloys,” *J. Nucl. Mater.*, vol. 418, no. 1, pp. 261–268, 2011.
- [99] V. Krsjak, J. Kuriplach, T. Shen, V. Sabelova, K. Sato, and Y. Dai, “Helium behavior in ferritic/martensitic steels irradiated in spallation target,” *J. Nucl. Mater.*, vol. 456, pp. 382–388, 2015.

Chapter 5 Accumulation of helium and hydrogen in a model bi-layer $Y_2O_3/FeCr$ system

The development of predictive models of ODS steel performance in irradiation conditions requires clear understanding of the mechanisms involved in the interaction of transmutation and/or directly implanted gases (helium, hydrogen) with nanosized oxide particles. The observations of microstructure evolution under the controlled gas introduction in industrial ODS steel discussed in chapters 3 and 4 contribute to further clarification of this understanding and, in particular, of the details of gas trapping on oxide particles. However, the small size of nano-oxide particles embedded in the massive iron-based matrix is able to impose non-negligible influence on the effects induced by the gas and cavity growth on nano-oxides, making their interpretation uncertain.

For example, the results of chapter 3 indicate that in all studies He^+ implantation regimes the nanoparticle-matrix interfaces serve as efficient nucleation sites for He-filled cavity nucleation and growth. However, that is not clear whether this observation can be interpreted in terms of only the efficient capture and transport of helium atoms at the particle-matrix interface, or is affected, as suggested by some first-principles simulations, by simultaneous He accumulation in the oxide particle itself. If the latter is true, one needs more detailed information on the mechanisms of helium accumulation and partitioning in the oxide, the matrix, and the associated interfacial features, such as He bubbles in order to reliably predict the helium inventory and the kinetics of bubble growth on oxide nanoparticles. The latter is, in turn, important for specifying the conditions (in terms of particle size and the environmental temperature) to prevent undesirable effects, such as bubble-to-void transition experimentally observed in the current study (see sections 3.2 and 3.3).

The potential role of hydrogen in the gas bubble development associated with oxide particles is also hard to understand based on the reported TEM investigations of ODS-EUROFER samples sequentially implanted with He^+ and H^+ ions. While it has been demonstrated that, at least at room temperature, H^+ implantation results in clearly detectable effects, such as the development of ~1 nm in size bubble arrays in the bulk and on oxide particles, or the smoothing of faceted bubble shape, it is less clear whether the increase of the bubble size during high-temperature H^+ implantation is due to the effect of hydrogen itself or to the acceleration of He diffusion via additional production of radiation damage.

One more open question concerns the role of oxide particles in the more efficient hydrogen accumulation in ODS-EUROFER steel as compared to its non-ODS reference EUROFER 97, as reported in section 4.2 of the manuscript. The observation can be ascribed to either the lower grain size of ODS-steel or the presence of high density of oxide nanoparticles. The performed analysis did not allow definite separation of relative contributions of these two microstructural features to the total hydrogen uptake.

In order to better understand the mechanisms involved in the microstructural development at and close to the metal/oxide interface during irradiation and/or gas accumulation, we have followed the approach recently implemented by several research groups [1–5]. This approach includes ion implantation and subsequent TEM investigation of model mesoscopic-scale bi-layer systems, providing enhanced control over the metal/oxide interfacial effects promoted by radiation and/or gas accumulation. Adopting this approach, we pursued four main purposes:

- To differentiate between the effects on microstructure development from radiation defect production and helium/hydrogen accumulation in systems with the metal/oxide interfaces;
- To study the differences in helium partitioning between metal, interface and oxide at room and elevated temperature;
- To investigate possible hydrogen partitioning between metal, interface and oxide;
- To search for synergetic effects of helium and hydrogen on microstructural development in systems with the metal/oxide interfaces.

The experimental approach used in this study was as follows. First of all, thin films consisting of pure Y_2O_3 compound and Fe-10at%Cr binary alloy were sequentially deposited onto different single-crystal ceramic substrates (MgO, SrTiO₃, and yttria-stabilized zirconia (YSZ)) combining the reactive MS deposition of Y elemental target in oxygen atmosphere with MBE deposition of elemental Fe and Cr metals using thermal effusion. The best Y_2O_3 /FeCr bi-layer films were obtained using SrTiO₃ (100) substrate, where the epitaxy of metal/oxide interface was achieved at least partially. The microstructural characterization of as-fabricated thin films is given in details in section 2.1.2.2. These samples were used for subsequent ion implantations.

Ion implantation was performed normally to the bi-layer sample surface in four different implantation/irradiation regimes, including:

- single-beam He⁺ ion implantation to the fluence of 1×10^{17} cm⁻² at room temperature and at 823 K;
- single-beam H⁺ ion implantation to the fluence of 2×10^{17} cm⁻² at RT;
- implantation with He⁺ ions to the fluence of 1×10^{17} cm⁻² at RT followed by H⁺ implantation to the fluence of 2×10^{17} cm⁻² at RT;
- heavy ion irradiation in transmission with Kr⁺ ions to the fluence of 3.6×10^{15} cm⁻² at RT.

He⁺ and H⁺ ion implantations were performed normally to the surface of the top Fe-10%Cr film. The energies for He⁺ and H⁺ ions were selected so as to obtain the peaks of implanted ion concentration close to the interface between Fe-10%Cr and Y_2O_3 thin films. For Kr⁺ ions irradiation, energy, flux and fluence of irradiating ions were selected so as to obtain dose rate and accumulated dose similar to the single-beam He⁺ implantation and, at the same time, to minimize Kr concentration in the region of interest. For the details of ion implantation/irradiation see section 2.2.3.5.

After implantation/irradiation, cross-section TEM samples were prepared by FIB lift-out technique (see section 2.1.2.3) and were investigated by TEM in BF TEM and HRTEM regimes. The chapter presents the results of these TEM investigations in sections 5.1-5.4, where each section comprises the data for that or other implantation regime as outlined above.

Finally, section 5.5 provides a discussion of TEM observations on helium and hydrogen partitioning between FeCr, interface and yttria and their rationalization in terms of the first principles simulation data available in the literature. The observed trends of microstructural development in model bi-layer system in different implantation regimes are correlated to those observed in industrial ODS-steels.

5.1 Microstructural development in bi-layer $\text{Y}_2\text{O}_3/\text{FeCr}$ system after single-beam He^+ ion implantation at room and elevated temperature

5.1.1 He^+ ion implantation at room temperature

Typical BF TEM through-focus images of a model bi-layer $\text{Y}_2\text{O}_3/\text{FeCr}$ system implanted at room temperature to the fluence of $1 \times 10^{17} \text{ cm}^{-2}$ are shown in Fig. 5.1(a-b).

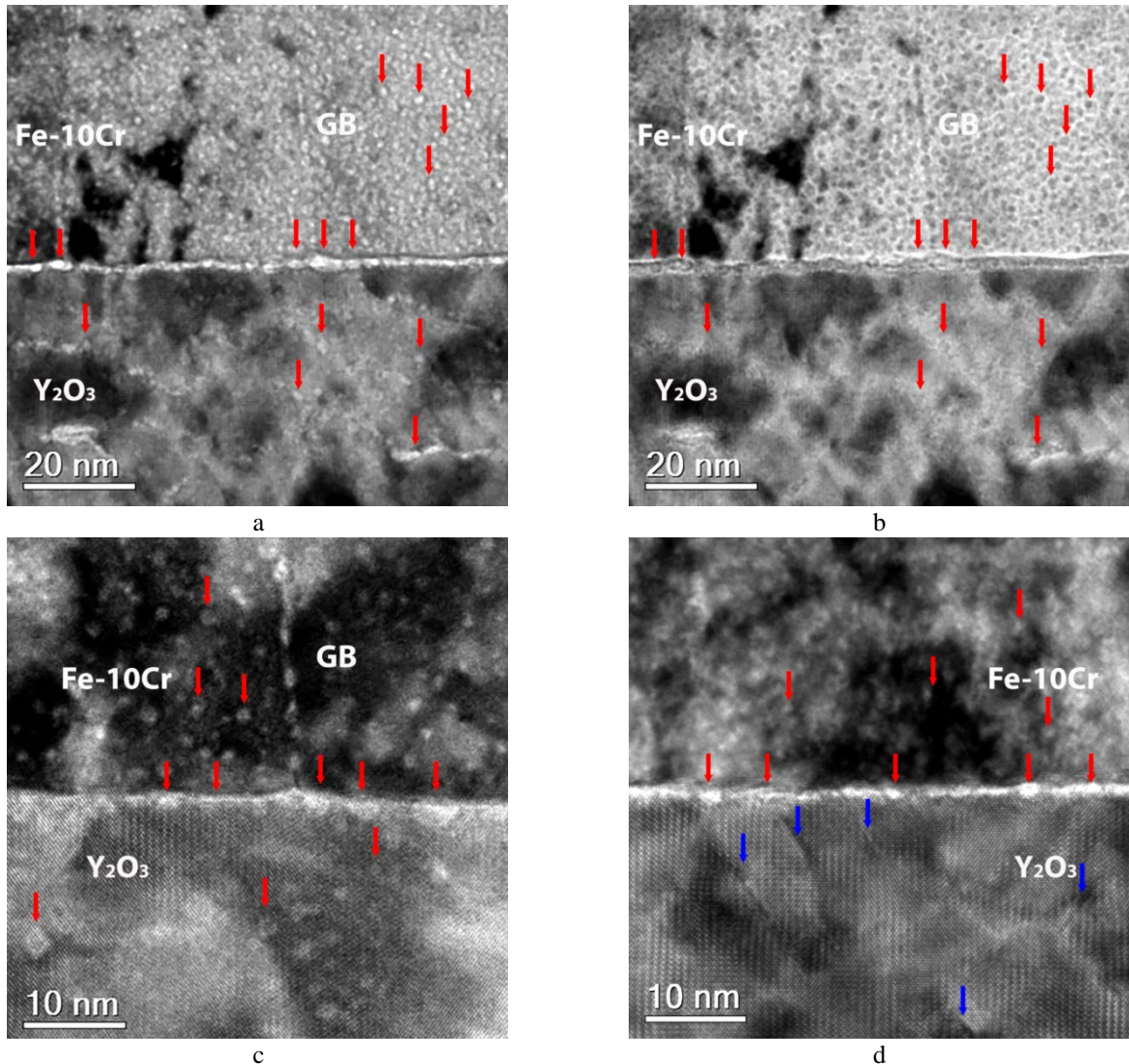


Fig. 5.1. Microstructure of a model bi-layer $\text{Y}_2\text{O}_3/\text{FeCr}$ system implanted at RT with 17 keV He^+ ions with the flux of $7 \times 10^{12} \text{ cm}^{-2} \text{ s}^{-1}$ to the fluence of $1 \times 10^{17} \text{ cm}^{-2}$: (a,b) through-focus image pair; (c) cavities at higher magnification; and (d) planar defects in Y_2O_3 layer at higher magnification. Red arrows denote cavities in all parts of the bi-layer system. Blue arrows denote planar defects in Y_2O_3 layer. BF TEM imaging conditions: (a) $\sim 0.6 \mu\text{m}$ underfocus; (b) $\sim 0.6 \mu\text{m}$ overfocus; (c,d) $\sim 0.3 \mu\text{m}$ underfocus.

Characteristic change in Fresnel contrast from the overfocus to underfocus conditions in Fig. 5.1(a,b) indicates cavities are present in Fe-10Cr and Y_2O_3 layers and at the interface between them after helium implantation at RT. Cavities at the interface are visibly larger than those inside of the Fe-10Cr or Y_2O_3 layers. In the Fe-10Cr layer, spherical cavities are uniformly distributed inside the grain bulk and clearly decorate grain boundaries. In contrast, cavities in the Y_2O_3 layer are faceted and aligned along some defects which are roughly parallel to the interface. Interfacial region of the bi-layer $\text{Y}_2\text{O}_3/\text{FeCr}$ is shown in Fig. 5.1(c) at higher magnification. As can be seen, the cavities located in the grain bulk and at grain boundaries of the Fe-10Cr film have similar sizes and both are typically smaller

than cavities at the $Y_2O_3/FeCr$ interface. The interfacial cavities more pronouncedly protrude into yttria layer than into the Fe-10Cr one. The distance between cavities at the interface seems to be noticeably smaller than between cavities inside either layer. When compared between the layers, the number density of cavities in Fe-10Cr looks higher than in Y_2O_3 . However the result of TEM observation of cavity size and number density in different parts of model bi-layer $Y_2O_3/FeCr$ system should be confirmed by quantitative analysis which considers the local thickness of sample when estimating the number density. In addition to cavities, another feature with lamellar shape and a characteristic contrast was observed in Y_2O_3 layer (see Fig. 5.1(d)).

HRTEM cross-sectional image taken close to $[110]$ zone axis and corresponding Fast Fourier Transform (FFT) image of a single faceted cavity in Y_2O_3 layer of the model $Y_2O_3/FeCr$ system implanted at RT to the fluence of $1 \times 10^{17} \text{ cm}^{-2}$ are shown in Fig. 5.2(a). As can be seen, cavities in Y_2O_3 layer demonstrate rhombic shape with facets parallel to $\{111\}$ planes. Taking into account that (111) plane is the lowest surface energy plane in the bixbyite structure of Y_2O_3 [6], the 3-dimensional shape of observed cavities is most probably an octahedral one.

Fig. 5.2(b) shows HRTEM cross-sectional image taken close to $[110]$ zone axis and corresponding FFT of the planar defect in Y_2O_3 layer shown in Fig. 5.1(d). The planar defect is located on $\{111\}$ plane. Such kind of planar defects in irradiated Y_2O_3 thin films was reported earlier in Refs. [7–9], where they were interpreted as dislocation loops on the anion sublattice. Such loops are presumably formed [7–9] as a result of clustering of irradiation-generated anion vacancies into discs on $\{111\}$ planes, followed by collapse of the surrounding lattice along the $\langle 111 \rangle$ direction and crystallographic shear along $\langle 211 \rangle$ direction. The resulting vacancy dislocation loops have Burgers vectors of the type $\mathbf{b} = \frac{a_0}{2} \langle 001 \rangle$, where $a_0 = 10.604 \text{ \AA}$ is the lattice parameter of the bixbyite Y_2O_3 structure. Being located on the anion sublattice, such vacancy loops do not affect ordering of yttrium atoms and thus do not distort notably the yttrium planes that are solely visible in HRTEM images due to the low electron scattering of oxygen. The lack of yttria pattern damage in our HRTEM images is strongly suggestive that the observed planar features in our case should be interpreted as anion vacancy dislocation loops.

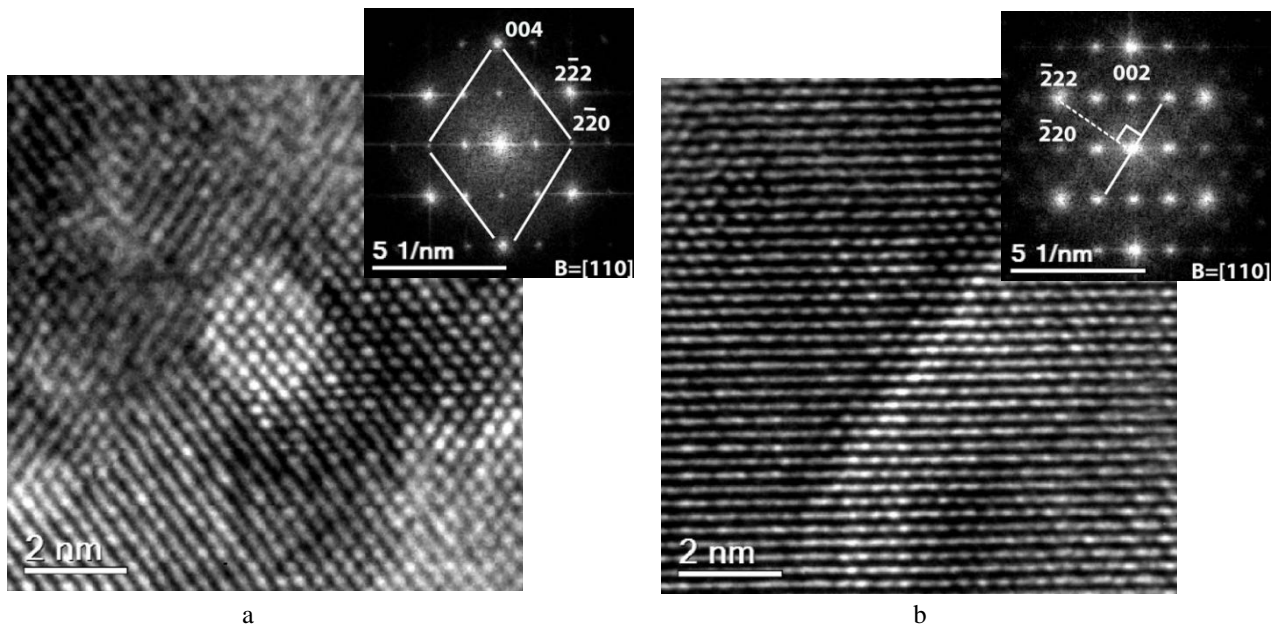


Fig. 5.2. HRTEM cross-sectional image of Y_2O_3 film after implantation of the model bi-layer $Y_2O_3/FeCr$ sample with 17 keV He^+ ions at RT with the flux of $7 \times 10^{12} \text{ cm}^{-2} \text{ s}^{-1}$ to the fluence of $1 \times 10^{17} \text{ cm}^{-2}$: (a) faceted cavity; (b) planar defect observed on $\{111\}$ plane. BF imaging conditions: $\sim 0.2 \text{ \mu m}$ underfocus.

Statistical analysis of cavity parameters inside Fe-10Cr and Y₂O₃ layers and on the interface follows the approach described in section 3.1.2.1. The specific cavity number densities $\langle N_c^k \rangle$ for the bulk of Fe-10Cr and Y₂O₃ layers are determined similar to N_c^V and for the interface is similar to $\langle N_c^{GB} \rangle$ (in this chapter $k = \text{Me, Ox, and Int}$ for cavities inside Fe-10Cr, Y₂O₃ and at the interface, respectively). It should be noted that the specific cavity number density at the interface cannot be converted into the number density normalized per unit sample volume. Therefore, only the calculated specific cavity number densities inside the layers can be compared directly. Table 5.1 summarizes statistical analysis results of cavity specific number densities and effective diameters inside both layers and at the interface. Errors given for $\langle N_c^k \rangle$ and $\langle D_c^k \rangle$ have the same meaning as in chapter 3.

Table 5.1. Statistical cavity ensemble parameters in the model bi-layer Y₂O₃/FeCr sample implanted with 17 keV He⁺ ions at RT with the flux of $7 \times 10^{12} \text{ cm}^{-2} \text{ s}^{-1}$ to the fluence of $1 \times 10^{17} \text{ cm}^{-2}$.

	Fe-10Cr film	Interface	Y₂O₃ film
$\langle D_c^k \rangle (\text{nm})$	2.02±0.23	4.10±0.42	3.28±0.35
$\langle N_c^k \rangle$	$(28.64 \pm 6.23) 10^{23} \text{ m}^{-3}$	$(9.98 \pm 1.00) 10^{15} \text{ m}^{-2}$	$(5.37 \pm 0.87) 10^{23} \text{ m}^{-3}$

The results of statistical analysis confirm the qualitative trend directly visible in TEM images, that is, significant difference of cavity sizes and number densities in different parts of model bi-layer Y₂O₃/FeCr system. The largest average effective diameter of ~4 nm is observed for the interfacial cavities. Despite the similar He content in the middle parts of both individual layers (of ~8 at. %), the cavities in Fe-10Cr are typically smaller than in yttria. The cavity number densities in the layers are also notably different; cavity number density in the Fe-10Cr layer is ~4 times higher than in the Y₂O₃ layer. Taking into account that He⁺ implantation was performed at room temperature and that He diffusivity at this temperature is low, no significant helium re-distribution between layers or desorption out of them are expected. Hence, the calculated values of average effective diameters and number densities suggest that the part of the implanted helium that is dissolved in the lattice or captured inside features (e.g. He-V clusters) invisible by TEM (which are always present after high dose helium implantation, see section 3.1.2.5.5) is notably larger for the oxide than for the metal part of the investigated system. Finally, even though the specific number densities of cavities inside the layers and at the interface cannot be compared directly, the abundance of relatively large cavities at the interface suggests that FeCr/Y₂O₃ interface is a favorable place for He-filled cavity formation as compared to the inner parts of layers.

5.1.2 He⁺ ion implantation at 823 K

As discussed in chapter 1 of this manuscript, industrial ODS-steels are planned to be used in future fission (Gen. IV) and fusion facilities with high operation temperatures (ranging within 723-923 K). Taking this into account, the response of the model oxide-metal bi-layer system to He accumulation at high temperatures was studied using He⁺ implantation at 823 K with the same ion energy, flux and fluence as in section 5.1.1.

Fig. 5.3(a,b) shows typical BF TEM cross-sectional through-focus images of model bi-layer Y₂O₃/FeCr system implanted at 823 K to the fluence of $1 \times 10^{17} \text{ cm}^{-2}$.

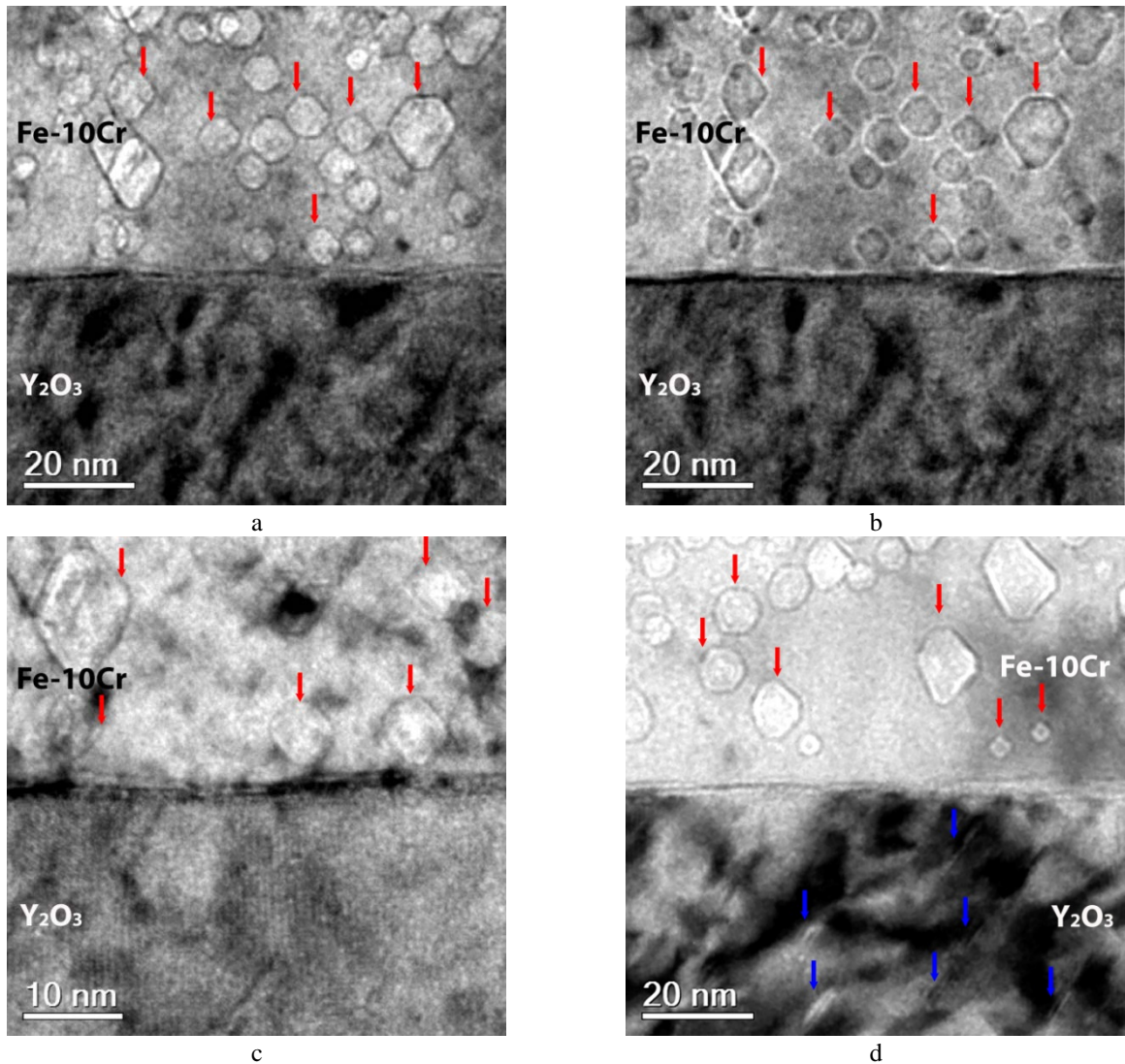


Fig. 5.3. (a,b) Microstructure of a model bi-layer $\text{Y}_2\text{O}_3/\text{FeCr}$ system implanted at 823 K with 17 keV He^+ ions with the flux of $7 \times 10^{12} \text{ cm}^{-2}\text{s}^{-1}$ to the fluence of $1 \times 10^{17} \text{ cm}^{-2}$. (c) Cavities at higher magnification. (d) Anion dislocation loops in the Y_2O_3 film. Red arrows denote cavities in the Fe-10Cr layer, while blue arrows in panel (d) denote dislocation loops in the Y_2O_3 layer. BF TEM imaging conditions: (a) $\sim 0.5 \mu\text{m}$ underfocus; (b) $\sim 0.5 \mu\text{m}$ overfocus; (c) $\sim 0.3 \mu\text{m}$ underfocus; and (d) $\sim 0.6 \mu\text{m}$ underfocus.

TEM images shown in Fig. 5.3 indicate no cavity formation either at the interface or inside of the Y_2O_3 layer after He^+ implantation at 823 K. In contrast, very large cavities are clearly visible in Fe-10Cr layer both at the grain boundaries and inside the grains. All the observed cavities have characteristic faceted shape. The interfacial region of the studied system at higher magnification is shown in Fig. 5.3(c) under BF TEM underfocused conditions. Even at this magnification, no evidence of cavity formation at the interface or inside Y_2O_3 layer can be found. However, similar to He^+ implantation at room temperature, the formation of anion vacancy dislocation loops inside Y_2O_3 film takes place (see Fig. 5.3(d)).

Fig. 5.4 shows HRTEM cross-sectional image taken close to [001] zone axis, which shows in detail a single faceted cavity and corresponding FFT pattern in the Fe-10Cr layer. As can be seen, cavity facets are lying on $\{100\}$ planes. A similar alignment of He-filled cavity faces was demonstrated earlier for ODS-EUROFER steel implanted to the fluence of $1 \times 10^{16} \text{ cm}^{-2}$ (see section 3.1.2.2) and is common for both voids and He bubbles in *bcc* Fe and Fe-Cr alloys [10,11].

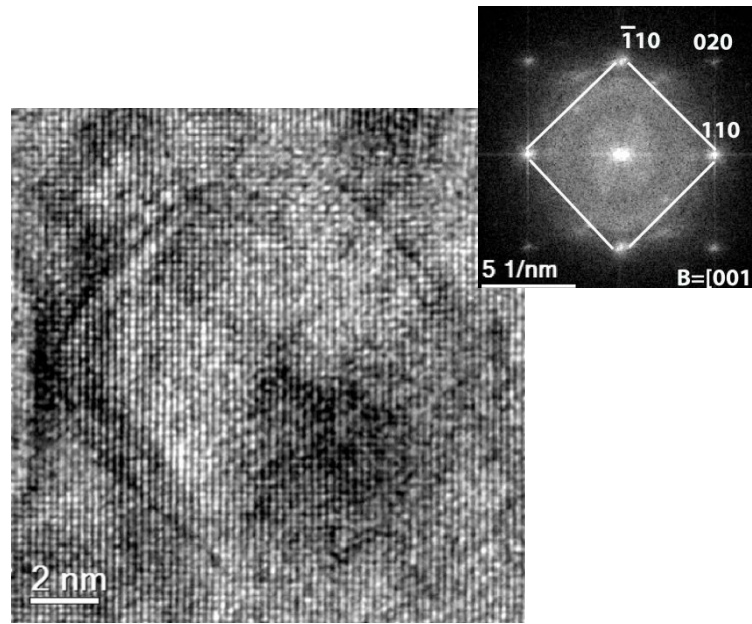


Fig. 5.4. HRTEM image of a faceted cavity in Fe-10Cr film after implantation of the model $Y_2O_3/FeCr$ bi-layer system at 823 K with 17 keV He^+ ions with the flux of $7 \times 10^{12} \text{ cm}^{-2} \text{ s}^{-1}$ to the fluence of $1 \times 10^{17} \text{ cm}^{-2}$. BF imaging conditions: $\sim 0.2 \mu\text{m}$ underfocus.

The results of statistical analysis of cavity parameters in the $Y_2O_3/FeCr$ bi-layer system implanted at 823 K with 17 keV He^+ ions to the fluence of $1 \times 10^{17} \text{ cm}^{-2}$ are given in Table 5.2.

Table 5.2. Number densities and average diameters of cavities in the model bi-layer $Y_2O_3/FeCr$ sample implanted at 823 K with 17 keV He^+ ions with the flux of $7 \times 10^{12} \text{ cm}^{-2} \text{ s}^{-1}$ to the fluence of $1 \times 10^{17} \text{ cm}^{-2}$.

	Fe-10Cr film	Interface	Y_2O_3 film
$\langle D_c^k \rangle (\text{nm})$	7.81 ± 0.81	-	-
$\langle N_c^k \rangle$	$(2.35 \pm 0.41) 10^{23} \text{ m}^{-3}$	-	-

The observed trends in the evolution of cavity population in different parts of the studied bi-layer system in reply to the change of implantation temperature can be summarized as follows:

- In the Fe-10Cr layer, the mean cavity size increases from $D_c^{Me} \approx 2 \text{ nm}$ to $D_c^{Me} \approx 8 \text{ nm}$ and the cavity number density decreases from $N_c^{Me} \approx 29 \times 10^{23} \text{ m}^{-3}$ down to $N_c^{Me} \approx 2.5 \times 10^{23} \text{ m}^{-3}$ as the implantation temperature increases from room temperature to 823 K. This trend is qualitatively in agreement with that observed in the experiments on He^+ implantation into ODS-EUROFER steel, as described in Chapter 3.
- In contrast, cavities at the interface and inside of the Y_2O_3 layer are observed only after room temperature implantation and are completely absent after He^+ implantation at 823 K.

5.2 Microstructural development in bi-layer $Y_2O_3/FeCr$ system after single-beam H^+ ion implantation at room temperature

Typical BF TEM trough-focus images of model $Y_2O_3/FeCr$ bi-layer system implanted at RT with H^+ to the fluence of $2 \times 10^{17} \text{ cm}^{-2}$ are shown in Fig. 5.5(a-b). Characteristic change in Fresnel contrast from the overfocus to underfocus conditions in Figs. 5.5(a) and 5.5(b) is indicative of spherical cavities with tiny size and high density in the Fe-10 Cr layer. The $Y_2O_3/FeCr$ interface is found to be heavily decorated with cavities. Hydrogen implantation at room temperature, in contrast to helium room temperature implantation, does not result in cavity nucleation inside the yttria layer. Instead of cavities, microcracks are formed in this region. Microcracks extend along the interface. Anion vacancy dislocation loops are not observed inside the Y_2O_3 layer after hydrogen implantation.

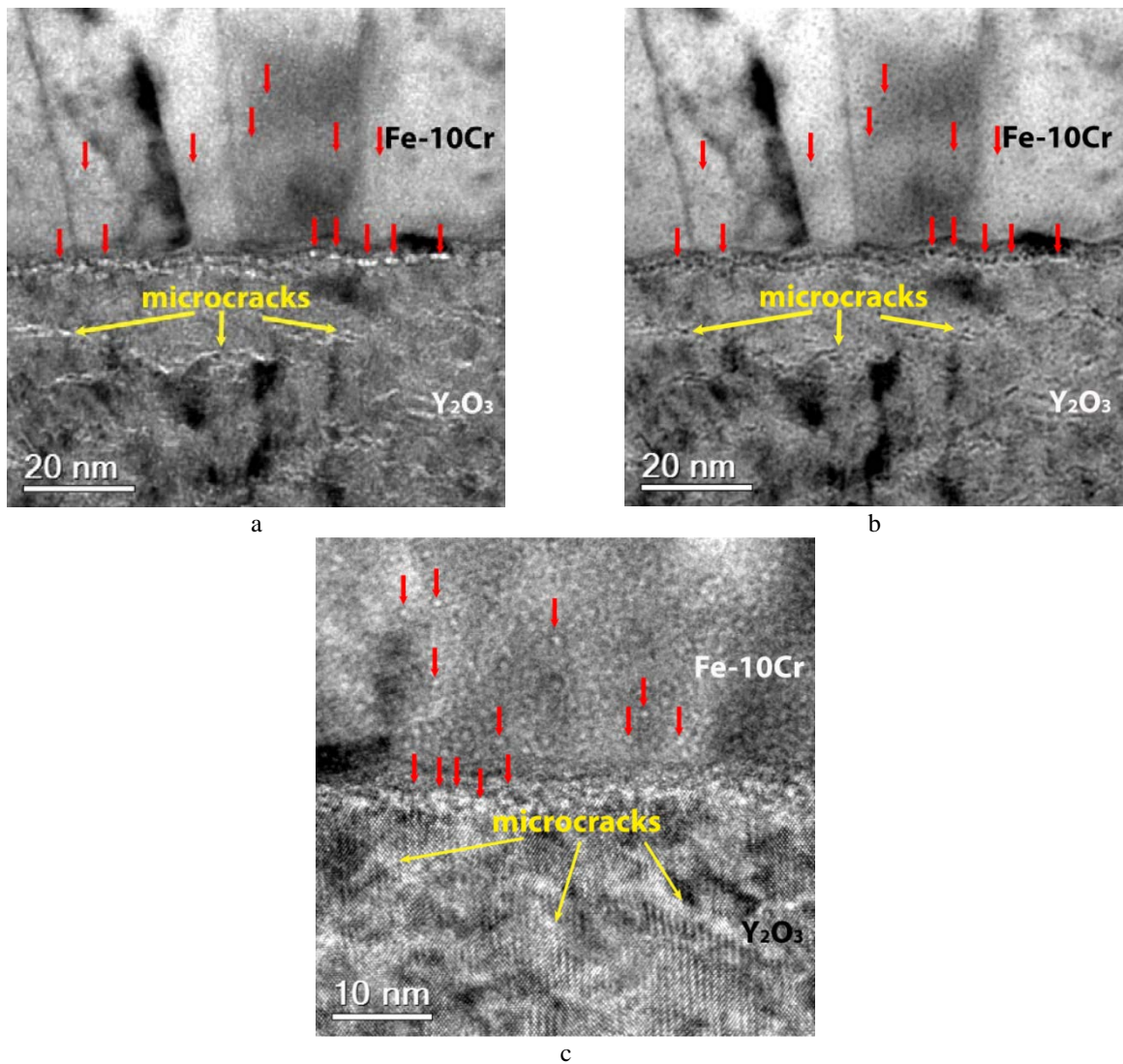


Fig. 5.5. The microstructure of model $Y_2O_3/FeCr$ bi-layer system implanted at RT with 10 keV H^+ ions with the flux of $1 \times 10^{13} \text{ cm}^{-2} \text{ s}^{-1}$ to the of fluence of $2 \times 10^{17} \text{ cm}^{-2}$: (a,b) through-focus image pair; (c) cavities and microcracks at higher magnification. Red arrows denote cavities in the Fe-10Cr film and at the interface of the bi-layer system. Yellow arrows denote microcracks in the Y_2O_3 film. BF TEM imaging conditions: (a) $\sim 0.5 \mu\text{m}$ underfocus; (b) $\sim 0.5 \mu\text{m}$ overfocus; (c) $\sim 0.3 \mu\text{m}$ underfocus.

Interfacial region of bi-layer $Y_2O_3/FeCr$ is shown in Fig. 5.5(c) at high magnification in BF TEM underfocused conditions. Similar to the case of single-beam He^+ implantation at RT, cavities at the interface are visibly larger than those observed in the Fe-10Cr layer. The interfacial cavities nucleated at the metal/oxide interface under H^+ implantation grow towards the oxide layer rather than the metal one.

Table 5.3 summarizes the results of statistical analysis of cavity effective diameter and specific number densities in $Y_2O_3/FeCr$ bi-layer system implanted at RT with H^+ ions to the fluence of $2 \times 10^{17} \text{ cm}^{-2}$. Quantitative analysis shows that interfacial cavities are ~ 3 times larger than cavities inside the Fe-10Cr layer. As compared to single-beam He^+ implantation at RT, the average effective diameter of interfacial cavities, D_c^{Int} , after H^+ implantation is $\sim 30\%$ smaller and that of cavities inside the Fe-10Cr layer, D_c^{Me} , is almost 2 times smaller. Specific cavity number density at the interface after H^+ implantation is $\sim 50\%$ higher than that observed after single-beam He^+ implantation. At the same time, the density of cavities in the metal layer is practically the same, $N_c^{Me} \approx 30 \times 10^{23} \text{ m}^{-3}$, after both He^+ and H^+ implantations at room temperature.

Table 5.3. Statistical analysis of number densities and mean diameters of cavities in the model $Y_2O_3/FeCr$ bi-layer system implanted at RT with 10 keV H^+ ions with the flux of $1 \times 10^{13} \text{ cm}^{-2}\text{s}^{-1}$ to the fluence of $2 \times 10^{17} \text{ cm}^{-2}$.

	Fe-10Cr film	Interface	Y_2O_3 film
$\langle D_c^k \rangle (\text{nm})$	1.14 ± 0.12	3.05 ± 0.35	microcracks
$\langle N_c^k \rangle$	$(34.77 \pm 3.56) 10^{23} \text{ m}^{-3}$	$(1.57 \pm 0.17) 10^{16} \text{ m}^{-2}$	

Fig. 5.6 presents a HRTEM cross-sectional image taken close to $[110]$ zone axis and showing multiple microcracks and a corresponding FFT pattern in the yttria layer of the model $Y_2O_3/FeCr$ bi-layer system implanted at RT with H^+ ions to the fluence of $2 \times 10^{17} \text{ cm}^{-2}$. A closer look shows that despite the micro-crack extension along the interface, the fracture occurs on planes distinct from $\{001\}$. From presented HRTEM image and FFT one can conclude that microcracks in yttrium oxide lie on $\{111\}$ type planes. Thus, crystallographic orientations of microcracks are the same as those of anion dislocation loops detected above in both He^+ implantation regimes. While no anion dislocation loops are observed after H^+ implantation, one cannot exclude that the formation of cracks is promoted by vacancy loops, e.g. as a result of hydrogen accumulation in them.

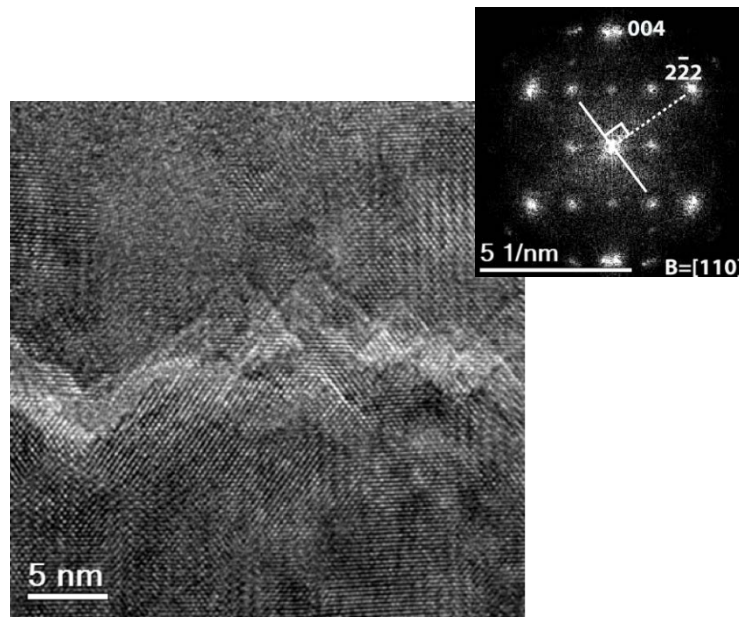


Fig. 5.6. HRTEM image $\sim 0.2 \mu\text{m}$ underfocus of microcrack in the Y_2O_3 layer of the model $Y_2O_3/FeCr$ bi-layer system after implantation with 10 keV H^+ ions at RT with the flux of $1 \times 10^{13} \text{ cm}^{-2}\text{s}^{-1}$ to the fluence of $2 \times 10^{17} \text{ cm}^{-2}$.

5.3 Microstructural development in bi-layer $Y_2O_3/FeCr$ system after sequential dual-beam implantation with He^+ and H^+ ions at room temperature

In section 4.1 it was reported that H^+ implantation of He pre-implanted industrial ODS-steel samples at RT promotes the appearance of $\sim 1 \text{ nm}$ large bubbles and suppresses bubble faceting. However, no major influence of implanted hydrogen on bubble population evolution (including the bubbles at the oxide particle/matrix interface) and overall swelling was noticed. TEM investigations do not allow definitely confirming or denying the presence of hydrogen inside bubbles of any kind and its potential influence on swelling. In order to get a deeper insight, the He pre-implanted samples of model $Y_2O_3/FeCr$ bi-layer system (see section 5.1) were additionally implanted at RT with H^+ ions to the fluence of $2 \times 10^{17} \text{ cm}^{-2}$, which is notably larger than that used in section 4.1.

Fig. 5.7(a) shows a low-magnification underfocused BF TEM image of the model $Y_2O_3/FeCr$ bi-layer system after room-temperature 17 keV He^+ implantation to the fluence of $1 \times 10^{17} \text{ cm}^{-2}$ followed by 10 keV H^+ implantation to the fluence of $2 \times 10^{17} \text{ cm}^{-2}$. It can be easily noticed that H^+ implantation leads to layer decohesion and blister formation at the interface between Fe-10Cr and Y_2O_3 layers.

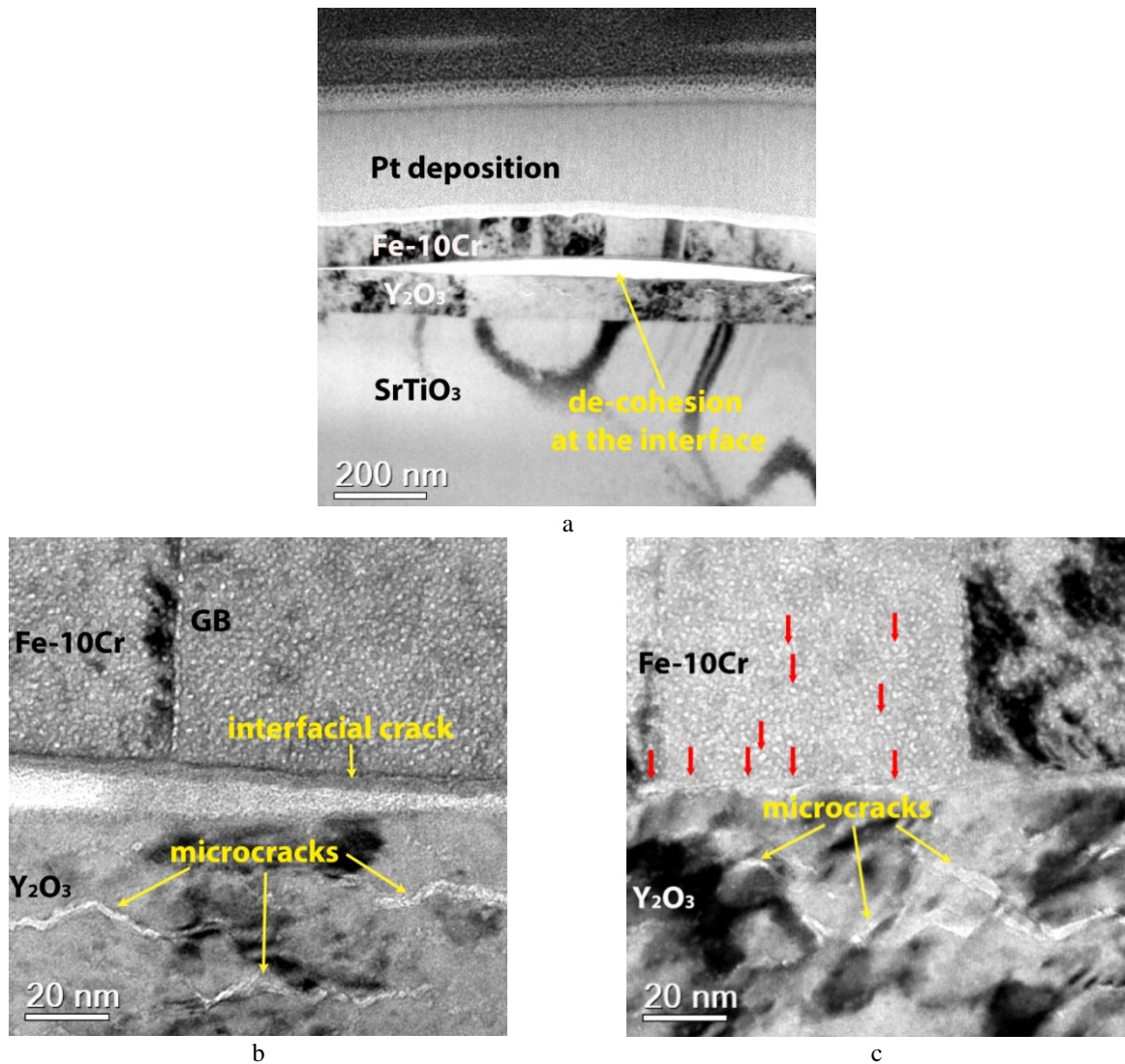


Fig. 5.7. The microstructure of the model $\text{Y}_2\text{O}_3/\text{FeCr}$ bi-layer system after sequential room temperature implantation with 17 keV He^+ ions with a flux of $7 \times 10^{12} \text{ cm}^{-2} \text{ s}^{-1}$ to the fluence of $1 \times 10^{17} \text{ cm}^{-2}$ and then with 10 keV H^+ ions with a flux of $1 \times 10^{13} \text{ cm}^{-2} \text{ s}^{-1}$ to the fluence of $2 \times 10^{17} \text{ cm}^{-2}$: (a) low-magnification view; (b) decohesion area; and (c) area without decohesion. Red arrows denote cavities in Fe-10Cr film and at the interface, while yellow arrows mark microcracks in the Y_2O_3 film and decohesion at the interface. BF TEM imaging conditions: (a) $\sim 1 \mu\text{m}$ underfocus; (b,c) $\sim 0.5 \mu\text{m}$ underfocus.

Typical BF TEM underfocused images of the decohesion area and an area without it are given in Figs. 5.7(b) and 5.7(c), respectively. The introduction of hydrogen into helium pre-implanted bi-layer system affects not only the metal/oxide interface but also the other parts of the system. Similar to the case of room temperature single-beam H^+ implantation into as-fabricated bi-layer, microcracks were formed inside the Y_2O_3 layer after the sequential He^+/H^+ implantation. In the area where interfacial decohesion does not occur, cavities at the interface, inside the Fe-10Cr grains, and at the Fe-10Cr grain boundaries were slightly larger than those observed after single-beam He^+ pre-implantation at RT. No noticeable change of cavity shapes was found after H^+ introduction for either interfacial cavities or cavities inside the Fe-10Cr layer.

Fig. 5.8(a-e) demonstrates elemental distributions in the decohesion region of the model $\text{Y}_2\text{O}_3/\text{FeCr}$ bi-layer system obtained by EDX together with a high angular annular dark field (HAADF) STEM image of the area used for the elemental mapping.

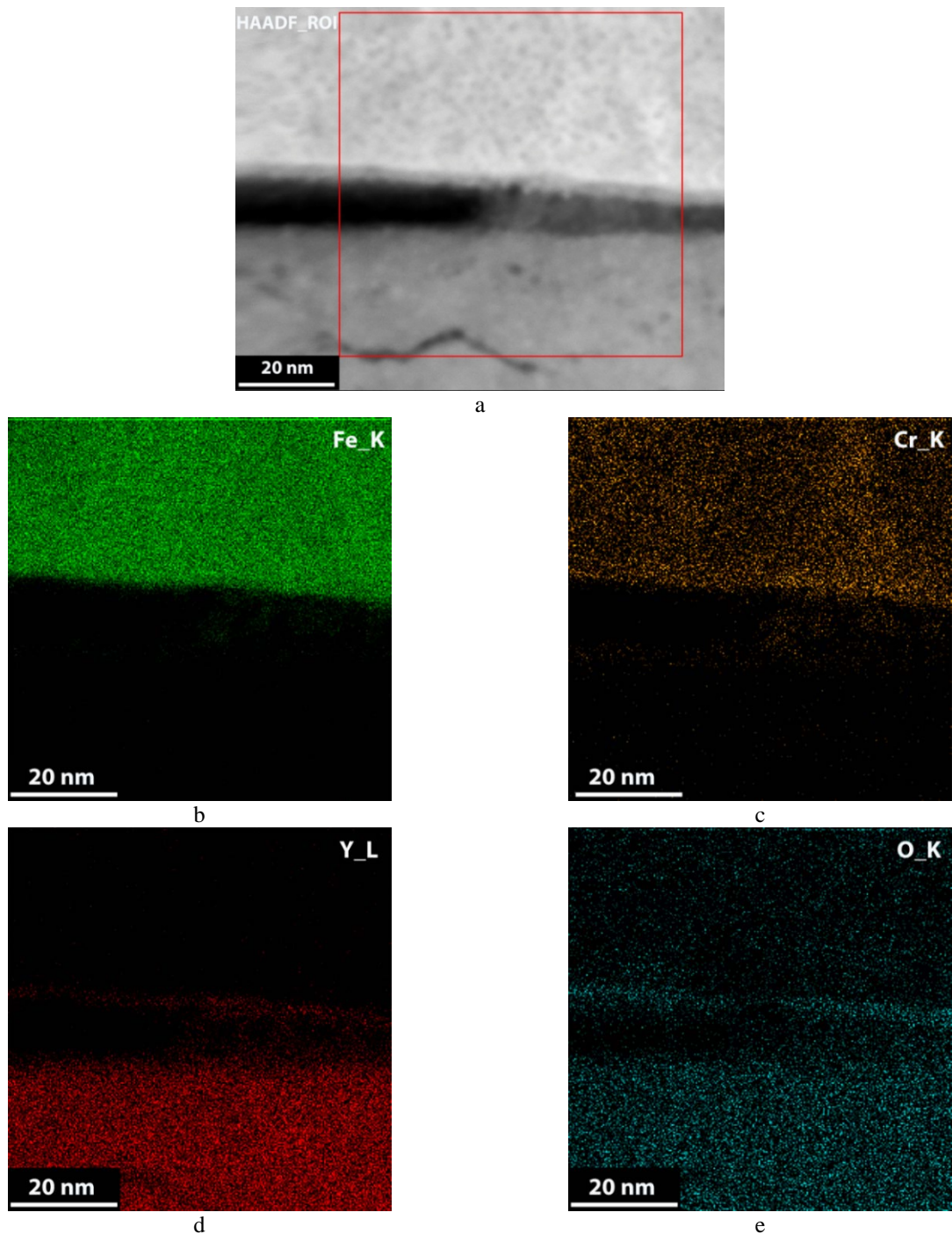


Fig. 5.8. EDX elemental mapping of the model $Y_2O_3/FeCr$ bi-layer system after RT sequential implantation with 17 keV He^+ ions to the fluence of $1 \times 10^{17} \text{ cm}^{-2}$ and 10 keV H^+ ions to the fluence of $2 \times 10^{17} \text{ cm}^{-2}$ at the decohesion area: (a) HAADF image of the area used for the elemental mapping; (b) iron elemental distribution; (c) chromium elemental distribution; (d) yttrium elemental distribution; (e) oxygen elemental distribution.

It can be noticed that on the top side of decohesion area (blister) one finds the enrichment not only in chromium (which segregates at the interface, see section 2.1.2.2) and possibly oxygen, but also in yttrium. As shown in section 5.1, single-beam He^+ pre-implantation at room temperature results in cavities at the metal/oxide interface that grow into the oxide layer rather than into the metal. Taking this into account, the observation of yttrium at the top side of the blister indicates that decohesion is somehow related to the presence of He-filled cavities formed during He^+ pre-implantation. In particular, blister formation can result from helium bubble coalescence [12,13] that leads to cracking at the interface. The decohesion is obviously triggered by hydrogen introduced into the interfacial area by secondary implantation, though the particular mechanism remains unclear; it can be related e.g. to pressure increase

in the interfacial bubbles due to hydrogen capture or to the weakening of the interface region as a result of the accumulation of implanted hydrogen.

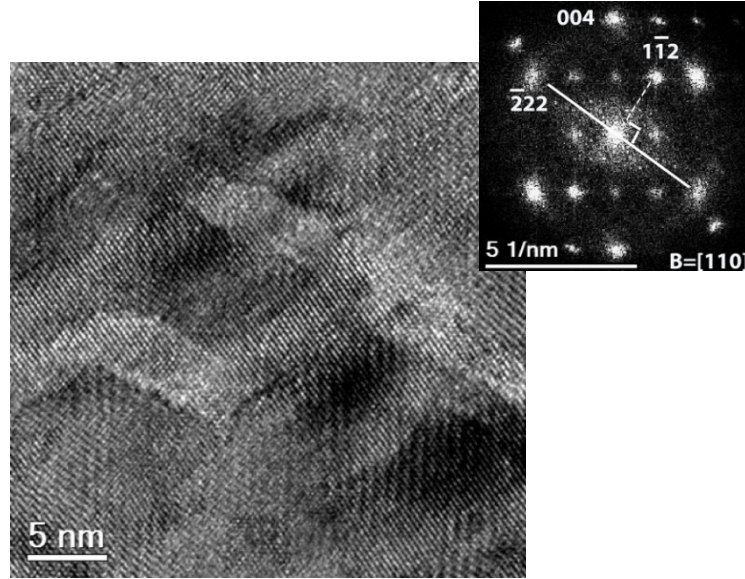


Fig. 5.9. HRTEM image at $\sim 0.2 \mu\text{m}$ underfocus of microcracks in Y_2O_3 film after sequential implantation at RT with 17 keV He^+ ions with the flux of $7 \times 10^{12} \text{ cm}^{-2} \text{ s}^{-1}$ to the fluence of $1 \times 10^{17} \text{ cm}^{-2}$ and then with 10 keV H^+ ions with the flux of $1 \times 10^{13} \text{ cm}^{-2} \text{ s}^{-1}$ to the fluence of $2 \times 10^{17} \text{ cm}^{-2}$.

Fig. 5.9 shows HRTEM cross-sectional image taken close to $[110]$ zone axis, which shows microcracks and a corresponding FFT pattern in the yttria layer of model $\text{Y}_2\text{O}_3/\text{FeCr}$ system implanted sequentially with He^+ and H^+ ions. The general pattern of microcracks is similar to that observed after single-beam H^+ implantation, i.e. microcracks are arranged along the interface and lie on planes different from $\{001\}$. However, one can notice also some differences. In contrast to H^+ implantation into as-fabricated bi-layer system, the fracture in yttrium oxide after H^+ introduction into He pre-implanted bi-layer system occurs rather on $\{112\}$ type planes than on $\{111\}$ type planes. Hence, the mechanisms of microcrack formation in Y_2O_3 layer after single-beam H^+ implantation and after sequential implantation with He^+ and H^+ might be different.

The results of statistical analysis of cavity parameters in $\text{Y}_2\text{O}_3/\text{FeCr}$ bi-layer system sequentially implanted at RT with He^+ and H^+ ions are given in Table 5.4. Note that cavity parameters for the interface are relevant for the area where decohesion did not occur.

Table 5.4. Number densities and average diameters of cavities in the model $\text{Y}_2\text{O}_3/\text{FeCr}$ bi-layer system sequentially implanted at RT with 17 keV He^+ ions with a flux of $7 \times 10^{12} \text{ cm}^{-2} \text{ s}^{-1}$ to the fluence of $1 \times 10^{17} \text{ cm}^{-2}$ and then with 10 keV H^+ ions with a flux of $1 \times 10^{13} \text{ cm}^{-2} \text{ s}^{-1}$ to the fluence of $2 \times 10^{17} \text{ cm}^{-2}$.

	Fe-10Cr film	Interface	Y_2O_3 film
$\langle D_c^k \rangle (\text{nm})$	2.33 ± 0.26	decohesion and 4.55 ± 0.59	
$\langle N_c^k \rangle$	$(27.87 \pm 3.17) 10^{23} \text{ m}^{-3}$	decohesion and $(1.00 \pm 0.11) 10^{16} \text{ m}^{-2}$	microcracks

Like in the case of single-beam He^+ implantation, the average interfacial cavity diameter after sequential dual-beam $\text{He}^+ + \text{H}^+$ implantation is notably larger than that of cavities in the metal layer, i.e. $D_c^{\text{Int}} \approx 4.6 \text{ nm}$ vs. $D_c^{\text{Me}} \approx 2.3 \text{ nm}$. The secondary H^+ implantation results in a moderate increase of cavity sizes as compared to implantation with helium only. Thus, mean cavity size inside the Fe-10Cr layer increases from $D_c^{\text{Me}} \approx 2 \text{ nm}$ up to $D_c^{\text{Me}} \approx 2.3 \text{ nm}$; for interfacial cavities the mean size increases from $D_c^{\text{Int}} \approx 4.1 \text{ nm}$ after single-beam He^+ implantation to $D_c^{\text{Int}} \approx 4.6 \text{ nm}$ after sequential implantation with He^+ and H^+ ions. As might be expected, H^+ introduction doesn't affect the specific cavity number density as compared to single-beam He^+ implantation for both interfacial cavities and cavities inside of metal layer,

implying that all visible cavities were formed already at the He⁺ implantation stage. The results obtained for the Fe-10Cr part of the model bi-layer system nicely agree with the data reported for the sequential ion implantation with helium and hydrogen of industrial ODS-steel (see section 4.1.2.1).

5.4 Microstructural development in bi-layer Y₂O₃/FeCr system after Kr⁺ irradiation at room temperature

In order to better understand the relative importance of gas (helium and, especially, hydrogen) accumulation and primary radiation damage production on cavity and crack nucleation in different parts of the bi-layer Y₂O₃/FeCr system, 2 MeV Kr⁺ irradiation was performed with a flux of $2 \times 10^{11} \text{ cm}^{-2}\text{s}^{-1}$ to the fluence of $3.6 \times 10^{15} \text{ cm}^{-2}$. The energy, flux and fluence of irradiating ions were selected such that the expected radiation damage dose were similar to that of the single-beam He⁺ implantation (where the highest damage among single-beam implantation regimes was achieved) and, at the same time, to minimize Kr accumulation in the region of interest.

Typical BF TEM through-focus images of model bi-layer Y₂O₃/FeCr system irradiated with Kr⁺ ions at room temperature to the fluence of $3.6 \times 10^{15} \text{ cm}^{-2}$ are shown in Fig. 5.10(a-b).

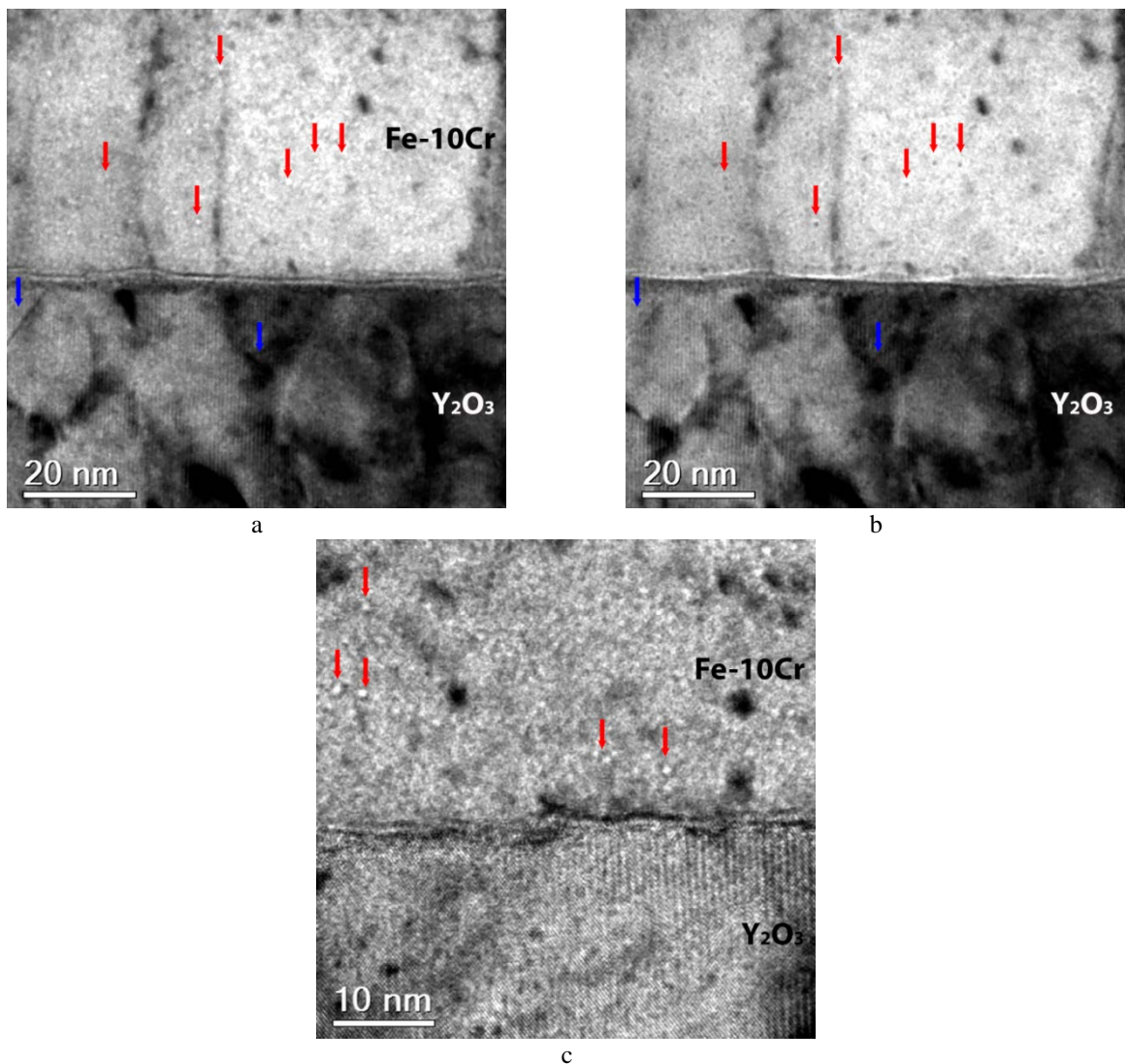


Fig. 5.10. The microstructure of the model bi-layer Y₂O₃/FeCr system irradiated with 2 MeV Kr⁺ ions at RT with the flux of $2 \times 10^{11} \text{ cm}^{-2}\text{s}^{-1}$ to the fluence of $3.6 \times 10^{15} \text{ cm}^{-2}$: (a,b) through-focus image pair; and (c) cavities at higher magnification. Red arrows denote cavities in Fe-10Cr film. Blue arrows denote dislocation loops in Y₂O₃ layer. BF TEM imaging conditions: (a) $\sim 0.6 \mu\text{m}$ underfocus; (b) $\sim 0.6 \mu\text{m}$ overfocus; (c) $\sim 0.3 \mu\text{m}$ underfocus.

Tiny spherical cavities with moderate number density can be noticed only in the Fe-Cr layer. In contrast to room temperature implantation with either He⁺ or H⁺ ions, no cavities or microcracks were observed after heavy ion (Kr⁺) irradiation at the interface and inside the yttrium oxide. At the same time, similar to the case of He⁺ implantation at room and elevated temperature, heavy ion irradiation promoted the formation of anion vacancy dislocation loops inside the Y₂O₃ layer.

The interfacial region of Y₂O₃/FeCr bi-layer is shown in Fig. 5.10(c) at a higher magnification in BF TEM underfocused conditions. Even at this magnification, no evidence of cavity formation at the interface and inside the Y₂O₃ layer could be noticed.

Table 5.5 summarizes the cavity parameters in the bi-layer Y₂O₃/FeCr system after Kr⁺ ion irradiation.

Table 5.5. The number densities and average diameters of cavities in model bi-layer Y₂O₃/FeCr system irradiated at RT with 2 MeV Kr⁺ ions with a flux of $2 \times 10^{11} \text{ cm}^{-2} \text{ s}^{-1}$ to the fluence of $3.6 \times 10^{15} \text{ cm}^{-2}$.

	Fe-10Cr film	Interface	Y ₂ O ₃ film
$\langle D_c^k \rangle (\text{nm})$	1.18±0.14	-	-
$\langle N_c^k \rangle$	$(6.61 \pm 1.95) 10^{23} \text{ m}^{-3}$	-	-

Having in mind that inside the Fe-Cr layer cavities were formed in all single-beam implantation regimes at room temperature, it is instructive to compare parameters of this cavity population in different implantation regimes. The data given in Tables 5.1, 5.3 and 5.5 indicate that specific cavity number density N_c^{Me} after heavy ion irradiation is roughly 4 times lower as compared to either H⁺ or He⁺ implantation. The largest mean cavity size $D_c^{Me} \approx 2 \text{ nm}$ was achieved after He⁺ implantation. In both H⁺ implantation and Kr⁺ irradiation conditions the final average cavity sizes are comparable, $D_c^{Me} \approx 1 \text{ nm}$, and notably smaller than after implantation with He⁺ ions.

5.5 Discussion

Let's start with a brief overview of the microstructures developed in the bi-layer samples in all studied implantation conditions. Table 5.6 summarizes the microstructural features observed after single-beam He⁺ and H⁺ implantations, sequential dual-beam He⁺+H⁺ implantation, and Kr⁺ irradiation.

Table 5.6. A summary of microstructural features observed after single-beam He⁺ and H⁺ implantation, sequential dual-beam He⁺+H⁺ implantation, and Kr⁺ irradiation.

Implantation / irradiation regime	Fe-10Cr film	Interface	Y ₂ O ₃ Film
He⁺, RT	cavity formation $\langle D_c^{Me} \rangle = 2.0 \text{ nm}; \langle N_c^{Me} \rangle = 28.6 \times 10^{23} \text{ m}^{-3}$	cavity formation $\langle D_c^{Int} \rangle = 4.1 \text{ nm}; \langle N_c^{Int} \rangle = 1.0 \times 10^{16} \text{ m}^{-2}$	cavity formation $\langle D_c^{Ox} \rangle = 3.3 \text{ nm}; \langle N_c^{Ox} \rangle = 5.4 \times 10^{23} \text{ m}^{-3}$
He⁺, 823 K	cavity formation $\langle D_c^{Me} \rangle = 7.8 \text{ nm}; \langle N_c^{Me} \rangle = 2.4 \times 10^{23} \text{ m}^{-3}$	-	-
H⁺, RT	cavity formation $\langle D_c^{Me} \rangle = 1.1 \text{ nm}; \langle N_c^{Me} \rangle = 34.8 \times 10^{23} \text{ m}^{-3}$	cavity formation $\langle D_c^{Int} \rangle = 3.1 \text{ nm}; \langle N_c^{Int} \rangle = 1.6 \times 10^{23} \text{ m}^{-2}$	cracking along the interface, fracture on {111} planes
He⁺+H⁺, RT	cavity growth at H ⁺ implantation stage $\langle D_c^{Me} \rangle = 2.3 \text{ nm}; \langle N_c^{Me} \rangle = 27.9 \times 10^{23} \text{ m}^{-3}$	(a) cavity growth at H ⁺ implantation stage $\langle D_c^{Int} \rangle = 4.6 \text{ nm}; \langle N_c^{Int} \rangle = 1.0 \times 10^{16} \text{ m}^{-2}$ (b) interface decohesion	cracking along the interface, fracture on {112} planes
Kr⁺, RT	cavity formation $\langle D_c^{Me} \rangle = 1.2 \text{ nm}; \langle N_c^{Me} \rangle = 6.6 \times 10^{23} \text{ m}^{-3}$	-	-

5.5.1 Irradiation with heavy (Kr⁺) ions

As can be seen in Table 5.6, krypton ion irradiation at room temperature promotes cavity nucleation in the Fe-Cr layer, but does not lead to visible defect structure formation either inside the oxide layer, or at the interface. There is little evidence in the literature on the effects of ion irradiation on layered oxide-FeCr structures is the absence of light gases. A similar study was conducted in Ref. [5], where FeCr-Y₂O₃ bi-layers were irradiated in transmission with 10 MeV Ni⁺ ions. Though the authors of Ref. [5] claim that they achieved the damage dose of 4 dpa inside the oxide, while in our case it is estimated as 2 dpa, the displacement energies for Y and O atoms used in Ref. [5] (25 eV) are nearly twice as low as those used here, so the doses in dpa in both experiments are, in fact, comparable. But the experiments in Ref. [5] used more than an order of magnitude higher ion flux ($\sim 3 \times 10^{13}$ ions/(cm²s)) than in the current study and substantially higher irradiation temperature of 500°C. As a result of ion irradiation, the yttria layer in Ref. [5] has undergone strong amorphization and the formation of cavities inside the yttria layer was observed. This is very different from our case, where neither oxide amorphization, nor void formation was found. Such difference in observations is most probably due to the difference in the irradiation conditions. Indeed, the authors of Ref. [5] convincingly relate the unexpected amorphization with the change of oxide chemical composition due to in-diffusion of chromium from the oxide-metal interface. Though Cr segregation at the interface was present also in our case, we observed no chromium diffusion into the oxide at RT and thus no amorphization. Also, the irradiation flux in our case was substantially lower, which could also contribute to the lack of crystallinity loss. From the comparison of our results with those of Ref. [5] we might suggest that preliminary amorphization is a prerequisite for cavity formation in oxide in the absence of light gases.

Another possible difference in the results is the observation of cavities in the metal layer. The published TEM micrograph (Fig. 3(a) in Ref. [5]) shows small features that might be interpreted as tiny cavities in the metal, but the authors of Ref. [5] make no explicit claims on these features. So it is hard to say if the observations of cavities in the metallic layer here and in Ref. [5] are really different. On the other hand, cavity formation in irradiated Fe-Cr alloys at elevated temperatures is known to occur in a rather narrow temperature region, so that the lack of cavities at 500°C would not be surprising. What is really surprising is the formation of cavities in Fe-Cr alloys at RT, which, to the best of our knowledge, has never been reported.

Finally, we observe no cavities located immediately at the metal/oxide interface and the authors of Ref. [5] do not claim to observe them either. The lack of cavity nucleation at the interface in the absence of stabilizing agents (such as gas atoms poorly soluble in the matrix) is quite natural, because the interface is expected to serve as a sink for vacancies, no matter if these vacancies are coming from oxide or from the metal. Additional arguments in support of this expectation come from the results of first-principles calculations on the interaction between iron vacancies and α -Fe/Y₂O₃ interface in Ref. [14]. It has been demonstrated there that, in the case of {100}<100>Fe||{100}<100>Y₂O₃ interface, single vacancies at the iron side tend to repel each other and avoid combining in subsurface di-vacancies, thus preventing the nucleation of vacancy clusters that might evolve into cavities.

Having in mind that the model metal/oxide interfaces were studied here in order to better understand the cavity formation on the oxide particle/matrix interfaces in ODS-steels, it is instructive to compare our data with the trends of cavity nucleation in industrial steels irradiated without explicit addition of either helium or hydrogen. Cavity nucleation at the interfaces between Y-based nano-oxides and the matrix was rarely reported under either heavy ion or neutron irradiation. In particular, interfacial voids at Y-Al-O nanoparticles in MA956 steel were observed by Chen et al. [15] and Zhang et al. [16] after heavy ion and neutron irradiation, respectively. Similar results were reported by Yamashita et al. [17] for Y-Ti-O oxides in MA957 steel after neutron irradiation at a high temperature. However, the formation of cavities might be promoted by argon that had been typically captured in as-received MA956 and MA957 steels compacted in argon atmosphere and segregated at the nano-

oxides/matrix interfaces [16,17]. Hence, the observed cavities should be treated as gas bubbles rather than voids and thus the direct comparison with our bi-layer experiment would not be fair.

Cavity formation associated with oxide nanoparticles was also reported for ODS PM2000 [18] and ODS-EUROFER [19] alloys after neutron irradiation. However, in both cases the authors claim that all nano-oxide particles associated with voids were found to be amorphous and, in contrast to the case of noble-gas-filled cavities, the detected cavities grew rather into the oxide particle than into iron-based matrix. These data are consistent with our conclusion above that cavity formation in the oxide is probably promoted by the oxide amorphization.

Summing up, the available experimental and simulation data are in favor of the assumption that both crystalline oxide and metal/oxide interface are not favorable for cavity nucleation without gas assistance.

5.5.2 The effects of light gases on the microstructural development in the implanted bi-layer systems

In contrast to heavy ion irradiation regime, helium and hydrogen implantation at room temperature promotes the formation of secondary microstructure (cavities or microcracks) in all parts of the studied bi-layer systems. The damage doses achieved in the individual parts of the bi-layer system after heavy ion irradiation and single-beam helium implantation are similar, while in the case of hydrogen implantation the dose is even lower than after heavy ion irradiation. Therefore, the crucial role of helium and, somewhat surprisingly, hydrogen, in cavity/microcrack formation at the interface and inside the yttria layer is evident. Cavities in the FeCr layer were nucleated in all implantation/irradiation regimes, but their number density after heavy ion irradiation was roughly four times lower than after single-beam helium or hydrogen implantation. The average cavity size after heavy ion irradiation was only half of that achieved after single-beam helium implantation but almost the same as that after single-beam hydrogen implantation. The obtained results suggest that cavities observed in all parts of the studied system after helium and hydrogen implantations are gas-stabilized and that microcrack formation is somehow promoted by the presence of implanted gas. The cavity formation pattern in helium-implanted FeCr layer is consistent with the experiments reported in chapter 3. In contrast, hydrogen is known to be a fast diffuser in iron-based alloys and is commonly assumed not to be retained at high concentrations, so that hydrogen-promoted cavity formation was rather unexpected. As far as we know, the only similar observation of cavity formation in Fe-Cr alloys after low energy single-beam H^+ implantation at RT has been reported in a very recent paper by Jin et al. [20]. In what follows, the helium and hydrogen partitioning between metal, oxide and metal/oxide interface and tentative mechanisms involved in the gas-assisted microstructure formation are discussed based on the available TEM results and in the context of experimental and modeling data found in literature.

5.5.2.1 Helium partitioning between oxide, matrix and interface

Helium-assisted cavity nucleation after single-beam He^+ implantation at room temperature was found everywhere, that is inside the FeCr layer, at the interface, and inside Y_2O_3 layer. The largest cavities were located at the metal/oxide interface, followed by slightly smaller cavities in oxide layer, while the smallest cavities corresponded to the FeCr layer. In contrast, cavity number density in the metal layer is notably higher than inside the oxide layer. In other words, at room temperature the metal/oxide interface manifests the highest helium trapping efficiency. Also, the reported data suggest higher helium diffusion rate in yttria and at the metal/oxide interface than in FeCr.

The observed trends in He-filled cavity partitioning between the parts of model FeCr/ Y_2O_3 system are in good agreement with the data reported in Refs. [1,3] for similar α -Fe/ Y_2O_3 layers. Interestingly, the qualitative trends of cavity formation in bi-layer metal/oxide systems are only weakly sensitive to

remarkable differences in implantation parameters, such as implantation geometry (from the surface in this study and on cross-section in Refs. [1,3]), flux, fluence, the type of interface orientation relationships, and interface chemistry (e.g. chromium segregation at the interface presents in this study). In all cases, the metal/Y₂O₃ interfaces served as efficient nucleation sites for He-filled-cavities at room temperature. This observation indicates that helium trapping at metal/oxide interface is related to some fundamental metal/oxide interface properties.

Moreover, efficient interfacial cavity formation well reproduces the situation in industrial ODS-steels subjected to helium or dual-beam (heavy ion+ He) irradiation (see chapter 3). However, one difference regarding the interfacial cavity formation between industrial ODS-steels and the model systems with planar metal/oxide interfaces should be noted. Typically, interfacial cavities in industrial steels after helium implantation grow into the iron-based matrix rather than into the oxide. The planar metal/oxide interfaces demonstrate an opposite behavior. A similar ‘one-sided’ growth of interfacial cavities has been reported in the literature for α -Fe/Y₂O₃ [3], Cu/Nb [21] and Cu/Ag [22] interfaces. A common explanation why cavities preferentially grow on one side of the interface is the difference in the surface energies of adjacent phases. According to this approach, one can define a wetting energy parameter, W , as

$$W = \gamma_A + \gamma_{AB} - \gamma_B,$$

where γ_A and γ_B are the surface energies of phases A and B, γ_{AB} the interface energy, and it is assumed that $\gamma_A < \gamma_B$. When $W > 0$, thermodynamics favors wetting, meaning that the cavity will stay in A phase and contact the interface. In contrast, when $W < 0$, wetting is not favored and the cavity has minimum energy when it is entirely contained within phase A. In our case, the phase with the lowest surface energy ($\sim 1.7 \text{ J/m}^2$ [23]) is cubic Y₂O₃, whereas the surface energies of α -Fe vary within 2.22-2.73 J/m² depending on surface crystallographic orientation (in particular, 2.43 J/m² for (110) surface) [24]. Hence, interfacial He-filled cavities are expected to nucleate on the oxide side and only wet the metal/oxide interface. This conclusion agrees with TEM results observed in this study for single-beam helium implantation at room temperature.

However, the treatment of cavity formation in terms of surface energies only would be highly oversimplified because it does not take into account such important factors as the energetics of lattice atom removal, helium and vacancy diffusion, stabilization of vacancy and He-vacancy-complexes and their growth. This is evidenced not only by the opposite trend of cavity growth into the metal matrix on the nano-oxide interfaces in industrial ODS-steels, but also by TEM results reported in this study for the planar metal/oxide interface after single-beam helium implantation at the elevated temperature. In contrast to both our data and observations of Refs. [1,3] at RT, the He-assisted cavity formation both inside the yttria layer and at the metal/oxide interface of model FeCr/Y₂O₃ system was completely suppressed during single-beam helium implantation at 823 K. The observed behavior is inconsistent with the typically reported intense He bubbles formation at the nano-oxide/matrix interfaces in industrial ODS-steels and puts forth the question which factors result in the absence of He-assisted cavities after high temperature helium implantation. In particular,

- might the lack of cavities in the yttria layer be due to helium diffusion out of the film as a consequence high He diffusion rate?
- if helium is retained in the yttria layer, might it be trapped inside some invisible by TEM clusters or simply dissolved in the lattice (as suggested by DFT calculation in Refs. [25–27])?
- where is it easier for a He-assisted cavity to form: at the metal/oxide interface or inside the oxide?

These questions are discussed below based on the available first-principles simulations of helium behavior at the metal/oxide interfaces.

Unfortunately, up to now there is no established database on required parameters for all existing ODS related metal/oxide system. The most comprehensively studied are helium atom and vacancies energies in all potential residence sites in a α -Fe/Y₂Ti₂O₇ planar interfacial system [26]. It has been

demonstrated that helium solution energy is effectively the same at interstitial sites inside the oxide (0.94 eV) and at the interface (0.95 eV) and both are significantly lower than the lowest helium interstitial formation energy in the iron matrix, either in the bulk (4.16 eV) or inside a vacancy (2.28 eV). Less detailed first-principles calculations for α -Fe/Y₂O₃ model system report quantitatively similar trends for helium solution energy in different parts of the studied system, namely Y₂O₃ cluster < α -Fe/Y₂O₃ interface \ll α -Fe [27]. Summing up, solution energies of He interstitial atom in Y-based oxide and at the interface are noticeably lower than inside iron. In other words, helium transport at the interface between oxide and steel is strongly asymmetric; He atoms that reach the interface from the steel side are easily transferred into oxide, whereas the reverse transition from oxide to steel is strongly suppressed due to the enormous difference between helium solution energies in oxide and steel [27].

In terms of the bi-layer implantation experiment discussed earlier in this chapter it means that all helium implanted into the oxide layer, as well as some helium transferred from the Fe-Cr layer into the oxide is available for cavity formation. However, the formation of cavities in the oxide is observed only in the case of implantation at room temperature, but not at 823 K. The reason for such difference is most probably related to the details of helium performance at low and high temperatures because radiation damage alone does not lead to cavity formation in oxide even at higher damage production rate than that typical for helium implantation experiment, as evidenced by the krypton irradiation experiment (see section 5.4). Assuming that cavity formation results from clustering of cation vacancies, the latter result can be explained by the lack of binding between nearby Y vacancies (estimated interaction energy of two Y vacancies at the 1st nearest neighbor separation is strongly repulsive, -0.6 eV, and practically vanishes at larger separations [28]). However, it can be expected that small vacancy clusters in yttria are stabilized by helium, which is known to be easily trapped in vacancies (especially in cation vacancies). According to first principles simulations, the lowest solution energy of interstitial He atom in Y₂O₃ crystal is \sim 0.73 eV, while He atom trapping in cation vacancies and small Y-O vacancy complexes gives an energy gain of 0.4-0.6 eV [29]. However, beneficial effect of trapped He atoms on vacancy cluster stabilization is possible only if He atom is trapped in the complex for sufficiently long time and if the He concentration in the matrix is sufficiently high. However, none of these conditions seems to be fulfilled when the implantation temperature is as high as 823 K.

In order to demonstrate it, let us estimate, first of all, the lifetime of He atoms in small vacancy clusters. Assuming a typical value of He binding energy in a small vacancy cluster $E_b^{\text{He}} = 0.55$ eV [29], this time can be roughly estimated as

$$t_l \approx \frac{1}{\nu} \exp\left(\frac{E_b^{\text{He}}}{kT}\right), \quad (5.1)$$

where ν is the atomic jump frequency ($\sim 10^{13}$ s⁻¹), k and T - the Boltzmann constant and implantation temperature, which gives $t_l \sim 3.1 \times 10^{-4}$ s and $\sim 2.4 \times 10^{-10}$ s at 293 K and 823 K, respectively. Thus, the trapping of He atoms in radiation-induced vacancy defects at the high temperature is negligible and the implanted helium is free to expand from the implantation region (close to the metal/oxide interface in our case) into the oxide and even further out of it (into the SrTiO₃ substrate or even out of the bi-layer system).

Indeed, He is known to be sufficiently mobile in Y₂O₃. Due to the presence of multiple stable positions for interstitial helium in the yttrium structure, there is a number of intermediate transitions between the ground state He configurations (in the oxygen structural vacancies), with the highest barrier on the shortest path between two neighboring ground state configurations being $E_m^{\text{He}} \sim 0.78$ eV [29]. The mean diffusion path of He interstitial within time t can then be estimated as

$$L_{\text{diff}} \approx \sqrt{D_{\text{He}} \cdot t}, \quad (5.2)$$

where D_{He} is the diffusion coefficient of helium in yttria,

$$D_{\text{He}} \approx a^2 \nu \exp\left(-\frac{E_m^{\text{He}}}{kT}\right), \quad (5.3)$$

where a denotes the jump length. He diffusion length in Y_2O_3 crystal at 293 K and 823 K estimated using equation (5.2) for the implantation time of 20000 s is 21.9 nm and 457 μm , respectively. It is clear that at room temperature helium in yttria is sufficiently mobile to be redistributed between vacancy defects created by ion implantation, but the profile of implanted He does not spread out much into the oxide layer (which was ~ 80 nm thick). On the contrary, after implantation at 823 K almost all the implanted He was re-distributed over the whole oxide layer and could even diffuse out of it. The possibility of helium desorption from oxide is supported by the data of Ref. [4], where it was mentioned that only 10% of helium implanted at 973 K remained inside the $Y_2Ti_2O_7$ layer.

While the transport of helium from oxide into the FeCr alloy can be excluded, bubbles might form at the oxide/matrix interface in case there would exist strong helium traps at the interface. However, the absence of cavities at the interface after single-beam helium implantation at 823 K indicates that even if such trapping sites do exist, they are not strong enough to promote cavity formation. A similar situation was met after He^+ implantation at 973 K into $\alpha\text{-Fe}/Y_2Ti_2O_7$ system [4], where helium was implanted into $\alpha\text{-Fe}$ layer. Due to helium diffusion from iron into oxide, bubble formation was observed not only in iron, but inside $Y_2Ti_2O_7$ as well, but no bubbles were observed at the metal/oxide interface.

Having in mind the discussed modes of He redistribution in mixed metal/oxide systems, it is instructive to discuss the reasons for very different patterns of He-assisted cavity nucleation on the studied planar metal/oxide interface and on nano-oxide particles in ODS steels at elevated temperatures. A sketch of possible paths of He re-distribution in ion implanted model FeCr/ Y_2O_3 system and an industrial ODS-steel is shown in Figs. 5.11(a) and 5.11(b), respectively. Note that in our case He^+ ions were implanted into both FeCr and yttria in similar concentrations and diffuse interstitially through the lattices of FeCr and yttria.

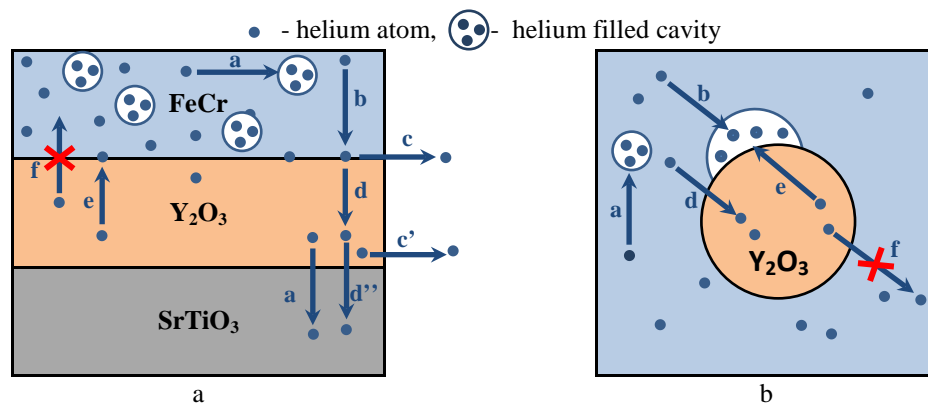


Fig. 5.11. A summary of possible redistribution paths of implanted He at 823 K for (a) the model FeCr/ Y_2O_3 system and (b) an oxide particle in steel matrix. The He redistribution modes include: **a**- trapping in cavities in the metal layer; **b**- diffusion to metal/oxide interface; **c**- out-diffusion along the interface; **c'**- out-diffusion from the yttria layer; **d**- diffusion away from the interface into yttria; **d'** and **d''**- escape to the substrate oxide; **e**- diffusion in yttria towards the interface; **f**- diffusion away from yttria into metal.

First of all, in both a planar metal/oxide system and an industrial ODS-steel, He atoms injected into FeCr layer or FeCr matrix during He^+ implantation diffuse and assist cavity nucleation inside the metal itself (scenario (a)). Helium atoms reaching a cavity are trapped in cavities because their energy is strongly decreased as a result. In the same way, the injected helium atoms that stop in the steel matrix in the vicinity of metal/oxide interface can reach the interface (scenario (b)) and their subsequent fate is largely determined by the properties of the interface. If the interface behaves as a strong trap for helium atoms and allows easy helium interfacial diffusion, this trapped helium can either escape from the interface into the environment (scenario (c)), or promote bubble formation at the interface by making small helium-vacancy clusters with radiation vacancies that also reach the interface. Already at this stage there is a clear difference between layered systems that allow helium loss into the environment as a result of fast interfacial helium diffusion and finite-size particles, where such mode of helium escape is

impossible. If, however, there is no strong helium trapping at the interface (as indicated by some modeling studies discussed above), helium atoms that reach the interface simply jump from the metal matrix into the oxide and continue their diffusion already inside the oxide matrix. The reverse transition from oxide to steel (scenario (f)) is strongly impeded by very large difference in solution energies and so the only reason that might prevent the transfer of helium atoms from the matrix into the oxide is sufficiently high concentration of helium inside the oxide, so that all low-energy sites in the oxide are already occupied with helium atoms trapped earlier or directly stopped inside the oxide during the implantation. As can be easily understood, this latter scenario is improbable for layered structures because, first of all, the available volume for helium storage can hardly be exhausted for any reasonable helium fluence and, second, there exist additional possibilities of helium escape, either through the oxide/substrate interface (scenarios (d) and (d')) or into the sample environment (either directly from the oxide, scenario (c'), or along the oxide-substrate interface). One more possible channel of helium immobilization in the oxide is trapping in radiation produced cavities, but, as evidenced by TEM investigations presented in sections 5.1.1 and 5.1.2, as well as in multiple studies on industrial ODS steels, this strongly temperature dependent effect is not relevant at high temperatures typical for in-reactor operation conditions. In any case, due to easy helium redistribution in the layered structure, helium that reaches oxide layer (either from the metal or as a result of direct implantation into the oxide) has little, if any, influence on the processes of helium-vacancy cluster formation at the interface. Considerably different situation takes place in the case of oxide particles, where the factor of limited particle size becomes crucial. First of all, the finite particle capacity for helium accumulation prevents particle 'charging' with helium after the limiting helium content in the particle is achieved and subsequent helium accumulation is possible only on the metal side of the interface. The basic mechanism of bubble formation at the particle interface is most probably the same as in the bulk (i.e. gradual accumulation of helium atoms accompanied with the trapping of vacancies to release growing helium pressure in the bubble), but the formation of bubbles on particles is additionally facilitated as compared to the bulk because helium atoms and vacancies are captured by the whole particle surface and not only by the surface of the bubble. Additional beneficial factor for the growth of sufficiently large bubbles (where helium/vacancy ratio is not too high) can be helium supply directly from the oxide particle (scenario (e)), because the transition of a helium atom from the particle to the empty space in the cavity would be energetically favorable [25]. Thus, the absence or presence of helium bubbles on the interface can be sensitive not only to the helium implantation conditions, but also to the oxide size factor, which should be taken into account when extrapolating the results obtained on model bi-layered systems to industrial ODS-steels.

Summing up, the analysis of obtained experimental results in conjunction with the available literature data leads us to the following conclusions:

(i) The oxide size factor plays a significant role when applied to bubble formation at metal/oxide interfaces. Thus, the model bi-layer metal/oxide systems are able to partially reproduce industrial materials trends only in the case of low temperature helium implantation. Moreover, the trend of preferential interfacial cavity formation observed at room temperature seems to be independent of either metal/oxide orientational relationship or the interfacial chemistry (in particular, interfacial chromium segregation). Helium diffusion during implantation at elevated temperature results in notably different helium partitioning between metal, Y-based oxide and interface as compared to industrial ODS-steels. Thus, even though the experiments with planar metal/oxide interfaces are useful for understanding the underlying mechanisms of He trapping and diffusion, care should be taken when extrapolating the observed trends to industrial materials.

(ii) Qualitatively similar patterns of He-assisted cavity nucleation were found inside the yttria layer and on metal/oxide interface. After room temperature implantation, cavities of similar size were formed at the interface and inside yttria, while after implantation at elevated temperature no cavities were

observed in both cases. This behavior indicates that cavity nucleation in both cases is controlled by helium solution and migration inside the Y-based oxide, in agreement with the results of first-principles calculations reported in literature.

(iii) The known energetics of helium solution and migration in Y_2O_3 suggests a ready explanation of the differences in cavity precipitation at room and elevated temperature. The easy helium diffusion allows helium to diffuse out of the yttria layer and the interface, while relatively weak trapping in radiation defects prevents stabilization of vacancy clusters on the cation sublattice. In contrast, at room temperature helium is efficiently captured in the radiation-produced cation vacancies and clusters, promoting their growth.

5.5.2.2 Hydrogen partitioning between oxide, matrix and interface

After single-beam H^+ implantation, hydrogen-assisted cavity formation was found inside the FeCr layer and at the oxide/matrix interface, while microcracks were formed in the Y_2O_3 layer. The interfacial cavities were notably larger than cavities in the FeCr layer. Hydrogen related cavities at the metal/oxide interface grew rather into the oxide layer and not towards the metal layer, indicating that hydrogen at the interface should behave more like hydrogen in the oxide than hydrogen in the metal layer.

The observation of hydrogen bubbles in FeCr alloy is highly interesting and demonstrates that at room temperature hydrogen does stabilize small vacancy clusters and is able to promote cluster growth up to at least 1 nm in size. A similar effect was observed in chapter 4 after sequential $He^+ + H^+$ implantation of industrial ODS-steel at RT, but there it remained unclear whether hydrogen was able to promote cavity formation alone or acted only as an assistant to helium and developed clusters that had already been formed during He^+ pre-implantation.

To the best of our knowledge, there are no relevant experimental data concerning hydrogen partitioning between α -Fe (and Fe-Cr), yttria and their interfaces. Therefore, the results of section 5.2 are discussed below in terms of recent first-principles calculations [30]. According to these calculations, hydrogen atom solution energies at different positions inside crystalline Y_2O_3 fall in the range of 2.4-2.7 eV depending on that or other interstitial position. At the same time, hydrogen solution energy in α -Fe is only 0.21 eV [31]. That is, the trend is completely opposite to that for helium; when iron and yttria are in contact, hydrogen dissolved in yttria tends to escape into iron, while hydrogen dissolved in iron avoids going into oxide. This trend is in agreement with the abundance of hydrogen-promoted cavities in the FeCr layer.

The formation of microcracks in Y_2O_3 layer is most probably related to the formation of anion dislocation loops during ion bombardment, as discussed in sections 5.2-5.3 of this chapter. Dislocation loops and fracture surfaces of microcracks both lie on $\{111\}$ planes of yttrium oxide. It is highly probable that vacant anion sites inside the loops serve as traps for hydrogen atoms injected into the oxide layer during hydrogen implantation. Hydrogen accumulation in the loops is potentially able to weaken chemical bonds between the opposite sides of the loop extra-plane and promote microcrack opening, similar to smart-cut effect in Si after hydrogen implantation [32,33].

The obtained experimental results in conjunction with the available literature data on hydrogen energetics in iron and yttria are instructive for predicting hydrogen effects in industrial ODS-steels in relevant fusion/fission environment. It can be expected that hydrogen from the steel matrix does not accumulate in the oxide particles, while hydrogen implanted directly into relatively small oxide particles quickly leaves them, unless trapped in some radiation defects in the particle. Due to the limited oxide particle size, microcrack formation under synergetic influence of radiation damage and hydrogen accumulation is unlikely, possibly excluding very large particles. Nevertheless, in the presence of irradiation-induced defects some trapping of hydrogen in vacant lattice positions or in vacancy clusters inside nanoparticles cannot be excluded, especially at not too high temperatures, because radiation damage in the oxide can be quite strong in certain conditions. A known example of radiation damage

effects is the formation of interfacial voids inside oxide particles in neutron irradiation of ODS-EUROFER steel [19].

An open issue remains the formation of cavities at the oxide side of the metal/oxide interface. Having in mind that the effect is observed under both helium and hydrogen implantation, cavity formation can equally well be due not only to the effect of implanted gases, but also to microchemical changes, such as the enrichment of subsurface yttria in chromium due to the cascade mixing, which, as discussed in section 5.5.1, facilitates yttria amorphization and cavity formation.

5.5.2.3 Possible synergism of helium and hydrogen influence on the implantation-induced damage in the oxide, metal matrix and at the interface

Gas-assisted cavity nucleation inside the FeCr layer and at the FeCr/Y₂O₃ interface was observed at room temperature after single-beam implantation with either helium or hydrogen. After sequential implantation of both gases the size of cavities in the FeCr layer increased by factors of 2 and 1.15 as compared to single-beam hydrogen and helium implantation regimes, respectively. The cavity number densities in the FeCr layer were comparable in all cases. This evolution of cavity parameters agrees well with the data for sequential implantation with helium and hydrogen ions reported for industrial ODS-steel in sections 4.1.2.1 and 4.1.2.2, indicating only minor hydrogen effect on the cavity growth in FeCr matrix.

However, a clear synergy of helium and hydrogen produced damage was observed in the oxide layer and at the oxide/metal interface. First of all, the pattern of microcrack formation promoted by hydrogen accumulation was somewhat different in the presence and absence of helium pre-implantation. While after single-beam hydrogen implantation microcracks were lying on {111} crystallographic planes, the microcrack planes in He pre-implanted sample corresponded rather to {112}. The reason for this modification remains, however, unclear.

Second, hydrogen injection into helium pre-implanted samples has led to the growth of interfacial cavities and interfacial decohesion in a blister-like-manner. Since interfacial cavities were already present in the He pre-implanted sample before hydrogen injection, interfacial decohesion occurred as a synergetic result of He-filled cavity nucleation and hydrogen accumulation either at the existing cavities or directly at the interface. Decohesion might occur as a result of several competing processes, such as

- (a) He-filled cavity coalescence due to the hydrogen promoted cavity growth;
- (b) fracture due to hydrogen accumulation inside He-filled cavities and subsequent pressure increase, as suggested in an interbubble fracture model of blister formation after He implantation [12,13];
- (c) lattice bond weakening at the metal/oxide interface by implanted hydrogen, similar to smart-cut effect in Si after hydrogen implantation [32,33].

The nucleation of interfacial cavities after single-beam hydrogen implantation and growth of pre-existing interfacial He-filled cavities after hydrogen injection along with the TEM and TDS results reported in sections 4.1 and 4.2 for industrial ODS-steel suggest possible hydrogen accumulation in the He-filled cavities. Hence, cavity coalescence or interbubble fracture seem more probable mechanisms responsible for the interfacial decohesion after sequential implantation with helium and hydrogen than interface bonding weakening.

5.6 Summary

(i) The model bi-layer metal/oxide systems were able to reproduce industrial material trends in He-assisted cavity formation in all parts of the system, i.e. metal, interface and oxide, but only after room temperature helium implantation. At room temperature, helium was efficiently trapped in small cavities in FeCr layer, and might be efficiently stored inside yttria particles. The tendency of preferential interfacial

cavity formation observed at room temperature indicates that helium trapping at metal/oxide interface is insensitive to both metal/oxide orientation relationship and the interfacial chemistry.

(ii) At the temperature of 823 K, cavity population development in response to helium implantation resembles that in ODS steels only in the metal layer. Helium-assisted cavity formation pattern at the metal/oxide interface is notably different from that typically observed for industrial ODS-steels. No helium bubble nucleation at the planar FeCr/yttria interface could be noticed, while large cavities decorating yttria nano-oxides were observed in industrial ODS-steels at the same temperature. Inside the oxide layer, no cavities were observed at this temperature as well; the implanted helium was either redistributed over the layer or escaped from it into the substrate or the sample environment. Such redistribution is impossible in ODS-steels, where nano-oxides are completely surrounded by FeCr matrix. Thus, though the experiments on the planar metal/oxide interfaces are useful for understanding underlying mechanisms of He trapping and diffusion, the extrapolation of their results onto industrial ODS steels should be done with caution.

(iii) Not only the nano-oxide particle number density but also particle size might serve as a tool for controlling He redistribution in industrial ODS-steels. In particular, the increase of oxide nanoparticle size increases the number of He trapping sites and helps to store larger amount of helium inside nano-oxides, which eventually reduces swelling. However, at high damage and He production rates too large oxide particles are able to strongly deteriorate swelling resistance of ODS steel. As shown in chapter 3, in certain conditions bubbles associated with oxide nanoparticle/matrix interfaces can undergo bubble-to-void transition that triggers continuous void swelling of industrial ODS-steels.

(iv) The critical role of helium and, surprisingly, hydrogen in cavity and/or microcrack formation in a model bi-layer FeCr/yttria system subjected to heavy ion, helium and hydrogen single-beam implantations has been demonstrated by TEM analysis. The hydrogen-assisted cavity formation inside the FeCr layer and at the metal/oxide interface caused by single-beam H^+ implantation was demonstrated. The interfacial cavities were larger than cavities in the metal layer. In contrast, microcracks rather than cavities were formed in the Y_2O_3 layer. The orientation of microcracks formed after single-beam hydrogen implantation indicates that hydrogen might be efficiently trapped in anion vacancy loops inside the yttria layer. The promotion of cavity formation by implanted hydrogen supports the possibility of hydrogen trapping at the metal/oxide interface suggested by TDS analysis presented in chapter 4.

(v) Strong synergetic effect of helium and hydrogen was observed after sequential implantation of a model bi-layer FeCr/yttria sample with helium and hydrogen. Hydrogen implantation into pre-implanted with helium system has led to interfacial decohesion and microcrack nucleation in the oxide layer. Decohesion and microcrack formation after hydrogen injection might result from several competing process such as hydrogen-promoted interfacial cavity growth and coalescence, or hydrogen-assisted interfacial bond weakening. An exact mechanism responsible for the detected processes remains unclear and further experimental and modeling research is required to explain the obtained results. At the same time, hydrogen had minor influence on the He-filled cavity population in the metal layer, just like in industrial ODS-steels. The growth of cavities inside the metal layer might be associated with hydrogen accumulation in cavities.

5.7 References

- [1] T. C. Kaspar, M. E. Bowden, C. M. Wang, V. Shutthanandan, N.R. Overman, R.M. van Ginhoven, B. D. Wirth, R. J. Kurtz, “Epitaxial Fe/Y₂O₃ interfaces as a model system for oxide-dispersion-strengthened ferritic alloys,” *J. Nucl. Mater.*, vol. 457, pp. 352–361, 2015.
- [2] T. Stan, Y. Wu, P. B. Wells, H. D. Zhou, and G. R. Odette, “Epitaxial Fe thin films on {100} Y₂Ti₂O₇: Model interfaces for nano-oxide dispersion strengthened steels,” *Metall. Mater. Trans. A*, vol. 48, no. 11, pp. 5658–5666, 2017.
- [3] A. Mairov, D. Frazer, P. Hosemann, and K. Sridharan, “Helium irradiation of Y₂O₃-Fe bilayer system,” *Scripta Materialia*, vol. 162, pp. 156–160, 2019.
- [4] T. Stan, “The role of oxides in nanostructured ferritic alloys and bilayers: Interfaces, helium partitioning and bubble formation,” 2017.
- [5] N. Li, S. K. Yadav, Y. Xu, J. A. Aguiar, J. K. Baldwin, Y. Q. Wang, H. M. Luo, A. Misra and B. P. Uberuaga, “Cr incorporated phase transformation in Y₂O₃ under ion irradiation,” *Scientific Reports*, vol. 7, no. 1, p. 40148, 2017.
- [6] R. J. Gaboriaud, F. Pailloux, P. Guerin, and F. Paumier, “Yttrium sesquioxide, Y₂O₃, thin films deposited on Si by ion beam sputtering: microstructure and dielectric properties,” *Thin Solid Films*, vol. 400, no. 1, pp. 106–110, 2001.
- [7] B. Lacroix, F. Paumier, and R. J. Gaboriaud, “Crystal defects and related stress in Y₂O₃ thin films: Origin, modeling, and consequence on the stability of the C-type structure,” *Phys. Rev. B*, vol. 84, no. 1, p. 14104, Jul. 2011.
- [8] R. J. Gaboriaud, F. Paumier, M. Jublot, and B. Lacroix, “Ion irradiation-induced phase transformation mechanisms in Y₂O₃ thin films,” *Nucl. Instruments Methods Phys. Res. Sect. B Beam Interact. with Mater. Atoms*, vol. 311, pp. 86–92, 2013.
- [9] B. Lacroix, R. J. Gaboriaud, and F. Paumier, “Fundamental aspects about the first steps of irradiation-induced phase transformations in fluorite-related oxides,” *Acta Mater.*, vol. 153, pp. 303–313, 2018.
- [10] D. Brimbal, E. Meslin, J. Henry, B. Décamps, and A. Barbu, “He and Cr effects on radiation damage formation in ion-irradiated pure iron and Fe–5.40wt.% Cr: A transmission electron microscopy study,” *Acta Mater.*, vol. 61, no. 13, pp. 4757–4764, 2013.
- [11] A. Bhattacharya, E. Meslin, J. Henry, B. Décamps, and A. Barbu, “Dramatic reduction of void swelling by helium in ion-irradiated high purity α -iron,” *Mater. Res. Lett.*, vol. 6, no. 7, pp. 372–377, Jul. 2018.
- [12] J. H. Evans, “The role of implanted gas and lateral stress in blister formation mechanisms,” *J. Nucl. Mater.*, vol. 76–77, pp. 228–234, 1978.
- [13] F. I. Allen, P. Hosemann, and M. Balooch, “Key mechanistic features of swelling and blistering of helium-ion-irradiated tungsten,” *Scripta Materialia*, vol. 178, pp. 256–260, 2020.
- [14] M.-M. Peng and W.-S. Lai, “Interaction between vacancies and the α -Fe/Y₂O₃ interface: A first-principles study,” *Nucl. Instruments Methods Phys. Res. Sect. B Beam Interact. with Mater. Atoms*, vol. 352, pp. 67–71, 2015.
- [15] T. Chen, H. Kim, J. G. Gigax, D. Chen, C.-C. Wei, F.A. Garner, L. Shao, “Radiation response of oxide-dispersion-strengthened alloy MA956 after self-ion irradiation,” *Nucl. Instruments Methods Phys. Res. Sect. B Beam Interact. with Mater. Atoms*, vol. 409, pp. 259–263, 2017.

- [16] Z. Zhang, T. A. Saleh, S. A. Maloy, and O. Anderoglu, "Microstructure evolution in MA956 neutron irradiated in ATR at 328 °C to 4.36 dpa," *J. Nucl. Mater.*, vol. 533, p. 152094, 2020.
- [17] S. Yamashita, N. Akasaka, S. Ukai, and S. Ohnuki, "Microstructural development of a heavily neutron-irradiated ODS ferritic steel (MA957) at elevated temperature," *J. Nucl. Mater.*, vol. 367–370, pp. 202–207, 2007.
- [18] H. J. Jung, D. J. Edwards, R. J. Kurtz, T. Yamamoto, Y. Wu, and G. R. Odette, "Structural and chemical evolution in neutron irradiated and helium-injected ferritic ODS PM2000 alloy," *J. Nucl. Mater.*, vol. 484, pp. 68–80, 2017.
- [19] M. Klimenkov, R. Lindau, U. Jäntschi, and A. Möslang, "Effect of irradiation temperature on microstructure of ferritic-martensitic ODS steel," *J. Nucl. Mater.*, vol. 493, pp. 426–435, 2017.
- [20] P. Jin, T. Shen, M. Cui, Y. Zhu, B. Li, T. Zhang, J. Li, S. Jin, E. Lu, X. Cao, Z. Wang, "Study on vacancy-type defects in SIMP steel induced by separate and sequential H and He ion implantation," *J. Nucl. Mater.*, vol. 520, pp. 131–139, 2019.
- [21] W. Z. Han, N. A. Mara, Y. Q. Wang, A. Misra, and M. J. Demkowicz, "He implantation of bulk Cu–Nb nanocomposites fabricated by accumulated roll bonding," *J. Nucl. Mater.*, vol. 452, no. 1, pp. 57–60, 2014.
- [22] S. Zheng, S. Shao, J. Zhang, Y. Wang, M. J. Demkowicz, I. J. Beyerlein, and N. A. Mara., "Adhesion of voids to bimetal interfaces with non-uniform energies," *Scientific Reports*, vol. 5, no. 1, p. 15428, 2015.
- [23] P. Zhang, A. Navrotsky, B. Guo, I. Kennedy, A. N. Clark, C. Leshner, and Q. Liu, "Energetics of cubic and monoclinic yttrium oxide polymorphs: Phase transitions, surface enthalpies, and stability at the nanoscale," *J. Phys. Chem. C*, vol. 112, no. 4, pp. 932–938, Jan. 2008.
- [24] L. Vitos, A. V. Ruban, H. L. Skriver, and J. Kollár, "The surface energy of metals," *Surface Science*, vol. 411, no. 1, pp. 186–202, 1998.
- [25] L. Yang, Y. Jiang, G. Robert Odette, T. Yamamoto, Z. Liu, and Y. Liu, "Trapping helium in $Y_2Ti_2O_7$ compared to in matrix iron: A first principles study," *J. Appl. Phys.*, vol. 115, no. 14, p. 143508, Apr. 2014.
- [26] L. Yang, Y. Jiang, Y. Wu, G. R. Odette, Z. Zhou, and Z. Lu, "The ferrite/oxide interface and helium management in nano-structured ferritic alloys from the first principles," *Acta Mater.*, vol. 103, pp. 474–482, 2016.
- [27] D. Sun, R. Li, J. Ding, S. Huang, P. Zhang, Z. Lu, J. Zhao, "Helium behavior in oxide dispersion strengthened (ODS) steel: Insights from ab initio modeling," *J. Nucl. Mater.*, vol. 499, pp. 71–78, 2018.
- [28] Y. D. Ou and W. S. Lai, "Vacancy formation and clustering behavior in Y_2O_3 by first principles," *Nucl. Instruments Methods Phys. Res. Sect. B Beam Interact. with Mater. Atoms*, vol. 269, no. 14, pp. 1720–1723, 2011.
- [29] W. Lai, Y. Ou, X. Lou, and F. Wang, "Ab initio study of He trapping, diffusion and clustering in Y_2O_3 ," *Nucl. Instruments Methods Phys. Res. Sect. B Beam Interact. with Mater. Atoms*, vol. 393, pp. 82–87, 2017.
- [30] D. Sun, J. Ding, Y. Yang, P. Zhang, and J. Zhao, "First-principles investigation of hydrogen behavior in different oxides in ODS steels," *Int. J. Hydrogen Energy*, vol. 44, no. 31, pp. 17105–17113, 2019.
- [31] W. A. Counts, C. Wolverton, and R. Gibala, "First-principles energetics of hydrogen traps in α -Fe: Point defects," *Acta Mater.*, vol. 58, no. 14, pp. 4730–4741, 2010.

- [32] B. Aspar, M. Bruel, H. Moriceau, C. Maleville, T. Poumeyrol, A.M. Papon, A. Claverie, G. Benassayag, A.J. Auberton-Hervé, T. Barge, “Basic mechanisms involved in the Smart-Cut process,” *Microelectron. Eng.*, vol. 36, no. 1, pp. 233–240, 1997.
- [33] T. Höchbauer, A. Misra, M. Nastasi, and J. W. Mayer, “Physical mechanisms behind the ion-cut in hydrogen implanted silicon,” *J. Appl. Phys.*, vol. 92, no. 5, pp. 2335–2342, Aug. 2002.

Conclusions and future work

Detailed summaries and conclusion in this manuscript are given within each chapter, while this section summarizes only the most important conclusions answering the global thesis objectives.

1. The efficiency of Y_2O_3 nanoparticles in ODS-EUROFER steel as helium trapping sites and potential risks associated with using oxide nanoparticles in a high He/dpa ratio environment

(i) Bubble growth kinetics on oxide particles is found to be notably different from that for bubble populations in the grain bulk, on extended microstructural defects (dislocations, grain boundaries) and carbide precipitates. The number density of bubbles on Y_2O_3 nanoparticles is predetermined by the number density of oxide particles that predominantly host a single bubble per particle for all implantation conditions. Bubbles on oxide particles are visibly larger than bubbles of other populations and their sizes are more controlled by the sizes of host nanoparticles than by variations in single-beam implantation conditions in the studied ranges. In contrast, size and density of all other bubble populations strongly depend on implantation conditions, but within each fixed single-beam implantation run, bubbles on grain boundaries, dislocations and carbides grow at approximately the same rate as bubbles in the grain bulk. Relative contributions of these bubble families to helium inventory and swelling are primarily controlled by their volumetric number densities, which are sensitive to particular irradiation conditions.

(ii) The contribution to helium inventory and swelling from bubbles associated with oxide particles is minor in all investigated single-beam regimes due to moderate number density of Y_2O_3 particles. Both contributions increase by only several percent with the decrease of helium implantation fluence or temperature and with the increase of implantation flux in the studied ranges. Among the bubble populations associated with structural defects, the most important contributors to both swelling and helium inventory are bubbles located on grain boundaries. Only bubbles in the grain bulk can serve as serious competitors in certain cases, mainly at high helium fluxes and, to less extent, at high helium fluences. Thus, our results do not support the widespread opinion that helium trapping in bubbles on oxide nanoparticles would always efficiently suppress helium accumulation on grain boundaries and thus reduce the risks of high-temperature intergranular embrittlement.

(iii) Even at the highest level of accumulated helium (12000 appm) and temperature (923 K) the extensive formation of bubbles on grain boundaries did not lead to bubble coalescence either in single-beam or in the dual-beam irradiation regime with enhanced damage production. Therefore, the high-temperature intergranular embrittlement seems not to be a lifetime restrictive issue for ODS-EUROFER steel in high He/dpa ratio environment.

(iv) The effect of accelerated damage produced by a secondary heavy ion (Au^{2+}) beam (*in situ* dual-beam irradiation) on helium redistribution between various microstructural features is relatively moderate and qualitatively similar to the case of single-beam helium implantation regime. The only important qualitative effect caused by strong acceleration of damage production is found to be the formation of large cavities on some oxide particles. The effect is interpreted as a manifestation of the bubble-to-void transition caused by the increase of the efficient vacancy supersaturation in the matrix as a result of irradiation with energetic gold ions. The effect is observed only on oxide particles because the largest bubbles were always those decorating oxide particles. Bubble-to-void transition observed in the dual-beam regime, even though taking place on a minor part of oxide particles, bears potential risk of accelerating swelling.

(v) The triggering of bubble-to-void transition by oxide nanoparticles was explained in the framework of the critical bubble growth model. The model predicts that the critical number of gas atoms necessary to initiate the transition decreases for bubbles on spherical particles as compared to bubbles in the bulk, even though the critical size for the transition increases. The effect is most pronounced for relatively large particles, which are thus the most probable candidates to launch the bubble-to-void transition, in agreement with observations.

2. Hydrogen retention in ODS-EUROFER steel and synergetic helium/hydrogen effects on swelling in a high H/dpa ratio environment at low and high temperatures

(i) ODS-EUROFER steel manifests ~3 times stronger hydrogen uptake as compared to ODS-free EUROFER 97 steel under single-beam H^+ and sequential dual-beam $He^+ + H^+$ ion implantations at room temperature. This stronger hydrogen retention cannot be attributed exclusively to the presence of oxide nanoparticles and should be related rather to differences in the volume densities of other trapping sites, such as dislocations, grain boundaries and single vacancies. Considering the estimated hydrogen binding energy to oxide particle/matrix interfaces of 0.36 eV, hydrogen trapping at nanoparticle/matrix interfaces can hardly affect swelling.

(ii) Sequential dual-beam $He^+ + H^+$ ion implantations leads to increased hydrogen retention via hydrogen accumulation in irreversible traps with the de-trapping energies of 0.78-0.81 eV. Combination of EELS and TDS analysis suggests that a chemisorption-like mechanism of hydrogen trapping at helium bubble walls plays the main role in hydrogen accumulation in the experimental conditions used.

(iii) The visible bubble microstructure after sequential dual-beam $He^+ + H^+$ ion implantations is mainly determined by the achieved helium concentration and the conditions of helium implantation or/and high-temperature processing. Hydrogen injection into ODS-EUROFER steel pre-implanted with helium did not reveal any potential hazards of notable swelling increase.

3. The effects of helium/hydrogen accumulation on secondary microstructure development near model metal/oxide interfaces, helium/hydrogen partitioning and synergetic helium/hydrogen effects

(i) Simultaneous helium-assisted cavity formation in all parts of the bi-layer metal/oxide systems was observed only after room temperature helium implantation. The tendency of preferential interfacial cavity formation observed at room temperature indicates that helium trapping at metal/oxide interface is insensitive to both metal/oxide orientation relationship and the interfacial chemistry.

(ii) In the case of high-temperature helium implantation, cavity population development in the metal layer closely resembles that in industrial ODS steels, but no helium bubble nucleation at the planar FeCr/yttria interface could be noticed, in contrast to ODS-steels, where large cavities decorating yttria nano-oxides are observed at the same temperature. Inside the oxide layer, no cavities were observed at this temperature as well; the implanted helium was either redistributed over the layer or escaped from it into the substrate or the sample environment.

(iii) Hydrogen-assisted cavity formation inside FeCr layer and at the metal/oxide interface caused by single-beam H^+ ion implantation was demonstrated. The interfacial cavities were larger than cavities in the metal layer. In contrast, microcracks rather than cavities were formed in the Y_2O_3 layer. The orientation of microcracks formed after single-beam H^+ ion implantation indicates that hydrogen might be efficiently trapped in anion vacancy loops inside oxide.

(iv) Strong synergetic effect of helium and hydrogen was observed after sequential implantation of a model bi-layer FeCr/yttria sample with helium and hydrogen. Hydrogen implantation into the system pre-implanted with helium has led to interfacial decohesion and microcrack nucleation in the oxide layer. At the same time, hydrogen had minor influence on the He-filled cavity population in the metal layer, just like in industrial ODS-steels. The moderate growth of cavities inside the metal layer might be associated with hydrogen accumulation in cavities.

The investigations performed in this PhD study have not only provided a new database contributing to fundamental understanding of gas-driven microstructure development in ferritic-martensitic ODS steels, but also have raised certain open questions that need further research to be better understood, in particular:

(i) Contribution of nanoparticles to helium inventory was calculated based on the average bubble size related to the average oxide particle size. Sometimes size distribution of nano-oxides in ODS steel is

quite wide and may include significant fraction of particles that strongly deviate from the average value. Therefore considering the real particle size distribution might improve the accuracy of helium inventory estimations. Moreover, since the nano-oxide detection via conventional TEM is challenging, the X-ray and EELS spectrum imaging might contribute.

(ii) Bubble-to-void conversion in bubble population associated with oxide nanoparticles after dual-beam He/heavy ion irradiation requires more attention. In this study quantitative dependence between oxide particle size and population of bubbles vs. voids could not be achieved due to poor statistics coming from large void size and relatively low area of TEM field of view. Consequently, only a possible range of swelling variation related to bubble-to-void conversion was estimated. An accurate correlation should be established in order to provide more relevant swelling estimations and guidelines for further design of advanced ODS steels in terms of particle size.

(iii) The dual-beam helium/heavy ion irradiation used in this thesis was oriented on the situation of high helium concentration accumulation at a relatively moderate damage level. Additional dual-beam experiments with variable He/dpa ratio are required to gain insight on the limiting He/dpa ratios that are able to promote conversion to voids for bubbles associated with oxide nanoparticles in order to justify the extrapolation of results to expected fusion or spallation reactor environments, where gas accumulation rates are expected to be few orders of magnitude lower than in our experiments.

(iv) Hydrogen accumulation in ODS steels is still far from being deeply understood. Additional TDS and EELS experiments after high temperature single-beam hydrogen implantation and multi-beam ion irradiation with hydrogen are required e.g. to clarify the major mechanisms that determine hydrogen influence on swelling, depending on temperature of hydrogen injection and the presence of radiation damage.

(v) Although preliminary EELS investigation in this study indicates hydrogen association with helium bubbles in the way of “helium core hydrogen shell”, more extensive data treatment is required. Confirmation of hydrogen presence can be achieved via complementary measurements by vibrational EELS spectroscopy and application of relevant modeling of hydrogen interaction with cavities in steel.

(vi) Model bi-layer metal/oxide systems show a good potential as templates for studying oxide interaction with secondary gas impurities and displacement damage. However, interpretation of experimental observations on planar systems in terms of their extrapolation to ODS steels requires application of appropriate simulations in order to better evaluate helium and hydrogen energetic characteristics in ODS relevant oxides and at their interfaces with Fe-based matrix.

Annex I. List of figures

- Fig. 1.1. Overview of operating temperatures and displacement damage regimes for structural materials in the current (generation II) and future Gen IV (VHTR, SCWR, LFR, GFR, SFR and MSR) and fusion energy systems [16]. 12
- Fig. 1.2. Examples of representative microstructures in irradiated materials as a function of irradiation temperature. The approximate onset temperatures for Stages I, III, and V of defect recovery are listed above the temperature scale, corresponding to initiation of long-range self-interstitial-atom migration, vacancy migration, and thermal dissolution of small vacancy clusters, respectively. T_M is the melting temperature [21]. 14
- Fig. 1.3. Comparison of swelling and maximal deformation of austenitic and ferritic-martensitic steels irradiated at 400–550°C to high doses in fast fission reactor spectrum: (a) volumetric void swelling in 304L, 316 and Ti-modified (D9) austenitic stainless steels and in tempered ferritic-martensitic steels with 9–12% Cr [15]; (b) maximum deformation (in term of swelling) of irradiated fuel pin claddings from base type 316 and type 316 Ti-modified steel, austenitic alloy alloyed with Ti, P, V, Nb, and ferritic-martensitic steels [28]. 16
- Fig. 1.4. Schematic diagram illustrating the difference in the microstructure of austenitic stainless steel and ferritic/martensitic steel [36]. 17
- Fig. 1.5. Summary of the effects of simultaneous DT fusion relevant He and H production on volumetric void swelling in ion and fission neutron irradiated F/M steels. The experimental studies include simultaneous heavy ion and He or He + H implantation at 470–510°C and fission reactor (HFIR or FFTF) irradiation at 400 °C of standard or boron-doped (to generate He) samples. The multi-ion beam irradiations used implantation rates of 10–18 appm He/dpa and 40–70 appm H/dpa. The boron doped HFIR neutron irradiated F82H samples generated ~60 or ~300 appm He, mainly created at doses <1 dpa [29]. 17
- Fig. 1.6. A schematic illustration of PM/MA fabrication route of ODS steels [69]. 19
- Fig. 1.7. Electron backscatter diffraction (EBSD) maps of a ferritic Fe-14Cr ODS alloy (a) and F/M Fe-9Cr ODS alloy (b) after hot extrusion [56]. 20
- Fig. 1.8. Comparison of the thermal creep behavior at 650 °C for ODS steels versus conventional F/M and RAFM steels [29]. 23
- Fig. 1.9. Comparison of void swelling under single ion irradiation at 450–480°C in conventional F/M steels and ODS steels [29]. 24
- Fig. 1.10. Correlation of different swelling regimes with the point defect mobility onset temperatures. (a) Schematic representation of different recovery stages as a function of temperature and associated mechanisms proposed for electron-irradiated Fe. Labels I, I2 and squares refer to mono- and di-interstitials and vacancies. (b) A simplified representation of three main volumetric swelling regimes that most materials follow under irradiation [22]. 26
- Fig. 1.11. A scheme of the cavity swelling evolution as a function of irradiation dose [22]. 27
- Fig. 1.12. (a) The dependence of the cavity radius growth rate on cavity radius showing stable bubble (r_b) and metastable void (r_v^*) radii for $n_g < n_g^*$, as well as $r^* = r_v^* = r^*$ condition at n_g^* . Here n_g is He content in a bubble and n_g^* is the critical number of gas atoms at which the bubble transforms to a growing void at the critical radius r^* . (b) Stress-driven growth of creep cavities formed on grain boundary (GB) bubbles. Based on [58]. 30
- Fig. 1.13. Bimodal cavity distributions in: (a) F/M steel F82H spallation proton-neutron irradiated to 20.3dpa/1800 appm He at ~400°C [102] and (b) ODS steel 14YW neutron irradiated to 21.2 dpa/1230 appm He at 500°C [108]. 32
- Fig. 1.14. Large cavity distribution in: (a) F/M steel F82H spallation proton-neutron irradiated to 20.3 dpa/1800 appm He at ~400°C [102] and (b) PM 2000 ODS steel neutron irradiated to 21.2 dpa/ 1230 appm at 500°C [108]. 32
- Fig. 1.15. Variation of cavity swelling rate in F/M steels as a function of sink strength ratio (Q). The areas where swelling can be suppressed by excess cavity nucleation (high He/dpa ratio) and by high dislocation density (low He/dpa ratio) are highlighted [22]. 33
- Fig. 1.16. Key elements of swelling resistance of ODS NFA steels (a) versus conventional F/M steels (b) [58]. 34

Fig. 1.17. (a) Energies of forming vacancies and trapping He at different locations in NFAs. Locations include the ferrite matrix, the bulk oxides, the oxide interfaces, and the iron grain boundaries. (b) The schematic formation of interfacial He bubbles in NFAs (ODS steel) [117].	35
Fig. 1.18. He induced cavity nucleation : (a) at grain boundaries in 14YWT [115]; (b) on prismatic dislocation loops in ultra-high purity Fe14%Cr alloy [22]; (c) Ti(C,N) precipitate [124] and (d) $M_{23}C_6$ carbide in F82H [126].	36
Fig. 1.19. Cavities associated with different nano-oxides in ODS steels neutron irradiated at 500 °C to 21 dpa with ~1200 appm He: (a) amorphous $YAlO_3$ in PM 2000 [110]; (b) crystalline Y_2O_3 in 14YW [108].	38
Fig. 1.20. Typical configuration of a VH_5 cluster. When 4 tetrahedral sites are occupied by H atoms (black small circles), only one of the tetrahedral sites marked with white small circles can be occupied to form VH_5 [153].	40
Fig. 1.21. Atomic structure of the fully H-decorated cavity in <i>bcc</i> Fe. Iron atoms are in violet, adsorbed atomic H and H_2 complexes (H dimers) - in blue [160].	41
Fig. 1.22. Hydrogen induced cavities in Fe-10Cr steel after implantation with 260 keV H^+ to the fluence of 1×10^{18} ions/cm ² (2.5 dpa at peak position) [166].	42
Fig. 1.23. Cavity development in ferrite phase of EP-450 steel after simultaneous irradiation at 480 °C with 1.8 MeV Cr^{3+} ions to 50 dpa and 20 keV H^+ ions at different H injection rates: (a) 0 appm H; (b) 1000 appm H; (c) 5000 appm H; (d) 10000 appm H [84].	42
Fig. 1.24. Swelling (a) cavity size (b) and cavity number density (c) of EP-450 steel after simultaneous irradiation at 480 °C with 1.8 MeV Cr^{3+} ions and 20 keV H^+ ions to 50 dpa as a function of H/dpa ratio [84].	43
Fig. 1.25. H saturated Al/ Al_2O_3 pillar at (a) 20°C; (b) 100°C; (c) 150°C; and (d) 200°C, respectively; (e) size evolution of proto-cavities and the cavity with temperature. From 20 to 10 °C, proto-cavities grow, but as the cavity on the corner begins to grow, the proto-cavities shrink. Scale bar corresponds to 100 nm [170].	43
Fig. 1.26. Calculated binding energies of H and He in <i>bcc</i> Fe. (a) H to H_x and $VHeH_x$ clusters [175]; (b) He to $V_nHe_mH_p$ clusters [175], (c) H to $H_mHe_jV_6$ clusters [176], (d) He to $H_mHe_jV_6$ [176].	45
Fig. 1.27. (a) The mean bubble diameter after irradiation to 1 dpa with 10 appm He/dpa and 40 appm H/dpa at 743 K in dual and triple ion-beam irradiation conditions calculated using rate theory approach. (b) Evolution of the mean bubble diameter with dose at 743 K as a function of the He/H ratio [86].	46
Fig. 1.28. Cavities developed in F82H steel irradiated at 470°C to 50 dpa in (a) triple ion beam regime Fe+He+H with 18 appm He/dpa and 70 appm H/dpa and (b) in dual ion beam regime Fe+He with 18 appm He /dpa, respectively [44]. (c) Swelling in 9Cr and 12Cr alloys irradiated at 510 °C to 50 dpa in triple ion beam regime Fe+He+H and in dual ion beam regimes with 10 appm He /dpa and 40 appm H/dpa [45].	47
Fig. 1.29. (a) Swelling and (b) number density and mean cube root diameter of cavities formed in F82H steel after self ion irradiated to 50 dpa in fusion-relevant dual-beam experiment with 18 appm He/dpa, fission-relevant triple-beam experiment with 18 appm He/dpa and 70 appm H/dpa, and spallation-relevant triple -beam experiment with 180 appm He/dpa and 1700 appm H/dpa [43].	48
Fig. 2.1. Typical microstructure of ODS-EUROFER (a,c) and EUROFER 97 steel in as-supplied state (b,d). (a,b) BSE SEM image; (c,d) BF TEM (imaging conditions ~0.5 μm underfocus). The inset shows an array of Y_2O_3 nanoparticles in ODS-EUROFER steel at a higher magnification.	64
Fig. 2.2. EBSD mapping of ODS-EUROFER in as-supplied state: (a) EBSD pattern quality map; (b) orientation image maps from EBSD data; high angle grain boundaries with misorientation angle $\geq 15^\circ$ (HAGBs) are shown as bold black lines and low angle grain boundaries (LAGBs) with misorientation between 2° and 15° are thin black lines; (c) grain boundary map showing HAGBs as black lines and LAGBs as red lines. Rolling (RD) and transverse (TD) directions marked in panel (a) are valid for all panels.	65
Fig. 2.3. Grain misorientation distribution in ODS-EUROFER steel in as-supplied state.	66
Fig. 2.4. A scheme of ODS-EUROFER and EUROFER97 sample preparation procedure used prior to ion implantation or irradiation.	68
Fig. 2.5. Typical BF TEM overview image of plane-view sample displaying a hole at the center surrounded by electron transparent areas (TEM ROI).	69

Fig. 2.6. (a) Overview and (b) schematic illustration of the UHV setup used for deposition and analysis of thin film structures.	70
Fig. 2.7. Samples fixed on the deposition holder.....	72
Fig. 2.8. LEED pattern of a pure SrTiO ₃ (001) surface.	72
Fig. 2.9. XRD patterns for Y ₂ O ₃ /FeCr thin films deposited on: (a) MgO(100); (b) YSZ(110) and (c) SrTiO ₃ (100) substrates.	73
Fig. 2.10. BF TEM image of as-fabricated bi-layer Y ₂ O ₃ /FeCr system deposited on SrTiO ₃ (100) substrate.	74
Fig. 2.11. HRTEM images and corresponding FFT images for two different as-fabricated bi-layer Y ₂ O ₃ /FeCr systems deposited on SrTiO ₃ (100) substrate. In-plane orientation relationships of films are: (a) [110] _{FeCr} [1 $\bar{1}$ 0] _{Y₂O₃} & (001) _{FeCr} (110) _{Y₂O₃} and (b) [11 $\bar{2}$] _{FeCr} [1 $\bar{1}$ 0] _{Y₂O₃} & (111) _{FeCr} (110) _{Y₂O₃}	75
Fig. 2.12. (a) HAADF STEM image of the area used for the elemental mapping; (b-c) STEM EDX elemental maps of as-fabricated bi-layer Y ₂ O ₃ /FeCr system deposited on SrTiO ₃ (100); (f) EDX line scan across the interface. Red line in panel (a) indicates the position of EDX line scan.....	76
Fig. 2.13. Typical BF TEM overview image of investigated FIB probe showing the electron transparent areas, ROI for TEM investigations and Pt protection layer.....	78
Fig. 2.14. An overview of the JANNuS-Orsay/SCALP facility [39].	79
Fig. 2.15. A scheme of goniometric heating stage for <i>ex situ</i> implantation in IRMA and ARAMIS chambers.....	81
Fig. 2.16. Scheme of ion beam injection under the IRMA+ ARAMIS +TEM mode.....	82
Fig. 2.17. SRIM-calculated depth profiles of implanted atoms (appm) and dose (dpa) in pure Fe implanted with 10 keV He ⁺ ions to the fluence of 5×10 ¹⁵ cm ⁻²	84
Fig. 2.18. SRIM-calculated depth profiles of implanted atoms (appm) and dose (dpa) in pure Fe implanted with 10 keV He ⁺ ions to the fluence of 5×10 ¹⁵ cm ⁻² and irradiated with 4 MeV Au ²⁺ to the fluence of 4.5×10 ¹⁵ cm ⁻² under: (a) simultaneous <i>in situ</i> dual ion beam regime and (b) sequential regimes with <i>ex situ</i> He ⁺ pre-injection.	87
Fig. 2.19. SRIM-calculated depth profiles of implanted atoms (appm) and dose (dpa) in pure Fe implanted with 10 keV He ⁺ ions to the fluence of 1×10 ¹⁶ cm ⁻² and with 5 keV H ⁺ to the fluence of 1×10 ¹⁷ cm ⁻²	89
Fig. 2.20. Implantation scheme of FeCr/Y ₂ O ₃ bi-layer system.....	91
Fig. 2.21. SRIM-calculated depth profiles of implanted atoms (appm) and dose (dpa) in pure Fe implanted with: ...	92
Fig. 2.22. Geometries for out-of-plane and in-plane XRD measurements [53].	95
Fig. 2.23. Schematic of SEM, TEM, and STEM imaging principles. (a) Serial collection of data by SEM (b) Parallel image acquisition by TEM. (c) Serial collection of transmitted electrons in STEM [56].	96
Fig. 2.24. The interaction of incident-beam electrons with solids. Useful signals generated by electron-matter interactions in a thin (TEM) (a) and a thick (b) sample. From Ref. [56].....	97
Fig. 2.25. (a) A scheme of the core components of SEM microscope [56]. (b) A picture of Zeiss Evo 50 XVP SEM microscope with analytical detectors.....	99
Fig. 2.26. (a) The cones (green and blue) generated by electrons from a divergent source which satisfy the Bragg conditions on a single lattice plane. These cones project onto the phosphor screen, and form the Kikuchi bands which are visible in the EBSP. (b) Generated EBSP pattern [62].	100
Fig. 2.27. (a) A scheme of the core components of an TEM microscope [56]. (b) A picture of FEI Tecnai G2 20 twin at JANNuS-Orsay facility.....	101
Fig. 2.28. Summary of the dominant contrast mechanisms in TEM and STEM operation modes [66].	102

Fig. 2.29. The relrod at \bar{g}_{hkl} when the beam is $\Delta\theta$ away from the exact Bragg condition. The Ewald sphere intercepts the relrod at a negative value of S. The intensity of the diffracted beam as a function of where the Ewald sphere cuts the relrod is shown on the right of the diagram. In this case the intensity has fallen to almost zero [55].	104
Fig. 2.30. Ray propagation diagrams showing how the objective lens and objective aperture are used in combination to produce: (a) a BF image by direct electron beam; (b) a displaced-aperture DF image with a specific off-axis scattered beam and (c) a DF image where the incident beam is tilted so that the scattered beam emerges on the optic axis [55].	104
Fig. 2.31. Example of the phase-contrast transfer function ($\sin \chi(\vec{k})$) at an accelerating voltage of 200 kV for: (a) Cs: 0.5 mm and for (b) Cs: 5 mm [119].	108
Fig. 2.32. A scheme of the different electron detectors in a STEM along with the range of electron scattering angles gathered by each detector [55].	109
Fig. 2.33. (a) An inner (K) shell electron is ejected from the atom by a high-energy electron. When the hole in the K shell is filled by an electron from the L shell, characteristic (K_{α}) X-ray emission occurs. The beam electron loses energy but continues moving through the sample [55]. (b) Example of an EDX spectrum from the interface of $Y_2O_3/FeCr$ bi-layer system.	110
Fig. 2.34. (a) Ray paths through a magnetic prism spectrometer showing the different dispersion and focusing of the no-loss and energy-loss electrons in the dispersion plane of the spectrometer. The inset shows the analogy with the dispersion of white light by a glass prism. (b) The lens focusing action in the plane normal to the spectrometer [55].	111
Fig. 2.35. An example of EELS spectrum displayed in logarithmic intensity scale. The zero-loss peak is an order of magnitude more intense than the low energy-loss portion (characterized by the plasmon peak), which is many orders of magnitude more intense than the small ionization edges [55].	112
Fig. 2.36. Energy-loss data collection in spectrum imaging acquisition mode. (a) STEM regime; (b) CTEM regime [78].	114
Fig. 2.37. In-focus BF TEM image of vacancy voids in the 16Cr–15Ni–3Mo–0.3Ti steels after irradiation in BN-600 reactor with fast neutrons to 60 dpa at 500°C [94].	116
Fig. 2.38. Through-focus TEM bright field micrographs of helium bubbles in Fe–9%Cr alloy after 8 keV He^+ implantation at 400 °C to 1.1×10^5 appm He. (a) +1 μm overfocused image; (b) -1 μm underfocused image [92].	117
Fig. 2.39. The size correlation between imaged Fresnel rings and the actual bubbles for small spherical voids in thick TEM sample. Dynamical two-beam conditions. The diameters (d_{in}/d_b) and (d_{out}/d_b) of the inner and outer first dark Fresnel fringe are shown as a function of the actual cavity diameter (d_b) for the underfocus of - 0.8 μm [71].	118
Fig. 2.40. The size correlation between imaged Fresnel fringes and the actual bubbles as a function of the: (a) deviation of illumination semi-angle ($\Delta\alpha$); (b) underfocus for cavities with different sizes [97].	119
Fig. 2.41. HAADF-STEM image of He-filled cavities and nano-oxides in 14YWT steel implanted with He^+ ions at 400°C [68].	119
Fig. 2.42. Qualitative evaluation of contrast in HAADF-STEM, BF-STEM, and BF-TEM images with respect to cavity and nano-oxides in 14YWT steel implanted with He^+ ions at 400°C [68]. Labels are the same as in Fig. 2.41.	120
Fig. 2.43. (a) HRTEM image of Y_2O_3 -particle with an attached He bubble [90]; (b) and (c) HAADF HRSTEM unprocessed and processed image of $Y_2Ti_2O_7$ particle with attached He bubbles [103].	121
Fig. 2.44. A summary of various hydrogen trapping sites in metallic alloys [106].	122
Fig. 2.45. Overview and principle scheme of TDS setup [108].	123
Fig. 2.46. TDS spectra for hydrogen release from: (a) EUROFER 97 and ODS-EUROFER (b) ODS-EUROFER and PM2000 [109].	123
Fig. 2.47. Schematic illustration of different energies involved in hydrogen diffusion and trapping.	124

- Fig. 3.1. FIB cross-section of ODS-EUROFER steel implanted with 40 keV He⁺ ions to the fluence of 5×10¹⁶ cm⁻² at 923 K (a) and with 10 keV He⁺ ions to the fluence of 5×10¹⁵ cm⁻² at 823 K (b). BF TEM imaging conditions: ~1 μm underfocus. Dash lines show projection range zone (with the highest He content)..... 136
- Fig. 3.2. FIB cross-section of ODS-EUROFER steel implanted with 10 keV He⁺ ions to the fluence of 5×10¹⁵ cm⁻² at 823 K with at the flux of 5×10¹¹ cm⁻²s⁻¹. BF TEM imaging conditions: (a,c) ~1 μm underfocus and (b,d) ~1 μm overfocus. Dash lines show limit the described zones, solid lines mark structural defects decorated with He bubbles. 137
- Fig. 3.3. He bubble size (a) and density (b) distribution with respect to distance from implanted surface in ODS-EUROFER steel implanted with 10 keV He⁺ ions at T=823 K with the flux of 5×10¹¹ cm⁻²s⁻¹ to the fluence of 5×10¹⁵ cm⁻²..... 137
- Fig. 3.4. Planar view of the sample of ODS-EUROFER steel implanted with 10 keV He⁺ ions to the fluence of 5×10¹⁵ cm⁻² at 823 K with at the flux of 5×10¹⁵ cm⁻²s⁻¹. Sample thickness is ~40 nm. BF TEM imaging conditions are: (a) ~1 μm underfocus and (b) ~1 μm overfocus. 138
- Fig. 3.5. Typical trough-focus images of high-angle grain boundaries and dislocations (a-b) and low-angle grain boundaries and dislocations (c-d) in ODS-EUROFER steel implanted with 10 keV He⁺ ions to the fluence of 5×10¹⁵ cm⁻² at 823 K with the flux of 5×10¹¹ cm⁻²s⁻¹. BF TEM imaging conditions are: (a,c) ~0.5 μm underfocus and (b,d) ~0.5 μm overfocus. 139
- Fig. 3.6. Typical trough-focus images of M₂₃C₆ carbide precipitates (a-b) and Y₂O₃ nanosized precipitates (c-d) in ODS-EUROFER steel implanted with 10 keV He⁺ ions to the fluence of 5×10¹⁵ cm⁻² at 823 K with the flux of 5×10¹¹ cm⁻²s⁻¹. BF TEM imaging conditions: (a,c) ~0.5 μm underfocus and (b,d) ~0.5 μm overfocus..... 140
- Fig. 3.7. Typical trough-focus images of Y₂O₃ nano-oxide precipitates in ODS-EUROFER steel implanted with 10 keV He⁺ ions to the fluence of 5×10¹⁵ cm⁻² at 823 K with a flux of 5×10¹¹ cm⁻²s⁻¹. BF TEM imaging conditions: (a) ~0.4 μm underfocus and (b) ~0.4 μm overfocus. 141
- Fig. 3.8. Microstructure of ODS-EUROFER steel implanted with 10 keV He⁺ ions at 823 K with flux of the 5×10¹¹ cm⁻²s⁻¹ to different fluencies: (a,b) 1×10¹⁵ cm⁻²; (c,d) 5×10¹⁵ cm⁻²; (e,f) 1×10¹⁶ cm⁻². BF TEM imaging conditions: (a,c,e) ~1 μm underfocus and (b,d,f) ~1 μm overfocus..... 145
- Fig. 3.9. He bubbles inside grain bulk interior of ODS-EUROFER steel implanted with 10 keV He⁺ ions at 823 K with the flux of 5×10¹¹ cm⁻²s⁻¹ to the fluence of 1×10¹⁶ cm⁻²; BF TEM imaging conditions are: (a) ~0.4 μm underfocus; (b) ~0.4 μm overfocus. 145
- Fig. 3.10. Association of He bubbles with Y₂O₃ nanoparticles of different size in ODS-EUROFER steel implanted with 10 keV He⁺ ions at 823 K with the flux of 5×10¹¹ cm⁻²s⁻¹ to the fluence of 1×10¹⁶ cm⁻². Oxide particles completely enveloped by He bubbles are marked by arrows. BF TEM imaging conditions: ~0.4 μm underfocus... 146
- Fig. 3.11. Bubble size on yttria nanoparticles vs. particle size for the ODS-EUROFER steel implanted with 10 keV He⁺ ions at 823 K with the flux of 5×10¹¹ cm⁻²s⁻¹ to the fluences of 1×10¹⁵; 5×10¹⁵; and 1×10¹⁶ cm⁻². Solid lines are best fits for each fluence. The grey marked area corresponds to the bubbles with the size smaller than that of the particle. Error bars are 10% uncertainties associated with the size of the first Fresnel fringe on bubble observed in underfocused images [9,16]..... 146
- Fig. 3.12. Microstructure of ODS-EUROFER steel implanted with 10 keV He⁺ ions at 823 K to the fluence of 5×10¹⁵ cm⁻² with different fluxes: (a,b) 5×10¹¹ cm⁻²s⁻¹; (c,d) 1×10¹² cm⁻²s⁻¹; (e,f) 5×10¹² cm⁻²s⁻¹. BF TEM imaging conditions are: (a,c,e) ~1 μm underfocus and (b,d,f) ~1 μm overfocus. 150
- Fig. 3.13. Bubble size on yttria nanoparticles vs. particle size for the ODS-EUROFER steel implanted with 10 keV He⁺ ions at 823 K with the fluxes varying from 5×10¹¹ to 5×10¹² cm⁻²s⁻¹ to the fluence of 5×10¹⁵ cm⁻². Solid lines are best fits for each flux. The grey marked area corresponds to the bubbles with the size smaller than that of the particle. Error bars are 10% uncertainties associated with the size of the first Fresnel fringe on bubble observed in underfocused images [9,16]..... 151
- Fig. 3.14. Microstructure of ODS-EUROFER steel implanted with 10 keV He⁺ ions with the flux of 5×10¹¹ cm⁻²s⁻¹ to fluence 5×10¹⁵ cm⁻² at different temperatures: (a,b) 723 K; (c,d) 823 K; (e,f) 923 K. BF TEM imaging conditions: (a,c,e) ~1 μm underfocus and (b,d,f) ~1 μm overfocus. 154
- Fig. 3.15. Bubble size on yttria nanoparticles vs. particle size for the ODS-EUROFER steel implanted with 10 keV He⁺ ions at temperatures 723, 823, and 923 K with the flux of 5×10¹¹ cm⁻²s⁻¹ to the fluence of 5×10¹⁵ cm⁻². Solid

lines are best fits for each temperature. The grey marked area corresponds to the bubbles with the size smaller than that of the particle. Error bars are 10% uncertainties associated with the size of the first Fresnel fringe on bubble observed in underfocused images [9,16].	155
Fig. 3.16. Approximation of the lens-shaped bubbles attached to a flat (a) or spherical surface (b) of the Y_2O_3 nanoparticle.	158
Fig. 3.17. Bubble volume calculated for curved surface, flat interface and equivalent sphere approximation; for $R=4.05$ nm and $\alpha = 48^\circ$.	159
Fig. 3.18. Various EOSs for He at $T = 825$ K [21].	160
Fig. 3.19. Graphical representation of the data from Table 3.7. Shades of grey used to differentiate between the data for different fluences are explained in the legend located in panel (a).	164
Fig. 3.20. Graphical representation of the data from Table 3.8. Shades of grey used to differentiate between the data for different fluxes are explained in the legend located in panel (a).	168
Fig. 3.21. Graphical representation of the data from Table 3.9. Shades of grey used to differentiate between the data for different temperatures are explained in the legend in panel (a).	172
Fig. 3.22. Relative contributions to total swelling from bubbles and HeV clusters for (a) fluence, (b) flux, and (c) temperature variation conditions.	174
Fig. 3.23. Microstructure of ODS-EUROFER steel implanted with 10 keV He^+ ions with a flux of $5 \times 10^{11} \text{ cm}^{-2}\text{s}^{-1}$ to the fluence of $5 \times 10^{15} \text{ cm}^{-2}$ at room temperature and subsequently annealed at 823 K for 90 minutes. BF TEM imaging conditions: (a,c) $\sim 0.8 \mu\text{m}$ underfocus and (b,d) $\sim 0.8 \mu\text{m}$ overfocus.	175
Fig. 3.24. Bubble size on yttria nanoparticles vs. particle size for the ODS-EUROFER steel samples implanted at RT with He^+ ions at the flux of $5 \times 10^{11} \text{ cm}^{-2}\text{s}^{-1}$ to the fluence of $5 \times 10^{15} \text{ cm}^{-2}$ and annealed at $T=823$ K. Red solid line fits current dataset, black solid line is the fit for He^+ implantation at 823 K. The grey marked area corresponds to the bubbles with the size smaller than that of the particle. Error bars are 10% uncertainties associated with the size of the first Fresnel fringe on bubble observed in underfocused images [9,16].	176
Fig. 3.25. Comparative statistical analysis of bubble mean size, volume density of bubbles, swelling and retained He fraction associated with different bubble populations in ODS-EUROFER implanted with He^+ ions at the flux of $5 \times 10^{11} \text{ cm}^{-2}\text{s}^{-1}$ to the fluence of $5 \times 10^{15} \text{ cm}^{-2}$ at RT followed by 90 minutes PIA at 823 K (red bars) and at 823 K with the flux of $1 \times 10^{12} \text{ cm}^{-2}\text{s}^{-1}$ to the fluence of $5 \times 10^{15} \text{ cm}^{-2}$ (grey bars). Color references provided in panel (a) are valid for all panels. Data for high-temperature regime are adapted from Table 3.8.	178
Fig. 3.26. The effect of nanoparticle number density N_p variation on (a) the particle-associated bubble contributions to swelling S_p and the captured helium fraction F_{He}^p and (b) on the cumulative swelling S and helium fraction F_{He} in all visible bubbles.	180
Fig. 3.27. Typical microstructure of EUROFER 97 implanted with He^+ ions to the fluence of $1 \times 10^{16} \text{ cm}^{-2}$ at 823 K. BF TEM imaging conditions: (a) $\sim 1 \mu\text{m}$ underfocus and (b) $\sim 1 \mu\text{m}$ overfocus.	181
Fig. 3.28. Carbide precipitates in EUROFER 97 implanted at 823 K with He^+ ions to the fluence of $1 \times 10^{16} \text{ cm}^{-2}$ (12.5×10^3 appm): (a) MC carbide; (b) $M_{23}C_6$ carbide. BF TEM imaging conditions: $\sim 0.5 \mu\text{m}$ underfocus.	182
Fig. 3.29. Microstructure of EUROFER 97 (a) and ODS-EUROFER (b) implanted at 823 K with He^+ ions to the fluence of $1 \times 10^{16} \text{ cm}^{-2}$ (12.5×10^3 appm). BF TEM imaging condition $\sim 0.8 \mu\text{m}$ underfocus.	182
Fig. 3.30. MX precipitate in EUROFER 97 (a) and yttria precipitate in ODS-EUROFER (b) steels implanted with He^+ ions to the fluence of $1 \times 10^{16} \text{ cm}^{-2}$ (12.5×10^3 appm) at 823 K. BF TEM imaging conditions: $\sim 0.5 \mu\text{m}$ underfocus.	183
Fig. 3.31. The average sizes of He bubbles associated with different microstructural defects in EUROFER 97 and ODS-EUROFER implanted to the fluence of $1 \times 10^{16} \text{ cm}^{-2}$ (12.5×10^3 appm) at $T= 823$ K with a flux $5 \times 10^{11} \text{ cm}^{-2}\text{s}^{-1}$. *MX precipitates are observed only in EUROFER 97.	183

- Fig. 3.32. Cumulative swelling (a) and fraction of implanted helium (b) in EUROFER 97 (red bars) and ODS-EUROFER (grey bars) implanted to fluence $1 \times 10^{16} \text{ cm}^{-2}$ (12.5×10^3 appm) at the $T = 823 \text{ K}$ with the flux $5 \times 10^{11} \text{ cm}^{-2} \text{ s}^{-1}$ 185
- Fig. 3.33. Microstructure of ODS-EUROFER steel implanted at RT with 10 keV He^+ ions at the flux of $5 \times 10^{11} \text{ cm}^{-2} \text{ s}^{-1}$ to the fluence of $5 \times 10^{15} \text{ cm}^{-2}$ and then *in situ* irradiated at 823 K with 4 MeV Au^{2+} at the flux of $4 \times 10^{11} \text{ cm}^{-2} \text{ s}^{-1}$ to the fluence of $4.5 \times 10^{15} \text{ cm}^{-2}$. BF TEM imaging conditions: (a,c) $\sim 0.8 \mu\text{m}$ underfocus and (b,d) $\sim 0.8 \mu\text{m}$ overfocus. 187
- Fig. 3.34. Bubble size on yttria nanoparticles vs. particle size for the ODS-EUROFER steel implanted at RT with 10 keV He^+ ions at the flux of $5 \times 10^{11} \text{ cm}^{-2} \text{ s}^{-1}$ to the fluence of $5 \times 10^{15} \text{ cm}^{-2}$ and then *in situ* irradiated at 823 K with 4 MeV Au^{2+} ions at the flux of $4 \times 10^{11} \text{ cm}^{-2} \text{ s}^{-1}$ to the fluence of $4.5 \times 10^{15} \text{ cm}^{-2}$. Red solid line fits the current dataset, black solid line is the fit for single-beam He^+ implantation at RT followed by PIA at 823 K. The grey marked area corresponds to the bubbles with the size smaller than that of the particle. Error bars are 10% uncertainties associated with the size of the first Fresnel fringe on bubble observed in underfocused images [9,16]. 188
- Fig. 3.35. Comparative statistical analysis of bubble mean size, the volume density of bubbles, swelling and retained He fraction associated with different bubble populations in ODS-EUROFER steel either sequentially dual-beam irradiated with 10 keV He^+ at RT and 4 MeV Au^{2+} ions at 823 K (red bars), or single-beam implanted with 10 keV He^+ ions at RT followed by 90 minutes PIA at 823 K (grey bars). Color references provided in panel (a) are valid for all panels. Data for He^+ single beam implantation is from Table 3.12. 190
- Fig. 3.36. Microstructure of ODS-EUROFER steel after simultaneous dual-beam *in situ* irradiation at 823 K with 10 keV He^+ ions at the flux of $5 \times 10^{11} \text{ cm}^{-2} \text{ s}^{-1}$ to the fluence of $5 \times 10^{15} \text{ cm}^{-2}$ and 4 MeV Au^{2+} ions with the flux of $4 \times 10^{11} \text{ cm}^{-2} \text{ s}^{-1}$ to the fluence of $4.5 \times 10^{15} \text{ cm}^{-2}$. BF TEM imaging conditions are: (a,c) $\sim 0.8 \mu\text{m}$ underfocus and (b,d) $\sim 0.8 \mu\text{m}$ overfocus. 192
- Fig. 3.37. Association of helium bubbles/voids with Y_2O_3 nanoparticles in ODS-EUROFER steel after simultaneous dual-beam *in situ* irradiation at 823 K with 10 keV He^+ ions at the flux of $5 \times 10^{11} \text{ cm}^{-2} \text{ s}^{-1}$ to the fluence of $5 \times 10^{15} \text{ cm}^{-2}$ and 4 MeV Au^{2+} ions with the flux of $4 \times 10^{11} \text{ cm}^{-2} \text{ s}^{-1}$ to the fluence of $4.5 \times 10^{15} \text{ cm}^{-2}$: (a,b) bubbles attached to particles and (c,d) large cavities attached to particles. BF TEM imaging conditions: $\sim 0.5 \mu\text{m}$ underfocus. 193
- Fig. 3.38. Bubble size on yttria nanoparticles vs. particle size for the ODS-EUROFER steel simultaneously *in situ* irradiated at 823 K with 10 keV He^+ ions at the flux of $5 \times 10^{11} \text{ cm}^{-2} \text{ s}^{-1}$ to the fluence of $5 \times 10^{15} \text{ cm}^{-2}$ and 4 MeV Au^{2+} ions at the flux of $4 \times 10^{11} \text{ cm}^{-2} \text{ s}^{-1}$ to the fluence of $4.5 \times 10^{15} \text{ cm}^{-2}$. (a) Black dots are full current data set. Black solid line is the fit for single-beam He^+ implantation. The grey marked area corresponds to the bubbles with the size smaller than that of the particle. (b) Data subset for “bubble” population satisfying the condition $D_c^p \leq D_p$; blue solid line is the data fit for single-beam He^+ implantation. (c) Data subset for “void” population satisfying the condition $D_c^p > D_p$; red solid line is the best data fit. Error bars are 10% uncertainties associated with the size of the first Fresnel fringe on bubble observed in underfocused images [9,16]. 194
- Fig. 3.39. Comparative statistical analysis of bubble mean size, the volume density of bubbles, swelling and retained He fraction associated with different bubble populations in ODS-EUROFER steel either simultaneously dual-beam irradiated with 10 keV He^+ + 4 MeV Au^{2+} ions at 823 K (red bars), or single-beam implanted with 10 keV He^+ ions at 823 K (grey bars). Color references provided in panel (a) are valid for all panels. Data for single-beam He^+ implantation are from Table 3.7. 197
- Fig. 3.40. Cumulative swelling in ODS-EUROFER irradiated at $T = 823 \text{ K}$ either simultaneously with a dual-beam of 10 keV He^+ ions with the flux of $5 \times 10^{11} \text{ cm}^{-2} \text{ s}^{-1}$ to the fluence of $5 \times 10^{15} \text{ cm}^{-2}$ and 4 MeV Au^{2+} ions with the flux of $4 \times 10^{11} \text{ cm}^{-2} \text{ s}^{-1}$ to the fluence of $4.5 \times 10^{15} \text{ cm}^{-2}$ (red bars) or by single-beam 10 keV He^+ ions with the flux of $5 \times 10^{11} \text{ cm}^{-2} \text{ s}^{-1}$ to the fluence of $5 \times 10^{15} \text{ cm}^{-2}$ (grey bar). Data for He^+ single-beam implantation are taken from Table 3.7. 198
- Fig. 3.41. The dependence of function Q on normalized cavity radius ρ at different values of normalized gas content in the cavity η_g . (a) $\eta_g = 0$; (b) $\eta_g = 0.1$; (c) $\eta_g = 0.5$; (d) $\eta_g = 1.0$; (e) $\eta_g = 1.5$ 203
- Fig. 3.42. (a) HRTEM image of a He-filled cavity attached to yttria nanoparticle in ODS-EUROFER steel irradiated with a single He^+ ion beam to $\sim 8.5 \times 10^3$ appm He (peak value). HRTEM imaging conditions: $\sim 0.3 \mu\text{m}$ underfocus. (b) Schematic representation of a lens-shaped cavity attached to spherical nanoparticle. 204
- Fig. 3.43. Variation of the factor $f_l = n_{gl}^* / n_g^*$ as a function of wetting angle α 206

- Fig. 3.44. The normalized bubble volume as a function of the cavity to particle size ratio ζ . Different curve colors correspond to different wetting angles as specified in the legend.206
- Fig. 3.45. The dependence of χ on the cavity to particle size ratio ζ . Different curve colors correspond to different wetting angles as specified in the legend.....207
- Fig. 3.46. The comparison of exact (solid lines) and approximate (dashed lines) values of (a) ρ_p^* and (b) η_{gp}^* as a function of the normalized particle size R_p/R^* at different α . Curve colors in both panels are specified in the legend.208
- Fig. 3.47. The critical parameters ρ_p^* (left column) and η_{gp}^* (right column) as a function of the normalized particle size R_p/R^* at different α (as indicated in the legends). Curves within each panel correspond either to the ideal gas law (solid) or to HSEOS with $s = 1$ (dash), 5 (das-dot) and 10 (dash-dot-dot).210
- Fig. 3.48. Relative contributions to retained He fraction and total swelling from bubbles and He-V clusters in ODS-EUROFER steel implanted with He⁺ ions: (a,b) as a function of fluence in the range 1×10^{15} - 1×10^{16} cm⁻² for the flux of 5×10^{11} cm⁻²s⁻¹ at T=823 K; (c,d) as a function of flux in the range of 5×10^{11} - 5×10^{12} cm⁻²s⁻¹ with the fluence of 5×10^{15} cm⁻² at T=823 K; (e,f) as a function of temperature in the range of 723-823 K to the fluence of 5×10^{15} cm⁻² with the flux of 5×10^{11} cm⁻²s⁻¹. Colors differentiate the data for bubbles and HeV clusters, as explained in the legend located in panel (a). The depicted helium shares are normalized to the total implanted helium concentrations. Presentation is based on the data collected in Table 3.10.....214
- Fig. 3.49. Contributions of bubbles associated with different microstructural features to retained He fraction in ODS-EUROFER steel implanted with He⁺ ions: (a,b) as a function of fluence in the range 1×10^{15} - 1×10^{16} cm⁻² with the flux of 5×10^{11} cm⁻²s⁻¹ at T=823 K; (c,d) as a function of flux in the range of 5×10^{11} - 5×10^{12} cm⁻²s⁻¹ to the fluence of 5×10^{15} cm⁻² at T=823 K; (e,f) as a function of temperature in the range of 723-823 K to the fluence of 5×10^{15} cm⁻² with the flux of 5×10^{11} cm⁻²s⁻¹. Colors differentiate between bubble populations, as explained in the legend located on top of the figure. The depicted helium shares are normalized to the total helium concentration contained in all bubbles. Presentation is based on the data collected in Tables 3.7-3.9.....216
- Fig. 3.50. Contributions to swelling from bubbles associated with different microstructural features in ODS-EUROFER implanted with He⁺ ions: (a,b) as a function of fluence in the range 1×10^{15} - 1×10^{16} cm⁻² with the flux of 5×10^{11} cm⁻²s⁻¹ at T=823 K; (c,d) as a function of flux in the range of 5×10^{11} - 5×10^{12} cm⁻²s⁻¹ to the fluence of 5×10^{15} cm⁻² at T=823 K with the; (e,f) as a function of temperature in the range of 723-823 K to the fluence of 5×10^{15} cm⁻² with the flux of 5×10^{11} cm⁻²s⁻¹. Colors differentiate between bubble populations, as explained in the legend located on top of the figure. Presentation is based on the data collected in Tables 3.7-3.9.217
- Fig. 3.51. Contributions of bubbles associated with different microstructural features to retained He fraction in ODS-EUROFER steel implanted at 823 K with He⁺ ions with the flux of 5×10^{11} cm⁻²s⁻¹ to the fluence of 5×10^{15} cm⁻²: (a) in a single-beam regime; (b) simultaneously with Au²⁺ ion beam with the flux of 4×10^{11} cm⁻²s⁻¹ to the fluence of 4.5×10^{15} cm⁻². Colors differentiate between bubble populations, as explained in the legend located on top of the figure. The depicted helium shares are normalized to the total helium concentration contained in all bubbles. Presentation is based on the data collected in Tables 3.7 and 3.18.....218
- Fig. 3.52. The influence of dpa/appm ratio on swelling contributions from bubbles on different microstructural defects. Colors differentiate between bubble populations, as explained in the legend located on top of the figure. Presentation is based on the data collected in Tables 3.7 and 3.18.....219
- Fig. 4.1. Microstructure of ODS-EUROFER steel (FIB-cut cross-section): (a,b) after sequential implantation with He⁺ ions at the flux of 1×10^{12} cm⁻²s⁻¹ to the fluence of 5×10^{15} cm⁻² and H⁺ ions at the flux of 7×10^{12} cm⁻²s⁻¹ to the fluence of 1×10^{17} cm⁻² and (c,d) after single-beam He⁺ implantation in the same conditions followed by tempering for the same duration of H⁺ implantation. BF TEM imaging conditions: (a,c) ~ 1 μ m underfocus and (b,d) ~ 1 μ m overfocus. Dash lines show implanted zone, arrows mark structural defects decorated by bubbles.228
- Fig. 4.2. The distribution of He bubble mean sizes (a) and number densities (b) depending on the distance from the implanted surface in ODS-EUROFER steel samples after either sequential dual-beam implantation with He⁺ and H⁺ ions or single-beam He⁺ implantation at 823 K. The colors of data bars correspond to different implantation regimes as indicated in the legend located in panel (a).229
- Fig. 4.3. Typical images of Y₂O₃ nano-precipitates in ODS-EUROFER steel implanted (a) sequentially with He⁺ ions with the flux of 1×10^{12} cm⁻²s⁻¹ to the fluence of 5×10^{15} cm⁻² and H⁺ ions with the flux of 7×10^{12} cm⁻²s⁻¹ to the fluence of 1×10^{17} cm⁻², and (b) after single-beam He⁺ implantation in the same conditions followed by tempering for the same duration of H⁺ implantation. BF TEM imaging conditions: ~ 0.8 μ m underfocus.229

Fig. 4.4. Bubble size on yttria nanoparticles vs. particle size for the ODS-EUROFER steel implanted at 823 K either sequentially with He⁺ and H⁺ ions (red dots) or with single He⁺ beam followed by tempering during H⁺ implantation. Red and blue lines fit data sets for sequential dual-beam He⁺+H⁺ and single-beam He⁺+tempering regimes, respectively. Black line is the fit for single-beam He⁺ implantation without tempering. The grey marked area corresponds to the bubbles with the size smaller than that of the particle. Error bars are 10% uncertainties associated with the size of the first Fresnel fringe on bubble observed in underfocused images [11,12]......230

Fig. 4.5. Comparative statistical analysis of bubble average sizes, volume densities of bubbles, swelling and retained He fraction associated with bubbles in ODS-EUROFER steel implanted at 823 K sequentially with He⁺ ions at the flux of 1×10¹² cm⁻²s⁻¹ to the fluence of 5×10¹⁵ cm⁻² and H⁺ ions at the flux of 7×10¹² cm⁻²s⁻¹ to the fluence of 1×10¹⁷ cm⁻² (red bars), and with single He⁺ beam at the flux of 1×10¹² cm⁻²s⁻¹ to the fluence of 5×10¹⁵ cm⁻² with and without tempering during H⁺ implantation (grey bars). Color references provided in panel (a) are valid for all panels. Data for single He⁺ beam implantation without tempering are borrowed from Table 3.8.232

Fig. 4.6. Microstructure of ODS-EUROFER steel implanted at RT: (a,b) with single He⁺ beam at the flux of 5×10¹¹ cm⁻²s⁻¹ to the fluence of 5×10¹⁵ cm⁻²; (c,d) after subsequent implantation with H⁺ ions at the flux of 7×10¹² cm⁻²s⁻¹ to the fluence of 1×10¹⁷ cm⁻²; and (e,f) sequentially with He⁺ and H⁺ ions followed by PIA at 823 K; BF TEM imaging conditions: (a,c,e) ~0.3 μm underfocus and (b,d,f) ~0.3 μm overfocus.....234

Fig. 4.7. Typical images of Y₂O₃ nano-oxide precipitates in ODS-EUROFER steel implanted at RT: (a,b) with single He⁺ beam at the flux of 5×10¹¹ cm⁻²s⁻¹ to the fluence of 5×10¹⁵ cm⁻²; (c,d) after subsequent implantation with H⁺ ions at the flux of 7×10¹² cm⁻²s⁻¹ to the fluence of 1×10¹⁷ cm⁻²; and (e,f) sequentially with He⁺ and H⁺ ions followed by PIA at 823 K; BF TEM imaging conditions: (a,c,e) ~0.3 μm underfocus and (b,d,f) ~0.3 μm overfocus.235

Fig. 4.8. Bubble size on yttria nanoparticles vs. particle size for the ODS-EUROFER steel sequentially implanted at RT with He⁺ ions at the flux of 1×10¹² cm⁻²s⁻¹ to the fluence of 5×10¹⁵ cm⁻² and H⁺ ions at the flux of 7×10¹² cm⁻²s⁻¹ to the fluence of 1×10¹⁷ cm⁻², followed by PIA at 823 K. Red solid line fits the current data set. Black solid line is the fit for single-beam He⁺ implantation at RT followed by PIA at 823 K. The grey marked area corresponds to the bubbles with the size smaller than that of the particle. Error bars are 10% uncertainties associated with the size of the first Fresnel fringe on bubble observed in underfocused images [11,12].236

Fig. 4.9. Comparative statistical analysis of bubble average sizes, volume densities of bubbles, swelling and retained He fraction associated with bubbles in ODS-EUROFER steel implanted at RT sequentially with He⁺ ions with the flux of 5×10¹¹ cm⁻²s⁻¹ to the fluence of 5×10¹⁵ cm⁻² and H⁺ ions with the flux of 7×10¹² cm⁻²s⁻¹ to the fluence of 1×10¹⁷ cm⁻² before and after PIA at 823 K (red bars), and with single He⁺ beam with the same parameters and PIA at 823 K (grey bars). Color references provided in panel (a) are valid for all panels. Data for single He⁺ beam implantation are from Table 3.12.238

Fig. 4.10. Microstructure of ODS-EUROFER steel implanted (a) with single He⁺ beam at the flux of 5×10¹¹ cm⁻²s⁻¹ to the fluence of 1×10¹⁶ cm⁻² at 823 K; (b) sequentially with He⁺ ions and then with H⁺ with the flux of 7×10¹² cm⁻²s⁻¹ to the fluence of 1×10¹⁷ cm⁻² at RT. BF TEM imaging condition ~0.5 μm underfocus.240

Fig. 4.11. Microstructure of ODS-EUROFER steel implanted sequentially with He⁺ ions at the flux of 5×10¹¹ cm⁻²s⁻¹ to the fluence of 1×10¹⁶ cm⁻² at 823 K and then with H⁺ ions with the flux of 7×10¹² cm⁻²s⁻¹ to the fluence of 1×10¹⁷ cm⁻² at RT. BF TEM imaging conditions: (a) ~0.3 μm underfocus, (b) ~0.3 μm overfocus.....241

Fig. 4.12. TDS curves of hydrogen release from ODS-EUROFER and EUROFER 97 steel samples implanted with H⁺ ions at the flux of 7×10¹² cm⁻²s⁻¹ to the fluence of 1×10¹⁷ cm⁻² at RT: (a) raw data; (b) spectra after filtering and background subtraction.243

Fig. 4.13. TDS spectra of hydrogen release from samples sequentially implanted at RT with He⁺ ions at the flux of 5×10¹¹ cm⁻²s⁻¹ to the fluence of 5×10¹⁵ cm⁻² and H⁺ ions at the flux of 7×10¹² cm⁻²s⁻¹ to the fluence of 1×10¹⁷ cm⁻²: (a) ODS-EUROFER; (b) EUROFER 97. For comparison, the data obtained for single-beam H⁺ implantation are shown as black curves.244

Fig. 4.14. Comparison of accumulated hydrogen concentrations measured by TDS analysis in samples of ODS-EUROFER and EUROFER 97 steels implanted at RT sequentially with He⁺ ions at the flux of 5×10¹¹ cm⁻²s⁻¹ to the fluence of 5×10¹⁵ cm⁻² and H⁺ ions at the flux of 7×10¹² cm⁻²s⁻¹ to the fluence of 1×10¹⁷ cm⁻² (red bars) and in the samples implanted with single H⁺ ion beam (grey bars).246

Fig. 4.15. TDS spectra of hydrogen release from ODS-EUROFER steel samples sequentially implanted with He⁺ ions at the flux of 5×10¹¹ cm⁻²s⁻¹ to the fluence of 1×10¹⁶ cm⁻² at 823 K and with H⁺ ions at the flux of 7×10¹² cm⁻²s⁻¹ to the fluence of 1×10¹⁷ cm⁻² at RT (red curve), and after single-beam H⁺ implantation with the flux of 7×10¹² cm⁻²s⁻¹ to the fluence of 1×10¹⁷ cm⁻² at RT (black curve).247

- Fig. 4.16. TDS curves of hydrogen release obtained from samples of ODS-EUROFER sequentially implanted at RT with He⁺ ions at the flux of $5 \times 10^{11} \text{ cm}^{-2}\text{s}^{-1}$ to the fluence of $1 \times 10^{16} \text{ cm}^{-2}$ and H⁺ ions at the flux of $7 \times 10^{12} \text{ cm}^{-2}\text{s}^{-1}$ to the fluence of $1 \times 10^{17} \text{ cm}^{-2}$. The curves corresponding to heating rates of 3K/min, 6K/min and 10 K/min are colored blue, red, and black, respectively: (a) raw spectra; (b) spectra after filtering and background subtraction. The inset in panel (b) shows a magnified portion of the curves in the region of peak 4. 249
- Fig. 4.17. An example of deconvolution of the TDS spectrum for ODS-EUROFER sample sequentially implanted at RT with He⁺ ions at the flux of $5 \times 10^{11} \text{ cm}^{-2}\text{s}^{-1}$ to the fluence of $1 \times 10^{16} \text{ cm}^{-2}$ and H⁺ ions at the flux of $7 \times 10^{12} \text{ cm}^{-2}\text{s}^{-1}$ to the fluence of $1 \times 10^{17} \text{ cm}^{-2}$. The heating rate is 6 K/min. The color coding for each deconvolution peak is explained in the legend. 250
- Fig. 4.18. Dependence of $\ln((\partial T/\partial t)/T_m^2)$ on $(1/T_m)$ for ODS-EUROFER samples sequentially implanted at RT with He⁺ ions at the flux of $5 \times 10^{11} \text{ cm}^{-2}\text{s}^{-1}$ to the fluence of $1 \times 10^{16} \text{ cm}^{-2}$ and H⁺ ions at the flux of $7 \times 10^{12} \text{ cm}^{-2}\text{s}^{-1}$ to the fluence of $1 \times 10^{17} \text{ cm}^{-2}$. The curve color coding is explained in Fig. 4.17. 250
- Fig. 4.19. High-angle annular dark-field image of ODS-EUROFER steel sequentially implanted with He⁺ ions with the flux of $5 \times 10^{11} \text{ cm}^{-2}\text{s}^{-1}$ to the fluence of $1 \times 10^{16} \text{ cm}^{-2}$ at 823 K and H⁺ ions with the flux of $7 \times 10^{12} \text{ cm}^{-2}\text{s}^{-1}$ to the fluence of $1 \times 10^{17} \text{ cm}^{-2}$ at RT: (a) HAADF survey image showing the regions from which SIs were recorded; (b) HAADF image recorded simultaneously with the SI dataset of zone 1 with He bubble attached to Y₂O₃ particle; 257
- Fig. 4.20. (a) HAADF image of zone 1 showing the regions from which the summed spectra were extracted. (b) Representative low-loss EEL spectra extracted at selected positions of the ODS-EUROFER steel sample sequentially implanted with He⁺ ions with the flux of $5 \times 10^{11} \text{ cm}^{-2}\text{s}^{-1}$ to the fluence of $1 \times 10^{16} \text{ cm}^{-2}$ at 823 K and H⁺ ions with the flux of $7 \times 10^{12} \text{ cm}^{-2}\text{s}^{-1}$ to the fluence of $1 \times 10^{17} \text{ cm}^{-2}$ at RT. Black, red, and green curves correspond to the matrix, He bubble, and Y₂O₃ particle, respectively. 258
- Fig. 4.21. The spatial distribution of components identified on raw LL EELS-SI data acquired from zone 1: (a) HAADF image; (b)-(j) EELS energy-selected window images associated with possible signals at (b) ~55–58 eV (Fe-M_{2,3}); (c) ~45–47 eV (Cr-M_{2,3}); (d) ~35–37 eV (Y- N_{2,3}); (e) ~24–26 eV (He-K); (f) ~22–24 eV (Fe-Cr bulk plasmon); (g) ~15.5–20.1 eV (bubble surface plasmon-BSP); (h) ~14–16 eV (Y₂O₃ bulk plasmon); (i) ~12–14 eV (H-K); (j) ~6.5–8.5 eV (surface oxide plasmon-SP). 259
- Fig. 4.22. The spatial distribution of components identified from raw LL EELS-SI data acquired from zone 2: (a) HAADF image; (b)-(h) EELS energy-selected window images associated with possible signals at (b) ~55–58 eV (Fe-M_{2,3}); (c) ~45–47 eV (Cr-M_{2,3}); (d) ~24–26 eV (He-K); (e) ~22–24 eV (Fe-Cr bulk plasmon); (f) ~15.5–20.1 eV (bubble surface plasmon-BSP); (g) ~12–14 eV (H-K); (h) ~6.5–8.5 eV (surface oxide plasmon-SP). 260
- Fig. 4.23. Composite color maps of EELS-SI of energy-selected window 12-14 eV (H-K, green) from Fig. 4.20(i) combined with either (a) the image for energy-selected window 24-26 eV (He-K, red), or (b) the image for energy-selected window 15.5-20 eV (bubble surface plasmon, blue). 261
- Fig. 4.24. Composite color maps of EELS-SI of energy-selected window 12-14 eV (H-K, green) from Fig. 4.21(g) combined with either (a) the image for energy-selected window 24-26 eV (He-K, red), or (b) the image for energy-selected window 15.5-20 eV (bubble surface plasmon, blue). 261
- Fig. 4.25. A comparison of the EEL spectrum extracted from ZL SI and the scaled spectrum from LL SI: (a) using time ratio as scaling factor and (b) using the ratio of intensities at the slope between ZLP and plasmon. 262
- Fig. 4.26. (a) The effect of the “bleed-through” between ZL and LL signals on the ZL spectrum. (b) Comparison of the corrected EEL spectrum from ZL SI and the spectrum from LL SI scaled by the time ratio 1:120. 263
- Fig. 4.27. (a) EEL spectra extracted from deconvoluted SI using 3x3 pixel areas in the matrix, close to He bubble center and at the He bubble edge (periphery). (b) The second differential curve of the EEL spectra shown in panel (a). (c) HAADF image of zone 2 showing the regions from which the spectra were extracted. 264
- Fig. 4.28. (a,b) EEL spectra subtracted from deconvoluted SI using 3x3 pixel areas and scaled to account for thickness differences: (a) close to He bubble center vs. the matrix; (b) close to He bubble edge vs. the matrix; (c) comparison of spectral differences in bubble center and bubble edge areas; (d) HAADF image of zone 2 showing the regions from which the spectra were extracted. He K-edge at ~25 eV and wide peak with a maximum at ~13.2 eV which is a result of superposed BSP (~16.6 eV-19.1), H-K edge (~13 eV) and SP (~7.5 eV) signals. 265

Fig. 4.29. (a) HAADF image of zone 2. Intensity maps of components identified in spectral difference SI of zone 2 generated by application of 4 eV integration windows: (b) 6-10eV (SP from surface oxide); (c) 11-15 eV (H-K); (d) ~16-20 eV (BSP from bubble); (e) ~22.5-26.5 eV (He-K).267

Fig. 4.30. Curve fitting of the superposed signals at the left shoulder of Fe-Cr bulk plasmon extracted from 3x3 pixel areas at bubble center and bubble periphery in spectral difference SI of zone 2. Fit peaks at ~7.2 eV, and 13.2-13.5 eV represent SP and H-K signals, respectively. (a) BSP peak position at 19.1 eV, as estimated for an empty cavity; (b) BSP peak position at 17.3 eV, as for a He-filled bubble with He density 94 at./nm³. The color model of the fit corresponds to that applied in Fig. 4.29.270

Fig. 4.31. Curve fitting using NLLS fitting GMS routine of the superposed signals extracted from 3x3 pixel areas at bubble center and bubble periphery in spectral difference SI of zone 2. Fit peaks at ~7.2, 13.2-13.5, 17.3-19.1 and 25 eV represent SP, H-K, BSP and He-K signals, respectively. (a) Bubble periphery, BSP energy $l=1$ estimated for empty bubble; (b) bubble center, BSP energy $l=1$ estimated for empty bubble; (c) bubble periphery, BSP energy $l=1$ estimated for bubble filled with He density 94 at./nm³; (d) bubble center, BSP energy $l=1$ estimated for bubble filled with He density 94 at./nm³.271

Fig. 4.32. Intensity maps obtained by NLLS Gaussian fitting of components identified in spectral difference SI of zone 2: (a) ~7.2 eV (SP of surface oxide interface); (b)~13.5 eV (H-K); (c)~19.1 eV (BSP of empty bubble); (d)~25 eV (He-K).272

Fig. 4.33. Intensity maps obtained by NLLS Gaussian fitting of components identified in spectral difference SI of zone 2: (a) ~7.2 eV (SP of surface oxide interface); (b) ~13.2 eV (H-K); (c) ~17.3 eV (BSP of filled bubble); (d) ~25 eV (He-K).272

Fig. 4.34. Intensity maps obtained by NLLS Gaussian fitting from spectral difference SI of zone 2: (a) ~25 eV (He-K); (b) ~13.2 eV H-K; (c) thickness map. For better visibility, the target H-K and He-K maps for the fitting results with BSP position of filled bubble are presented using color model different from that in Figs. 4.32-4.33.273

Fig. 5.1. Microstructure of a model bi-layer Y₂O₃/FeCr system implanted at RT with 17 keV He⁺ ions with the flux of 7×10¹² cm⁻²s⁻¹ to the fluence of 1×10¹⁷ cm⁻²: (a,b) through-focus image pair; (c) cavities at higher magnification; and (d) planar defects in Y₂O₃ layer at higher magnification. Red arrows denote cavities in all parts of the bi-layer system. Blue arrows denote planar defects in Y₂O₃ layer. BF TEM imaging conditions: (a) ~0.6 μm underfocus; (b) ~0.6 μm overfocus; (c,d) ~0.3 μm underfocus.291

Fig. 5.2. HRTEM cross-sectional image of Y₂O₃ film after implantation of the model bi-layer Y₂O₃/FeCr sample with 17 keV He⁺ ions at RT with the flux of 7×10¹² cm⁻²s⁻¹ to the fluence of 1×10¹⁷ cm⁻²: (a) faceted cavity; (b) planar defect observed on {111} plane. BF imaging conditions: ~0.2 μm underfocus.292

Fig. 5.3. (a,b) Microstructure of a model bi-layer Y₂O₃/FeCr system implanted at 823 K with 17 keV He⁺ ions with the flux of 7×10¹² cm⁻²s⁻¹ to the fluence of 1×10¹⁷ cm⁻². (c) Cavities at higher magnification. (d) Anion dislocation loops in the Y₂O₃ film. Red arrows denote cavities in the Fe-10Cr layer, while blue arrows in panel (d) denote dislocation loops in the Y₂O₃ layer. BF TEM imaging conditions: (a) ~0.5 μm underfocus; (b) ~0.5 μm overfocus; (c) ~0.3 μm underfocus; and (d) ~0.6 μm underfocus.294

Fig. 5.4. HRTEM image of a faceted cavity in Fe-10Cr film after implantation of the model Y₂O₃/FeCr bi-layer system at 823 K with 17 keV He⁺ ions with the flux of 7×10¹² cm⁻²s⁻¹ to the fluence of 1×10¹⁷ cm⁻². BF imaging conditions: ~0.2 μm underfocus.295

Fig. 5.5. The microstructure of model Y₂O₃/FeCr bi-layer system implanted at RT with 10 keV H⁺ ions with the flux of 1×10¹³ cm⁻²s⁻¹ to the fluence of 2×10¹⁷ cm⁻²: (a,b) through-focus image pair; (c) cavities and microcracks at higher magnification. Red arrows denote cavities in the Fe-10Cr film and at the interface of the bi-layer system. Yellow arrows denote microcracks in the Y₂O₃ film. BF TEM imaging conditions: (a) ~0.5 μm underfocus; (b) ~0.5 μm overfocus; (c) ~0.3 μm underfocus.296

Fig. 5.6. HRTEM image ~0.2 μm underfocus of microcrack in the Y₂O₃ layer of the model Y₂O₃/FeCr bi-layer system after implantation with 10 keV H⁺ ions at RT with the flux of 1×10¹³ cm⁻²s⁻¹ to the fluence of 2×10¹⁷ cm⁻².297

Fig. 5.7. The microstructure of the model Y₂O₃/FeCr bi-layer system after sequential room temperature implantation with 17 keV He⁺ ions with a flux of 7×10¹² cm⁻²s⁻¹ to the fluence of 1×10¹⁷ cm⁻² and then with 10 keV H⁺ ions with a flux of 1×10¹³ cm⁻²s⁻¹ to the fluence of 2×10¹⁷ cm⁻²: (a) low-magnification view; (b) decohesion area; and (c) area without decohesion. Red arrows denote cavities in Fe-10Cr film and at the interface, while yellow arrows mark

microcracks in the Y_2O_3 film and decohesion at the interface. BF TEM imaging conditions: (a) $\sim 1 \mu m$ underfocus; (b,c) $\sim 0.5 \mu m$ underfocus.....298

Fig. 5.8. EDX elemental mapping of the model $Y_2O_3/FeCr$ bi-layer system after RT sequential implantation with 17 keV He^+ ions to the fluence of $1 \times 10^{17} cm^{-2}$ and 10 keV H^+ ions to the fluence of $2 \times 10^{17} cm^{-2}$ at the decohesion area: (a) HAADF image of the area used for the elemental mapping; (b) iron elemental distribution; (c) chromium elemental distribution; (d) yttrium elemental distribution; (e) oxygen elemental distribution.299

Fig. 5.9. HRTEM image at $\sim 0.2 \mu m$ underfocus of microcracks in Y_2O_3 film after sequential implantation at RT with 17 keV He^+ ions with the flux of $7 \times 10^{12} cm^{-2}s^{-1}$ to the fluence of $1 \times 10^{17} cm^{-2}$ and then with 10 keV H^+ ions with the flux of $1 \times 10^{13} cm^{-2}s^{-1}$ to the fluence of $2 \times 10^{17} cm^{-2}$300

Fig. 5.10. The microstructure of the model bi-layer $Y_2O_3/FeCr$ system irradiated with 2 MeV Kr^+ ions at RT with a flux of $2 \times 10^{11} cm^{-2}s^{-1}$ to the fluence of $3.6 \times 10^{15} cm^{-2}$: (a,b) through-focus image pair; and (c) cavities at higher magnification. Red arrows denote cavities in Fe-10Cr film. Blue arrows denote dislocation loops in Y_2O_3 layer. BF TEM imaging conditions: (a) $\sim 0.6 \mu m$ underfocus; (b) $\sim 0.6 \mu m$ overfocus; (c) $\sim 0.3 \mu m$ underfocus.....301

Fig. 5.11. A summary of possible redistribution paths of implanted He at 823 K for (a) the model $FeCr/Y_2O_3$ system and (b) an oxide particle in steel matrix. The He redistribution modes include: **a**- trapping in cavities in the metal layer; **b**- diffusion to metal/oxide interface; **c**- out-diffusion along the interface; **c'**- out-diffusion from the yttria layer; **d**- diffusion away from the interface into yttria; **d'** and **d''**- escape to the substrate oxide; **e**- diffusion in yttria towards the interface; **f**- diffusion away from yttria into metal.307

Annex II. List of tables

Table 1.1. Comparison of neutron fluxes, displacement rates, He and H production (in Fe-based alloys) for fusion (DEMO FW), spallation (SINQ, European spallation source (ESS), Experimental Accelerator Driven System (XADS)), fission materials testing reactors (high flux reactor (HFR) and Jules Horowitz reactor (JHR)), and the fast neutron BOR60 reactor. Abbreviation fpy stands for 'full power year' [17,18].	13
Table 1.2. Examples of nominal key element contents (in wt.%) for ferritic (F) and F/M ODS steels (balance Fe with other elements at < 0.5 wt%) [59].	21
Table 1.3. Comparison of average cavity sizes $\langle d \rangle$, average cavity number density $\langle N \rangle$ and swelling detected in commercial ferritic and ferritic-martensitic steels after dual and triple-beam irradiations simulating fusion conditions	47
Table 2.1. Chemical composition of ODS- EUROFER and EUROFER-97 steels (in wt.%) [1–3].	63
Table 2.2. Typical microstructural parameters of ODS-EUROFER and EUROFER steel in as-supplied state.	67
Table 2.3. Summary of implantation conditions with 10 keV He ⁺ ions.	86
Table 2.4. Summary of implantation/irradiation conditions with 10 keV He ⁺ ions and 4 MeV Au ²⁺ ions.	88
Table 2.5. Summary of implantation conditions with 10 keV He ⁺ and 5 keV H ⁺ ions.	90
Table 2.6. Summary of implantation conditions for bi-layer Y ₂ O ₃ /FeCr system.	93
Table 3.1. Parameters for the power law fitting used in Fig. 3.11.	147
Table 3.2. Statistical analysis of specific number densities and average diameters of bubbles in ODS-EUROFER steel implanted with 10 keV He ⁺ ions at the flux of $5 \times 10^{11} \text{ cm}^{-2} \text{ s}^{-1}$ to different fluencies at T=823 K, for several zones.	148
Table 3.3. Parameters for the power law fitting used in Fig. 3.13.	151
Table 3.4. Statistical analysis of specific number densities and average diameters of bubbles in ODS-EUROFER steel implanted with 10 keV He ⁺ ions at different fluxes to the fluence of $5 \times 10^{15} \text{ cm}^{-2}$ at T=823 K, for several zones.	152
Table 3.5. Parameters for the power law fitting used in Fig. 3.15.	155
Table 3.6. Statistical analysis of specific number densities and average diameters of bubbles in ODS-EUROFER steel implanted with 10 keV He ⁺ ions at the flux of $5 \times 10^{11} \text{ cm}^{-2} \text{ s}^{-1}$ to the fluence of $5 \times 10^{15} \text{ cm}^{-2}$ at different temperatures, for several zones.	156
Table 3.7. The average sizes and volume number densities of bubbles, swelling, V/He ratio and retained He fraction associated with different bubble populations in ODS-EUROFER steel implanted with He ⁺ ions at the flux of $5 \times 10^{11} \text{ cm}^{-2} \text{ s}^{-1}$ to different fluencies at T=823 K.	163
Table 3.8. The average sizes and volume number densities of bubbles, swelling, V/He ratio and retained He fraction associated with different bubble populations in ODS-EUROFER steel implanted with He ⁺ ions at three different fluxes to the fluence of $5 \times 10^{15} \text{ cm}^{-2}$ at T=823 K.	167
Table 3.9. The average sizes and volume number densities of bubbles, swelling, V/He ratio and retained He fraction associated with different bubble populations in ODS-EUROFER steel implanted with He ⁺ ions at the flux of $5 \times 10^{11} \text{ cm}^{-2} \text{ s}^{-1}$ to the fluence of $5 \times 10^{15} \text{ cm}^{-2}$ at different temperatures.	171
Table 3.10. Cumulative values of V/He ratio, retained He fraction, swelling estimated by TEM data and total swelling that includes contribution from helium dissolved in small He-vacancy clusters.	174
Table 3.11. Statistical analysis of specific number densities and average diameters of bubbles in ODS-EUROFER steel implanted with 10 keV He ⁺ ions at the flux of $5 \times 10^{11} \text{ cm}^{-2} \text{ s}^{-1}$ to the fluence of $5 \times 10^{15} \text{ cm}^{-2}$ at RT after annealing at 823 K, for several zones.	177

Table 3.12. The average sizes and volume number densities of bubbles, swelling, V/He ratio and retained He fraction associated with different bubble populations in ODS-EUROFER steel implanted at RT with He ⁺ ions at the flux of 5×10 ¹¹ cm ⁻² s ⁻¹ to the fluence of 5×10 ¹⁵ cm ⁻² followed by PIA at 823 K.....	177
Table 3.13. Comparative statistical analysis of specific number densities and average diameters of bubbles in the bulk and at different microstructural defect for EUROFER 97 and ODS-EUROFER steels implanted with 10 keV He ⁺ ions.....	184
<i>Data on EUROFER 97 include detailed information over 5 different zones of the sample; data for ODS-EUROFER are copied from Table 3.2.</i>	184
Table 3.14. Cumulative values of helium bubble number density, V/He ratio, swelling estimated by TEM data and retained He fraction for EUROFER 97 and ODS-EUROFER steels.....	185
Table 3.15. Statistical analysis of specific number densities and average diameters of bubbles in ODS-EUROFER steel implanted with 10 keV He ⁺ ions at the flux of 5×10 ¹¹ cm ⁻² s ⁻¹ to the fluence of 5×10 ¹⁵ cm ⁻² at RT and then irradiated <i>in situ</i> with 4 MeV Au ²⁺ ions at the flux of 4×10 ¹¹ cm ⁻² s ⁻¹ to the fluence of 4.5×10 ¹⁵ cm ⁻² at 823 K.....	188
Table 3.16. The average sizes and volume number densities of bubbles, swelling, V/He ratio and retained He fraction associated with different bubble populations in the ODS-EUROFER steel implanted at RT with 10 keV He ⁺ ions at the flux of 5×10 ¹¹ cm ⁻² s ⁻¹ to the fluence of 5×10 ¹⁵ cm ⁻² and then irradiated <i>in situ</i> at 823 K with 4 MeV Au ²⁺ ions at the flux of 4×10 ¹¹ cm ⁻² s ⁻¹ to the fluence of 4.5×10 ¹⁵ cm ⁻²	189
Table 3.17. Statistical analysis of specific number densities and average diameters of bubbles/cavities in the ODS-EUROFER steel after simultaneous <i>in situ</i> dual-beam irradiation with 10 keV He ⁺ ions at the flux of 5×10 ¹¹ cm ⁻² s ⁻¹ to the fluence of 5×10 ¹⁵ cm ⁻² and 4 MeV Au ²⁺ ions at the flux of 4×10 ¹¹ cm ⁻² s ⁻¹ to the fluence of 4.5×10 ¹⁵ cm ⁻² at 823 K.....	195
Table 3.18. The average sizes and volume number densities of bubbles, swelling, V/He ratio and retained He fraction associated with different bubble populations in the ODS-EUROFER steel after simultaneous <i>in situ</i> dual-beam irradiation at 823 K with 10 keV He ⁺ ions at the flux of 5×10 ¹¹ cm ⁻² s ⁻¹ to the fluence of 5×10 ¹⁵ cm ⁻² and 4 MeV Au ²⁺ ions with the flux of 4×10 ¹¹ cm ⁻² s ⁻¹ to the fluence of 4.5×10 ¹⁵ cm ⁻²	196
Table 3.19. Typical microstructural parameters of ODS-EUROFER steel in tempered state.....	212
Table 3.20. Comparison of average sizes and volume number densities of cavities and swelling contributions for different cavity populations in the ODS-EUROFER steel sample after dual-beam He ⁺ +Au ²⁺ irradiation and single-beam He ⁺ implantation. Data are adapted from Tables 3.7 and 3.18.....	212
Table 3.21. Estimated sink strengths for ODS-EUROFER steel samples after dual-beam He ⁺ +Au ²⁺ irradiation and single-beam He ⁺ implantation. For cavities on oxide particles, the calculated effective diameters are also included.	213
Table 4.1. Parameters for the power law fitting used in Fig. 4.3.....	230
Table 4.2. The average sizes and volume number densities of bubbles, swelling, V/He ratio and retained He fraction associated with different bubble populations in the ODS-EUROFER steel implanted at 823 K both sequentially with He ⁺ ions at the flux of 1×10 ¹² cm ⁻² to the fluence of 5×10 ¹⁵ cm ⁻² and H ⁺ ions at the flux of 7×10 ¹² cm ⁻² s ⁻¹ to the fluence of 1×10 ¹⁷ cm ⁻² , and with single He ⁺ beam at the flux of 1×10 ¹² cm ⁻² s ⁻¹ to the fluence of 5×10 ¹⁵ cm ⁻² with and without subsequent tempering.....	231
Table 4.3. The average sizes and volume number densities of bubbles, swelling, V/He ratio and retained He fraction associated with different bubble populations in the ODS-EUROFER steel implanted at RT both sequentially with He ⁺ ions at the flux of 5×10 ¹¹ cm ⁻² s ⁻¹ to the fluence of 5×10 ¹⁵ cm ⁻² and H ⁺ ions with the flux of 7×10 ¹² cm ⁻² s ⁻¹ to the fluence of 1×10 ¹⁷ cm ⁻² s ⁻¹ before and after PIA at 823 K, and with single He ⁺ beam with the same parameters after PIA at 823 K.....	237
Table 4.4. Estimated desorbed hydrogen content in ODS- EUROFER and EUROFER 97 steels implanted at room temperature with 5 keV H ⁺ ions with the flux of 7×10 ¹² cm ⁻² s ⁻¹ to the fluence of 1×10 ¹⁷ cm ⁻²	244
Table 4.5. Estimated desorbed hydrogen content in ODS- EUROFER and EUROFER 97 steels sequentially implanted at room temperature with He ⁺ ions at the flux of 5×10 ¹¹ cm ⁻² s ⁻¹ to the fluence of 5×10 ¹⁵ cm ⁻² and H ⁺ ions at the flux of 7×10 ¹² cm ⁻² s ⁻¹ to the fluence of 1×10 ¹⁷ cm ⁻²	245

Table 4.6. The estimated content of hydrogen in ODS-EUROFER steel implanted at RT with H ⁺ ions at the flux of 7×10 ¹² cm ⁻² s ⁻¹ to the fluence of 1×10 ¹⁷ cm ⁻² into pristine samples and into samples preliminary implanted with He ⁺ ions at the flux of 5×10 ¹¹ cm ⁻² s ⁻¹ to the fluence of 1×10 ¹⁶ cm ⁻² at 823 K.	247
Table 4.7. Summary of maximum peak temperatures and activation energies corresponding to the deconvoluted peaks of TDS spectra for ODS-EUROFER samples sequentially implanted at RT with He ⁺ ions at the flux of 5×10 ¹¹ cm ⁻² s ⁻¹ to the fluence of 1×10 ¹⁶ cm ⁻² and H ⁺ ions at the flux of 7×10 ¹² cm ⁻² s ⁻¹ to the fluence of 1×10 ¹⁷ cm ⁻²	250
Table 4.8. Published data on trapping (activation) energies E_a for hydrogen isotopes in <i>bcc</i> iron-based alloys. Notice that the main part of the data in the references is compiled from secondary sources.	251
Table 4.9. Summary of hydrogen effects on ODS-EUROFER steel samples pre-implanted with helium ions.	276
Table 4.10. Average cavity sizes $\langle d \rangle$ detected in commercial ferritic, ferritic-martensitic and ODS-steels after triple-beam irradiations simulating fusion conditions.	280
Table 5.1. Statistical cavity ensemble parameters in the model bi-layer Y ₂ O ₃ /FeCr sample implanted with 17 keV He ⁺ ions at RT with the flux of 7×10 ¹² cm ⁻² s ⁻¹ to the fluence of 1×10 ¹⁷ cm ⁻²	293
Table 5.2. Number densities and average diameters of cavities in the model bi-layer Y ₂ O ₃ /FeCr sample implanted at 823 K with 17 keV He ⁺ ions with the flux of 7×10 ¹² cm ⁻² s ⁻¹ to the fluence of 1×10 ¹⁷ cm ⁻²	295
Table 5.3. Statistical analysis of number densities and mean diameters of cavities in the model Y ₂ O ₃ /FeCr bi-layer system implanted at RT with 10 keV H ⁺ ions with the flux of 1×10 ¹³ cm ⁻² s ⁻¹ to the fluence of 2×10 ¹⁷ cm ⁻²	297
Table 5.4. Number densities and average diameters of cavities in the model Y ₂ O ₃ /FeCr bi-layer system sequentially implanted at RT with 17 keV He ⁺ ions with a flux of 7×10 ¹² cm ⁻² s ⁻¹ to the fluence of 1×10 ¹⁷ cm ⁻² and then with 10 keV H ⁺ ions with a flux of 1×10 ¹³ cm ⁻² s ⁻¹ to the fluence of 2×10 ¹⁷ cm ⁻²	300
Table 5.5. The number densities and average diameters of cavities in model bi-layer Y ₂ O ₃ /FeCr system irradiated at RT with 2 MeV Kr ⁺ ions with a flux of 2×10 ¹¹ cm ⁻² s ⁻¹ to the fluence of 3.6×10 ¹⁵ cm ⁻²	302
Table 5.6. A summary of microstructural features observed after single-beam He ⁺ and H ⁺ implantation, sequential dual-beam He ⁺ +H ⁺ implantation, and Kr ⁺ irradiation.	302
Table 2. Résumé des caractéristiques microstructurales observées dans le système bicouche Y ₂ O ₃ /FeCr après implantation d'He ⁺ et H ⁺ en simple faisceau, implantation séquentielle d'ions He ⁺ +H ⁺ , et irradiation avec des ions Kr ⁺	345
Table 2. A summary of microstructural features observed after single-beam He ⁺ and H ⁺ implantation, sequential dual-beam He ⁺ +H ⁺ implantation, and Kr ⁺ irradiation.	360

Annex III. List of abbreviations

AC	Alternative current
ADF	Annular dark field
ADS	Accelerator driven systems
appm	Atomic parts per million
bcc	Body-centered cubic
bct	Body-Centered Tetragonal
BF	Bright-field
BSE	Back-scattered secondary electrons
BSP	Bubble surface plasmon
CBM	Critical bubble model
CTEM	Conventional transmission electron microscopy
DC	Direct current
DF	Dark-field
dpa	Displacement per atom
EBSD	Electron backscatter diffraction
EELS	Electron energy-loss spectroscopy
EDX	Energy Dispersive X-ray spectroscopy
EOS	Equation of state
fcc	Face-centered cubic
F/M	Ferritic-martensitic
FFTF	Fast Fourier transformation
GB	Grain boundary
Gen IV	Generation IV
GFR	Gas-cooled fast reactor
H	Hydrogen
HAADF	High-angle annular dark field
HAGB	High-angle grain boundary
He	Helium
HE	Hot Extrusion
HIP	Hot isostatic pressing
HSEOS	Hard sphere equation of state
HRTEM	High-resolution transmission electron microscopy
HTIE	High temperature irradiation embrittlement
ISHI	<i>In situ</i> helium injection
JANNuS	Joint accelerators for nano-science and nuclear simulation
LAGB	Low-angle grain boundary
LEED	Low energy electron diffraction
LFR	Lead fast reactor
LL SI	Low-loss spectrum image
LWR	Light water reactor
NFA	Nanostructured ferritic alloys
MA	Mechanical alloying
MBE	Molecular beam epitaxy
MC	Bubble migration and coalescence
MD	Molecular dynamic
MS	Magnetron sputtering
MSR	Molten salt reactor

ODS	Oxide dispersion strengthened
OR	Ostwald ripening
PIA	Post implantation annealing
PM	Powder metallurgy
QCM	Quartz crystal microbalance
RAFM	Reduced activation ferritic-martensitic
RHEED	Reflection high-energy electron diffraction
RT	Room temperature
SAED	Selection area electron diffraction
SCWR	Supercritical water reactor
SE	Secondary electrons
SEM	Scanning electron microscopy
SFT	Stacking fault tetrahedra
SFR	Sodium fast reactor
SI	Spectrum imaging
SIA	Self-interstitial atoms
SIMS	Mass spectrometry of secondary ions
SP	Surface plasmon
STEM	Scanning transmission electron microscopy
TEM	Transmission electron microscopy
TDS	Thermal desorption spectroscopy
TMT	Thermo-mechanical treatment
UHV	Ultra high vacuum
UHR EELS	Ultra high resolution electron energy-loss spectroscopy
VHTR	Very high-temperature reactor
XPS	X-ray photoemission spectroscopy
XRD	X-ray Diffraction
ZL SI	Zero-loss spectrum image
ZLP	Zero-loss peak

Annex IV. Résumé détaillé en Français

Compte tenu des avantages d'un rendement élevé et de la réduction des limitations liées à l'impact environnemental, les systèmes avancés de génération IV de fission, ceux de fusion et ceux pilotés par accélérateur (ADS) ont un grand potentiel pour devenir une partie importante des sources d'énergie non carbonées actuelles et futures en mode continu de production d'énergie [1-4]. Les conditions de service des installations de fission et de fusion avancées sont caractérisées par des températures élevées (~550-1000°C), des champs de rayonnement neutronique intenses (~5-30 dpa/fpy, dommages de déplacement par atome par année de pleine puissance) et l'utilisation de réfrigérants chimiquement agressifs. Les principaux matériaux de structure candidats pour les prochaines installations de fission et de fusion sont les aciers ferritiques-martensitiques [5-9]. Cependant, certains systèmes devraient fonctionner à des températures bien supérieures à la limite (~550° C) de performance fiable de ces aciers. Le renforcement par dispersion d'oxyde élimine l'inconvénient le plus grave des aciers ferritiques-martensitiques qui sont par ailleurs très bons (comme EUROFER), à savoir la résistance insuffisante à la ductilité de fluage à haute température. Cela rend les aciers renforcés par dispersion d'oxyde (ODS) particulièrement intéressants pour les futures installations énergétiques. La densité élevée des particules d'oxyde dispersées dans la matrice de l'acier améliore non seulement ses propriétés mécaniques pour les applications à haute température, mais aide également à sa bonne stabilité sous irradiation [10-15]. Malgré les recherches internationales intensives sur les aciers ODS au cours de la dernière décennie, de nombreuses questions fondamentales concernant l'utilisation des nano-oxydes pour l'amélioration des propriétés de l'acier restent en débat. Une question importante est le rôle relatif joué par les nano-oxydes dans le développement de la microstructure des matériaux dans des environnements d'irradiation complexes où les dommages dus aux déplacements intensifs s'accompagnent à des niveaux extrêmement élevés d'une accumulation de gaz légers - hélium et hydrogène.

Deux risques majeurs d'accumulation de l'hélium dans les aciers sont (i) la diminution de la dose d'incubation de gonflement et (ii) la fragilisation par irradiation à haute température (HTIE). On s'attend actuellement à ce que les particules d'oxyde de taille nanométrique dans l'acier ODS soient bénéfiques pour atténuer à la fois le gonflement et la fragilisation à haute température, en fournissant des sites de recombinaison supplémentaires pour les défauts ponctuels aux interfaces particules d'oxyde/matrice, et des sites de piégeage de l'hélium [13,16-20]. Cependant, les aciers ODS ont une microstructure complexe avec de multiples puits (joints de grains, dislocations, précipités) qui se font concurrence pour les défauts ponctuels et les atomes d'hélium, et le rôle relatif des composants supplémentaires tels que les nanoparticules d'oxyde est loin d'être évident, surtout si l'on tient compte de la grande variété de nano-oxydes (Y_2O_3 , $Y_2Ti_2O_7$, $Y_3Al_5O_{12}$, $YAlO_3$, etc.) utilisés dans les différentes nuances d'acier. Selon l'acier et les conditions d'essai, la fraction de bulles d'hélium associée aux nano-oxydes varie de 30 à 100% [15-17,21-24]. Étant donné que la nucléation et la cinétique de croissance des bulles d'hélium sont sensibles à de multiples paramètres d'irradiation (dose, température et taux d'injection/génération d'hélium), les connaissances disponibles dans la littérature restent non systématiques et souvent mal reproductibles en raison du manque de compréhension de base des mécanismes microstructuraux impliqués. Il n'est pas non plus évident de savoir si une forte accumulation d'hélium sur les nano-oxydes ne risque pas d'avoir des conséquences indésirables en termes de tolérance à l'irradiation des ODS-acier [25,26].

Les effets de l'hydrogène sur la modification microstructurale des aciers ODS ont été moins étudiés que ceux de l'hélium. On s'attend généralement à ce que les aciers conventionnels ne contiennent pas d'hydrogène à des concentrations élevées, mais des études récentes ont montré que les aciers ODS sont capables d'accumuler plus d'hydrogène que les matériaux conventionnels [27,28]. L'explication proposée de cet effet en termes de piégeage de l'hydrogène par des nanoparticules d'oxyde est plausible, mais n'a pas de preuves solides. Une question ouverte reste également la synergie de l'action de l'hydrogène et de l'hélium sur les propriétés des aciers ODS. Des expériences d'irradiation ionique multifaisceaux montrent que l'hélium et l'hydrogène peuvent agir en synergie sur le développement de la

microstructure des défauts induits par l'irradiation [29-36] et provoquer un gonflement supplémentaire notable en cas de dommages dus à un déplacement intense [30-33,36], mais seulement dans une certaine plage de température [30-32,36]. Les mécanismes de ces effets de l'hydrogène restent obscurs.

La plupart des recherches expérimentales non systématiques de matériaux complexes dans un environnement radiatif complexe ne sont pas en mesure de guider la conception des matériaux car pour recommander les aciers ODS pour une application particulière, un concepteur doit également connaître leur réponse à l'effet des conditions de fonctionnement (historique des températures de fonctionnement, dommages et hélium, taux d'accumulation d'hydrogène, etc). Pour atteindre cet objectif, il est nécessaire d'effectuer des études systématiques de la sensibilité de la microstructure aux gaz lors d'une variation des paramètres clés, qui comprennent la taille et la densité des nano-oxydes, la teneur en gaz et les températures de traitement. L'utilisation de la technique d'implantation ionique pour simuler expérimentalement des changements microstructuraux dans des conditions bien contrôlées avec un large éventail de paramètres variables, combinée à une caractérisation post-implantation minutieuse, est une approche très prometteuse. Cependant, les expériences d'implantation ionique sont affectées par des limitations géométriques (telles que la profondeur d'implantation ionique relativement faible). Afin de permettre l'extrapolation des résultats à des cas plus généraux et plus pertinents, la recherche expérimentale doit être complétée par une modélisation pertinente afin d'extraire les tendances générales du développement des microstructures sous l'effet du gaz à partir des données sensibles à l'environnement et de suggérer les moyens d'appliquer les connaissances obtenues dans un contexte plus large.

L'objectif principal de cette étude de doctorat est d'étudier systématiquement les tendances fondamentales du développement de la microstructure induite par les gaz dans les aciers ferritiques-martensitiques ODS dans des expériences ciblées d'irradiation/implantation examinant les dépendances à un seul paramètre de la teneur en gaz accumulé, de l'accumulation de gaz et des taux de dommages, et de la température, avec une attention particulière au rôle des particules d'oxyde. L'approche expérimentale proposée consiste à saturer des échantillons d'acier ODS-EUROFER avec diverses quantités d'atomes d'hélium et d'hydrogène par implantation ionique à l'aide de l'installation JANNuS-Orsay dans des conditions bien contrôlées. Les méthodes de caractérisation comprennent diverses techniques d'examen par microscopie électronique à transmission (MET), ainsi que des techniques complémentaires appropriées telles que la spectroscopie de thermodésorption (TDS). Pour une meilleure compréhension des mécanismes de base de l'interaction hélium/hydrogène avec les oxydes, les expériences sur le matériau industriel sont complétées par celles sur le système modèle $Y_2O_3/FeCr$ en couches minces et par une modélisation pertinente.

Afin d'atteindre cet objectif, cette thèse de doctorat poursuit les buts suivants:

1. Étude systématique des effets de l'accumulation d'hélium et d'hydrogène sur le développement microstructural et le gonflement de l'acier commercial ODS-EUROFER, notamment

(i) l'étude de l'efficacité des nanoparticules Y_2O_3 comme sites de piégeage de l'hélium lors de l'irradiation, soit avec un seul faisceau d'ions He, soit simultanément avec des ions He et des ions lourds (avec des rapports He/dpa très différents) ;

ii) l'estimation des risques potentiels liés à l'utilisation de nanoparticules d'oxyde dans un environnement à rapport He/dpa élevé.

(iii) l'étude du rôle de l'hydrogène dans l'évolution des différentes populations de cavités dans l'acier ODS dans un environnement à rapport H/dpa élevé et les effets de l'hydrogène sur le gonflement qui en résultent ;

(iv) l'étude de la rétention d'hydrogène sous implantation d'ions H à faisceau unique et sous implantation séquentielle d'ions He + H à la fois à basse et à haute température, avec une attention particulière sur le rôle des nanoparticules Y_2O_3 dans le piégeage de l'hydrogène.

2. Étude des effets de l'implantation d'hélium et d'hydrogène dans un système modèle bicouche $Y_2O_3/FeCr$

(v) l'élucidation des contributions de la production de défauts par rayonnement et de l'accumulation d'hélium/hydrogène sur le développement de microstructures secondaires près des interfaces métal/oxyde ;

(vi) l'étude des effets de la température sur la répartition de l'hélium entre les couches de métal, d'interface et d'oxyde ;

(vii) l'étude d'une éventuelle partition de l'hydrogène entre le métal, l'interface et l'oxyde ;

(viii) la recherche d'effets synergétiques de He et H sur le développement microstructural dans les systèmes ayant des interfaces métal/oxyde.

Le manuscrit se compose de cinq chapitres.

Le **chapitre 1** résume les défis liés aux matériaux pour la fission de génération IV, les réacteurs de fusion et les systèmes pilotés par accélérateur, couvre les résultats expérimentaux et de simulation pertinents sur le gonflement des cavités dans les alliages ferritiques-martensitiques et les ODS, et examine les mécanismes possibles de l'influence de l'hélium et de l'hydrogène sur le gonflement.

Le **chapitre 2** précise les techniques expérimentales utilisées dans l'étude et est principalement axé sur la méthode d'implantation ionique et les différentes techniques liées au MET, qui sont les principales méthodes de caractérisation utilisées dans cette étude. Les résultats de la caractérisation microstructurale initiale de l'acier ODS-EUROFER et du système modèle en bicouche $Y_2O_3/FeCr$ sont également fournis dans ce chapitre.

Le **chapitre 3** présente l'analyse détaillée des effets de He sur l'évolution de la microstructure de l'acier ODS-EUROFER lors de l'implantation d'ions hélium en simple faisceau et de l'irradiation en double faisceau avec des ions hélium et or dans différents régimes. Le rôle des nanoparticules d'oxyde dans l'inventaire de l'He et la transition bulle-vide est discuté.

Le **chapitre 4** couvre les effets synergiques de l'accumulation d'hélium et d'hydrogène sur l'évolution microstructurale de l'acier ODS-EUROFER grâce à une combinaison d'études par spectroscopie de perte d'énergie des électrons, MET et TDS.

Le **chapitre 5** couvre le développement de microstructures à base de gaz dans un système modèle bicouche $Y_2O_3/FeCr$. Le schéma d'accumulation de l'hélium et de l'hydrogène observé dans les matériaux industriels est analysé de manière critique pour prendre en compte les résultats obtenus pour le système modèle à deux couches $Y_2O_3/FeCr$

Pour étudier systématiquement l'évolution de l'acier ODS-EUROFER sous l'effet des gaz, différentes options d'implantation *ex situ* utilisant un seul faisceau He^+ de 10 keV ont été utilisées. Au cours de la procédure expérimentale d'implantation d'ions He^+ uniquement dans des échantillons d'acier ODS-EUROFER, la fluence, le flux et la température étaient compris dans les intervalles $1 \times 10^{15} - 1 \times 10^{16} \text{ cm}^{-2}$, $5 \times 10^{11} - 5 \times 10^{12} \text{ cm}^{-2}\text{s}^{-1}$ et 293-923 K, respectivement. Après l'implantation, des examens MET conventionnels détaillés ont été effectués et se sont principalement concentrés sur la visualisation des cavités remplies d'hélium (bulles) par l'imagerie en champ clair (BF) sous- et sur-focus, et sur l'étude des paramètres des bulles (tailles et densités de nombre). Pour clarifier la contribution relative à l'accumulation d'hélium et au gonflement des nanoparticules d'oxyde au sein de la microstructure complexe de l'ODS-EUROFER, les populations de bulles associées à tous les défauts microstructuraux ont été étudiées. Les paramètres des ensembles de bulles d'hélium associés aux joints de grains, aux dislocations, aux carbures $M_{23}C_6$ et aux particules Y_2O_3 , en plus des bulles situées à l'intérieur du grain, ont été évalués quantitativement en fonction de la fluence, du flux et de la température lors de l'implantation d' He^+ . Une analyse détaillée des effets de l'He sur l'évolution microstructurale de l'acier ODS-EUROFER lors de l'implantation d' He^+ en simple faisceau a révélé que la cinétique de croissance des bulles sur les particules d'oxyde est sensiblement différente de celle des populations de bulles dans le grain, sur les défauts étendus (dislocations, joints de grains) et les précipités de carbure (voir Fig.1).

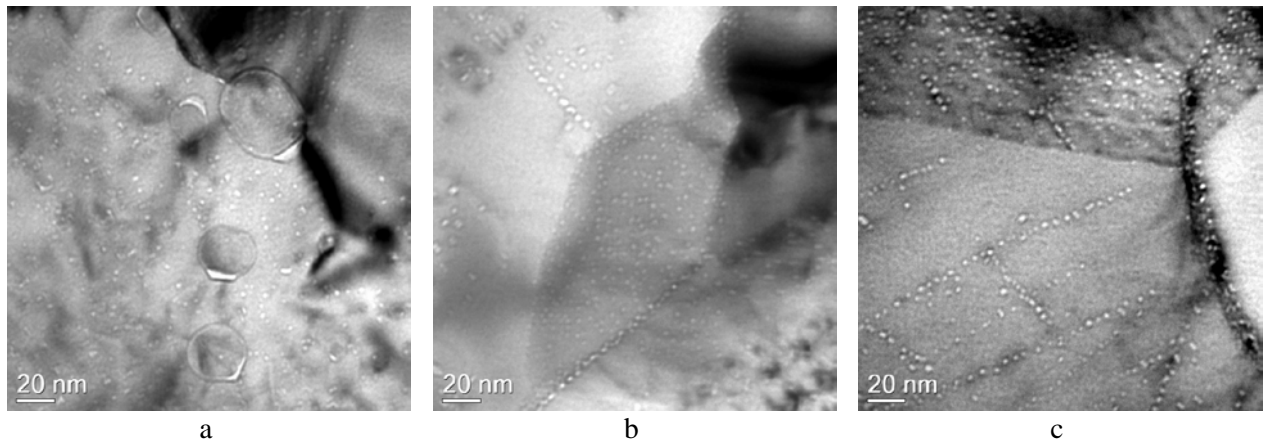


Fig. 1. Images typiques de MET BF sous-focalisées de (a) précipités nanométriques de Y_2O_3 ; (b) précipités de carbure $M_{23}C_6$ et (c) dislocations et joints de grains fortement désorientés dans de l'acier ODS-EUROFER implanté avec des ions He^+ de 10 keV jusqu'à la fluence de $5 \times 10^{15} \text{ cm}^{-2}$ à 823 K avec un flux de $5 \times 10^{11} \text{ cm}^{-2}\text{s}^{-1}$.

La densité numérique des bulles sur les nanoparticules d' Y_2O_3 est prédéterminée par la densité numérique des particules d'oxyde qui accueillent principalement une seule bulle par particule dans toutes les conditions d'implantation appliquées. Les bulles sur les particules d'oxyde sont plus grandes que les bulles des autres populations et leur taille est contrôlée plutôt par la taille des nanoparticules hôtes que par les variations des conditions d'implantation d'un seul faisceau dans les gammes étudiées. En revanche, la taille et la densité des bulles dans toutes les autres populations dépendent fortement des conditions d'implantation, mais il a été observé qu'à l'intérieur de chaque série d'implantation simple faisceau, les bulles sur les joints de grains, les dislocations et les carbures croissent à peu près au même rythme que les bulles visibles dans le cœur des grains. Sur la base d'une analyse statistique des données MET, le gonflement et la fraction d'hélium accumulée dans les bulles visibles ont été calculés en utilisant une approche indirecte pour combiner les contributions des bulles d'hélium associées à différentes caractéristiques de la microstructure, en tenant compte de la géométrie et de la densité volumique de ces défauts microstructuraux dans le volume du matériau. Dans la majorité des régimes d'implantation étudiés, le gonflement et l'inventaire de He étaient largement contrôlés par les populations de bulles sur les défauts structuraux (particules, dislocations et joints de grains), tandis que les bulles dans le cœur des grains apportaient une contribution relativement mineure. En termes quantitatifs, les contributions relatives à l'accumulation d'hélium et par conséquent au gonflement des bulles sur les défauts structuraux et dans le cœur des grains sont principalement sensibles aux variations du flux d'implantation. À mesure que le flux d'implantation augmente, le rôle relatif des bulles dans le grain devient plus important et, au flux le plus élevé utilisé, cette population de bulles apporte à peu près la même contribution au gonflement et à l'inventaire d'hélium que les bulles sur les défauts structuraux. Avec l'augmentation de la fluence d'implantation (concentration d'hélium) et la diminution de la température, la contribution relative des bulles dans le cœur des grains augmente également, mais pour la fluence et les variations de température dans les plages étudiées, elle reste bien inférieure à celle des bulles sur les défauts structuraux. La contribution à l'inventaire He et au gonflement des bulles associées aux particules d'oxyde était mineure dans tous les régimes d'implantation en simple faisceau étudiés, en raison de la densité numérique modérée des particules Y_2O_3 (voir Fig. 2) dans l'acier ODS-EUROFER. Ces deux contributions n'ont augmenté que de plusieurs pour cent avec la diminution de la fluence d'implantation de l'hélium ou de la température et avec l'augmentation du flux d'implantation dans les gammes étudiées. Parmi les populations de bulles associées à des défauts structuraux, les plus importantes contributions au gonflement et à l'inventaire d'He provenaient de bulles situées aux joints de grains. Seules les bulles situées dans le cœur des grains pouvaient être de concurrents sérieux dans certains cas, principalement à des flux d'He élevés et, dans une moindre mesure, à des fluences d'hélium élevées. Ainsi, nos résultats ne confirment pas l'opinion largement répandue selon laquelle le piégeage de l'hélium dans les bulles sur les nanoparticules d'oxyde supprimerait toujours efficacement l'accumulation d'hélium aux joints de grains,

ce qui devrait être un facteur important de suppression de la fragilisation intergranulaire à haute température. Malgré cela, même au plus haut niveau d'accumulation d'hélium (12 000 appm) et de température (923 K) étudiés, la formation extensive de bulles aux joints de grains n'a pas conduit à la coalescence des bulles, que ce soit en régime d'implantation à simple ou à double faisceau, avec une production accrue de dommages. Par conséquent, la fragilisation intergranulaire à haute température ne semble pas être un problème limitant la durée de vie de l'acier ODS-EUROFER dans un environnement à rapport He/dpa élevé.

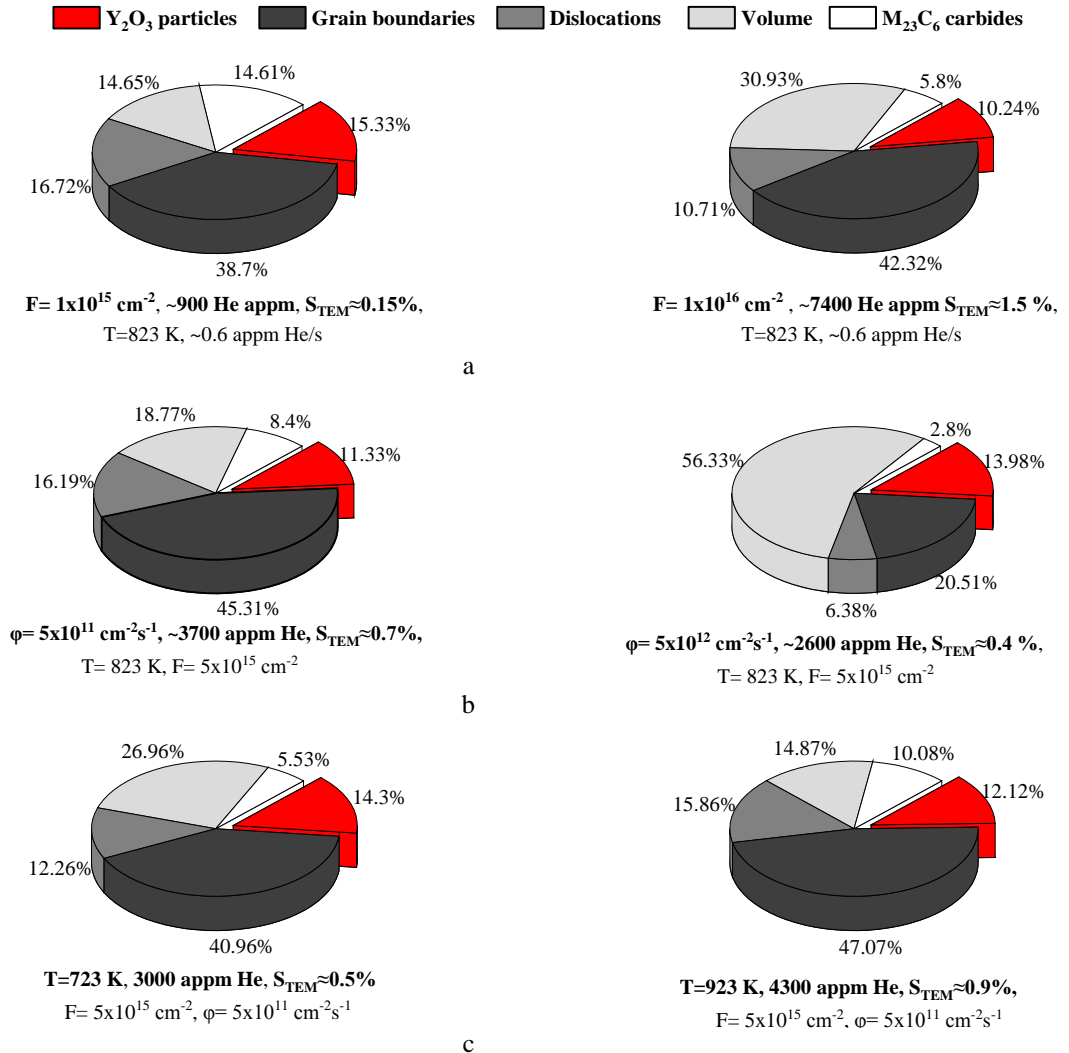


Fig. 2. Contributions des bulles associées à différentes caractéristiques microstructurales à la fraction He accumulée dans l'acier ODS-EUROFER implanté avec des ions He⁺ de 10 keV : (a) en fonction de la fluence dans la plage de 1x10¹⁵-1x10¹⁶ cm⁻² pour le flux de 5x10¹¹ cm⁻²s⁻¹ à T=823 K; (b) en fonction du flux dans la plage de 5x10¹¹ - 5x10¹² cm⁻²s⁻¹ à la fluence de 5x10¹⁵ cm⁻² à T=823 K; (c) en fonction de la température dans la plage de 723-823 K pour la fluence de 5x10¹⁵ cm⁻² avec le flux de 5x10¹¹ cm⁻²s⁻¹. Les couleurs différencient les populations de bulles, comme l'explique la légende située en haut de la figure. Les parts d'hélium représentées sont normalisées par rapport à la concentration totale d'hélium contenue dans toutes les bulles.

Les résultats de l'analyse statistique des paramètres de la population de bulles et les estimations du gonflement et de la fraction d'hélium accumulée dans les bulles obtenues pour l'acier ODS-EUROFER dans des conditions d'implantation fixes de He⁺ en simple faisceau ont été comparés au matériau de référence exempt d'oxyde, c'est-à-dire l'acier EUROFER 97. Dans les mêmes conditions d'implantation à simple faisceau, les bulles dans l'acier EUROFER 97 étaient légèrement plus grandes que celles dans l'acier ODS-EUROFER, qu'elles soient situées dans le cœur des grains ou sur des défauts microstructuraux, à l'exception des précipités de carbure. Une tendance similaire a été constatée pour la densité des bulles d'hélium pour chaque type de défaut. On prévoit pour EUROFER 97 des valeurs de gonflement et de fraction d'hélium accumulée environ 1,5 fois plus élevées que pour ODS-EUROFER.

En gardant à l'esprit que les aciers ODS en service dans les réacteurs seront soumis à des dommages intenses causés par l'irradiation par des neutrons rapides, l'effet augmenté du rapport dpa/He appm sur le gonflement et l'inventaire d'hélium dans l'ODS-EUROFER a été étudié dans cette thèse au moyen d'une irradiation ionique simultanée *in situ* en double faisceau à 823 K avec des ions He⁺ de 10 keV à une fluence de 5×10¹⁵ cm⁻² et un second faisceau d'ions lourds (Au²⁺) de 4 MeV à une fluence de 4,5×10¹⁵ cm⁻². Les paramètres des bulles d'hélium corrélés aux caractéristiques microstructurales ont été estimés par analyse MET au moyen de la même approche indirecte que pour le régime d'implantation d'He⁺ à simple faisceau. Les résultats de l'analyse statistique des paramètres de la population de bulles et les estimations du gonflement et de la fraction d'hélium accumulée dans les bulles ont été comparés aux résultats similaires obtenus pour l'implantation d'He⁺ en simple faisceau. Il a été constaté que la redistribution de l'hélium entre les différentes caractéristiques microstructurales était relativement modérément affectée par les dommages accélérés produits par le faisceau secondaire d'ions lourds et restait qualitativement similaire au cas du régime d'implantation d'hélium en simple faisceau. En termes d'inventaire d'hélium, le rapport dpa/He appm a augmenté les contributions d'He pour toutes les populations de bulles, soit dans le cœur du grain, soit sur les défauts microstructuraux. L'effet le plus fort a été observé pour les bulles dans le grain ; leur contribution à la fraction d'hélium retenue a augmenté environ deux fois. En conséquence, la part totale d'He implanté capturé dans les bulles a augmenté sous l'action synergétique de l'accumulation d'hélium et de l'accélération des dommages jusqu'à ~70%, alors que dans le régime He⁺ en simple faisceau, il ne constitue que ~54%, soit un peu plus de la moitié de tout He implanté capturé dans les bulles visibles. Dans l'ensemble, l'effet des dommages accélérés sur la rétention d'hélium est relativement modéré et, parmi les défauts microstructuraux, la plus grande contribution est fournie par les bulles des joints de grain, comme c'était le cas dans le régime d'implantation d'hélium en simple faisceau. L'effet qualitatif important causé par une forte accélération de la production de dommages est la formation de grandes cavités sur certaines particules d'oxyde (voir la figure 3 (a)). L'effet est interprété comme une manifestation de la transition bulle-cavité causée par l'augmentation de la sursaturation efficace de lacunes dans la matrice suite à l'irradiation avec des ions d'or énergétiques. Dans la littérature, on ne trouve que quelques rapports [25,37] mentionnant une transition bulle-cavité dans la population de bulles associée à des nanoparticules dans des alliages ODS qui avaient accumulé plus de 1000 appm He après une irradiation neutronique à une dose >20 dpa à une température de 773 K.

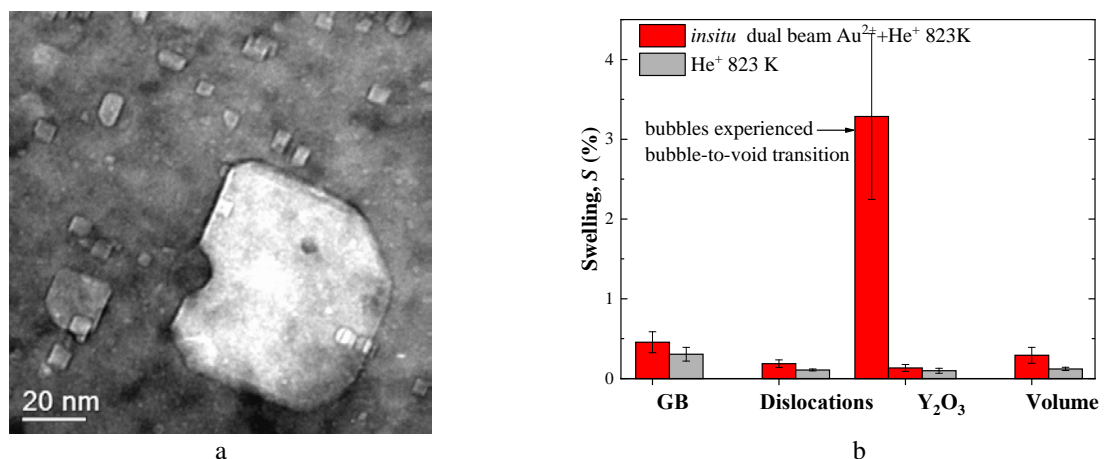


Fig. 3. (a) Image sous-focalisée par BF MET de l'acier ODS-EUROFER après irradiation simultanée *in situ* à 823 K d'ions He⁺ de 10 keV (avec un flux de 5×10¹¹ cm⁻²s⁻¹ à la fluence de 5×10¹⁵ cm⁻²) et d'ions Au²⁺ de 4 MeV (avec un flux de 4×10¹¹ cm⁻²s⁻¹ à la fluence de 4,5×10¹⁵ cm⁻²) ; (b) Analyse statistique comparative du gonflement associé à différentes populations de bulles dans des échantillons ODS-EUROFER irradiés à 823 K soit simultanément avec des ions He⁺ 10 keV avec un flux de 5×10¹¹ cm⁻²s⁻¹ à la fluence 5×10¹⁵ cm⁻², puis avec des ions Au²⁺ de 4 MeV avec un flux de 4×10¹¹ cm⁻²s⁻¹ à la fluence de 4,5×10¹⁵ cm⁻² (barres rouges), soit seulement avec des ions He⁺ 10 keV à la même température et avec les mêmes paramètres d'implantation (barres grises).

Le fait que la transition ne se produise que sur les particules d'oxyde semble naturel car on a constaté que les plus grosses bulles décoraient toujours les particules d'oxyde de l'acier ODS. Dans cette thèse, la transition bulle-cavité déclenchée par les nanoparticules d'oxyde a été expliquée en termes d'un modèle théorique qui prédit que le nombre critique d'atomes de gaz requis pour favoriser la transition bulle-cavité pour une bulle d'hélium située sur une particule est sensiblement inférieur à celui d'une bulle critique située dans le grain. Notez que selon le modèle théorique et les observations expérimentales, la transition est déclenchée par des particules hôtes suffisamment grandes. La création de grandes cavités sur les nanoparticules d'oxyde affecte fortement le gonflement, comme l'illustre la figure 3(b). Malgré une certaine augmentation de la contribution au gonflement des bulles aux joints de grains dans le régime d'irradiation à double faisceau, il n'y a toujours pas de coalescence des bulles aux joints de grains qui pourrait entraîner une fragilisation à haute température de l'hélium dans l'acier ODS-EUROFER. Si, toutefois, toutes les bulles associées aux nanoparticules devaient subir une telle transition, leur contribution au gonflement augmenterait de près d'un ordre de grandeur, (Fig. 3(b)), dépassant largement les contributions des bulles situées aux joints de grains, ou de toute autre population de bulles. Le gonflement cumulé attendu serait alors supérieur d'un facteur d'environ 7 à la valeur de l'implantation à simple faisceau. En réalité, la véritable valeur de gonflement pour l'irradiation à double faisceau devrait se situer quelque part entre les deux valeurs limites. Avec l'augmentation de la dose d'irradiation, la contribution au gonflement des grandes cavités sera finalement beaucoup plus importante que celle que pourraient fournir toutes les autres populations de bulles, car la croissance des grandes cavités n'est plus contrôlée par la quantité d'hélium qu'elles retiennent. Par conséquent, la transition bulle-cavité observée dans le régime à double faisceau comporte le risque de modifier qualitativement la résistivité de l'acier au gonflement.

Pour étudier l'effet synergétique de l'accumulation d'hélium et d'hydrogène sur l'évolution microstructurale dans l'ODS-EUROFER, une série d'expériences d'irradiation a été réalisée en mode séquentiel *ex situ* à double faisceau avec pré-implantation d'ions He^+ de 10 keV à une fluence de $5 \times 10^{15} \text{ cm}^{-2}$, suivie d'une implantation d'ions H^+ de 5 keV à une fluence de $1 \times 10^{17} \text{ cm}^{-2}$ dans les régimes de température suivants:

- (i) régime de haute température, introduction de He^+ et H^+ à 823 K,
- (ii) régime de basse température, introduction de He^+ et H^+ à la température ambiante. Une partie des échantillons implantés en régime de basse température a été soumise à un recuit post-implantation pendant 90 minutes à 823 K sous vide,
- (iii) régime de température « combiné », pré-implantation d'ions He^+ à $T=823 \text{ K}$ suivie d'une implantation de H^+ à température ambiante.

Des études MET conventionnelles détaillées d'échantillons d'ODS-EUROFER implantés *ex situ* à double faisceau dans tous les régimes de température ont été axées sur l'évolution des paramètres des bulles d'hélium (taille, densité numérique et forme, le cas échéant) causées par l'implantation de H^+ . Les cavités remplies d'hélium formées au stade de l'implantation de l' H^+ ont été traitées comme des marqueurs de tout changement microstructural survenu au cours de l'implantation de l' H^+ . Compte tenu du fait que les bulles fixées aux nanoparticules d'oxyde d'yttrium sont toujours sensiblement plus grandes que les bulles dans le cœur du grain ou les bulles associées à d'autres défauts structuraux, seule cette population de bulles a été analysée en détail. Le gonflement cumulé a été estimé par une approche indirecte. Pour étudier le rôle de l'hydrogène dans l'évolution de la microstructure dans des échantillons ODS-EUROFER pré-implantés avec des ions He^+ dans des régimes de température basse et « combiné », la teneur en hydrogène retenue a été quantifiée par des mesures de TDS et comparée à celle des échantillons sans He (implantés avec de l'hydrogène uniquement). Afin de mieux comprendre le rôle possible des nanoparticules d'oxyde d'yttrium dans l'accumulation d'hydrogène dans l'acier ODS-EUROFER, les tendances générales de l'absorption et du piégeage de l'hydrogène dans l'ODS-EUROFER ont été comparées à celles de l'acier EUROFER 97, qui a une composition similaire mais pas de particules d'oxyde. En outre, les mesures de TDS pour l'acier ODS-EUROFER après implantation séquentielle à

double faisceau avec des ions He⁺ et H⁺ réalisées à différents taux de chauffage ont été utilisées pour déterminer les énergies d'activation du piégeage de l'H de divers composants microstructuraux. Des recherches sur l'association possible de l'hydrogène avec les bulles d'hélium ont été effectuées en utilisant les résultats des mesures EELS en mode d'acquisition d'imagerie spectrale (SI) effectuées sur des échantillons ODS-EUROFER implantés séquentiellement à double faisceau en régime de température dit combiné.

Un résumé des effets de l'hydrogène observés expérimentalement sur l'acier ODS-EUROFER pré-implanté avec He⁺ est donné dans le tableau 1. Les résultats MET et TDS pour les échantillons implantés séquentiellement sont comparés aux résultats d'implantation de He⁺ et de H⁺ en simple faisceau, respectivement.

Tableau 1. Résumé des effets de l'hydrogène sur les échantillons d'acier ODS-EUROFER pré-implantés avec des ions hélium.

	MET conventionnel	TDS	EELS-SI
<p>He⁺ F=5×10¹⁵ - 1×10¹⁶ cm⁻² à la RT</p>	<ul style="list-style-type: none"> • Nucléation de bulles de faible taille et de forte densité numérique ; • L'augmentation de la taille des bulles après recuit à 823 K de ~6 % pour les bulles sur les particules de Y₂O₃ et de ~12 % pour les bulles dans la masse et sur d'autres défauts structuraux ; 	<ul style="list-style-type: none"> • L'augmentation de la rétention totale de H de 40% due à l'accumulation d'hydrogène dans les pièges irréversibles avec les énergies de déblocage de 0,78-0,81 eV • Faible signal des forts pièges à hydrogène avec une énergie de déblocage de ~3 eV 	Pas d'enquête
<p>H⁺ F= 1×10¹⁷ cm⁻² à la RT</p>	<ul style="list-style-type: none"> • Pas de changement dans la densité numérique des bulles • Une légère augmentation du gonflement de 25 % après un recuit supplémentaire à 823 K 		
<p>He⁺ F=1×10¹⁶ cm⁻² à 823 K</p>	<ul style="list-style-type: none"> • Suppression des facettes des bulles • Nucléation de bulles de taille sub-nanométrique et de haute densité numérique 	<ul style="list-style-type: none"> • L'augmentation de la rétention totale de H de 80% due à l'accumulation d'hydrogène dans les pièges irréversibles avec les énergies de déblocage de 0,78-0,81 eV 	Le signal H est associé aux bulles He. Le signal est spatialement distribué sur toute la surface de la bulle avec un renforcement modéré à la périphérie de la bulle
<p>H⁺ F= 1×10¹⁷ cm⁻² à la RT</p>	<ul style="list-style-type: none"> • Modification du gonflement en dessous du seuil de détection 		
<p>He⁺ F=5×10¹⁵ cm⁻² à 823 K</p>	<ul style="list-style-type: none"> • Les bulles attachées aux particules de Y₂O₃ croissent d'environ 7 %; tandis que les bulles associées à d'autres défauts et situées au cœur des grains restent inchangées 	Pas d'enquête	Pas d'enquête
<p>H⁺ F= 1×10¹⁷ cm⁻² à 823 K</p>	<ul style="list-style-type: none"> • Pas de changement dans la densité numérique des bulles • L'augmentation du gonflement cumulé de 21 		

Les données MET conventionnelles indiquent une influence relativement mineure de l'hydrogène implanté sur le gonflement global pour tous les régimes d'implantation séquentiels utilisés. L'implantation de l'hydrogène augmente le gonflement cumulé de moins de 25 % par rapport à celui observé après une pré-implantation de He⁺ en simple faisceau. La microstructure visible des bulles dans ODS-EUROFER est principalement déterminée par la concentration d'hélium obtenue et les conditions d'implantation d'hélium et/ou de traitement à haute température. Pour les conditions expérimentales à haute température utilisées, la densité du nombre de bulles est faiblement affectée par l'implantation de H⁺. La comparaison de l'évolution des bulles dans les échantillons ODS-EUROFER soumis à une pré-implantation d'ions He⁺ à haute température ou à un recuit post-implantation à 823 K a révélé qu'après une implantation séquentielle de He⁺+H⁺ en double faisceau, les bulles observées étaient systématiquement légèrement plus grandes qu'après une implantation de He⁺ en simple faisceau. Cependant, une part notable des atomes d'hélium après l'étape d'implantation de He a été retenue dans la matrice sous la forme d'atomes de He

substitutifs et/ou de petits amas He_nV_m . La diffusion d'atomes de He et/ou d'amas He_nV_m vers des bulles d'He pendant l'implantation d'hydrogène à haute température ou le recuit post-implantation entraîne la croissance de bulles et augmente la valeur estimée du gonflement. Il semble que les changements microstructuraux observés à température élevée (823 K) ont été déterminés plutôt par la redistribution de l'hélium due à l'accélération de la mobilité des défauts, et par les dommages supplémentaires causés par le rayonnement créés par le faisceau H^+ , que par l'accumulation d'hydrogène. Cette conclusion est soutenue par les estimations de la fraction d'hélium retenue dans les bulles après recuit et par les mesures de la libération d'hydrogène par TDS. Dans les échantillons implantés avec un double faisceau, la fraction d'hélium retenue dans les bulles a augmenté après recuit de 33% à 87%, alors que la majeure partie de l'hydrogène est libérée à des températures inférieures à 750 K.

Bien que l'implantation d'hydrogène joue peu de rôle dans le développement microstructural après l'implantation à des températures élevées ou pendant le recuit post-implantation, certains effets de l'hydrogène sur la population de bulles ont été détectés lors de l'implantation d'hydrogène à température ambiante. L'implantation d'ions H^+ dans l'acier ODS-EUROFER pré-implanté avec de l'hélium soit à température ambiante soit à 823 K a favorisé la nucléation de bulles avec une forte densité et des tailles de $\sim 0,5\text{-}1$ nm. La nucléation de bulles observée peut être due soit à une stabilisation supplémentaire des amas vacants par des atomes d'hydrogène piégés, soit à la diffusion renforcée par irradiation de l'He retenu dans de petits amas He-V à la suite de la production de dommages supplémentaires par le faisceau d'hydrogène. De plus, pour les échantillons ODS-EUROFER implantés séquentiellement par double faisceau dans le régime de température dit combiné (He^+ à 823 K et H^+ à la température ambiante), on observe un net arrondi des bulles à facettes développées au stade de pré-implantation de He^+ . La suppression des facettes des bulles est difficile à expliquer en termes de dommages causés par les radiations et est plus probablement due à l'accumulation d'hydrogène au niveau des parois des bulles d'hélium par un mécanisme de type chimisorption. Le piégeage de l'hydrogène au niveau des bulles d'hélium est également confirmé par les observations de TDS et de l'EELS-SI. L'implantation d' He^+ à température ambiante ou à 823 K suivie de l'implantation de H^+ à température ambiante augmente la rétention totale d'hydrogène dans l'ODS-EUROFER de, respectivement, 40% ou 80% par rapport à l'implantation de H^+ en simple faisceau. L'augmentation de la rétention d'hydrogène résulte de l'accumulation d'hydrogène dans des pièges irréversibles avec des énergies de dé-piégeage de 0,78-0,81 eV, qui sont couramment associées dans la littérature à la liaison de l'hydrogène aux surfaces des bulles. La distribution spatiale de l'hélium et de l'hydrogène obtenue par la technique SI EELS sur des échantillons implantés séquentiellement avec de l' He^+ à 823 K et H^+ à RT soutient fortement cette identification provisoire (voir Fig. 4). Le signal EELS-SI de l'hélium a l'intensité maximale au centre de la bulle, ce qui suggère que l'hélium remplit uniformément le volume de la bulle. En revanche, le signal de l'hydrogène extrait est distribué de manière plus ou moins uniforme sur les zones de la bulle avec une augmentation d'intensité définie à la périphérie de la bulle, ce qui devrait plutôt être le cas pour la couverture de la surface de la bulle par l'hydrogène. La distribution spatiale des atomes de gaz dans les bulles après une implantation séquentielle avec He^+ à 823 K et H^+ à RT peut être interprétée en termes de structure "cœur-coquille", où le cœur d'hélium à l'intérieur de la cavité est entouré d'une coquille d'atomes d'hydrogène au niveau des parois de la cavité. La présence d'hydrogène moléculaire dans les bulles nucléées après une implantation séquentielle avec He^+ et H^+ à la température ambiante est suggérée par les résultats de l'analyse TDS, mais la part d'hydrogène retenue sous forme moléculaire est extrêmement faible.

L'analyse TDS montre que l'acier ODS-EUROFER présente une absorption d'hydrogène environ 3 fois plus importante que l'acier EUROFER 97 sans ODS, sous implantation H^+ en simple faisceau et sous implantation séquentielle $\text{He}^+\text{+H}^+$ à température ambiante. Cependant, l'analyse des résultats expérimentaux en conjonction avec les données de la littérature disponible indique que la plus forte rétention d'hydrogène dans l'acier ODS-EUROFER par rapport à EUROFER 97 ne peut pas être exclusivement attribuée à la présence de nanoparticules d'oxyde et devrait plutôt être liée aux différences

de densités de volume d'autres sites de piégeage, comme les dislocations, les joints de grains et les lacunes. L'accumulation directe d'hydrogène à l'intérieur des particules d'oxyde n'est pas très probable en raison de la faible solubilité de l'hydrogène dans l'oxyde d'yttrium [38], mais il ne peut être exclu que l'hydrogène s'accumule soit à la surface des nanoparticules, soit dans les bulles associées aux nanoparticules. Compte tenu de l'énergie de liaison de l'hydrogène aux interfaces particules/matrice d'oxyde estimée à 0,36 eV, le piégeage de l'hydrogène aux interfaces nanoparticules/matrice ne peut guère affecter le gonflement, même si l'on peut s'attendre à des effets sur les propriétés mécaniques de l'acier ODS-EUROFER [28,39]. L'influence de l'hydrogène sur la population de bulles associée aux nanoparticules d'oxyde d'yttrium s'est également avérée mineure dans toutes les conditions d'implantation utilisées dans cette thèse. Après une implantation séquentielle avec He^+ et H^+ à température ambiante, des bulles se sont formées à la fois dans le cœur des grains et sur les défauts structuraux, mais aucune augmentation préférentielle de la taille des bulles sur les interfaces nanoparticules/matrice d'oxyde n'a été observée. Après implantation d' H^+ à haute température (823 K) ou le recuit post-implantation d'échantillons pré-implantés séquentiellement avec de l'hélium à la température ambiante, les bulles associées aux nanoparticules de Y_2O_3 étaient plus grandes que dans le cœur du grain ou sur d'autres défauts structuraux. Cependant, comme pour d'autres populations de bulles, les bulles attachées aux nanoparticules ont montré une faible sensibilité à l'implantation d' H^+ ; leur taille moyenne a augmenté de moins de 7 % par rapport à celle observée après l'implantation d' He^+ en simple faisceau. Comme la désorption de l'hydrogène des bulles se produit principalement à des températures inférieures à 750 K, cette croissance mineure des bulles devrait être liée plutôt à la redistribution de l'hélium qu'à l'accumulation d'hydrogène dans les bulles.

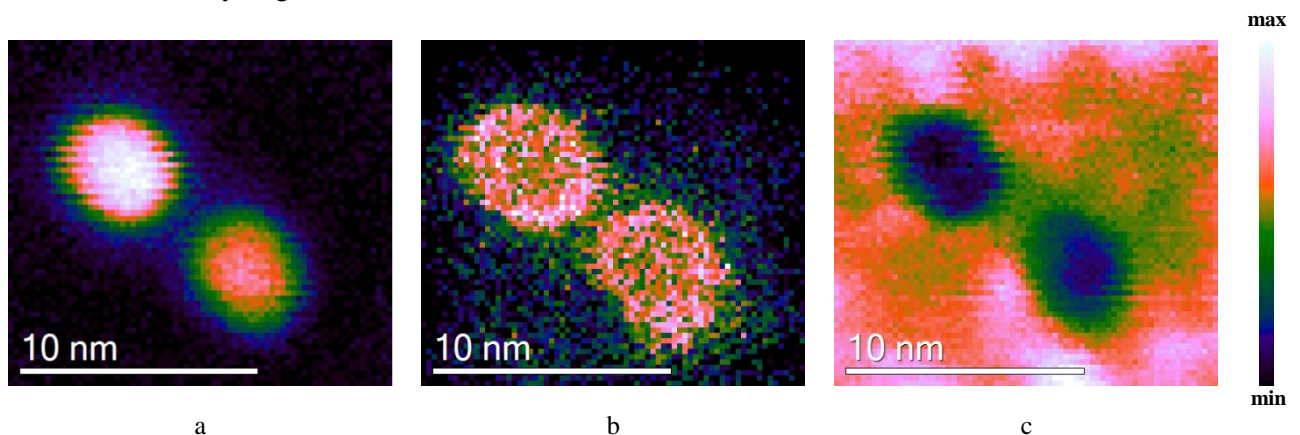


Fig. 4. Cartes d'intensité de deux bulles dans l'acier ODS-EUROFER séquentiellement à double faisceau implanté avec des ions He^+ de 10 keV à la fluence de $1 \times 10^{16} \text{ cm}^{-2}$ à 823 K et des ions H^+ à la fluence de $1 \times 10^{17} \text{ cm}^{-2}$ à RT obtenues par ajustement gaussien NLLS à partir de la différence spectrale EELS-SI: (a) $\sim 25 \text{ eV}$ (He-K); (b) $\sim 13,2 \text{ eV}$ H-K; (c) carte d'épaisseur.

En résumé, dans les conditions expérimentales utilisées dans cette thèse, l'injection d'hydrogène dans l'acier ODS-EUROFER pré-implanté avec de l'hélium n'a pas révélé de risques potentiels d'augmentation notable du gonflement, contrairement à la production de dommages supplémentaires qui est capable de déclencher une transition de bulle à cavité dans la population de bulles associée aux nanoparticules d' Y_2O_3 . Le mécanisme spécifique de type chimisorption de piégeage de l'hydrogène au niveau des parois des bulles d'hélium semble jouer le rôle principal dans l'accumulation d'hydrogène dans les conditions expérimentales étudiées.

Afin de mieux comprendre les mécanismes impliqués dans le développement microstructural à l'interface métal/oxyde et à proximité de celle-ci pendant l'irradiation et/ou l'accumulation de gaz, l'approche récemment proposée par plusieurs groupes de recherche [40-44] a été appliquée. Cette approche comprend l'implantation ionique et l'étude subséquente par MET de systèmes modèles bicouches à l'échelle mésoscopique, ce qui permet de mieux contrôler les effets à l'interface métal/oxyde, favorisés par l'irradiation et/ou l'accumulation de gaz. À cette fin, des films minces constitués d'un

composé Y_2O_3 pur et d'un alliage binaire de Fe-10at%Cr ont été déposés successivement sur différents substrats céramiques monocristallins (MgO, SrTiO₃ et zircone stabilisée à l'oxyde d'yttrium (YSZ)) en combinant le dépôt par pulvérisation magnétron réactive (MS) d'une cible élémentaire Y sous atmosphère d'oxygène avec le dépôt par épitaxie par faisceau moléculaire (MBE) de métaux élémentaires Fe et Cr par effusion thermique. Les meilleurs films en bicouche $Y_2O_3/FeCr$ ont été obtenus en utilisant un substrat de SrTiO₃ (100), où l'épitaxie de l'interface métal-oxyde a été réalisée au moins partiellement. Les films en bicouche $Y_2O_3/FeCr$ tels que fabriqués et déposés sur le substrat en SrTiO₃ (100) ont été caractérisés en détail et utilisés pour des implantations ioniques ultérieures.

L'implantation ionique a été effectuée perpendiculairement à la surface de l'échantillon en bicouche selon quatre régimes d'implantation/irradiation différents, dont

- (i) implantation de He^+ à 17 keV à la fluence de $1 \times 10^{17} \text{ cm}^{-2}$, à température ambiante et à 823 K
- (ii) implantation de 10 keV H^+ à la fluence de $2 \times 10^{17} \text{ cm}^{-2}$ à RT
- (iii) implantation avec des ions He^+ de 17 keV à la fluence de $1 \times 10^{17} \text{ cm}^{-2}$ à température ambiante, suivie d'une implantation de H^+ de 10 keV à la fluence de $2 \times 10^{17} \text{ cm}^{-2}$ à température ambiante
- (iii) irradiation par des ions lourds Kr^+ d'énergie 2 MeV à la fluence de $3,6 \times 10^{15} \text{ cm}^{-2}$ à température ambiante.

Les énergies des ions He^+ et H^+ ont été sélectionnées de manière à obtenir les pics de concentration des ions implantés à proximité de l'interface entre les couches minces de Fe-10%Cr et de Y_2O_3 . Pour l'irradiation avec des ions Kr^+ , l'énergie, le flux et la fluence des ions ont été sélectionnés de manière à obtenir un débit de dose et une dose accumulée similaires à ceux de l'implantation d' He^+ en simple faisceau et, en même temps, à minimiser la concentration de Kr dans la région d'intérêt. Après l'implantation/l'irradiation, des échantillons de MET en coupe transverse ont été préparés par la technique d'extraction FIB et ont été étudiés par MET en champ clair (BF) et MET haute résolution (HRTEM).

Le tableau 2 résume les caractéristiques microstructurales observées dans le système bicouche $Y_2O_3/FeCr$ après des implantations d' He^+ et H^+ en simple faisceau, une implantation séquentielle d' $He^+ + H^+$, et une irradiation avec des ions Kr.

Table 2. Résumé des caractéristiques microstructurales observées dans le système bicouche $Y_2O_3/FeCr$ après implantation d' He^+ et H^+ en simple faisceau, implantation séquentielle d'ions $He^+ + H^+$, et irradiation avec des ions Kr^+ .

Implantation/ régime d'irradiation	Film Fe-10Cr	Interface	Film Y_2O_3
He^+ , RT	formation de la cavité $\langle D_c^{Me} \rangle = 2.0 \text{ nm}$; $\langle N_c^{Me} \rangle = 28.6 \times 10^{23} \text{ m}^{-3}$	formation de la cavité $\langle D_c^{Int} \rangle = 4.1 \text{ nm}$; $\langle N_c^{Int} \rangle = 1.0 \times 10^{16} \text{ m}^{-2}$	formation de la cavité $\langle D_c^{Ox} \rangle = 3.3 \text{ nm}$; $\langle N_c^{Ox} \rangle = 5.4 \times 10^{23} \text{ m}^{-3}$
He^+ , 823 K	formation de la cavité $\langle D_c^{Me} \rangle = 7.8 \text{ nm}$; $\langle N_c^{Me} \rangle = 2.4 \times 10^{23} \text{ m}^{-3}$	-	-
H^+ , RT	formation de la cavité $\langle D_c^{Me} \rangle = 1.1 \text{ nm}$; $\langle N_c^{Me} \rangle = 34.8 \times 10^{23} \text{ m}^{-3}$	formation de la cavité $\langle D_c^{Int} \rangle = 3.1 \text{ nm}$; $\langle N_c^{Int} \rangle = 1.6 \times 10^{23} \text{ m}^{-2}$	Fissuration le long de l'interface, fracture sur les plans {111}.
$He^+ + H^+$, RT	croissance des cavités lors de l'implantation H $\langle D_c^{Me} \rangle = 2.3 \text{ nm}$; $\langle N_c^{Me} \rangle = 27.9 \times 10^{23} \text{ m}^{-3}$	a) Croissance des cavités lors de l'implantation d'H $\langle D_c^{Int} \rangle = 4.6 \text{ nm}$; $\langle N_c^{Int} \rangle = 1.0 \times 10^{16} \text{ m}^{-2}$ b) Dé-cohésion de l'interface	Fissuration le long de l'interface, fracture sur les plans {112}.
Kr^+ , RT	formation de la cavité $\langle D_c^{Me} \rangle = 1.2 \text{ nm}$; $\langle N_c^{Me} \rangle = 6.6 \times 10^{23} \text{ m}^{-3}$	-	-

Les systèmes modèles bicouche métal/oxyde ont pu reproduire les tendances des matériaux industriels en matière de formation de cavités assistée par l'H dans toutes les parties du système, c'est-à-dire le métal, l'interface et l'oxyde, mais seulement après l'implantation d'hélium à température ambiante (voir figure 5).

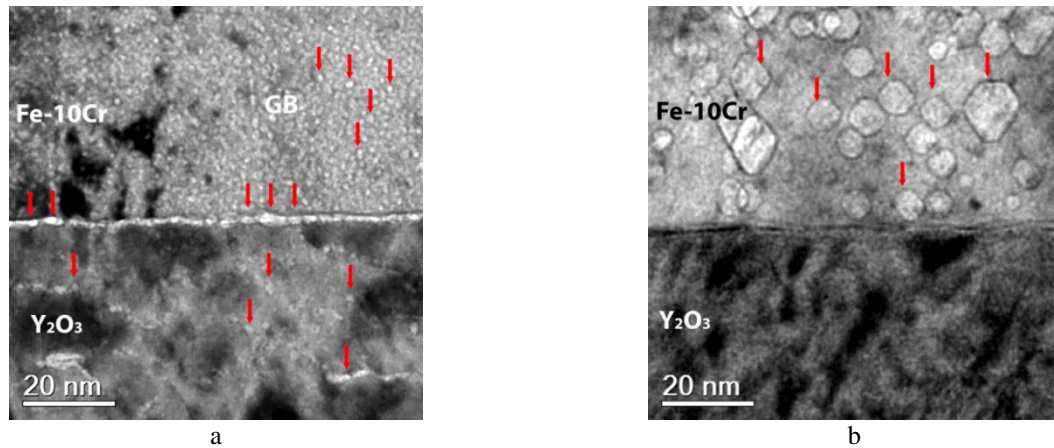


Fig. 5. Image sous-focalisée par MET en champ clair d'un système modèle en bicouche $Y_2O_3/FeCr$ implanté avec des ions He^+ de 17 keV à la fluence de $1 \times 10^{17} \text{ cm}^{-2}$: (a) à RT; (b) à 823 K.

À température ambiante, l'hélium était efficacement piégé dans de petites cavités de la couche de FeCr, et pouvait être efficacement stocké à l'intérieur de particules d'oxyde d'yttrium. La tendance à la formation préférentielle de cavités à l'interface observées à température ambiante indique que le piégeage de l'hélium à l'interface métal/oxyde est insensible à la fois à la relation d'orientation métal/oxyde et à la chimie de l'interface. À la température de 823 K, le développement de la population de cavités en réponse à l'implantation d'hélium ressemble à celui des aciers ODS uniquement dans la couche métallique. Le schéma de formation des cavités assistée par l'hélium à l'interface métal/oxyde est sensiblement différent de celui généralement observé pour les aciers industriels ODS. Aucune nucléation de bulles d'hélium à l'interface plane FeCr/oxyde d'yttrium n'a été remarquée, alors que de grandes cavités décorant les nano-oxydes d'oxyde d'yttrium ont été observées dans les aciers industriels ODS à la même température (voir Fig. 1(a)). À l'intérieur de la couche d'oxyde, aucune cavité n'a été observée à cette température également ; l'hélium implanté était soit redistribué dans la couche, soit s'était échappé de celle-ci dans le substrat ou dans l'environnement de l'échantillon. Une telle redistribution est impossible dans les aciers ODS, où les nano-oxydes sont complètement entourés d'une matrice de FeCr. Ainsi, bien que les expériences sur les interfaces planaires métal/oxyde soient utiles pour comprendre les mécanismes sous-jacents du piégeage et de la diffusion de l'He, l'extrapolation de leurs résultats sur les aciers industriels ODS doit être faite avec prudence.

Le rôle critique de l'hélium et, étonnamment, de l'hydrogène dans la formation de cavités et/ou de microfissures dans un système modèle en bicouche FeCr/oxyde d'yttrium soumis à des implantations d'ions lourds, d'hélium et d'hydrogène en simple faisceau a été démontré par l'analyse MET. La formation de cavités assistée par l'hydrogène à l'intérieur de la couche de FeCr et à l'interface métal/oxyde, provoquée par l'implantation de H^+ , a été démontrée. Les cavités à l'interface étaient plus grandes que les cavités dans la couche métallique. En revanche, des microfissures plutôt que des cavités se sont formées dans la couche d' Y_2O_3 . L'orientation des microfissures formées après l'implantation d'hydrogène indique que l'hydrogène pourrait être efficacement piégé dans des boucles lacunaires anioniques à l'intérieur de la couche d'oxyde d'yttrium. La promotion de la formation de cavités par l'hydrogène implanté soutient la possibilité de piégeage de l'hydrogène à l'interface métal/oxyde suggérée par l'analyse TDS effectuée sur l'acier industriel ODS-EUROFER.

Un fort effet synergétique de l'hélium et de l'hydrogène a été observé après l'implantation séquentielle d'un échantillon modèle en bicouche FeCr/oxyde d'yttrium implanté avec de l'hélium et de l'hydrogène. L'implantation d'hydrogène dans le système pré-implanté d'hélium a conduit à une dé-cohésion de l'interface et à la nucléation de micro-fissures dans la couche d'oxyde. La dé-cohésion et la formation de micro-fissures après l'injection d'hydrogène pourraient résulter de plusieurs processus concurrents tels que la croissance et la coalescence des cavités à l'interface favorisées par l'hydrogène, ou l'affaiblissement des liaisons de l'interface assisté par l'hydrogène. Le mécanisme exact responsable des processus détectés reste incertain et des recherches expérimentales et de modélisation supplémentaires

sont nécessaires pour expliquer les résultats obtenus. En même temps, l'hydrogène a eu une influence mineure sur la population de cavités remplies d'He dans la couche métallique, tout comme dans les aciers industriels ODS. La croissance des cavités à l'intérieur de la couche métallique pourrait être associée à l'accumulation d'hydrogène dans les cavités.

Les recherches menées dans le cadre de cette thèse de doctorat fournissent non seulement une nouvelle base de données contribuant à la compréhension fondamentale du développement de la microstructure des aciers ferritiques-martensitiques ODS, mais soulèvent également un certain nombre de questions qui doivent être approfondies pour être mieux comprises, en particulier :

(i) La contribution des nanoparticules à l'inventaire d'hélium a été calculée sur la base de la taille moyenne des bulles par rapport à la taille moyenne des particules d'oxyde. Parfois, la distribution de taille des nano-oxydes dans l'acier ODS est assez large et peut inclure une fraction importante de particules qui s'écartent fortement de la valeur moyenne. Par conséquent, la prise en compte de la distribution réelle de la taille des particules pourrait améliorer la précision des estimations de l'inventaire de l'hélium. En outre, comme la détection des nano-oxydes par les méthodes conventionnelles en MET est difficile, les rayons X et l'imagerie par EELS (SI) pourrait y contribuer.

(ii) La conversion bulle-cavité dans la population de bulles associée aux nanoparticules d'oxyde après une irradiation avec des ions H/lourds en double faisceau requiert une plus grande attention. Dans cette étude, la dépendance quantitative entre la taille des particules d'oxyde et la population de bulles par rapport aux cavités n'a pas pu être réalisée en raison de statistiques médiocres provenant de la grande taille des cavités et de la surface relativement faible du champ de vision par MET. Par conséquent, seule une plage possible de variation de gonflement liée à la conversion des bulles en cavités a été estimée. Une corrélation précise devrait être établie afin de fournir des estimations de gonflement plus pertinentes et des lignes directrices pour la conception future d'aciers avancés ODS en termes de taille des particules.

(iii) L'irradiation d'hélium/ions lourds en double faisceau utilisée dans cette thèse était orientée sur la situation d'une accumulation de forte concentration en He à un niveau de dommage relativement modéré. Des expériences supplémentaires en double faisceau avec un rapport He/dpa variable sont nécessaires pour avoir un aperçu des rapports He/dpa limitatifs qui sont capables de favoriser la conversion en cavités des bulles associées aux nanoparticules d'oxyde afin de justifier l'extrapolation des résultats aux environnements prévus des réacteurs de fusion ou de spallation, où les taux d'accumulation de gaz devraient être inférieurs de quelques ordres de grandeur à ceux de nos expériences.

(iv) L'accumulation d'hydrogène dans les aciers ODS est encore loin d'être bien comprise. Des expériences supplémentaires de TDS et d'EELS après implantation d'hydrogène à haute température en simple faisceau et après irradiation d'ions hydrogène en faisceaux multiples sont nécessaires, par exemple pour clarifier les principaux mécanismes qui déterminent l'influence de l'hydrogène sur le gonflement, en fonction de la température de l'injection d'hydrogène et de la présence de dommages causés par les radiations.

(v) Bien que l'enquête préliminaire de l'EELS dans cette étude indique une association de l'hydrogène avec les bulles d'hélium à la manière d'une "enveloppe d'hydrogène et d'un noyau d'hélium", un traitement plus approfondi des données est nécessaire. La confirmation de la présence d'hydrogène peut être obtenue par des mesures complémentaires par spectroscopie vibratoire EELS et par l'application d'une modélisation pertinente de l'interaction de l'hydrogène avec les cavités dans l'acier.

(vi) Les modèles de systèmes en bicouche métal/oxyde présentent un bon potentiel en tant que modèles pour l'étude de l'interaction des oxydes avec les impuretés gazeuses secondaires et les dommages dus au déplacement. Cependant, l'interprétation des observations expérimentales sur les systèmes planaires en termes d'extrapolation aux aciers ODS nécessite l'application de simulations appropriées afin de mieux évaluer les caractéristiques énergétiques de l'hélium et de l'hydrogène dans les oxydes concernés et à leurs interfaces avec la matrice à base de Fe.

Références

- [1] *Climate Change and Nuclear Power 2018*. Vienna: International Atomic Energy Agency, 2018.
- [2] P. Yvon, Ed., *Structural Materials for Generation IV Nuclear Reactors*. Woodhead Publishing, 2017.
- [3] G. R. Odette and S. Zinkle, Eds., *Structural Alloys for Nuclear Energy Applications*. Elsevier, 2019.
- [4] I. L. Pioro, Ed., *Handbook of Generation IV Nuclear Reactors*. Woodhead Publishing, 2016.
- [5] R. L. Klueh, “Analysis of swelling behaviour of ferritic/martensitic steels,” *Philos. Mag.*, vol. 98, no. 28, pp. 2618–2636, Oct. 2018.
- [6] S. J. Zinkle and G. S. Was, “Materials challenges in nuclear energy,” *Acta Mater.*, vol. 61, no. 3, pp. 735–758, 2013.
- [7] A. Bhattacharya and S. J. Zinkle, “1.12 - Cavity swelling in irradiated materials,” in *Comprehensive Nuclear Materials (Second Edition)*, R. J. M. Konings and R. Stoller, Eds. Oxford: Elsevier, 2020, pp. 406–455.
- [8] *Structural Materials for Liquid Metal Cooled Fast Reactor Fuel Assemblies-Operational Behaviour*, no. NF-T-4.3. Vienna: International Atomic Energy Agency, 2012.
- [9] F. A. Garner, M. B. Toloczko, and B. H. Sencer, “Comparison of swelling and irradiation creep behavior of fcc-austenitic and bcc-ferritic/martensitic alloys at high neutron exposure,” *J. Nucl. Mater.*, vol. 276, no. 1, pp. 123–142, 2000.
- [10] R. Lindau, A. Moeslang, M. Rieth, M. Klimiankou, E. Materna-Morris, A. Alamo, A.-A. F. Tavassoli, C. Cayron, A.-M. Lancha, P. Fernandez, N. Baluc, R. Schaubelin, E. Diegele, G. Filacchioni, J.W. Rensman, B.v.d. Schaaf, E. Lucon, W. Dietz, “Present development status of EUROFER and ODS-EUROFER for application in blanket concepts,” *Fusion Eng. Des.*, vol. 75–79, pp. 989–996, 2005.
- [11] S. Ukai, S. Ohtsuka, T. Kaito, Y. de Carlan, J. Ribis, and J. Malaplate, “10 - Oxide dispersion-strengthened/ferrite-martensite steels as core materials for Generation IV nuclear reactors,” in *Structural Materials for Generation IV Nuclear Reactors*, P. Yvon, Ed. Woodhead Publishing, 2017, pp. 357–414.
- [12] S. J. Zinkle, J. L. Boutard, D. T. Hoelzer, A. Kimura, R. Lindau, G. R. Odette, M. Rieth, L. Tan and H. Tanigawa, “Development of next generation tempered and ODS reduced activation ferritic/martensitic steels for fusion energy applications,” *Nucl. Fusion*, vol. 57, no. 9, p. 92005, 2017.
- [13] G. R. Odette and D. T. Hoelzer, “Irradiation-tolerant nanostructured ferritic alloys: Transforming helium from a liability to an asset,” *JOM*, vol. 62, no. 9, pp. 84–92, Sep. 2010.
- [14] G. R. Odette, M. J. Alinger, and B. D. Wirth, “Recent developments in irradiation-resistant steels,” *Annu. Rev. Mater. Res.*, vol. 38, no. 1, pp. 471–503, Jul. 2008.
- [15] G. R. Odette, N. J. Cunningham, T. Stan, M. E. Alam, and Y. De Carlan, “Chapter 12 - Nano-oxide dispersion-strengthened steels,” in *Structural Alloys for Nuclear Energy Applications*, G. R. Odette and S. Zinkle, Eds. Boston: Elsevier, 2019, pp. 529–583.
- [16] P. D. Edmondson, C. M. Parish, Y. Zhang, A. Hallén, and M. K. Miller, “Helium bubble distributions in a nanostructured ferritic alloy,” *J. Nucl. Mater.*, vol. 434, no. 1, pp. 210–216, 2013.
- [17] A. I. Ryazanov, O. K. Chugunov, S. M. Ivanov, S. T. Latushkin, R. Lindau, A. Möslang, A. A. Nikitina, K. E. Prikhodko, E. V. Semenov, V. N. Unezhev, P. V. Vladimirov, “Tensile properties and microstructure of helium implanted EUROFER ODS,” *J. Nucl. Mater.*, vol. 442, no. 1, Supplement 1, pp. S153–S157, 2013.

- [18] T. Chen, H. Kim, J. G. Gigax, D. Chen, C.-C. Wei, F.A. Garner, L. Shao, “Radiation response of oxide-dispersion-strengthened alloy MA956 after self-ion irradiation,” *Nucl. Instruments Methods Phys. Res. Sect. B Beam Interact. with Mater. Atoms*, vol. 409, pp. 259–263, 2017.
- [19] Q. Li, C. M. Parish, K. A. Powers, and M. K. Miller, “Helium solubility and bubble formation in a nanostructured ferritic alloy,” *J. Nucl. Mater.*, vol. 445, no. 1, pp. 165–174, 2014.
- [20] C. M. Parish and M. K. Miller, “Aberration-corrected X-ray spectrum imaging and fresnel contrast to differentiate nanoclusters and cavities in helium-irradiated alloy 14YWT,” *Microsc. Microanal.*, vol. 20, no. 2, pp. 613–626, 2014.
- [21] C. M. Parish, K. A. Unocic, L. Tan, S. J. Zinkle, S. Kondo, L. L. Snead, D. T. Hoelzer, Y. Katoh, “Helium sequestration at nanoparticle-matrix interfaces in helium + heavy ion irradiated nanostructured ferritic alloys,” *J. Nucl. Mater.*, vol. 483, pp. 21–34, 2017.
- [22] T. Yamamoto, G. R. Odette, P. Miao, D. J. Edwards, and R. J. Kurtz, “Helium effects on microstructural evolution in tempered martensitic steels: In situ helium implanter studies in HFIR,” *J. Nucl. Mater.*, vol. 386–388, pp. 338–341, 2009.
- [23] G. R. Odette, P. Miao, D. J. Edwards, T. Yamamoto, R. J. Kurtz, and H. Tanigawa, “Helium transport, fate and management in nanostructured ferritic alloys: In situ helium implanter studies,” *J. Nucl. Mater.*, vol. 417, no. 1, pp. 1001–1004, 2011.
- [24] T. Yamamoto, Y. Wu, G. Robert Odette, K. Yabuuchi, S. Kondo, and A. Kimura, “A dual ion irradiation study of helium-dpa interactions on cavity evolution in tempered martensitic steels and nanostructured ferritic alloys,” *J. Nucl. Mater.*, vol. 449, no. 1–3, pp. 190–199, 2014.
- [25] B. Yao, D. J. Edwards, R. J. Kurtz, G. R. Odette, and T. Yamamoto, “Microstructure characterization of neutron irradiated and helium injected PM2000, 14YW, and modified F82H alloys,” *Fusion Mater. Semiannul Prog. Rep. June 2012*, vol. DOE-ER-031, p. 26, 2012.
- [26] H. J. Jung, D. J. Edwards, R. J. Kurtz, T. Yamamoto, Y. Wu, and G. R. Odette, “Structural and chemical evolution in neutron irradiated and helium-injected ferritic ODS PM2000 alloy,” *J. Nucl. Mater.*, vol. 484, pp. 68–80, 2017.
- [27] E. Malitckii, Y. Yagodzinskyy, M. Ganchenkova, S. Binyukova, H. Hänninen, R. Lindau, P. Vladimirov, A. Moeslang, “Comparative study of hydrogen uptake and diffusion in ODS steels,” *Fusion Eng. Des.*, vol. 88, no. 9, pp. 2607–2610, 2013.
- [28] Y. Yagodzinskyy, E. Malitckii, M. Ganchenkova, S. Binyukova, O. Emelyanova, T. Saukkonen, H. Hänninen, R. Lindau, P. Vladimirov, A. Moeslang, “Hydrogen effects on tensile properties of EUROFER 97 and ODS-EUROFER steels,” *J. Nucl. Mater.*, vol. 444, no. 1, pp. 435–440, 2014.
- [29] K. Farrell and E.H. Lee, “Ion damage in a Fe-10Cr-6Mo-0.5Nb ferritic Steel,” *Radiation-Induced Changes in Microstructure: 13th International Symposium (Part I)*, vol. STP 955, pp. 498–507, Jan. 1987.
- [30] E. Wakai, T. Sawai, K. Furuya, A. Naito, T. Aruga, K. Kikuchi, S. Yamashita, S. Ohnuki, S. Yamamoto, H. Naramoto, S. Jistukawa, “Effect of triple ion beams in ferritic/martensitic steel on swelling behavior,” *J. Nucl. Mater.*, vol. 307–311, pp. 278–282, 2002.
- [31] E. Wakai, K. Kikuchi, S. Yamamoto, T. Aruga, M. Ando, H. Tanigawa, T. Taguchi, T. Sawai, K. Oka, S. Ohnuki, “Swelling behavior of F82H steel irradiated by triple/dual ion beams,” *J. Nucl. Mater.*, vol. 318, pp. 267–273, 2003.
- [32] T. Tanaka, K. Oka, S. Ohnuki, S. Yamashita, T. Suda, S. Watanabe, E. Wakai, “Synergistic effect of helium and hydrogen for defect evolution under multi-ion irradiation of Fe–Cr ferritic alloys,” *J. Nucl. Mater.*, vol. 329–333, pp. 294–298, 2004.

- [33] J. Marian, T. Hoang, M. Fluss, and L. L. Hsiung, “A review of helium–hydrogen synergistic effects in radiation damage observed in fusion energy steels and an interaction model to guide future understanding,” *J. Nucl. Mater.*, vol. 462, pp. 409–421, 2015.
- [34] Y. E. Kupriyanova, V. V. Bryk, O. V. Borodin, A. S. Kalchenko, V. N. Voyevodin, G. D. Tolstolutskaia, F. A. Garner, “Use of double and triple-ion irradiation to study the influence of high levels of helium and hydrogen on void swelling of 8–12% Cr ferritic-martensitic steels,” *J. Nucl. Mater.*, vol. 468, pp. 264–273, 2016.
- [35] D. Brimbal, L. Beck, M. Payet, and F. Jomard, “The synergistic effect of hydrogen and helium implantations in forming H₂ molecules in a Fe-12 wt.%Cr-ODS steel characterized by Raman spectroscopy and SIMS,” *Nucl. Instruments Methods Phys. Res. Sect. B Beam Interact. with Mater. Atoms*, vol. 461, pp. 191–196, 2019.
- [36] N. Zimber, P. Vladimirov, M. Klimenkov, U. Jaentsch, R. Vila, V. Chakin, F. Mota, “Microstructural evolution of three potential fusion candidate steels under ion-irradiation,” *J. Nucl. Mater.*, vol. 535, p. 152160, 2020.
- [37] H. J. Jung, D. J. Edwards, R. J. Kurtz, G. R. Odette, Y. Wu, and T. Yamamoto, “Microstructural summary of ODS ferritic alloys (14YW, 14YWT, 12YWT, MA957FR, PM2000) and RAFM steels (F82H Mod.3-CW, Eurofer97) from JP27 in-Situ He injection (ISHI) experiment at 500°C,” *Fusion Mater. Semiannual Prog. Rep. June 2015*, vol. DOE-ER-031, p. 55, 2015.
- [38] D. Sun, J. Ding, Y. Yang, P. Zhang, and J. Zhao, “First-principles investigation of hydrogen behavior in different oxides in ODS steels,” *Int. J. Hydrogen Energy*, vol. 44, no. 31, pp. 17105–17113, 2019.
- [39] E. Malitckii, Y. Yagodzinskyy, M. Ganchenkova, T. Saukkonen, H. Hänninen, R. Lindau, P. Vladimirov, A. Moeslang, “Hydrogen uptake and its effect on mechanical properties of Eurofer 97-2 and ODS-Eurofer steels,” in *SMiRT 22 - San Francisco, USA. August 18-23, 2013*, 2013.
- [40] T. C. Kaspar, M. E. Bowden, C. M. Wang, V. Shutthanandan, N. R. Overman, R. M. van Ginhoven, B. D. Wirth, R. J. Kurtz, “Epitaxial Fe/Y₂O₃ interfaces as a model system for oxide-dispersion-strengthened ferritic alloys,” *J. Nucl. Mater.*, vol. 457, pp. 352–361, 2015.
- [41] T. Stan, Y. Wu, P. B. Wells, H. D. Zhou, and G. R. Odette, “Epitaxial Fe thin films on {100} Y₂Ti₂O₇: Model interfaces for nano-oxide dispersion strengthened steels,” *Metall. Mater. Trans. A*, vol. 48, no. 11, pp. 5658–5666, 2017.
- [42] A. Mairov, D. Frazer, P. Hosemann, and K. Sridharan, “Helium irradiation of Y₂O₃-Fe bilayer system,” *Scripta Materialia*, vol. 162, pp. 156–160, 2019.
- [43] T. Stan, “The role of oxides in nanostructured ferritic alloys and bilayers: Interfaces, helium partitioning and bubble formation,” 2017.
- [44] N. Li, S. K. Yadav, Y. Xu, J. A. Aguiar, J. K. Baldwin, Y. Q. Wang, H. M. Luo, A. Misra and B. P. Uberuaga, “Cr incorporated phase transformation in Y₂O₃ under ion irradiation,” *Scientific Reports*, vol. 7, no. 1, p. 40148, 2017.

Annex V. Detailed summary in English

Given the advantages of high efficiency and fewer limitations from environmental impact, advanced Generation IV fission, fusion and accelerator driven systems (ADS) have a great potential to become an important part of current and future non-carbon energy sources with continuous mode of energy generation [1–4]. Advanced fission and fusion facilities service conditions are characterized by high temperatures ~550-1000°C, intense neutron radiation fields ~5-30 dpa/fpy (displacement damage per atom per full power year) and utilization of chemically aggressive coolants. The primary candidate structural materials for the forthcoming fission and fusion facilities are ferritic-martensitic steels [5–9]. However, some designs are expected to operate at temperatures well above the limit (~550°C) of reliable performance of these steels. Oxide strengthening eliminates the most serious drawback of otherwise very good ferritic-martensitic steel grades (such as EUROFER) – the insufficient creep ductility resistance at high temperatures. This makes oxide dispersion strengthened (ODS) steels especially attractive for forthcoming advanced energy facilities. The high density of nano-oxide particles dispersed in the steel matrix not only improves its mechanical properties for high-temperature applications, but also adds to its radiation stability [10–15]. In spite of intensive international research on ODS steels in the last decade, many fundamental questions concerning the nano-oxide usage for the improvement of steel properties remain under debate. An important issue is the relative role in material microstructure development played by nano-oxides in complex irradiation environments where intensive displacement damage is accompanied with the accumulation of extremely high levels of light gases - helium and hydrogen.

Two major risks of helium accumulation in steels are (i) the decrease of swelling incubation dose and (ii) high temperature irradiation embrittlement (HTIE). It is currently expected that nanosized oxide particles in ODS steel should be beneficial for mitigation of both swelling and high temperature embrittlement, providing additional recombination sites for point defects at the oxide particle/matrix interfaces and He trapping sites [13,16–20]. However, ODS steels have complicated microstructure with multiple sinks (grain boundaries, dislocations, second phase precipitates) competing for point defects and helium atoms, and the relative role of additional components such as oxide nanoparticles is far from obvious, especially having in mind a broad variety of nano-oxides (Y_2O_3 , $Y_2Ti_2O_7$, $Y_3Al_5O_{12}$, $YAlO_3$, etc.) employed in different steel grades. Depending on particular steel and testing conditions, the fraction of helium bubbles affiliated with nano-oxides varies from 30 to 100% [15-17,21–24]. Taking into account that the nucleation and growth kinetics of helium bubbles is sensitive to multiple parameters of irradiation (dose, temperature and helium injection/generation rate) as well, the available literature knowledge remains unsystematic and often badly reproducible due to the lack of basic understanding of the involved microstructural mechanisms. Neither is it clear whether strong helium accumulation on nano-oxides bears no risks of undesirable consequences in terms of ODS-steel radiation tolerance [25,26].

The effects of hydrogen on the microstructural modification of ODS steels have been less extensively investigated than those of helium. It is commonly expected that in conventional steels hydrogen would not be retained at high concentrations but recent investigations have shown that ODS steels are able to accumulate more hydrogen than conventional materials [27,28]. The proposed explanation of this effect in terms of hydrogen trapping by oxide-nanoparticles is plausible, but has no firm proofs. An open question remains also a synergy in the action of hydrogen and helium on the properties of ODS steels. Multi-beam ion irradiation experiments evidence that helium and hydrogen are able to act in a synergistic manner on the development of irradiation-induced defect microstructure [29–36] and promote notable extra swelling under intense displacement damage [30–33,36], but only in a certain temperature range [30–32,36]. The mechanisms of such hydrogen effects remain unclear.

Mostly unsystematic experimental research of complex materials under complex radiations environment is not in a position to guide materials design because in order to recommend ODS steels for particular heavy-duty application, a designer must not only know their response to the effect of operation conditions (operation temperature history, damage and helium, hydrogen accumulation rates, etc.), but

also have a possibility to make the reliable long-term predictions and extrapolations of the existing experimental data beyond the parameter range, where these data were obtained. To reach this goal it is necessary to perform systematic studies of the sensitivity of gas-driven microstructure to the variation of key parameters, which include the nano-oxide sizes and densities, gas content and processing temperatures. The use of ion implantation technique for the imitation of microstructural changes in well-controlled conditions with a wide range of variable parameters combined with careful post-implantation characterization is a highly promising approach. However, ion implantation experiments are affected by geometry limitations (such as the relatively low ion implantation depth). In order to allow extrapolation of the results to more general and relevant cases, the experimental research must be supplemented with relevant modeling in order to extract the general trends of gas-driven microstructure development from the environment-sensitive data and suggest the ways of applying the obtained knowledge in a broader context.

The major objective of this PhD study is to systematically investigate fundamental trends in gas-driven microstructure development in ferritic-martensitic ODS steels in targeted ion implantation experiments examining single-parameter dependencies of accumulated gas content, gas accumulation and damage rates, and temperature, with particular attention to the role of oxide particles. The proposed experimental approach involves saturation of ODS-EUROFER steel samples with various amounts of helium and hydrogen atoms using ion implantation at the JANNuS-Orsay facility in well-controlled conditions. The characterization methods include various transmission electron microscopy examinations (TEM) based techniques, as well as appropriate supplementary techniques such as thermo-desorption spectroscopy (TDS). For better understanding of the basic mechanisms of helium/hydrogen interaction with oxides, the experiments on the industrial material are supplemented with those on self-fabricated model $Y_2O_3/FeCr$ bilayer thin film system and with relevant modeling.

In order to achieve this objective, this PhD study pursues the following aims:

1. Systematic investigation of the effects of helium and hydrogen accumulation on microstructural development and swelling of commercial ODS-EUROFER steel, including

- (i) the investigation of the efficiency of Y_2O_3 nanoparticles as helium trapping sites under irradiation with either single He ion beam or simultaneously with He and heavy ions (with strongly different He/dpa ratios);
- (ii) the estimation of potential risks associated with using oxide nanoparticles in a high He/dpa ratio environment.
- (iii) the investigation of the role of hydrogen in the evolution of different cavity populations in ODS steel in a high H/dpa ratio environment and the resulting hydrogen effects on swelling;
- (iv) the study of hydrogen retention under single-beam H^+ and sequential $He^+ + H^+$ ion implantations at both low and high temperatures with particular attention on the role of Y_2O_3 nanoparticles in hydrogen trapping.

2. Investigation of the effects of helium and hydrogen implantation into a model $Y_2O_3/FeCr$ bi-layer system

- (v) the elucidation of contributions from radiation defect production and helium/hydrogen accumulation on secondary microstructure development near metal/oxide interfaces;
- (vi) the investigation of the temperature effects on helium partitioning between metal, interface and oxide layers;
- (vii) the investigation of possible hydrogen partitioning between metal, interface and oxide;
- (viii) the search for synergetic effects of He and H on microstructural development in systems with the metal/oxide interfaces.

The manuscript consists of five Chapters.

Chapter 1 summarizes materials challenges for Generation IV fission, fusion reactors and accelerator driven systems, covers relevant experimental and simulation results on cavity swelling in ferritic-martensitic and ODS alloys, and discusses possible mechanisms of helium and hydrogen influence on swelling.

Chapter 2 specifies experimental techniques used in the study and is mostly focused on ion implantation method and the various TEM-related techniques, which are the main characterization methods used in this study. The results on initial microstructural characterization of ODS-EUROFER steel and model $Y_2O_3/FeCr$ bilayer system are also provided in this chapter.

Chapter 3 presents the detailed analysis of He effects on the microstructure evolution in ODS-EUROFER steel during single-beam helium ion implantation and dual-beam irradiation with helium and gold ions in different regimes. The role of oxide nanoparticles in He inventory and bubble-to-void transition is discussed.

Chapter 4 covers synergetic effects of helium and hydrogen accumulation on the microstructural evolution in ODS-EUROFER steel by means of a combination of TEM, TDS and electron energy loss spectroscopy investigations.

Chapter 5 covers gas-driven microstructure development in a model bi-layer $Y_2O_3/FeCr$ system. Helium and hydrogen accumulation pattern observed in industrial material are critically analyzed to take into account the results obtained for the model bi-layer $Y_2O_3/FeCr$ system

To systematically investigate the gas-driven evolution of ODS-EUROFER steel, different *ex situ* implantation options using single 10 keV He^+ beam were applied. During the experimental procedure of single-beam He^+ ion implantation into ODS-EUROFER steel samples, the fluence, flux and temperature were varied in the ranges of 1×10^{15} - 1×10^{16} cm^{-2} , 5×10^{11} - 5×10^{12} $cm^{-2}s^{-1}$, and 293-923 K, respectively. After implantation, detailed conventional TEM examinations were performed and were mainly focused on visualization of helium filled cavities (bubbles) via through-focus bright-field (BF) imaging and investigations of bubble parameters (sizes and number densities). To clarify the relative contribution to helium accumulation and swelling from oxide nanoparticles as a part of the complex microstructure of ODS-EUROFER, bubble populations associated with all microstructural defects were investigated. Parameters of helium bubble ensembles associated with grain boundaries, dislocations, $M_{23}C_6$ carbides and Y_2O_3 particles in addition to bubbles located in the grain bulk interior were quantitatively evaluated as a function of He^+ fluence, flux and temperature variation. Detailed analysis of He effects on the microstructural evolution in ODS-EUROFER steel during single-beam He^+ implantation has revealed that bubble growth kinetics on oxide particles is notably different from that for bubble populations in the grain bulk, on extended microstructural defects (dislocations, grain boundaries) and carbide precipitates (see Fig.1).

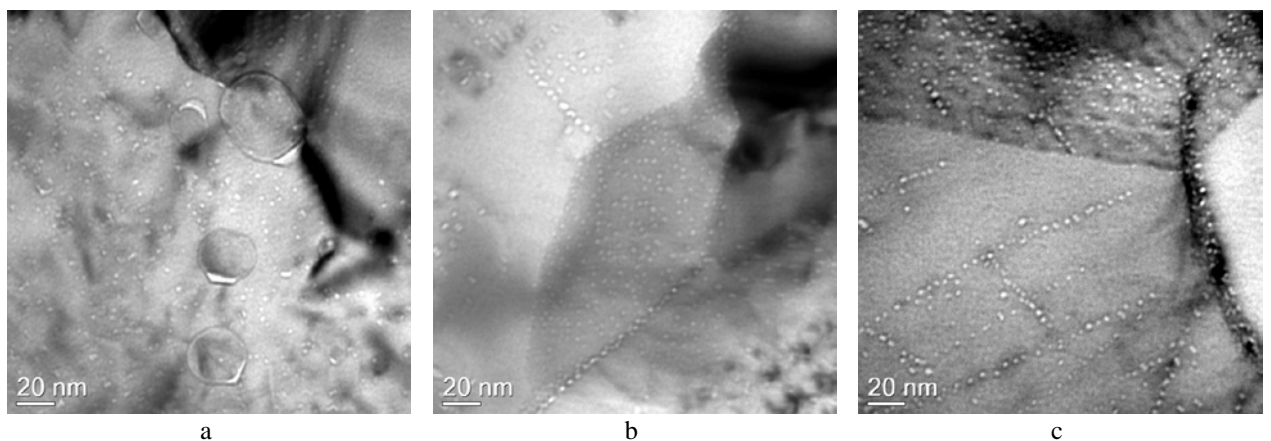
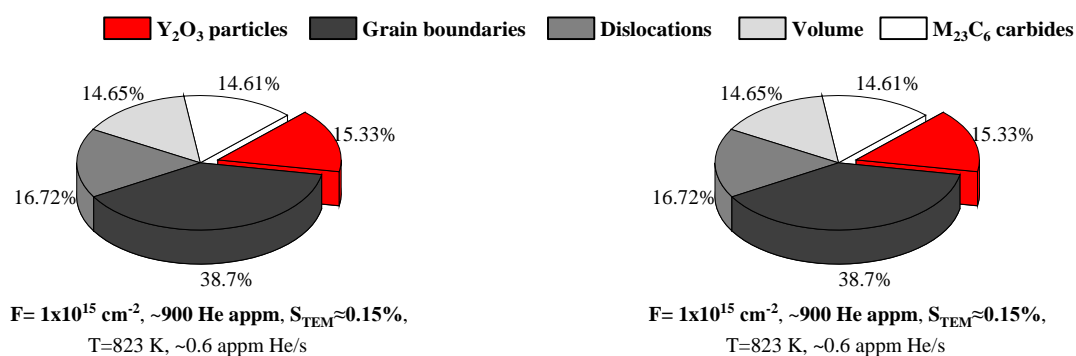


Fig. 1. Typical BF TEM underfocused images of (a) Y_2O_3 nanosized precipitates; (b) $M_{23}C_6$ carbide precipitates and (c) high-angle grain boundaries and dislocations in ODS-EUROFER steel implanted with 10 keV He^+ ions to the fluence of 5×10^{15} cm^{-2} at 823 K with the flux of 5×10^{11} $cm^{-2}s^{-1}$.

The number density of bubbles on Y_2O_3 nanoparticles is predetermined by the number density of oxide particles that predominantly host a single bubble per particle under all implantation conditions applied. Bubbles on oxide particles are found to be larger than bubbles of other populations and their sizes are controlled rather by the sizes of host nanoparticles than by variations in single-beam implantation conditions in the studied ranges. In contrast, sizes and number densities of bubbles in all other populations strongly depend on implantation conditions, but within each fixed single-beam implantation run, bubbles on grain boundaries, dislocations and carbides grow at approximately the same rate as bubbles in the grain bulk. Based on statistical analysis of TEM data, swelling and the fraction of helium accumulated in visible bubbles were calculated utilizing indirect approach for combining contributions of helium bubbles associated with different features of the microstructure, taking into account the geometry and volume density of these microstructural defects in the material volume. In the majority of studied implantation regimes both swelling and He inventory were largely controlled by bubble populations on structural defects (particles, dislocations and grain boundaries), while bubbles in the grain bulk provided relatively minor contribution. In quantitative terms, the relative contributions to helium accumulation and consequently swelling from bubbles on structural defects and in the grain bulk are mostly sensitive to variations of implantation flux. As the implantation flux increases, the relative role of bubbles in the bulk becomes stronger and at the highest flux used this bubble population provided roughly the same contribution to swelling and helium inventory as bubbles on structural defects. With the increase of implantation fluence (helium concentration) and the decrease of temperature the relative contribution of bubbles in the grain bulk also increases, but for fluence and temperature variations within the studied ranges remains well below that from bubbles on structural defects. The contribution to He inventory and swelling from bubbles associated with oxide particles was minor in all investigated single-beam regimes due to moderate number density of Y_2O_3 particles (see Fig. 2) in ODS-EUROFER steel. Both contributions increased by only several percent with the decrease of helium implantation fluence or temperature and with the increase of implantation flux in the studied ranges. Among the bubble populations associated with structural defects, the most important contributions to both swelling and He inventory came from bubbles located on grain boundaries. Only bubbles in the grain bulk could serve as serious competitors in certain cases, mainly at high He fluxes and, to less extent, at high helium fluences. Thus, our results do not support the widespread opinion that helium trapping in bubbles on oxide nanoparticles would always efficiently suppress helium accumulation on grain boundaries, which is expected to be an important factor of suppressing high-temperature intergranular embrittlement. In spite of that, even at the highest level of accumulated He (12000 appm) and temperature (923 K) the extensive formation of bubbles on grain boundaries did not lead to bubble coalescence either in single-beam or in the dual-beam regime with enhanced damage production. Therefore, the high-temperature intergranular embrittlement seems not to be a lifetime restrictive issue for ODS-EUROFER steel in high He/dpa ratio environment.



a

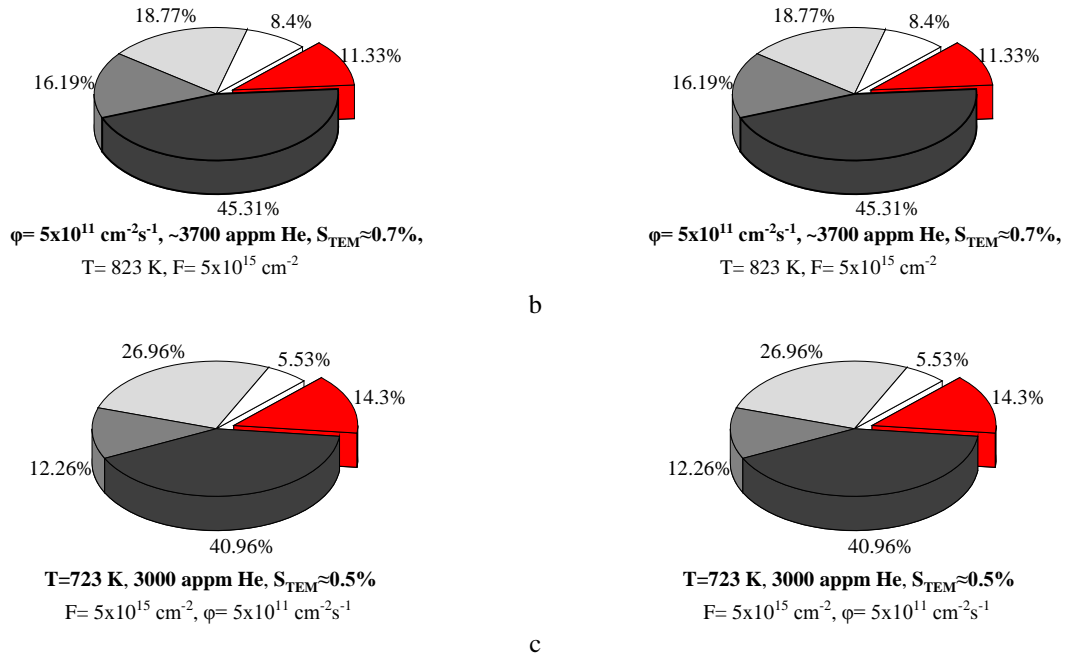


Fig. 2. Contributions of bubbles associated with different microstructural features to the accumulated He fraction in ODS-EUROFER steel implanted with 10 keV He^+ ions: (a) as a function of fluence in the range 1×10^{15} - $1 \times 10^{16} \text{ cm}^{-2}$ with the flux of $5 \times 10^{11} \text{ cm}^{-2}\text{s}^{-1}$ at $T=823 \text{ K}$; (b) as a function of flux in the range of 5×10^{11} - $5 \times 10^{12} \text{ cm}^{-2}\text{s}^{-1}$ to the fluence of $5 \times 10^{15} \text{ cm}^{-2}$ at $T=823 \text{ K}$; (c) as a function of temperature in the range of 723-823 K to the fluence of $5 \times 10^{15} \text{ cm}^{-2}$ with the flux of $5 \times 10^{11} \text{ cm}^{-2}\text{s}^{-1}$. Colors differentiate between bubble populations, as explained in the legend located on top of the figure. The depicted helium shares are normalized to the total helium concentration contained in all bubbles.

The results of statistical analysis of bubble population parameters and the estimates of swelling and helium fraction accumulated in the bubbles obtained for ODS-EUROFER steel under fixed single-beam He^+ implantation conditions were compared with the oxide-free reference material, i.e. EUROFER 97 steel. Under the same single-beam implantation conditions bubbles in EUROFER 97 steel were slightly larger than in ODS-EUROFER, no matter whether they were located in the bulk or on microstructural defects, except carbide precipitates. A similar trend was found for the density of helium bubbles (per defect). Around a factor of 1.5 higher values of swelling and accumulated helium fraction are predicted for EUROFER 97 in comparison with ODS-EUROFER.

Having in mind that ODS steels in reactor service environment will be subject to intense radiation damage by fast neutrons, the effect of enhanced dpa/He appm ratio on swelling and helium inventory in ODS-EUROFER was studied in the thesis by means of simultaneous *in situ* dual-beam irradiation at 823 K with 10 keV He^+ with the fluence of $5 \times 10^{15} \text{ cm}^{-2}$ and secondary 4 MeV heavy (Au^{2+}) ions with the fluence of $4.5 \times 10^{15} \text{ cm}^{-2}$. The parameters of helium bubbles correlated with microstructural features were estimated via TEM analysis by means of the same indirect approach as for single-beam He^+ implantation regime. The results of statistical analysis of bubble population parameters and the estimates of swelling and helium fraction accumulated in the bubbles were compared with similar results for single-beam He^+ implantation. It was found that helium redistribution between various microstructural features was relatively moderately affected by accelerated damage produced by the secondary heavy ion beam and remained qualitatively similar to the case of single-beam helium implantation regime. In terms of helium inventory, the enhanced dpa/He appm ratio increased the retained He contributions for all bubble populations, either in the bulk or on microstructural defects. The strongest effect was observed for bubbles in the bulk; their contribution to the fraction of retained helium increased approximately twice. Correspondingly, the total share of implanted He captured in the bubbles has increased under synergetic action of helium accumulation and damage acceleration up to $\sim 70\%$, whereas in the single-beam He^+ regime it constitutes only $\sim 54\%$, that is only slightly more than a half of all implanted He was captured in the visible bubbles. Overall, the effect of accelerated damage on helium retention is relatively moderate

and, among the microstructural defects, the largest contribution is provided by grain boundary bubbles, just as it was the case in single-beam helium implantation regime. The important qualitative effect caused by strong acceleration of damage production is found to be the formation of large cavities on some oxide particles (see Fig. 3 (a)). The effect is interpreted as a manifestation of the bubble-to-void transition caused by the increase of the efficient vacancy supersaturation in the matrix as a result of irradiation with energetic gold ions. In the literature, one can find only a couple of reports [25,37] mentioning bubble-to-void transition in bubble population associated with nanoparticles in ODS alloys that had accumulated more than a thousand appm He after neutron irradiation to >20 dpa at 773 K.

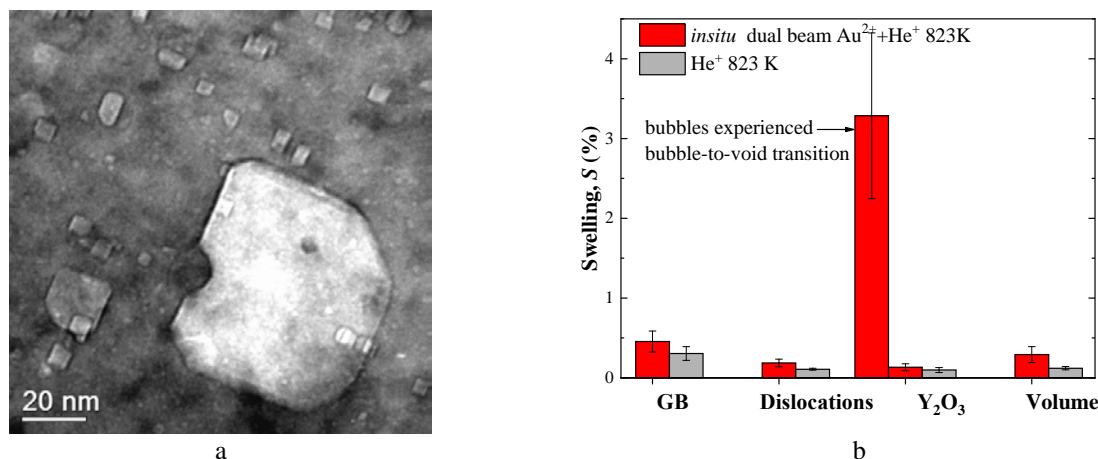


Fig. 3. (a) BF TEM underfocused image of ODS-EUROFER steel after simultaneous *in situ* dual-beam irradiation at 823 K with 10 keV He⁺ ions with the flux of $5 \times 10^{11} \text{ cm}^{-2} \text{ s}^{-1}$ to the fluence $5 \times 10^{15} \text{ cm}^{-2}$ and 4 MeV Au²⁺ ions with the flux of $4 \times 10^{11} \text{ cm}^{-2} \text{ s}^{-1}$ to the fluence of $4.5 \times 10^{15} \text{ cm}^{-2}$; (b) Comparative statistical analysis of swelling associated with different bubble populations in ODS-EUROFER samples irradiated at 823 K either simultaneously with 10 keV He⁺ ions with the flux of $5 \times 10^{11} \text{ cm}^{-2} \text{ s}^{-1}$ to fluence $5 \times 10^{15} \text{ cm}^{-2}$ and 4 MeV Au²⁺ ions with the flux of $4 \times 10^{11} \text{ cm}^{-2} \text{ s}^{-1}$ to the fluence of $4.5 \times 10^{15} \text{ cm}^{-2}$ (red bars) or implanted only with 10 keV He⁺ ions at the same temperature and implantation parameters (grey bars).

The fact that the transition occurs only on the oxide particles seems natural because the largest bubbles in ODS steel were found to always decorate oxide particles. In this thesis, the bubble-to-void transition triggering by oxide nanoparticles was explained in terms of a theoretical model that predicts that the critical number of gas atoms required to promote the bubble-to-void transition for a helium bubble located on a particle is noticeably lower than that for a critical bubble in the bulk. Note that according to both the theoretical model and the experimental observations the transition is triggered by sufficiently large host particles. The creation of large cavities on oxide nanoparticles strongly affects swelling, as illustrated in Fig. 3(b). In spite of a certain increase of swelling contribution from grain boundary bubbles in the dual-beam irradiation regime, there is still no bubble coalescence on grain boundaries that might result in high-temperature helium embrittlement in ODS-EUROFER steel. If, however, all bubbles associated with nanoparticles would undergo such a transition, their contribution to swelling would increase nearly by an order of magnitude, (Fig. 3(b)), largely exceeding the contributions of grain boundary or any other bubble population. The expected cumulative swelling would then be higher than the single-beam implantation value already by a factor of ~ 7 . In reality, the true swelling value for dual-beam irradiation should fall somewhere between the two limiting values. With the increase of irradiation dose the swelling contribution from large cavities will eventually become much larger than could be provided by all the other bubble populations because the growth of large cavities is no longer controlled by the amount of helium they retain. Therefore the bubble-to-void transition observed in the dual-beam regime bears the risk of qualitatively changing steel resistivity to swelling.

To investigate synergetic effect of helium and hydrogen accumulation on the microstructural evolution in ODS-EUROFER, a set of irradiation experiments was carried out in sequential *ex situ* dual-

beam mode with pre-implantation of 10 keV He⁺ ions to fluence $5 \times 10^{15} \text{ cm}^{-2}$ followed by 5 keV H⁺ implantation to the fluence of $1 \times 10^{17} \text{ cm}^{-2}$ in the following temperature regimes:

- (i) high temperature regime, introduction of both He⁺ and H⁺ at 823 K,
- (ii) low temperature regime, introduction of both He⁺ and H⁺ at RT. A part of samples implanted in low temperature regime was subjected to post-implantation annealing during 90 minutes at 823 K under vacuum and
- (iii) combined temperature regime, pre-implantation of He⁺ ions at T=823 K followed by H⁺ implantation at RT.

Detailed conventional TEM investigations of *ex situ* dual-beam implanted samples of ODS-EUROFER in all temperature regimes were focused on evolution of parameters of helium bubbles (size, number density and shape, if relevant) caused by H⁺ implantation. Helium filled cavities formed at the He⁺ implantation stage were treated as markers for any microstructural changes that occurred during H implantation. Taking into account that bubbles attached to yttria nanoparticles are always noticeably larger than bubbles in the bulk or bubbles associated with other structural defects, only this bubble population was analyzed in detail. Cumulative swelling was estimated by means of indirect approach. To investigate the role of hydrogen in the microstructure evolution in ODS-EUROFER samples pre-implanted with He⁺ ions in low and combined temperature regimes, the retained hydrogen content was quantified through TDS measurements and compared to that in the He-free samples (implanted with hydrogen only). In order to clearer understand the possible role of yttria nanoparticles in the hydrogen accumulation in ODS-EUROFER steel, the general trends in hydrogen uptake and trapping in ODS-EUROFER were compared with those in EUROFER 97 steel, which has a similar composition but no oxide particles. In addition, TDS measurements for ODS-EUROFER steel after sequential dual-beam implantation with He⁺ and H⁺ ions conducted at different heating rates were used to determine the activation energies of H de-trapping from various microstructural components. Investigations of possible hydrogen association with helium bubbles were done using the results of EELS measurements in spectrum imaging (SI) acquisition mode performed on ODS-EUROFER samples sequentially dual-beam implanted in combined temperature regime.

A summary of experimentally observed hydrogen effects on ODS-EUROFER steel pre-implanted with He⁺ ions is given in Table 1. TEM and TDS results for the sequentially implanted samples are compared to single-beam He⁺ and single-beam H⁺ implantation results, respectively.

Conventional TEM data indicate relatively minor influence of implanted hydrogen on overall swelling for all sequential implantation regimes used. Hydrogen implantation increases cumulative swelling by less than 25% as compared to that observed after single-beam He⁺ pre-implantation. The visible bubble microstructure in ODS-EUROFER is mainly determined by the achieved helium concentration and the conditions of helium implantation or/and high-temperature processing. For high temperature experimental conditions used, bubble number density is weakly affected by H⁺ implantation. The comparison of bubble evolution in ODS-EUROFER samples subjected to high-temperature He⁺ ion pre-implantation or post-implantation annealing at 823 K has revealed that after sequential dual-beam He⁺+H⁺ implantation the observed bubbles were systematically slightly larger than after single-beam He⁺ implantation. However, a notable share of helium atoms after the He implantation stage was retained in the matrix in the form of substitutional He atoms and/or small He_nV_m clusters. Diffusion of He atoms and/or He_nV_m clusters to He bubbles during high-temperature hydrogen implantation or post-implantation annealing leads to bubble growth and increases the estimated swelling value. It looks like the observed microstructural changes at the elevated temperature (823 K) were determined rather by helium redistribution due to acceleration of defects mobility and additional radiation damage created by H⁺ beam than by hydrogen accumulation. This conclusion is supported by the estimates of helium fraction retained in bubbles after annealing and by TDS measurements of hydrogen release. In dual-beam implanted samples the fraction of helium retained in bubbles has increased after annealing from 33% to 87 %, while the major part of hydrogen releases at temperatures below 750 K.

Table 1. Summary of hydrogen effects on ODS-EUROFER steel samples pre-implanted with helium ions.

	Conventional TEM	TDS	EELS- SI
<p>He⁺ F=5×10¹⁵ - 1×10¹⁶ cm⁻² at RT + H⁺ F= 1×10¹⁷ cm⁻² at RT</p>	<ul style="list-style-type: none"> • Nucleation of bubbles with low size and high number density; • The increase of bubble size after annealing at 823 K by ~6 % for bubbles on Y₂O₃ particles and by ~12 % for bubbles in the bulk and on other structural defects; • No changes in the number density of bubbles • A minor increase of swelling by 25 % after additional annealing at 823 K 	<ul style="list-style-type: none"> • The increase of total H retention by 40% due to hydrogen accumulation in irreversible traps with the de-trapping energies of 0.78-0.81 eV • Weak signal from strong hydrogen traps with de-trapping energy of ~3 eV 	Not investigated
<p>He⁺ F=1×10¹⁶ cm⁻² at 823 K + H⁺ F= 1×10¹⁷ cm⁻² at RT</p>	<ul style="list-style-type: none"> • Suppression of bubble faceting • Nucleation of bubbles with sub-nanometer size and high number density • Swelling modification below detection limit 	<ul style="list-style-type: none"> • The increase of total H retention by 80% due to hydrogen accumulation in irreversible traps with the de-trapping energies of 0.78-0.81 eV 	H signal is associated with He bubbles. The signal is spatially distributed over the entire bubble area with moderate enhancement at the bubble periphery
<p>He⁺ F=5×10¹⁵ cm⁻² at 823 K + H⁺ F= 1×10¹⁷ cm⁻² at 823 K</p>	<ul style="list-style-type: none"> • The bubbles attached to Y₂O₃ particles grow by ~7 %; while bubbles associated to other defects and located in the grain bulk remain unchanged • No changes in the number density of bubbles • The increase of cumulative swelling by 21 % 	Not investigated	Not investigated

While hydrogen implantation plays little role in the microstructural development after implantation at elevated temperatures or during post-implantation annealing, some hydrogen effects on the bubble population were detected when room temperature hydrogen implantation was used. H⁺ ion implantation into ODS-EUROFER steel pre-implanted with helium either at RT or at 823 K has promoted nucleation of bubbles with high number density and the sizes of ~0.5-1 nm. The observed bubble nucleation can be due either to additional stabilization of vacancy clusters by trapped hydrogen atoms or to the radiation-enhanced diffusion of He retained in small He-V clusters as a result of additional damage production by hydrogen beam. In addition, for ODS-EUROFER samples sequentially dual-beam implanted in the combined temperature regime (He⁺ at 823 K and H⁺ at RT) one observes a clear rounding of faceted bubbles developed at the He⁺ pre-implantation stage. The suppression of bubble faceting is hard to explain in terms of radiation damage effects and is more probably due to hydrogen accumulation at the walls of helium bubbles via chemisorption-like mechanism. The trapping of hydrogen at helium bubbles is supported also by TDS and EELS-SI observations. Implantation of He⁺ at RT or 823 K followed by H⁺ implantation at RT increases total hydrogen retention in ODS-EUROFER by, respectively, 40% or 80% as compared to single-beam H⁺ implantation. The increased hydrogen retention results from hydrogen accumulation in irreversible traps with the de-trapping energies of 0.78-0.81 eV, which are commonly associated in the literature with hydrogen binding to bubble surfaces. Helium and hydrogen spatial distribution obtained by EELS-SI technique on samples sequentially implanted with He⁺ at 823 K and H⁺ at RT strongly supports this tentative identification (see Fig. 4). Helium EELS-SI signal has the maximum intensity at the bubble center suggesting that helium uniformly fills bubble volume. In contrast, the extracted hydrogen signal is distributed mostly uniformly over the bubble areas with a definite intensity increase at the bubble periphery, which should be expected rather for bubble surface coverage by hydrogen. The spatial distribution of gas atoms in the bubbles after sequential implantation with He⁺ at 823 K and H⁺ at RT can be interpreted in terms of a “core-shell” structure, where the helium core inside the cavity is surrounded by a shell of hydrogen atoms at cavity walls. The presence of

molecular hydrogen in bubbles nucleated after sequential implantation with both He⁺ and H⁺ at RT is suggested by the results of TDS analysis, but the share of hydrogen retained in molecular form is extremely small.

TDS analysis shows that ODS-EUROFER steel manifests ~3 times stronger hydrogen uptake as compared to ODS-free EUROFER 97 steel under single-beam H⁺ implantation and sequential dual-beam He⁺+H⁺ implantations at RT. However, the analysis of experimental results in conjunction with available literature data indicates that the stronger hydrogen retention in ODS-EUROFER steel as compared to EUROFER 97 cannot be attributed exclusively to the presence of oxide nanoparticles and should be related rather to differences in the volume densities of other trapping sites, such as dislocations, grain boundaries and single vacancies. The direct accumulation of hydrogen inside the oxide particles is not very probable because of the low hydrogen solubility in yttria [38], but it cannot be excluded that hydrogen accumulates either at nanoparticle surfaces or at bubbles associated with nanoparticles. Considering the estimated hydrogen binding energy to oxide particle/matrix interfaces of 0.36 eV, hydrogen trapping at nanoparticle/matrix interfaces can hardly affect swelling, even if the effects on mechanical properties of ODS-EUROFER steel might be expected [28,39]. The influence of hydrogen on bubble population associated with yttria nanoparticles was also found to be minor in all implantation conditions used in this thesis. After sequential implantation with He⁺ and H⁺ at RT, bubbles were formed both in the bulk and on structural defects but no preferential bubble size increase on oxide nanoparticle/matrix interfaces occurred. After high-temperature (823 K) H⁺ implantation or post-implantation annealing of samples sequentially pre-implanted with helium at RT, bubbles associated with Y₂O₃ nanoparticles were larger than in the grain bulk or on other structural defects. However, similar to other bubble populations, bubbles attached to nanoparticles have demonstrated low sensitivity to H⁺ implantation; their average size has increased by less than 7 % in comparison with that observed after single-beam He⁺ implantation. Since hydrogen desorption from bubbles occurs mostly at temperatures below 750 K, this minor bubble growth should be related rather to helium re-distribution than to hydrogen accumulation in bubbles.

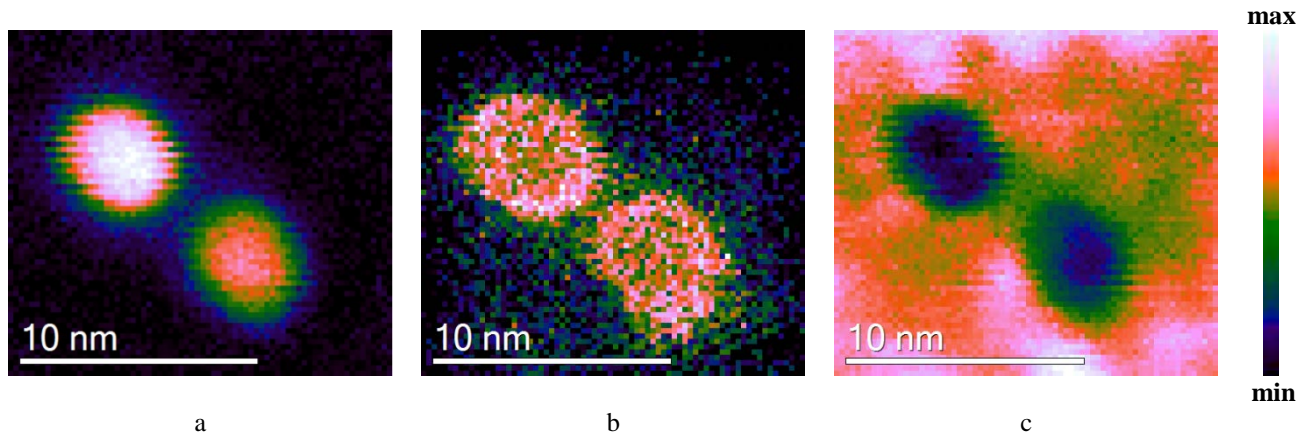


Fig. 4. Intensity maps of two bubbles in ODS-EUROFER steel sequentially dual-beam implanted with 10 keV He⁺ ions to the fluence of 1×10^{16} cm⁻² at 823 K and H⁺ ions to the fluence of 1×10^{17} cm⁻² at RT obtained by NLLS Gaussian fitting from spectral difference EELS-SI: (a) ~25 eV (He-K); (b) ~13.2 eV H-K; (c) thickness map.

Summing up, under experimental conditions used in this thesis hydrogen injection into ODS-EUROFER steel pre-implanted with helium did not reveal any potential hazards of notable swelling increase, in contrast to additional damage production which is able to trigger bubble-to-void transition in bubble population associated with Y₂O₃ nanoparticles. The specific chemisorption-like mechanism of hydrogen trapping at helium bubble walls is suggested to play the main role in hydrogen accumulation under investigated experimental conditions.

In order to better understand the mechanisms involved in the microstructural development at and close to the metal/oxide interface during irradiation and/or gas accumulation, the approach recently

suggested by several research groups [40–44] was applied. This approach includes ion implantation and subsequent TEM investigation of model mesoscopic-scale bi-layer systems, providing enhanced control over the metal/oxide interfacial effects promoted by radiation and/or gas accumulation. For this purpose, thin films consisting of pure Y_2O_3 compound and Fe-10at%Cr binary alloy were sequentially deposited onto different single-crystal ceramic substrates (MgO, SrTiO₃, and yttria-stabilized zirconia (YSZ)) combining the reactive magnetron sputtering (MS) deposition of Y elemental target in oxygen atmosphere with molecular beam epitaxy (MBE) deposition of elemental Fe and Cr metals using thermal effusion. The best Y_2O_3 /FeCr bi-layer films were obtained using SrTiO₃ (100) substrate, where the epitaxy of metal/oxide interface was achieved at least partially. As-fabricated Y_2O_3 /FeCr bi-layer films deposited on SrTiO₃ (100) substrate were characterized in detail and used for subsequent ion implantations.

Ion implantation was performed normally to the bi-layer sample surface in four different implantation/irradiation regimes, including:

- (i) single-beam 17 keV He⁺ implantation to the fluence of 1×10^{17} cm⁻² at RT and at 823 K
- (ii) single-beam 10 keV H⁺ implantation to the fluence of 2×10^{17} cm⁻² at RT
- (iii) implantation with 17 keV He⁺ ions to the fluence of 1×10^{17} cm⁻² at RT followed by 10 keV H⁺ implantation to the fluence of 2×10^{17} cm⁻² at RT
- (iiii) heavy ion irradiation in transmission with 2 MeV Kr⁺ ions to the fluence of 3.6×10^{15} cm⁻² at RT.

The energies for He⁺ and H⁺ ions were selected so as to obtain the peaks of implanted ion concentration close to the interface between Fe-10%Cr and Y_2O_3 thin films. For Kr⁺ ion irradiation, the energy, flux and fluence of irradiating ions were selected so as to obtain dose rate and accumulated dose similar to the single-beam He⁺ implantation and, at the same time, to minimize Kr concentration in the region of interest. After implantation/irradiation, cross-section TEM samples were prepared by FIB lift-out technique and were investigated by TEM in BF TEM and high-resolution TEM (HRTEM) regimes. Table 2 summarizes the microstructural features observed in Y_2O_3 /FeCr bi-layer system after single-beam He⁺ and H⁺ implantations, sequential He⁺+H⁺ implantation, and Kr⁺ irradiation

Table 2. A summary of microstructural features observed after single-beam He⁺ and H⁺ implantation, sequential dual-beam He⁺+H⁺ implantation, and Kr⁺ irradiation.

Implantation/ irradiation regime	Fe-10Cr film	Interface	Y ₂ O ₃ Film
He ⁺ , RT	cavity formation $\langle D_c^{Me} \rangle = 2.0$ nm; $\langle N_c^{Me} \rangle = 28.6 \times 10^{23}$ m ⁻³	cavity formation $\langle D_c^{Int} \rangle = 4.1$ nm; $\langle N_c^{Int} \rangle = 1.0 \times 10^{16}$ m ⁻²	cavity formation $\langle D_c^{Ox} \rangle = 3.3$ nm; $\langle N_c^{Ox} \rangle = 5.4 \times 10^{23}$ m ⁻³
He ⁺ , 823 K	cavity formation $\langle D_c^{Me} \rangle = 7.8$ nm; $\langle N_c^{Me} \rangle = 2.4 \times 10^{23}$ m ⁻³	-	-
H ⁺ , RT	cavity formation $\langle D_c^{Me} \rangle = 1.1$ nm; $\langle N_c^{Me} \rangle = 34.8 \times 10^{23}$ m ⁻³	cavity formation $\langle D_c^{Int} \rangle = 3.1$ nm; $\langle N_c^{Int} \rangle = 1.6 \times 10^{23}$ m ⁻²	cracking along the interface, fracture on {111} planes
He ⁺ + H ⁺ , RT	cavity growth at H ⁺ implantation stage $\langle D_c^{Me} \rangle = 2.3$ nm; $\langle N_c^{Me} \rangle = 27.9 \times 10^{23}$ m ⁻³	(a) cavity growth at H ⁺ implantation stage $\langle D_c^{Int} \rangle = 4.6$ nm; $\langle N_c^{Int} \rangle = 1.0 \times 10^{16}$ m ⁻² (b) interface decohesion	cracking along the interface, fracture on {112} planes
Kr ⁺ , RT	cavity formation $\langle D_c^{Me} \rangle = 1.2$ nm; $\langle N_c^{Me} \rangle = 6.6 \times 10^{23}$ m ⁻³	-	-

The model bi-layer metal/oxide systems were able to reproduce industrial material trends in He-assisted cavity formation in all parts of the system, i.e. metal, interface and oxide, but only after room temperature helium implantation (see Fig. 5).

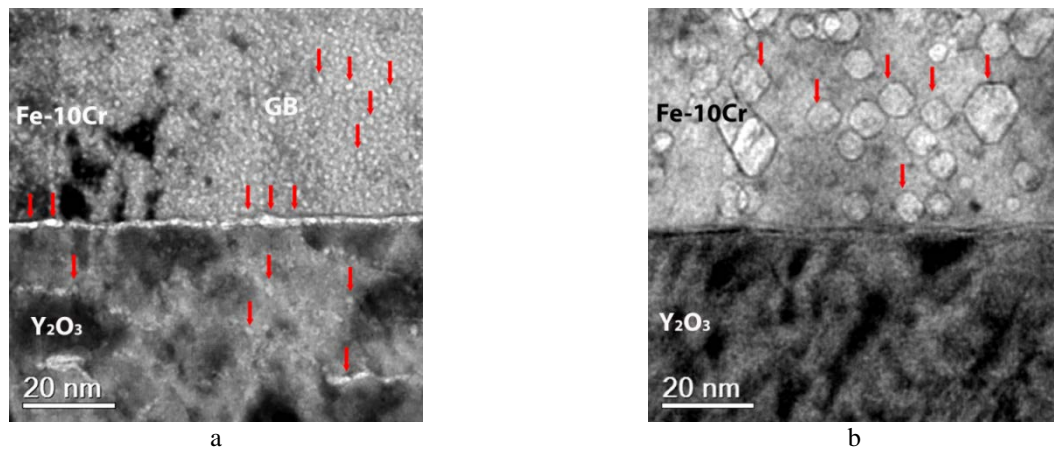


Fig. 5. BF TEM underfocused image of a model bi-layer $Y_2O_3/FeCr$ system single-beam implanted with 17 keV He^+ ions to the fluence of $1 \times 10^{17} \text{ cm}^{-2}$: (a) at RT, (b) at 823 K.

At room temperature, helium was efficiently trapped in small cavities in FeCr layer, and might be efficiently stored inside yttria particles. The tendency of preferential interfacial cavity formation observed at room temperature indicates that helium trapping at metal/oxide interface is insensitive to both metal/oxide orientation relationship and the interfacial chemistry. At the temperature of 823 K, cavity population development in response to helium implantation resembles that in ODS steels only in the metal layer. Helium-assisted cavity formation pattern at the metal/oxide interface is notably different from that typically observed for industrial ODS-steels. No helium bubble nucleation at the planar FeCr/yttria interface was noticed, whereas large cavities decorating yttria nano-oxides were observed in industrial ODS-steels at the same temperature (see Fig. 1(a)). Inside the oxide layer, no cavities were observed at this temperature as well; the implanted helium was either redistributed over the layer or had escaped from it into the substrate or the sample environment. Such redistribution is impossible in ODS-steels, where nano-oxides are completely surrounded by FeCr matrix. Thus, though the experiments on the planar metal/oxide interfaces are useful for understanding underlying mechanisms of He trapping and diffusion, the extrapolation of their results onto industrial ODS steels should be done with caution.

The critical role of helium and, surprisingly, hydrogen in cavity and/or microcrack formation in a model bi-layer FeCr/yttria system subjected to heavy ion, helium and hydrogen single-beam implantations has been demonstrated by TEM analysis. The hydrogen-assisted cavity formation inside the FeCr layer and at the metal/oxide interface caused by single-beam H^+ implantation was demonstrated. The interfacial cavities were larger than cavities in the metal layer. In contrast, microcracks rather than cavities were formed in the Y_2O_3 layer. The orientation of microcracks formed after single-beam hydrogen implantation indicates that hydrogen might be efficiently trapped in anion vacancy loops inside the yttria layer. The promotion of cavity formation by implanted hydrogen supports the possibility of hydrogen trapping at the metal/oxide interface suggested by TDS analysis on industrial ODS-EUROFER steel.

Strong synergetic effect of helium and hydrogen was observed after sequential implantation of a model bi-layer FeCr/yttria sample with helium and hydrogen. Hydrogen implantation into helium pre-implanted system has led to interfacial decohesion and microcrack nucleation in the oxide layer. Decohesion and microcrack formation after hydrogen injection might result from several competing process such as hydrogen-promoted interfacial cavity growth and coalescence, or hydrogen-assisted interfacial bond weakening. An exact mechanism responsible for the detected processes remains unclear and further experimental and modeling research is required to explain the obtained results. At the same time, hydrogen had minor influence on the He-filled cavity population in the metal layer, just like in industrial ODS-steels. The growth of cavities inside the metal layer might be associated with hydrogen accumulation in cavities.

The investigations performed in this PhD study not only provide a new database contributing to fundamental understanding of gas-driven microstructure development in ferritic-martensitic ODS steels, but also raise a number of questions that need further research to be better understood, in particular:

(i) Contribution of nanoparticles to helium inventory was calculated based on the average bubble size related to the average oxide particle size. Sometimes size distribution of nano-oxides in ODS steel is quite broad and may include significant fraction of particles that strongly deviate from the average value. Therefore considering the real particle size distribution might improve the accuracy of helium inventory estimations. Moreover, since the nano-oxide detection via conventional TEM is challenging, the X-ray and EELS spectrum imaging might contribute.

(ii) Bubble-to-void conversion in bubble population associated with oxide nanoparticles after dual-beam He/heavy ion irradiation requires more attention. In this study quantitative dependence between oxide particle size and population of bubbles vs. voids could not be achieved due to poor statistics coming from large void size and relatively low area of TEM field of view. Consequently, only a possible range of swelling variation related to bubble-to-void conversion was estimated. An accurate correlation should be established in order to provide more relevant swelling estimations and guidelines for further design of advanced ODS steels in terms of particle size.

(iii) The dual-beam helium/heavy ion irradiation used in this thesis was oriented on the situation of high He concentration accumulation at a relatively moderate damage level. Additional dual-beam experiments with variable He/dpa ratio are required to gain insight on the limiting He/dpa ratios that are able to promote conversion to voids for bubbles associated with oxide nanoparticles in order to justify the extrapolation of results to expected fusion or spallation reactor environments, where gas accumulation rates are expected to be few orders of magnitude lower than in our experiments.

(iv) Hydrogen accumulation in ODS steels is still far from being deeply understood. Additional TDS and EELS experiments after high temperature single-beam hydrogen implantation and multi-beam ion irradiation with hydrogen are required e.g. to clarify the major mechanisms that determine hydrogen influence on swelling, depending on temperature of hydrogen injection and the presence of radiation damage.

(v) Although preliminary EELS investigation in this study indicates hydrogen association with helium bubbles in the way of “helium core hydrogen shell”, more extensive data treatment is required. Confirmation of hydrogen presence can be achieved via complementary measurements by vibrational EELS spectroscopy and application of relevant modeling of hydrogen interaction with cavities in steel.

(vi) Model bi-layer metal/oxide systems show a good potential as templates for studying oxide interaction with secondary gas impurities and displacement damage. However, interpretation of experimental observations on planar systems in terms of their extrapolation to ODS steels requires application of appropriate simulations in order to better evaluate helium and hydrogen energetic characteristics in ODS relevant oxides and at their interfaces with Fe-based matrix.

References

- [1] *Climate Change and Nuclear Power 2018*. Vienna: International Atomic Energy Agency, 2018.
- [2] P. Yvon, Ed., *Structural Materials for Generation IV Nuclear Reactors*. Woodhead Publishing, 2017.
- [3] G. R. Odette and S. Zinkle, Eds., *Structural Alloys for Nuclear Energy Applications*. Elsevier, 2019.
- [4] I. L. Pioro, Ed., *Handbook of Generation IV Nuclear Reactors*. Woodhead Publishing, 2016.
- [5] R. L. Klueh, “Analysis of swelling behaviour of ferritic/martensitic steels,” *Philos. Mag.*, vol. 98, no. 28, pp. 2618–2636, Oct. 2018.

- [6] S. J. Zinkle and G. S. Was, "Materials challenges in nuclear energy," *Acta Mater.*, vol. 61, no. 3, pp. 735–758, 2013.
- [7] A. Bhattacharya and S. J. Zinkle, "1.12 - Cavity swelling in irradiated materials," in *Comprehensive Nuclear Materials (Second Edition)*, R. J. M. Konings and R. Stoller, Eds. Oxford: Elsevier, 2020, pp. 406–455.
- [8] *Structural Materials for Liquid Metal Cooled Fast Reactor Fuel Assemblies-Operational Behaviour*, no. NF-T-4.3. Vienna: International Atomic Energy Agency, 2012.
- [9] F. A. Garner, M. B. Toloczko, and B. H. Sencer, "Comparison of swelling and irradiation creep behavior of fcc-austenitic and bcc-ferritic/martensitic alloys at high neutron exposure," *J. Nucl. Mater.*, vol. 276, no. 1, pp. 123–142, 2000.
- [10] R. Lindau, A. Moeslang, M. Rieth, M. Klimiankou, E. Materna-Morris, A. Alamo, A.-A. F. Tavassoli, C. Cayron, A.-M. Lancha, P. Fernandez, N. Baluc, R. Schaubelin, E. Diegele, G. Filacchioni, J.W. Rensman, B.v.d. Schaaf, E. Lucon, W. Dietz, "Present development status of EUROFER and ODS-EUROFER for application in blanket concepts," *Fusion Eng. Des.*, vol. 75–79, pp. 989–996, 2005.
- [11] S. Ukai, S. Ohtsuka, T. Kaito, Y. de Carlan, J. Ribis, and J. Malaplate, "10 - Oxide dispersion-strengthened/ferrite-martensite steels as core materials for Generation IV nuclear reactors," in *Structural Materials for Generation IV Nuclear Reactors*, P. Yvon, Ed. Woodhead Publishing, 2017, pp. 357–414.
- [12] S. J. Zinkle, J. L. Boutard, D. T. Hoelzer, A. Kimura, R. Lindau, G. R. Odette, M. Rieth, L. Tan and H. Tanigawa, "Development of next generation tempered and ODS reduced activation ferritic/martensitic steels for fusion energy applications," *Nucl. Fusion*, vol. 57, no. 9, p. 92005, 2017.
- [13] G. R. Odette and D. T. Hoelzer, "Irradiation-tolerant nanostructured ferritic alloys: Transforming helium from a liability to an asset," *JOM*, vol. 62, no. 9, pp. 84–92, Sep. 2010.
- [14] G. R. Odette, M. J. Alinger, and B. D. Wirth, "Recent developments in irradiation-resistant steels," *Annu. Rev. Mater. Res.*, vol. 38, no. 1, pp. 471–503, Jul. 2008.
- [15] G. R. Odette, N. J. Cunningham, T. Stan, M. E. Alam, and Y. De Carlan, "Chapter 12 - Nano-oxide dispersion-strengthened steels," in *Structural Alloys for Nuclear Energy Applications*, G. R. Odette and S. Zinkle, Eds. Boston: Elsevier, 2019, pp. 529–583.
- [16] P. D. Edmondson, C. M. Parish, Y. Zhang, A. Hallén, and M. K. Miller, "Helium bubble distributions in a nanostructured ferritic alloy," *J. Nucl. Mater.*, vol. 434, no. 1, pp. 210–216, 2013.
- [17] A. I. Ryazanov, O. K. Chugunov, S. M. Ivanov, S. T. Latushkin, R. Lindau, A. Möslang, A. A. Nikitina, K. E. Prikhodko, E. V. Semenov, V. N. Unezhev, P. V. Vladimirov, "Tensile properties and microstructure of helium implanted EUROFER ODS," *J. Nucl. Mater.*, vol. 442, no. 1, Supplement 1, pp. S153–S157, 2013.
- [18] T. Chen, H. Kim, J. G. Gigax, D. Chen, C.-C. Wei, F.A. Garner, L. Shao, "Radiation response of oxide-dispersion-strengthened alloy MA956 after self-ion irradiation," *Nucl. Instruments Methods Phys. Res. Sect. B Beam Interact. with Mater. Atoms*, vol. 409, pp. 259–263, 2017.
- [19] Q. Li, C. M. Parish, K. A. Powers, and M. K. Miller, "Helium solubility and bubble formation in a nanostructured ferritic alloy," *J. Nucl. Mater.*, vol. 445, no. 1, pp. 165–174, 2014.
- [20] C. M. Parish and M. K. Miller, "Aberration-corrected X-ray spectrum imaging and fresnel contrast to differentiate nanoclusters and cavities in helium-irradiated alloy 14YWT," *Microsc. Microanal.*, vol. 20, no. 2, pp. 613–626, 2014.

- [21] C. M. Parish, K. A. Unocic, L. Tan, S. J. Zinkle, S. Kondo, L. L. Snead, D. T. Hoelzer, Y. Katoh, "Helium sequestration at nanoparticle-matrix interfaces in helium + heavy ion irradiated nanostructured ferritic alloys," *J. Nucl. Mater.*, vol. 483, pp. 21–34, 2017.
- [22] T. Yamamoto, G. R. Odette, P. Miao, D. J. Edwards, and R. J. Kurtz, "Helium effects on microstructural evolution in tempered martensitic steels: In situ helium implanter studies in HFIR," *J. Nucl. Mater.*, vol. 386–388, pp. 338–341, 2009.
- [23] G. R. Odette, P. Miao, D. J. Edwards, T. Yamamoto, R. J. Kurtz, and H. Tanigawa, "Helium transport, fate and management in nanostructured ferritic alloys: In situ helium implanter studies," *J. Nucl. Mater.*, vol. 417, no. 1, pp. 1001–1004, 2011.
- [24] T. Yamamoto, Y. Wu, G. Robert Odette, K. Yabuuchi, S. Kondo, and A. Kimura, "A dual ion irradiation study of helium-dpa interactions on cavity evolution in tempered martensitic steels and nanostructured ferritic alloys," *J. Nucl. Mater.*, vol. 449, no. 1–3, pp. 190–199, 2014.
- [25] B. Yao, D. J. Edwards, R. J. Kurtz, G. R. Odette, and T. Yamamoto, "Microstructure characterization of neutron irradiated and helium injected PM2000, 14YW, and modified F82H alloys," *Fusion Mater. Semiannual Prog. Rep. June 2012*, vol. DOE-ER-031, p. 26, 2012.
- [26] H. J. Jung, D. J. Edwards, R. J. Kurtz, T. Yamamoto, Y. Wu, and G. R. Odette, "Structural and chemical evolution in neutron irradiated and helium-injected ferritic ODS PM2000 alloy," *J. Nucl. Mater.*, vol. 484, pp. 68–80, 2017.
- [27] E. Malitckii, Y. Yagodzinskyy, M. Ganchenkova, S. Binyukova, H. Hänninen, R. Lindau, P. Vladimirov, A. Moeslang, "Comparative study of hydrogen uptake and diffusion in ODS steels," *Fusion Eng. Des.*, vol. 88, no. 9, pp. 2607–2610, 2013.
- [28] Y. Yagodzinskyy, E. Malitckii, M. Ganchenkova, S. Binyukova, O. Emelyanova, T. Saukkonen, H. Hänninen, R. Lindau, P. Vladimirov, A. Moeslang, "Hydrogen effects on tensile properties of EUROFER 97 and ODS-EUROFER steels," *J. Nucl. Mater.*, vol. 444, no. 1, pp. 435–440, 2014.
- [29] K. Farrell and E.H. Lee, "Ion damage in a Fe-10Cr-6Mo-0.5Nb ferritic Steel," *Radiation-Induced Changes in Microstructure: 13th International Symposium (Part I)*, vol. STP 955, pp. 498–507, Jan. 1987.
- [30] E. Wakai, T. Sawai, K. Furuya, A. Naito, T. Aruga, K. Kikuchi, S. Yamashita, S. Ohnuki, S. Yamamoto, H. Naramoto, S. Jistukawa, "Effect of triple ion beams in ferritic/martensitic steel on swelling behavior," *J. Nucl. Mater.*, vol. 307–311, pp. 278–282, 2002.
- [31] E. Wakai, K. Kikuchi, S. Yamamoto, T. Aruga, M. Ando, H. Tanigawa, T. Taguchi, T. Sawai, K. Oka, S. Ohnuki, "Swelling behavior of F82H steel irradiated by triple/dual ion beams," *J. Nucl. Mater.*, vol. 318, pp. 267–273, 2003.
- [32] T. Tanaka, K. Oka, S. Ohnuki, S. Yamashita, T. Suda, S. Watanabe, E. Wakai, "Synergistic effect of helium and hydrogen for defect evolution under multi-ion irradiation of Fe–Cr ferritic alloys," *J. Nucl. Mater.*, vol. 329–333, pp. 294–298, 2004.
- [33] J. Marian, T. Hoang, M. Fluss, and L. L. Hsiung, "A review of helium–hydrogen synergistic effects in radiation damage observed in fusion energy steels and an interaction model to guide future understanding," *J. Nucl. Mater.*, vol. 462, pp. 409–421, 2015.
- [34] Y. E. Kupriyanova, V. V. Bryk, O. V. Borodin, A. S. Kalchenko, V. N. Voyevodin G. D. Tolstolutsкая, F. A. Garner, "Use of double and triple-ion irradiation to study the influence of high levels of helium and hydrogen on void swelling of 8–12% Cr ferritic-martensitic steels," *J. Nucl. Mater.*, vol. 468, pp. 264–273, 2016.

- [35] D. Brimbal, L. Beck, M. Payet, and F. Jomard, “The synergistic effect of hydrogen and helium implantations in forming H₂ molecules in a Fe-12 wt.%Cr-ODS steel characterized by Raman spectroscopy and SIMS,” *Nucl. Instruments Methods Phys. Res. Sect. B Beam Interact. with Mater. Atoms*, vol. 461, pp. 191–196, 2019.
- [36] N. Zimmer, P. Vladimirov, M. Klimenkov, U. Jaentsch, R. Vila, V. Chakin, F. Mota, “Microstructural evolution of three potential fusion candidate steels under ion-irradiation,” *J. Nucl. Mater.*, vol. 535, p. 152160, 2020.
- [37] H. J. Jung, D. J. Edwards, R. J. Kurtz, G. R. Odette, Y. Wu, and T. Yamamoto, “Microstructural summary of ODS ferritic alloys (14YW, 14YWT, 12YWT, MA957FR, PM2000) and RAFM steels (F82H Mod.3-CW, Eurofer97) from JP27 in-Situ He injection (ISHI) experiment at 500°C,” *Fusion Mater. Semiannual Prog. Rep. June 2015*, vol. DOE-ER-031, p. 55, 2015.
- [38] D. Sun, J. Ding, Y. Yang, P. Zhang, and J. Zhao, “First-principles investigation of hydrogen behavior in different oxides in ODS steels,” *Int. J. Hydrogen Energy*, vol. 44, no. 31, pp. 17105–17113, 2019.
- [39] E. Malitckii, Y. Yagodzinsky, M. Ganchenkova, T. Saukkonen, H. Hänninen, R. Lindau, P. Vladimirov, A. Moeslang, “Hydrogen uptake and its effect on mechanical properties of Eurofer 97-2 and ODS-Eurofer steels,” in *SMiRT 22 - San Francisco, USA. August 18-23, 2013*, 2013.
- [40] T. C. Kaspar, M. E. Bowden, C. M. Wang, V. Shutthanandan, N. R. Overman, R. M. van Ginhoven, B. D. Wirth, R. J. Kurtz, “Epitaxial Fe/Y₂O₃ interfaces as a model system for oxide-dispersion-strengthened ferritic alloys,” *J. Nucl. Mater.*, vol. 457, pp. 352–361, 2015.
- [41] T. Stan, Y. Wu, P. B. Wells, H. D. Zhou, and G. R. Odette, “Epitaxial Fe thin films on {100} Y₂Ti₂O₇: Model interfaces for nano-oxide dispersion strengthened steels,” *Metall. Mater. Trans. A*, vol. 48, no. 11, pp. 5658–5666, 2017.
- [42] A. Mairov, D. Frazer, P. Hosemann, and K. Sridharan, “Helium irradiation of Y₂O₃-Fe bilayer system,” *Scripta Materialia*, vol. 162, pp. 156–160, 2019.
- [43] T. Stan, “The role of oxides in nanostructured ferritic alloys and bilayers: Interfaces, helium partitioning and bubble formation,” 2017.
- [44] N. Li, S. K. Yadav, Y. Xu, J. A. Aguiar, J. K. Baldwin, Y. Q. Wang, H. M. Luo, A. Misra and B. P. Uberuaga, “Cr incorporated phase transformation in Y₂O₃ under ion irradiation,” *Scientific Reports*, vol. 7, no. 1, p. 40148, 2017

Annex VI. Scientific Communications

Publications

1. O. Emelyanova, A. Gentils, V.A. Borodin, M.G. Ganchenkova, P.V. Vladimirov, P. S. Dzhumaev, I. Golovchanskiy, R. Lindau, A. Möslang. Bubble-to-void transition promoted by oxide nanoparticles in ODS-EUROFER steel ion implanted to high helium content. *Journal of Nuclear Materials*, Vol. 545, 2021, 152724, <https://doi.org/10.1016/j.jnucmat.2020.1527242>.
2. O. Emelyanova, A. Gentils, V.A. Borodin, M.G. Ganchenkova, P.V. Vladimirov, P. S. Dzhumaev. Microstructural response of ODS-EUROFER steel to helium ion implantation up to high doses, in preparation
3. O. Emelyanova, A. Gentils, M. G. Ganchenkova, V. A. Borodin, K. March, Y.N. Yagodzinskiy, P. S. Dzhumaev, P. V. Vladimirov. Synergetic effects of helium and hydrogen accumulation on the microstructural evolution of ODS-EUROFER steel, in preparation
4. O. Emelyanova, A. Gentils, M.G. Ganchenkova, A. Gumarov, I.Yanilkin, I.Vakhitov, I. Golovchanskiy, V. Stolyarov, I. Shchetinin; L. Tagirov, V.A. Borodin. Modeling of helium bubble development in $Y_2O_3/FeCr$ bi-layers by high-dose ion implantation, in preparation
5. O. Emelyanova, A. Gentils, M.G. Ganchenkova, A. Gumarov, I.Yanilkin, I.Vakhitov, I. Golovchanskiy, L. Tagirov, V.A. Borodin. The effects of high-dose helium and hydrogen ion implantation on the microstructural development in a bi-layer $Y_2O_3/FeCr$ system, in preparation

Conference Presentations

1. O. Emelyanova, A. Gentils, M.G. Ganchenkova, V.A. Borodin, P.V. Vladimirov, P. Dzhumaev, I. Golovchanskiy, A. Moeslang. Microstructural response of ODS-EUROFER steel to helium ion implantation up to high doses. European Materials Research Society 2019 (E-MRS 2019 Spring Meeting), Nice (France), May 27-31, 2019.
Contribution: Oral presentation
2. O.V. Emelyanova, A. Gentils, M.G. Ganchenkova, V.A. Borodin, Yu.N. Yagodzinskiy, P.V. Vladimirov, P.S. Dzhumaev, I. Golovchanskiy. Modeling of gas driven microstructural evolution of ODS-EUROFER steel by high dose ion implantation. European Congress and Exhibition on Advanced Materials and Processes 2019 (EUROMAT 2019), Stockholm (Sweden), September 1-5, 2019.
Contribution: Oral presentation
3. Olga Emelyanova, Aurelie Gentils, Maria G. Ganchenkova, Vladimir A. Borodin, Katia March, Yuriy N. Yagodzinskiy, Pavel S. Dzhumaev, Pavel V. Vladimirov. The effects of high-dose He and H ion implantation on the microstructural development in EUROFER-ODS steel. The 19th International Conference on Fusion Reactor Materials (ICFRM-19), La Jolla (California, USA), October 27-November 1, 2019.
Contribution: Oral presentation
4. Olga Emelianova; Aurelie Gentils; Maria Ganchenkova; Amir Gumarov; Igor Yanilkin; Iskander Vakhitov; Igor Golovchanskiy; Igor Shchetinin; Lenar Tagirov; Vladimir A. Borodin. Microstructural response of $FeCr/Y_2O_3$ bilayer system to He/H implantation. The Minerals, Metals and Materials Society Annual Meeting & Exhibition 2020 (TMS 2020), San Diego, California, USA, February 23-27, 2020.
Contribution: Poster presentation

Titre : Modélisation de l'évolution de la microstructure induite par des gaz dans l'acier ODS-EUROFER par implantation ionique à haute dose d'hélium et d'hydrogène

Mots clés : modélisation et simulation, implantation ionique, aciers renforcés par dispersion d'oxydes (aciers ODS), hydrogène/hélium, gonflement, microscopie électronique en transmission (TEM)

Résumé : Les aciers ferritiques-martensitiques renforcés par dispersion d'oxydes (ODS) sont des matériaux de structure de haute performance pour les futures installations nucléaires de fission et de fusion. Un problème important pour la performance de ces aciers sous irradiation est leur résistance aux effets néfastes des gaz de transmutation, l'hélium et l'hydrogène, avec une attention particulière aux effets liés à la forte densité de nanoparticules d'oxyde.

L'objectif de la thèse est une étude systématique et fondamentale de l'évolution de la microstructure induite par les gaz légers dans les aciers ODS ferritiques-martensitiques en fonction de la teneur en gaz accumulée, du taux d'endommagement et de la température, en accordant une attention particulière au rôle des nanoparticules d'oxyde. L'approche expérimentale utilisée a consisté à saturer des échantillons avec différentes quantités d'hélium et d'hydrogène, par implantation ionique à JANNuS-Orsay, dans des conditions bien contrôlées. Le matériau de référence utilisé était l'acier ODS-EUROFER. Les modifications microstructurales accompagnant l'accumulation de gaz ont été révélées par microscopie électronique à transmission. Pour une meilleure compréhension des mécanismes d'interaction de l'hélium avec les nanoparticules d'oxyde, les expériences ont été complétées par des implantations ioniques dans un système modèle de couches minces $Y_2O_3/FeCr$, et par une modélisation analytique et numérique pertinente. Cependant, leurs contributions au

gonflement sont généralement relativement mineures par rapport aux autres populations de bulles. Au contraire, les grosses bulles comportent le risque d'une transition accélérée d'une bulle à une cavité dans des conditions défavorables, ce qui provoque un gonflement non contrôlé des cavités. La viabilité d'un tel effet a été démontrée dans des expériences d'implantation d'ions He et d'irradiation d'ions Au simultanées, et quantifiée à l'aide d'une modélisation analytique. Lors de l'implantation séquentielle d'hélium et d'hydrogène dans l'acier ODS-EUROFER, une augmentation notable de l'absorption d'hydrogène a été observée par rapport à l'acier ne contenant pas d'oxyde. Cependant, la résistance globale à l'irradiation de l'acier n'a été que faiblement influencée par l'hydrogène, aussi bien dans l'acier ODS-EUROFER que dans le système modèle $Y_2O_3/FeCr$. Les effets visibles de l'hydrogène sur la microstructure des bulles étaient mineurs et ne se manifestaient qu'après l'implantation d'H à température ambiante.

En résumé, l'acier ODS s'avère résistant au gonflement jusqu'à des niveaux très élevés d'hélium et d'hydrogène accumulés. La présence de nano-oxydes à haute densité est généralement bénéfique pour la tolérance à l'irradiation de l'acier, mais leur influence n'est pas aussi forte que celle attendue. Le piégeage de l'hydrogène dans les bulles d'hélium ne présente aucun risque potentiel pour la tolérance à l'irradiation de l'acier ODS dans les conditions expérimentales étudiées.

Title : Modeling gas-driven microstructural evolution in ODS-EUROFER steel by high dose helium and hydrogen ion implantation

Keywords : modeling and simulation, ion implantation, oxide dispersion strengthened steels (ODS steels), hydrogen/helium, swelling, transmission electron microscopy (TEM)

Abstract : Oxide dispersion strengthened (ODS) ferritic-martensitic steels are advanced high-performance structural materials for next generation nuclear and fusion facilities. An important issue for operation performance of these steels is their resistance to detrimental effects of transmutation gases, helium and hydrogen, with a particular attention to the effects from dense population of nano-size oxide particles.

The objective of the thesis is a systematic investigation of fundamental trends in gas-driven microstructure development in ferritic-martensitic ODS steels in reply to variations in the accumulated gas content, gas accumulation and damage rates, and temperature, with particular attention to the role of oxide particles. The applied experimental approach involved saturation of steel samples with various amounts of helium and hydrogen atoms using ion implantation at the JANNuS-Orsay facility in well-controlled conditions. The reference material used was ODS-EUROFER steel. The microstructural changes accompanying gas accumulation were revealed using transmission electron microscopy (TEM). For the better understanding of the mechanisms of helium interaction with oxide particles, the experiments were backed up with ion implantation into a model $Y_2O_3/FeCr$ bilayer system and with relevant analytical and numerical modeling. Microstructural investigations of ODS-EUROFER samples implanted to high He fluences reveal a persistent partitioning of introduced gas between different microstructural features. In addition to gas bubbles in the grain bulk, extensive bubble precipitation on extended defects (grain boundaries and dislocations) and precipitates (carbides and oxides) was observed. The relative abundance of bubbles associated with different microstructural features is found to be sensitive to implantation conditions and changes in uncorrelated manner with the variation of implantation parameters. Overall, the main contributions to steel volume expansion (swelling) and the He inventory were from bubbles

on grain boundaries and, at lower implantation temperatures and higher fluxes, from bubbles in the grain matrix. However, the preferential He accumulation at grain boundaries does not lead to bubble coalescence and growth of huge grain boundary cavities, without causing high-temperature helium embrittlement. Oxide nanoparticles were found to be efficient centers for helium bubble nucleation, each hosting a single bubble typically noticeably larger than bubbles in other populations. However, their contributions to both swelling and He inventory were estimated to be generally relatively minor as compared to other bubble populations, implying that oxide particles provide no substantial improvement of steel radiation performance. On the contrary, the large bubbles bear the risk of accelerated bubble-to-void transition in unfavorable conditions, launching uncontrolled void swelling. The viability of such effect was demonstrated in experiments on simultaneous steel implantation with He and Au ions and quantified using analytical modeling. Under sequential helium and hydrogen implantation into ODS-EUROFER steel, notable increase of hydrogen uptake was observed as compared to oxide-free steel. However, the parameters of He bubble microstructure and, hence, the overall steel radiation resistance were found to be only weakly influenced by hydrogen, in both ODS-EUROFER steel and in $Y_2O_3/FeCr$ bilayer system. Visible hydrogen effects on bubble microstructure were minor and manifested only after the room temperature H implantation.

Summing up, ODS steel is shown to be resistant to void swelling up to very high levels of accumulated helium and hydrogen. The presence of high density of nano-oxides is generally beneficial for steel radiation tolerance, but their influence is not as strong as commonly expected. Hydrogen trapping in helium bubbles doesn't manifest any potential risks for ODS steel radiation tolerance under experimental conditions studied.